

Observational Studies of Galactic Cataclysmic Variables

by

Keith Inight

Thesis

Submitted to the University of Warwick for the degree of

Doctor of Philosophy in Physics

Department of Physics

June 2023

THE UNIVERSITY OF
WARWICK

Contents

Acknowledgments	v
Declarations	vi
Abstract	viii
Abbreviations	ix
Chapter 1 Introduction	1
1.1 Motivation	1
1.2 White dwarfs	3
1.3 Cataclysmic variable stars and accretion	5
1.3.1 Roche-lobe overflow	5
1.3.2 Accretion discs	7
1.3.3 Magnetic accretion	9
1.3.4 Winds	10
1.4 Cataclysmic variable evolution	11
1.4.1 Evolution and angular momentum	11
1.4.2 Formation and the common envelope phase	13
1.4.3 Magnetic braking	15
1.4.4 The period gap	15
1.4.5 Gravitational wave radiation	16
1.4.6 Additional ways to lose angular momentum	17
1.4.7 The period minimum and beyond	18
1.4.8 Novae	18
Chapter 2 Methods	20
2.1 Distances from <i>Gaia</i>	20
2.2 CV Sub-types	22
2.2.1 Non-magnetic CVs	23

2.2.2	Magnetic CVs	32
2.3	CV Classification	38
2.3.1	Spectral analysis	38
2.3.2	Light curves	39
2.3.3	Hertzsprung–Russell and Colour-Colour Diagrams	40
2.3.4	Imaging	44
2.4	Identification of tertiary systems	45
2.5	Summary	45
Chapter 3	An extraordinary windy novalike	47
3.1	Introduction	47
3.2	Observations	48
3.2.1	Spectroscopy	48
3.2.2	Photometry	50
3.2.3	<i>Swift</i>	51
3.3	Analysis	55
3.3.1	Orbital period	55
3.3.2	The mass transfer rate	57
3.3.3	Orbital inclination	62
3.3.4	From <i>Gaia</i> DR2 to EDR3: improved precision and overall changes due to variability	64
3.3.5	Photometric variability	64
3.3.6	X-ray emission	66
3.3.7	Spectral variability and detection of a wind outflow	68
3.4	Discussion	68
3.4.1	Winds	68
3.4.2	Disc structure	72
3.4.3	Mass transfer rate	73
3.4.4	Quasi-periodic outbursts	74
3.4.5	Novalikes and dwarf novae – secular changes in mass transfer rate	75
3.5	Conclusions	76
Chapter 4	Reference samples of close binaries	77
4.1	Introduction	77
4.2	Close white dwarf binaries	78
4.3	Reference samples	80
4.3.1	PCEBs: White dwarfs with M-type companions	83
4.3.2	PCEBs - White Dwarf + A/F/G/K stars	90
4.3.3	Cataclysmic variables	94
4.3.4	Double white dwarfs	101

4.4	Evolution of white dwarf binaries within the HR diagram.	103
4.4.1	PCEBs	105
4.4.2	CVs	108
4.4.3	DWDs	111
4.5	Conclusions	111
Chapter 5 Cataclysmic variables from SDSS III and IV		113
5.1	Introduction	113
5.2	Methods	115
5.2.1	Identification	115
5.3	Results	120
5.3.1	Unusual systems	121
5.3.2	Non-CVs	140
5.4	Discussion	143
5.4.1	Distribution of periods	143
5.4.2	Distribution of CV sub-types	147
5.4.3	Variability of CVs	148
5.4.4	Space Density	150
5.4.5	Low accretion rate systems	158
5.4.6	Unusual state changes	159
5.4.7	Tertiary systems	164
5.5	Summary	165
Chapter 6 Cataclysmic variables from the SDSS-V plate survey		166
6.1	Introduction	166
6.2	Target selection	167
6.3	Observations	169
6.3.1	SDSS Spectroscopy	169
6.3.2	Photometric survey data	170
6.3.3	Follow-up observations	170
6.4	Analysis	172
6.4.1	Classification	172
6.4.2	Orbital Periods	173
6.5	Results	180
6.5.1	New CVs	185
6.5.2	Spectral confirmation of previously known systems	188
6.5.3	Well known systems	199
6.5.4	Misclassified systems	205
6.5.5	Unusable observations	209
6.6	Discussion	210

6.6.1	Period Bouncers	210
6.6.2	Orbital period distribution	214
6.6.3	CV sub-types	214
6.7	Summary	216
Chapter 7 Conclusion		218
Bibliography		221
Appendix A Supplementary Material - Chapter 4		247
A.1	List of WD+M	248
A.2	List of WD+AFGK	254
A.3	List of CVs	255
A.4	List of CVs with data quality issues	263
A.5	List of Double White Dwarfs	266
Appendix B Supplementary Material - Chapter 5		270
B.1	Introduction	270
B.2	List of CVs	271
B.3	Details	286
B.3.1	New systems	286
B.3.2	Previously known systems	298
B.4	Spectra and light curves	344
B.5	SDSS plate, MJD and fibre list	408
Appendix C Supplementary Material - Chapter 6		427
C.1	Spectra and light curves of previously known CVs	427

Acknowledgments

Firstly I would like to offer profuse thanks to Boris Gänsicke for all his support, guidance and help. He has been a patient and tolerant supervisor, teacher and mentor and above all shown flexibility when dealing with the novel experience of a (very) mature student.

This research draws heavily upon archive data which has been placed in the public domain. This data represents the fruits of the labour of hundreds, and probably thousands, of dedicated astronomers. Without their work this thesis would not have been possible; thank you for all that you have done.

I have been fortunate through the difficult times brought on by the covid pandemic to obtain observing time on the Liverpool Telescope. Some of the results appear in this work but more widely I would like to acknowledge the positive and practical support that their team has always shown me.

Last but not least my grateful thanks to my long-suffering wife, Gwenda, who has supported me throughout this time.

Declarations

This thesis is submitted to the University of Warwick for the degree of Doctor of Philosophy and has not been submitted for a degree at another university.

This work contains material from the following peer-reviewed publications written by me:-

- Inight et al. (2021) MNRAS, 504(2),2420 *Towards a volumetric census of close white dwarf binaries - I. Reference samples*. Material from this paper has been used in Chapters 2 and 3.
- Inight et al. (2022) MNRAS, 510(3),3605 *ASAS J071404+7004.3 - a close, bright nova-like cataclysmic variable with gusty winds*. Material from this paper has been used in Chapters 1 and 4.
- Inight et al. (2023a) (MNRAS - Accepted for publication) *A catalogue of cataclysmic variables from 20 years of the Sloan Digital Sky Survey with new classifications, periods, trends and oddities*. Material from this paper has been used in Chapters 1,2 and 5.
- Inight et al. (2023b) (Submitted to MNRAS) *Cataclysmic Variables from Sloan Digital Sky Survey V - the search for period bouncers continues*. Material from this paper has been used in Chapter 6.

The work presented in this thesis was performed by the author with the following exceptions:-

- In Chapter 3 Viktor Ivanov and Dominic Blondel used machine learning to identify ASAS J0714+7004. Tonny Vanmunster and the AAVSO contributed to the light

curve in Figure 3.2. David Boyd contributed a spectrum. Danny Steeghs arranged for the *Swift* observation and Peter Wheatley assisted with the reduction of the x-ray data. Paul Kuin (Mullard Space Science Laboratory, University College London) processed the *Swift* UVOT data. John Thorstensen provided additional spectroscopy.

- In Chapter 4 Elmé Breedt and Anna Pala provided an initial list of candidate CVs for further analysis. Tom Marsh provided an initial list of double white dwarfs. Roberto Raddi provided grids of data for the donor cooling curves.
- In Chapter 5 Boris Gänsicke provided an initial list of candidate CVs, accumulated over 10 years by many people including Tom Marsh, Chris Manser, Tim Mulvany and Henry Israel, for further analysis. John Thorstensen provided some unpublished spectra and periods.
- In Chapter 6 an extended group shared the task of creating an initial shortlist which I then refined and analysed. Knox Long provided guidance in the use of PYTHON. John Thorstensen provided some unpublished spectra of NS Per. Sean Morrison provided advice regarding flux calibration problems.

Abstract

Cataclysmic variables (CVs) are binary stars consisting of a white dwarf accreting from a main sequence donor. They are important laboratories for studying accretion and binary evolution in multiple contexts. In this thesis I describe my work to build volume-limited samples and spectroscopically-identified samples of CVs thereby reducing the observational bias and enabling robust estimates of population density that can be reconciled with theoretical evolutionary models.

As a foundation I have produced a set of reliable volume-limited samples to aid future targeting of spectroscopic surveys. These have already been used to inform the targeting of SDSS-V.

The first 20 years of CVs observed by SDSS have also been analysed; with data from the last 10 years published for the first time. The sub-type of each CV, and hence its place in the evolutionary timeline, has been established. Light curves and radial velocities of CVs have also been used where available to find the orbital period. This analysis has enabled me to estimate the space density of each of the major subtypes of CV.

The most recent SDSS survey, SDSS-V, has for the first time systematically targeted white dwarfs and CVs. Significantly the targeted nature of the survey has enabled me to put an upper limit on the space density of *accreting* period bouncers. This is an important result providing input to the long running debate regarding the ultimate fate of CVs.

In the course of my analysis I also made some other discoveries. Firstly the analysis of ASAS J071404+7004.3 spectroscopy yielded a new insight into disc winds from nova-likes and, by using computer simulation, I was able to show that the Balmer emission lines could originate entirely in the wind far from the CV thereby offering a potential explanation for the single-peaked emission lines in SW Sex nova-likes. Secondly whilst analysing the ZTF light curves of SDSS-identified CVs a small number stood out because of their unusual state changes. I found seven examples of such systems that exhibit significant state changes on timescales that indicate the cause is a change in mass transfer rate, rather than storage in the disc. This phenomenon is most unexpected and further investigation is needed.

Whilst a significant step forward there is still far more that can be achieved as new tools including *JWST*, Vera Rubin telescope, UVEX, 4MOST and WEAVE become available and I outline how this work can be taken forward.

Abbreviations

2MASS	Two Micron All-Sky Survey
4MOST	4-metre Multi-Object Spectroscopic Telescope
AAVSO	American association of variable star observers
AML	Angular momentum loss
AOV	Analysis of variance
APO	Apache Point Observatory
ASAS-SN	All-Sky Automated Survey for Supernovae
BOSS	Baryon Oscillation Spectroscopic Survey
CAML	Consequential angular momentum loss
CE	Common envelope
CV	Cataclysmic Variable
DD	Double-degenerate
DR2	<i>Gaia</i> Data Release 2
DSS	Digitized Sky Survey
DWD	Duble White Dwarf
EDR3	<i>Gaia</i> Early Data Release 3
ESA	European Space Agency
ESO	European Southern Observatory
eBOSS	Extended Baryon Oscillation Spectroscopic Survey
eCAML	Empirical consequential angular momentum loss
ELM	Extremely Low Mass (white dwarf)
EUV	Extreme Ultra Violet
FITS	Flexible Image Transport System
FoV	Field of view
FUV	Far ultraviolet

FWHM	Full width half maximum
GWR	Gravitational wave radiation
HR	Hertzsprung–Russell
HRD	Hertzsprung–Russell Diagram
<i>HST</i>	Hubble Space Telescope
INT	Isaac Newton Telescope
JWST	James Webb Space Telescope
LIGO	Laser Interferometer Gravitational–Wave Observatory
MB	Magnetic braking
MCMC	Markov–chain Monte Carlo
MCV	Magnetic CV
MS	Main Sequence
NASA	National Aeronautics and Space Administration
NIR	Near–infrared
NUV	Near–ultraviolet
Pan–STARRS	Panoramic Survey Telescope and Rapid Response System
PCEB	Post common envelope binary
PREP	Pre-Polar
R&K	Ritter & Kolb
RGB	Red giant branch
RMS	Root mean square
SD	Single–degenerate
SDSS	Sloan Digital Sky Survey
SED	Spectral energy distribution
SNR	Signal–to–noise ratio
SNe Ia	Supernovae Ia
STIS	Space Telescope Imaging Spectrograph
STScI	Space Telescope Science Institute
UVEX	Ultraviolet Explorer item[UVB] Ultraviolet–blue
VIS	Visible
VLT	Very Large Telescope
VSNET	Variable Star Network
VST	VLT Survey Telescope
WD	White Dwarf
WEAVE	William Herschel Telescope Enhanced Area Velocity Explorer
YSO	Young Stellar Object
ZTF	Zwicky Transient Facility

Chapter 1

Introduction

1.1 Motivation

Cataclysmic variables (CVs) are binary stars consisting of a white dwarf accreting from a mass-transferring secondary. They are important laboratories for studying accretion and binary evolution, both topics highly relevant in a panoply of contexts from star forming galaxies to the supermassive black holes in the centres of galaxies.

CV outbursts were noted from around 1500 BCE ([Clark & Stephenson, 1976, 1977](#)) but the first documented discovery occurred in 1670 when an outburst of CK Vul was described by Père Dom Anthelme; the exact nature of CK Vul is still unknown ([Eyres et al., 2018](#)). Other CVs were identified in subsequent centuries by virtue of their outbursts and 31 were known by 1900 ([Downes & Szkody, 1989](#)). Photographic surveys identified more CVs; by 1948 the first General Catalog of Variable Stars recorded 231 ([Kukarkin & Parenago, 1949](#)) and by 1992 this had grown to 751 ([Downes & Shara, 1993](#)). The first spectroscopic observation of a CV was of T CrB in 1866 ([Huggins, 1866](#)) and photographic plates were progressively used to record observations. The advent of photo-multipliers in the 1940's and charge coupled devices in the 1970's greatly increased the precision of observations whilst satellite missions from 1968 onwards revealed wavebands unobservable from the ground.

These observational advances inspired and underpinned theoretical work. As we shall see in Section [1.3.2](#) a typical insight was the realisation that dwarf novae arise from a thermal instability in a viscous disc ([Osaki, 1974](#)) with the viscosity caused by magnetic turbulence ([Balbus & Hawley, 1998](#)). Closely related is the evolutionary model of a CV driven by the progressive loss of angular momentum from its formation in a post-common-envelope binary to reach a period minimum. This model has been used ([Kolb, 1993](#)) to predict the space density of CVs as a function of time and orbital period. This combination of theory and observational evidence was encapsulated by

Warner (2003) which remains the standard reference work to this day.

A fundamental observational problem has been the huge bias in favour of CVs with frequent outbursts. CVs with no, or infrequent, outbursts were greatly under-represented until the advent of multi-fibre spectrographs which revealed large numbers of such short-period CVs (Gänsicke et al., 2009). Technological advances such as the Sloan Digital Sky Survey (SDSS) have exposed shortcomings in our theories such as the predicted rate of angular momentum loss being unable to account for the observed space density and a large missing population of CVs that have evolved past the period minimum. High cadence (a few days) photometric surveys such as the Zwicky Transient Facility (ZTF) have also revealed phenomena including surprising secular changes in mass transfer rate.

Progress depends upon building volume-limited samples as well as spectroscopically-identified samples of CVs thereby reducing the observational bias and enabling robust estimates of the space density that can be reconciled with theoretical evolutionary models. This work pursues this objective by using the latest observational tools and analytical techniques to obtain modern and reliable samples.

Chapter 1 summarises the generally accepted theories for CV evolution and Chapter 2 discusses the methods that have been used.

Chapter 3 analyses a classic example of a CV that, despite being close and bright, has until now remained undiscovered. This chapter is a comprehensive multi-wavelength study exemplifying the data that can be obtained with current tools.

Chapter 4 was motivated by the need to derive target lists for the next generation of multi-fibre spectroscopic surveys. Identification of targets required a high quality set of observational characteristics of the different types of CV and a volumetric analysis within 300 pc was undertaken.

Chapter 5 is a major analytical work encompassing ten years of spectroscopic observations by SDSS resulting in accurate classifications of both new and known CVs. Although this is a magnitude-limited survey it has been possible to derive appropriate space densities whilst the detailed study of these objects has revealed new phenomena requiring further investigation.

Chapter 6 describes a recent survey carried out by SDSS targeting, for the first time, white dwarfs in general and CVs in particular. The dedicated nature of this survey has yielded new insights into the density of post-period-minimum CVs.

Chapter 7 looks forward to the exciting opportunities offered by new tools both in space, for example using the James Webb Space Telescope (*JWST*), and on the ground, with surveys such as the Vera Rubin Telescope.

1.2 White dwarfs

Every CV contains at least one white dwarf by definition. However white dwarfs have far wider significance; being the progenitors of Type Ia supernovae (Hillebrandt & Niemeyer, 2000) and thereby a key source of galactic iron-peak elements as well as cosmological probes for dark energy (Riess et al., 1998; Perlmutter, 2003). White dwarfs are the ultimate destination of ~ 95 per cent of main sequence stars (Althaus et al., 2010) with only the highest mass stars ($M \gtrsim 11 M_{\odot}$) resulting in neutron stars or black holes.

Stars destined to become white dwarfs have initial masses $M \lesssim 11 M_{\odot}$ depending upon metallicity (Ibeling & Heger, 2013). They traverse the main sequence with thermal pressure from the fusion of hydrogen to helium in the core maintaining hydrostatic equilibrium with gravity (Kippenhahn et al., 2013). What happens when the core hydrogen has all been fused depends upon the mass of the star.

Stars with an initial mass $M \lesssim 0.7 M_{\odot}$ will not reach the temperature needed to fuse helium ($\approx 10^8$ K) and the core nuclear reaction stops, hydrostatic equilibrium is lost and the core contracts under the influence of gravity. Eventually the core contracts to the point where it is degenerate with gravitational forces being opposed by electron degeneracy pressure. When shell burning of hydrogen is complete the star will consist predominantly of helium and form a helium white dwarf. Such low mass stars cannot transition the main sequence within the life of the universe and so the observed helium white dwarfs have followed a different channel (discussed later in the context of binary evolution).

Stars with an initial mass $0.7 M_{\odot} \lesssim M \lesssim 2.3 M_{\odot}$ collapse when core hydrogen burning ceases and become degenerate. When the temperature rises above $\approx 10^8$ K helium burning commences fusing helium to create carbon and oxygen as a result of the ‘triple- α ’ process. However unlike an ideal gas the degenerate gas does not expand in response to increased temperature and the situation becomes unstable and results in a helium flash. The flash raises the core temperature further thereby removing the degeneracy and allowing the core to expand. When all of the helium in the core has been burnt into carbon and oxygen the core contracts again and, following the ejection of the outer layers, forms a carbon-oxygen white dwarf.

Stars with an initial mass $2.3 M_{\odot} \lesssim M \lesssim 8 M_{\odot}$ follow a similar path except that core helium burning commences before the end of hydrogen burning and hence the core does not become degenerate and stable burning occurs without a helium flash; the end result is also a carbon-oxygen white dwarf.

Stars with an initial mass $8 M_{\odot} \lesssim M \lesssim 11 M_{\odot}$ attain higher core temperatures resulting in carbon being burnt to magnesium and/or neon and forming an oxygen-neon or oxygen-neon-magnesium white dwarf (Iben et al., 1997).

White dwarfs, by virtue of their degeneracy, are very compact with $M \sim M_{\odot}$ but

$R \sim 0.01R_{\odot}$. Their surface gravity is consequently very high with $\log g \simeq 8$ compared with $\log g \simeq 4$ for the Sun. This extreme gravity causes gravitational settling with helium and particularly hydrogen rising to the surface. These surface layers are opaque and so the optical spectrum of many white dwarfs is dominated by hydrogen absorption lines even though the hydrogen proportion of the total mass is only $X_{\text{H}} \simeq 10^{-4}$.

With no source of energy white dwarfs will gradually cool down and their effective temperature and luminosity can be used as cosmic clocks (Fontaine et al., 2001). An important caveat is that the onset of crystallisation results in the release of latent heat thereby delaying the cooling process.

This analysis of single white dwarfs is only part of the story; many (~ 25 per cent) white dwarfs are actually members of binaries (Toonen et al., 2017). On the one hand this can result in a population of higher mass white dwarfs formed through mergers. Conversely it provides one solution to the enigma referred to earlier where helium white dwarfs could not evolve within Hubble time; the high mass progenitor of the helium white dwarf loses its hydrogen envelope by unstable mass transfer to a companion during common envelope evolution (Section 1.4.2 and Iben & Livio 1993).

The average mass of isolated white dwarfs is $M \simeq 0.6 M_{\odot}$ with the mass of most white dwarfs in the range $0.4 - 0.7 M_{\odot}$ (Kepler et al., 2007). However the average mass of white dwarfs in pre-CVs is higher with $M \simeq 0.67 M_{\odot}$ (Zorotovic et al., 2011) and in CVs is even higher with $M \simeq 0.83 M_{\odot}$ (Zorotovic et al., 2011; McAllister et al., 2019; Pala et al., 2020). The reason for this higher average mass is still being debated. An early assumption was that it is the result of accretion; which would imply that older CVs would have higher mass; however this was disproved by McAllister et al. (2019) who essentially showed that the mass did not depend upon age. Schreiber et al. (2016) have proposed an alternative model whereby CVs with low mass white dwarfs ($M \lesssim 0.4 M_{\odot}$) become unstable to mass transfer and merge with their donor and thereby increasing the average mass. Observational evidence from McAllister et al. (2019) supports this (see Fig. 1.1).

Finally, as we shall see, the magnetic field of the white dwarf in a CV can control the mode of accretion and the incidence of outbursts. These magnetic fields can be very large ranging up to 1000MG. Until recently it was believed that these were fossil fields inherited from the stellar progenitor of the white dwarf (Wickramasinghe & Ferrario, 2005). However as Ferrario et al. (2020) points out the stellar birth rate of highly magnetic main sequence (Ap/Bp) stars is insufficient to fully account for the incidence of magnetic white dwarfs. Three additional formation mechanisms have been proposed; convective dynamos driven by binary mergers (Wickramasinghe et al., 2014), convective dynamos driven by crystallisation in the white dwarf as it cools down (Schreiber et al., 2021) and convective dynamos arising in the giant phase (Lehtinen et al., 2020). It is likely that all four mechanisms contribute to the overall population of magnetic white

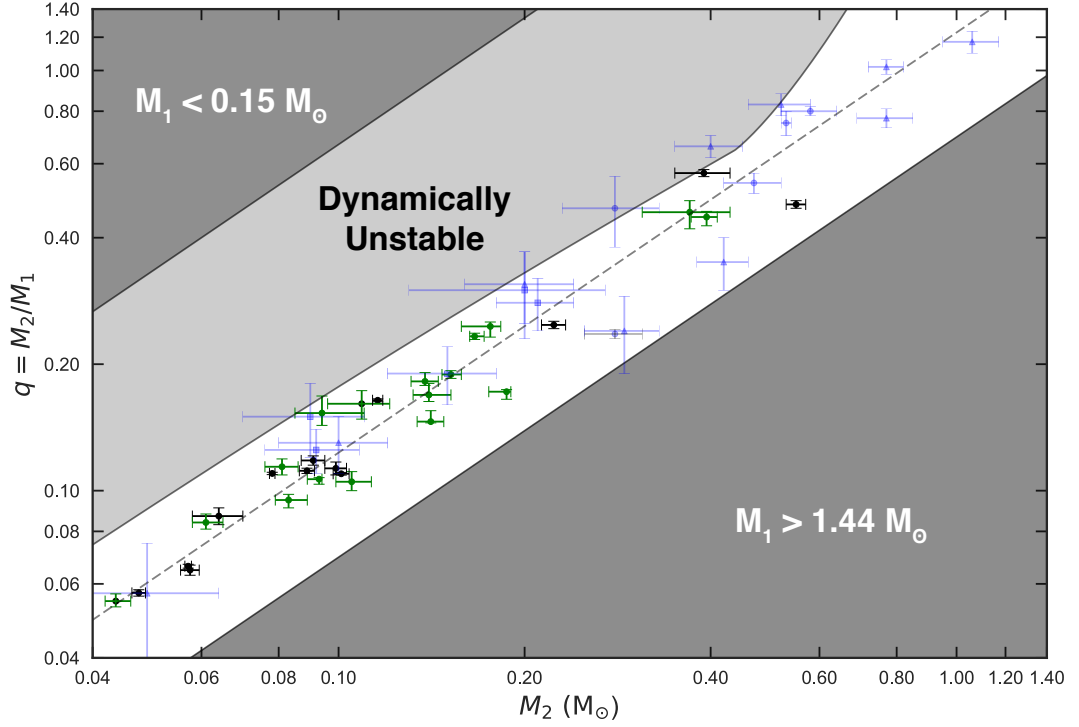


Figure 1.1: Figure 5 from [McAllister et al. \(2019\)](#). M_1 is the mass of the white dwarf in a CV and M_2 is the mass of the donor. The dark grey regions cover unrealistically low white dwarf masses ($\lesssim 0.15 M_\odot$) and masses greater than the Chandrasekhar mass limit ($1.44 M_\odot$), while the light grey region is forbidden by the empirical consequential angular momentum loss (eCAML) model of [Schreiber et al. \(2016\)](#). The green and black points represent masses obtained from eclipse modelling of ULTRACAM/ULTRASPEC data whilst the faint blue points represent measured CV masses from other methods.

dwarfs.

1.3 Cataclysmic variable stars and accretion

CVs are binary stars that interact resulting in matter being accreted onto the white dwarf. There are three mechanisms that govern how the accretion takes place distinguished by the strength of the magnetic field of the white dwarf. Roche-lobe overflow is a pre-requisite for disc and magnetic accretion and we discuss this before exploring the accretion mechanisms in detail.

1.3.1 Roche-lobe overflow

Consider a close binary system consisting of a white dwarf with mass M_1 and radius R_1 and a donor with mass M_2 and radius R_2 . The centres of the white dwarf and donor are separated by a distance a and their orbital angular frequency is Ω . Hereafter we shall also refer to the mass ratio $q = M_2/M_1$. Assume further that tidal forces have

caused the orbit to circularise. The gravitational potential at any point in space can be modelled as the sum of the gravitational potentials of the white dwarf and donor plus that of the notional centrifugal force (equation 2.2 in [Warner 2003](#)):

$$\phi = -\frac{GM_2}{\sqrt{x^2 + y^2 + z^2}} - \frac{GM_2}{\sqrt{(x-a)^2 + y^2 + z^2}} - \frac{1}{2}\Omega^2 ((x - \mu a)^2 + y^2) \quad (1.1)$$

where

$$\mu = \frac{M_2}{M_1 + M_2} \quad (1.2)$$

Plotting equipotential lines reveals teardrop shapes around each object and a point where the gravitational attraction balances out - the inner (or L_1) Lagrange point (see Fig. 1.2). The equipotential surface that contains L_1 (shown in red in Fig. 1.2) is referred to as the Roche lobe. There is no simple analytical expression to work with Roche Lobe geometry and so the volume radius of the Roche lobe (R_L) is defined as the radius of a sphere of equal volume. Approximate formulae for the volume radius are

$$\frac{R_L}{a} = 0.46224 \left(\frac{q}{1+q} \right)^{1/3} \quad (1.3)$$

([Paczynski, 1971](#)) accurate within 2 per cent for $q < 0.8$ and

$$\frac{R_L}{a} = \frac{0.49q^{2/3}}{0.6q^{2/3} + \ln(1 + q^{1/3})} \quad (1.4)$$

([Eggleton, 1983](#)) accurate within 1 per cent for all q .

The compact white dwarf is too small to fill its Roche lobe but the donor will do so if the separation is sufficiently small. Defining the average density of the donor as $\rho = 3M_2/4\pi R_2^3$ and substituting Kepler's law $4\pi^2 a^3 = GMP^2$ equation 1.3 becomes

$$P = \sqrt{\frac{3\pi}{0.46224^3 G \rho}} \quad (1.5)$$

showing that the orbital period of a Roche lobe filling star is solely dependent upon its average density.

‘Roche-lobe overflow’ therefore results in mass transfer from the donor forming a stream through the inner Lagrange point. The cross-section of this stream is perhaps one thousandth of the surface area of the donor ([Hellier, 2001](#)). The stream initially crosses the L_1 point at the local sound speed of the gas but the orbital rotation imparts a much greater tangential velocity and the stream follows a ballistic track (Fig. 1.3).

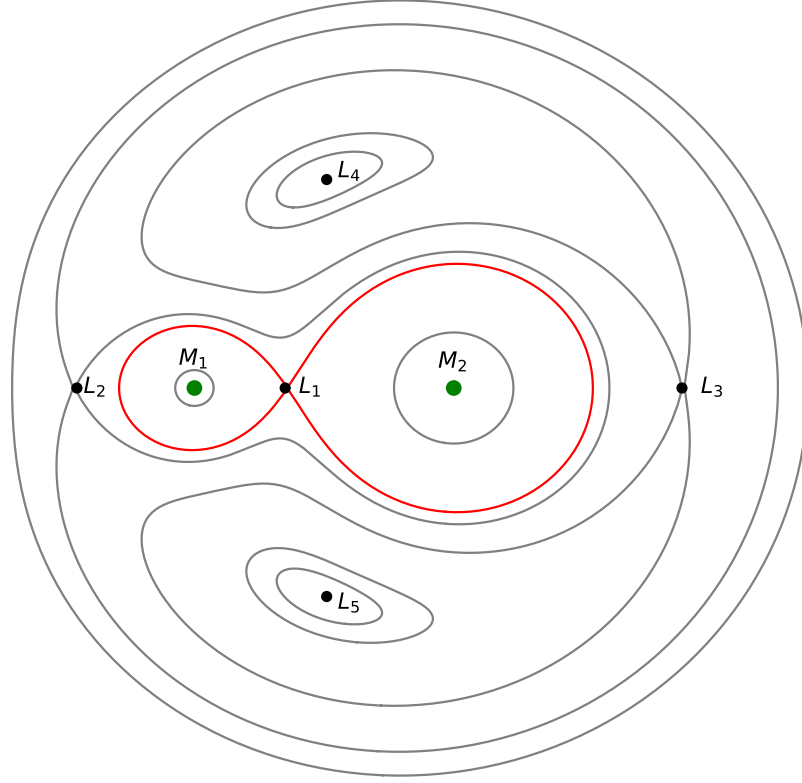


Figure 1.2: Diagram of the orbital plane of a CV where $M_1 = 0.75 M_\odot$, $M_2 = 0.18 M_\odot$, $a = 0.835 R_\odot$ and $P_{\text{orb}} = 2.2 \text{ h}$ showing equipotential lines calculated using equation 1.1. The Roche lobes are shown in red and the Lagrange points, where $\nabla\phi = 0$, labelled L_1 to L_5 . $L_1 - 3$ are unstable and $L_4 - 5$ are stable.

1.3.2 Accretion discs

In the absence of a strong magnetic field ($B \lesssim 1 \text{ MG}$) an individual blob of material in the accretion stream would, by conservation of angular momentum, end up orbiting the white dwarf with a Keplerian velocity at the circularisation radius (R_c) of $v_K = \sqrt{GM_1/R_c}$. Multiple blobs, with slightly different radii and hence different (Keplerian) velocities result in friction as they pass. As a consequence the outer (slower) blob will speed up and the inner (faster) blob will slow down thereby transferring angular momentum. Pringle (1981) showed that the cumulative effect of this process is for material to diffuse both inwards and outwards to form a disc (see Fig. 1.4).

Once established a disc can be considered as a collection of thin concentric annuli rotating with Keplerian velocities. Shakura & Sunyaev (1973) assumed that the frictional viscosity between annuli (ν) arises from turbulence whose eddies would have a size limited by the height of the disc (H) and travelling at the sound speed in the disc (c_s). They then encapsulated the effect of these viscous forces in a parameter (α)

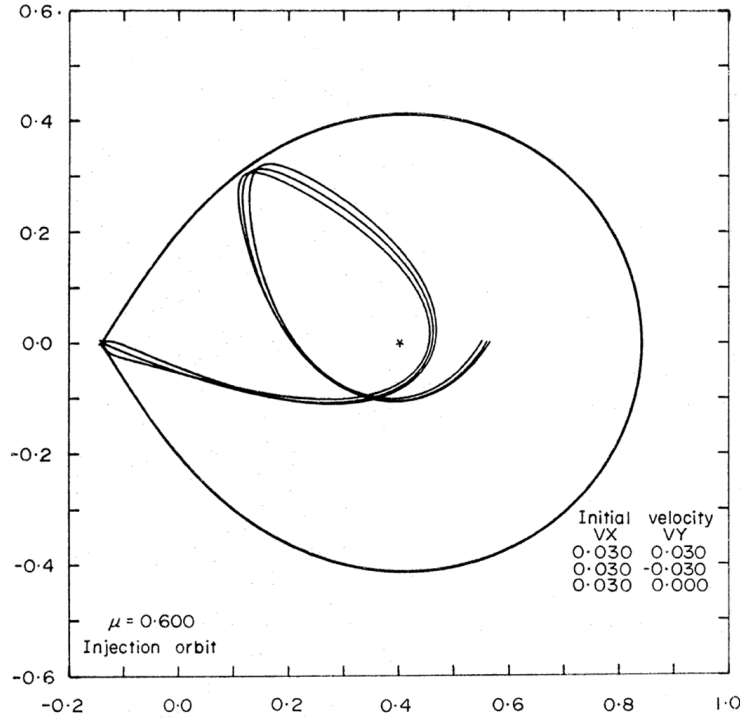


Figure 1.3: Stream trajectory after passing the inner Lagrange point (Flannery, 1975). μ is the mass ratio: the ratio of the white dwarf mass to the total mass of the system.

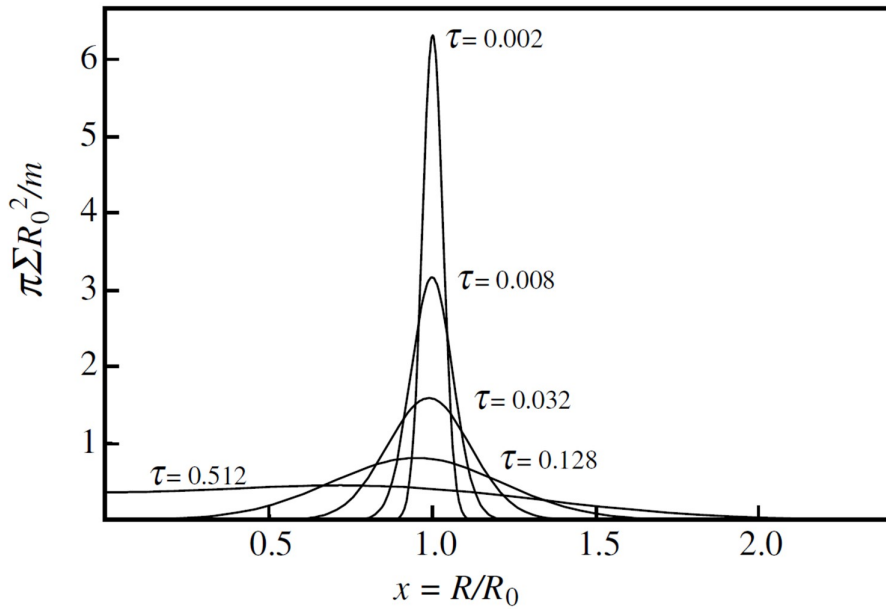


Figure 1.4: The viscous evolution of a ring of matter of mass m at a radius R_0 showing how a disc forms. The surface density is shown as a function of dimensionless radius $x = R/R_0$ and of dimensionless time $\tau = 12\nu t/R_0^2$ where ν is the viscosity (Pringle, 1981).

where $\nu = \alpha c_s H$ giving rise to the term ‘alpha disc’. The turbulence underlying the viscosity is believed to be a result of magnetic instability (Hawley & Balbus, 1998). This instability can be understood by considering two ionised blobs within the disc joined by a magnetic field line; the inner (faster rotating) one will stretch the field line which will act to bring the blobs together - reducing the velocity of the inner blob and increasing the velocity of the outer one. The inner blob will move inwards to a new Keplerian orbit and the outer blob outwards thereby stretching the field line even more until it reaches a limit and reconnection occurs. This fundamentally unstable process amplifies the field strength and the effective turbulence - the Balbus-Hawley instability.

The presence of an accretion disc gives rise to observable phenomena, two of which are the bright spot and the boundary layer. When the accretion stream meets the disc shock heating occurs and the resulting bright spot can become the most optically luminous part of the CV (Section 2.4.3 in Warner 2003). On the other hand when material leaves the inner disc with a Keplerian orbital velocity and drops to the surface of the white dwarf, which is spinning far more slowly, large amounts of kinetic energy (up to half the total disc luminosity) are released as electromagnetic radiation (Drew & Kley, 1993).

Accretion discs are also the source of dwarf novae. Dwarf novae outbursts are, as the name suggests, dimmer than novae, with a typical magnitude of $\Delta m = 3 - 5$. They are also shorter, lasting for only a few days to weeks, and recur much more frequently (from several weeks to a few decades). Both the temperature and the luminosity of the disc depend upon the rate of gravitational energy released which in turn depends upon \dot{M}_2 . If \dot{M}_2 is greater than a critical value the disc remains fully ionised with a high viscosity and stable accretion, without outbursts (Shafter et al., 1986), is maintained (see Section 7 in Knigge et al. 2011); these CVs are termed novalikes. Conversely, in principle (but observationally impossible to prove), if \dot{M}_2 is below a different threshold then the disc will not ionise and stable accretion will occur with no outbursts. \dot{M}_2 between these two critical values yields unstable accretion due a thermal limit cycle (Osaki, 1974).

1.3.3 Magnetic accretion

The magnetosphere of a star is defined as the volume within which the magnetic pressure of the star’s magnetic field dominates the ram pressure of any infalling gas. When the magnetosphere is spherical equilibrium occurs at the Alfvén radius. The magnetosphere of a white dwarf with a large magnetic field ($B \gtrsim 10$ MG) in a CV extends beyond the typical radius of an accretion disc. Within the magnetosphere ionised particles, and in particular the accretion stream, will be forced to follow field lines to the magnetic poles (Cropper, 1990; Kube et al., 2000). The stream is therefore forced to co-rotate with the white dwarf resulting in the white dwarf spinning at the orbital period. Without

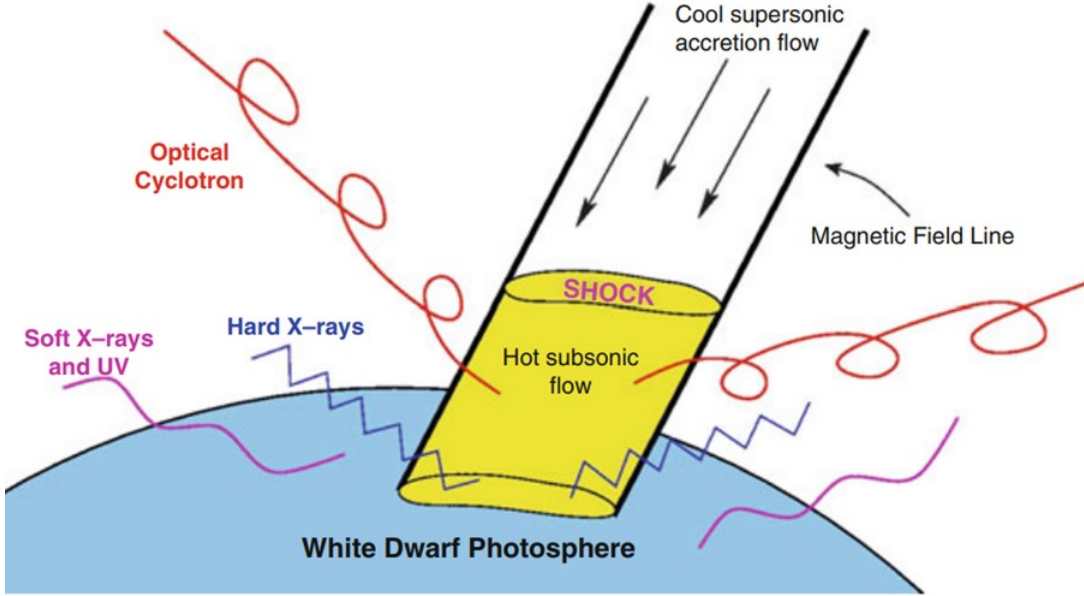


Figure 1.5: Schematic of a magnetic accretion column showing the origin of emissions. (Potter, 2016)

the moderating effect of a disc the stream follows magnetic field lines and accelerates to supersonic speed ($\sim 3000 \text{ km s}^{-1}$) as it approaches the white dwarf surface forming an accretion column (Fig. 1.5). This results in shock heating to $\sim 10^8 \text{ K}$ which causes X-ray emissions via thermal bremsstrahlung and optical cyclotron emissions from the infrared to the ultraviolet. As we shall discuss later it is possible for a moderately magnetic ($1 \lesssim B \lesssim 10 \text{ MG}$) CV to have a hollowed-out disc that terminates where it meets the magnetosphere; the accretion stream leaves the inner edge of the disc and follows field lines to the magnetic poles of the white dwarf Patterson (1994).

1.3.4 Winds

If the donor does not fill its Roche lobe a small amount of accretion is possible due to the donor wind. Winds emanating from the donor and driven by the donor magnetic field eject material some of which can be captured and accreted by the white dwarf. This wind-driven accretion has a very low mass transfer rate compared with the streams arising from Roche-lobe overflow (Schwope et al., 2002a; Debes, 2006; Schwope et al., 2009; Pyrzas et al., 2012; Hakala et al., 2022).

1.4 Cataclysmic variable evolution

1.4.1 Evolution and angular momentum

Binary interaction results in changes to the system angular momentum as well as its geometry (separation and Roche lobes). We now analyse this relationship.

By definition the angular momentum, J is given by:-

$$J = M_1 a_1 \frac{2\pi a_1}{P_{\text{orb}}} + M_2 a_2 \frac{2\pi a_2}{P_{\text{orb}}} \quad (1.6)$$

where a_1 , a_2 are the respective distances of M_1 and M_2 from their joint centre of mass. Kepler's Law states

$$P_{\text{orb}}^2 = \frac{4\pi^2 a^3}{G(M_1 + M_2)} \quad (1.7)$$

and substituting into 1.6 to eliminate P_{orb} yields

$$J = M_1 M_2 \left(\frac{Ga}{M} \right)^{1/2} \quad (1.8)$$

where $M = M_1 + M_2$. Taking natural logarithms and differentiating with respect to time yields

$$\frac{\dot{J}}{J} = \frac{\dot{M}_1}{M_1} + \frac{\dot{M}_2}{M_2} - \frac{1}{2} \frac{\dot{M}}{M} + \frac{1}{2} \frac{\dot{a}}{a} \quad (1.9)$$

If total mass is conserved then $\dot{M} = 0$ and $\dot{M}_1 + \dot{M}_2 = 0$

$$\frac{\dot{a}}{a} = 2 \frac{\dot{J}}{J} - 2 \frac{\dot{M}_2}{M_2} \left(1 - \frac{M_2}{M_1} \right) \quad (1.10)$$

Assuming that $q < 0.8$ we recall the empirical equation (1.3) for the volume radius of the Roche lobe of donors:-

$$\frac{R_L}{a} = 0.46224 \left(\frac{q}{1+q} \right)^{1/3} = 0.46224 \left(\frac{M_2}{M} \right)^{1/3} \quad (1.11)$$

Taking logarithms, setting $\dot{M} = 0$ and differentiating results in

$$\frac{\dot{R}_L}{R_L} - \frac{\dot{a}}{a} = \frac{1}{3} \left(\frac{\dot{M}_2}{M_2} \right)^{1/3} \quad (1.12)$$

and merging with 1.10

$$\frac{\dot{R}_L}{R_L} = 2 \frac{\dot{J}}{J} - 2 \frac{\dot{M}_2}{M_2} \left(\frac{5}{6} - \frac{M_2}{M_1} \right) \quad (1.13)$$

As $q < 0.8$ the bracketed term is positive. So if angular momentum is conserved (i.e. $\dot{J} = 0$) then accretion ($\dot{M}_2 < 0$) will result in $\dot{R}_L > 0$ and hence the donor Roche lobe

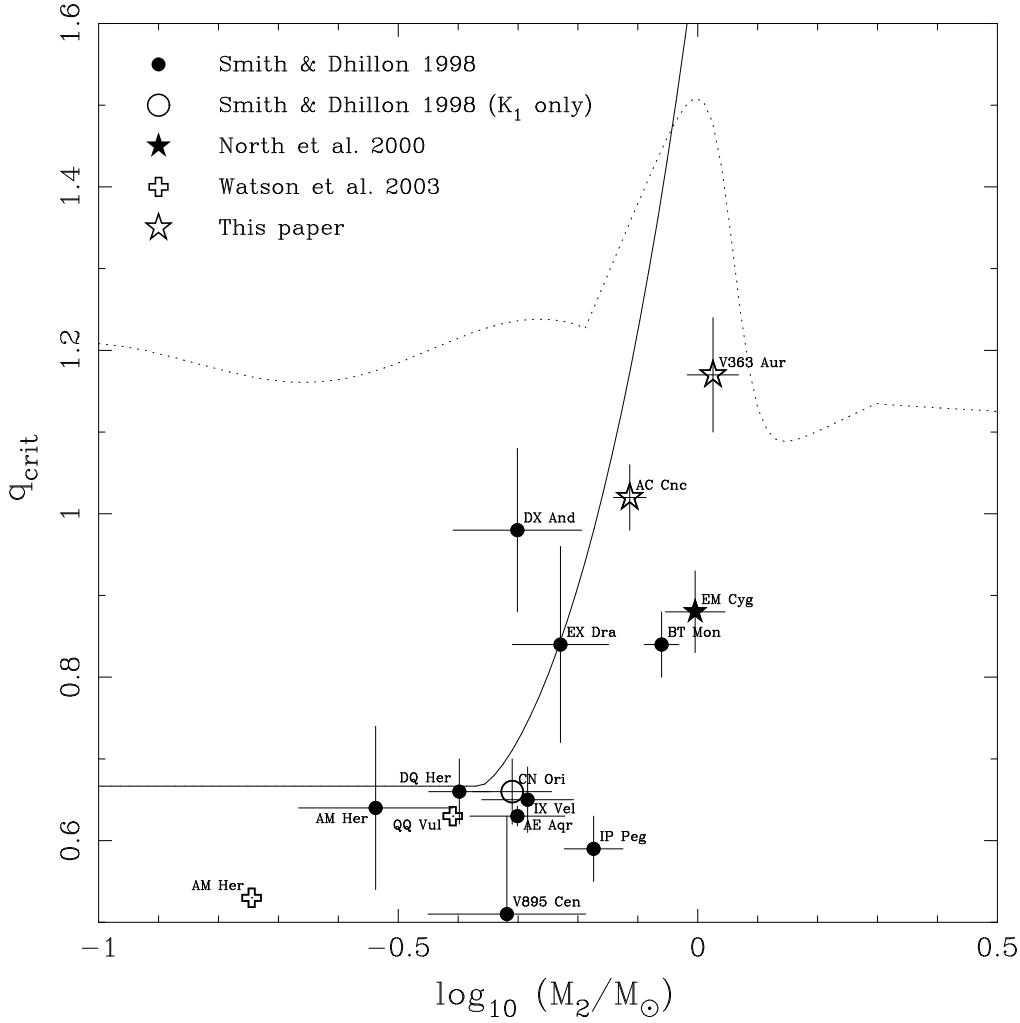


Figure 1.6: Figure 12 from [Thoroughgood et al. \(2004\)](#) showing the critical mass ratios for mass transfer stability. The dotted line represents the condition for thermal instability; the solid line represents the condition for dynamical instability ([Politano, 1996](#)). Both curves assume the star is on the main sequence and is initially in thermal equilibrium.

will expand losing contact with the donor thereby terminating accretion. Sustained mass transfer (i.e. $\dot{R}_L < 0$) can therefore only occur if $\dot{J} < 0$ leading to the key result that angular momentum loss, AML, is required for continued stable accretion and hence all CVs with $q < 0.8$ must have mechanisms for achieving this.

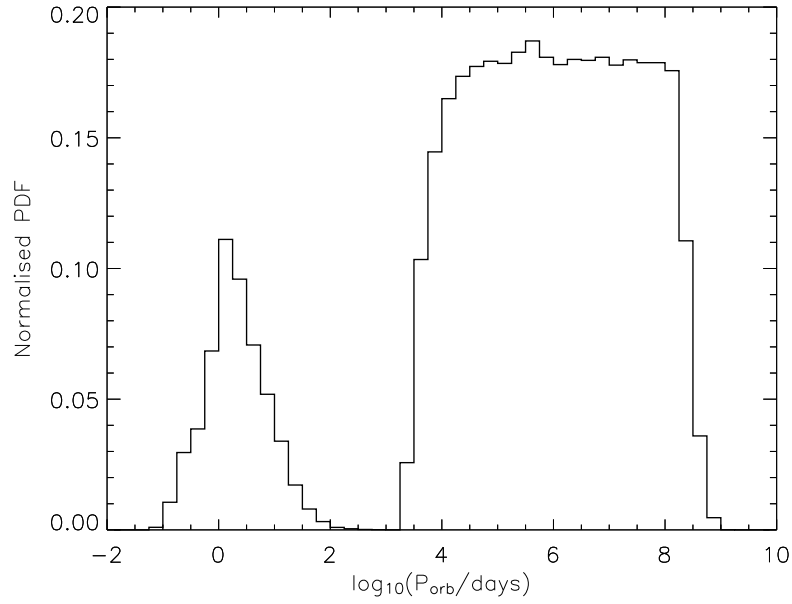


Figure 1.7: Theoretical orbital period distribution of present-day white dwarf plus main sequence binaries following the common envelope phase showing the bi-modality. The distribution is normalised so that the integral over all systems found is equal to one (Fig. 10 in [Willems & Kolb 2004](#)).

Stable accretion is dependent upon the response of the radius and Roche lobe radius of the donor to mass-loss ([Belloni & Schreiber, 2023](#)). This response occurs on two timescales; dynamical and thermal. [Hjellming \(1989\)](#) showed that lower mass donors with significant convective envelopes contract on the dynamical timescale in response to mass-loss. The solid line in Fig. 1.6 shows the limiting value of q in this case. Higher mass donors ($M > 0.8M_{\odot}$) generally do not have convective envelopes and their adiabatic response to mass loss is to shrink with the limiting value of q due to maintaining thermal equilibrium shown by the dotted line in Fig. 1.6 ([Belloni & Schreiber, 2023](#)).

1.4.2 Formation and the common envelope phase

Between 50 and 80 per cent of stars are formed as part of a binary system ([Eggleton & Tokovinin, 2008](#); [Raghavan et al., 2010](#)). Both stars will evolve normally through the main sequence until the higher mass primary runs out of hydrogen in its core and ascends the giant branch. If the initial binary separation is sufficiently small, it will eventually fill its Roche lobe, initiating unstable (see Section 1.4.1) mass transfer onto the lower-mass companion ([Paczynski, 1976](#); [Webbink, 1984](#)). The mass transfer timescale is faster than the rate at which the companion can accrete (the Eddington Limit) and the two stars are rapidly engulfed in a common envelope. Friction within this envelope drains energy and angular momentum from the binary orbit, shrinking

their separation. The envelope acquires this angular momentum and is ejected leaving a short-period binary consisting of a white dwarf and a main-sequence star. This process is very rapid lasting less than 1000 years (Meyer & Meyer-Hofmeister, 1979) and therefore not surprisingly has never been observed. Models of this process are therefore hard to validate and focus upon the transfer of energy and angular momentum to the envelope to estimate the final separation of the white dwarf and companion. Zorotovic et al. (2010) describes the classical approach as follows. The key assumption is that the change in orbital energy of the binary is used to provide the energy required to unbind the envelope. This assumes that the reduction in orbital energy is transferred to the envelope so that it can achieve escape velocity. In practice the envelope velocity may exceed the escape velocity, energy can be radiated away or conversely there may be additional sources of energy such as recombination of ionised material. All of these possibilities are encapsulated in the efficiency factor α :-

$$E_{\text{env}} = \alpha \left(-\frac{GM_{\text{d}}M_2}{2a_i} + \frac{GM_{\text{core}}M_2}{2a_f} \right), \quad (1.14)$$

where E_{env} is the binding energy of the envelope, G is the gravitational constant, M_{d} is the mass of the pre-CE donor, M_2 is the mass of the secondary, M_{core} is the mass of the donor's core and a_i, a_f are the pre- and post-CE orbital separations. The binding energy of the envelope can be expressed as:-

$$E_{\text{env}} = \frac{GM_{\text{d}}M_{\text{env}}}{\lambda R_{\text{d}}}, \quad (1.15)$$

where $M_{\text{env}} \equiv M_{\text{d}} - M_{\text{core}}$ is the envelope mass, R_{d} is the donor radius and λ is a parameter that encapsulates the density distribution of the donor. Equating 1.14 and 1.15 yields the standard α -formalism:-

$$\frac{GM_{\text{d}}M_{\text{env}}}{\lambda R_{\text{d}}} = \alpha \left(-\frac{GM_{\text{d}}M_2}{2a_i} + \frac{GM_{\text{core}}M_2}{2a_f} \right), \quad (1.16)$$

This formula is used in population studies where all the values prior to the common envelope phase are known and assumptions for α and λ yield the final separation. Research continues into the values of α and λ ; for example Zorotovic & Schreiber (2022) used observational evidence together with the prescription for λ from Appendix A of (Claeys et al., 2014) (yielding values in the range $\lambda = 0.25 - 2.0$) to find that the value of α is in the range $0.2 - 0.4$ for systems consisting of a white dwarf plus either an M-dwarf or a brown dwarf.

The orbital shrinkage caused by common envelope evolution implies that the resulting population of white dwarf binaries is bi-modal (see Fig. 1.7) with post common envelope binaries (PCEBs) having periods of hours to days, and wide white dwarf plus main sequence star binaries (that avoided a common envelope and evolved as single

stars) having periods in excess of a few years. The longest period PCEBs are probably a result of unusually massive progenitor companions and can emerge with periods of ~ 100 d (Kruse & Agol, 2014; Zorotovic et al., 2014). This bi-modal distribution has been observationally confirmed with high-resolution *HST* imaging and radial velocity studies of a sample of white dwarf binaries (Farihi et al., 2010; Ashley et al., 2019).

1.4.3 Magnetic braking

Magnetic braking in a single star is caused by ionised winds interacting with the magnetic field of the star. Within the Alfvén radius the wind is forced to co-rotate with the star causing a torque and thereby reducing the angular momentum of the star and increasing its spin period. In the case of a CV the donor is tidally locked to the orbital period and its loss of angular momentum due to a wind is ultimately drained from the orbital angular momentum of the CV. There have been many attempts to model magnetic braking in CVs with radically different results (see Fig. 2 and Appendix A in Knigge et al. 2011). The most commonly used model in population studies is attributed to Rappaport et al. (1983) and in essence is based upon an empirical relation between equatorial rotation speed and age of G-type stars from Skumanich (1972). Knigge et al. (2011) present this model as

$$\dot{J} = -5 \times 10^{-29} k_2^2 f^{-2} M_2 R_2^4 \Omega^3 \left(\frac{R_2}{R_\odot} \right)^{-1} \quad (1.17)$$

where k_2 is the radius of gyration with $k_2^2 \simeq 0.1$ and $f \simeq 1$ is a constant. The situation changes when the white dwarf has a strong magnetic field (see Section 2.2.2) which probably traps part of the wind resulting in ‘reduced’ magnetic braking (Wickramasinghe & Wu, 1994; Webbink & Wickramasinghe, 2002; Belloni et al., 2020).

A recent study by El-Badry et al. (2022) cast doubt on the fundamental model of rotation speed by Skumanich (1972) in the case of detached binaries; it is not clear whether their findings would apply to CVs because both mass and angular momentum are changing at the same time as a result of mass loss from the donor.

1.4.4 The period gap

The observed distribution of orbital periods shows a significant dip between 2 – 3 h (Whyte & Eggleton, 1980), and this deficiency is known as the *period gap*. The currently accepted explanation for the period gap is that CVs undergo a major drop in the rate at which they lose angular momentum once the donor stars become fully convective at $\simeq 3$ h (Rappaport et al., 1983; Howell et al., 2001) and hence $\tau_j > \tau_{\text{kh}}$. Prior to this point the donor was bloated with a larger radius than a detached star of the same mass. The bloating was because the mass loss timescale was much less than the thermal timescale

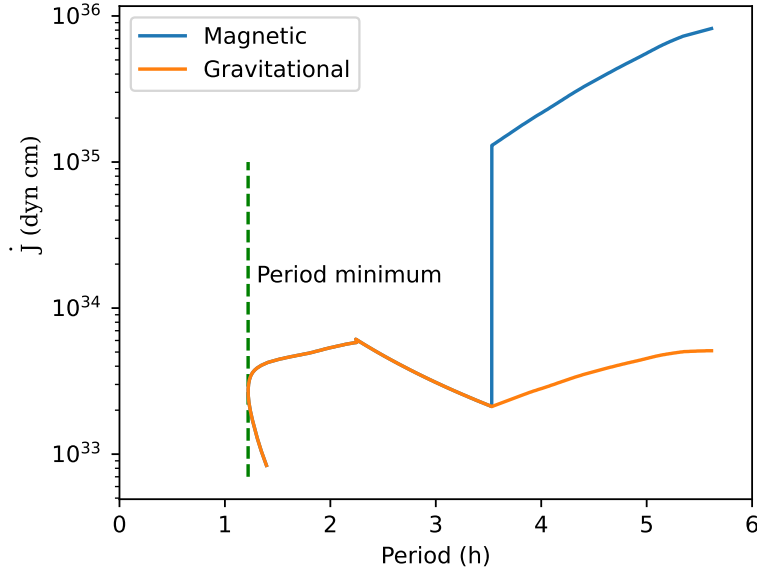


Figure 1.8: Schematic redrawn using data from [Knigge et al. \(2011\)](#) showing the rate of AML due to magnetic braking up to the period gap and the rate of AML due to gravitational wave radiation. The magnetic braking is calculated according to [Rappaport et al. \(1983\)](#) whilst the gravitational wave radiation uses the prescription of [Peters \(1964\)](#); [Chau \(1978\)](#).

(i.e. $\tau_{\dot{M}_2} < \tau_{\text{kh}}$). On reaching the period gap the donor shrinks and is no longer bloated thereby losing contact with its Roche lobe. CVs then evolve as *detached* systems across the period gap ([Davis et al., 2008](#); [Zorotovic et al., 2016](#)), until the Roche-lobe shrinks sufficiently to re-establish a semi-detached configuration and re-start the mass transfer, albeit at a much lower rate. The drop in AML is referred to as Disrupted Magnetic Braking.

1.4.5 Gravitational wave radiation

The small separation and high angular frequency of CVs result in significant gravitational wave radiation (GWR) thereby resulting in AML. Gravitational radiation ([Paczynski, 1967](#); [King, 1988](#)) was originally proposed in [Einstein \(1916\)](#) and indirect evidence came from the binary pulsar system PSR B1913+16 ([Hulse & Taylor, 1975](#)) but it was not until the advent of the Laser Interferometer Gravitational-Wave Observatory (LIGO) that the first direct detection of gravitational waves took place * ([Abbott et al., 2016](#)). From fundamental physics the formula for the rate of AML due to GWR ([Peters, 1964](#); [Chau, 1978](#)) is:-

$$\dot{J} = -\frac{32}{5} \frac{G^{7/2}}{c^5} \frac{M_1^2 M_2^2 M^{1/2}}{a^{7/2}} \quad (1.18)$$

*The gravitational wave radiation was inferred from the precise measurement of the orbital decay of main sequence (MS+MS) and white dwarf (WD+WD) binaries

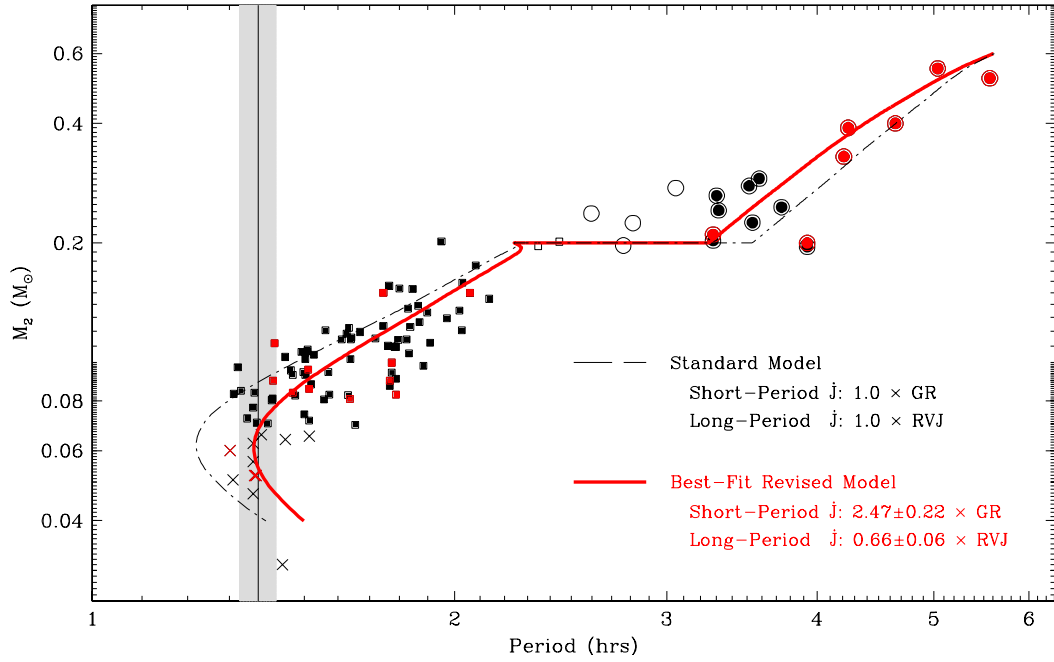


Figure 1.9: Self-consistent model fits to the observed properties of CV donors from Fig. 9 in [Knigge et al. \(2011\)](#). The broken black line uses the standard models for magnetic braking and gravitational wave radiation. The revised model (in red) assumes that $\dot{J} = 2.47\dot{J}_{\text{GW}}$ below the period gap (i.e., enhanced AML) and $\dot{J} = 0.66\dot{J}_{\text{MB}}$ above the period gap (i.e., slightly reduced AML) where \dot{J}_{GW} and \dot{J}_{MB} are the predictions from the standard formulae. The vertical line marks the observed location of the period spike (which presumably corresponds to the period minimum) whilst the width of the shaded area corresponds to the FWHM of the spike as measured in [Gänsicke et al. \(2009\)](#).

The denominator shows that GWR falls off rapidly with separation ($\propto a^{-7/2}$) and is therefore only dominant in very close, and hence short-period, CVs. This is demonstrated in Fig. 1.8 where magnetic braking is dominant down to the period gap and it is only at shorter periods that GWR becomes the main cause of AML.

1.4.6 Additional ways to lose angular momentum

Figure 1.9 (from [Knigge et al. 2011](#)) demonstrates that additional means of AML are needed to accurately fit the model to observations. One possibility is residual magnetic braking below the period gap whilst another possibility is that angular momentum could be lost due to accretion ([King & Kolb, 1995](#)), now referred to as Consequential Angular Momentum Loss (CAML). A number of mechanisms have been proposed for CAML. One mechanism is a magnetic wind arising from the accretion disc with sufficient velocity to escape the CV's gravity and hence removing angular momentum ([Livio & Pringle, 1994](#)). Accretion disc winds are discussed further in Chapter 3. Alternatively [Schenker et al. \(1998\)](#) and subsequently [Schreiber et al. \(2016\)](#) and [Nelemans et al.](#)

(2016) discuss the loss of angular momentum due to a classical nova (see Section 1.4.8). In this scenario the ejecta can not only convey angular momentum from the surface of the white dwarf (the origin of the nova) but can also interact with the donor with angular momentum being transferred due to friction. A third possibility is the existence of a circumbinary disc around the CV. In this scenario a proportion of the mass lost by the donor is fed into the circumbinary disc. As the mass of the circumbinary disc grows it will exert an increasing gravitational torque on the CV thereby transferring angular momentum from the CV (Spruit & Taam, 2001; Willems et al., 2005).

1.4.7 The period minimum and beyond

Continuing mass loss will ultimately result in the mass of the donor dropping to the point where hydrogen fusion cannot be sustained ($M_2 \simeq 0.064 - 0.087 M_\odot$, Auddy et al. 2016). The donor then becomes degenerate with mass loss resulting in an *increasing* radius ($R_2 \propto M_2^{-1/3}$ Oppenheimer et al. 1998). Transferring terms in Kepler's Law (equation 1.7) yields

$$P_{\text{orb}} \propto \frac{a^{3/2} q^{1/2}}{M_2^{1/2} (1+q)^{1/2}} \quad (1.19)$$

Transferring terms from equation 1.11

$$a = \frac{R_L}{0.46224} \left(\frac{q}{1+q} \right)^{-1/3} \quad (1.20)$$

As the donor is accreting it must be in contact with its Roche lobe ($R_2 = R_L$) and hence $R_L \propto M_2^{-1/3}$. Consolidating these three equations yields $P_{\text{orb}} \propto M_2^{-1}$ implying that mass loss causes the orbital period to increase. It follows that there is a period minimum. CVs that have evolved past the period minimum are colloquially referred to as period bouncers and these are extensively discussed in Chapters 5 and 6.

Population synthesis models predict that a large fraction of CVs should have evolved past the period minimum: 38 – 60 per cent (Goliaşch & Nelson, 2015) to 70 – 75 per cent (Kolb, 1993; Belloni et al., 2018). Observations generally have found relatively few period bouncers; Patterson (2011) identified 22 candidates and in Chapter 5 we identified 0.7 per cent of the CVs discovered by SDSS. Their fraction in the practically complete volume-limited 150 pc sample is only $\simeq 7 - 14$ per cent (Pala et al., 2020). This inconsistency remains an open question.

1.4.8 Novae

Classical novae (Bode & Evans, 2012) were first observed by ancient Chinese astronomers as eruptions of 8 – 15 magnitudes that decayed over a period of tens to several hundred days (Clark et al., 1977). They occur in CVs and also symbiotic stars. The eruptions

are caused by an accumulation of hydrogen on the surface of the white dwarf which eventually reaches a critical mass and pressure thereby initiating a runaway nuclear reaction that expels an expanding shell (Nelemans et al., 2016; Shen & Quataert, 2022) and may also influence the evolution of the CV by causing frictional angular momentum loss (Schreiber et al., 2016). Classical novae can therefore occur in all types of CVs including magnetic ones (Stockman et al., 1988) particularly ones with high mass white dwarfs. The accumulation of hydrogen is influenced by \dot{M}_2 and therefore classical novae are more common in high \dot{M}_2 systems typically with periods $P_{\text{orb}} \gtrsim 3$ h. Classical novae were originally thought to be singular events for a given system but it is now believed that they recur over unobservably long periods (thousands of years) (Darnley et al., 2012). The small (around ten) number of observed recurrent novae all have very high mass white dwarfs approaching the Chandrasekhar limit.

Chapter 2

Methods

Many commonly used methods have been applied as part of this research. This chapter focuses upon methods specific to this research work in particular justifying the approaches used for measurement of stellar distances and for the classification of CVs.

2.1 Distances from *Gaia*

The astrometry of the *Gaia* space mission ([Gaia Collaboration et al., 2016, 2018](#)) is revolutionising Galactic and stellar astronomy. *Gaia* has vastly increased the number of stars with accurate parallaxes, ϖ , however, a large fraction of the objects have substantial parallax uncertainties, such that $d = 1/\varpi$ is no longer a reliable estimate of their distances. [Bailer-Jones \(2015\)](#) has used a probabilistic model using the known geometric distributions of stars to derive distance estimates that avoid the errors in traditional methods, such as spectro-photometric estimates which are subject to assumptions regarding interstellar extinction and stellar effective temperatures. We illustrate ([Figure 2.1](#)) the difference between *Gaia* DR2 $d = 1/\varpi$ and the distances of [Bailer-Jones et al. \(2018\)](#) using the sample of 42 CVs (top panel) known within 150 pc ([Pala et al., 2020](#)), all of which have $\sigma_\varpi \leq 0.24$ mas and $\varpi/\sigma_\varpi > 27.7$. This contrasts with the 374 CVs and CV candidates from our collection of all known CVs with distances beyond 1000 pc with $\varpi > 1$ mas and $1 < \varpi/\sigma_\varpi < 3$. [Figure 2.1](#) demonstrates that $1/\varpi$ results in substantial underestimates with respect to the distances of [Bailer-Jones et al. \(2018\)](#) for data with large parallax uncertainties. We note from [Lindgren et al. \(2018\)](#) that faint sources or those in crowded areas of the sky are most susceptible to errors in the five-parameter solution (and the parallax in particular). We have therefore split the sources in [Fig. 2.1](#) according to their location on sky, with those in crowded areas (defined as the Galactic plane, $|b| < 10^\circ$) shown as circles, and those in uncrowded areas as stars. It appears that for CVs and CV candidates, there is no clear correlation between

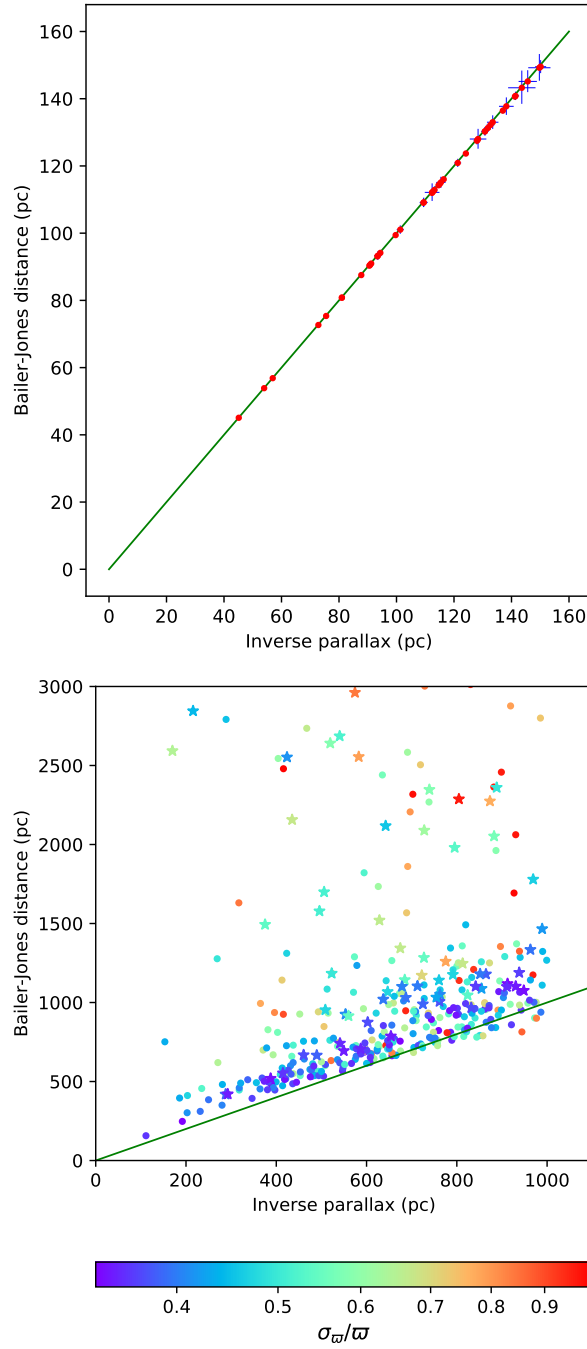


Figure 2.1: Comparison between $d = 1/\varpi$ and the distances of [Bailer-Jones et al. \(2018\)](#). Upper panel: 42 CVs known within 150 pc ([Pala et al., 2020](#)), with $\sigma_{\varpi} \leq 0.24$ mas and $\varpi/\sigma_{\varpi} > 27.7$, illustrating that for accurate parallaxes, the inverse of the parallax is a very good approximation for the distance. Lower panel: 374 CVs and CV candidates from our collection of all known CVs with $\sigma_{\varpi} > 0.33$ mas and $1 < \varpi/\sigma_{\varpi} < 3$. A star indicates that the object is outside the Galactic plane ($|b| > 10^\circ$). It is evident that for large parallax uncertainties, $1/\varpi$ often significantly underestimates the likely distance of the systems. In both panels the solid green line indicates a 1:1 correspondence.

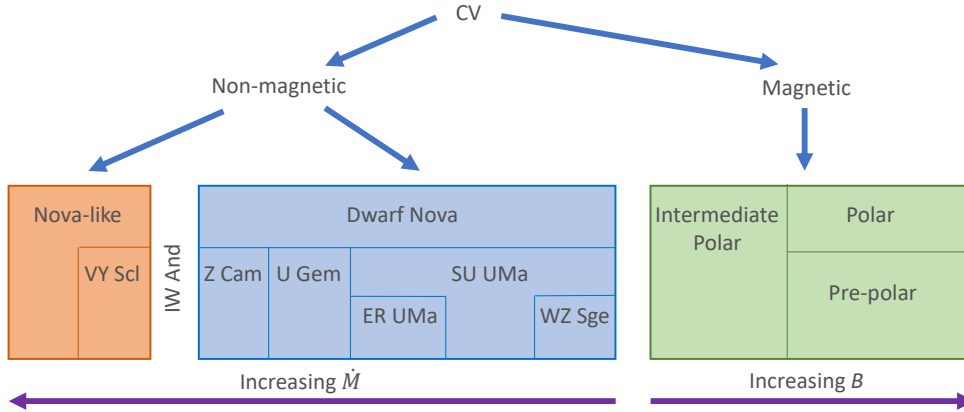


Figure 2.2: Diagram depicting the CV classification scheme used in this thesis. The physical key parameters that define the boundaries between different classes are \dot{M}_2 , P_{orb} (which, together, establish whether or not the accretion disc is subject to thermal instabilities) and B (which determines whether, or not a disc forms in the first place). Depending on the exact physical setup, some individual CVs may straddle the boundaries between the sub-classes defined above. AM CVns, with three possible formation channels (Section 2.2.1), follow the same distribution as non-magnetic CVs.

the magnitude of the discrepancy between $1/\varpi$ and the distances of [Bailer-Jones et al. \(2018\)](#) and whether a source is in the Galactic plane.

A second, photogeometric, method was developed for EDR3 which additionally uses the colour and apparent magnitude of a star and exploits the fact that stars of a given colour have a restricted range of probable absolute magnitudes ([Bailer-Jones et al., 2021](#)). Throughout this work we have used distances based upon the geometric priors^{*} rather than the photometric distances as CVs are likely to have a different colour/magnitude profile from the overall *Gaia* sample. Figure 8 in [Fouesneau et al. \(2022\)](#) confirms that the geometric distances are generally more reliable than the photogeometric ones.

2.2 CV Sub-types

CVs are classified into a number of subtypes. Historically they have been categorised based upon their observable characteristics with categories typically being named after a prototype system, frequently the first discovery. The number of sub-classes, their definition, and relationship between different sub-classes remain in flux, making their use challenging for scientists not regularly working in this research area – and some

^{*}[Bailer-Jones et al. \(2021\)](#) states that this is a direction dependent prior based upon the Galaxy’s stellar population. Whilst not specifically designed for CVs it should be a reasonable proxy as the progenitors of CVs were main sequence stars and presumably shared the same spacial distribution as present-day main-sequence stars.

care has to be taken with the temptation to define new sub-classes for each additional observational wrinkle in a particular CV. Nevertheless, dividing CVs into sub-classes is meaningful, as their observational characteristics depend on a small number of physical parameters, which link to the evolutionary state and the accretion geometry of an individual system (see Fig. 2.2).

Here we provide an overview of the main CV categories that have been historically used, and detail their state of evolution and mode of accretion. The key physical parameters are the orbital period, P_{orb} , the rate of mass loss from the donor, \dot{M} , and the white dwarf magnetic field strength, B .

The strength of the magnetic field of the white dwarf is of particular importance in determining the accretion geometry (Norton et al., 2008). We therefore discuss the evolution of magnetic and non-magnetic systems separately.

2.2.1 Non-magnetic CVs

Dwarf Novae

Dwarf novae are characterised by having at least one recorded outburst. In the literature they are frequently incorrectly treated as synonymous with U Gem CVs. However we follow Osaki (1996) in defining the U Gem subtype of dwarf novae by CVs that exhibit quasi-periodic outbursts without superoutbursts or standstills. In practice these have periods ($P_{\text{orb}} \gtrsim 3$ h) above the period gap. In quiescence their spectra (Fig. 2.3) exhibit hydrogen and also sometimes helium emission lines whilst in outburst their spectra resemble those of novalike variables (see below). Four other subtypes of dwarf novae are discussed below (SU UMa, WZ Sge, ER UMa and Z Cam).

SU UMa CVs (Osaki, 1989; Buat-Ménard & Hameury, 2002; Patterson et al., 2005b) are characterised by occasional ‘superoutbursts’ (Fig. 2.4) usually lasting several weeks and recurring with a supercycle of typically a few hundred days. These superoutbursts are significantly brighter than the regular dwarf novae which occur in between the superoutbursts. Hirose & Osaki (1990) show that when the separation of CVs decreases as a result of mass loss, tidal forces eventually cause the disc to become eccentric and non-axisymmetric. The disc rotates more rapidly than the orbital period and will stabilise at a resonant ratio of 3:1. The gradual accumulation of mass in the disc eventually results in a superoutburst; Hirose & Osaki (1990) show analytically that superoutbursts only occur when $q = M_2/M_1 \lesssim 0.3$. Assuming a typical value of $M_1 \simeq 0.8 M_{\odot}$ and using the relation $M_2 \approx 0.065 P_{\text{orb}}^{5/4}$ (Warner 1995 Section 2.8) implies $P_{\text{orb}} \lesssim 2.8$ h. After the peak luminosity of superoutbursts the light curves of SU UMa CVs are modulated by periodic oscillations called superhumps. The superhump period is a few per cent longer than P_{orb} and the relation $P_{\text{orb}} = 0.9162 \times P_{\text{sh}} + 5.39/60$ h can be used to estimate P_{orb} (Gänsicke et al., 2009). In reverse, if P_{sh} and P_{orb} are

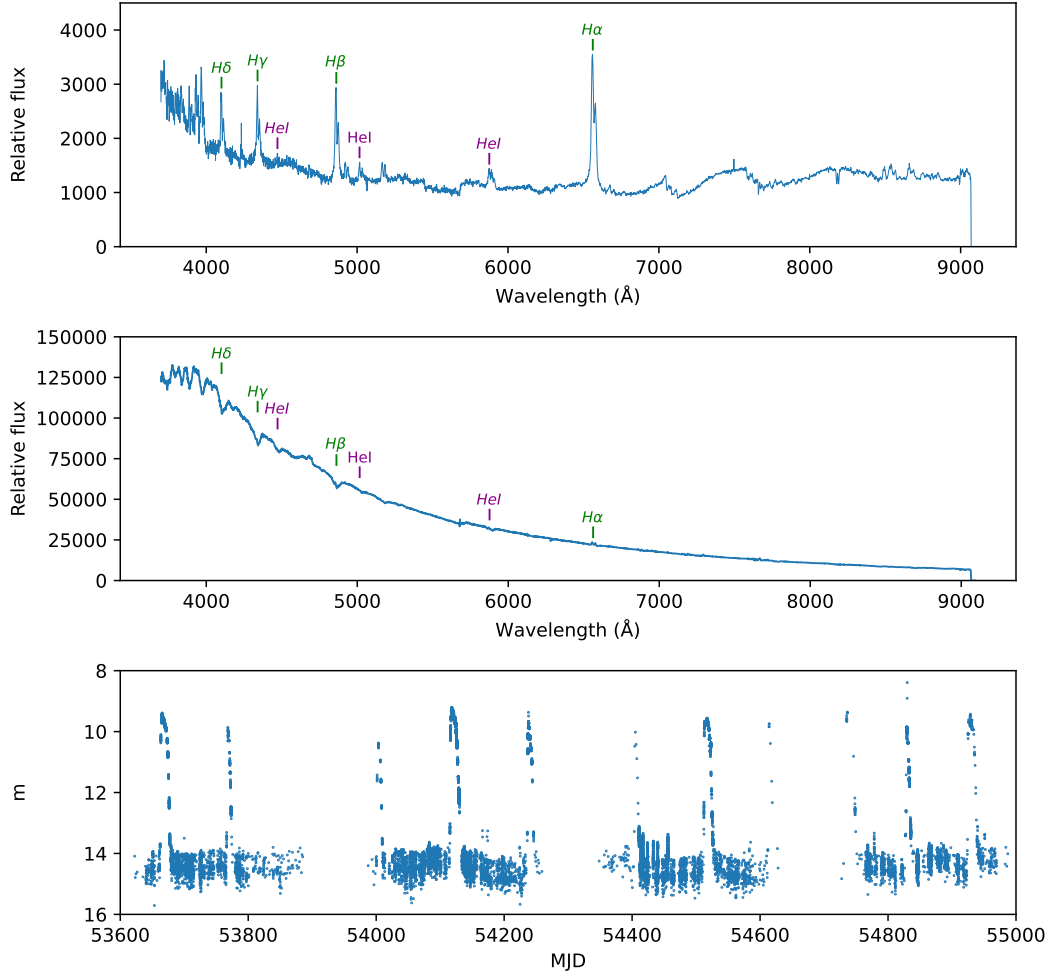


Figure 2.3: U Gem is the prototype of a dwarf nova. Top panel: LAMOST DR5 spectrum in quiescence showing strong emission lines. Middle panel: LAMOST DR5 spectrum in outburst. Bottom panel: light curve based on observations from the AAVSO International Database showing the decay of an outburst is $\simeq 20$ d.

both measured, the superhump period excess $\epsilon = (P_{\text{sh}} - P_{\text{orb}})/P_{\text{orb}}$ can be used to estimate q (Patterson et al., 2005b; Kato & Osaki, 2013) with a relation of the form $q = R + S \times \epsilon$ where R and S are empirically-derived constants. The period of the superhumps evolves through three stages (A, B and C) with different constants for each – for example McAllister et al. (2019) used $A = 0.00675$ and $B = 4.45$ for stage B superhumps.

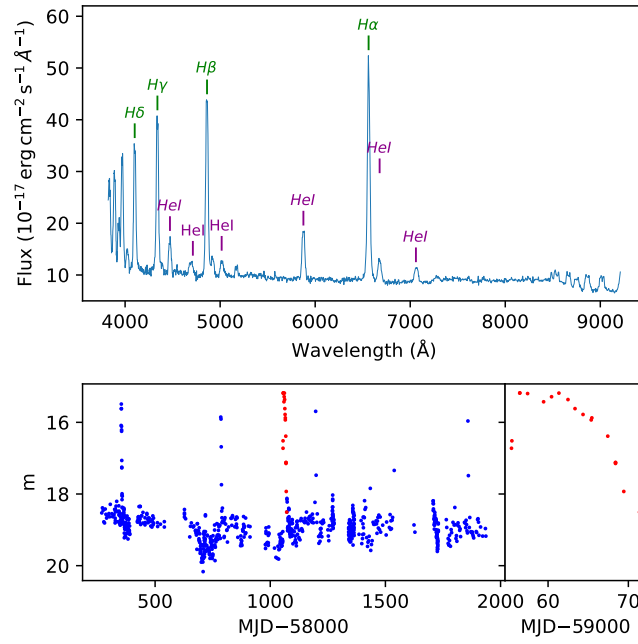


Figure 2.4: SDSS J003203.62+314510.4 is an example of an SU UMa CV. Top panel: Smoothed SDSS spectrum in quiescence showing typical slightly double-peaked Balmer emission lines. The Helium emission lines are not always present in SU UMas. Bottom left panel: ZTF (g -band) light curve showing outbursts and a superoutburst in red. Bottom right panel: Expanded light curve showing the decay of the superoutburst and characteristic superhumps.

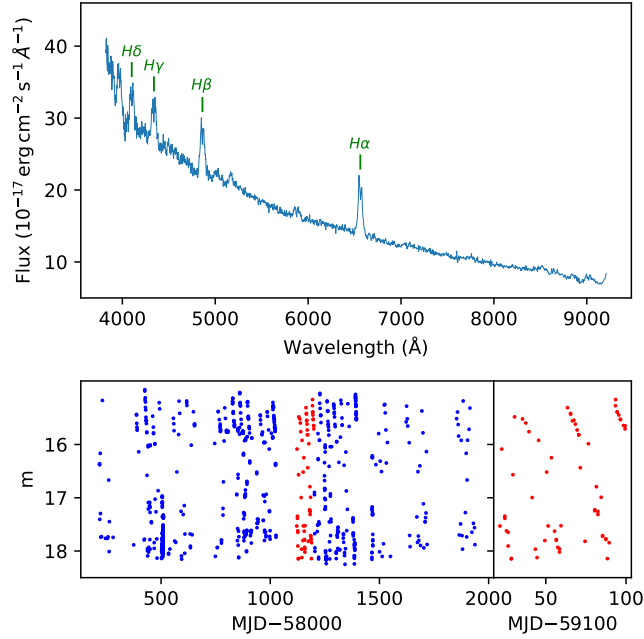


Figure 2.5: SDSS J091216.20+505353.8 (DIUMa) is an example of an ER UMa CV. It has a high \dot{M} which is inconsistent with its short orbital period of 78 min at the period minimum (Kato et al., 1996; Fried et al., 1999), resulting in extremely frequent superoutbursts. The supercycle is 25 d whilst normal outbursts occur every four days. Top panel: Smoothed SDSS spectrum in quiescence showing Balmer emission lines. Bottom left panel: ZTF (g - band) light curve showing frequent superoutbursts. Bottom right panel: Expanded light curve showing the frequency of the superoutbursts.

ER UMa dwarf novae (Fig. 2.5) are a subtype of SU UMa CVs characterised by an unusually short supercycle (20 – 50 d) so that they spend over a third of the time in superoutburst. The intervening time between superoutbursts is punctuated by normal outbursts every few days. (Robertson et al., 1995; Kato et al., 2013a). The cause for this behaviour is an \dot{M} around four times that of a typical SU UMa CV.

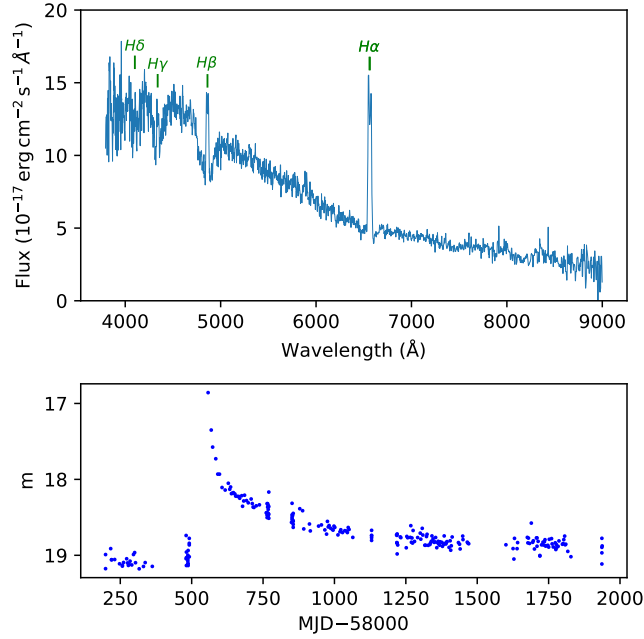


Figure 2.6: SDSS J161033.63-010223.2 (V386 Ser) is an example of a WZ Sge CV. Top panel: Smoothed SDSS spectrum in quiescence showing double-peaked Balmer emission lines from the accretion disc. The spectrum of the white dwarf is visible at the blue end with characteristic wide Balmer absorption lines. Bottom panel: ZTF (g -band) light curve showing a single characteristically large superoutburst. Many systems, believed to be WZ Sge CVs based on their spectra and periods, have no recorded outbursts.

WZ Sge dwarf novae are also a subtype (Patterson et al., 2002; Kato, 2015) of SU UMa CVs. Their donors have lost most of their mass and they have low \dot{M} with very infrequent, albeit bright, outbursts (Fig. 2.6). The low \dot{M} , and consequential low disc luminosity, often result in the white dwarf being visible in the optical spectrum. In many cases this is the best evidence for a WZ Sge classification as the original definition was based upon observation of an outburst, together with the characteristic early superhumps, which may not occur for decades. Note that low \dot{M} is not sufficient in itself for a classification; there also needs to be evidence of the low mass of the donor.

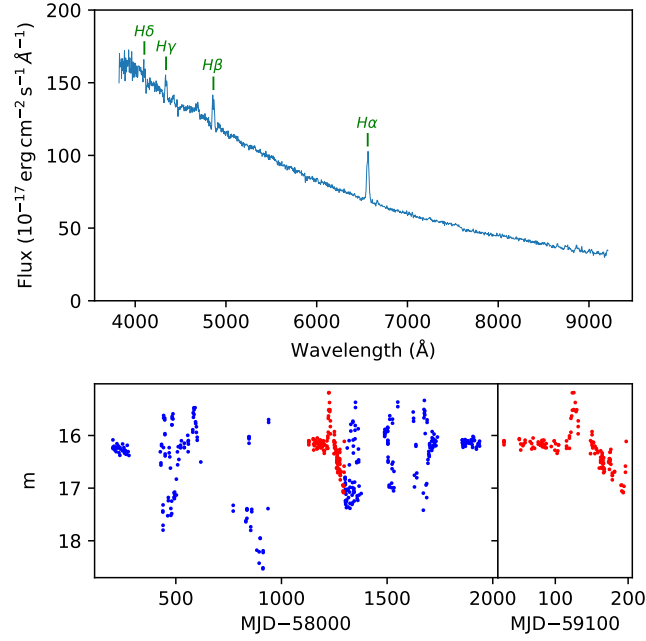


Figure 2.7: The prototype system Z Cam. Left panel: light curve based on observations from the AAVSO International Database showing standstill periods as well as outbursts and the low, quiescent, level. The standstill is highlighted in red. Right panel: Expanded light curve showing a period of ‘standstill’.

Z Cam dwarf novae have an unusual characteristic (Fig. 2.7) of having ‘standstills’ of luminosity midway between the quiescent level and the elevated level associated with a dwarf nova outburst (Simonsen et al., 2014). This is believed to be due to having an \dot{M} that fluctuates around the critical level and is too high to sustain the thermal limit cycle associated with dwarf novae. The IW And stars (Hameury & Lasota, 2014) form a sub-category of Z Cam and show continual outbursts (not unlike dwarf novae) during the ‘standstill’.

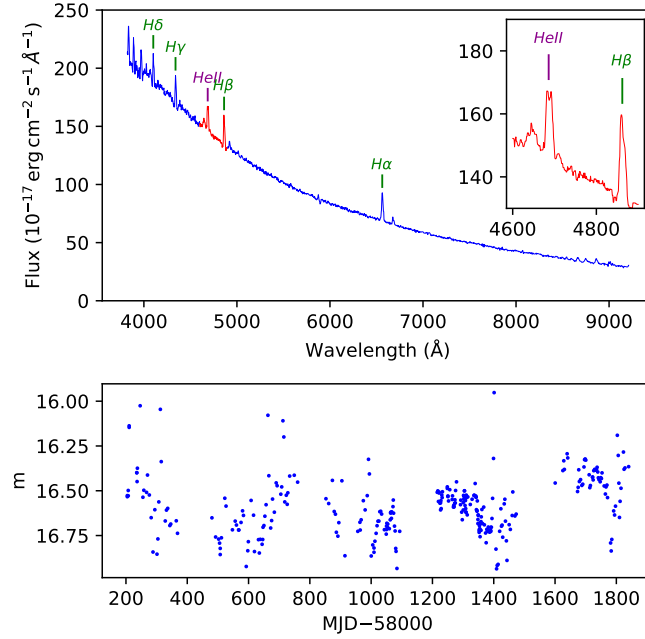


Figure 2.8: SDSS J154539.08+142231.4 (CT Ser) is an example of an old nova that erupted in 1948. Top panel: Smoothed SDSS spectrum showing Balmer and He II emission lines. Top inset panel: Expanded spectrum showing the relative strength of the H β and He II lines (Munari et al., 2014). Bottom panel: The ZTF (g –band) light curve illustrates the relatively constant emission from the disc in its high state.

Classical Novae

By definition an eruption of a classical nova has been recorded at some time. The spectrum of a classical nova varies considerably depending upon the time since this eruption. After the eruption the spectrum is the sum of the spectrum from the CV itself and the spectrum of the ejected shell which is rapidly expanding. The shell will initially be dominant and contribute broad emission lines of hydrogen and helium. As it expands further and becomes more diffuse it resembles a planetary nebula and exhibits forbidden lines such as S II 6717 \AA . The rapid expansion of the shell also results in spectral lines exhibiting the P Cygni profile. Eventually (years) the spectrum becomes that of the pre-eruption CV. Most classical novae revert to being novalike variables (Fig. 2.8), which is unsurprising as the nova recurrence time is inversely related to the accretion rate, and hence the nova population is dominated by novalike variables (Townesley & Bildsten, 2005).

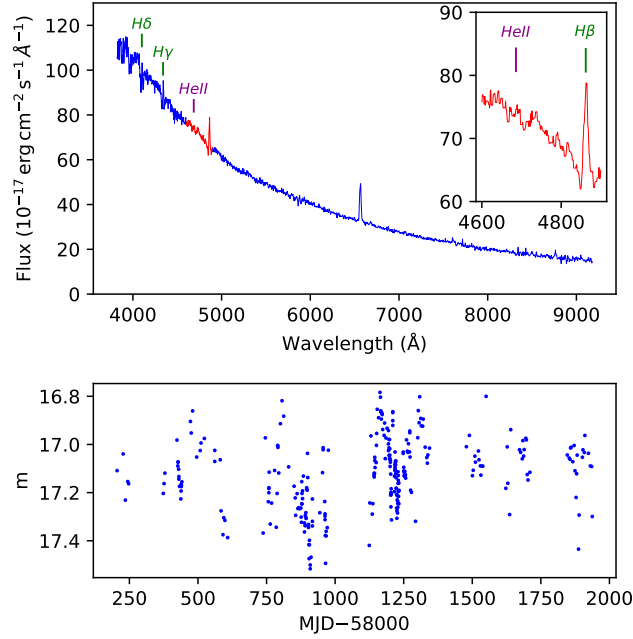


Figure 2.9: SDSS J075808.81+104345.5 is an example of a novalike variable. Top panel: Smoothed SDSS spectrum showing Balmer $H\alpha$ and $H\beta$ emission lines together with $H\gamma$ and $H\delta$ absorption lines. Top inset panel: Expanded spectrum showing the $H\beta$ line and absence of $HeII$ lines. The strength of $HeII$ 4686 Å emission lines varies with orbital phase far more than Balmer emission lines – often exceeding the strength of the $H\beta$ line (Hoard et al., 2014). Bottom panel: ZTF (g -band) light curve showing the relatively constant emission from the disc in its high state.

Novalike variables

Novalike variables (Dhillon, 1996) have bright spectra dominated by the hot disc (Fig. 2.9). The hydrogen in their discs is almost fully ionised and their spectra therefore exhibit absorption lines, often with inset emission lines. They often have strong disc winds which can appear as P Cygni spectral lines (Inight et al., 2022). Novalikes sometimes exhibit secular changes in mass transfer rates; the resulting high and low states visible in their light curves have given rise to a number of subtypes (Section 3.4.5 and Fig. 3.14). The VY Scl sub-category of novalikes shows (see Fig. 2.10) relatively deep ($2 - 5$ mag) low states which can last a few weeks to about a year, and during which small outbursts occur. This contrasts with the IW And sub-category (Section 2.2.1) in which characteristic outbursts occur during the (higher state) standstills. The SW Sex sub-category of novalikes (Schmidtobreick, 2017) are believed to have high inclinations, and are often eclipsing. However SW Sex novalikes have single-peaked emission lines unlike other CVs that are double-peaked.

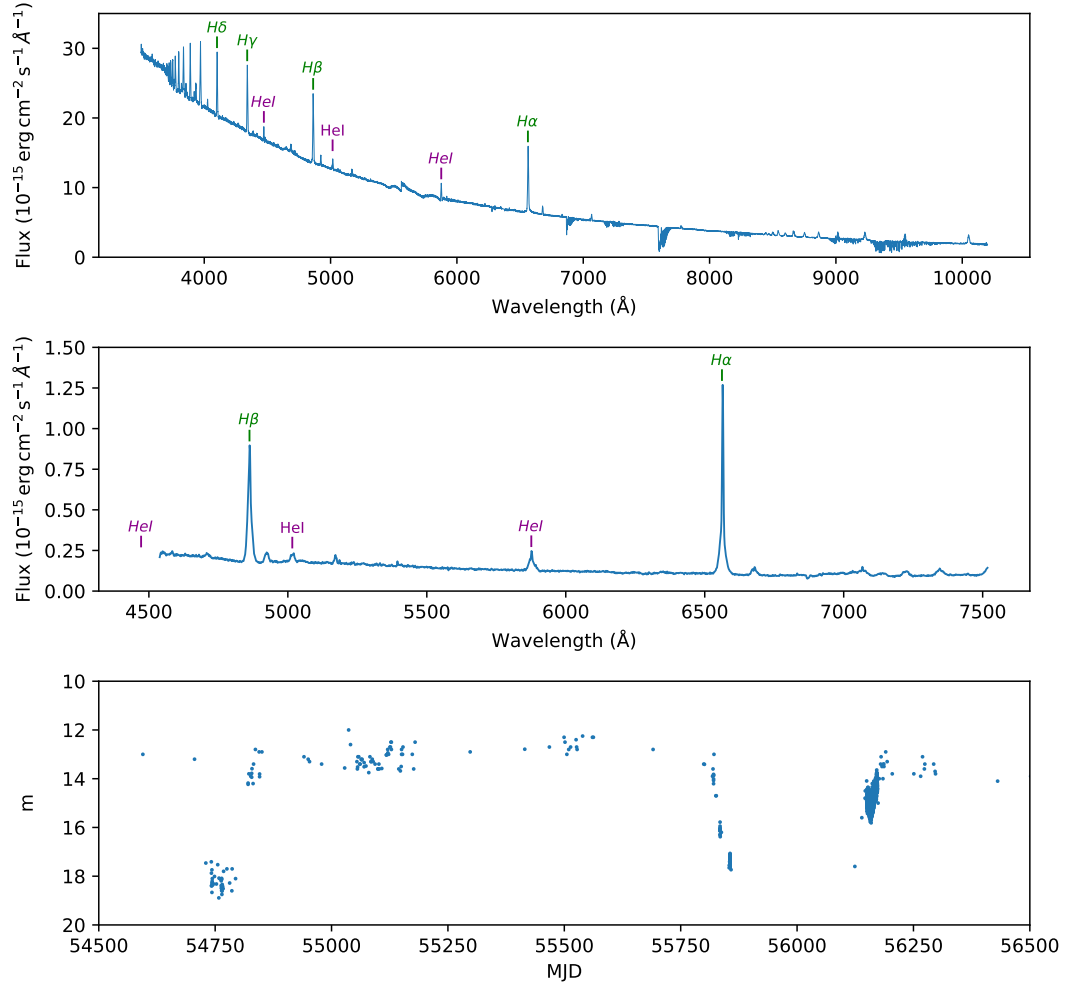


Figure 2.10: The prototype system VY Scl. Top panel: Spectrum using XSHOOTER on 2020-11-12 when VY Scl was in the high state showing Balmer and He I emission lines with a blue continuum. Middle panel: Spectrum using FORS1 (on the VLT) on 2008-11-18 (MJD = 54788) when VY Scl was in the low state showing emission lines above a much weaker and redder continuum (Schmidtobreick et al., 2018). Bottom panel: light curve based on observations from the AAVSO International Database showing the low state lasting ≈ 400 d around MJD = 56000 and also a shorter one around MJD = 54750 exhibiting outbursts whilst in the low state.

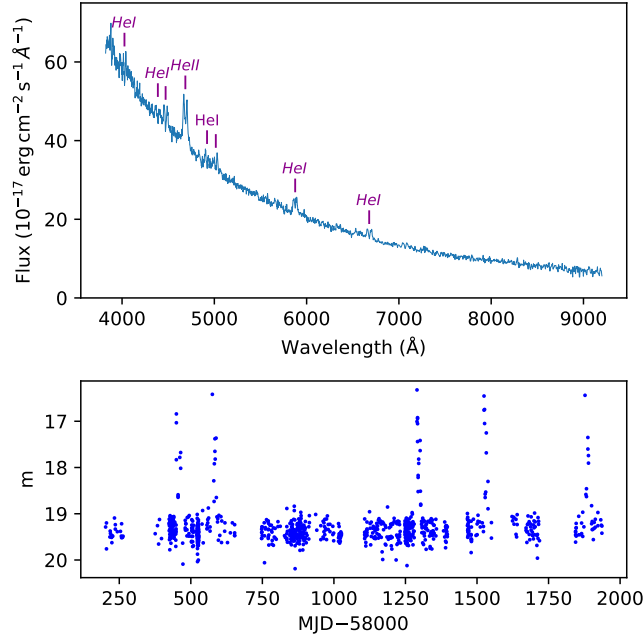


Figure 2.11: SDSS J092638.71+362402.4 is an example of an AM CVn CV. Top panel: The smoothed SDSS spectrum shows He I and He II emission lines but no hydrogen lines. The absence of hydrogen lines is a characteristic of AM CVn CVs. Bottom panel: ZTF (merged and scaled r - and g -bands) light curve showing outbursts.

AM CVn

AM CVn systems (Fig. 2.11) are identified by helium lines and an absence of, or very weak, hydrogen lines in their optical spectra (van Roestel et al., 2022). They are short-period systems ($P_{\text{orb}} \simeq 5 - 65 \text{ min}$ Deloye et al. 2007; Ramsay et al. 2018) but their origin is unclear with at least three potential formation channels leading from their progenitors (Solheim, 2010). AM CVn systems are uncommon with only ~ 60 systems known (Ramsay et al., 2018). These systems evolve through a similar set of subtypes as non-magnetic CVs; the first magnetic AM CVns have only recently been discovered (Maccarone et al., 2023). AM CVn systems are good verification binaries for *LISA* (Amaro-Seoane et al., 2017) given their short periods and separations (Nelemans et al., 2004; Liu et al., 2021).

2.2.2 Magnetic CVs

Perhaps a third (Pala et al., 2020) of CVs have a white dwarf with a magnetic field $B \gtrsim 1 \text{ MG}$ and these are termed magnetic. The origin of this strong field is not well understood; it may be formed during the common-envelope event or sometime later (Belloni & Schreiber, 2020). Schreiber et al. (2021) propose a model inspired by observational evidence whereby the white dwarf in a magnetic CV is born without a strong field and acquires it as a consequence of crystallisation (see Fig. 2.12 for details) whilst

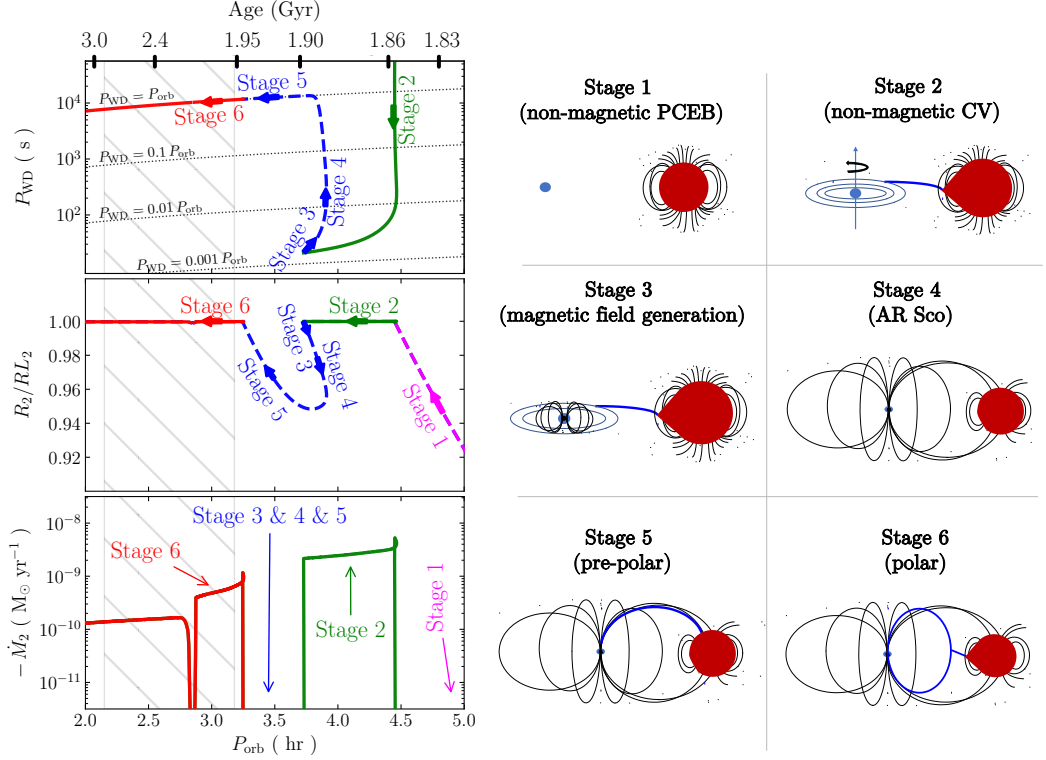


Figure 2.12: The [Schreiber et al. \(2021\)](#) model. In stage 1 a post-common-envelope binary contains a slowly rotating white dwarf. In stage 2 the binary has evolved to shorter periods and become a CV with accretion due to Roche lobe overflow of the donor. During this stage the white dwarf is spun-up by accretion. Stage 3 occurs if the white dwarf starts crystallising generating a strong magnetic field by a dynamo. If this magnetic field is strong enough to interact with the magnetic field of the donor the resulting torque causes the donor to detach from its Roche lobe. The system initially resembles the radio pulsing white dwarf binary AR Sco ([Marsh et al., 2016](#)). The white dwarf then spins down until it is synchronised with the orbital motion (stage 5) where accretion from the donor wind occurs; at this point the system is referred to as a pre-polar ([Hakala et al., 2022](#)). Angular momentum loss eventually causes the donor to fill its Roche lobe forming a polar (stage 6). When the secondary becomes fully convective, a second short detached phase occurs (hatched region) forming a variation of the classical orbital period gap. The magnetic field in intermediate polars ([Wilson et al., 2021](#)) would not be sufficient to cause the system to detach and evolution would proceed directly to stage 5.

being spun up by accretion. As expected this model is consistent with observational evidence (Fig. 9 in [Ferrario et al. 2015](#)) as intermediate polars (with $B \lesssim 10$ MG) are, in general, observed to have orbital periods $P_{\text{orb}} \gtrsim 3$ h whilst polars (with $B \gtrsim 10$ MG) are observed to have orbital periods $P_{\text{orb}} \lesssim 2$ h. The model is also consistent with our findings (Fig. 5.16).

Polars

The magnetic field of the white dwarf in polar CVs (Cropper, 1990; Wu, 2000), typified by the prototype AM Her, is generally greater than 10 MG. In this case the Alfvén radius (see Section 1.3.3) is beyond the circularisation radius, preventing the formation of an accretion disc, and the accretion flow follows field lines from the inner Lagrange point to impact on the white dwarf. These shock-heated impact zones ($\approx 10^8$ K) give rise to X-ray radiation and also characteristic He II emission lines (Fig. 2.13). The cyclotron radiation is sometimes observed in spectra as ‘humps’ (see for example Thomas et al. 2000). These humps are harmonics of the cyclotron frequency $f = (eB)/(2\pi m_e)$, with e and m_e the charge and the mass of the electron, due to the magnetic field B and can appear in the infrared (e.g. AM Her, $B \simeq 15$ MG Bailey et al. 1991), optical (e.g. MR Ser, $B \simeq 25$ MG; Schwobe et al. 1993) or ultraviolet (e.g. AR UMa, $B \simeq 200$ MG; Gänsicke et al. 2001) according to field strength. Cyclotron emission is directional and results in cyclotron beaming which manifests itself as periodic behaviour. Polars can also be identified either by polarimetry, as cyclotron radiation is polarised (Shahbaz, 2019), or by the Zeeman splitting of Balmer lines from the white dwarf (Ferrario et al., 1995) that is sometimes visible in spectra obtained during low states when accretion nearly ceases (Fig. 2.14) and can be used to estimate the strength of the magnetic field. A consequence of the strong magnetic field is that the spin period of the white dwarf normally equals P_{orb} . This is thought to be due to the interaction of the strong white dwarf magnetic field with the donor magnetic field generating a torque which over time causes the white dwarf to spin down until it equals P_{orb} ; the equilibrium situation (Campbell, 1984). Asynchronous polars (Campbell & Schwobe, 1999) have a white dwarf spin period slightly different from P_{orb} which can be detected in periodograms. Asynchronous polars are believed to have been knocked out of exact synchronisation by an event such as a nova (Pavlenko et al., 2018).

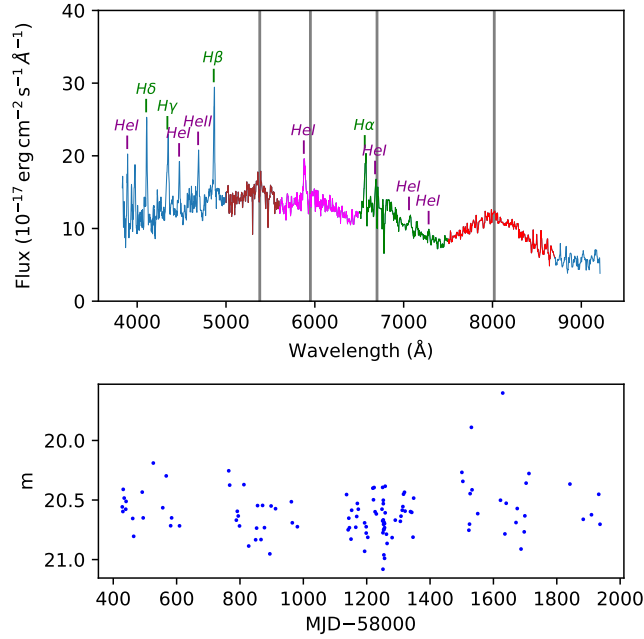


Figure 2.13: SDSS J092122.84+203857.1 is an example of a polar. Top panel: The smoothed SDSS spectrum (blue) shows Balmer, He I and characteristic He II emission lines. The four cyclotron humps (brown, magenta, green and red) provide clear evidence that this is a polar. [Schmidt et al. 2008](#) determined that these are the fifth, sixth, seventh and eighth harmonics (shown in grey) due to a magnetic field of $B = 32$ MG. Bottom panel: ZTF (g -band) light curve showing the variability due to cyclotron beaming. There are no outbursts as polars do not have discs in which to store accreting material and hence they do not undergo a thermal limit cycle.

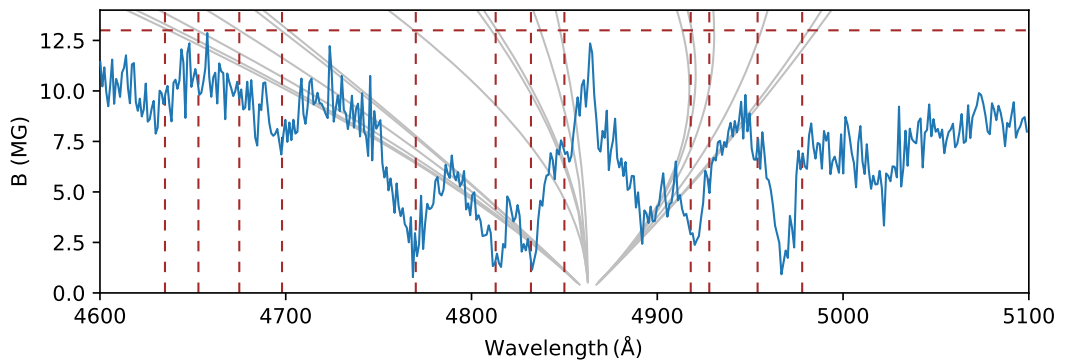


Figure 2.14: SDSS J110539.76+250628.6 is an example of a polar showing Zeeman splitting (grey lines) of the $H\beta$ line evolving vertically with increased magnetic field ([Schimeczek & Wunner, 2014](#)). The spectrum is over-plotted in blue with flux scaled to roughly match the amplitude of the grey lines. The split lines are identified by vertical dashes; they coincide with the grey lines at $B \simeq 13$ MG.

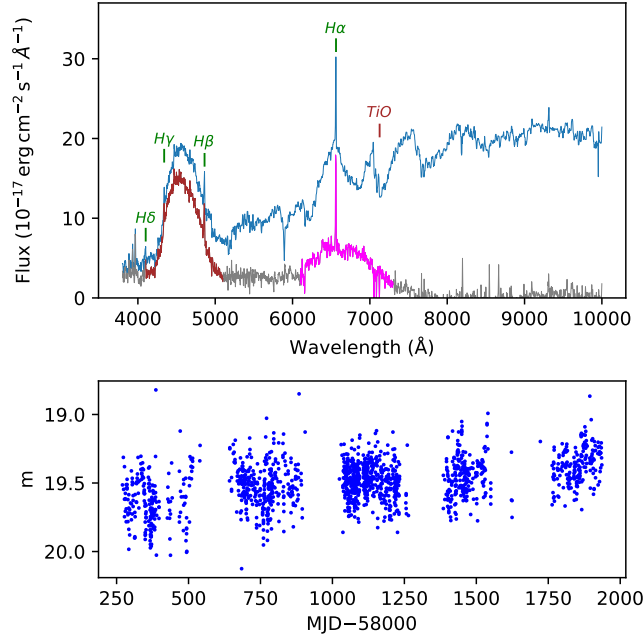


Figure 2.15: SDSS J004924.50+222617.9 is an example of a pre-polar CV. Top panel: The smoothed SDSS spectrum (blue) shows Balmer emission lines. The donor is visible at the red end of the spectrum. The cyclotron hump visible between 4200Å and 5000Å (brown) is clear evidence that this is a polar or pre-polar CV. Following [Parsons et al. \(2021\)](#) we subtracted a model spectrum ([Kesseli et al., 2017](#)) of an M3 dwarf (grey) to reveal a further cyclotron hump (magenta) at 6840 Å. Modelling of harmonic frequencies for varying magnetic fields yielded a good fit for a magnetic field strength of $B \simeq 78$ MG with the humps forming the second and third harmonics. The fact that the donor is visible implies that the accretion rate is low and this implies that this is a pre-polar accreting from the donor wind ([Schreiber et al., 2021](#)). Bottom panel: ZTF (g -band) light curve showing the variability attributable to cyclotron beaming which revealed the orbital period ($P_{\text{orb}} = 5.92$ h).

Pre-polars

White dwarfs in pre-polars ([Schwope et al., 2002a](#); [Parsons et al., 2021](#)) (also called low-accretion rate polars) accrete via a stellar wind from the donor rather than through Roche-lobe overflow. These detached systems therefore have very low accretion rates with \dot{M} less than one per cent of that of other CVs ([Schmidt et al., 2005b](#)). Cyclotron humps are the defining characteristic of pre-polars; typically the second and third harmonics are visible in the optical – although the humps can be masked by the donor spectrum (Fig. 2.15). In the evolutionary scenario of [Schreiber et al. \(2021\)](#) pre-polars represent a natural phase in the evolution of CVs once the white dwarf develops a strong magnetic field.

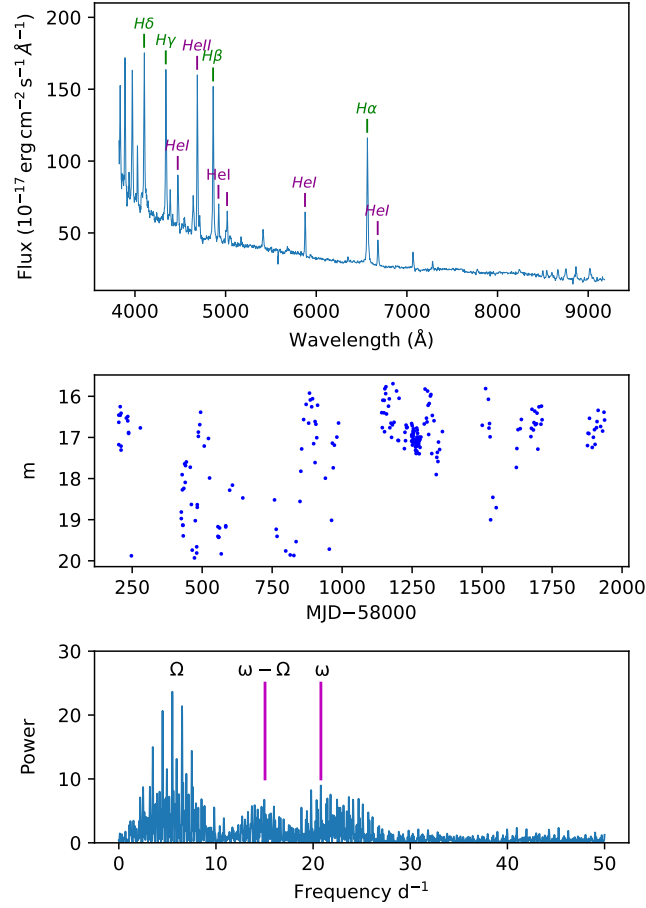


Figure 2.16: SDSS J094634.46+135057.8 (HY Leo, HS 0943+1404) is an example of an intermediate polar. Top panel: The smoothed SDSS spectrum shows Balmer, He I and He II emission lines. Middle panel: ZTF (g -band) light curve showing the variability due to the spin of the white dwarf and the accretion stream. The alternation between high and low states is also evident. Bottom panel: Periodogram taken from archival Jacobus Kapteyn Telescope data showing the orbital frequency (Ω), spin period (ω) and the beat period together with numerous aliases. For a detailed period analysis see [Rodríguez-Gil et al. \(2005b\)](#).

Intermediate polars

Intermediate polars (IPs, [Patterson 1994](#)) such as their prototype DQ Her, have weaker white dwarf magnetic fields than polars. The magnetic field is too weak to force synchronisation of the spin period of the white dwarf resulting in a spin period significantly shorter than the orbital period ([Norton et al., 2004](#)) – the defining characteristic of an IP (Fig. 2.16). The vast majority of IPs have a truncated accretion disc ([Hameury & Lasota, 2017](#)). In common with non-magnetic CVs material from the donor passes through the inner Lagrange point and pursues a ballistic path until it merges with the disc. The disc is truncated at the Alfvén radius and material then follows field lines

from the innermost part of the disc to one or both magnetic poles. The presence of the disc can result in outbursts (Hameury & Lasota, 2017). Magnetically funneled accretion onto the magnetic poles of the white dwarf results in pulsations in X-ray light curves (Hellier et al., 1991), which are the definitive observational proof of a CV being an intermediate polar.

2.3 CV Classification

We used a number of methods to classify the CVs. There is no single method that can reliably classify CVs – it is necessary to consider all the available information and seek a classification that is consistent with all of the data. In some cases only high level classifications such as dwarf nova or magnetic CV (MCV), are possible due to the limited amount of data. In other cases where a classification is very likely but not certain a colon (:) has been appended.

Classification starts with a literature search using Simbad (Wenger et al., 2000) and a search of the AAVSO VSX database. Where an existing classification exists it still needs checking to ensure that it is consistent with the SDSS spectra together with data from *Gaia* (Gaia Collaboration, 2020), VizieR (Allen et al., 2014), ZTF (Masci et al., 2019; Bellm et al., 2019), CRTS (Djorgovski et al., 2011; Breedt et al., 2014) and *TESS* (Ricker et al., 2015). This checking has resulted in refining many classifications and also identifying some systems that are not CVs (see sections 5.3.2 and 6.5.4). The references both for the initial discovery and subsequent measurement of the orbital period as well as spectroscopic observations are documented.

Detailed consideration of the available data is discussed in the following sections.

2.3.1 Spectral analysis

We first plotted the SDSS spectrum and then used the spectrum to calculate a synthetic *Gaia* *G* magnitude using the PYTHON PYPHOT[†] package. In addition to the SDSS spectrum we also created a broad-band (ultraviolet to infrared) spectral energy distribution (SED) diagram using data downloaded from VizieR (Allen et al., 2014) and over-plotted the spectrum.

We initially compared the SED with the spectrum. There can be a number of possible explanations if the spectrum is not consistent with the SED. Firstly the flux calibration of all or part of the spectrum may be faulty. Secondly the spectrum may have been taken at a time when the CV was in a high or outburst state in which case it will be above the other SED data. Thirdly the SED may have been contaminated by observations of a nearby object – we check the PanSTARRS image for such objects (see Section 2.3.4). When a CV has changed state and hence luminosity (see for example

[†]<https://github.com/mfouesneau/pyphot>

Fig. 3.8) this will be evident in the SED with two distinct curves – the epochs of the SED observations can be compared with the light curve (section 2.3.2).

We next tried to identify the donor and/or the white dwarf. At the blue end of the spectrum broad Balmer absorption lines are indicative of the white dwarf. Conversely if the Balmer jump is visible in emission then the disc is much brighter than the white dwarf. Absorption from the Mg triplet at 5200 \AA is indicative of an M dwarf donor as is a rising continuum broken by TiO ‘sawtooth’ absorption lines. In addition a blackbody curve in the ultraviolet or infrared SED can identify a white dwarf or M dwarf respectively. Care was taken to distinguish absorption lines due to a white dwarf from those of a disc. Disc absorption lines tend to be flat-bottomed as they are influenced by Doppler broadening due to Keplerian velocities whilst photospheric Balmer absorption lines are affected by pressure broadening due to the high surface gravities of white dwarfs. A clear white dwarf signature in the spectrum is indicative of a low level of accretion; if the donor is also not visible then this is typically a WZ Sge candidate.

We then considered the wavelengths of the lines in the spectrum. In addition to the lines exhibited in the examples in section 2.2 we firstly looked for the presence of S II 6717 \AA which is indicative of contamination by a nebula and is not seen in CV spectra. Secondly we looked for the strong wide emission lines at arbitrary wavelengths which are associated with highly red-shifted extra-galactic sources such as quasars and thirdly we looked for He II 4686 \AA emission which is indicative of a polar or intermediate polar particularly if the ratio of its equivalent width to that of $H\beta$ is greater than 0.4 (Silber, 1992)

The shape of emission lines was also considered. Wide Balmer lines are indicative of an accretion disc and hence dwarf novae – the width will depend upon the inclination of the system (Horne & Marsh, 1986). Furthermore if they are double-peaked with a central absorption core then they are likely to be eclipsing. Asymmetric emission lines are associated with the velocity dispersion of the accretion stream of polars whilst very thin lines are typical of nebulae and detached systems.

Lastly we also superimposed upon the SDSS spectrum the five SDSS photometric magnitudes obtained in the original observations. These can reveal inconsistencies and in particular can reveal cyclotron humps (due to one observation being taken at an orbital phase when the cyclotron emission peaked).

2.3.2 Light curves

Archival light curves from the CRTS, ZTF and *TESS* were obtained from online archives; Caltech, IRSA (Rebull et al., 2019) and Lightkurve (Lightkurve Collaboration et al., 2018) respectively. We inspected these for historical outbursts, to provide confirmation of a dwarf nova classification, and also for eclipses to obtain orbital periods. The long

span of this data (over 20 years) also reveals many state changes that are indicative of certain magnetic CVs (see Figs. 2.13 and 2.16) and novalike variables (Fig. 2.9).

We generated periodograms in an attempt to determine orbital periods, from these light curves. Prior to generating the periodogram we cropped any outbursts from the light curve which was then de-trended typically using a polynomial fit. Periodograms of the light curve were then produced using a Fourier transform and also an orthogonal multi-harmonic analysis of variance (Schwarzenberg-Czerny, 1996)[‡]. Potential periods were identified from peaks in the periodogram that exceeded a false alarm probability of five per cent; the results were then validated by phase-folding the original light curve on the potential period (see Fig. 2.17). The shape of the phase-folded light curve not only validates the period but also determines the orbital period which may be twice as long. This is because there are many potential causes for modulation of the light curve. Eclipses may occur once or twice per orbital cycle whilst ellipsoidal modulation, caused by light from the tidally-distorted donor, will yield two peaks per orbital cycle. Cyclotron beaming is another case where the waveform may show multiple peaks per orbital cycle.

Knowledge of the period assists classification; SU UMa and ER UMa CVs typically have $P_{\text{orb}} < 3\text{ h}$ (Ritter & Kolb, 1998), WZ Sge CVs have even shorter periods whilst U Gem and Z Cam CVs typically have $P_{\text{orb}} > 3\text{ h}$.

Whilst some periodograms show an unambiguous period others leave room for doubt due to aliases and harmonics for example; we have indicated such periods with a colon (:). Ellipsoidal modulation of the light curve can also result in the true orbital period being twice the strongest period in the periodogram; this can often (but not always) be revealed by folding the light curve on the longer period.

2.3.3 Hertzsprung–Russell and Colour–Colour Diagrams

The position of a CV on the Hertzsprung–Russell (HR) diagram aids classification as many CV types congregate in specific sections of the diagram (see Fig. 2.18 Fig. 2 in Abril et al. 2020 and Fig. 4.7). Absolute magnitudes require knowledge of the distance of a CV which is normally derived from *Gaia* parallaxes and hence CVs without a *Gaia* counterpart cannot be positioned. Even when *Gaia* data exists positions can be misleading if the parallax accuracy is poor or the CV is subject to significant reddening. A further issue is that CVs are intrinsically variable with outbursts, eclipses and orbital variations contributing to observed errors. Figure 2.18 shows a subset of the CVs from SDSS I to IV where systems with inaccurate parallaxes ($\varpi/\sigma_{\varpi} < 10$) or inaccurate colour magnitudes (`phot_g_mean_flux_over_error`<10,

[‡]The analysis of variance (ANOVA) algorithm is designed for obtaining the periodogram from a non-sinusoidal light curve with periodic short duration pulses such as that of an eclipsing CV. For a given SNR it will more reliably recover the periodogram of a pulsating signal than a Fourier transform (which remains the most effective algorithm for a sinusoidal signal).

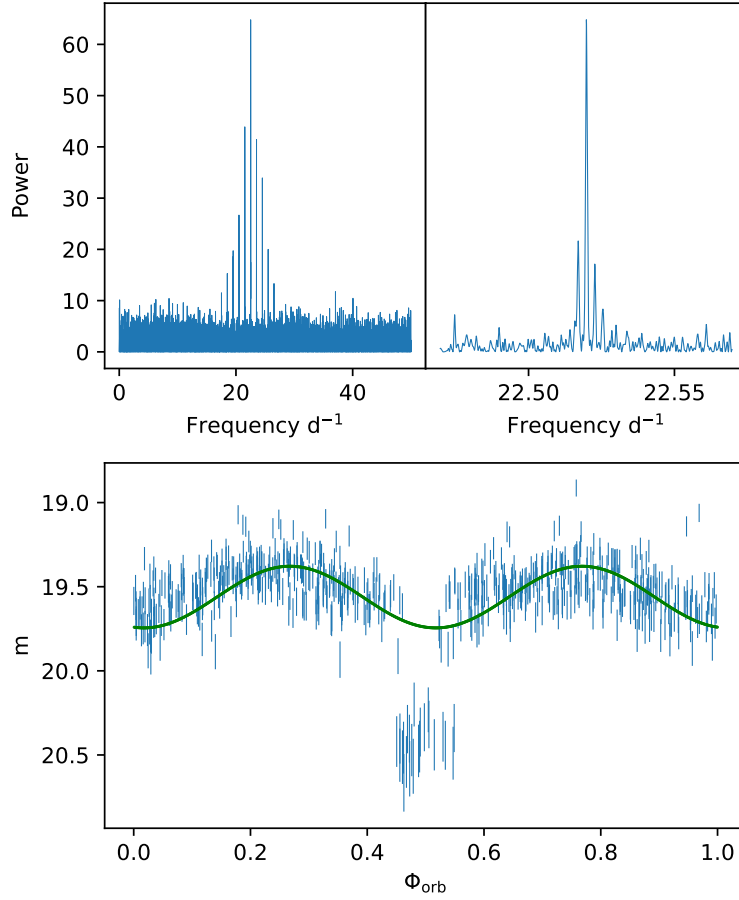


Figure 2.17: A Fourier transform of the light curve of SDSS J015803.40+282303.6, an eclipsing CV, yields a particularly clear periodogram. Top left panel: The aliases around the central frequency are separated by a frequency of once per day – reflecting the nightly sampling. Top right panel: The central peak provides a good estimate of a period which can then be used to seed a sine fit of the data yielding $f = 22.51981(3) \text{ d}^{-1}$. Bottom panel: A plot of the data folded at twice the period with the best fit superimposed. In this case $P_{\text{orb}} = 2/f$ due to ellipsoidal modulation although the corresponding frequency (11.2599 d^{-1}) is barely visible in the periodogram. This can be seen in the bottom plot with the deep eclipse of the white dwarf by the donor at $\phi \simeq 0.5$ and the two peaks at 0.25 in phase either side. In this case there is no doubt which is the correct alias but more generally the error has to take account of the possibility of an incorrect alias being selected.

phot_bp_mean_flux_over_error<10, or phot_rp_mean_flux_over_error<10) have been removed in line with [Lindgren et al. \(2018\)](#); [Lindgren \(2018\)](#).

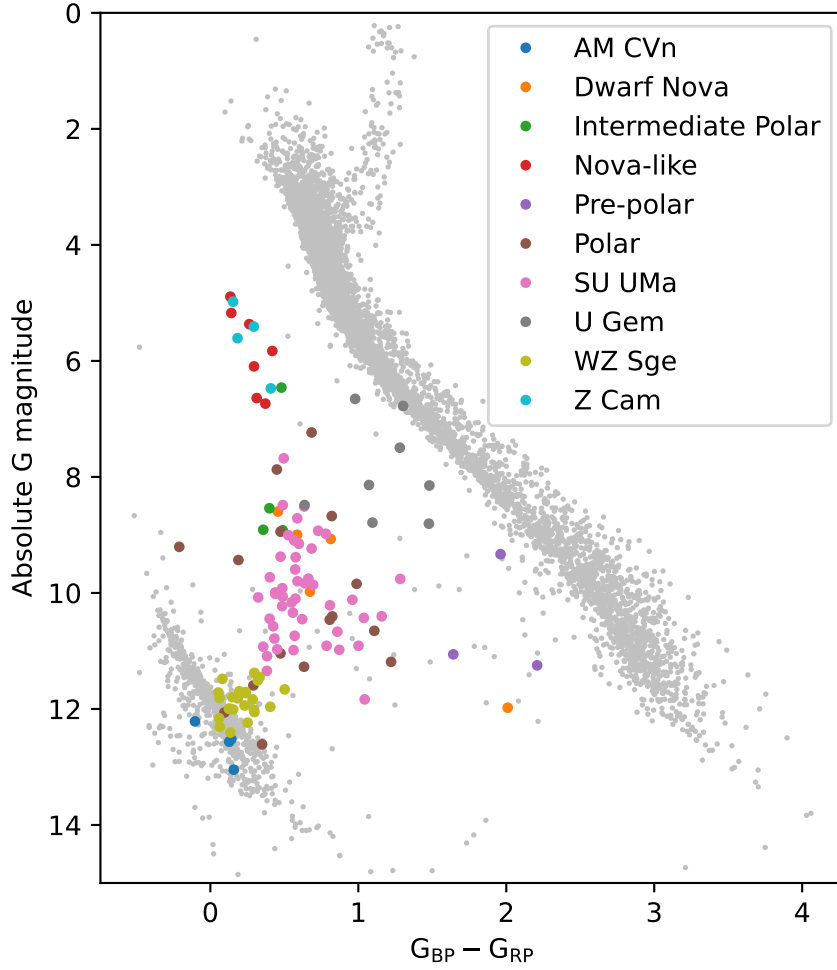


Figure 2.18: HR diagram showing the CVs from SDSS I to IV where the astrometric and photometric errors are less than 10 per cent. The grey background consists of those *Gaia* objects closer than 100 pc with *GALEX* observations to increase the proportion of white dwarfs (which are UV-bright). The colours refer to CV types (see section 2.2). Note the concentration of AM CVn and WZ Sge CVs near the white dwarf cooling sequence with SU UMa CVs spreading out towards the main sequence. Novalike variables and Z Cam CVs are concentrated around $5 < G_{\text{abs}} < 7$ as their high \dot{M} results in large optical luminosity.

Where a *Gaia* counterpart does not exist, or does not have a parallax, a colour-colour diagram based on SDSS photometry is an alternative (see Fig. 2.19). This is typically the case for faint systems with apparent magnitude $m \gtrsim 20$. These approaches are somewhat complementary as SDSS photometry saturates at $m \simeq 15$ and so cannot position bright CVs.

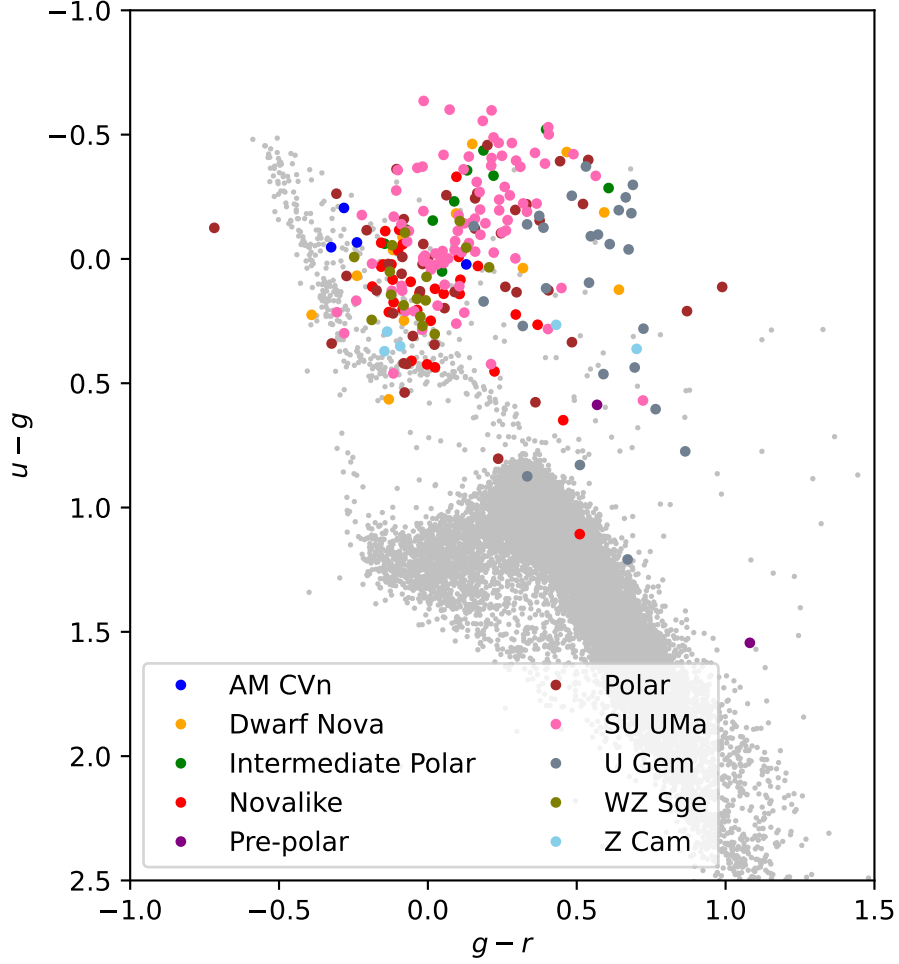


Figure 2.19: Colour-colour diagram showing the CVs from SDSS I to IV which have reliable SDSS photometry (where the magnitude of each colour is greater than 15.5 to avoid saturation and the magnitude error is less than 0.05). The grey background shows a collection of spectroscopically observed SDSS stars to guide the eye. The dense lower area forms the main sequence and the upper area is the white dwarf cooling sequence. Note the concentration of SU UMa and WZ Sge CVs on and above the white dwarf cooling sequence.

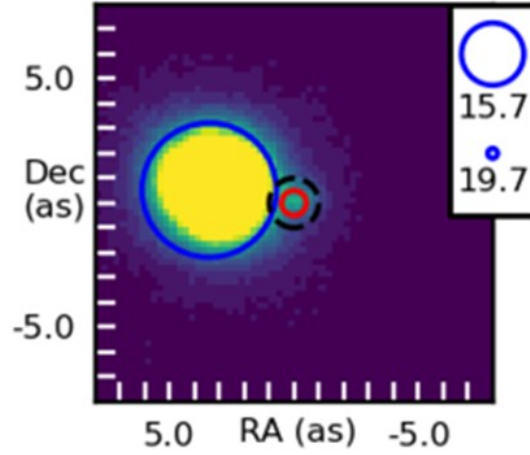


Figure 2.20: Pan-STARRS cutout of SDSS J075117.09+144423.5 showing the potential for the contamination of fibre spectroscopy. SDSS J075117.09+144423.5 has an apparent *Gaia* magnitude $m_G = 17.7$ whereas its neighbour, at a distance of 3.38 arcsec, has $m = 14.1$. The red circle denotes the target, the black dotted circle denotes the nominal coverage of an SDSS fibre (2 arcsec) and the blue circle is centred on the *Gaia* coordinates of the neighbour scaled according to the *Gaia* G magnitude. The *Gaia* coordinates are based upon EDR3 with an epoch of 2016 whilst the Pan-STARRS epoch is around 2012 and so a lack of alignment is a prompt to check proper motions to see if the contaminant was closer when the spectrum was observed.

2.3.4 Imaging

Pan-STARRS (Chambers et al., 2016) cutout images for each CV were obtained from the PS1 Image Cutout Server at STScI (Flewelling et al., 2020). We superimposed circles for each *Gaia* object and the nominal coverage (2 arcsec) of an SDSS fibre (Fig. 2.20). The resulting image shows whether there is potential contamination of a spectrum from neighbouring objects, nebulae or background galaxies. In addition we superimposed circles for any *GALEX* observations. CVs often have *GALEX* observations but the accuracy of the coordinates of *GALEX* observations can be incorrect by a few arcsec and the image shows whether an observation could be associated with the wrong object.

2.4 Identification of tertiary systems

Close binaries can be part of multiple systems accompanied by one or more distant companions. It is an open question how frequently this occurs; Tokovinin et al. (2006) concluded that 63 per cent of close solar-type binaries had additional companions whilst Raghavan et al. (2010) suggest that around eight per cent of close solar-type binaries are part of a triple system and have a distant companion. They are significant as the distant star can influence the evolution of the inner binary through Lidov-Kozai cycles (Fabrycky & Tremaine, 2007; Toonen et al., 2016). We searched *Gaia* EDR3 for such systems by identifying candidate stars within 30 arcsec of each of the CVs in our sample. Potential companions can be expected to have similar proper motions. Proper motions, and hence differences between them, will scale inversely with distance. We therefore adopted the following metric where the denominator is a proxy for distance:

$$\sqrt{\frac{(\text{pmra}_{\text{cv}} - \text{pmra}_{\text{cand}})^2 + (\text{pmdec}_{\text{cv}} - \text{pmdec}_{\text{cand}})^2}{\text{pmra}_{\text{cv}}^2 + \text{pmdec}_{\text{cv}}^2}} < 0.05 \quad (2.1)$$

The 2D separation was calculated by multiplying the angular separation by the Bailer-Jones et al. (2018) distance; the errors on the Bailer-Jones et al. (2018) distances are too large to estimate the radial separation. Estimating the binding energy is a test of whether these systems are gravitationally bound to the CV by comparison with known wide systems (see Fig. 2.21 and Faherty et al. 2011). We calculate the binding energy using:-

$$-E_{\text{bind}} = G \frac{(M_{\text{WD}} + M_2)M_3}{D} \quad (2.2)$$

where M_3 is the mass of the companion at a distance D . A rough estimate is sufficient for this purpose and so we assume typical values of $M_{\text{WD}} = 0.83 M_{\odot}$ and a donor of mass $M_2 = 0.14 M_{\odot}$. We estimate M_3 from the position of the star in the *Gaia* HR diagram.

2.5 Summary

In this chapter we have explained the taxonomy of CVs and the methods used to classify them based on observations and archived data. These methods are applied in subsequent chapters.

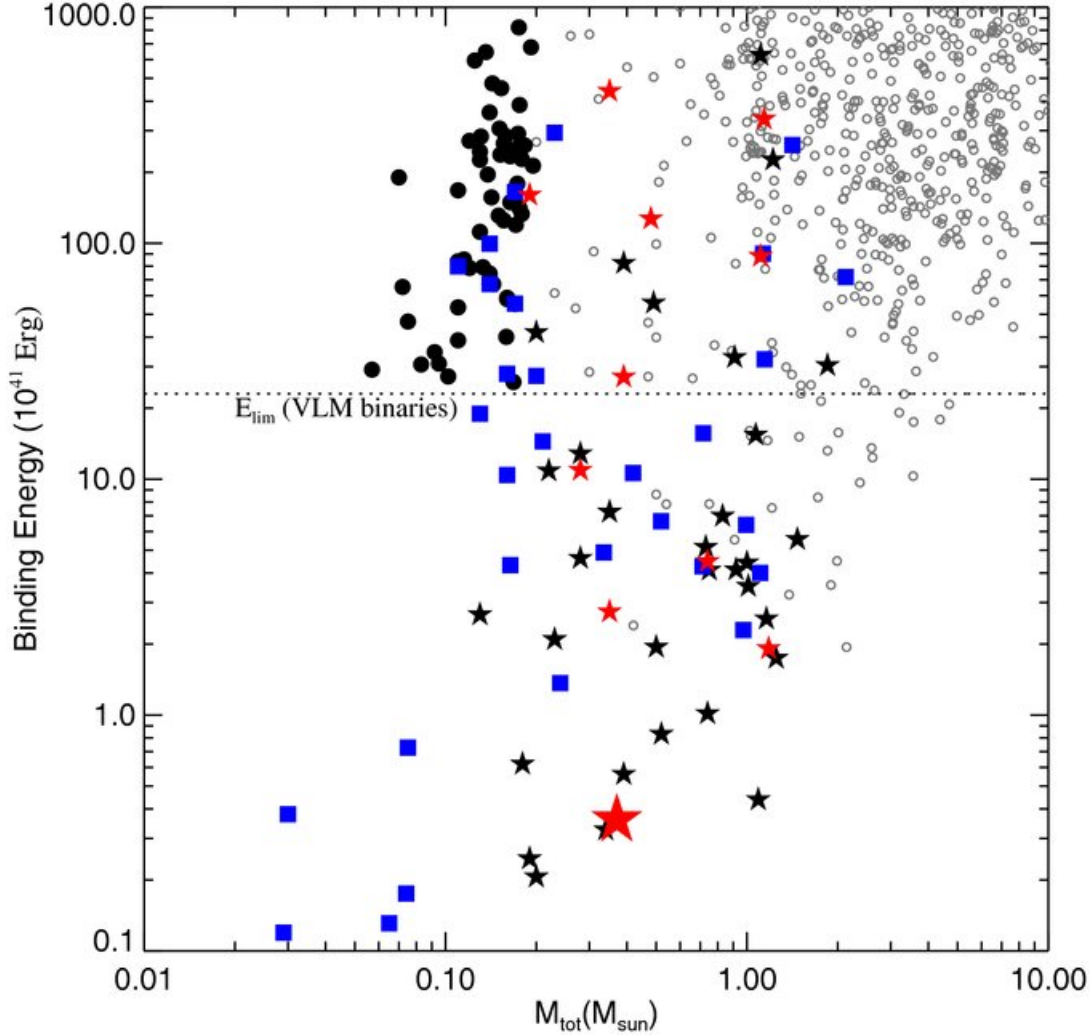


Figure 2.21: Figure 8 from [Faherty et al. \(2011\)](#) showing the binding energies from known stellar systems as open circles. Objects marked with filled circles are tight low-mass systems (typically $M_{\text{tot}} < 0.2 M_{\odot}$ and $D < 20$ AU). The other objects are not relevant here: wide systems ($D > 100$ AU) containing an ultracool dwarf companion are marked as five point stars and those highlighted in red also contain a very low mass binary ($M_{\text{tot}} < 0.2 M_{\odot}$). Those marked as squares are systems containing a tight or widely separated ultracool dwarf with an age < 500 Myr. The brown dwarf 2MASS J0850+1057 system is the enlarged five-point star.

Chapter 3

An extraordinary windy novalike

3.1 Introduction

As explained in Section 2.2.1 CVs above a critical \dot{M} appear as novalikes which have steady, hot and luminous discs (Meyer & Meyer-Hofmeister, 1984; Shafter et al., 1986; Cannizzo et al., 1988). Some novalikes have mass transfer rates close to the critical value of \dot{M} , and cycle between undergoing regular outbursts and states where their discs are in a steady hot state (Buat-Ménard et al., 2001). Even though the accretion discs in novalikes are in a (relatively) steady luminous state, they can exhibit small ‘stunted’ outbursts (Honeycutt et al., 1998). In addition, some novalikes occasionally enter a low state during which mass loss from the donor drops significantly, or even shuts off completely (Honeycutt & Kafka, 2004). During this time they may exhibit dwarf nova outbursts (King & Cannizzo, 1998).

Discovering new, bright examples of CVs remains important to grow the arsenal of diagnostic tools that are available to investigate these topics. However, because of their steady discs, novalike variables have remained difficult to identify, in contrast with dwarf novae that stand out in photometric time-domain surveys because of their large-amplitude variability (Gänsicke, 2005; Drake et al., 2014b; Breedt et al., 2014; Szkody et al., 2020).

Here we report a detailed study of the bright and nearby novalike ASAS J071404+7004.3 (hereafter ASAS J0714+7004). ASAS J0714+7004 was identified as the optical counterpart to the X-ray source 1RXS J071404.0+700413, and a potential variable star, by Kiraga & Stepień (2013) who suggested it might be a CV with a putative period of 22.4 d. ASAS J0714+7004 came to our attention as part of a project to identify white dwarf binary candidates located between the main sequence and the white dwarf cooling sequence, using a combination of *Gaia* and *GALEX* photometry and astrometry (Inight et al. in prep).

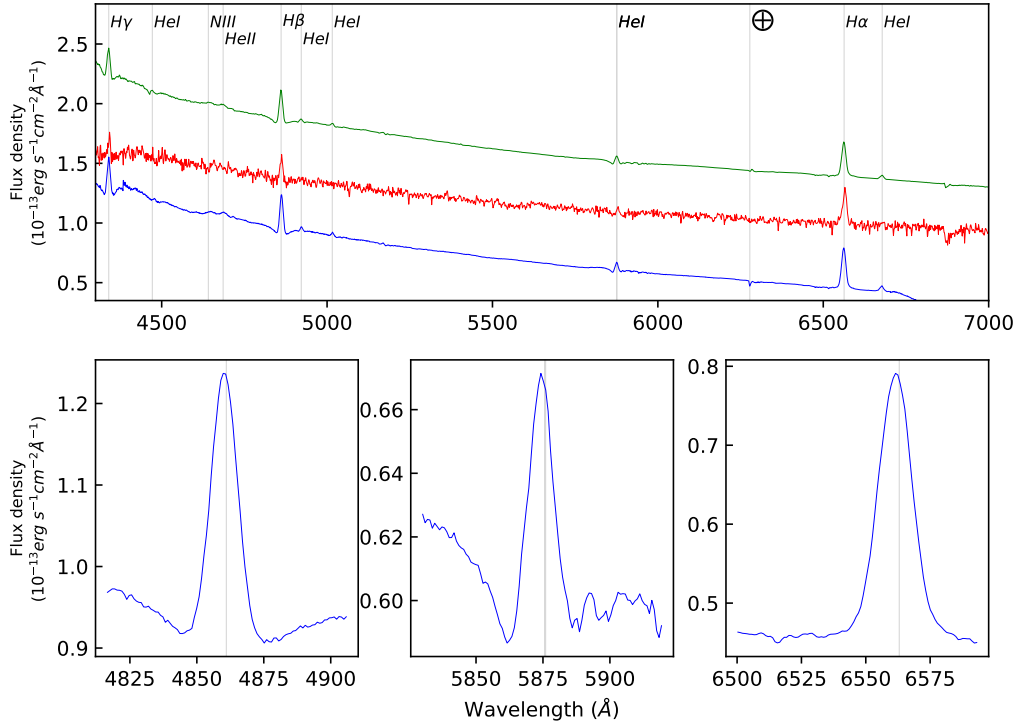


Figure 3.1: Spectra of ASAS J071404+7004.3. Top panel: The first spectrum (red – offset by 0.6 flux units) was obtained on 2020 February 6. The second spectrum (blue) is the average of the INT observations. The third spectrum (green – offset by 1.0 flux units) is the average of the MDM observations. Bottom panel: The average INT spectra for H β (left), He I 5876 Å (centre) and H α (right). The H β line shows an emission line sitting in a broad absorption line, the He I 5876 Å triplet line shows a P Cygni profile and the H α line is purely in emission although showing slight traces of a P Cygni profile.

We summarise our observations and provide a qualitative description of the system in Section 3.2, analyse these observations to extract the physical parameters of the system in Section 3.3 and then discuss the implications (Section 3.4) and conclusions (Section 3.5).

3.2 Observations

3.2.1 Spectroscopy

We obtained an identification spectrum on 2020 February 6 using a 280 mm Schmidt Cassegrain telescope (SCT) equipped with a Shelyak LISA spectroscope, giving a spectral resolution of $R \simeq 1000$. The spectrum was integrated for 30 min before being stopped by clouds which limited the signal-to-noise ratio. The data were corrected with bias, dark and flat frames, wavelength calibrated using the integrated ArNe lamp, and corrected for the instrumental response function and atmospheric losses using the

spectrum of a spectrophotometric standard star taken at the same altitude immediately prior to the target. Processing was performed using the ISIS spectral analysis software^{*}. The spectrum was then calibrated in absolute flux using a concurrently recorded V magnitude observation using the method described on the BAA website[†]. The SCT spectrum (Fig. 3.1) exhibits a blue slope in the continuum with broad and shallow $H\beta$ and $H\gamma$ absorption lines filled in by single-peaked Balmer emission lines, and additional emission lines from He I, unambiguously identifying this system as a CV. With a median magnitude of $V \simeq 11.8$, ASAS J0714+7004 is among the $\simeq 20$ brightest CVs known (Ritter & Kolb, 2003).

ASAS J0714+7004 was then observed using the Intermediate Dispersion Spectrograph (IDS) mounted on the 2.54 m Isaac Newton Telescope (INT) on the island of La Palma, using the R632V grating at a central wavelength of 5720 Å. This setup covers the wavelength range 4383–6704 Å at a dispersion of 0.89 Å/pixel. A total of 264 120 s exposures were taken over a period of 13 days in February 2020 (hereafter the February INT data) and a further long sequence on 2020 December 13 (hereafter the December INT data) – see Table 3.3 for details.

All of the INT spectra were optimally extracted and reduced using the PAMELA and MOLLY reduction software (Marsh, 1989). In order to perform the flux calibration we fitted a spline to the continua of spectrophotometric standard stars taken on the same night as the observations. We then used their published flux as a reference, see e.g. Marsh (1990). For the wavelength calibration, Cu+Ne and Cu+Ar arcs were observed at the start and end of each observation, and approximately once every hour in between during the longer sequences. As a final step in wavelength calibration we extracted the sky spectrum and measured the deviation of the telluric O I emission line at 5577.4 Å from its laboratory wavelength and shifted our science spectra to align with this feature.

Additional spectra of ASAS J0714+7004 were obtained prior to the SCT and ING observations[‡] with the 1.3 m McGraw-Hill and 2.4 m Hiltner telescopes at the MDM Observatory on Kitt Peak in Arizona; Table 3.2 gives a journal. These data will be referred to as the MDM spectra hereafter. On both telescopes we used the modular spectrograph (modspec), which covered from 4210 to 7560 Å with a resolution of about 4 Å (full-width at half maximum). To calibrate the wavelengths, we took spectra of Hg, Ne, and Xe lamps in twilight, and derived zero-point shifts to the solution using the night-sky background lines. We flux-calibrated the spectra using observations of standard stars; experience suggests that the zero point of these calibrations is accurate to $\simeq 30$ per cent. In addition, the continua in modspec data sometimes show unphysical distortions, which tend to average out.

^{*}<http://www.astrosurf.com/buil/isis-software.html>

[†]<https://britastro.org/sites/default/files/absfluxcalibration.pdf>

[‡]Upon posting the submitted version of this paper to arXiv, John Thorstensen reminded the other authors that he had observed this star already in 2013.

Table 3.1: Stellar parameters of ASAS J0714+7004.

Parameter		Value	Refs
RA J2000	α [h:m:s]	$07:14:04.654486 \pm 0.00001$	1
Dec J2000	δ [d:m:s]	$+70:04:18.400755 \pm 0.00001$	1
<i>Gaia</i> EDR3 source_id		1109608206832496512	1
Parallax	ϖ [mas]	4.703 ± 0.02	1
Distance	d [pc]	210.15 ± 1.0	2
Apparent magnitude	G [mag]	11.814 ± 0.01	1
Absolute magnitude	M_G [mag]	5.20 ± 0.016	1,2,4
Proper motion	μ_α [mas yr ⁻¹]	26.007 ± 0.02	1
	μ_δ [mas yr ⁻¹]	-36.923 ± 0.025	1
Mass transfer rate	\dot{M} [$10^{-9} M_\odot$ yr ⁻¹]	4-9	3
Period	P_{orb} [h]	3.2794894 ± 0.0000008	3
Epoch	HJD [d]	2456597.8330 ± 0.0005	
Inclination	i [°]	50 – 70	3

¹ [Gaia Collaboration et al. \(2021\)](#); ² [Bailer-Jones et al. \(2021\)](#); ³ this paper;

⁴ Not taking account of extinction

The average of the 264 INT spectra (Fig. 3.1) is very similar to the SCT identification spectrum and the MDM average spectrum, although it has a higher spectral resolution and signal-to-noise ratio. It contains strong single-peaked Balmer emission lines embedded within broad and shallow absorption lines. Overall, the morphology of the spectrum is that of a novalike, with the absorption arising from an optically thick disc ([Dhillon, 1996](#); [Haug & Drechsel, 1985](#); [Rosino et al., 1993](#)). Unlike dwarf novae, single-peaked Balmer lines are not indicative of low inclination ([Thorstensen et al., 1991a](#); [Rodríguez-Gil et al., 2007a](#); [Neustroev et al., 2011](#)). Strong emission lines in novalikes are in fact associated with high inclination (see e.g. Fig. 1 in [Matthews et al. 2015](#)). This is because they are believed to originate in the disc winds and hence appear strongest relative to the underlying disc emission at higher inclinations. The He I 5876 Å line exhibits a P Cygni profile which supports this theory.

3.2.2 Photometry

The long-term light curve of ASAS J0714+7004 obtained by ASAS-SN ([Shappee et al., 2014](#)) displays quasi-periodic brightness variations on time scales of $\simeq 20$ d with an amplitude of $\simeq 0.5$ mag (panels (a), (b) and (c) in Fig. 3.2). In order to investigate the nature of these variations, we began intensive photometric monitoring of the system using small-aperture telescopes throughout February and March 2020. However, during this campaign, ASAS J0714+7004 did not display much variability, remaining at an average magnitude of $V \simeq 11.85 \pm 0.12$ mag, although the quasi-periodic brightening resumed again in June 2020 (panel (d) in Fig. 3.2).

A peculiar event captured by the ASAS-SN data was a drop in the minimum

brightness in between the quasi-periodic brightening in April 2015, whereas the maximum brightness remained constant (panel (b) in Fig. 3.2). This ‘low state’ lasted at least two months; unfortunately the ASAS-SN observations were stopped due to ASAS J0714+7004 moving into day time. When the observations resumed in August 2015, the system had returned to the normal state.

The *TESS* satellite (Ricker et al., 2015) observed ASAS J0714+7004 in short-cadence (2 min exposures) during Sector 20 (2019 December 24 to 2020 January 21) and Sector 26 (2020 June 8 to July 4) and in ultra-short cadence (20 s exposures) during Sector 40 (2021 June 24 to July 23). The space-based photometry covers part of the inactive phase (panels (e) and (f) in Fig. 3.2), the first brightening following this inactive phase (panels (g) and (h)), and two further brightenings (Fig. 3.2, panel (d)). All the *TESS* data sets reveal substantial periodic short-term variability.

3.2.3 *Swift*

ASAS J0714+7004 was observed in January 2021 using the Neil Gehrels *Swift* Observatory (Evans et al., 2009). Data were obtained from both the ultraviolet optical telescope (UVOT) (Roming et al., 2005) and X-ray telescope (XRT) (Burrows et al., 2005). Ten observations were obtained over a 22 d period with exposure times $\simeq 10$ min, see Table 3.4. Six of the ultraviolet observations used the *U* filter (mean wavelength 3492 Å and width 866 Å) and four used the *M2* filter (mean wavelength 2272.21 Å and width 533.85 Å). The XRT covers the range 0.2 – 10 keV and has two modes – Windowed Timing (WT) with continuous readout (and only one-dimensional imaging) and Photon Counting (PC) where the exposure length is 2.5 s. We have only used PC data. The XRT data were processed using the automated pipeline to produce an average spectrum and a light curve. The UVOT data were saturated in both *U* and *M2* filters and therefore a modified approach (Page et al., 2013) was used to obtain photometry by measuring the ‘streak’ as the CCD is read out.

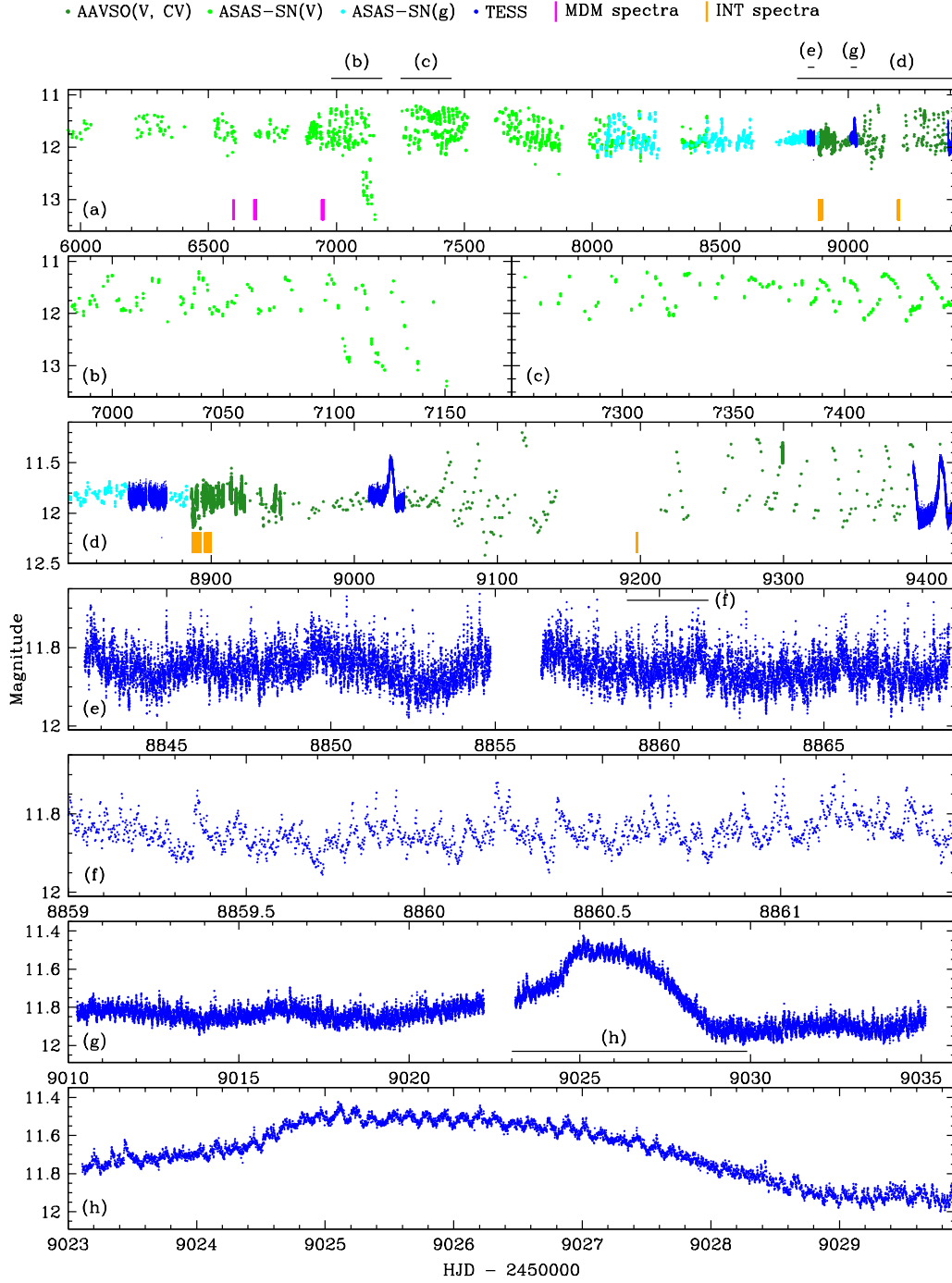


Figure 3.2: Ground and space-based photometry of ASAS J0714+7004. The horizontal bars above the top panel, and within panels (e) and (g), indicate the date range of the zoom-in views. Note the change in the scale of the magnitude axis in the different panels. The system exhibits quasi-periodic brightenings most of the time, but experienced a fainter state (a,b) as well as a phase of relative inactivity (a,e,f). The high-cadence *TESS* data reveals short-term flickering (e,f) and low-amplitude orbital modulations at the orbital period (g,h).

Table 3.2: Journal of MDM observations.

UT (start)	Tel.	HA start	HA end	Exp(s)	N_{exp}
2013-11-01 09:39	M	−02:19	+00:55	600	3
2014-01-22 11:05	H	+04:30	+05:04	480	4
2014-01-26 11:06	H	+04:47	+05:05	240	4
2014-01-27 06:22	H	+00:06	+00:50	480	4
2014-10-12 12:37	H	−00:40	−00:32	480	1
2014-10-13 12:49	H	−00:24	−00:19	300	1
2014-10-14 12:55	H	−00:15	−00:04	300	2
2014-10-15 12:10	H	−00:56	−00:06	300	9
2014-10-16 07:17	H	−05:46	−00:03	240	17

Telescopes are: M - McGraw-Hill 1.3 m; H - Hiltner 2.4 m.

Hour angles are in hours and minutes.

Table 3.3: The journal of INT observations for the February and December proposals.

Date	JD (start)	N (observations)	Duration (min)
2020-02-08	2458887.583423	52	117.61
2020-02-09	2458888.530952	52	124.56
2020-02-10	2458889.465164	54	122.25
2020-02-12	2458891.600877	2	4.20
2020-02-13	2458892.455516	49	113.99
2020-02-13	2458892.543982	44	117.47
2020-02-16	2458895.603163	1	2.00
2020-02-17	2458896.607681	2	4.20
2020-02-18	2458897.602185	2	4.20
2020-02-19	2458898.575209	2	4.20
2020-02-20	2458899.526425	2	4.20
2020-02-20	2458899.581305	2	4.20
2020-12-13	2459197.430520	195	522.0

Table 3.4: The journal of *Swift* observations. The central wavelengths of the *U*-band and *M2*-filter are 3492.67 Å and 2272.71 Å, respectively.

Date (UTC)	UVOT exposure (s)	XRT PC exposure (s)	UV Filter	UV Mag (Vega)
2020-12-29 23:28:31	76.2	70.0	<i>U</i>	10.947(129)
2021-01-02 17:56:34	702.8	699.2	<i>U</i>	11.040(45)
2021-01-04 00:13:36	583.5	574.7	<i>M2</i>	10.510(39)
2021-01-06 08:10:35	557.9	552.3	<i>U</i>	10.785(43)
2021-01-08 09:25:38	374.1	684.5	<i>M2</i>	9.828(32)
	316.2		<i>M2</i>	9.680(32)
2021-01-10 11:08:21	412.8	402.8	<i>U</i>	10.409(38)
2021-01-14 08:56:35	425.2	423.7	<i>U</i>	
2021-01-16 07:05:34	747.3	782.5	<i>M2</i>	10.627(38)
2021-01-18 08:32:35	564.5	557.5	<i>U</i>	10.897(44)
2021-01-20 06:27:34	544.8	540.0	<i>M2</i>	10.430(38)

3.3 Analysis

The morphology of the spectroscopic and photometric data argues against a dwarf nova nature of ASAS J0714+7004. Although, at a first glance, the quasi-regular brightenings may seem unusual (see the discussion in Sect. 3.4.4), we conclude that this system is best classified as a novalike variable.

3.3.1 Orbital period

The primary motivation for obtaining the fast cadence INT observations was to measure the evolution of radial velocities, which we carried out using the MOLLY software package (Marsh, 2019). We also used MOLLY to process the MDM spectra. We normalised the continuum of the spectra using a straight line fit, and then determined the central wavelength of the H α emission line by convolving each spectrum with a Gaussian template with a standard deviation of $\sigma = 300 \text{ km s}^{-1}$. A Fourier analysis (Deeming, 1975) of the resulting INT and MDM radial velocity time-series was then used to compute a periodogram (Fig. 3.3 green line in the top panel). The highest peak in the periodogram identifies the orbital period as $P_{\text{orb}} \simeq 3.28 \text{ h}$, albeit the periodogram is plagued by a substantial alias structure due to the sparse sampling of the radial velocities (Fig. 3.3 middle panel).

The Fourier transform of the Sector 20,26 and 40 *TESS* photometry results in a much less aliased periodogram (blue in Fig. 3.3) which, however, also contains some alias structure resulting from the gaps in the middle of the *TESS* observations (panel (d) in Fig. 3.2). We note that our time-series analysis of the *TESS* data did not reveal any other periodic signal such as that seen in the novalike V341 Ara (which was interpreted as a beat frequency between the orbital period and the retrograde precession of the accretion disc in that system (Fig. 8 in Castro Segura et al. 2021)).

The combined radial velocity and photometric periodograms overlap only for one unique period, which we therefore identify as the true orbital period of ASAS J0714+7004 (middle panel in Fig. 3.3). In order to improve the precision of the orbital period, we performed a sinusoidal fit to the INT and MDM radial velocity data, which spans a much longer temporal baseline, with five distinct epochs, than the *TESS* photometry, and hence provides a more accurate value of the period. We found $P = 3.2794894(8) \text{ h}$ and an epoch of $\text{HJD(UTC)} = 2456597.8330(5)$. We define the epoch as being the blue to red crossing of the radial velocity. The velocity amplitude of the fit is $143.5(2.2) \text{ km s}^{-1}$. The phase-folded data are shown in (Fig. 3.3 bottom panel). A trailed spectrum of the December INT data is shown in Fig. 3.12.

The integrated flux from the H α line measured from the December INT data appears to lag the radial velocity variation by $\simeq 90^\circ$ (see Fig. 3.4). Assuming that the H α emission originates in the disc, then the radial velocity variation will track the

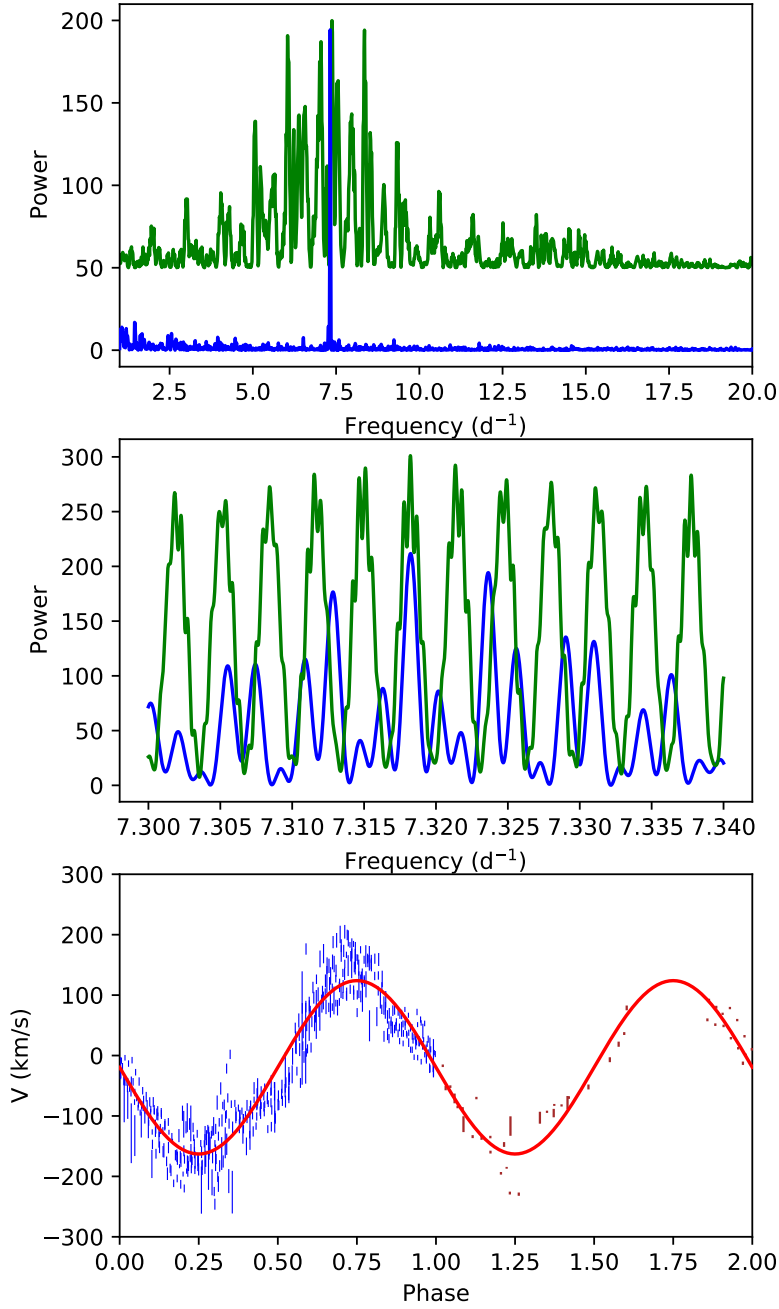


Figure 3.3: Top panel: Power spectra of the time-resolved radial velocity variations measured from the H_{α} line (in green with offset added) and the Sector 20, 26 and 40 *TESS* light curves (blue). There is a clear peak at ~ 3.28 h. Central panel: Detail from the top plots with the radial velocity plot rescaled. Bottom panel: The radial velocities of the INT data (blue) and the MDM data (brown) phase-folded using the adopted period of 3.2794894 h, superimposed by a sine-fit to the data.

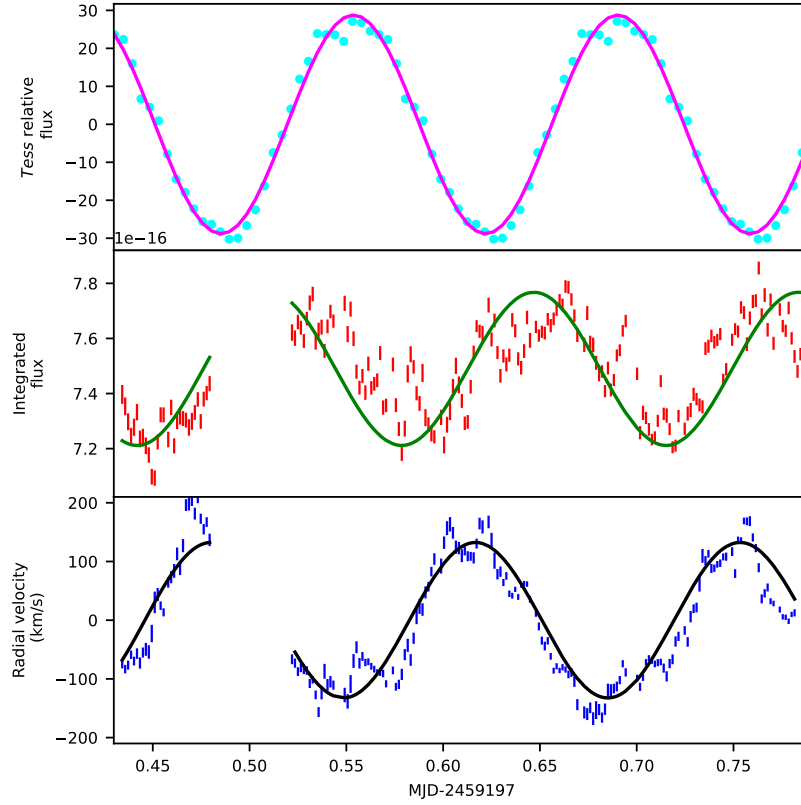


Figure 3.4: The radial velocity of the $H\alpha$ core (bottom panel) and the integrated flux from the $H\alpha$ line (centre panel) for the December INT data together with the *TESS* photometry (top panel) binned and folded at the orbital period and projected onto the December timeline. Each dataset was fitted with a sinusoid at the orbital period. The integrated flux is offset by 0.241 cycles from the radial velocities whilst the *TESS* photometry is offset by 0.5 cycles.

movement of the disc (and hence the white dwarf at its centre) around the centre of gravity of the system. The peak of the integrated flux therefore occurs at the superior conjunction when the white dwarf is at its furthest point and the donor is at its closest. Thus, the relative phasing of the integrated line fluxes and radial velocities argues against the emission originating on the irradiated donor star.

3.3.2 The mass transfer rate

A key parameter of CVs is their mass transfer rate, \dot{M} . This parameter is difficult to determine in dwarf novae, where the disc effectively buffers the mass lost from the companion (Hessman et al., 2000), and cyclically flushes it onto the white dwarf. However novalikes such as ASAS J0714+7004 can be in a quasi-steady-state, facilitating the measurement of \dot{M} . Here, we estimate \dot{M} in ASAS J0714+7004 by modelling its spectral energy distribution (SED).

We have assembled the overall SED of ASAS J0714+7004 making use of available X-ray to infrared photometry (Pan-STARRS1, [Chambers et al. 2016](#); 2MASS, [Cutri et al. 2003](#); *WISE*, [Cutri et al. 2021](#); *Gaia*, [Gaia Collaboration 2020](#); ATLAS, [Tonry et al. 2018](#); APASS, [Henden et al. 2015](#) and *GALEX*, [Morrissey et al. 2007](#)) and of our *Swift* observations (Sect. 3.2.3).

The SED of ASAS J0714+7004 (Fig. 3.5) presents a steep blue slope from the infrared into the ultraviolet, with a significant drop in the spectral energy density in the X-ray regime. The system is sufficiently bright that the *GALEX* observations suffer from saturation effects ([Morrissey et al., 2007](#)) – the *Swift* UVOT photometry confirms that the *GALEX* photometry is not reliable, and therefore it was not included in the fit.

The optical magnitude of ASAS J0714+7004 is $\simeq 12$ mag and this can also be expected to saturate the Pan-STARRS1 data (saturation occurs at 12 – 14 mag dependent upon seeing [Magnier et al. 2013](#)) and the ATLAS data ([Tonry et al., 2021](#)). The saturated points were therefore ignored when obtaining the best fit and are not shown (except for *GALEX*) in Fig. 3.5.

In order to model the SED of ASAS J0714+7004, we have to account for the flux emitted by the individual components of the system, i.e. the disc, the white dwarf, the donor star and potentially also a hot boundary layer close to the white dwarf where up to half of the gravitational potential energy is released. The detailed structure, and even the presence of a boundary layer in CVs has been subject to decades of discussion ([Ferland et al., 1982](#); [Long et al., 1996](#); [Hertfelder et al., 2013](#); [Nixon & Pringle, 2019](#)), and, on the observational side, is severely limited by the fact that interstellar absorption severely hinders access to the extreme ultraviolet (EUV) emission of CVs[§]. In the case of ASAS J0714+7004, we note that whereas a putative boundary layer may contribute in the EUV, it will make only a minimal contribution when fitting the ultraviolet to infrared emission of the system (see Fig. 3.5). Here, we model the SED of ASAS J0714+7004 by the sum of the disc, the white dwarf, the donor and the boundary layer. In novalikes, the accretion disc is expected to be the primary source of optical and ultraviolet flux, in contrast the two stellar components have only relatively small contributions.

[§]The boundary layer is expected to have temperatures of a few 10^5 K, and hence its emission will peak in the Extreme Ultraviolet. This wavelength region is heavily absorbed by interstellar neutral hydrogen, and hence only a handful of nearby CVs have adequate observations, which led to conflicting results: [Long et al. \(1996\)](#) observed U Gem during outburst and concluded that the peak spectrum resembled a blackbody with $T_{\text{eff}} \simeq 140\,000$ K. Conversely a joint *ROSAT* and *EUVE* data analysis of the novalike IX Vel showed no blackbody emission ([van Teeseling et al., 1995](#)).

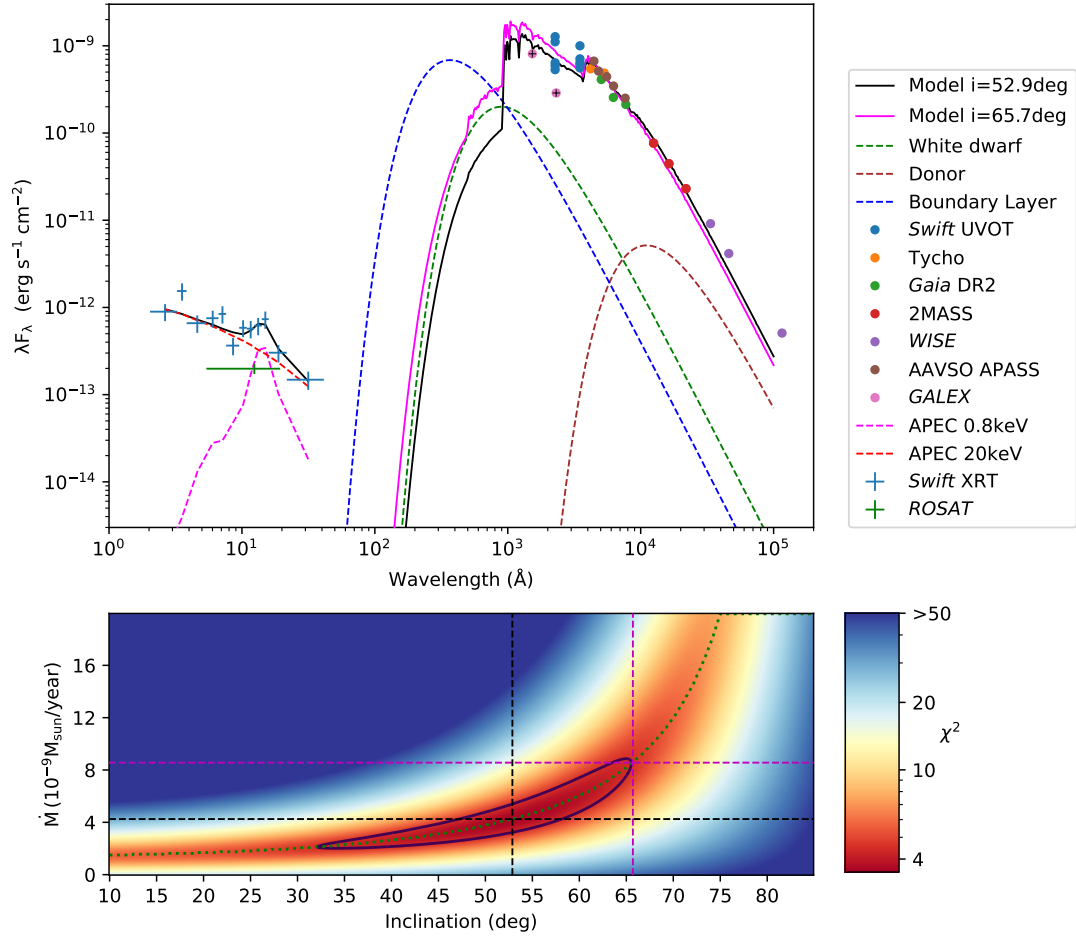


Figure 3.5: Multi-wavelength observations of ASAS J0714+7004 (see text for details). Top panel: Spectral energy density as a function of wavelength. The disc dominates the SED in the optical; dashed lines show the contribution of the other components. The boundary layer contribution is only notionally constrained by the observations. The black solid line shows the optimum fit whilst the magenta line plots a fit constrained by the estimate of inclination from Sect. 3.3.3. It is noticeable that the fits consistently undershoot the infrared observations. Such an infrared excess has been observed in other novalikes (e.g. Hoard et al., 2014), indicating that the adopted model is not accounting for all components in the system. The excess may be due to a dusty circumstellar disc (Hoard et al., 2007, 2009). Bottom panel: A heat map of the chi-squared of our model fit to the observed SED as a function of the two free parameters, i and \dot{M} . The green dotted line traces the degeneracy between the orbital inclination and the mass transfer rate, illustrating that the two parameters cannot be determined independently. The black line indicates the best fit to the SED, and the magenta line shows the estimate from Sect. 3.3.3. The solid purple line traces the 1 σ contour.

We model the disc as a set of 1000 concentric annuli of constant width between the inner and outer radii of the disc, $R_{\text{disc,i}}$ and $R_{\text{disc,o}}$, respectively. To determine the temperature $T(r)$ of each annulus we assume that the flux per unit surface area at radius r in the disc is given by (see chapter 5 of [Frank et al. 1992](#)):

$$F = \frac{3GM_1\dot{M}}{8\pi r^3} \left(1 - \left(\frac{R_1}{r} \right)^{1/2} \right) \quad (3.1)$$

where M_1 and R_1 are the mass and radius, respectively, of the white dwarf and \dot{M} is the rate of mass transfer. Given that the integrated flux is a function of the temperature,

$$F = \sigma T^4 \quad (3.2)$$

we obtain

$$T = \left(\frac{3GM_1\dot{M}}{8\pi\sigma r^3} \left(1 - \left(\frac{R_1}{r} \right)^{1/2} \right) \right)^{1/4} \quad (3.3)$$

We then used the BT-Settl (AGSS2009) spectral models ([Allard et al., 2012](#)) to represent the spectrum for each annulus based on the temperature from Eq. 3.3, $\log g = 4.0$ [¶] The shortcomings of using synthetic stellar spectra to model the emission of an accretion disc have been discussed at length, ([Wade, 1988](#)) however they are better than the alternative which is to use a blackbody spectrum.

The white dwarf temperature was treated as a function of \dot{M} using Eq. 2 in ([Townsley & Gänsicke, 2009](#)):

$$T_1 = 17\,000[\text{K}] \left(\frac{\langle \dot{M} [\text{M}_\odot \text{yr}^{-1}] \rangle}{10^{-10}} \right)^{\frac{1}{4}} \left(\frac{M_1 [\text{M}_\odot]}{0.9} \right) \quad (3.4)$$

For the donor star, we adopted a mass, radius, and effective temperature based upon the evolutionary track from Table 2 by [Knigge et al. \(2011\)](#). The emission of the white dwarf and the donor were modelled by two blackbodies of the corresponding temperatures and radii.

The fit shown in Fig. 3.5 was obtained by fixing $M_1 = 0.83 \text{ M}_\odot$ (the average value for CVs from [Zorotovic et al. 2011](#)) and $R_1 = 0.0122 \text{ R}_\odot$ (using the mass/radius relationships from [Bédard et al. 2020](#) available at ^{||}).

We also followed [Godon et al. \(2017\)](#) and assumed that the inner edge of the accretion disc is located one R_1 above the white dwarf surface. We followed [Harrop-](#)

[¶]The choice of $\log g = 4.0$ was constrained by the available coverage of the parameter space for values of $T_{\text{eff}} > 50000 \text{ K}$ and solar metallicity. CV discs are flat with typical surface gravities $\log g = 4-6$ depending upon radial distance from the centre of the disc; although in practice this is not a critical factor as pressure broadening will be dominated by Doppler broadening due to the Keplerian rotation of the disc.

^{||}<https://www.astro.umontreal.ca/~bergeron/CoolingModels/>

Table 3.5: System parameters adopted for fitting the spectral energy distribution.

Parameter		Value
Mass (white dwarf)	$M_1 [M_\odot]$	0.83
Mass (donor)	$M_2 [M_\odot]$	0.22
Separation	$a [R_\odot]$	1.11
Radius (white dwarf)	$R_1 [R_\odot]$	0.0122
Radius (donor)	$R_2 [R_\odot]$	0.30
Inner radius (disc)	$R_{\text{disc,i}} [R_\odot]$	0.0244
Outer radius (disc)	$R_{\text{disc,o}} [R_\odot]$	0.49
Temperature (donor)	$T_2 [\text{K}]$	3324

Allin & Warner (1996) and assumed that the outer radius of the disc (due to tidal truncation) is $0.7 \times R_{\text{L1}}$ where R_{L1} is the distance from the centre of the white dwarf to the inner Lagrange point given by:

$$R_{\text{L1}} = a (1.0015 + q^{0.4056})^{-1} \quad (3.5)$$

The inclination of the accretion disc and \dot{M} were treated as free parameters.

We assumed extinction based on the galactic formulae in Howarth 1983. We then fitted the data using the system parameters in table 3.5 and a 320×600 linearly spaced grid of values of \dot{M} from $0.5 - 20 \times 10^{-9} M_\odot \text{ yr}^{-1}$, and inclination $10 - 85^\circ$ to produce the heat map in Fig. 3.5. In order to account for the fact that the object is intrinsically slightly variable, we adopted for the fit either the published uncertainties on the photometric data, or a value of 10 per cent, whichever was larger.

To demonstrate the contribution of a potential boundary layer we also modelled the effect of adding a circular band with $H = 0.1R_1$, $R = R_1$ and $T_{\text{bl,eff}} = 100\,000 \text{ K}$. This does not significantly affect the fit as its emission in the optical and near-ultraviolet is far less than that of the disc (see Fig. 3.5).

There is considerable degeneracy between the angle of inclination and \dot{M} . This is evident from the dotted green line in Fig. 3.5 showing the best fit for a given inclination. The overall best fit is found for $i = 52.9^\circ$ (see table 3.6), consistent with the estimate calculated in section 3.3.3 ($65.7^\circ_{-13}^{+8}$). The disc luminosity is better constrained, $3 \pm 1 \times 10^{33} \text{ erg s}^{-1}$ (see Table 3.6).

The white dwarf temperature determined from the SED fit only mildly depends on the inclination (Table 3.6) and is consistent with those found in other novalikes and VY Scl stars from direct modelling of the white dwarf spectrum: DW UMa ($\simeq 50\,000 \text{ K}$, Araujo-Betancor et al. 2003), TT Ari ($\simeq 39\,000 \text{ K}$, Gänsicke et al. 1999) and MV Lyr ($\simeq 47\,000 \text{ K}$, Hoard et al. 2004).

Table 3.6: Estimated values from fitting the spectral energy distribution.

Parameter		$i = 52.9^\circ$	$i = 65.7^\circ$
Mass transfer rate	$\dot{M} [10^{-9} M_\odot \text{ yr}^{-1}]$	4.75	8.13
Temperature (white dwarf)	$T_1 \text{ [K]}$	41 158	48 777
Disc luminosity	$L_{\text{disc}} [10^{33} \text{ erg s}^{-1}]$	2.59	3.66

3.3.3 Orbital inclination

As discussed in Sect. 3.3.2, the inclination of ASAS J0714+7004 is not tightly constrained from the SED fit. Here, we will follow an alternative approach to estimate the inclination based on the absolute magnitude of the system. Its location within the Hertzsprung-Russell diagram (HRD) places it firmly among the novalikes (Fig. 3.6), which are characterised by high mass-transfer rates that keep their accretion discs in the hot state. We therefore adopt the absolute magnitude-orbital period relation of Paczynski & Schwarzenberg-Czerny (1980), see also (Warner 1987)

$$M = 5.7 \pm 0.13 - 0.287 \pm 0.024 \times P_{\text{orb}} \quad (3.6)$$

which is adjusted for inclination by:

$$\Delta M_V = -2.5 \times \log \left(\left(1 + \frac{3}{2} \cos i \right) \cos i \right) \pm 0.4 \quad (3.7)$$

Based on the *Gaia* *G*-band data in Table 3.1, the mean absolute *G*-band magnitude of ASAS J0714+7004 is 5.20 ± 0.016 . Using Eq. 3.6 and the orbital period of 3.28 h gives a predicted absolute magnitude of $4.76^{+0.21}_{-0.16}$ and therefore $\Delta M_V = 0.44 \pm 0.21$. Solving Eq. 3.7 for i (and taking account of the error in the formula of ± 0.4) yields an inclination of $65.7^{+8.0}_{-13.0}^\circ$. This estimate is also consistent with the SED fit, the strong Balmer emission lines and the fact that it is not eclipsing. It is also consistent with Fig. 1 in Howell & Mason (2018).

The *Gaia* astrometry provides the opportunity to test the absolute magnitude-orbital period relation: most novalikes, including ASAS J0714+7004, have orbital periods of 3 – 4 h, and hence their absolute magnitudes should primarily depend on their inclinations. Inspecting Fig. 3.6 (lower panel), this is indeed the case, where the fainter systems have higher inclinations – in particular the green and yellow coded SW Sex systems (Section 2.2.1) are eclipsing and will therefore inevitably have large inclinations. We caution, however, that some care needs to be taken when considering cataclysmic variables in the *Gaia* HRD, as their exact location is subject to the state(s) that *Gaia* sampled. As such, CVs may move by some amount within the HRD when comparing their DR2 and EDR3 data (see Section 3.3.4).

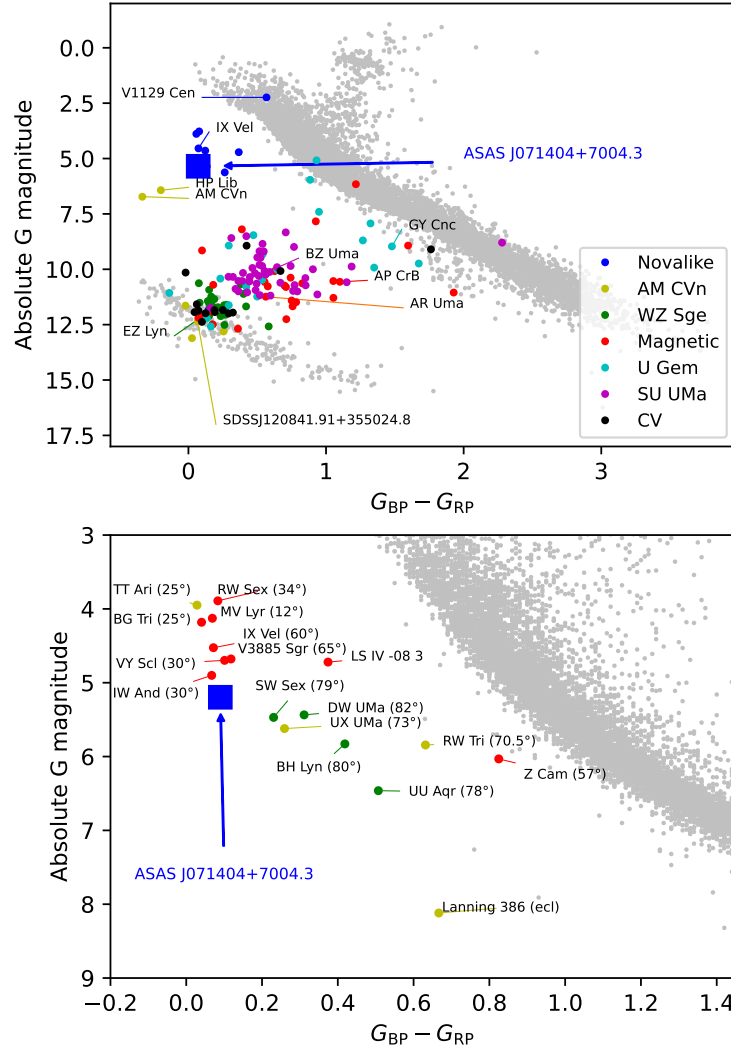


Figure 3.6: Top panel: The ‘Gold Sample’ of known CVs within 300pc with reliable astrometry and astrometry from [Inight et al. \(2021\)](#). ASASJ0714+7004 is marked with a blue square. Bottom panel: Detail showing the area of the HRD occupied by a representative selection of well-studied novalikes. Confirmed SW Sex stars are shown using green dots and candidate SW Sex stars using yellow whilst the remaining novalikes are shown in red. The data is from *Gaia* EDR3 ([Gaia Collaboration et al., 2021](#)) without adjusting the absolute magnitudes for extinction. The inclination (where known) is shown in brackets (references ‘SW Sex’, ([Groot et al., 2001](#)) ‘BH Lyn’, ([Dhillon et al., 1992](#)) ‘DW UMa’, ([Bíró, 2000](#)) ‘Lanning 386’, ([Brady et al., 2008](#)) ‘MV Lyr’, ([Hoard et al., 2004](#)) ‘BG Tri’, ([Hernández et al., 2021b](#)) ‘RW Tri’, ([Smak, 2019](#)) ‘UX UMa’, ([Suleimanov et al., 2004](#)) ‘TT Ari’, ([Bruch, 2019](#)) ‘UU Aqr’, ([Baptista et al., 1994](#)) ‘RW Sex’, ([Beuermann et al., 1992](#)) ‘IW And’, ([Szkody et al., 2013](#)) ‘VY Scl’, ([Martínez-Pais et al., 2000](#)) ‘Z Cam’, ([Szkody & Wade, 1981](#)) ‘V3885 Sgr’, ([Hartley et al., 2002](#)) ‘IX Vel’, ([Hartley et al., 2002](#))). Lanning 386 is an interesting outlier. It is an eclipsing system ([Kennedy et al., 2017, 2016](#)) and more significantly it is most often, unusually for a novalike, in its low state.

3.3.4 From *Gaia* DR2 to EDR3: improved precision and overall changes due to variability

Gaia EDR3 is a complete re-release of the astrophysical and photometric data and inevitably the absolute magnitudes and colours of any source are expected to differ somewhat with respect to DR2. For the set of novalikes shown in Fig. 3.6, the median uncertainties in the G , G_{BP} , G_{RP} magnitudes were 0.0101, 0.0355 and 0.0308 mag respectively in EDR3 compared with 0.0144, 0.0423, 0.0346 mag in DR2. The median parallax uncertainty was 0.0267 mas in EDR3 compared with 0.0634 mas in DR2. Figure 3.7 shows the corresponding changes in the *Gaia* HRD as black arrows. In most cases, these changes are quite small but one system (MV Lyr) stands out as its absolute magnitude decreased by $\simeq 1$. The reason is an important reminder that novalikes are variable stars and *Gaia* EDR3 essentially computes a weighted average of measurements taken between 25 July 2014 and 28 May 2017 (whereas DR2 data collection stopped on 23 May 2016). Figure 3.8 shows that MV Lyr was in a prolonged low state for about 2/3 of the DR2 observations, whereas EDR3 sampled the system for a substantially longer period in the high state – explaining the large change in G , G_{BP} , and G_{RP} .

3.3.5 Photometric variability

The uninterrupted *TESS* observations provide the opportunity to investigate the broad-band variability of ASAS J0714+7004 on timescales of minutes to days. The Fourier transform (Deeming, 1975) computed from the entire Sector 40 data that was obtained in the ultra-short 20 s cadence mode (Fig. 3.9) shows clearly the 3.28 h orbital period, and a flat distribution (-1 powerlaw) in power density down to $\simeq 6.3$ mHz, after which the power law breaks to -2 . A weak signal at 2000 s was detected in the Sector 40 data, but was absent in the other *TESS* observations, and may have been related to intermittent quasi-periodic oscillations (Warner & Woudt, 2002). The power law slopes and break frequency are typical of those observed in other accreting white dwarfs which display strong broad-band variability components (see e.g. MV Lyr, Scaringi et al. 2012; Scaringi 2014; Scaringi et al. 2015). This phenomenology is generally explained by the so-called fluctuating accretion disc model, which was originally developed to explain the broad-band noise properties observed in X-ray binaries and active galactic nuclei (see Lyubarskii 1997; Arévalo & Uttley 2006; Ingram & Done 2011, 2012; Ingram & van der Klis 2013). In this model mass transfer variations through the disc couple multiplicatively as matter is moved inwards through the disc. The observed power spectrum is then the result of the faster variability driven by mass transfer fluctuations and emitted in the inner-disc regions (Scaringi et al., 2015). In reality the variability is generated across a range of disc radii, and is observed in a specific pass-band given an emissivity profile for the disc. A similar power spectral density observed in the

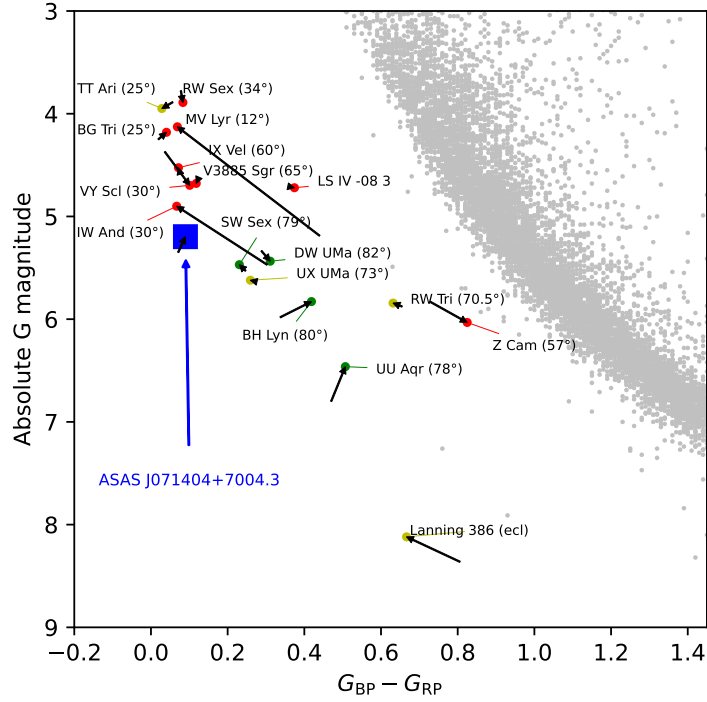


Figure 3.7: Selected novalikes in the *Gaia* EDR3 HRD showing the changes (black arrows) in absolute magnitude and colour between *Gaia* DR2 and EDR3. Whilst some minor changes are due to refinement in *Gaia* astrometry and photometry the major changes are due to transitory changes in the observed light curve. MV Lyr is a good example of this where it was mostly in a low state during the 162 observations contained in DR2 but in a high state during the remaining 107 observations in EDR3 (see Fig. 3.8).

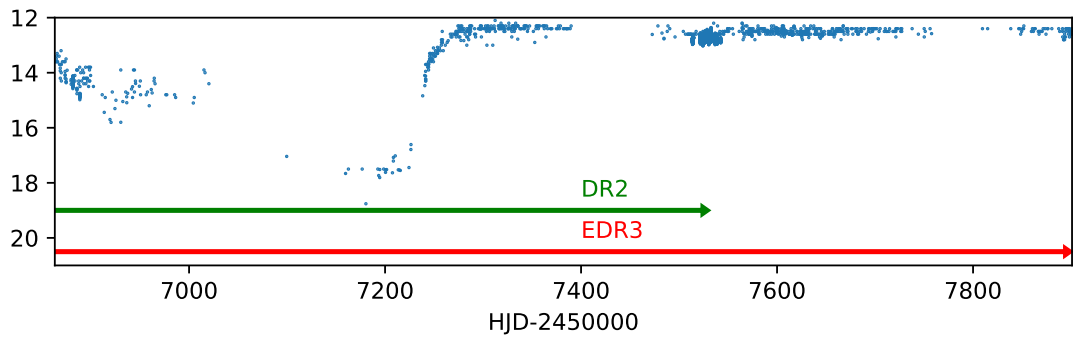


Figure 3.8: Long-term light curve of MV Lyr, obtained from the AAVSO data base. The arrows indicate the date range covered by the observations contained in *Gaia* DR2 and EDR3, illustrating why the absolute magnitude of this system brightened significantly in EDR3 compared to DR2.

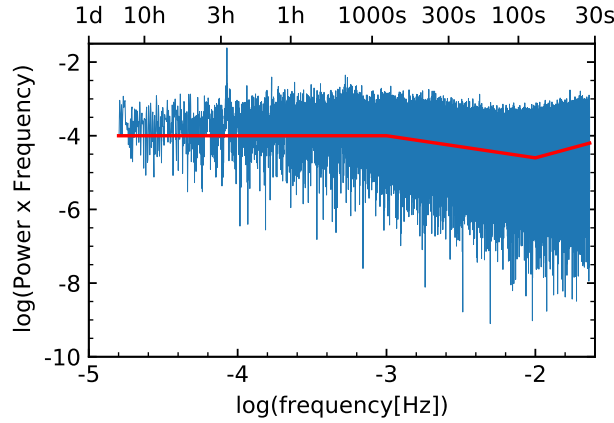


Figure 3.9: Power density spectrum of ASAS J0714+7004 computed from the Sector 40 observations, which were obtained with at a 20 s cadence. The orbital period of 3.28 h is clearly detected. The slight peak at $\simeq 2000$ s does not appear in the data of the other sectors. It first appears with a period of 1883 s on day 5 and varies between 1594 s and 1931 s before disappearing after day 11. It may be related to intermittent quasi-periodic oscillations. The overall shape of the broad-band noise can be fit with three simple power laws. The frequency break at $\approx 10^{-3}$ Hz is typical of accretion-induced variability. The rise in power at $\approx 10^{-2}$ Hz is attributed to Poisson noise dominating the power spectrum.

novalike MV Lyr has been modelled by [Scaringi \(2014\)](#) using the fluctuating accretion disc model. From the modelling, the power spectral break reveals that the variability is driven by a geometrically thick (and optically thin) disc component which extends from the white dwarf surface up to a few white dwarf radii ([Scaringi, 2014](#)). By analogy, the same disc component, as inferred from the break in the power spectrum shown in Fig. 3.9 may also be present in ASAS J0714+7004. This would also be consistent with the inference of the boundary layer discussed in Sect. 3.3.2, although the geometrical extent inferred from the broad-band variability would suggest this component to be substantially extended.

3.3.6 X-ray emission

ASAS J0714+7004 was observed by *ROSAT* during its all sky survey ([Voges et al., 1999](#)). The *ROSAT* Position Sensitive Proportional Counter (PSPC) observation, covering 0.1–2.4 keV, detected a count rate of 0.17 ± 0.023 ct s $^{-1}$. *ROSAT* derives two different values for the flux based on either a power law (designed for AGN and clusters of galaxies) and a stellar model. The stellar model (resulting in Flux2 = 1.92×10^{-15} W m $^{-2}$) is more appropriate for a novalike as the x-ray emission will resemble a dwarf nova in outburst and consist of predominantly soft x-rays (Section 3.3.6 in [Warner 1995](#)). The stellar model ([Voges et al., 1999](#)) is based on an empirical conversion between count-rates and fluxes following [Schmitt et al. 1995](#) that was originally

Table 3.7: Flux and luminosity based on *Swift* XRT observations.

	Range		Flux ($10^{-12} \text{erg s}^{-1} \text{cm}^{-2}$)	X-ray luminosity ($10^{30} \text{erg s}^{-1}$)
	keV	Å		
Observed	0.3–6.0	2.1–41	1.67	9.07
Extrapolated	0.3–10	1.2–41	2.33	12.65
Extrapolated	0.1–10	1.2–124	2.57	13.95
Extrapolated	0.01–10	1.2–1242	2.66	14.44

developed to obtain flux values for stars and we use it to illustrate the *ROSAT* detection in Fig. 3.5.

Our *Swift* XRT spectrum consists of a set of counts binned by energy (see Fig. 3.10) in the range 0.3 to 6 keV. To obtain an estimate for the luminosity we fitted the data using XSPEC. We have used a model with two components – one with a temperature over 16 keV and the other with a temperature of 0.83 ± 0.15 keV. This model was then used to extrapolate upwards into harder X-rays and downwards into the EUV (see Table 3.7). Absorption is based on assuming an interstellar hydrogen column density of $N_{\text{H}} = 3.2 \times 10^{19} \text{cm}^{-2}$; in practice this has a minimal effect.

The *Swift* pipeline spectrum is shown in Fig. 3.10 and qualitatively resembles those of BZ Cam and MV Lyr (Figures 2 and 3 in Balman et al. 2014). The X-ray lumi-

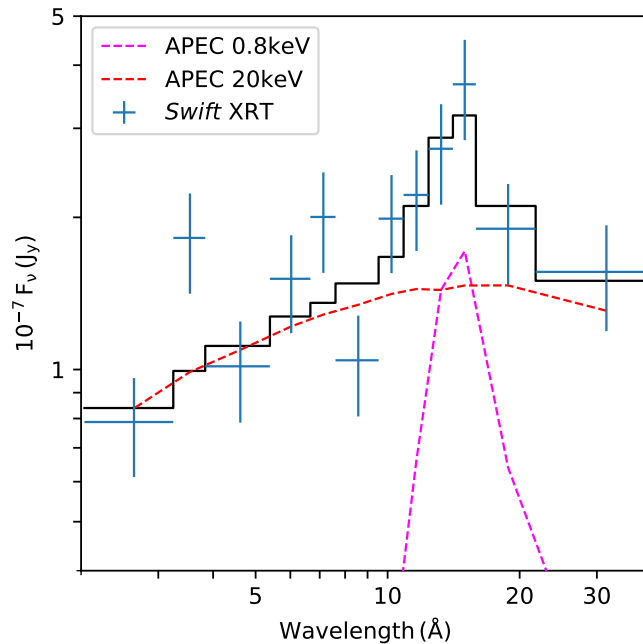


Figure 3.10: Spectrum of the *Swift* XRT observations (crosses). We assumed interstellar absorption fixed at $N_{\text{H}} = 3.2 \times 10^{19} \text{cm}^{-2}$ and solar abundances. The spectrum was then fitted using the sum of two APEC** components with temperatures of 0.8 keV and 20 keV respectively, and the sum is shown as the grey line, binned to the observed energy channels.

osity of ASAS J0714+7004 of $1.17 \pm 0.27 \times 10^{31} \text{ erg s}^{-1}$ is lower than that of some dwarf novae (Byckling et al., 2010), although an order of magnitude greater than that of the average CV (Reis et al., 2013). The optically-thin spectrum and inferred temperatures are similar to other non-magnetic CVs (Baskill et al., 2005; Mauche & Mukai, 2002).

We inspected the average count rates for each of our *Swift* XRT observations, and we note that there is mild (1σ) evidence for variability across the 22 d spanned by the data.

3.3.7 Spectral variability and detection of a wind outflow

The high cadence of our INT spectroscopy reveals rapid variations in the morphology of the emission lines. This is evident in the H_α trailed spectrum (see Fig. 3.12) and is particularly striking in the variability of a P Cygni-like feature in He I $\lambda 5876$ (see bottom panel in Fig. 3.11). These variations appear to be stochastic with no relation to orbital phase or indeed variations in other lines (see Fig. 3.11).

3.4 Discussion

3.4.1 Winds

The optical P Cygni lines are clear evidence of the presence of winds (Kafka & Honeycutt, 2004). Our INT spectroscopy demonstrates variability within the wind structure on the time scale of minutes – probably due to clumping. The lack of correlation of the wind features with the orbital phase precludes a stable and localised origin within the disc. The blue absorption wing of the He I $\lambda 5876$ P Cygni line is unusually strong compared to other well-studied novalikes (e.g. Kafka & Honeycutt 2004; Kafka et al. 2009) and this may be due to a fortuitous inclination. Proga et al. (1998) finds that slower dense winds are confined to within 45° of the orbital plane. The radial velocity component of the winds will therefore be greater in high inclination systems such as ASAS J0714+7004. We did not detect the concentration of winds at the superior conjunction of the donor as reported by Honeycutt et al. (2013) in BZ Cam.

To explore whether a wind outflow is plausible in the case of ASAS J0714+7004, we have calculated simulated spectra for bi-conical outflow using the Monte Carlo radiative transfer code PYTHON (Long & Knigge, 2002), which has been used in several previous attempts to model winds in disc-dominated cataclysmic variables at ultraviolet (Noebauer et al., 2010) and optical wavelengths (Matthews et al., 2015). PYTHON starts with a parameterised description of a biconical outflow, in this case one originally formulated by Shlosman & Vitello (1993). It then solves for the ionisation structure

****Smith et al. (2001)** defined Astrophysical Plasma Emission Codes (APECs) using atomic data in the companion Astrophysical Plasma Emission Database (APED) to calculate spectral models for hot plasmas.

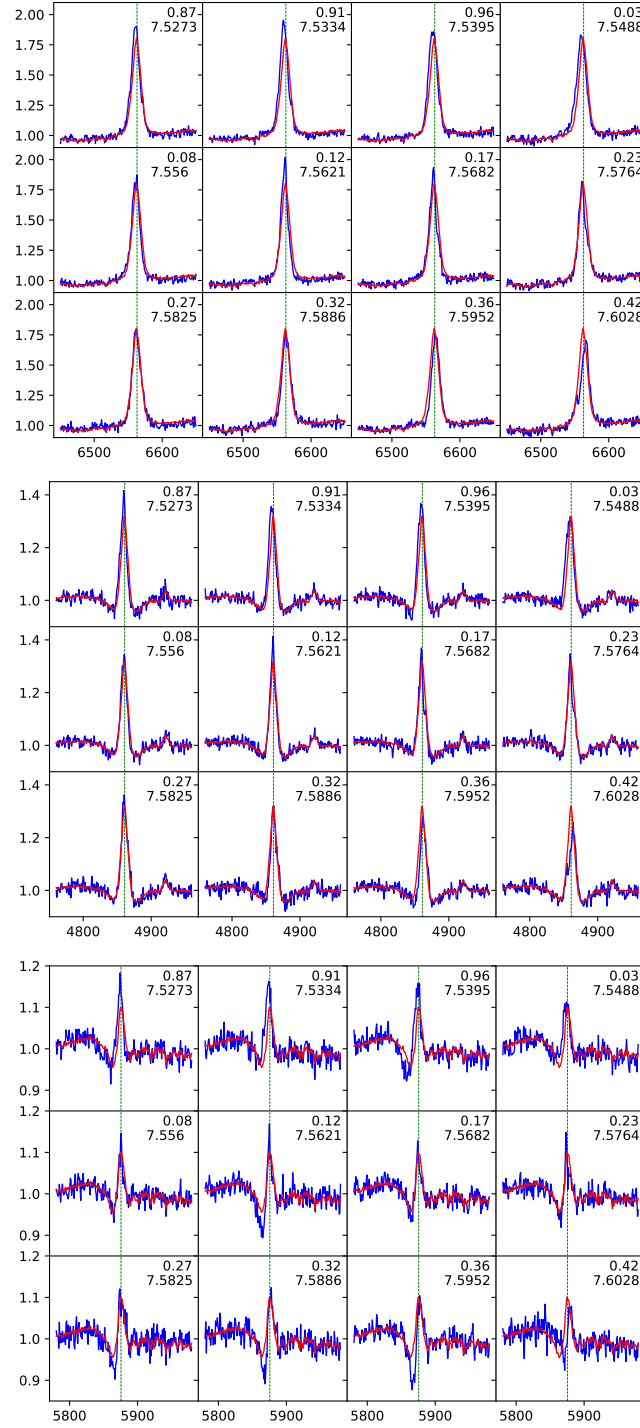


Figure 3.11: Phase resolved spectra centred on H α (top), H β (middle) and He I 5876 Å (bottom) from the December INT data. The individual exposures were binned such that each sub-panel in the sequence covers $\simeq 8$ min. The top number in each panel is the orbital phase and the lower number is HJD - 2 459 190. The red line is the time averaged spectrum of the December sample. Note the stochastic variability in the emission lines.

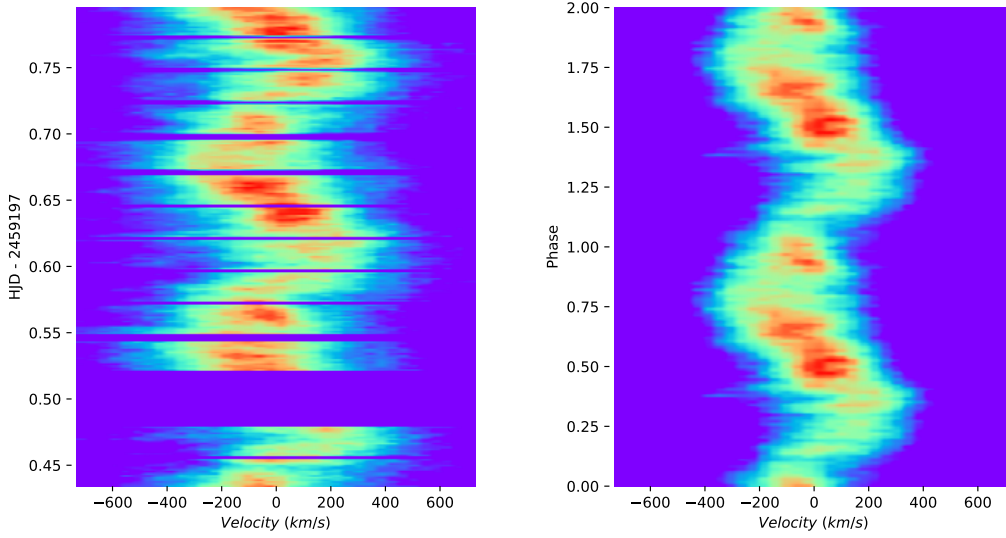


Figure 3.12: (left) The trailed spectrum of the H α line in the December sample and (right) the same data phase-folded using the fitted period and epoch. The ‘S’ shape is clearly visible. Note also the stochastic peaks in the left plot that are less evident in the right hand plot due to averaging and orbital binning. We inspected the trailed spectra of the earlier observations which provided partial orbital coverage, and did not find repeating orbital behaviour.

of the outflow given the nature of the white dwarf and disc, and then simulates the emergent spectrum as a function of the inclination angle^{††}. The Shlosman & Vitello (1993) models have a large number of parameters. For the modelling discussed here, we explored a small fraction of the allowable parameter space, beginning with models that were similar to those described by Matthews et al. (2015). For the models we used parameter values consistent with those derived earlier (Table 3.5), and varied various of the parameters in Table 3.8. The external radiation sources were the white dwarf and the disc; solar abundances were assumed; H and He were treated as multi-level macro-atoms, while the metals were treated in the so-called two-level approximation.

A comparison of the simulated to the observed spectra for the best model we calculated is shown in Fig. 3.13. The line strengths and line shapes of the H and He lines are approximately correct. He I λ 5876 shows evidence of a P Cygni like feature. Despite being produced from a wind that arises from the disc at distances between 4 and 12 white dwarf radii, the lines in the simulated spectra and in the observed INT spectra are single peaked. The reason that the lines are single peaked in the model spectra (at the resolution of the INT spectra) is likely to be due to two effects. First, there is emission from fairly far out in the wind which reduces the azimuthal velocity

^{††}PYTHON is a collaborative open-source project available at github.com/agnwinds/python.

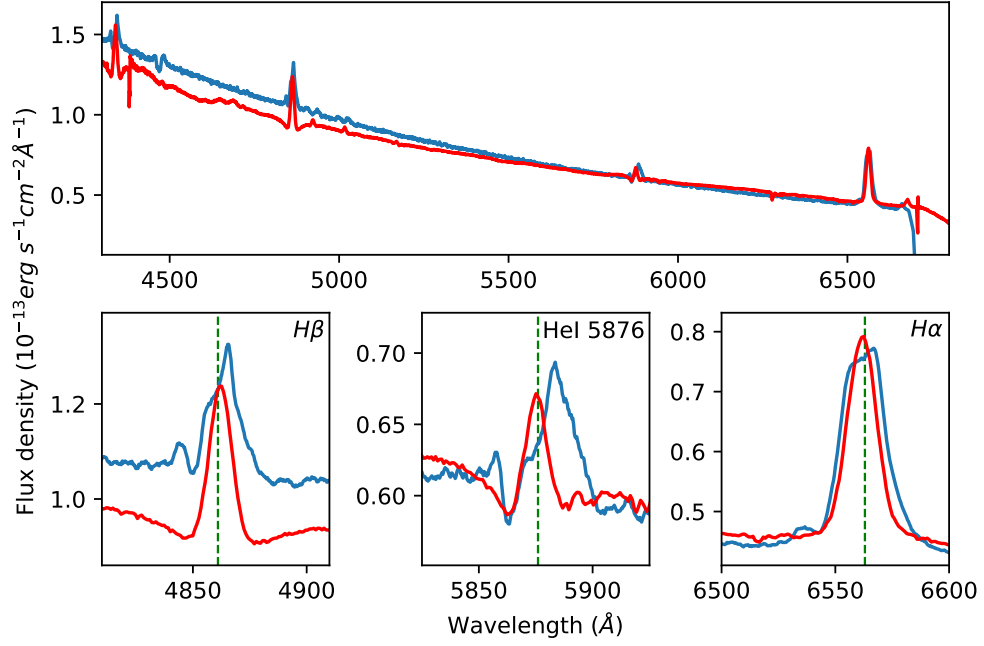


Figure 3.13: Top panel: the PYTHON model fit (blue) to the observed average spectrum (red). An inclination of 62° was found to best reproduce the observed data. Bottom panel: enlargements of the $H\beta$, He I $\lambda 5876$ and $H\alpha$ lines.

Table 3.8: Adopted values used to model the bi-conical outflow using the PYTHON model. See [Matthews et al. \(2015\)](#) for more details of the model and parameter definitions.

Parameter		Value
Wind fill factor		0.008
Wind mass transfer rate	$\dot{M} [10^{-10} M_\odot \text{yr}^{-1}]$	5.0
Mass (white dwarf)	$M_1 [M_\odot]$	0.83
Mass (donor)	$M_2 [M_\odot]$	0.22
Radius (white dwarf)	$R_1 [R_\odot]$	0.0122
Radius (donor)	$R_2 [R_\odot]$	0.30
Inner radius (disc)	$R_{\text{disc,i}} [R_\odot]$	0.0244
Outer radius (disc)	$R_{\text{disc,o}} [R_\odot]$	0.49
Temperature (white dwarf)	$T_1 [\text{K}]$	41158
Temperature (donor)	$T_2 [\text{K}]$	3324
Orbital period	$P_{\text{orb}} [\text{hr}]$	3.2794
Wind inner radius	$r_{\text{min}} [R_1]$	4
Wind outer radius	$r_{\text{max}} [R_1]$	12
Inner opening angle	$\theta_{\text{min}} [^\circ]$	20.0°
Outer opening angle	$\theta_{\text{max}} [^\circ]$	65.0°
Angle exponent	γ	1
Terminal velocity	$v_\infty [v_{\text{esc}}]$	3
Wind Acceleration length	$R_v [10^{11} \text{cm}]$	1.0
Acceleration exponent	α	1.2

since the flow is designed to conserve angular momentum. In this model, the fact that the P Cygni absorption line is $\simeq 600 \text{ km s}^{-1}$ implies that the interaction with the wind occurs at a considerable distance ($\sim 5 - 6 R_{\odot}$ i.e. > 5 times the binary separation) from the system. Second, the blue edge of a double peaked line tends to be absorbed by material further out in the flow. With somewhat different parameters one often sees a double $H\alpha$ profile with the blue wing suppressed.

Although the comparison of model spectra to the observations suggests that this might be a plausible wind model for ASAS J0714+7004, and although the model is not that different from those that [Matthews et al. \(2015\)](#) used to model the spectra of UX UMa and RW Tri, there are a number of critiques of the model that might be made. First, while the model spectra resemble the observed spectra, the model spectra are quite sensitive to the inclination angle. The nature of the simulated spectra change fairly rapidly with inclination angle near 62° because this is very close to the outer opening angle of the conical flow; at lower angles the P Cygni lines grow more prominent; at higher angles the emission lines grow in strength. Changing the outer opening angle to a somewhat lower value, would allow one to produce similar spectra at similarly lower inclination angles. Second, the wind model we use has a mass accretion rate of $10^{-9} M_{\odot} \text{ yr}^{-1}$, which compares with the mass accretion rate we have derived at high inclination of $8.9 \times 10^{-9} M_{\odot} \text{ yr}^{-1}$; this is probably the maximum value that is plausible. Furthermore we have assumed that the wind is clumped, and only occupies three per cent of the volume. If one preferred a lower mass loss rate, one could have simply assumed that the wind occupied an even smaller fraction of the volume, and obtained a fairly similar spectrum, since the ionisation parameter at any particular point depends on the density of the filled fraction of the wind. Finally, we note in passing, that there are several He I lines that appear double peaked in our models, but which are single peaked in the time-averaged spectra. Despite these difficulties, we would suggest that the models indicate that ASAS J0714+7004 has a relatively wide-angle outflow with properties that are similar to those in the model, and similar to those in other novalike systems.

3.4.2 Disc structure

The extensive INT spectroscopy never shows evidence of the double-peaked emission lines we would expect from a high inclination disc ([Horne & Marsh, 1986](#)). We considered the possibility that ASAS J0714+7004 was an SW Sex star ([Dhillon et al., 2013](#)) as this would explain the lack of double-peaked lines^{††} even though it did not have the other SW Sex defining characteristics (deep continuum eclipses and emission lines that do not share the orbital motion of the white dwarf and exhibit transient absorption

^{††}[Dhillon et al. \(2013\)](#) studied the prototype SW Sex and concluded that the emission lines originated in a single region of the disc, the hot spot resulting in a single peak.

features).

However, in contrast to a large fraction of the confirmed SW Sex stars, ASAS J0714+7004 is not eclipsing and the trailed spectrum shows no evidence of a second peak. A wide flared disc, as proposed to explain the lack of double-peaked lines in SW Sex stars (Dhillon et al., 2013), would require a flare angle of over 20° which is geometrically unlikely. The alternative explanation is that the single-peaked emission lines originate in the wind, as discussed above.

3.4.3 Mass transfer rate

The widely accepted thermal disc instability model (Meyer & Meyer-Hofmeister, 1981; Osaki, 1996) predicts that CVs with a mass transfer rate (\dot{M}) below a critical value (\dot{M}_{crit}) will exhibit outbursts, and such systems are known as dwarf novae. Novalikes are CVs with \dot{M} above this critical value and are expected to have discs in a steady high-luminosity state. The actual value for \dot{M}_{crit} depends on the size of the disc, and hence largely on the orbital period, and is somewhat model dependent (Shafter et al., 1986; Knigge et al., 2011). The estimated range of the mass transfer rate for ASAS J0714+7004 is typical for that found among novalikes (e.g. Table 4 from Hewitt et al. 2020), and places it above \dot{M}_{crit} .

We have used a simple blackbody model for a boundary layer as, in the optical, it has little effect on the fitted value of \dot{M} . However this is not the whole story. Puebla et al. (2007) concluded that the standard model needed to be augmented with a modification to the temperature profile of the inner disc, either by increasing the temperature close to the white dwarf or by the addition of a wind or corona component (Meyer & Meyer-Hofmeister, 1994). Balman et al. (2014) analysed three novalikes and confirmed this conclusion. These authors suggested that the boundary layer consists of either optically thin regions traversed by advection-dominated accretion flows or X-ray corona regions close to the white dwarf but above the disc plane. This then leads to speculation as to why optically thin regions of this sort form in novalikes but not in dwarf novae. Nixon & Pringle (2019) suggests that the cause is a magnetically controlled zone that builds up due to the persistently ionised disc; dwarf nova outbursts do not last long enough for the field to build up.

In this context we note that the X-ray spectrum of ASAS J0714+7004 is less than one percent of the optical flux which is typical of novalikes (Fig. 3 in Mukai 2017) and clearly shows that the expected 50 per cent of gravitational energy released at the white dwarf boundary does not escape in the form of X-rays. ASAS J0714+7004 is therefore another example of where the standard model fails to account for this energy.

3.4.4 Quasi-periodic outbursts

The photometry in Fig. 3.2 displays quasi-periodic variability of $\simeq 1$ mag on time scales of $\simeq 10 - 20$ d, reminiscent of the ‘stunted’ outbursts seen in some other novalikes (Honeycutt et al., 1998). We investigated the possibility of non-orbital periodic variability and found no evidence for this despite a number of apparently regular structures. The *TESS* power spectrum (Fig. 3.9) clearly confirms the absence of any other periodicities. This quasi-periodic variability is distinct from lower level and rapid ‘flickering’ (Bruch, 1992) which is evident in the *TESS* light curves (Fig. 3.2, particularly panels (e) and (f)). The cause of the stunted outbursts remains unclear. One possibility is stochastic changes in the mass transfer rate whilst another is a form of disc instability similar to the cause of dwarf nova outbursts that involves only a small fraction of the disc. Honeycutt (2001) strongly favoured the model of dwarf nova outbursts arising from a disc instability – the apparent stunting of the outbursts being caused by dilution from an additional source of illumination within the system. Honeycutt (2001) also argued that the presence of stunted outbursts is not correlated with \dot{M} which suggests that they are not due to those novalikes displaying them being close to \dot{M}_{crit} . Inspecting the long-term light curve of ASAS J0714+7004 (top panel in Fig. 3.2) shows that the (dis)appearance of the quasi-periodic variability does indeed not correlate strongly with the average brightness of the system.

Robertson et al. (2018) propose a contrary view based on observational evidence of UU Aqr that about half of the stunted outbursts coincided with increased hot spot emissions and hence higher \dot{M} . Subsequently Schlegel & Honeycutt (2019) studied an eclipsing novalike (AC Cnc) and found that the stunted outbursts were eclipsed by the disc suggesting that either the outbursts originated on the facing hemisphere of the donor or were due to changes in the disc.

Closer investigation of an outburst observed at two minute cadence by *TESS* (see Fig. 3.2, panel (g)) shows a gradual rise and fall typical of an ‘inside out’ dwarf nova. The *Swift* ultraviolet observations show a similar outburst with AAVSO optical observations also peaking at the same time. Given that the bulk of the disc must be ionised to sustain the high \dot{M} we speculate that there is an outer part of the disc that occasionally becomes sufficiently cool for H to recombine, and that this outburst starts at the inner edge of this area and subsequently spreads outwards. As such, we conclude that the quasi-periodic variability seen in ASAS J0714+7004 is likely related to the standard thermal disc instability acting in a small outer part of the disc, leaving the inner disc in a steady hot state which provides the ‘background’ luminosity that Honeycutt (2001) required to dilute the amplitude of the outbursts.

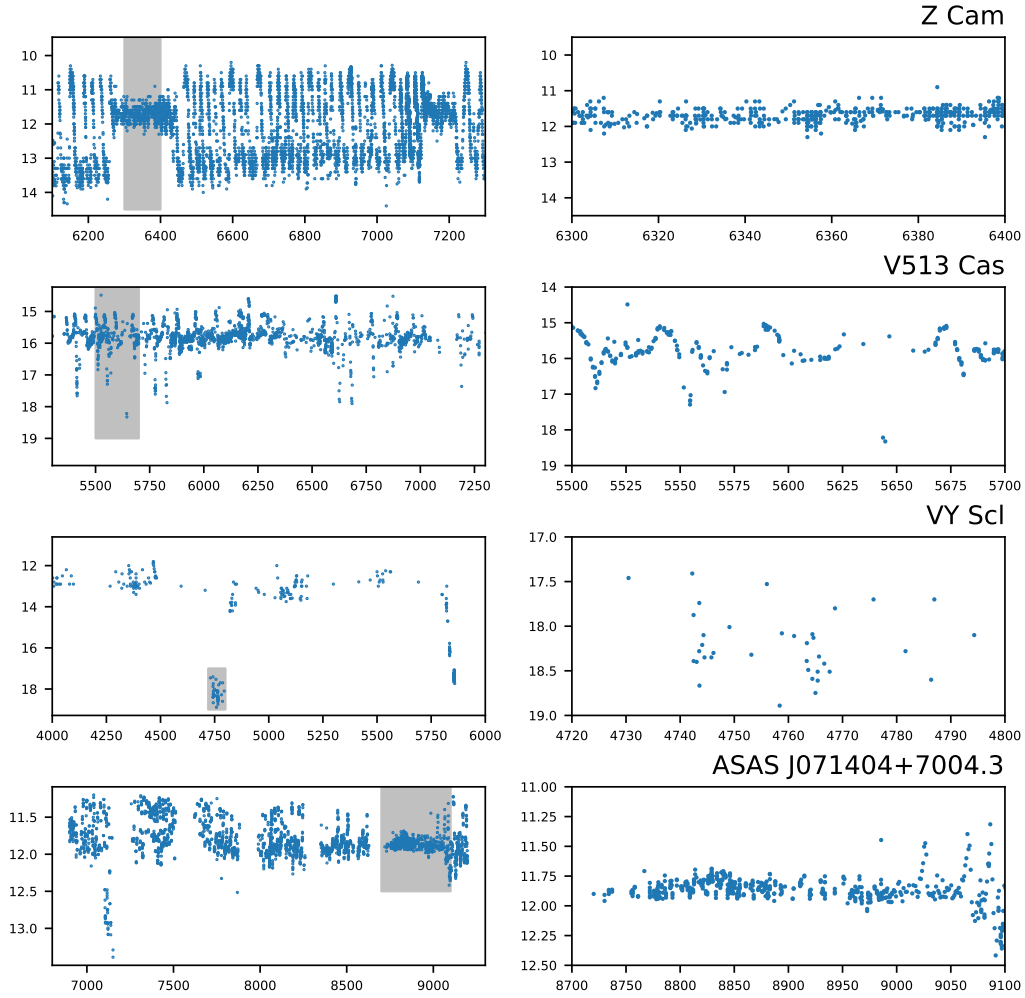


Figure 3.14: Light curves of several typical dwarf nova and novalike sub-classes. Dates are HJD $- 2\,450\,000$. The panels on the right are enlargements of the grey areas in the left panels. The dwarf nova Z Cam shows classic ‘standstills’ of $\simeq 100 - 200$ d during which there are no outbursts whilst exhibiting large-amplitude outbursts between standstills; standstills are normally terminated by a decline to quiescence. This contrasts with the IW And class (of which V513 Cas is an example) in which characteristic outbursts occur during standstills. VY Scl stars show relatively deep ($2 - 5$ mag) low states which can last a few weeks to about a year, and during which small outbursts occur. (Observations from the AAVSO International Database, <https://www.aavso.org>).

3.4.5 Novalikes and dwarf novae – secular changes in mass transfer rate

The observed temporary change to a low state in 2015 (HJD $- 2\,450\,000 = 7150$) is interesting as it leads to a potential explanation for the under-representation of dwarf novae with orbital periods between $\simeq 3 - 4$ hours – just above the so-called ‘period gap’ (Shafter et al., 1986).

Knigge et al. (2011) showed that populations of dwarf novae and novalikes coexist at these orbital periods and so the direct association between orbital period and mass transfer rate breaks down in this region. Our observation supports the idea that CVs can change back and forth between dwarf novae and novalikes more frequently (a few years) – particularly when mass transfer rates are close to \dot{M}_{crit} . Novalikes are brighter (by $\simeq 5$ mag) than dwarf novae and hence there will be a large selection effect leading to the under-representation of dwarf novae at such periods.

In the light of our observations it is interesting to compare ASAS J0714+7004 with known sub-classes of novalikes (see Fig. 3.14).

Z Cam stars (e.g. Schreiber et al. 2002) are dwarf novae that experience occasional standstills of constant magnitude of 1–1.5 mag below maximum usually following an outburst. The remainder of the time Z Cam stars exhibit frequent dwarf novae commencing $\simeq 1$ mag below the standstill level and peaking above it. The bottom right light curve in Fig. 3.14 shows ASAS J0714+7004 has a high-level standstill but the amplitude of the outbursts at other times is far lower than Z Cam.

The IW And stars (Hameury & Lasota, 2014) form a sub-category of Z Cam (see Fig. 3.14) and show continual outbursts (not unlike dwarf novae) during the high state (i.e. during the ‘standstill’). Again this is not consistent with our light curve except for our low state in 2015.

The VY Scl stars (Schmidtobreick et al., 2018) are novalikes that show occasional $\sim 3 - 6$ mag low states similar to ASAS J0714+7004 in 2015 and typically have orbital periods of 3–4 h. Whilst the cause of the low state is not well understood it is clear that the previously hot steady-state disc will continue to deposit its mass onto the white dwarf until it is exhausted – potentially causing dwarf nova outbursts which we do see (panel (b) in Fig. 3.2). Based on these observations we conclude that ASAS J0714+7004 is a VY Scl star.

3.5 Conclusions

Our study of ASAS J0714+7004 has shown it to be a bright and nearby novalike CV. It exhibits the low states characteristic of the VY Scl sub-class. We have obtained a reliable estimate of the orbital period and estimated the mass transfer rate and inclination (see Table 3.1). We have identified strong wind signatures that are highly variable – coming and going in a few minutes in veritable gusts, and uncorrelated with orbital phase. A better understanding of disc winds is important for clarifying the evolution of all CVs not just novalikes and because of its brightness and proximity, this system is an excellent target for future detailed studies of its accretion disc and wind outflow.

Chapter 4

Reference samples of close binaries

4.1 Introduction

The work in this chapter was completed and published before *Gaia* EDR3 was available and is based on DR2.

Chapter 1 showed that binary evolution involves complex physical processes including common envelope (CE) evolution and orbital angular momentum loss that are not well understood (Ivanova et al., 2013; Knigge et al., 2011). Models describing these physical processes involve a number of free parameters, that require observational calibrations. However, the currently known samples of different types of binaries are severely incomplete, and subject to observational biases that are difficult to quantify (Pretorius et al., 2007a; Gänsicke, 2004). Consequently, predictions of binary populations have to be considered with some reservations, as the parameters used to encapsulate the physics of binary evolution are not well calibrated.

Progress requires the identification of representative populations of binaries with well-understood selection effects that sample the entire phase-space of physical parameters, as well as evolutionary stages. The key motivation of this chapter is to assemble a volume-limited sample that includes a homogeneous representation of all major sub-types of close white dwarf binaries: detached white dwarf plus main-sequence post-common envelope binaries (PCEBs), interacting white dwarf binaries (cataclysmic variables, CVs), and double white dwarfs (DWDs). One example of such a study is the joint population study of all types of white dwarfs, single and in binaries, within the volume-limited and complete 20 pc sample (Toonen et al., 2017).

The key information required for constructing a truly representative sample of white dwarf binaries is the accurate knowledge of their distances which have only now become systematically available, thanks to the all-sky astrometry provided by the *Gaia* mission. *Gaia* DR2 provides parallax measurements for ~ 1.3 billion stars, with a lim-

iting magnitude of $G \simeq 20$.

[Pala et al. \(2020\)](#) used the *Gaia* DR2 data to establish the first truly volume-limited study of CVs within 150 pc. Whilst limited to only 42 systems this study provided the most robust estimate of the space density of CVs to date ($\rho_0 = 4.8^{+0.6}_{-0.8} \times 10^{-6} \text{ pc}^{-3}$), as well as an assessment of the intrinsic make-up of the CV population, with the surprising conclusion that about one third of all CVs contain a magnetic white dwarf (a much higher proportion than seen in previous observations).

With the *Gaia* astrometry of $\simeq 1.3$ billion stars in hand, the limitation in extending the study of [Pala et al. \(2020\)](#) to a larger volume, and including all types of close white dwarf binaries, is the incompleteness of the known members of the different sub-classes. [Pala et al. \(2020\)](#) estimated a $\simeq 77$ per cent completeness for the CVs within 150 pc, that value drops for larger distances, and is poorly constrained for PCEBs.

The first step within this project is to establish reference samples of each sub-type of white dwarf binaries that are as representative as possible. The definition of these samples, and a discussion of their overall properties within the *Gaia* Hertzsprung-Russell (HR) diagram is the focus of this chapter. These reference samples will then be used to define algorithms that identify white dwarf binary candidates, combining *Gaia* data with observations extending over a wider wavelength range.

In this chapter we define the reference ‘Gold’ samples for each sub-type (Sect. 4.3) including a discussion of the selection effects that affect these samples, and finally use the Gold Samples to discuss the evolution of close white dwarf binaries in the *Gaia* Hertzsprung-Russell diagram (Sect. 4.4). The tabular data for each Gold sample is provided in Appendix A.

4.2 Close white dwarf binaries

In this chapter, we focus on close white dwarf binaries that have undergone interactions in the past, in the vast majority of cases in the form of a common envelope event. Some of these are currently in a mass transferring state, others are in a detached configuration but may interact again in the future. A graphical overview of the evolutionary links between the different types of white dwarf binaries discussed below is shown in Fig. 4.1. Whilst our primary focus is upon CVs we need to account for these other types of white dwarf binaries including helium-rich donors and double white dwarfs.

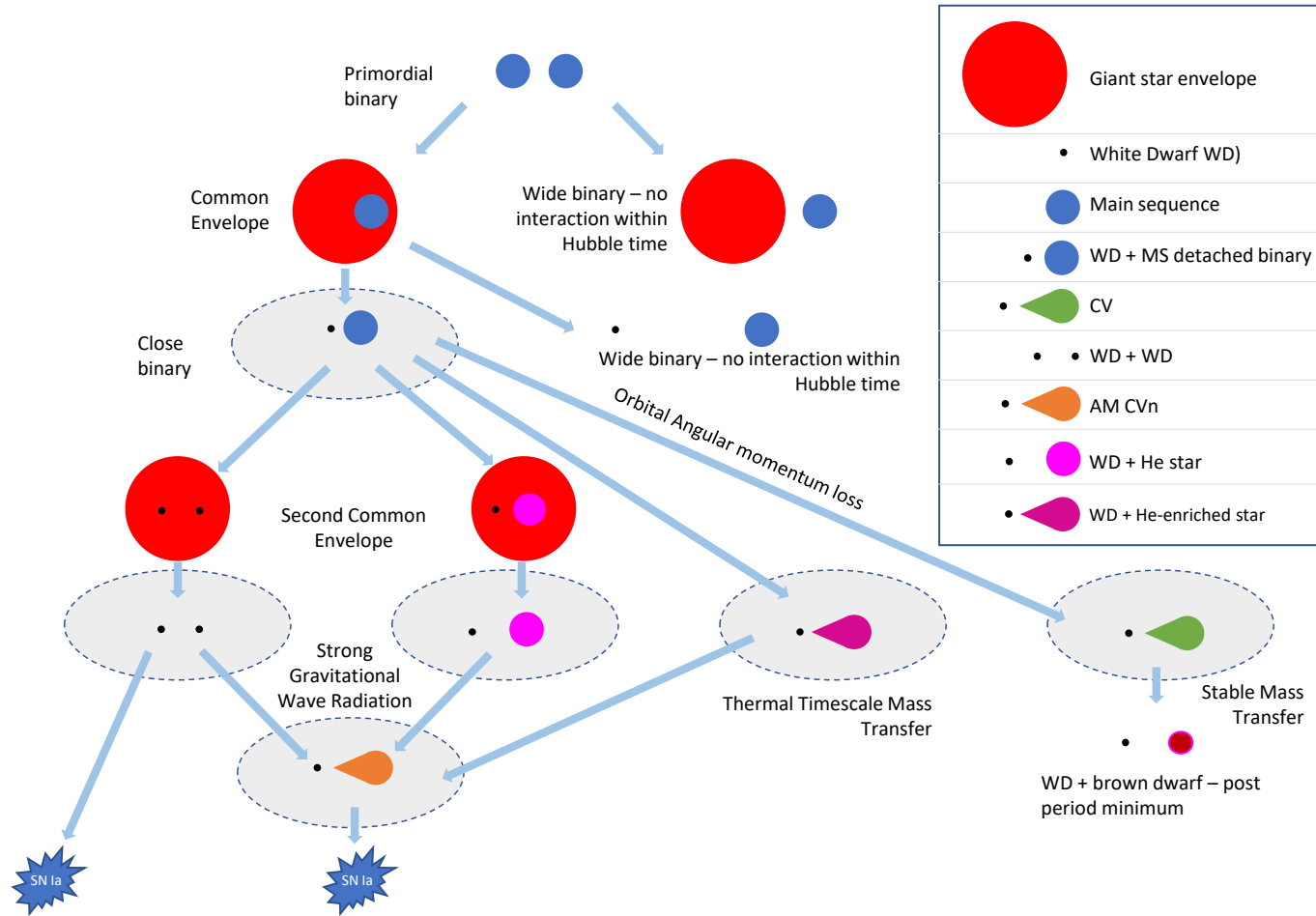


Figure 4.1: A schematic overview of the evolutionary channels leading to the different sub-classes of close white dwarf binaries discussed in this chapter. A number of these channels potentially lead to the ignition of white dwarfs as type Ia supernovae and to the emission of gravitational waves detectable by the *LISA* mission, highlighting the importance of these systems for a wide range of astrophysical problems. The grey ellipses show the sub-classes that are included in our census. Adapted from [Tolosa et al. \(2019\)](#).

4.3 Reference samples

The objective of this section is to define a prototypical Gold Sample for each type of close white dwarf binary based on the known systems that can then be used to define selection criteria for an all-sky search. The ultimate goal of this search is to establish a view of the Galactic white dwarf binary populations that is homogeneous, representative, and as complete as possible within a given volume limit. We emphasise that each Gold Sample will inevitably be subject to the selection effects underlying the known populations of white dwarf binaries. However, our goal here is not to achieve completeness at any level, but to map out the parameter space occupied by these white dwarf binaries.

For the goal of completeness within a given volume, two aspects limit the maximum distance for which it will be possible to identify white dwarf binaries, i.e. the requirement for (1) a *Gaia* parallax, and (2) spectroscopic confirmation. Within *Gaia* DR2, parallaxes require a 5-parameter astrometric solution; which exists for $\simeq 83$ per cent of targets with $G \leq 20$, dropping to $\simeq 16$ per cent at $G \leq 21$ (interpolated from Fig. B1 in Lindegren et al. 2018). The required follow-up spectroscopy of a large number ($\simeq 100\,000$) of candidate white dwarf binaries can only be achieved via multi-object spectroscopic surveys, such as DESI (DESI Collaboration et al., 2016a,b), WEAVE, (Dalton et al., 2012), 4MOST, (de Jong et al., 2016), and SDSS-V, (Kollmeier et al., 2017). These experiments will deliver spectroscopy with a sufficient quality for a reliable identification for sources as faint as $G \simeq 20$

We therefore adopt a magnitude limit of $G = 20$, and using $m = 20 - 5 \log(d/10)$, we determine the intrinsically faintest systems (assuming minimal extinction) we can detect for a given distance limit, as illustrated in Figs. 4.2, 4.7, 4.10 for the different classes of white dwarf binaries. The overall volume limit of our census is a compromise between sample size and completeness and we have chosen

$$\mathbf{r_est} < 300 \text{ pc} \quad (4.1)$$

where $\mathbf{r_est}$ is the distance estimate of Bailer-Jones et al. (2018), with the exception of the DWDs (Sect. 4.3.4). This choice will introduce well-quantifiable selection effects (some types of white dwarf binaries are inherently fainter than others), which we explore further in the context of each individual sub-class.

Accurate astrometry and photometry are needed to avoid misleading conclusions when we use the samples to evaluate potential cuts. Following Lindegren et al. (2018)

and [Lindgren \(2018\)](#) we filter the astrometry by:

$$\text{ruwe} < 1.4 \quad (4.2)$$

$$\varpi/\sigma_{\varpi} > 10 \quad (4.3)$$

where **ruwe** is the ‘re-normalised unit weight errors’, and ϖ and σ_{ϖ} are the parallaxes and its uncertainties. The **ruwe** is not unduly impacted by the binarity of the CVs due to their short periods ($P_{\text{orb}} \lesssim 1$ d) ([Belokurov et al., 2020](#)).

To ensure that the precision of the red and blue photometry is within 10 per cent ($\simeq 0.1$ mag) we again followed [Lindgren et al. \(2018\)](#) and filtered on:

$$\text{phot_bp_mean_flux_over_error} > 10 \quad (4.4)$$

$$\text{phot_rp_mean_flux_over_error} > 10 \quad (4.5)$$

Known CVs that failed these quality cuts are listed in Table A.4. These filters do not just exclude dim stars. Two examples closer than 100 pc are U Gem (excluded because **ruwe** = 1.48) and AM Her (excluded because **phot_rp_mean_flux_over_error** = 6.04). Although it may seem counter-intuitive to omit well-known systems it must be remembered that the purpose of a Gold Sample is not to be complete, but to be clean, with good *Gaia* data.

The accurate astrometry enables the derivation of an important parameter of the various white dwarf binary classes: their space density. The space density makes assumptions about the age and hence the scale height of systems and can be calculated using the approximation:-

$$\rho = \rho_0 e^{-|z|/h} \quad (4.6)$$

where h is the scale height. The effective volume for a given radius (R) is then calculated by integration:-

$$V_{\text{eff}} = \int_0^R \int_{-\sqrt{R^2-x^2}}^{\sqrt{R^2-x^2}} (2\pi x) \left(\exp^{-|z|/h} \right) dz dx \quad (4.7)$$

Using this expression, the space density of the considered type of white dwarf binary is then given by the size of the sample divided by $\rho = N/V_{\text{eff}}$. This requires an assumption for the value of h , which depends upon the age of the stars in the sample ([Pretorius et al., 2007a](#)). Below, we follow [Pala et al. \(2020\)](#) and calculate the space densities of the Gold Samples for three different values of h (100, 280, 500 pc). The estimates of ρ_0 will represent lower limits to the true space densities of the respective white dwarf binary populations as the Gold Samples are not complete.

Table 4.1: Assembling the Gold samples. Positive numbers indicate the initial sample size, negative numbers indicate the effects of the individual cuts that were subsequently applied. The requirement for a complete set of accurate attributes dramatically reduces the final sample size. ‡ see Equations 4.2-4.5

System type	WD+M					WD+AFGK			CV	DWD		
Source	SDSS	Ashley sample	Zorotovic sample	RK sample	Other	Ren sample	RK sample	Other		20 pc sample	40 pc sample	Other
Source Systems	3287	16	25	190	2	23	25	7	5192	5	24	198
Duplicates	-1	-6	-3	-131				-2			-3	-2
Systems with no <i>Gaia</i> match	-213	-1		-2								
Systems with no parallax	-429			-3					-1150			-6
Systems >300pc	-2049		-4	-26		-10	-23		-3737			-129
Systems failing quality criteria ‡	-272	-2	-7	-5		-3	-1	-1	-104	-1	-10	-9
Unreliable/invalid Systems				-8					-50			
Wide binaries	-125											
Possible wide binaries	-119											
Final Gold Sample	79	7	11	15	2	10	1	4	151	4	11	52
	114					15			151	67		

4.3.1 PCEBs: White dwarfs with M-type companions

Establishing the Gold Sample

There has been a continuing effort over many years to build a comprehensive catalogue of binaries consisting of a white dwarf and a main sequence M-type star (hereafter WD+M, see [Rebassa-Mansergas et al. 2007, 2010, 2012b, 2013, 2016](#)). This catalogue contains WD+M binaries identified from the detection of both stellar components in their SDSS spectroscopy. Whereas these systems are unresolved in the SDSS imaging data, given the typical spatial resolution $\simeq 1.5$ arcsec, and distances of several 100 pc, they can be either short-period (hours to days) PCEBs or wide binaries with separations of tens of AU that never interacted. Extensive radial velocity studies of the SDSS WD+M binary sample showed that $\simeq 21 - 24$ per cent are PCEBs, with a period distribution peaking at $\simeq 10.3$ h ([Nebot Gómez-Morán et al., 2011](#)). In the online catalogue of SDSS WD+M binaries*, PCEBs are defined as systems where a $\geq 3\sigma$ radial velocity variation has been detected in the spectroscopy, and we select these ‘SDSS’ systems for our Gold Sample.

To these we added confirmed WD+M binaries from [Farihi et al. \(2006, 2010\)](#), some of which were later followed up by [Ashley et al. \(2019\)](#). These WD+Ms (hereafter the ‘Ashley sample’) were identified from catalogues of white dwarfs due to their infrared excess and were unresolved in high-resolution *HST* imaging. [Ashley et al. \(2019\)](#) obtained radial velocity measurements of these systems, and corroborated the bi-modality of the orbital separations referred to earlier, i.e. that we can expect WD+M binaries to be either close (with periods of hours to days) or wide (with periods $>$ years).

*<http://www.sdss-wdms.org> ([Rebassa-Mansergas et al., 2012a](#))

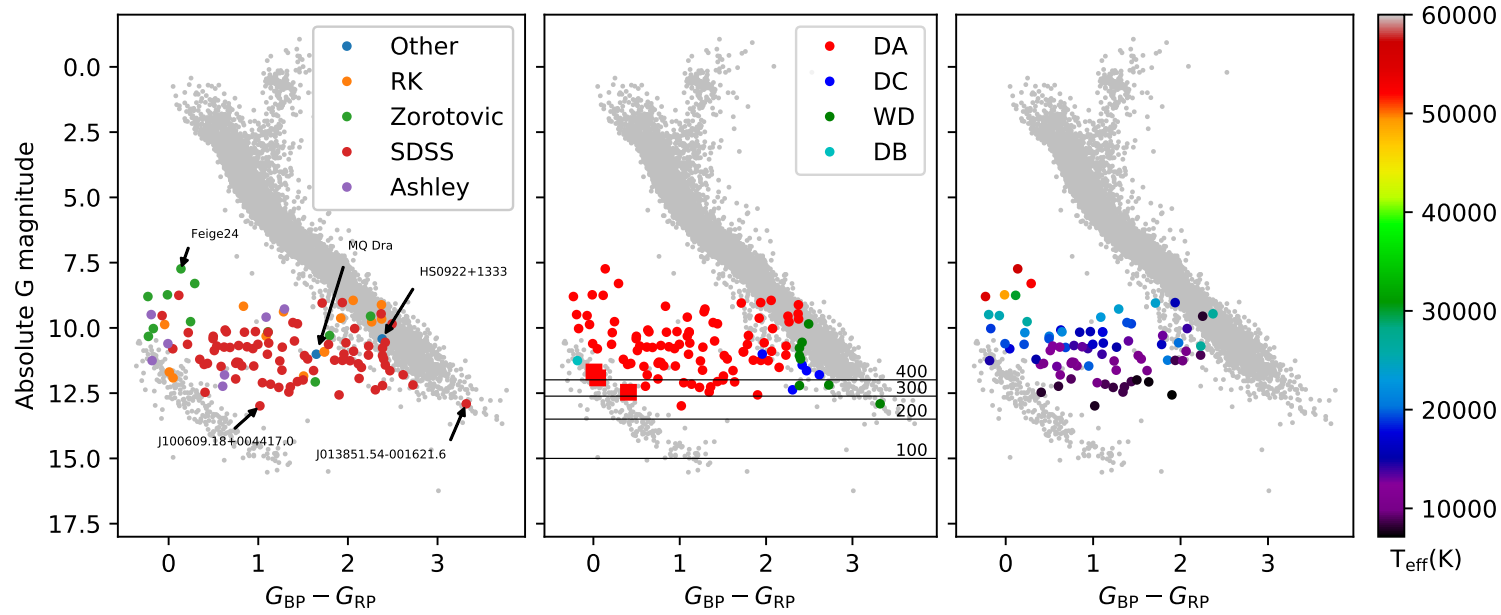


Figure 4.2: The WD+M Gold Sample in the HR diagram. Left panel: distribution of the sub-samples. Middle panel: distribution of the white dwarf spectral types. The concentration of systems with no spectroscopic classification (WD, green symbols) near the main sequence indicates that the companion dominates the optical flux of these systems. Systems with brown dwarf companions are indicated by squares; their location within the white dwarf cooling sequence is consistent with the low luminosity of the brown dwarfs. The minimum absolute magnitude to be detectable at an apparent magnitude of $G = 20$ is indicated by grey lines for distances of 200, 300 and 400 pc. Right panel: The white dwarf effective temperatures of the WD+M Gold Sample plotted on the HR diagram. The decrease in absolute magnitude with decreasing effective temperature is evident.

We also added confirmed PCEBs from appendix A2 of [Zorotovic et al. \(2010\)](#) (hereafter the ‘Zorotovic sample’) as well as the confirmed PCEBs from the catalogue of [Ritter & Kolb \(2003\)](#) that were not contained in any of the other published lists (hereafter the ‘RK sample’).

The process for assembling the Gold Sample is illustrated in Table 4.1. We first match each system to the closest *Gaia* source within 2 arcsec and then removed those with distances (r_{est} from [Bailer-Jones et al. 2018](#)) greater than 300 pc even if their uncertainties might bring them under 300 pc ($r_{\text{lo}} < 300$). We then removed any systems that fail the data quality criteria (4.2) to (4.5) and finally rejected wrongly classified systems, e.g. those with an A to K class companion (which we incorporate in the sample discussed in the next Section), or those considered to be unreliable.

The WD+M Gold Sample includes four systems containing strongly magnetic white dwarfs in which accretion of the wind from the M-dwarf companion results in the emission of cyclotron radiation: MQ Dra ([Szkody et al., 2008](#)), WX LMi ([Reimers et al., 1999](#)), SDSS J030308.35+005444.1 ([Parsons et al., 2013b](#)) and HS0922+1333 ([Reimers & Hagen, 2000](#)). These systems are considered to be progenitors of magnetic CVs, and hence called pre-polars, or PREPs.

Finally, whilst we refer to the set binaries assembled here as the WD+M Gold Sample, we have also included four systems with brown dwarf companions, as their properties and evolution are very similar to those of white dwarfs with low-mass M-dwarf companions: SDSS J013532.97+144555.9 (= NLTT 5306, [Steele et al. 2013](#)), WD 0137–3457, ([Burleigh et al., 2006a](#)), SDSS J141126.20+200911.1 ([Casewell et al., 2018](#)) and GD1400, ([Farihi et al., 2005a](#)).

As mentioned above, we defined 300 pc as the limit for the WD+M Gold Sample yielding 114 systems, which are listed in Table A.1.

Selection effects

The distribution of the WD+M binaries in the *Gaia* HR diagram is illustrated in Fig. 4.2, where they define a horizontal ‘bridge’ between the white dwarf cooling sequence and the main sequence. The evolutionary interpretation of this bridge is discussed in more detail in Sect. 4.4.1. We discuss a few individual systems to illustrate the effect of the white dwarf and M-dwarf spectral type on the location in the HR diagram. Feige 24 is a well-studied PCEB ([Kawka et al., 2008](#)) that contains a particularly hot ($\simeq 56\,000$ K, [Vennes et al. 2000](#)) white dwarf, consistent with having the smallest absolute magnitude among the WD+M Gold Sample.

In contrast SDSS J100609.18+004417.0 contains a cold (7819 K) white dwarf and a late-type (M7), low-mass ($0.12 M_{\odot}$) secondary ([Nebot Gómez-Morán et al., 2011](#)). Both stellar components are intrinsically faint, and the system has one of the largest absolute magnitudes in the Gold Sample. Despite the low white dwarf temperature, the

system is located relatively close to the white dwarf cooling track, a consequence of the feeble luminosity of its M-dwarf companion. Finally SDSS J013851.54-001621.6 contains an ultra-cool (3570 K) white dwarf and an M5 companion (Parsons et al., 2012). The white dwarf contributes hardly anything to the optical flux of the system, and it is hence located within the low-mass end of the main sequence. These two systems illustrate that the limit for a truly volumetric sample is $\simeq 250$ pc to ensure faint systems such as SDSS J100609.18+004417.0 are fully represented (see Fig. 4.2, left panel).

A global selection effect that affects the WD+M sample is that it has been primarily constructed from systems identified by SDSS. Consequently, the restricted sky coverage of SDSS has to be taken into account. Based on the sky distribution of $\simeq 5.8$ million optical spectra contained within DR16 (Ahumada et al., 2020), we estimate that SDSS spectroscopy has been obtained over $\simeq 29$ per cent of the sky.

The known population of WD+M binaries will be subject to additional selection effects that will affect both the completeness and distribution in the HR diagram parameter space of the Gold Sample defined here. As these systems are, for the vast majority, selected from optical spectroscopy, a key criterion necessary for their identification is that both stellar components contribute noticeable amounts of flux in the visual wavelength range. That immediately implies that a WD+M in which one of the components strongly dominates the optical spectrum will be difficult if not impossible to identify (see Sect. 4.3.2). One example consists of hot white dwarfs with very late type M-dwarf companions. The detection of emission lines from the irradiated companion may mitigate the low overall flux contribution of the companion, although that introduces another selection effect, i.e. the binary separation. Very cool white dwarfs with relatively early M-dwarf companions form another example. In addition to these intrinsic limitations in the identification of WD+M binaries, there will be additional biases related to the specific observations that were used in a given study, such as the wavelength range covered by the spectroscopy, and brightness limits.

The following discussion focuses on the SDSS WD+M sample, which was identified and analysed in a homogeneous fashion, and which makes up the bulk of the Gold Sample. Specifically, the SDSS WD+M sample has a bright-limit of $g \simeq 15$ to avoid saturation of the CCDs and contamination of the spectra of fainter objects on adjacent fibres (Strauss et al., 2002). This limit will introduce a bias, that we have mitigated by including the systems from Ritter & Kolb (2003), Ashley et al. (2019), and Zorotovic et al. (2010). More subtle, and hard-to-quantify effects arise from the fact that the SDSS sample was obtained using the 640-fibre SDSS and the 1000-fibre BOSS spectrographs sampling a seven square degree field-of-view (York et al., 2000; Smee et al., 2013). The allocation of these fibres is subject to a complex selection algorithm, that has evolved over the course of the SDSS, and will result in both incompleteness and magnitude and colour-dependent selection effects. Rebassa-Mansergas et al. (2010, 2012b, 2013,

Table 4.2: The number of each WD sub-type (where known) in the WD+M Gold Sample.

Sub-type		n
DA	Only hydrogen features	94
DC	Featureless continuum	5
WD	No WD spectral type	8
DB	Only helium features	1

2016) reported spectral types for the white dwarf and M-dwarf components, as well as effective temperatures for a sub-set of the white dwarfs. We discuss the distributions of those parameters in turn.

White dwarf spectral type. The white dwarfs within the SDSS WD+M sample were classified, according to the key features in their optical spectra, into DAs (clearly detected Balmer lines), DB (clearly detected helium lines), DC (featureless continua), and WD (definite blue excess over the M-dwarf, but insufficient to assess the intrinsic spectrum of the white dwarf); the respective numbers of these types are listed in Table 4.2. The vast majority of the WD+M binaries contain DA white dwarfs, and that fraction may be somewhat higher than among single field white dwarfs in a magnitude-limited sample (e.g. Kleinman et al. 2013). Accretion of the wind of the companion (Debes, 2006) would relatively rapidly build up a sufficient amount of hydrogen to convert an initially helium-dominated white dwarf into a DA. Figure 4.2 (centre panel) illustrates the distribution of white dwarf spectral types within the *Gaia* HR diagram. As expected, the WD+M systems with barely recognisable contributions from the white dwarf are mostly localised close to or in the main sequence.

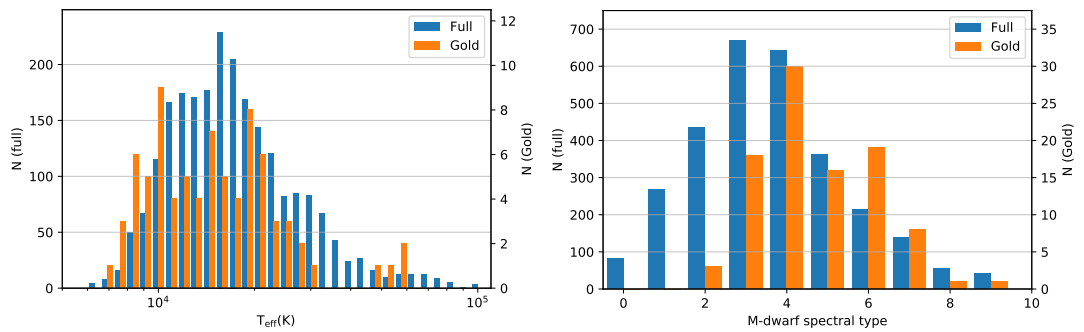


Figure 4.3: Left panel: The distribution of the effective temperatures (where known) of the white dwarfs in the WD+M Gold Sample contrasted with the full (not volume-limited) set from Rebassa-Mansergas et al. (2016). Right panel: The distribution of the spectral types (where known) of the white dwarf companions. The WD+M Gold Sample is contrasted with the full (not volume-limited) set from Rebassa-Mansergas et al. (2016) and shows that the WD+M Gold Sample has a higher proportion of late companions.

White dwarf temperature. The temperature distribution of the white dwarfs within the Gold WD+M sample in the HR diagram is shown in Fig. 4.2 (right panel). Again, as expected, the WD+M binaries with the lowest temperatures have the largest absolute magnitudes. Comparing the white dwarf temperatures in the Gold WD+M sample ($d \lesssim 300$ pc) with those in the full sample (Fig. 4.3) reveals a bias against hot white dwarfs within the Gold Sample. This relatively small bias is a consequence of the brightness limit of the SDSS spectroscopy – whilst the actual value of that limit varied throughout the different instalments of the survey, and its diverse sub-programs, very few stars brighter than $g \simeq 16$ were observed with the SDSS or BOSS spectrographs, and the hottest white dwarfs will violate that limit at $d < 300$ pc [†].

Spectral type of the companion. Rebassa-Mansergas et al. (2010) provide the spectral types of the M-dwarf companions of their sample. Figure 4.3 shows that the distribution of the WD+M Gold Sample is biased in favour of later stars. This again shows the difference between a volume-limited and a magnitude-limited sample, with the intrinsically fainter late spectral types being under-represented in the latter one. A more subtle selection effect is the correlation between donor spectral type and white dwarf temperature: for the WD+M to be detected as such, the white dwarf will need to be brighter, and hence hotter, for earlier type donors. It follows that a magnitude-limited sample will favour intrinsically bright white dwarfs and hence earlier type donors.

The Gold Sample as a fraction of the total population

The space density of the WD+M Gold Sample (Table A.1 including periods where available) is reported in Table 4.3 for the three adopted values of the scale height. Remembering the selection effect caused by the SDSS sky coverage these space densities should be multiplied by ~ 3.4 before making comparisons with the intrinsic space density of WD+M binaries. Few published studies on observational estimates of the space density

[†]There are 229338 white dwarfs in the Gentile Fusillo et al. (2021a) white dwarf catalogue within 300 pc of which 2113 (~ 1 per cent) have $G < 16$.

Table 4.3: The estimated effective volume (V_{eff}) and space density of the Gold Samples as a function of scale height (h). These ignore selection effects such as SDSS sky coverage (see text for details).

h (pc)	V_{eff} (10^6 pc^3)	ρ_0 (10^{-6} pc^{-3})			
		WD+M	WD+AFGK	CV	DWD
100	46.5	2.47	0.37	3.27	1.35
280	65.4	1.76	0.26	2.23	1.04
500	93.3	1.23	0.18	1.63	0.73

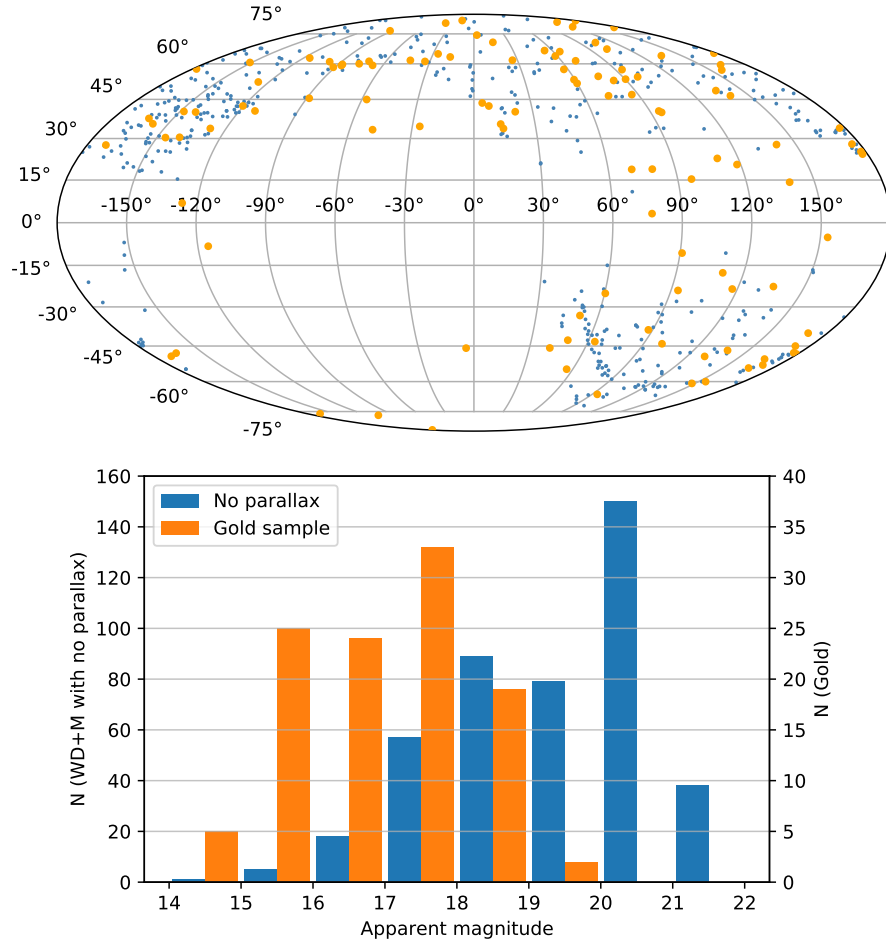


Figure 4.4: Top panel: The distribution of the WD+M Gold Sample (orange) and candidates without a *Gaia* parallax (blue) in Galactic coordinates. Bottom panel: The *G*-band magnitude distribution of the WD+M Gold Sample compared with the WD+M systems without a parallax. It is evident that most of the systems without a parallax are fainter than the Gold Sample – although the parallax incompleteness is already rising when $G \gtrsim 17$, which is several magnitudes brighter than *Gaia*’s magnitude limit.

of WD+M binaries exist, [Schreiber & Gänsicke \(2003\)[‡]](#) quote $6\text{--}30 \times 10^{-6} \text{ pc}^{-3}$ which is substantially higher than the values we derive here – however, these authors accounted for the selection effects introduced by the dimming of the white dwarf throughout the PCEB evolution. The WD+M Gold Sample clearly forms a small subset (~ 10 per cent) of the underlying population, and is biased in favour of systems with hot white dwarfs and early-type M-dwarfs.

[‡]The sample of [Schreiber & Gänsicke \(2003\)](#) includes a small number of PCEBs with companion spectral types earlier than M.

Candidates with no parallax

Of the 3520 candidates (Table 4.1) 432 did not have a *Gaia* parallax. We consider the distribution of these 429 systems across the sky area and magnitude range (Fig. 4.4). Whereas the sky coverage of the SDSS footprint is evident (see Blanton et al. 2017), there is no apparent spatial pattern among the systems without parallax. However, the magnitude distribution reveals a clear drop in the fraction of WD+M candidates with parallaxes towards fainter systems. The parallax incompleteness is already very noticeable for $G \gtrsim 17$, which is substantially above the *Gaia* magnitude limit. The reason for the apparent difficulty of *Gaia* in measuring parallaxes of WD+M systems is not clear, but we speculate that some of those systems might be wide binaries that exhibit sufficient astrometric accelerations to foil the DR2 five-parameter astrometric solution. This hypothesis is supported by the large number of systems found between the white dwarf cooling track and the main sequence that have excessive `ruwe` values (see fig. 1 in Belokurov et al. 2020).

4.3.2 PCEBs - White Dwarf + A/F/G/K stars

PCEBs consisting of a white dwarf and a star of spectral type A, F, G and K (hereafter WD+AFGK) present very different observational issues from those with M-dwarf companions as the optical flux of the companion star is so much greater than that of even hot and young white dwarfs. Nevertheless, the process of establishing systems as close WD+AFGK binaries is the same as for the WD+M ones, i.e. firstly identifying candidate systems, and secondly establishing whether they are wide binaries, PCEBs or close binaries formed through stable Roche-lobe overflow (Parsons et al., 2023) via the appropriate follow-up observations.

Establishing the Gold Sample

WD+AFGK binary candidates have been identified by searching for systems with an ultraviolet excess – which in most case signals the presence of the white dwarf. As PCEBs have short periods their confirmation requires the detection of radial velocity variations related to the orbital motion. Given that the companions in these systems totally dominate the optical flux, their spectra are rich in sharp photospheric features, and they are typically relatively bright compared with WD+M systems.

The identification of WD+AFGK binary candidates has been pioneered by Parsons et al. (2016) and Rebassa-Mansergas et al. (2017b) who cross-matched AFGK-type stars spectroscopically confirmed by the RAVE and LAMOST surveys respectively, with the *GALEX* ultraviolet photometry. Parsons et al. (2016) obtained *HST* spectroscopy of nine of these potential WD+AFGK binaries, all of which contained white dwarfs

(see also [Werner et al. 2020](#)).[§] Follow-up spectroscopy of TGAS-selected WD+AFGK candidates led to the confirmation of 23 PCEBs ([Ren et al. \(2020\)](#), hereafter the ‘Ren sample’). Four additional PCEBs were confirmed by [Parsons et al. \(2015b\)](#) and [Hernandez et al. \(2021a\)](#). We included also the well-studied PCEBs V741 Tau ([Nelson & Young, 1970](#)) and IK Peg ([Wonnacott et al., 1993](#)), as well as the recently discovered GPX-TF16E-48 ([Krushinsky et al., 2020](#)).

We also consider in this sample the EL CVn binaries, short-period ($\simeq 1 - 3$ d) binaries containing A/F-type stars with extremely low-mass (ELM) white dwarf companions. These systems are identified as eclipsing binaries ([Maxted et al., 2014](#); [van Roestel et al., 2018](#)). EL CVn stars represent a different evolutionary channel from the WD+M and most WD+AFGK binaries discussed so far, forming via dynamically stable mass transfer that initiates once the initially more massive star in a main-sequence binary enters the sub-giant branch ([Chen et al., 2017](#); [Sun & Arras, 2018](#)). There is strong evidence that most EL CVn systems are inner binaries of hierarchical triples ([Lagos et al., 2020b](#)). We include the EL CVn stars listed by [Ritter & Kolb \(2003\)](#) (hereafter the ‘RK sample’). As before systems without a *Gaia* match or parallax were dropped and quality filters (Eq. 4.1 to 4.5) were applied (see Table 4.1)[¶]. The WD+AFGK Gold Sample contains 15 systems (Table A.2).

HR Diagram

The distribution of the WD+AFGK binaries in the *Gaia* HR diagram is shown in Fig. 4.5. As the size of this Gold Sample is small (Table 4.1), we include in this diagram, purely for the purpose of visualisation, systems beyond the 300 pc volume limit; these systems are not included in the Gold Sample.

WD+A binaries are located at the top of the main sequence, and the intrinsic brightness of the main sequence companions in these systems results in a significant selection effect: All but one are EL CVn binaries with a low mass pre-He white dwarf formed by stable mass transfer rather than in the common envelope phase. These systems have been almost exclusively discovered because of mutual eclipses of the two stellar components. The Gold Sample contains one EL CVn star: the prototype itself.

The one non-EL CVn system among the WD+A binaries is IK Peg. Whereas it is not included in the Gold Sample because of *Gaia* quality issues, it deserves mention as it further underlines the difficulty in finding WD binaries with luminous companions. IK Peg had long been known as a single-lined spectroscopic binary with a period of 21.7 d ([Harper, 1928](#)), but the white dwarf component was discovered only much later

[§]This does leave the possibility that some systems are triples. [Lagos et al. \(2020a\)](#) estimated this fraction to be less than 10 per cent.

[¶]In the case of WD+AFGK binaries, the main sequence star is intrinsically so bright that it will be reliably detected to well over 300 pc. However for compatibility with the other Gold Samples, we use the same limiting volume.

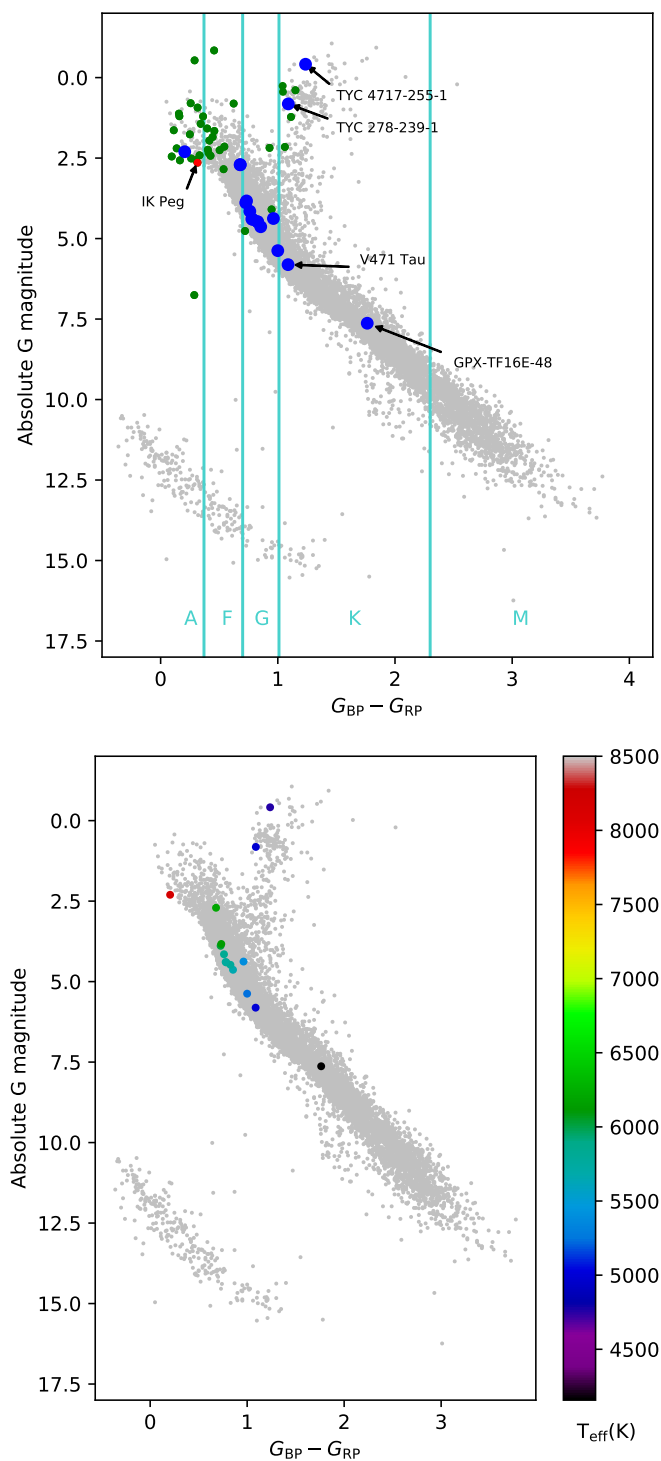


Figure 4.5: Upper panel: The WD+AFGK Gold Sample in the HR diagram contrasting the WD+AFGK PCEBs over 300 pc (green), IK Peg (red) and the Gold Sample (blue). The boundaries between spectral types are shown in turquoise. Lower panel: The distribution of the effective temperatures of the main-sequence (and sub-giant) companions of the WD+AFGK Gold Sample.

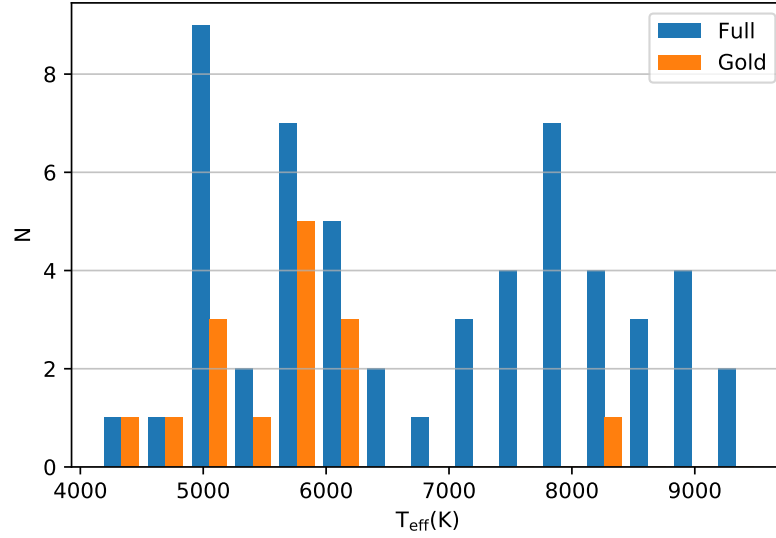


Figure 4.6: The distribution of the effective temperatures of the systems in the WD+AFGK Gold Sample contrasted with the full (not volume-limited) set. The volume-limited sample has a significantly lower average effective temperature.

via ultraviolet spectroscopy (Wonnacott et al., 1993). The fact that IK Peg is nearby, $\simeq 47$ pc, suggests that WD+A PCEBs may be relatively common.

Whereas the Gold Sample contains a number of white dwarf binaries with F- and G-type companions, there is a distinct lack of systems with K-type companions. Noticeable exceptions are V471 Tau (with a K2-type companion, Kamiński et al. 2007) and GPX-TF16E-48 (with a K7-type companion, Krushinsky et al. 2020). This is probably related to selection effects caused by a gap between the two different approaches used to identify white dwarf plus main-sequence binaries (i.e using either optical spectroscopy or ultraviolet excess detections).

Within the HR diagram (Fig. 4.5), the majority of the WD+AFGK Gold Sample occupies the expected well-confined area within the main-sequence, albeit two Gold systems are located within the giant branch: TYC 4717-255-1 is a K0 III star (Houk & Swift, 1999) at 299 pc and TYC 278-239-1 is also a K0 III star at 159 pc (Fabricius et al., 2002).

Given that the contribution of the white dwarf to the optical fluxes of the WD+AFGK binaries is negligible, the effective temperatures (taken from *Gaia* DR2 where available) are essentially those of the main sequence or sub-giant stars. The Gold sample is dominated by systems with cooler, G/K-type companions (Fig. 4.6), with only a single WD+A system, i.e. the prototypical EL CVn. This reflects the difficulty in identifying white dwarf binaries with early type companions, the exception being the EL CVn systems which are identified photometrically via the detection of eclipses.

The Gold Sample as a fraction of the total population

As before (Sect. 4.3.1) we calculate the space density of this Gold Sample for three different values of h (100, 280, 500 pc) (see Table 4.3). These figures compare with $\rho_0 \simeq 4 - 10 \times 10^{-6} \text{ pc}^{-3}$ for the EL CVn stars alone (Chen et al., 2017) and a lower limit on WD+FGK binaries of $\rho_0 > 1.9 \times 10^{-6} \text{ pc}^{-3}$ (Ren et al., 2020), both of which suggest that the WD+AFGK Gold Sample forms a small subset of the underlying population. Moreover this subset is heavily biased in favour of systems where the white dwarf signal can be detected, i.e. namely hot white dwarfs, and we conclude that the population of known WD+AFGK binaries is likely the most incomplete out of all the close white dwarf binary sub-types discussed in this chapter.

4.3.3 Cataclysmic variables

Historically CVs, or more specifically CV candidates, were primarily discovered because of their large-amplitude optical variability, either by visual observers, or from the comparison of photographic plates taken at different epochs (Breedt et al., 2014). Examples of early discoveries include the dwarf nova U Gem (Pogson, 1857) and SS Cyg (Pickering & Fleming, 1896). Variability is still a major source of new CV candidate discoveries, with time-domain surveys such as CRTS (Drake et al., 2014b), ASAS-SN (Shappee et al., 2014), ZTF (Bellm et al., 2019) and *Gaia* alerts (Hodgkin et al., 2013) continually generating new candidates for investigation. Given that a number of phenomena can be mistaken for CVs, such as minor planets (Schmadel et al., 1996) or large-amplitude pulsating stars (Dupke, 1992), the unambiguous confirmation of CVs typically requires follow-up spectroscopy (Zwitter & Munari, 1994; Szkody et al., 2020).

CV candidates discovered because of their optical variability are biased towards systems that undergo frequent, and/or large-amplitude brightness changes. Alternative characteristic hallmarks of CVs are their blue colour, Balmer and helium emission, and X-ray emission, which allow their identification in multi-colour photometric surveys (e.g. Green et al., 1986), spectroscopic surveys (e.g. Aungwerojwit et al., 2006; Szkody et al., 2009), and X-ray surveys (Schwope et al., 2002c; Landi et al., 2009). The relative contributions of the different CV identification methods to the overall population of known CVs, and their affinity with different CV sub-classes are discussed by Gänsicke et al. (2005b). Despite all efforts, CVs that mimic either single white dwarfs, or main-sequence stars, and have low accretion rates remain very difficult to discover (e.g. Rebassa-Mansergas et al. 2014; Teyssier 2019; Yu et al. 2019).

Establishing the Gold Sample

An extensive literature review was conducted as part of Pala et al. (2020) to obtain a comprehensive inventory of both confirmed CVs and CV candidates. This list has

been updated for new CV candidates that have been discovered since that study, and contains 5192 systems of which 4042 have a *Gaia* parallax (see Table 4.1). Applying the distance limit we were left with 305 CV candidates. We then applied the quality filters outlined in Sect. 2.1 resulting in 201 systems.

As discussed by Pala et al. (2020), a fraction of CV candidates reported in the literature are contaminants, including flaring M-dwarfs, young stellar objects, single white dwarfs and detached binaries being mistakenly identified as CVs. In order to establish the CV Gold Sample, we therefore proceeded to validate the CV nature of these 201 candidates.

We began by adopting the CV classification for the 42 systems with $d \lesssim 150$ pc, that were already vetted by Pala et al. (2020), as well as 139 with $150 \lesssim d \lesssim 300$ pc that were in the catalogue of bona-fide CVs compiled by Ritter & Kolb (2003). We then extracted light curves, where available, for the 124 remaining candidates from ZTF (Masci et al., 2019), ASAS-SN (Jayasinghe et al., 2019; Masci et al., 2019) and CRTS (Masci et al., 2019) together with spectra from SDSS (Smeed et al., 2013) and LAMOST (Zhao et al., 2012). We found a total of 152 CVs with reliable spectra and a history of variability and these are henceforth referred to as the CV Gold Sample (Table A.3). The CVs in the Gold Sample have reliable parallax measurements with an average distance uncertainty (based on the estimated errors in Bailer-Jones et al. 2018) of 2.7 per cent.

In passing we note that we have excluded $\simeq 50$ potential CV candidates from the Gold Sample primarily due to a lack of spectroscopy. Follow-up observations are planned and will be reported in a subsequent paper. We also expect that a number of the CV candidates rejected due to poor data quality will be confirmed by *Gaia* EDR3 astrometry.

The CV Gold Sample in the *Gaia* HR diagram

The distribution of the CV Gold Sample within the *Gaia* HR diagram is shown in Fig. 4.7. We re-iterate that the CV Gold Sample is not intended to be complete, but to establish the parameter space that CVs inhabit, and to assess how their location within this parameter space links to their physical properties (the evolution of CVs across the HR diagram is discussed in more detail in Sect. 4.4). We review how well the CV Gold Sample meets those goals in four ways – firstly by checking that the variety of sub-types are well-represented, secondly by checking that there is a spread in evolutionary states (for which orbital period is a proxy), thirdly by comparing the number of CVs in the Gold Sample with the estimated size for a complete 300 pc CV sample, and lastly by investigating whether the CV candidates from our initial list that do not have a parallax introduce some major bias in the CV Gold Sample.

CV sub-types. The CV Gold Sample contains examples of all six major different sub-types, their respective numbers are listed in Table 4.4. The different sub-types form clearly distinct clusters in the *Gaia* HR diagram (Fig. 4.7, left panel)[†], and the location of these clusters closely links to the spectro-photometric properties of each sub-type (Fig. 4.7, right panel).

The novalike variables are characterised by stable high mass transfer rates and hot accretion discs that dominate the optical emission of these systems. Correspondingly, their cluster is located at small absolute magnitudes and blue colours. Two AM CVn stars, HP Lib and the prototype AM CVn itself (Faulkner et al., 1972) are novalike variables with stable, hot helium discs that are somewhat bluer and fainter than their cousins with hydrogen-rich discs.

The three sub-classes of dwarf novae exhibit clear trends in their location within

[†]A similar HR diagram has been shown by Abril et al. (2020), presenting overall similar features. However, these authors included a much larger number of CVs with much looser selection criteria than those defining the Gold Sample. Consequently, the clustering in their diagram is less pronounced.

Table 4.4: The number of each type in the CV Gold Sample together with the range of their orbital periods.

Type	N	Period (hours)		
		Median	Min	Max
Novalike	9	4.42	1.51	5.88
AM CVn	6	0.31	0.29	0.88
WZ Sge	26	1.37	1.12	1.82
Magnetic	28	1.89	1.37	9.88
U Gem	23	2.09	0.99	21.43
SU UMa	45	1.63	1.07	2.81
CV	14	1.44	1.3	4.26

the HR Diagram. The U Gem type dwarf novae have lower mass transfer rates than the novalike variables, their quiescent discs are therefore less luminous, and their donor stars can contribute noticeably to the optical flux of the systems, which is reflected by a number of these systems being located close to the main sequence. The donors and accretion discs in the SU UMa systems are less luminous than those in U Gem-type dwarf novae, hence they are concentrated closer to the white dwarf cooling sequence. Finally, the WZ Sge type dwarf novae have the dimmest accretion discs and donor stars, in fact some of them contain brown dwarf companions (GD552 [Unda-Sanzana et al. 2008](#), QZ Lib ([Pala et al., 2018](#)), 1RXS J105010.3–140431 ([Mennickent et al., 2001](#)), SDSS J102905.21+485515.2 ([Thorstensen et al., 2016](#)), SDSS J143317.78+101123.3 ([Hernández Santisteban et al., 2016](#)), SSS J122221.7–311525 ([Neustroev et al., 2017](#))). WZ Sge are therefore inherently the faintest CVs, and merge into the white dwarf cooling sequence.

A noticeable outlier among the dwarf novae is V1129 Cen, a long-period ($\simeq 21.4$ h) CV that exhibits low-amplitude ($\simeq 0.6$ mag) outbursts about once per year, but no emission lines are detected in its spectrum ([Bruch, 2017](#)). The donor is a luminous F-type+ star, explaining the location in the HR diagram.

Magnetic CVs have a larger spread due to their more varied spectral appearances. During states of low mass transfer they resemble the detached WD+M binaries whilst during high states their optical spectra can contain cyclotron emission lines ([Wickramasinghe, 1988](#)) that will affect their colour and absolute magnitude.

Overall, the CV Gold Sample contains a representative mix of the different CV sub-types that well sample the spread of the underlying CV population in the HR diagram.

Distribution of periods. As outlined earlier, the evolution of CVs is driven by orbital angular momentum loss, which results in their periods decreasing down to the period minimum before reversing to longer periods as the donor stars become degenerate. The orbital periods of the Gold Sample (Fig. 4.8) span the typical range occupied by CVs, $\simeq 80$ min to $\simeq 600$ min, and the distribution of the periods broadly resembles that of the volume-limited 150 pc sample ([Pala et al., 2020](#)). However, both the distributions of the 150 pc and 300 pc Gold Sample differ markedly from that of the overall population of known CVs, drawn from the [Ritter & Kolb \(2003\)](#) catalogue, which displays a steep increase in the number of CVs with periods in the range 3 – 4 h. This difference highlights the importance of using a volume-limited sample for population studies, as intrinsically bright novalikes (with mass transfer rates that in fact exceed the predictions of the standard CV evolution model - see [Townesley & Gänsicke 2009](#); [Knigge et al. 2011](#)) are detected out to much larger distances than other CVs and dominate the period distribution of the [Ritter & Kolb](#) sample.

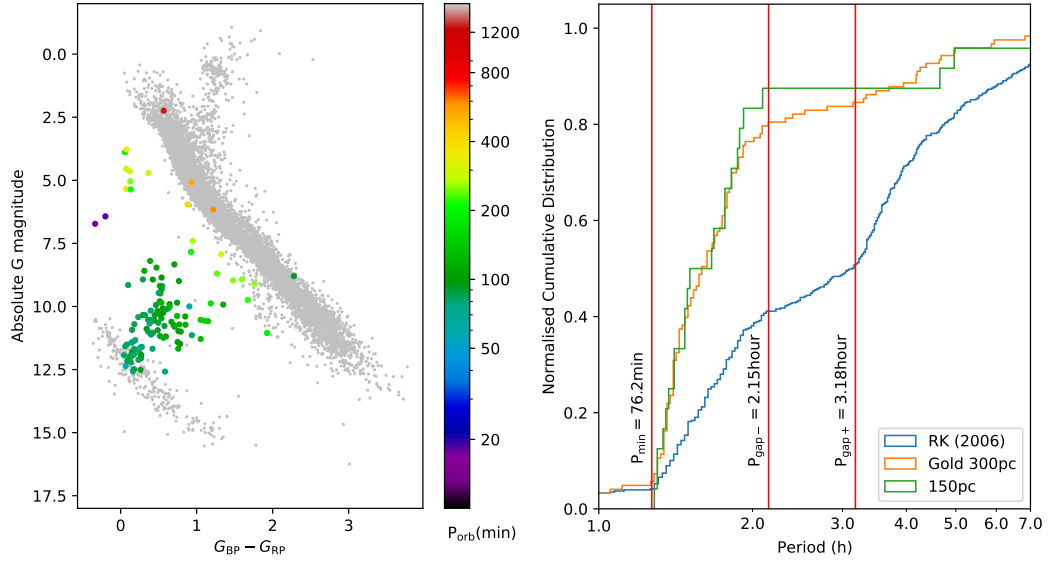


Figure 4.8: Left panel: An HR diagram showing the distribution of CVs in the Gold Sample with their measured orbital periods colour-coded (in minutes). As CVs evolve towards shorter periods, they move from the main sequence towards the white dwarf cooling track. Right panel: Comparison of cumulative orbital period distributions of the 150 pc sample (green, [Pala et al. 2020](#)), the 300 pc CV Gold Sample (orange) and the [Ritter & Kolb \(2003\)](#) sample (blue - we use V7.6 which enables a direct comparison with fig. 4 in [Knigge 2006](#)), which is a heterogeneous mix of CVs identified by all identified selection methods. The period gap starting at two hours is very evident in each case.

We note in passing that the upper edge of the canonical period gap at $\simeq 3$ h is much less pronounced in the volume-limited sample when compared to the overall population of CVs in the RK catalogue, which is subject to a multitude of selection effects. This underlines once more that great care has to be taken when using heterogeneous CV samples as the underpinning of generic CV evolution models.

The Gold Sample as a fraction of the total population. In the same manner as the other Gold Samples, we compute the space density of the Gold CVs for three different values of h (100, 280, 500 pc), resulting in $\rho_0 \simeq 1.6 - 3.3 \times 10^{-6} \text{ pc}^{-3}$ (see Table 4.3). These values should be compared with $\rho_0 = 4.8 \times 10^{-6} \text{ pc}^{-3}$ for the volume-limited 150 pc sample ([Pala et al., 2020](#)), and suggest that the CV Gold Sample represents a substantial fraction ($\simeq 50$ per cent) of the underlying population within 300 pc.

Candidates with no parallax

Among the 5192 CV candidates we began with, 1150 have no *Gaia* parallax, and an important question is whether any of those are within 300 pc. A characteristic of *Gaia* is that the *G*-band magnitude of variable systems with only a 2-parameter solution (i.e. no parallax) will tend to be the (brighter) outburst magnitude not the (fainter)

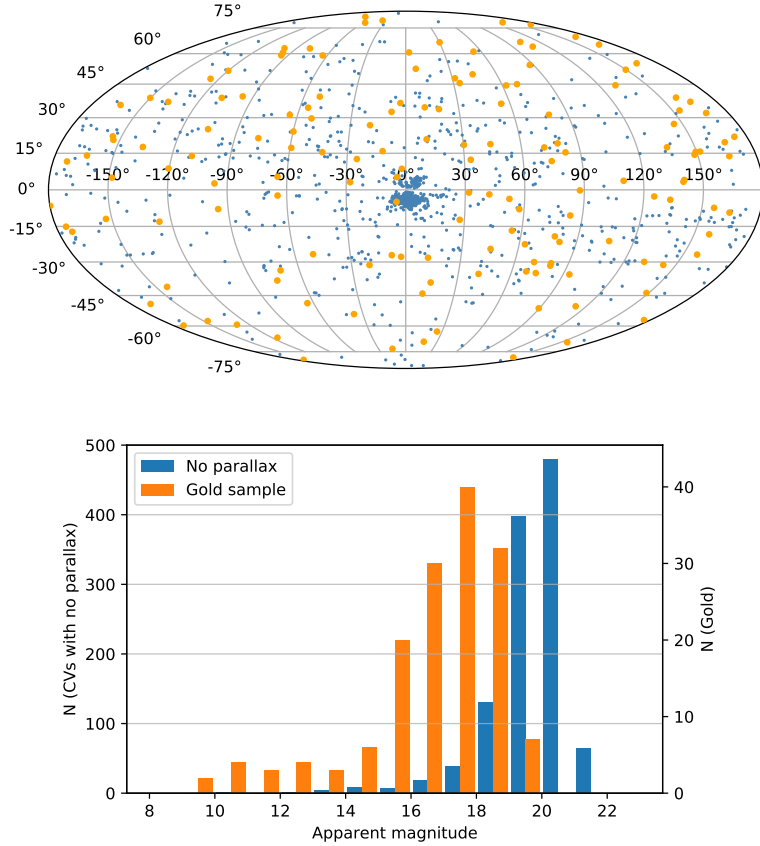


Figure 4.9: Top panel: The distribution of the CV Gold Sample (orange) and the CV candidates without a valid parallax (blue) in Galactic coordinates. The concentration of systems with no parallax close to the Galactic centre is very noticeable, with $\simeq 44$ per cent contained within the area bounded by $-12 < l < 12$ and $-8 < b < 5$. Most ($\simeq 79$ per cent) of this concentration were identified by the OGLE survey (Mróz et al., 2015). Bottom panel: The distribution of apparent magnitudes of the Gold Sample contrasted with the CVs without a parallax. It is evident that most of the CVs without a parallax have apparent magnitudes $\gtrsim 19$, i.e. near the limiting magnitude of *Gaia*.

quiescent one. Figure 10.10 in Antoja et al. (2018) illustrates this effect, and upon closer inspection of a sample, we have found that the majority of CVs with *G*-band magnitudes in the range $\simeq 17 - 20$ (Fig. 4.9, left panel), and no parallax have indeed fainter quiescent magnitudes, $\gtrsim 20$, in SDSS and PanSTARRS1 imaging, suggesting that the *Gaia* detections were obtained during outburst(s) or high states.

For an assumed distance $\lesssim 300$ pc, these very faint quiescent apparent magnitudes would imply that these systems are intrinsically extremely faint with low mass transfer rates, cool white dwarfs and very low-mass donors. Whereas we cannot rule out that a small number of intrinsically faint WZSge type dwarf novae with distances near the volume-limit fall into this category, inspection of the spatial distribution of the 1150 CVs without parallaxes shows a strong concentration towards the Galactic centre

(Fig. 4.9, right panel). CVs within a 300 pc volume limit are expected to be approximately isotropic in their sky distribution, and we conclude that the majority of CVs without a parallax are beyond our adopted distance limit.

4.3.4 Double white dwarfs

Over recent years many DWDs have been documented in the literature. Volumetric surveys of white dwarfs encompassing 20 pc (Hollands et al., 2018) and 40 pc (McCleery et al., 2020) contain a number of confirmed DWDs and these were supplemented by a collection of systems from various other publications, which include most of the known DWDs. As before (see table 4.1) we remove duplicates and systems for which there is no *Gaia* parallax or which fail our quality criteria outlined in Sect. 2.1. The remaining 67 form the Gold Sample (Table A.5).

The DWD Gold Sample in the *Gaia* HRD

A system consisting of two white dwarfs typically has a similar colour to a single white dwarf but is somewhat (up to $\simeq 0.75$ magnitudes depending upon their temperatures and to a lesser extent masses) brighter and therefore appears slightly higher in the HR diagram (Fig. 4.10). The four outliers bounded by NLTT11748 (Kaplan et al., 2014; Kawka et al., 2010) and GALEX J1717+6757 (Vennes et al., 2011) include an extremely low mass (ELM) white dwarf (Brown et al., 2020; Kosakowski et al., 2020). ELM white dwarfs (typically $\sim 0.2 M_{\odot}$) have greater luminosities than more massive white dwarfs because of their larger radii ($R \propto M^{-1/3}$). This increased luminosity therefore causes them to appear above the white dwarf cooling sequence in the HR diagram.

The lack of DWDs at the cool end ($T_{\text{eff}} \lesssim 7000$ K) of the white dwarf sequence is a selection effect. The vast majority of DWDs were identified as spectroscopic binaries (e.g. Morales-Rueda et al., 2005; Napiwotzki et al., 2020), only a very small number were photometrically detected because of eclipses (e.g. Steinfadt et al., 2010) or because of inconsistencies in their spectroscopic features (Bergeron et al., 1990). At low temperatures, the Balmer lines weaken and eventually disappear, therefore the confirmation of DWD candidates (e.g. selected because they are over-luminous, Giammichele et al. 2012; Hollands et al. 2018) becomes very difficult for cool white dwarfs.

Only 38 of the DWDs in the Gold Sample have an orbital period measurement, and there is no apparent correlation between period and position in the HR diagram (Fig. 4.10).

The Gold Sample as a fraction of the total population

As before (Sect. 4.3.1) we calculate the space density for three different values of h (100, 280, 500 pc) (see Table 4.3). These figures compare with $> 0.62 \times 10^{-3} \text{ pc}^{-3}$ from

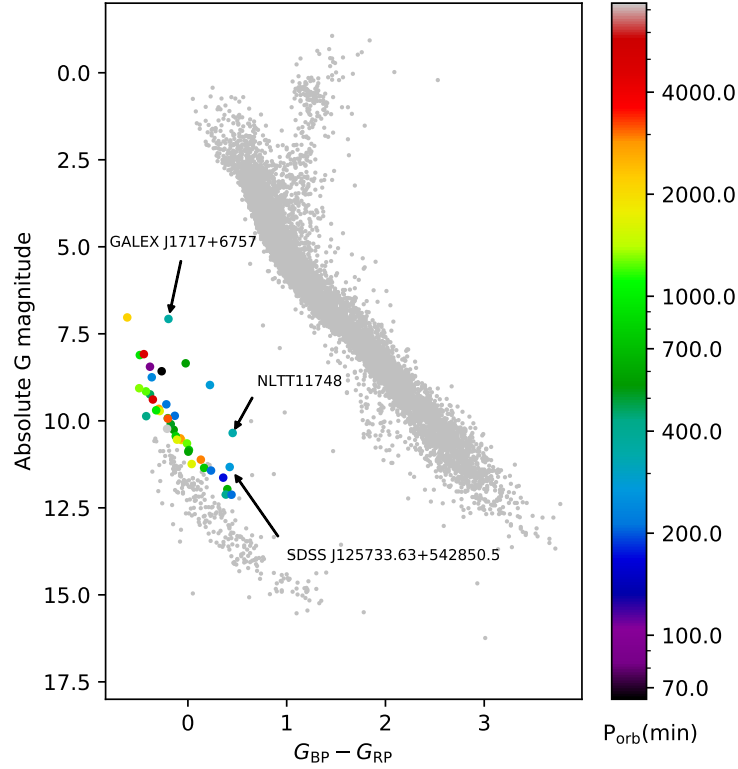


Figure 4.10: The Gold Sample of DWDs with known orbital periods (colour-coded) are located slightly above the general white dwarf cooling sequence in the HR diagram, reflecting the combined luminosity of the two white dwarfs. The lack of DWDs at the faint end of the white dwarf sequence is an observational selection effect.

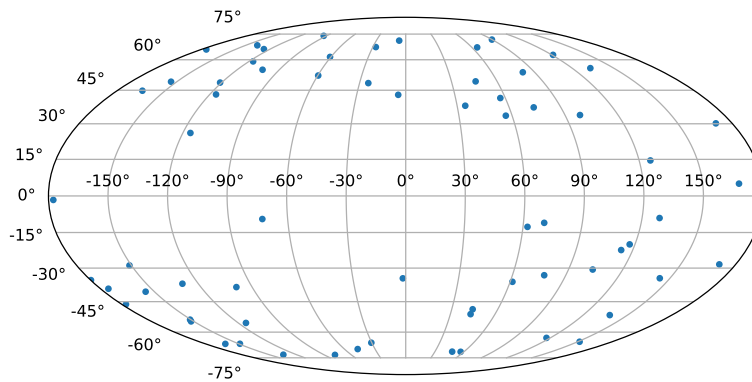


Figure 4.11: The distribution of the DWD Gold Sample in Galactic coordinates. They appear to be evenly distributed away from the Galactic plane. The lack of DWDs near the Galactic plane is a selection effect due to the difficulty in identifying white dwarf candidates in crowded regions.

[Holberg et al. \(2016\)](#) which demonstrates that the DWD Gold Sample forms a tiny subset (~ 0.2 per cent) of the underlying population. This is partly a reflection of the inherently low luminosity of these systems – [Holberg et al. \(2016\)](#) derived their estimates from a volume-limited survey of 25 pc – and partly the difficulty in distinguishing DWDs from single white dwarfs.

Candidates with no parallax

Only six of the 67 candidates (Table [A.5](#)) had no *Gaia* parallax and in each case their *G*-band magnitude was larger than any of the members of the Gold Sample. It is therefore likely that they are all at a distance of more than 300 pc.

This volume-limited sample is weighted towards normal mass white dwarfs rather than the rare, but more luminous ELM DWDs that are detectable out to larger distances, again highlighting the difference between a volume-limited survey and a magnitude-limited one.

4.4 Evolution of white dwarf binaries within the HR diagram.

The discussion so far has focused on establishing and validating the various white dwarf binary sub-samples, and to discuss their observational properties. Here we will briefly investigate the evolution of white dwarf binaries across the HR diagram, as well as the effects of systems moving from one sub-sample into another one.

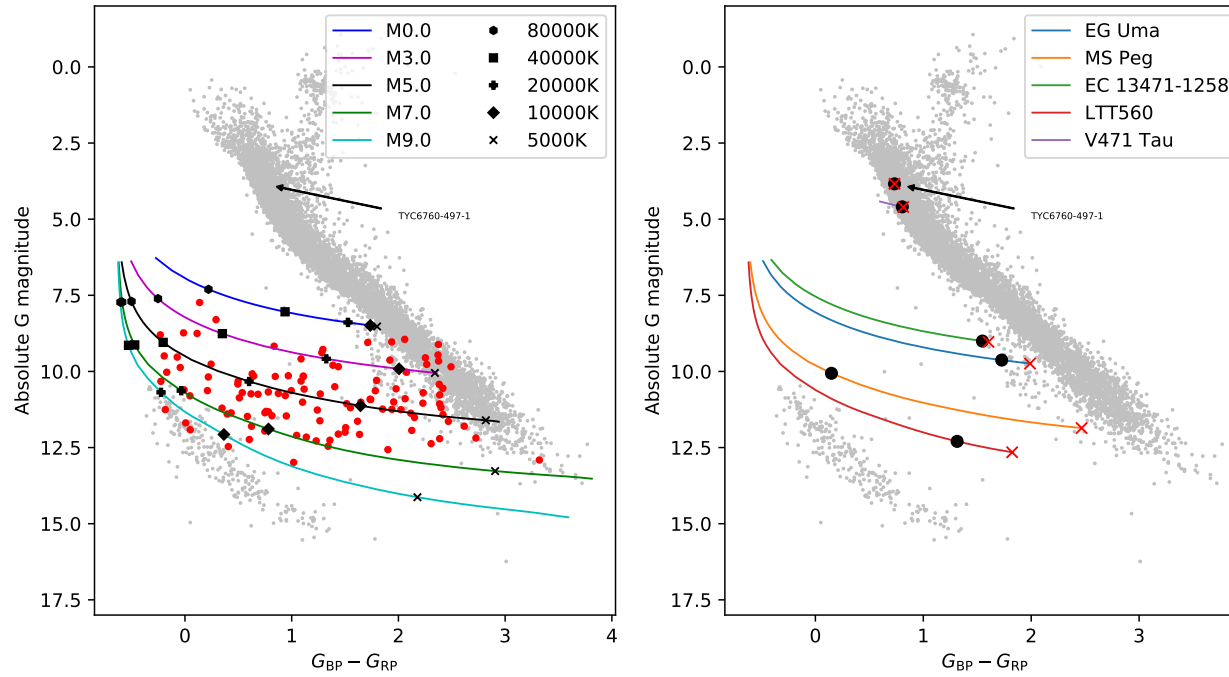


Figure 4.12: Left panel: The evolution of WD+M PCEBs across the *Gaia* HR diagram is illustrated by the coloured tracks showing a range of companion spectral types, the black markers indicate a sequence of white dwarf temperatures. White dwarfs cool very fast initially and then gradually slow down (the cooling ages for a $0.6 M_{\odot}$ white dwarf for the five temperatures annotated in the left panel are $\simeq 3.4 \times 10^5, 4.2 \times 10^6, 6.2 \times 10^7, 6.3 \times 10^8, 6.3 \times 10^9$ yr)**. This results in a selection effect as most (i.e. except the youngest) WD+M0 PCEBs will be seen near the main sequence whilst white dwarfs with less massive companions of the same age will be found in the area between the main sequence and the white dwarf cooling sequence. As the white dwarfs cool, and the flux contribution of the M-dwarfs remains constant, the systems fade and become redder, moving to the right in the HR diagram, until eventually merging into the main sequence. The WD+M Gold Sample is shown as red dots. Right panel: Evolutionary paths for five PCEBs adapted from (Schreiber & Gänsicke, 2003) and (Zorotovic et al., 2011). Their current locations in the HR diagram are indicated by the black dot, and the positions where they will evolve into CVs once the companion star becomes Roche-lobe filling are shown by the red crosses. TYC 6760-497-1 (Parsons et al., 2015b) is a WD+F type. Due to its high mass ratio, this system will undergo a short phase of thermal-timescale mass transfer during which the white dwarf will accrete at a rate that is sufficiently high to sustain nuclear shell burning (Fujimoto, 1982; Iben, 1982) – and will be a super-soft X-ray source, and correspondingly bright and blue (Kahabka & van den Heuvel, 1997).

4.4.1 PCEBs

A PCEB emerges from the common envelope as a detached binary consisting of a hot ($\simeq 100\,000\text{ K}$) white dwarf and a main sequence star companion with a spectral type A to M (and a small number of brown dwarfs). These systems have typical orbital periods of hours to days, are hence always spatially unresolved, and *Gaia* will consequently detect and characterise them based on the combined flux from both stars. In the optical passbands of *Gaia*, PCEBs with K-type or earlier companions are indistinguishable from single main-sequence stars even in the early stages of their evolution (Sect. 4.3.2).

As angular momentum losses drive the evolution of these binaries towards shorter orbital periods, the white dwarf gradually cools, fades, and becomes redder in colour – a process that takes $\simeq 415\text{ Myr}$ to 2.6 Gyr to reach $10\,000\text{ K}$ for white dwarfs with masses of $0.4 - 1.2\text{ M}_{\odot}$. In contrast, companion stars with masses $\lesssim 0.9\text{ M}_{\odot}$ will not significantly evolve, and their flux contribution consequently remains constant throughout the evolution of the binary.

We have computed the evolutionary tracks of a range of WD+M binaries by combining the synthetic G , G_{BP} and G_{RP} magnitudes for a typical 0.6 M_{\odot} white dwarf (Tremblay et al., 2011; Bergeron et al., 2011), with the cooling models provided by Pierre Bergeron**. The M-dwarf companions were modelled using the Phoenix (Husser et al., 2013) and ATLAS9 (Castelli & Kurucz, 2003) grids.

Comparison between these evolutionary tracks and the WD+M Gold Sample (Fig. 4.12, left panel) shows reasonably good agreement, highlighting that WD+M PCEBs containing early or late M-type companions are relatively rare (see also Fig. 9 in Rebassa-Mansergas et al. 2010). This is likely a combination of the slope of the initial mass function of low-mass stars, which drops off for very low stellar masses (Kroupa et al., 1993)^{††} and the selection effects discussed in Sect. 4.3.1. Similarly, WD+M PCEBs with very hot white dwarfs are relatively rare in the Gold Sample (again, see Fig. 9 in Rebassa-Mansergas et al. 2010) which is a consequence of the fact that white dwarfs cool quasi-exponentially together with the selection effects examined in Sect. 4.3.1.

Once the orbital separation reduces sufficiently for the companion to fill its Roche lobe, the system will morph into a CV, and the onset of mass transfer will drastically alter its properties within the HR diagram (Sect. 4.3.3 and 4.4.2). We have used the parameters of five PCEBs in the WD+M and WD+AFGK Gold Samples to compute their tracks within the HR diagram, illustrating both their past evolution as well as the location at which they will transition into CVs and hence disappear from the PCEB

**<http://www.astro.umontreal.ca/~bergeron/CoolingModels> (Holberg & Bergeron, 2006; Kowalski & Saumon, 2006; Fontaine et al., 2001; Tremblay et al., 2011; Bédard et al., 2020).

^{††}Farihi et al. (2005b) already noted (see their fig. 6 & 7) the very similar distribution in M-dwarf spectral types among a 20 pc volume-limited sample of field M-dwarfs and their sample of WD+M binaries.

population (Fig. 4.12, top panel). Except for LTT 560, which contains a relatively cool M-dwarf, the onset of mass transfer will occur close to the main sequence, when the white dwarf has cooled below 10 000 K (Schreiber & Gänsicke, 2003; Zorotovic et al., 2010). V471 Tau illustrates that PCEBs with a K-type companion exit the common envelope very close to the main sequence, and rapidly descend into it (even though the white dwarf in this system is still fairly hot, $\simeq 35\,000$ K, O’Brien et al. 2001).

Although detached white dwarf plus main-sequence binaries are mostly formed via common envelope evolution, the standard theory of CV evolution predicts that some WD+M binaries with periods of $\simeq 2-3$ h are actually CVs in which the donor detached from its Roche lobe (Rappaport et al., 1983; Davis et al., 2008; Zorotovic et al., 2016). Angular momentum loss will still drive the evolution of these systems towards shorter orbital periods until the donor fills its Roche lobe again at $P_{\text{orb}} \simeq 2$ h, when they will transit back into the CV population. Abril et al. (2020) have suggested that these ‘interlopers’ among the WD+M PCEBs population may be identified because of their, on average, higher white dwarf mass (Zorotovic et al., 2011), resulting in larger absolute magnitudes compared to the WD+M PCEBs that have not yet reached the first onset of mass transfer.

A final note concerns those white dwarfs with companions that are sufficiently massive ($\gtrsim 0.9 M_{\odot}$) to evolve off the main sequence within a Hubble time. In the *Gaia* HR diagram, those systems will emerge from the common envelope within the main-sequence. Given their relatively small orbital separations, they will initiate mass transfer before the companion evolves significantly into the giant branch, and will hence transform into CVs ‘in situ’. Their effective temperature can also fall because the AFGK star is pushed out of thermal equilibrium (El-Badry et al., 2021). An interesting example is the WD+F binary TYC 6760-497-1 (Parsons et al., 2015b): because of the high mass ratio, $M_2/M_{\text{wd}} \simeq 2$, this system will undergo a short phase of thermal-timescale mass transfer during which the white dwarf will accrete at a rate that is sufficiently high to sustain nuclear shell burning (Fujimoto, 1982; Iben, 1982) – and will be a super-soft X-ray source, and correspondingly bright and blue (Kahabka & van den Heuvel, 1997). There is no super-soft source known within the 300 pc CV Gold Sample.

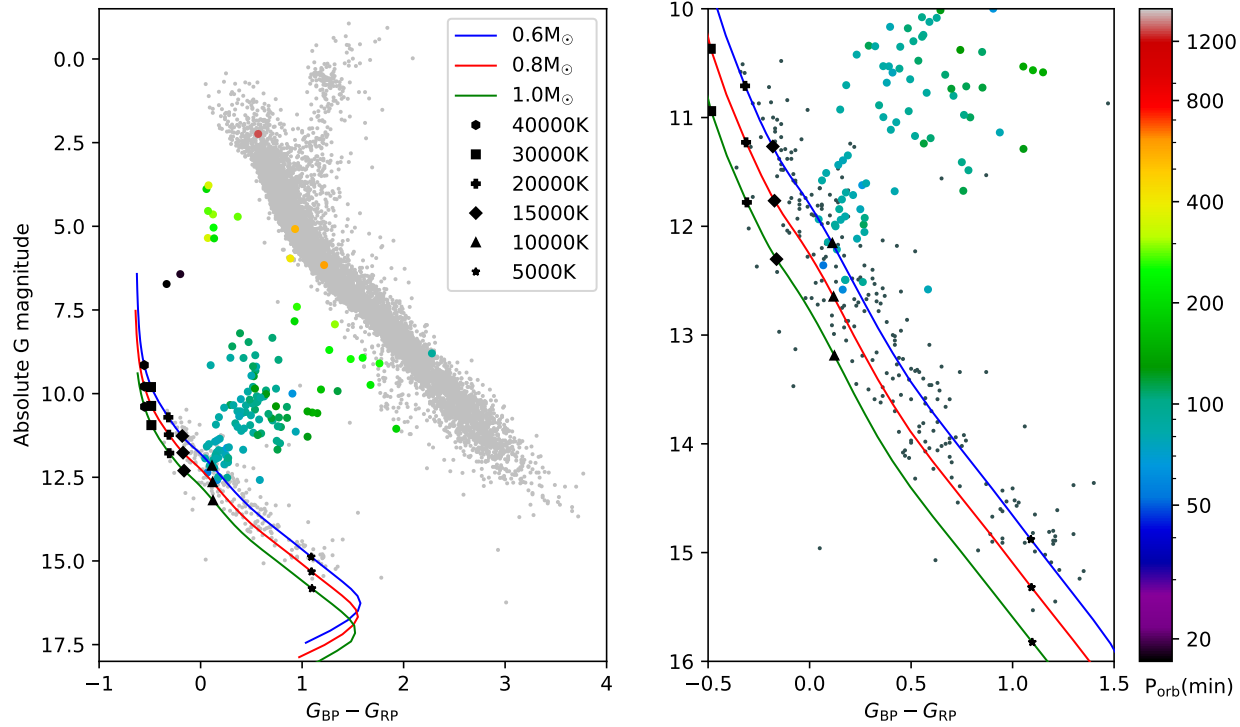


Figure 4.13: The evolutionary channel from the main sequence is clearly evident with a wide range of long period CVs near the main sequence funnelling in as their periods fall towards a small locus in the white dwarf area of the HR diagram (left panel with expanded view in the right panel). By this time CVs have become dominated by their white dwarfs, following prolonged mass transfer. The effective temperature of the CV is essentially that of the white dwarf and is focused towards a region with $T_{\text{eff}} \simeq 10\,000 - 15\,000$ K. Subsequent evolution follows the cooling track of a white dwarf - the cooling tracks of the white dwarf component are shown for white dwarf masses of 0.6, 0.8, 1.0 M_{\odot} (Bergeron et al., 2011).

4.4.2 CVs

CVs commence mass transfer resulting in the formation of a luminous accretion flow, and heating of the surface of the white dwarf (Towneley & Bildsten, 2003). As discussed in Sect. 4.3.3, the location of a CV within the HR diagram depends on the relative contributions of the white dwarf, the donor star, and the accretion flow to the overall flux.

As shown in the previous section, the location of most CVs within the HR diagram at the onset of mass transfer is expected to be close to, or within, the main sequence. Once a companion in a PCEB fills its Roche lobe, the system will very quickly move blue-wards, and, if the mass transfer rate is within the regime of dwarf novae, sit slightly below the main sequence (Fig. 4.7). The distinct cluster of novalike CVs (see Fig. 4.7) with bright, blue accretion discs and very similar orbital periods of $\simeq 3 - 4$ h, i.e. sandwiched between the longer-period U Gem type dwarf novae, and the shorter-period SU UMa type dwarf novae, is noteworthy: these systems appear to have mass transfer rates that exceed the predictions of the standard evolution model (Towneley & Gänsicke, 2009), and very likely reflect a peculiar phase in CV evolution, and/or a specific set of initial parameters.

As CVs evolve the mass, radius, and effective temperature of the secondary decrease, and so does the mass transfer rate, and hence the evolutionary curve moves back towards the white dwarf cooling sequence. This explains the funnel-shaped distribution of CVs in Fig. 4.8 (see also Abril et al. 2020), which clearly illustrates the decrease of P_{orb} as the systems come closer to the white dwarf cooling sequence. An interesting question is whether the 2 – 3 h period gap, i.e. when CV donors detach from their Roche lobes and the systems turn into detached WD+M binaries (see previous section) will leave a detectable imprint in the population of CVs within the *Gaia* HR diagram. We would argue that, at the moment, the number of CVs within a well-defined sample with accurate *Gaia* data is not sufficiently large to assess this question, and we caution that the intrinsic variability of CVs might smear out the effect of the period gap within the HR diagram.

As the mass of the donors continues to decrease, they will eventually change into brown dwarfs^{††}. These are inherently faint systems, and their optical appearance is entirely dominated by the accretion-heated white dwarf, hence their location lies very close to or within the white dwarf cooling track. It is noticeable that the evolutionary path of CVs ends in a small area of the HR diagram corresponding to white dwarf temperatures of $\simeq 10\,000$ K (Fig. 4.13, right panel). The mass transfer rates implied by these accretion rates, $\dot{M} \simeq 5 \times 10^{-11} M_{\odot} \text{ yr}^{-1}$ are consistent with the predictions for

^{††}The CV Gold Sample contains at least five potentially ‘period bouncer’ systems with brown dwarf donors: 1RXS J105010.3-140431 (Mennickent et al., 2001), GD 552 (Unda-Sanzana et al., 2008), SDSS J102905.21+485515.2 (Thorstensen et al., 2016), SDSS J143317.78+101123.3 (Hernández Santisteban et al., 2016), QZ Lib, (Pala et al., 2018).

systems that have reached the period minimum, however, as CVs evolve back towards longer periods (Howell et al., 2001), the mass transfer rates are predicted to drop by an order of magnitude – the known ‘period bouncers’ have mass accretion rates much higher than these predictions. This exhibits the problem of the ‘missing period bouncers’ (Howell et al., 2001; Pala et al., 2020).

A final note concerns the evolution of AM CVn stars within the *Gaia* HR diagram. As they may be formed via three different channels, their locations at the onset of mass transfer may radically differ. In the case of a double-degenerate progenitor (Paczynski, 1967; Deloye et al., 2007), they will start mass transfer in, or close to, the white dwarf cooling sequence. In the case of a white dwarf plus a helium-burning star (Savonije et al., 1986; Yungelson, 2008), they would probably start mass transfer within the region occupied by subdwarfs ($M_G \simeq 4$, $G_{BP} - G_{RP} \simeq -0.5$, Geier 2020). Finally, if they descend from CVs with nuclearily evolved donor stars (Podsiadlowski et al., 2003; Goliash & Nelson, 2015), they would begin mass transfer within the main sequence, and TYC 6760-497-1 (Parsons et al., 2015b) may be a relevant example (Fig. 4.12). The AM CVn stars within the Gold Sample appear bi-modal, with two luminous blue ‘high state’ systems, and the remaining four ‘low state’ systems close to the white dwarf cooling sequence. This may be a result of small number statistics, the larger sample in fig. 2 of Ramsay et al. (2018) exhibits a larger spread – however, that sample is very likely subject to observational biases. The two luminous AM CVn stars within the Gold Sample (AM CVn with a period of 17.14 min and HP Lib with a period of 18.38 min) have high mass transfer rates that maintain their accretion discs in a hot, stable state – in other words, they are miniature novalike variables. They appear bluer and less luminous than the ‘normal’ novalikes with typical periods of 3 – 4 h, reflecting their much more compact size with their spectral energy distribution (SED) dominated by very small and hot accretion discs.

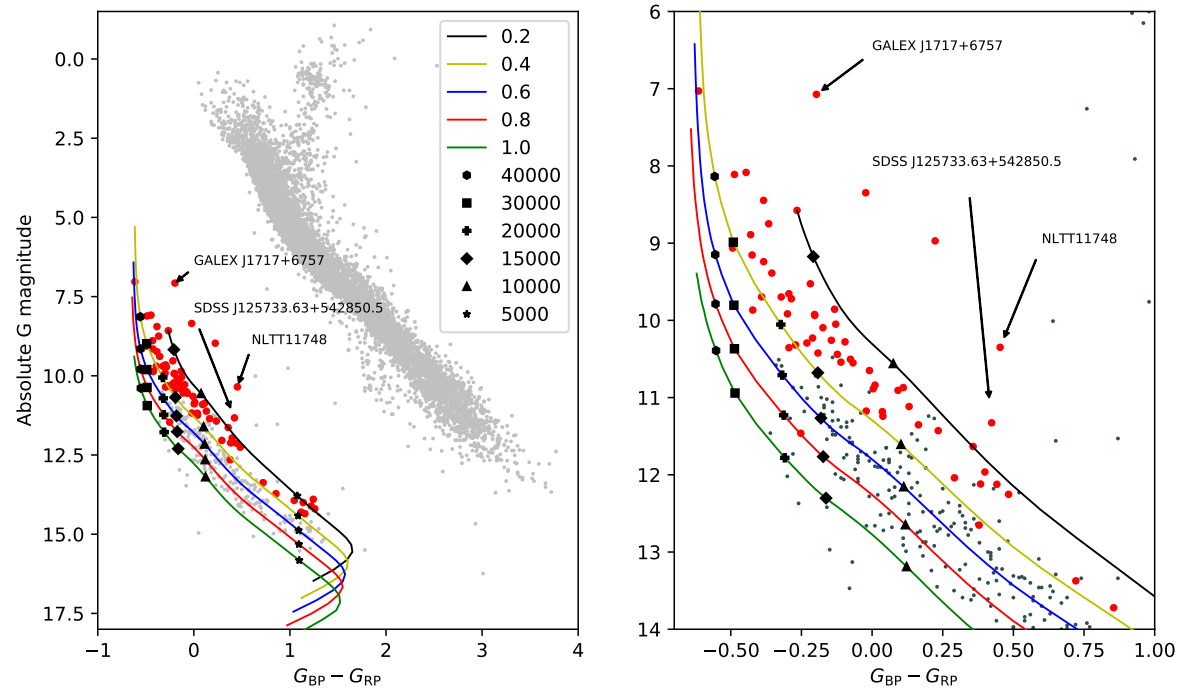


Figure 4.14: The position of the DWD Gold Sample on the HR diagram together with the cooling tracks of single white dwarfs for masses of 0.2, 0.4, 0.6, 0.8, 1.0 M_{\odot} (Bergeron et al., 2011). The colours of the DWDs will be the weighted average of the colours of its constituents whilst the absolute magnitude will be the sum of their fluxes. The position will therefore be similar to that of a single white dwarf but $\simeq 0.75$ magnitudes brighter – in practice the more massive white dwarf will have formed first and hence have progressed further down the cooling track leaving the secondary dominant. The clumping between the 0.2 M_{\odot} and 0.4 M_{\odot} cooling curves indicates that the brighter star in these systems typically has a low mass ($\lesssim 0.4 M_{\odot}$), highlighting possible observational selection effects. *GALEX* J1717+6757 and NLTT11748 are ELMs with $M_{\text{wd}} \lesssim 0.2 M_{\odot}$, which, despite containing relatively cool white dwarfs ($\simeq 10\,000 - 15\,000$ K) are substantially more luminous thanks to their large radii. (Kawka et al., 2010; Steinfadt et al., 2010; Vennes et al., 2011; Hermes et al., 2014)

4.4.3 DWDs

Double white dwarfs tend to sit towards, or just above, the bright edge of the white dwarf cooling sequence. Just as single white dwarfs, they will evolve along the cooling track, though not necessarily follow any single-mass track, as the relative contribution of the two stars gradually changes (Fig. 4.14). DWDs will have experienced at least one common-envelope event and hence their constituents are likely to have differing masses and luminosities. With the exception of the extremely low mass white dwarfs mentioned earlier (well above even the $0.2 M_{\odot}$ cooling track) the majority of the Gold Sample sits around the cooling curves of $0.2 - 0.4 M_{\odot}$ single white dwarfs. This implies that the brighter dwarf is of low mass – the dimmer companion may be an older and/or cooler, higher mass white dwarf (see [Napiwotzki et al. 2020](#)). This almost certainly represents a selection effect, as the brighter low-mass white dwarfs in these systems are easier to find. There are a few DWDs scattered within the cooling curves of higher mass white dwarfs, which suggests that the Gold Sample captures the range of mass ratios found among DWDs, though it may not be representative. An exception is SDSS J125733.63+542850.5 ([Bours et al., 2015](#)) (see Fig. 4.14) which paradoxically has a low mass white dwarf that is older ($\simeq 5$ Gyr) than the more massive one (~ 1 Gyr), highlighting the potentially complex intricacies of the formation of DWDs. As noted in Sect. 4.3.4, the Gold Sample has a sharp cut-off at $G_{BP} - G_{RP} \simeq 0.6$, corresponding to $\simeq 7000$ K due to the disappearance of the Balmer lines.

4.5 Conclusions

We have defined ‘Gold’ reference samples within $d < 300$ pc of the most common populations of close white dwarf binaries: CVs, PCEBs and DWDs. We have used those samples, which encompass most of the parameter space of physical properties (component masses, orbital periods, ages) spanned by close white dwarf binaries, to map out their distribution in the *Gaia* HR diagram. CVs are inherently easier to discover than PCEBs and DWDs. Whereas the CV Gold Sample is likely to be $\simeq 50$ per cent complete, this figure drops to ~ 10 per cent (section 4.3.1) for PCEBs (with a large uncertainty) and less than 0.2 per cent (section 4.3.4) for DWDs. We have furthermore explored how close white dwarf binaries evolve through the *Gaia* HR diagram, criss-crossing between the white dwarf cooling track and the main sequence, occupying similar parameter spaces during different evolutionary phases. We have investigated the differences between magnitude and volume limited close white dwarf binary samples, and have demonstrated the importance of a volume-limited sample to further improve our understanding of the evolution of these systems. The Gold Samples established here will be used to develop selection functions that will reliably identify close white dwarf binary candidates for spectroscopic and photometric confirmation, with the overarch-

ing goal to assemble a volumetric 300 pc sample that is representative of the underlying population of these systems, and sufficiently large to provide accurate statistical insight into the relative numbers, and physical properties of the various sub-types.

Chapter 5

Cataclysmic variables from SDSS III and IV

5.1 Introduction

In Chapter 1 we explained that cataclysmic variables are an important class of white dwarf binaries within multiple astrophysical contexts, including accretion disc physics (González Martínez-País et al., 2014) and potential gravitational wave sources for *LISA* (Danzmann & LISA Study Team, 1996). These compact binaries will become increasingly important as the inventory becomes more complete and the emerging population statistics can be used to test evolutionary models. Although $\sim 10\,000$ CV candidates are known (see for example Watson et al. 2017) that sample contains a fair amount of contaminants, including flaring M-dwarfs, young stellar objects, variable AGN and unexplained transients (see discussion in section 2 of Pala et al. 2020). To be useful for evolutionary modelling a sample of CVs needs not only to be reasonably complete over a given volume but also possess astrometric data for each CV and, crucially, an identification spectrum.

The sample of 507 CVs spectroscopically observed by the Sloan Digital Sky Survey (SDSS) (Gunn et al., 1998; York et al., 2000) presented here is a magnitude-limited sample covering over 25.6 per cent of the sky (section 5.4.4).

The four phases of SDSS (hereafter SDSS I to IV) were executed between 2000 and 2020 (Abazajian et al., 2003; Adelman-McCarthy et al., 2008; Aihara et al., 2011; Aguado et al., 2019) and addressed many science goals of which the search for quasars (Richards et al., 2002) and latterly luminous red galaxies and quasars (Dawson et al., 2013) in the Baryon Oscillation Spectroscopic Survey (BOSS and eBOSS) are of particular relevance here. Between 2000 and 2009 SDSS obtained photometry, using the five *ugriz* filter passbands, of over 14 000 square degrees, predominantly of the northern

sky. The imaging camera (Gunn et al., 1998) was installed on a purpose-built 2.5 m telescope at Apache Point, New Mexico. This photometry was used to select targets for subsequent spectroscopic surveys using a multi-object, fibre-fed spectrograph capable of taking 640 (SDSS I and II) and 1000 (SDSS III and IV) simultaneous spectra spanning $\simeq 3800 - 9200 \text{ \AA}$ (SDSS I and II) and $\simeq 3600 - 10\,000 \text{ \AA}$ (SDSS II and IV, Smee et al. 2013).

Whereas CVs were targeted within SDSS I via a multi-dimensional colour selection (Szkody et al., 2002b), the vast majority of CVs were serendipitously identified from the spectroscopy of quasar candidates. SDSS I (York et al., 2000) and II (Dilday et al., 2005; Yanny et al., 2009) have proven to be a major source of optical spectroscopy of CVs, both of previously known systems and new discoveries (Szkody et al., 2002b, 2003a, 2004a, 2005, 2006, 2007, 2009, 2011).

SDSS III and IV were two subsequent phases spanning from July 2008 until June 2014 (Eisenstein et al., 2011; Dawson et al., 2013) and from July 2014 until August 2020 (Blanton et al., 2017; Dawson et al., 2016) respectively.

SDSS I and II yielded spectra of 285 CVs (Szkody et al., 2011) and have been particularly successful in identifying CVs with no history of outbursts (Gänsicke et al., 2009). Specifically they provided a rich source of short period (80 – 86 min) CVs that provided the crucial observational evidence for the existence of a ‘period minimum spike’. Other groundbreaking achievements include the identification of low accretion rate, X-ray weak, polars (Schmidt et al. 2008 and references therein) and CVs with pulsating white dwarfs (Woudt et al., 2005; Gänsicke et al., 2006; Mukadam et al., 2007). Beyond these individual discoveries the systematic detection of all types of CVs has enabled statistical studies of population density and CV evolution (Gänsicke, 2005). These achievements from SDSS I and II provided the motivation to identify CVs in SDSS III and IV. Further motivation came from the opportunity to refine the attributes of the known CVs using new astrometric and photometric survey data.

We report here the identification of 70 new CVs found in SDSS I to IV (see Table 5.1). We have also revisited the remaining 437 CVs observed during SDSS I to IV in the light of *Gaia* (Gaia Collaboration, 2020) astronomy and photometry from the Catalina Real-Time Transient Survey (CRTS, Djorgovski et al. 2011), Zwicky Transient Facility (ZTF, Masci et al. 2019; Bellm et al. 2019) and the Transiting Exoplanet Survey Satellite (*TESS*, Ricker et al. 2015) which was not previously available. This has resulted in 59 new orbital periods (including some unpublished orbital periods from other sources, details are provided in the supplementary information) and 262 new/revised classifications. SDSS objects are identified by their coordinates, e.g. SDSS J152212.20+080340.9, which we abbreviate throughout this chapter as J1522+0803.

5.2 Methods

In compiling this CV catalogue, we followed a two-step process. In the first step we identified a shortlist of potentially new CVs from the 5 789 200 spectra of SDSS III and IV. In the second step we then undertook a detailed classification of these potential CVs using the methodology described in Section 2.2 as well as revisited all the CVs previously identified in SDSS I and II.

5.2.1 Identification

SDSS I to IV focused upon a number of surveys none of which explicitly targeted CVs. Fortuitously the BOSS and eBOSS targets (Dawson et al., 2013, 2016) included quasars which share a similar colour parameter space to CVs. Since the publication of the first comprehensive orbital period distribution of SDSS (Gänsicke et al., 2009), we progressively built up a list of candidate CVs based upon visual inspection of the flux and wavelength calibrated SDSS spectra (Weaver et al., 2015; Dawson et al., 2016). The spectra were reviewed multiple times by a range of individuals using a number of pre-selections in terms of colour and filtering on the redshifts determined by the SDSS project.

Timothy Mulvany and Henry Israel augmented this visual process by a supervised machine learning process. A data set of known CVs and proven non-CVs was used to train a Random Forest (RF) classifier (Liaw & Wiener, 2001). The RF model used features extracted from the equivalent widths of 12 spectral lines and the average gradient of the spectrum measured over five intervals. The different identification methods resulted in a substantial overlap in the sub-sets of CV candidates that they identified, and whereas we cannot claim to have identified all the CVs that were spectroscopically observed by SDSS, we are confident that our search has picked up the majority of them. CVs that remain overlooked will either have extremely low signal-to-noise ratio spectroscopy, or have colours very close to those of single main-sequence stars, and weak emission lines.

Table 5.1: New CVs from SDSS III and IV. Geometric distances are from (Bailer-Jones et al., 2021). Apparent magnitudes are from SDSS data release 7 (Abazajian et al., 2009). Tentative values are indicated by a ‘:’ suffix.

SDSS name	Gaia EDR3 source_id	Period (d)	SDSS g (mag)	Distance (pc)	Variable type
J000014.74+255603.1			22.17		CV:
J001231.54+280011.1	2859847683924640384		20.98		WZ Sge:
J002910.96+324125.8			22.12		DN
J004849.86+332832.9	361363704879572736		20.61	763^{+358}_{-230}	SU UMa:
J005421.90+334815.7			22.12		WZ Sge:
J010340.75+200525.9	2788762156951156864	0.158(1):	21.45		IP:
J012212.21+075546.8	2578454444735885056		20.33	343^{+119}_{-78}	WZ Sge:
J012402.25+211359.7	289388711652054912	0.083475(1)	21.38	688^{+357}_{-241}	Polar
J013421.83+042200.0			21.41		Polar:
J013540.99+340132.9	316371177970255232		22.42		Polar:
J014121.21+062007.6	2562434457240098432		20.77		WZ Sge:
J014732.85+144443.3	2588313902941290112		22.38	907^{+722}_{-310}	Polar
J015253.39-004350.4			20.81		SU UMa:
J015803.40+282303.6	298356019250182016	0.0888104(1)	20.37	254^{+20}_{-16}	DN
J020712.71-014116.2	2494386992562185088		21.43		Polar:
J023046.26-004531.1			21.68		WZ Sge:
J024215.05-011054.4			22.3		CV:

SDSS name	Gaia EDR3 source_id	Period (d)	SDSS g (mag)	Distance (pc)	Variable type
J072827.34+330741.6			21.94		WZ Sge:
J073605.07+182709.8	672172522242684800		21.83		Polar
J073648.03+200959.7			22.0		CV
J080249.06+363716.4			21.9		WZ Sge:
J080625.73+343244.4		0.0637(1):	21.46		SU UMa:
J081017.41+262238.3			21.31		SU UMa:
J081520.83+335634.1			21.6		WZ Sge:
J082809.87+222004.2	665816516105274496		20.79		CV:
J083404.24+185416.8	662643501643372544		19.23	1634^{+726}_{-438}	Polar
J083549.86+292636.9	704773999783239808		19.88	1244^{+657}_{-442}	Polar
J084228.13+462334.4			22.17		CV
J090947.82+110637.0	592059145810439808		20.83	601^{+631}_{-232}	WZ Sge:
J091107.84+260617.3			21.53		SU UMa:
J093130.75+335651.2	797435239135183744	0.0799(2):	20.44	797^{+990}_{-248}	SU UMa
J101335.56+393826.3	802734507224071936		20.78	882^{+741}_{-316}	WZ Sge:
J101723.18+375343.4	754291266149306496		21.65		SU UMa
J104245.15+371819.8	751777469035821312		19.7	507^{+95}_{-91}	Polar
J104521.19+362433.0			21.44		WZ Sge:
J115030.59+404151.8	768134186262349568	5.902(2)	21.9	1273^{+549}_{-451}	Polar
J115419.05+575751.1	845441772229861760		20.62	1144^{+449}_{-352}	ER UMa

SDSS name	Gaia EDR3 source_id	Period (d)	SDSS g (mag)	Distance (pc)	Variable type
J121015.61+351334.4	4029016667559886080		19.38	356^{+64}_{-58}	WZ Sge:
J122808.73+454516.3	1541836947948009472	0.07829(1):	21.66	1599^{+778}_{-608}	Polar
J123717.98+365535.2	1519559914656417920		21.22		WZ Sge:
J125716.08+582501.5	1578799436498250368		20.13	953^{+109}_{-99}	CV
J133816.44+371639.8			21.66		WZ Sge:
J140430.98+525811.1			21.93		CV
J140430.98+552558.5	1609460864427043072		21.48	1413^{+776}_{-636}	DN
J152603.67+382216.4			21.35		WZ Sge:
J155538.12+380250.5	1373544697473750272	0.104(1)	20.39	486^{+46}_{-49}	Polar
J160712.11+392450.6	1379871940214896640	0.08071(1)	21.57		Polar
J160813.59+301952.2			21.46		WZ Sge:
J161853.16+303845.5	1319026547281204480		20.69	1822^{+1404}_{-922}	WZ Sge:
J163620.62+472442.4	1410251583929439744		20.59	708^{+318}_{-227}	WZ Sge:
J171016.94+403127.5			22.08		WZ Sge:
J211652.28+014144.3	2692060074926640000		20.43	2752^{+2087}_{-1558}	SU UMa:
J212406.75+010029.8	2691114426208274176		20.84		WZ Sge:
J213040.11-001319.1			22.34		WZ Sge:
J220818.52+135330.0			21.33		WZ Sge
J220935.78-001332.5	2678822818216797056		21.8		WZ Sge:
J221333.38+245059.3			21.94		WZ Sge:

SDSS name	Gaia EDR3 source_id	Period (d)	SDSS g (mag)	Distance (pc)	Variable type
J221900.24+201831.1	1778468682222798080	0.140(1)	19.85	821^{+124}_{-98}	DN
J223212.79+260725.1	1880505014843117696		22.26		Polar
J223352.56+225913.4	1875338547143938944		19.89	1294^{+491}_{-329}	Polar
J223623.52+323913.1			21.02		WZ Sge:
J225613.53+191132.9			22.12		WZ Sge:
J225926.51+223902.4			21.81		WZ Sge:
J230319.85+274736.0			22.43		DN:
J232113.45+251822.3	2841125848466425856		20.96	1189^{+715}_{-482}	WZ Sge:
J232553.47+011527.3			21.39		WZ Sge:
J233705.01+314149.4	2871487075361158400		19.64	2574^{+939}_{-1150}	SU UMa:
J235131.68+270907.7	2854471033409793024		21.9	1089^{+467}_{-451}	DN:
J235603.71+001833.3			21.45		WZ Sge:
J183131.63+420220.2	2111270034246759424		16.9	1490^{+162}_{-155}	AM CVn:

5.3 Results

In the interests of brevity the full observational data and analysis of the over 500 SDSS I to IV CVs has been consigned to Appendix B. Illustrative examples are given here in Fig. 5.1 together with a brief discussion of a small set of the most interesting systems. Spectra have been smoothed by using a box-car median filter of width five points. A list of the 70 newly discovered CVs is included in Table 5.1.

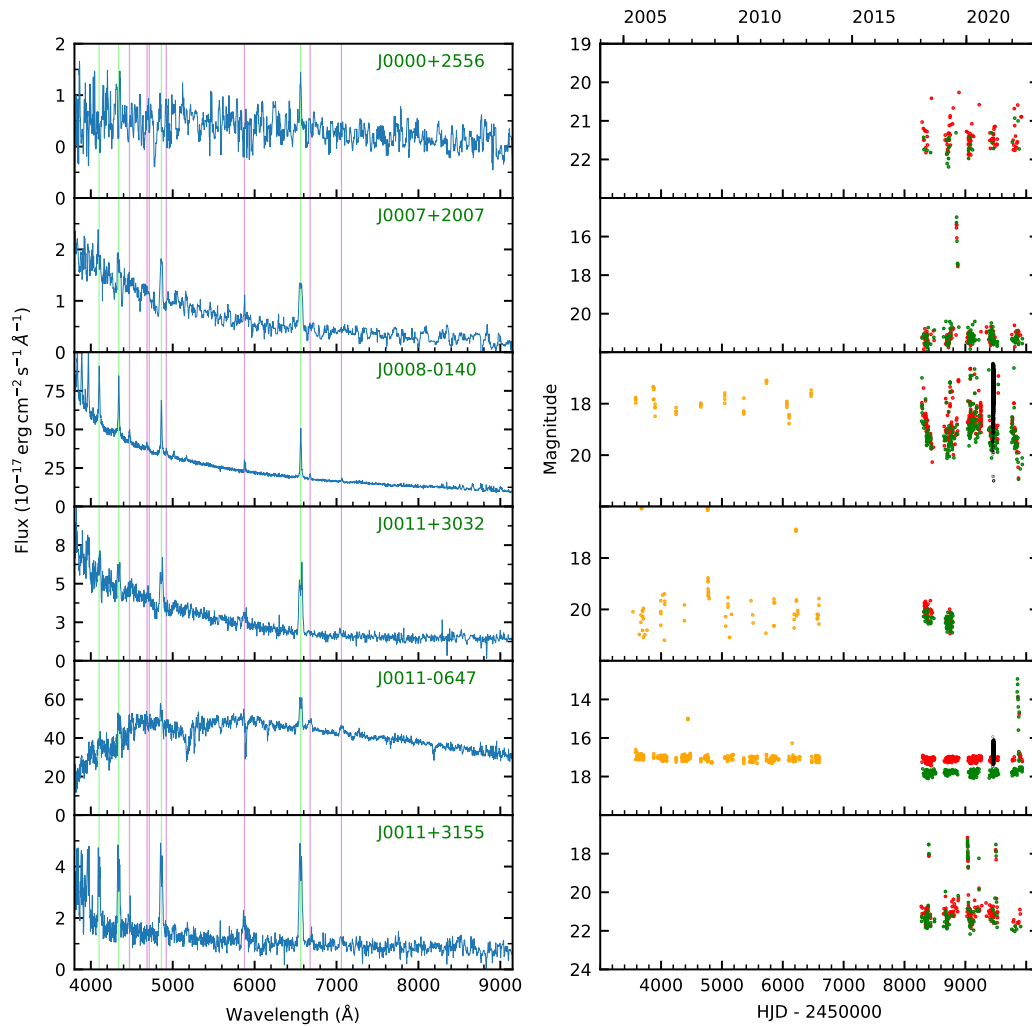


Figure 5.1: Left panels: Spectra with Balmer lines shown in green and He lines in pink. Right panels: Light curves with CRTS shown in orange, ZTF in red (*r*-band) and green (*g*-band) and *TESS* in black. This is a short extract of the data: the complete set is included in the supplementary information.

5.3.1 Unusual systems

The following notes discuss a small selection of the systems in SDSS I to IV which have unusual features and are worthy of further study.

J0028+3118

The spectrum displays single-peaked Balmer emission lines above a flat continuum as well as a very strong He II 4686 Å emission line. The system is located close to the main sequence in the HR diagram. There is a $\simeq 1$ yr state change of $\simeq 2$ magnitudes at MJD $\simeq 58750$ together with three shorter and smaller brightening events in the ZTF light curve. The ZTF light curve (Fig. 5.2) suggests that $P_{\text{orb}} = 29.20(1)\text{h}$ and also that the system is eclipsing. J0028+3118 is a high-accretion novalike system but the very long period is unusual. The extraordinarily strong He II 4686 Å suggests a hot and helium-rich accretion stream – possibly the result of a hydrogen depleted donor that is still burning (Harrison, 2018).

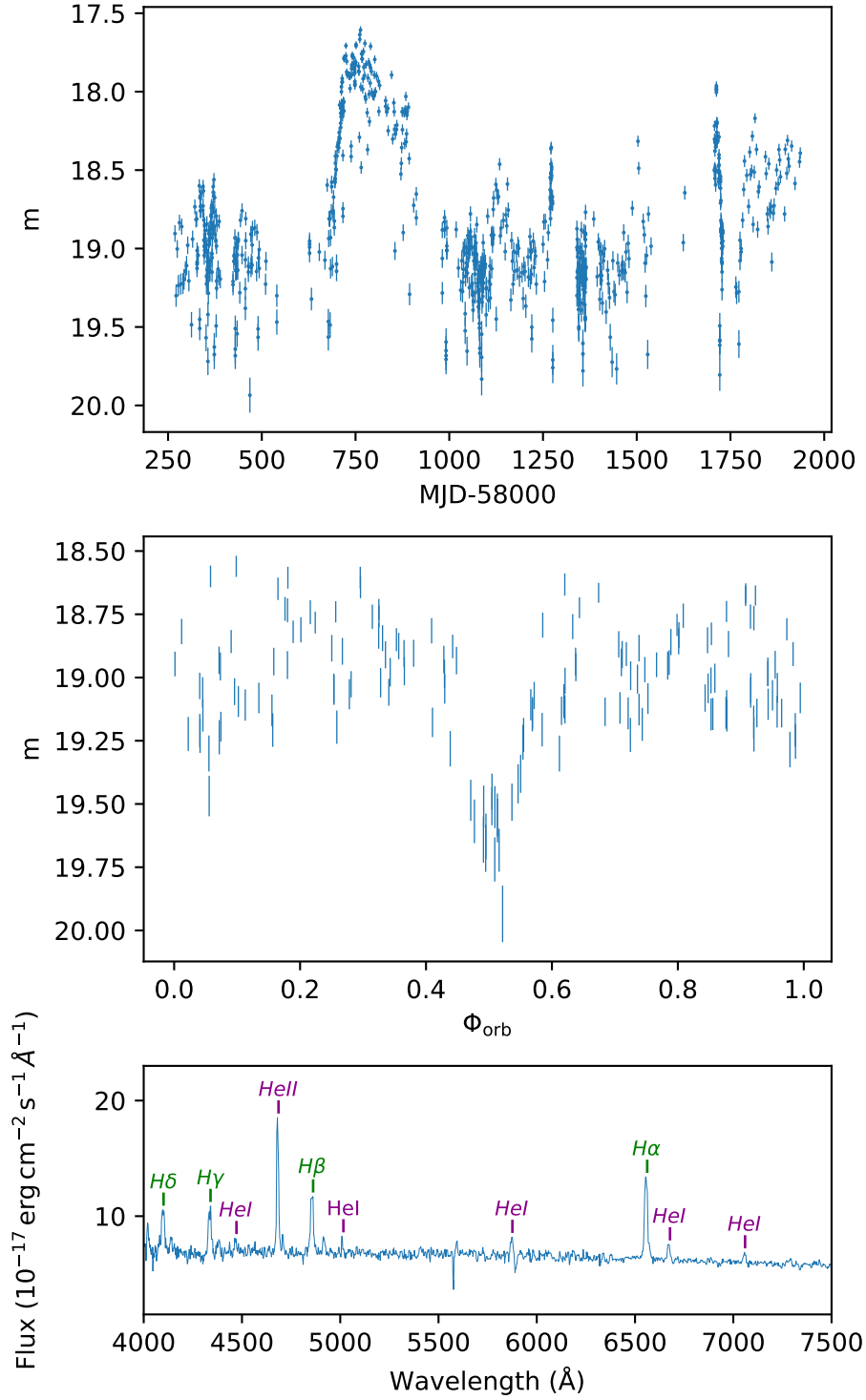


Figure 5.2: J0028+3118 is an eclipsing CV with an unusually long orbital period. Top panel: ZTF light curve (r -band) showing a brightening event lasting about one year. Middle panel: The section of the light curve with MJD < 58600 folded on the 29.2 h period. Bottom panel: SDSS spectrum with a prominent He II 4686 \AA emission line.

J0223–0520

The spectrum shows double-peaked Balmer emission lines with the higher order ones embedded in broad absorption lines from the white dwarf (Fig. 5.3). The blue slope of the continuum, and the shape of the white dwarf absorption lines suggest a relatively high white dwarf temperature, which is consistent with the SED being dominated by the white dwarf. The system is brighter in the far-ultraviolet (*GALEX* $m_{\text{FUV}} = 19.5$) than in the optical ($g = 19.9$). This is not consistent with its position at the lower end of the white dwarf cooling sequence in the HR diagram with $G_{\text{BP}} - G_{\text{RP}} = 0.35$, which would imply a temperature $T_{\text{eff}} \simeq 8000$ K. The ZTF light curve shows variability but does not reveal an orbital period. There is an *XMM* X-ray detection which is unusual for a low- \dot{M} system (Webb et al., 2020). This is probably a WZ Sge. It is possible that the raised temperature of the white dwarf is the consequence of a previous eruption.

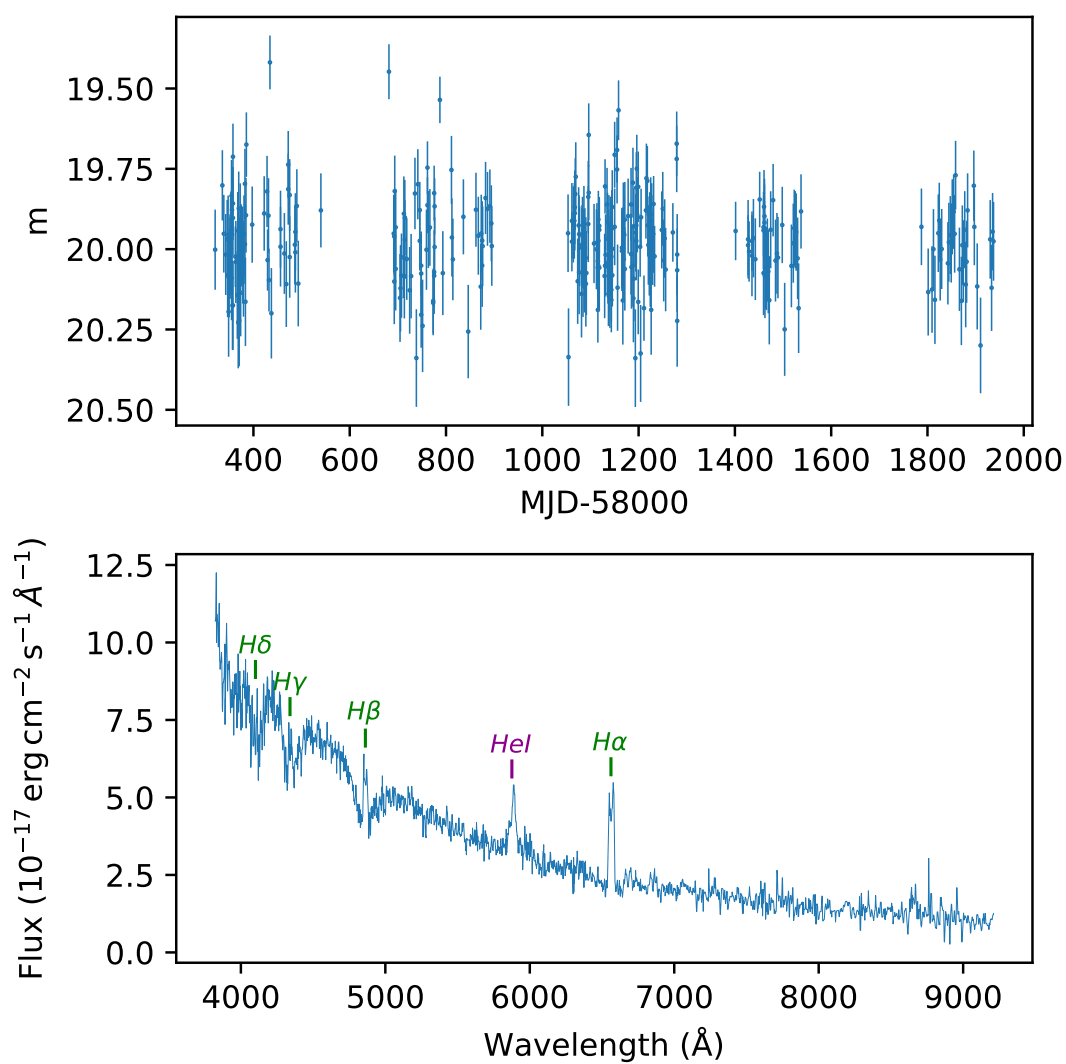


Figure 5.3: J0223–0520 is a CV with an unusually hot white dwarf. Top panel: ZTF light curve (r -band) showing variability. Bottom panel: SDSS spectrum showing the white dwarf absorption lines.

J0932+4725 and J0947+4524

Double-peaked Balmer, He I, He II and Ca emission lines are visible in the SDSS spectra of these systems as well as the Balmer jump in emission (Fig. 5.4). There is deep central absorption in the emission lines suggesting that they are eclipsing – which is confirmed by Homer et al. (2006a) for J0932+4725, and by the ZTF light curve for J0947+4524. Both are closer to the white dwarf cooling sequence than the main sequence in the HR diagram. In the CRTS and ZTF light curves J0932+4725 exhibits outbursts and super-outbursts whilst J0947+4524 exhibits two small ($\Delta m \simeq 1$ mag) outbursts. J0932+4725 has a period of 1.588 h (Homer et al., 2006a) whilst we obtained a period of 1.34963(2) h from the ZTF light curve.

The large ratio of the helium to hydrogen line strengths suggests that the donor is likely He-enriched. An *HST* observation of J0932+4725 by Pala et al. (2017) shows a large N V/C IV line flux ratio. Gänsicke et al. (2003) attribute this type of nitrogen excess to a system having passed through a phase of thermal timescale mass transfer and now accreting CNO processed material from a donor stripped of its external layers. J0932+4725 is therefore most probably such an evolved system. Whilst there are no *HST* spectra of J0947+4524 the optical spectrum is very similar to that of J0932+4725 and suggests that this may also have an evolved donor. Systems with evolved donors are interesting as they are potential precursors to AM CVn systems (Podsiadlowski et al., 2003; Goliasch & Nelson, 2015)

The superoutbursts confirm that J0932+4725 is an SU UMa CV. J0947+4524 is a dwarf nova but we cannot classify it more precisely.

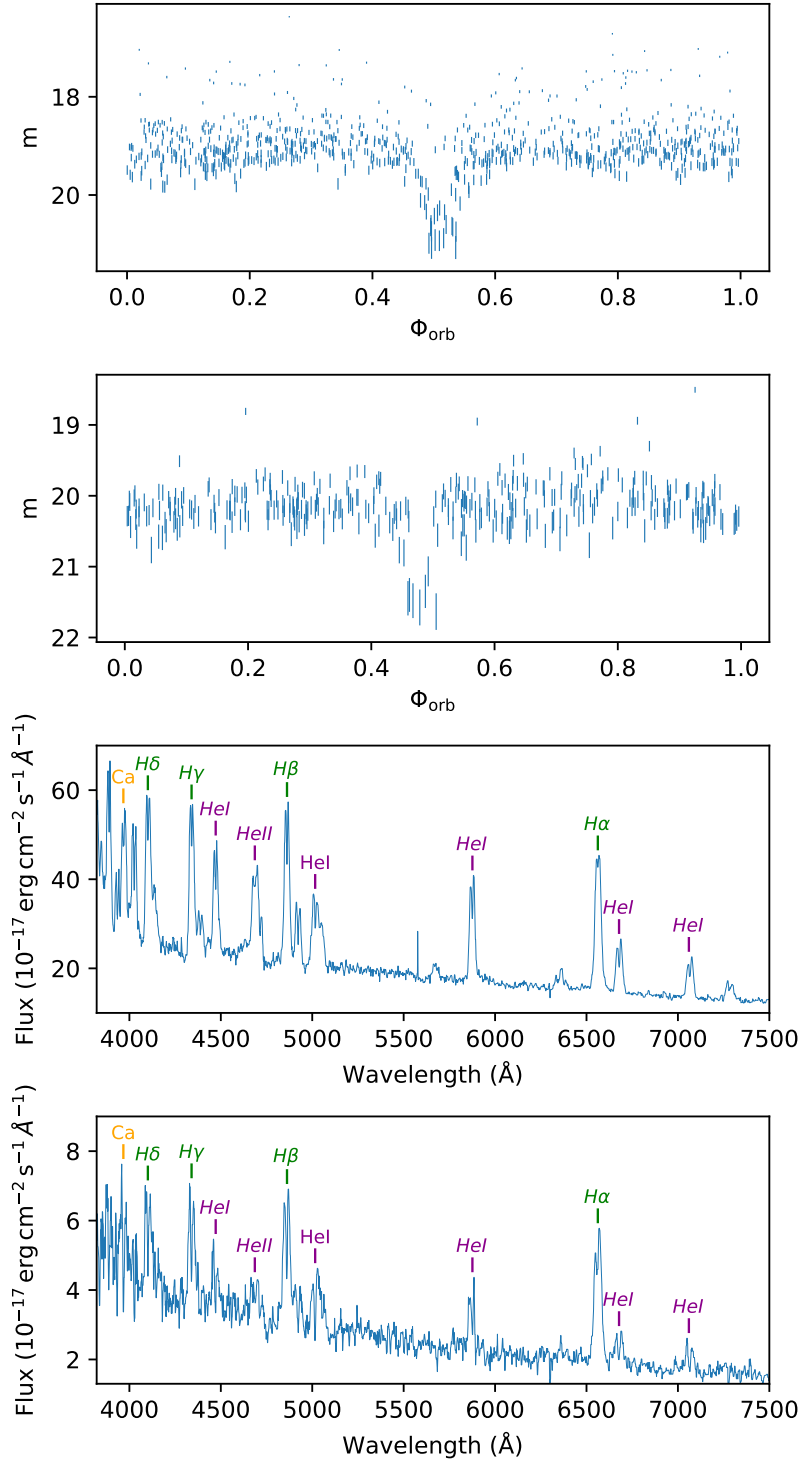


Figure 5.4: Two eclipsing CVs with unusually strong He I emission lines, which very likely contain stripped nuclear evolved donor stars. Top panel: Folded ZTF light curve of J0932+4725. Second panel: Folded ZTF light curve of J0947+4525. Third panel: Spectrum of J0932+4725. Bottom panel: Spectrum of J0947+4524.

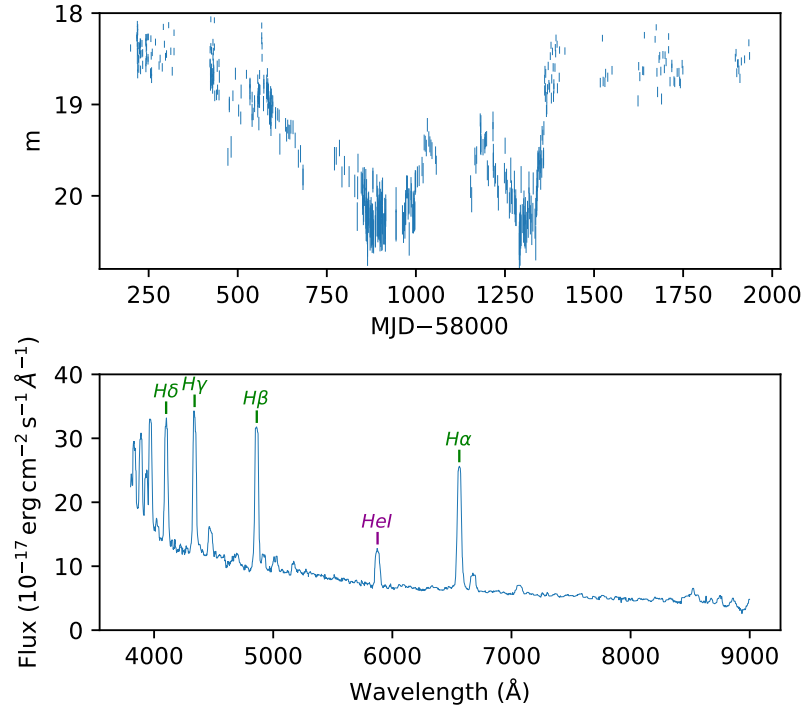


Figure 5.5: J1146+6759 has been classified as an SU UMa dwarf nova, but has an unusual ZTF light curve (r -band) showing a slow decline into a faint state without outbursts.

J1146+6759

Double-peaked Balmer and He I emission lines are visible in the spectrum as well as the Balmer jump in emission. The donor is not detected. J1146+6759 is located midway between the main sequence and the white dwarf cooling sequence in the HR diagram. The system was observed in a superoutburst on 2011 January 4 and a superhump period of 0.0615(8) was reported (vsnet-alert 12567*), classifying this system as an SU UMa dwarf nova. The ZTF light curve shows very unusual variability (Fig. 5.5) with a steady decline in amplitude of $\simeq 1.5$ mag over three years. This is followed by a rapid return to the original magnitude and then an outburst. It demonstrates that some dwarf novae can undergo state changes (section 5.4.6)

*<http://ooruri.kusastro.kyoto-u.ac.jp/mailarchive/vsnet-alert/12567>

J1150+4041

The spectrum shows strong Balmer, He I and He II asymmetric emission lines, suggesting that this is a magnetic CV. Neither the white dwarf nor the donor are visible. The ZTF light curve shows continuous variability with an amplitude of $\Delta m \simeq 1$, but no outbursts. The periodogram computed from the ZTF data shows a clear and strong signal at an unusually long period of 141.65(5) h, or 5.9 d (Fig. 5.6). If this signal is genuinely the orbital period of the system, it would exceed that of the current record of 5.7 d (V1017 Sgr, [Sekiguchi 1992](#)). However, in contrast to V1017 Sgr, the spectrum of J1150+4041 does not reveal any signature of a donor star, normally detected at such a long orbital period. Moreover, the system is located relatively close to the white dwarf cooling sequence in the *Gaia* HR diagram, i.e. intrinsically faint. We have currently no consistent explanation for the observed properties of J1150+4041, but speculate that the long period might be the beat between the white dwarf spin and the orbital period in a slightly asynchronous polar. Radial velocity and fast photometry follow-up is required to unravel the true nature of this system.

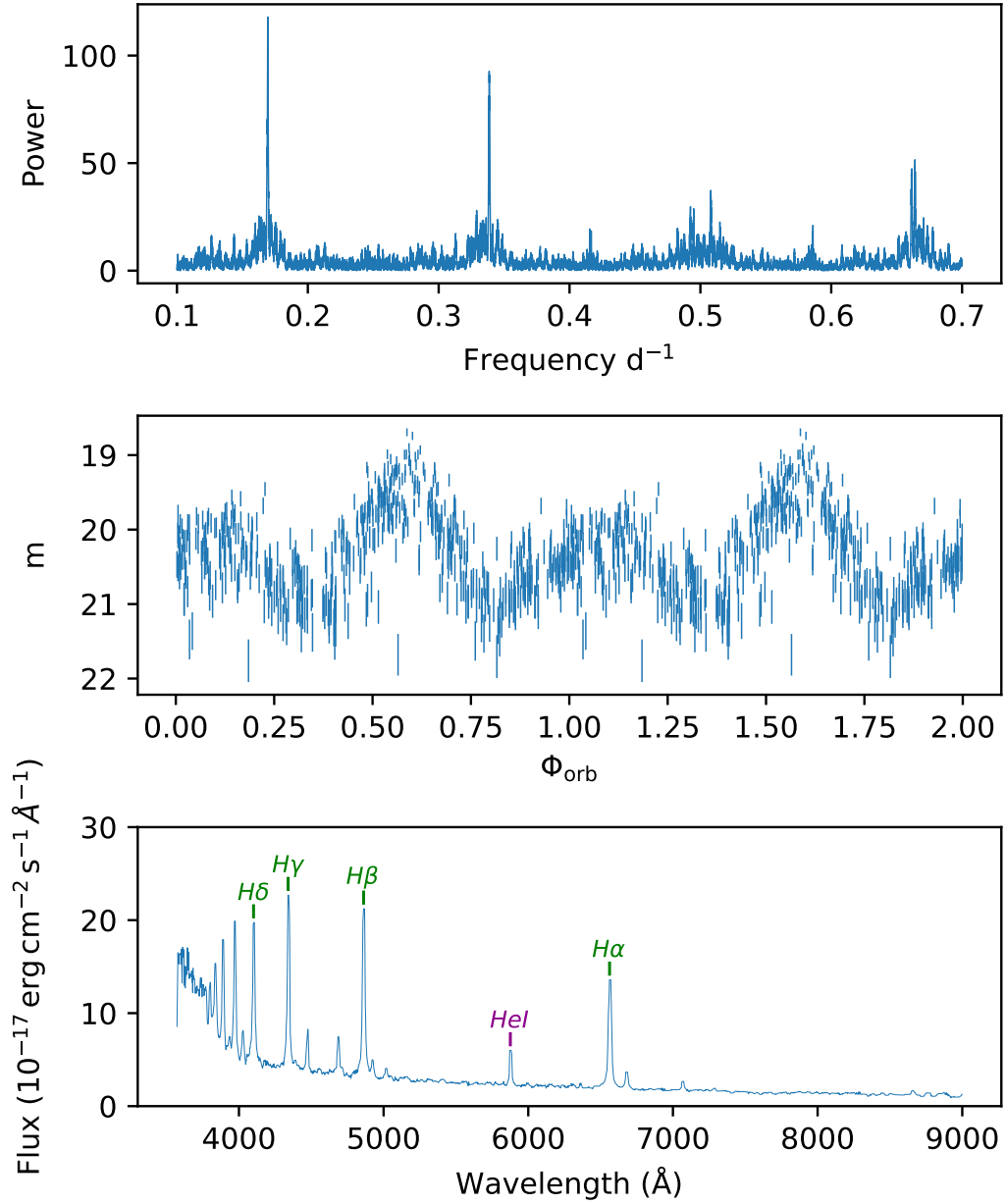


Figure 5.6: The ZTF data of J1150+4041 shows a very clear and strong signal at an unusually long period of 141.65(5) h. Top panel: The highest peak in the periodogram from the ZTF light curve is the second harmonic. Centre panel: The folded light curve shows a double humped profile. Bottom panel: Spectrum of J1150+4041.

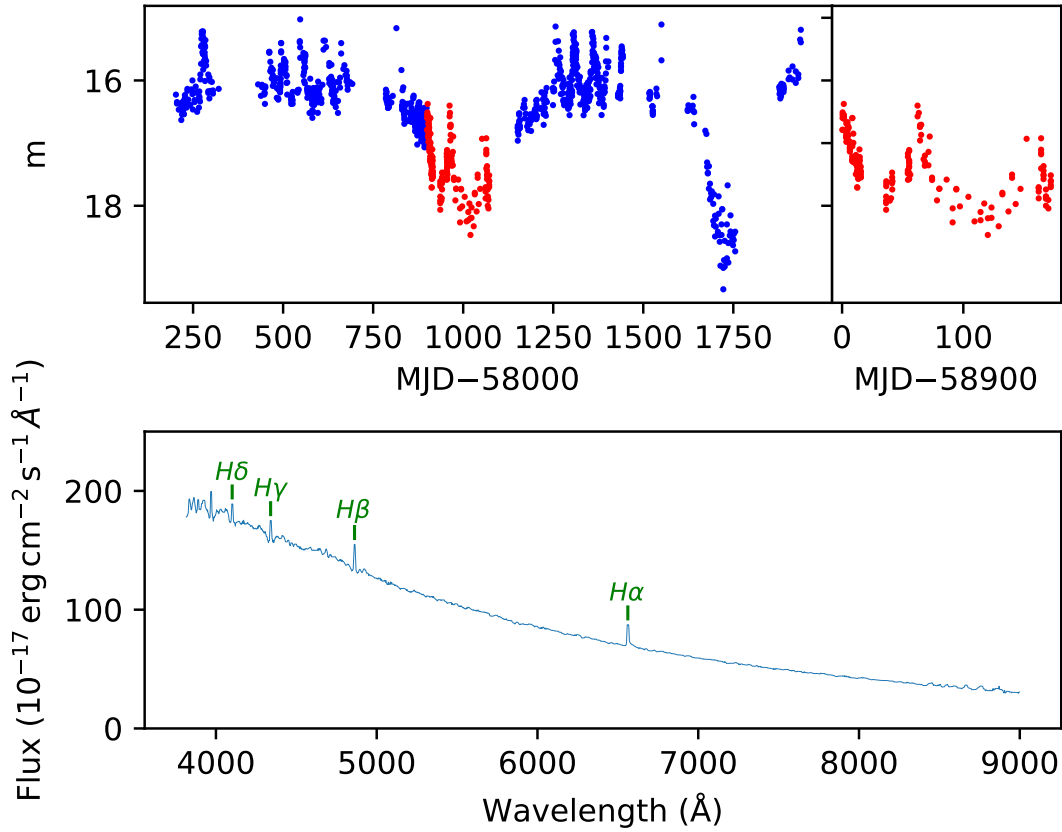


Figure 5.7: J1224+1841 is a transitional object between novalike variables and dwarf novae. Top panels: The ZTF light curve showing both outbursts and a drop-out (red). Outbursts also appear to occur during the faint state. Bottom panel: Spectrum of J1224+1841.

J1224+1841

The spectrum shows a blue continuum with Balmer emission lines, which are embedded in Balmer absorption lines for $H\beta$ and the higher Balmer lines. J1224+1841 is located in the area of the HR diagram occupied by novalike variables. The ZTF light curve shows multiple outbursts and also a drop of $\simeq 2$ magnitudes to a low state lasting several hundred days (Fig. 5.7). There appear to be outbursts during the low state although it is possible that they are very short reversion to the high state. The CRTS light curve shows two similar low states. J1224+1841 belongs to the growing family of CVs bordering between novalike variables and dwarf novae (Kato, 2019; Kato et al., 2021; Inight et al., 2022). Radial velocity follow-up should be carried out to determine the orbital period of this system.

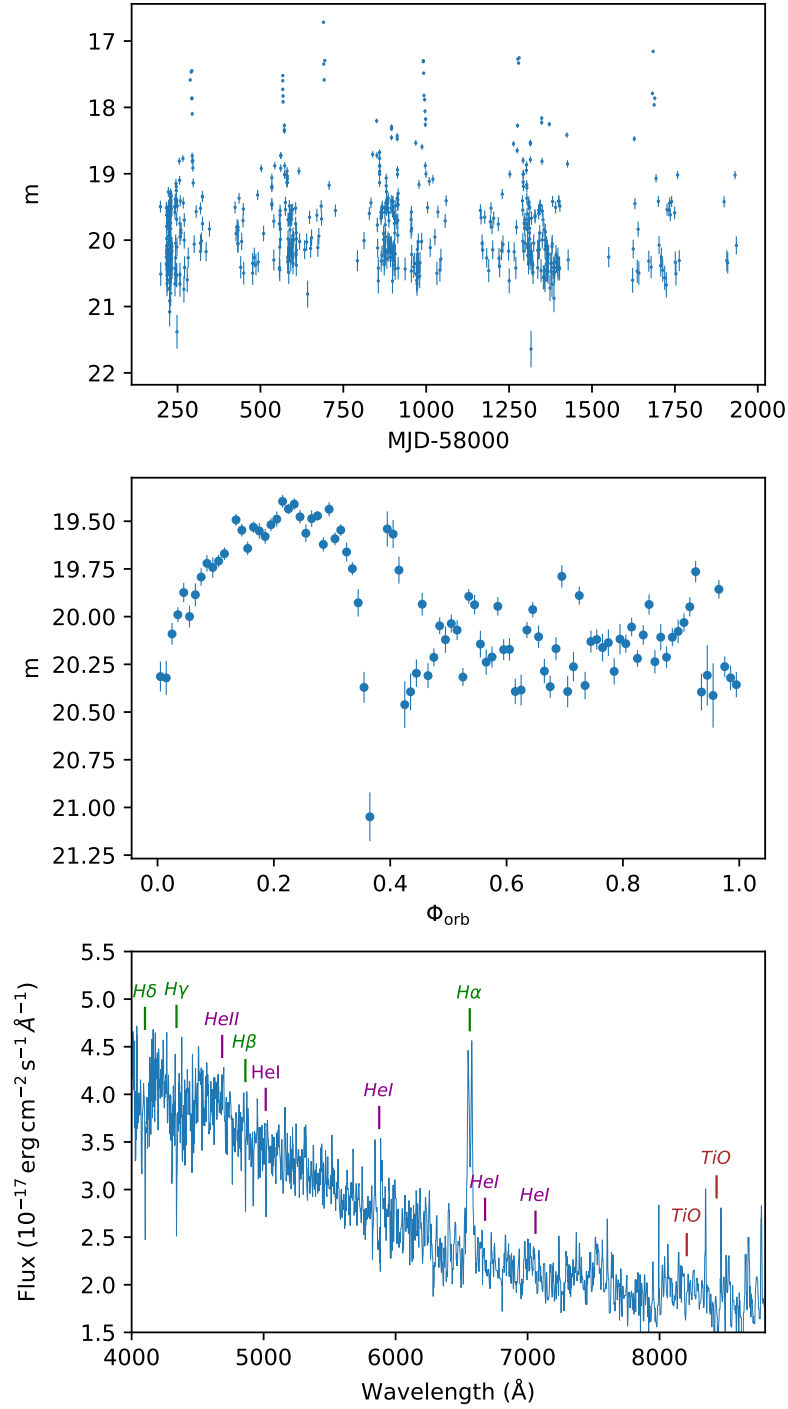


Figure 5.8: J1244+5936 (Gaia16adi) is an eclipsing system with a very low accretion rate. Top panel: ZTF light curve (r -band). Middle panel: Light curve folded at the orbital period of 1.75 h, and rebinned into 30 phase bins. Note the eclipse of the white dwarf at $\Phi_{\text{orb}} \simeq 0.4$ and the eclipse of the hot spot at $\Phi_{\text{orb}} \simeq 0.45$. Bottom panel: SDSS spectrum showing $H\gamma$ and $H\delta$ absorption lines from the white dwarf and TiO absorption lines from the donor in the red.

J1244+5936

This system is also known as Gaia16adi (Wyrzykowski et al., 2012). A double-peaked $H\alpha$ emission line is visible in the spectrum as well as other Balmer, He I and He II emission lines (Fig. 5.8). The deep central absorption features in the higher Balmer lines, dipping below the continuum flux level, suggest that the system is eclipsing, which is confirmed by the ZTF photometry. Absorption lines from the white dwarf are visible together with TiO molecular bands from the donor. It is closer to the white dwarf cooling sequence than the main sequence in the HR diagram. The ZTF and CRTS light curves show $\simeq 10$ outbursts with at least one low amplitude superoutburst accompanied by superhumps. We obtained a reliable period of 1.74954(1) h from the ZTF light curve and a consistent period from the CRTS light curve. The folded light curve shows that it is eclipsing with a hot spot just before the eclipse. J1244+5936 appears to be an SU UMa albeit with a very low \dot{M} . It may have recently started accreting – possibly after passing through the period gap; although theory (D’Antona et al., 1989) suggests that this transitional period will be short ($\sim 10^6$ yr).

J1522+3913

The spectrum shows Balmer emission lines above a relatively red continuum. Narrow absorption lines reveal a \simeq G-type donor star. The SED of the system exhibits a clear ultraviolet excess in the *GALEX* bands, most likely from the accretion disc. The *Gaia* HR diagram shows that J1522+3913 is just evolving off the main sequence into the giant branch. The ZTF light curve shows at least one outburst. We obtained a reliable period of 10.7686 d (258.4464 h) from the ZTF light curve confirming the period found by Drake et al. (2014a) from the CRTS data. The folded light curve shows a clear double hump, consistent with the detection of ellipsoidal modulation. To our knowledge J1522+3913 is the longest known orbital period for a CV – twice that of V1017 Sgr ($P_{\text{orb}} = 5.714$ d, Sekiguchi 1992). We note that a small number of symbiotic stars are located in this region of the HR diagram as well, however, J1522+3913 does not show any of the defining features in its spectrum (see the definition in section 1.1 of Merc et al. 2021). Instead, we suggest that the very long orbital period, and the location in the HR diagram are consistent with a CV in which the donor has evolved off the main sequence (e.g. for example GK Per Álvarez-Hernández et al. 2021).

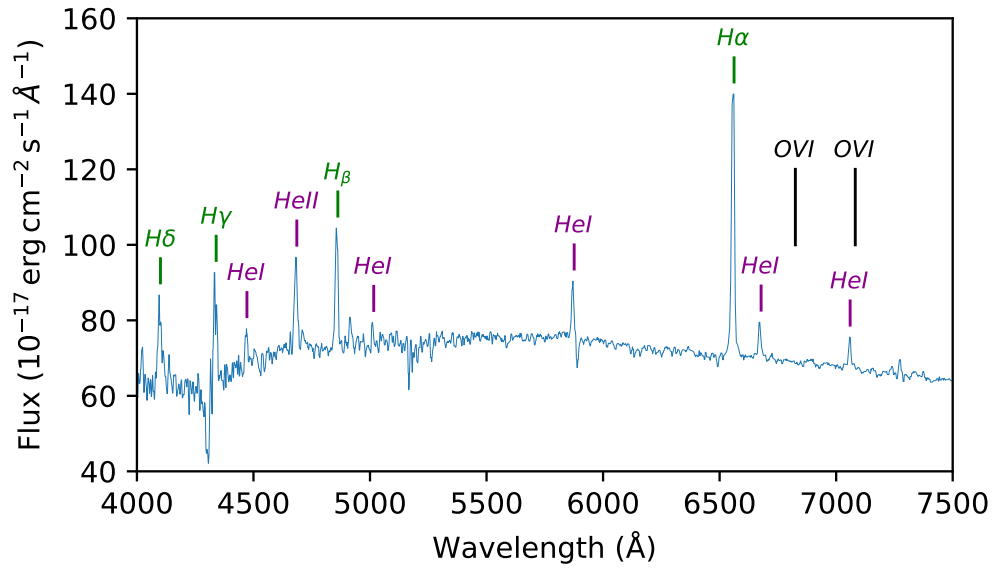


Figure 5.9: The spectrum of the long-orbital period (10.8 d) J1522+3913 contains narrow absorption features from a G-type donor. The helium emission lines suggest that the donor is evolved. There are no molecular and metallic absorption lines or Raman-scattered O VI lines; two of the conditions in [Merc et al. \(2021\)](#) for a symbiotic star classification.

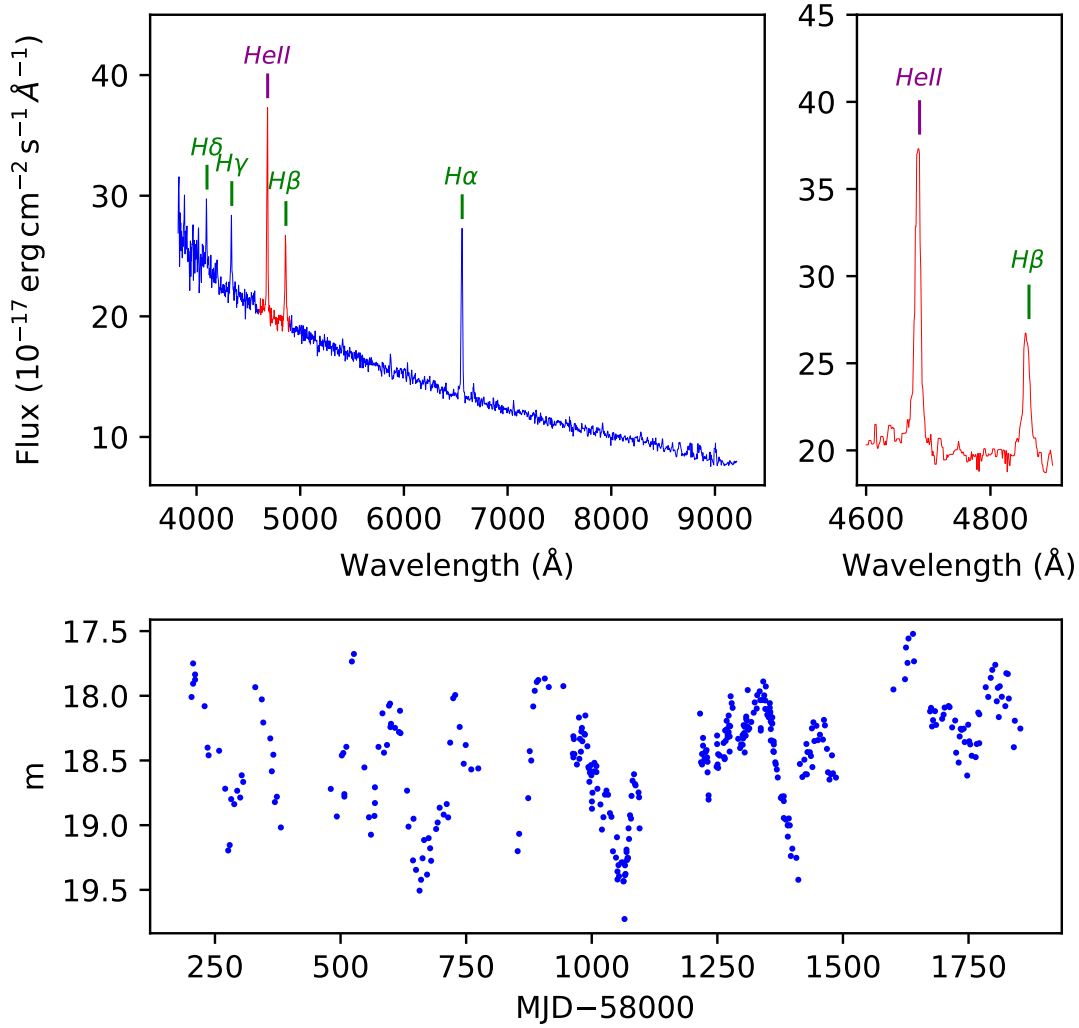


Figure 5.10: J1549+1739 is probably a novalike variable. Top panel: The spectrum shows an unusually strong He II line (expanded in the inset panel). Bottom panel: The ZTF light curve (r -band) shows repeated changes of magnitude on timescales of about a year.

J1549+1739

The SDSS spectrum shows single-peaked Balmer emission lines and a very strong He II emission line on top of a strong blue continuum (Fig. 5.10). There is no sign of the white dwarf or the donor. J1549+1739 is located in the novalike variable area of the HR diagram. Whilst there are no outbursts in the CRTS and ZTF light curves, the system meanders on time scales of about a year between $m \simeq 17.5$ –19. This is probably a novalike variable but the strong He II and its light curve are unusual. Spectroscopic follow up is encouraged to explore the spectral changes between the bright and faint states, and to determine the orbital period of the system.

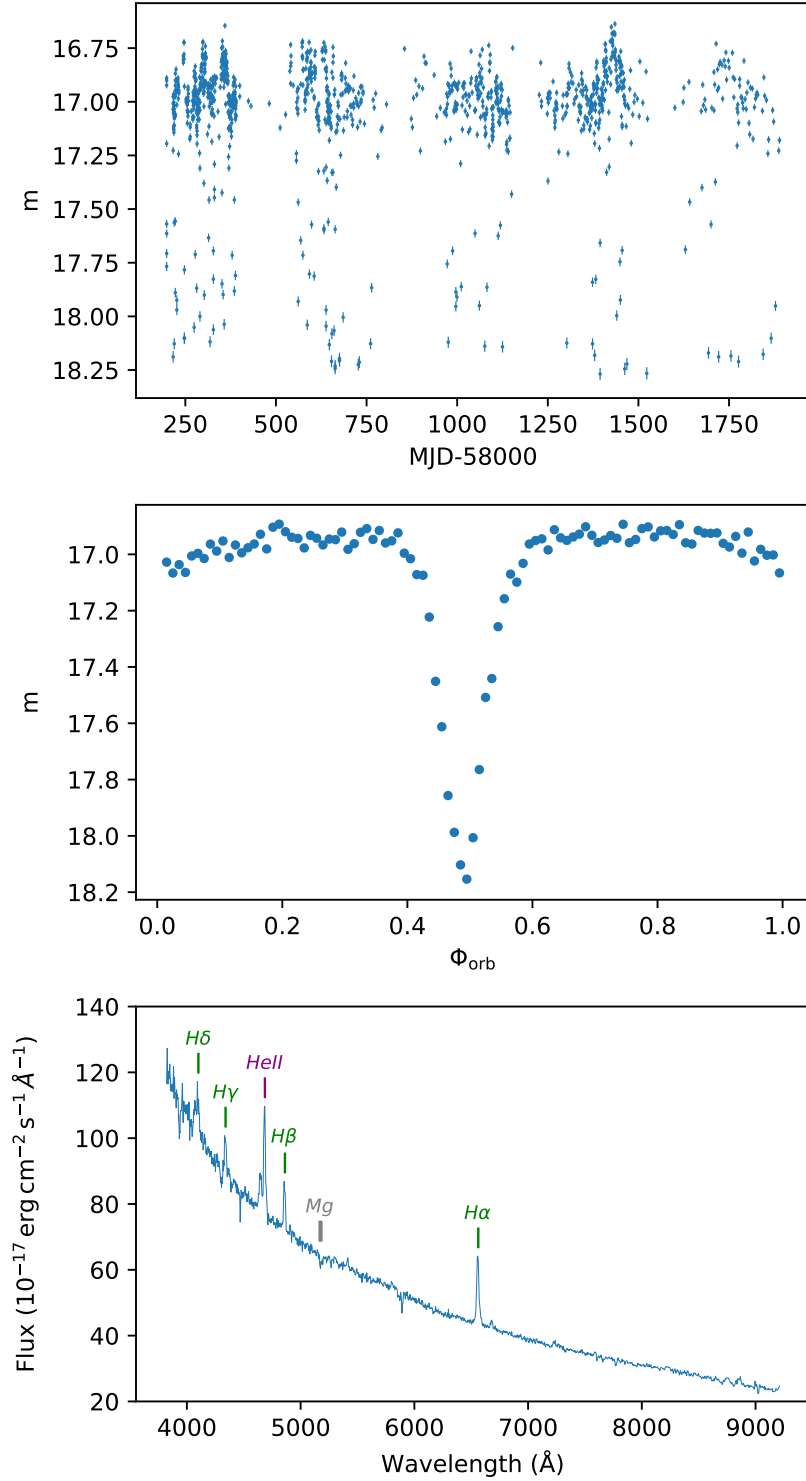


Figure 5.11: J1712+3218 is a novalike variable with an unusually long orbital period. Top panel: ZTF light curve (r -band) showing eclipses. Middle panel: ZTF light curve folded on 8.96 h showing the eclipse. Bottom panel: The spectrum shows absorption lines that may be from an early-type donor (Mg is indicated).

J1712+3218

The spectrum (Fig. 5.11) shows Balmer and Helium emission lines, including strong He II, and the Bowen blend above a blue continuum. Narrow absorption lines of Mg, Na and Ca are detected, which may be from the donor star. J1712+3218 is located in the novalike variable area of the HR diagram. The ZTF light curve shows variability with clear eclipsing behaviour. Drake et al. (2014a) report an orbital period of 17.998 h and concluded that this is a Beta Persei system. We determine $P_{\text{orb}} = 8.9599(1)$ h from the eclipses in the ZTF light curve. We also have unpublished MDM time series spectroscopy confirming the orbital period. We classify J1712+3218 as a novalike variable. This is an unusually long period for a novalike variable although it would be consistent with an early donor that is visible even though the disc is in a high state.

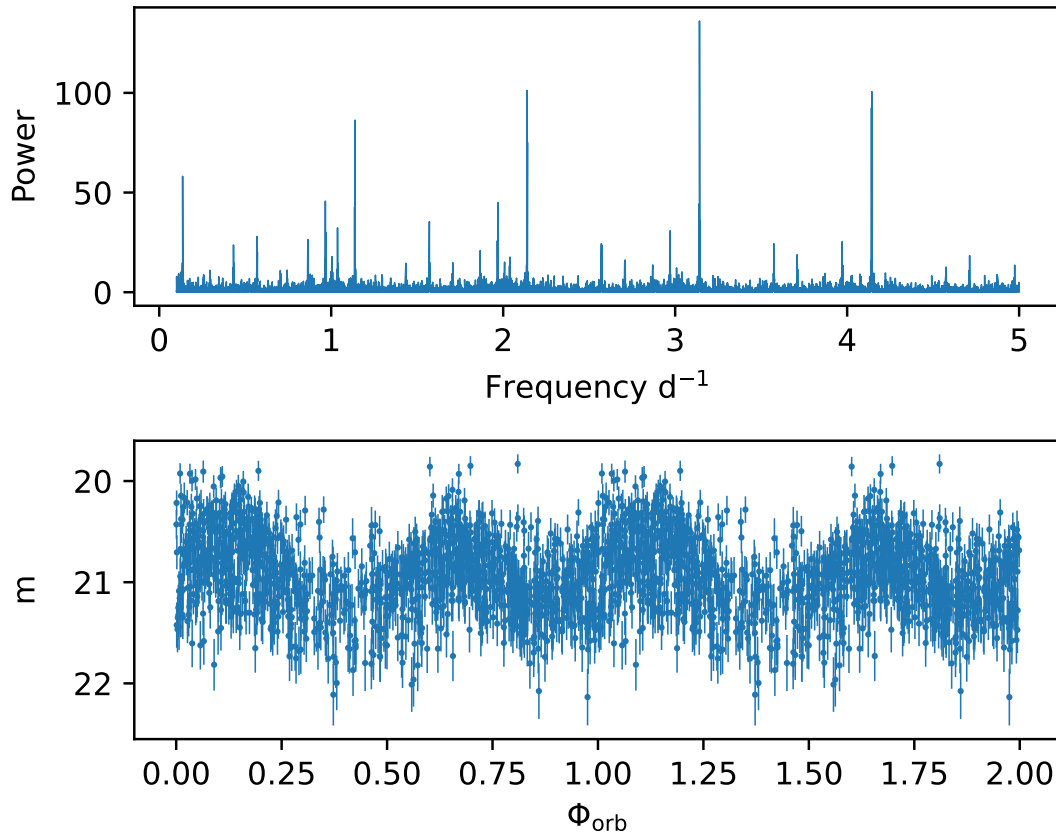


Figure 5.12: J1726+5432 has an unusually long period of $P_{\text{orb}} = 15.2783(3)$ h. Top panel: The periodogram peak at 3.14 per day is at twice P_{orb} . Bottom panel: Light curve folded at P_{orb} .

J1726+5432

This system has two SDSS spectra obtained at MJDs 51813 and 51997. Both spectra show single-peaked Balmer, He I and He II emission lines as well as the Balmer jump in emission (Fig. 5.12). The SED shows that it has historically been brighter. There is no *Gaia* parallax. It is above the white dwarf cooling sequence in the SDSS $u - g, g - r$ diagram, although the SDSS photometry was obtained during a brighter state. The ZTF light curve shows no outbursts but low-level variability. We find an unusually long period of 15.2783(3) h from the ZTF light curve which, together with the helium-rich spectrum may indicate an evolved donor. In the absence of outbursts we cannot assign a sub-type and have classified this generically as a CV.

J1831+4202

He I absorption lines are detected in the spectrum superimposed on a blue continuum (Fig. 5.13). There is no sign of the white dwarf or the donor. J1831+4202 has previously been classified as a CV (Girven et al., 2011) and a DB white dwarf (Genest-Beaulieu & Bergeron, 2019; Geier et al., 2019) however the DB classification is inconsistent with the variability in the *Gaia* and ZTF light curves which indicates that this is an interacting binary. It is close to AM CVn in the HR diagram and we hence classify this system as an accretion-disc dominated AM CVn. The drop-outs in the *Gaia* and ZTF light curves are unusual for this type of system.

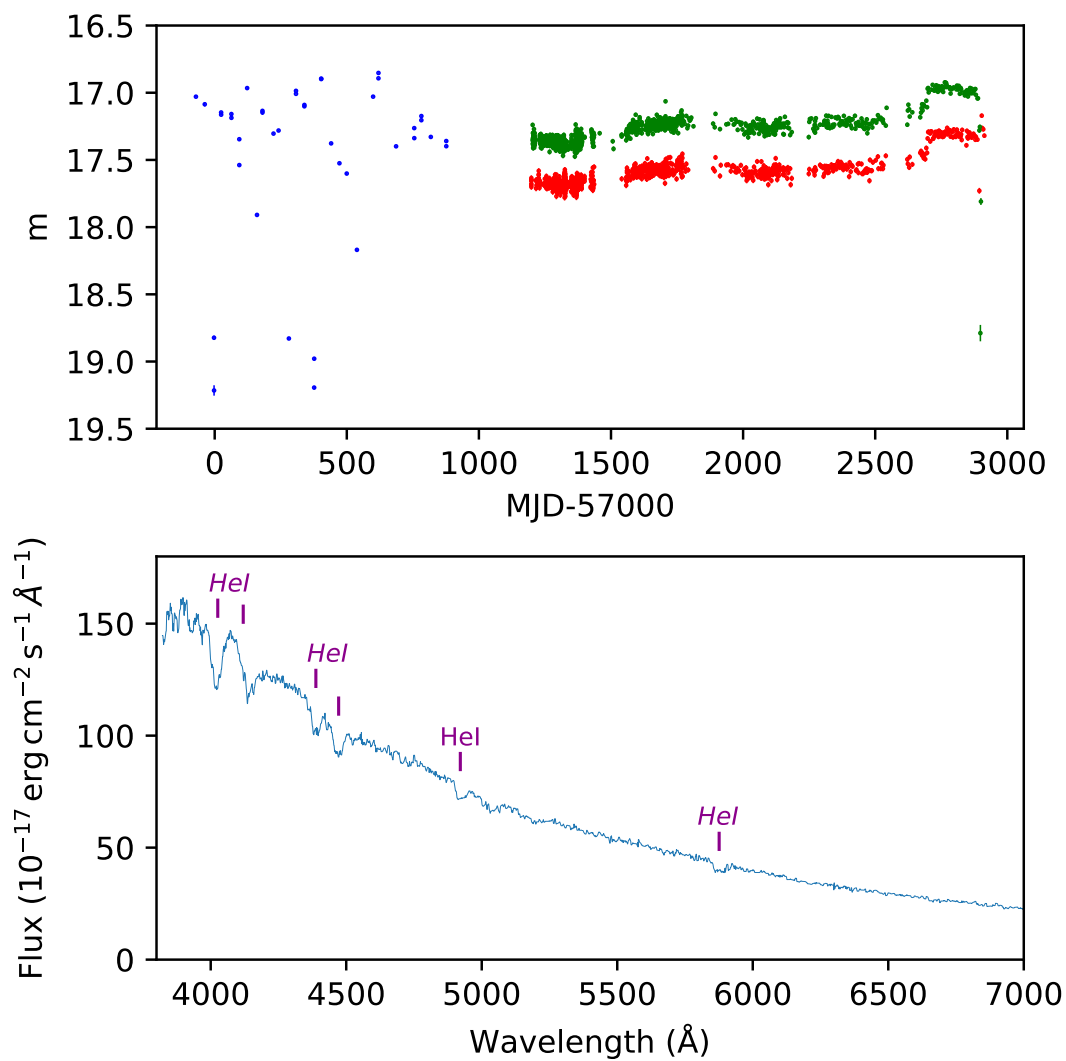


Figure 5.13: J1831+4202 is an AM CVn with a helium-dominated absorption line spectrum and it exhibits low-amplitude brightness variations on time scales of about a year with occasional drop-outs. Top panel: The ZTF light curve (r - and g -band data shown in red and green respectively) and the *Gaia* light curve (shown in blue). Bottom panel: Spectrum showing helium absorption lines and an absence of hydrogen lines.

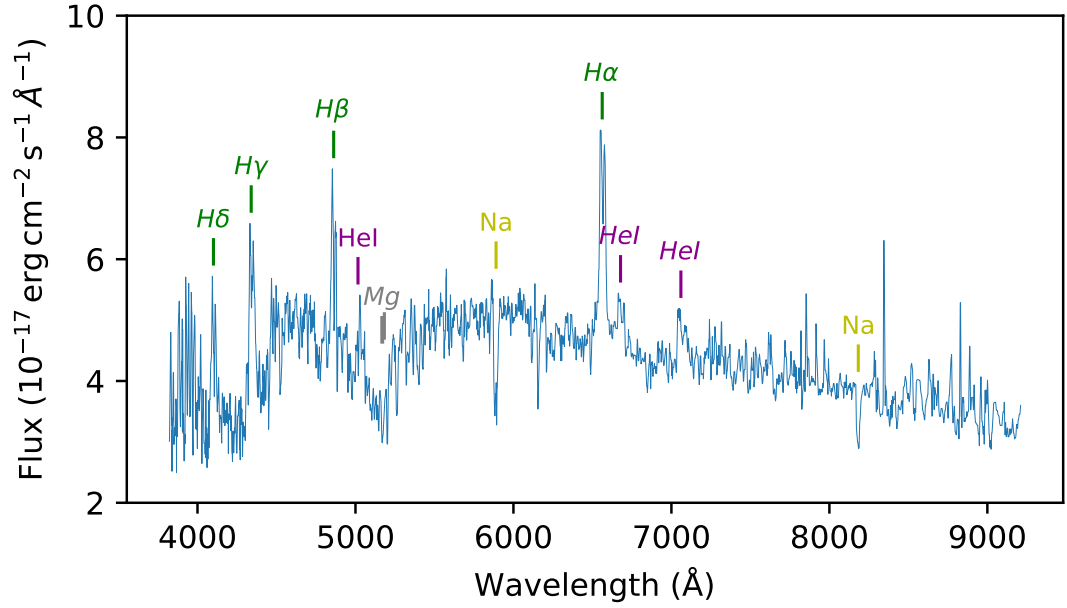


Figure 5.14: The spectrum of J2119+0332 shows Na and Mg lines consistent with a K-type star. Whilst bright enough to outshine the disc the spectrum is too dim for a main sequence K-type suggesting a nuclear evolved stripped donor. This hypothesis is corroborated by the short orbital period of 2.4 h.

J2119+0332

Double-peaked Balmer and He I lines are visible in the spectrum as well as the Balmer jump in emission (Fig. 5.14). There are also Na absorption lines at $\simeq 8190\text{\AA}$ and at $\simeq 5890\text{\AA}$ together with broad Mg at $\simeq 5170\text{\AA}$ suggesting a K-type donor. J2119+0332 is closer to the main sequence than the white dwarf cooling sequence in the HR diagram. There are no outbursts in either the CRTS or the ZTF light curves. We found ellipsoidal modulation and a reliable orbital period of 2.37223(3) h from the ZTF light curve, i.e. within the period gap. The period and relatively low luminosity are inconsistent with a main-sequence K-type donor and reminiscent of SDSS J001153.08–064739.2 (Rebassa-Mansergas et al., 2014) and QZ Ser (Thorstensen et al., 2002b) where the donor has undergone nuclear evolution on the main sequence before mass transfer to the white dwarf commences. In these cases a period of rapid mass transfer has resulted in a stripped donor and a short period. The strong Na absorption lines are consistent with CNO burning.

5.3.2 Non-CVs

The classification of a number of systems that were previously classified as CVs have now, with the benefit of new data such as from *Gaia* and ZTF, been revised. Most of the systems previously classified as CVs turned out to be either single white dwarfs or white dwarf plus main sequence binaries, in which emission lines from a nebular background or from the chromosphere of the companion were mistaken for signatures of accretion flows. The new classifications of these non-CV systems are listed in Table 5.2.

Table 5.2: Systems identified as CVs in the literature which we have reclassified as detached binaries or isolated stars. Unless otherwise stated the original classification was taken from [Szkody et al. \(2011\)](#). Each system may include a white dwarf (WD), M dwarf (M) or other type of main sequence star (MS).

SDSS name	Notes	New type
002603.80-093021.0	Thorstensen & Skinner (2012) determined that the spectrum was not that of a CV. Kleinman et al. (2013) classified the object as a (hydrogen) DA white dwarf. We found a ZTF period of 9.3086hh confirming that this is probably a binary.	WD+MS
034420.16+093006.8	Parsons et al. (2015a) found that this is a detached, eclipsing system.	WD+MS
035409.32+100924.4	Kleinman et al. (2013) found that this was an eclipsing system including a DA white dwarf. This system is within the Eridanus superbubble (see fig. 1 in Ryu et al. 2006) and this is likely to be the source of the Balmer emission lines; the remaining spectrum is that of an isolated white dwarf.	WD
053659.12+002215.1	Thorstensen & Skinner (2012) determined that the spectrum was not that of a CV. Kleinman et al. (2013) classified the system as a DA white dwarf. This system is on the edge of the Eridanus superbubble (see fig. 1 in Ryu et al. 2006) and this is likely to be the source of the Balmer emission lines; the remaining spectrum is that of an isolated white dwarf.	WD

SDSS name	Notes	New type
075117.09+144423.5	The spectrum shows emission lines but these are contamination from a nearby CV (PQ Gem) and the object is actually an M-dwarf.	MS Star
102347.67+003841.2	Wang et al. (2009) found that this object is a millisecond radio pulsar - a low mass X-ray binary including a neutron star.	Low mass X-ray binary
105443.06+285032.7	Rebassa-Mansergas et al. (2010) concluded that the object is a detached binary including a DA white dwarf. Thorstensen & Skinner (2012) also determined that the spectrum was not that of a CV. We note that the weak Balmer emission lines appear to vary in strength between multiple SDSS spectra.	WD+M
111703.53+182558.1	Thorstensen & Skinner (2012) determined that the spectrum was not that of a CV. We classify the system as a detached binary containing a hot white dwarf and a main sequence star. The SDSS and LAMOST (He et al., 2017) spectra show that the emission lines vary in strength consistent with coming from the irradiated secondary at different phases of the orbit. We find a period of 9.33 h from the ZTF light curve.	WD+MS
121929.46+471522.8	Gänsicke et al. (2020) concluded that this was an isolated magnetic white dwarf with Zeeman-split Balmer line emission.	WD
124959.76+035726.6	Rebassa-Mansergas et al. (2010) concluded that the object is a detached binary including a DA white dwarf. Thorstensen & Skinner (2012) also determined that the spectrum was not that of a CV. We find a period of 17.84 h from the ZTF light curve.	WD+M

SDSS name	Notes	New type
130236.21+060148.0	Thorstensen & Skinner (2012) determined that the spectrum was not that of a CV.	M/L dwarf
131424.68+455528.3	Kiman et al. (2019) found that it was an isolated system – either an M or L dwarf. Kepler et al. (2016) identified this as a CV from SDSS data release 12. However the spectrum only shows very narrow emission lines and there are no recorded outbursts. The coordinates lie in a nearby galaxy, UGC 8320 (4.3 Mpc, Karachentsev et al. 2003), and so the object is most likely to be a hot star with the emission lines arising from the background galaxy.	MS Star
131709.07+245644.2	Thorstensen & Skinner (2012) determined that the spectrum was not that of a CV.	WD+M
132856.71+310846.0	Thorstensen & Skinner (2012) determined that the spectrum was not that of a CV. Geier et al. (2019) found that it was a hot luminous subdwarf.	Hot luminous subdwarf?
151500.56+191619.6	Thorstensen & Skinner (2012) determined that the spectrum was not that of a CV. It appears to be a detached binary with emission lines caused by irradiation.	WD+MS
155904.62+035623.4	Thorstensen & Skinner (2012) determined that the spectrum was not that of a CV. Parsons et al. (2013a) concluded that it was a WD+MS. We find a period of 2.5h from the ZTF light curve.	WD+MS
202520.13+762222.4	The spectrum is very noisy with only the H α emission line clearly visible. There are no recorded outbursts and it is on the main sequence. The SED is consistent with this being a single M-dwarf. This is most likely to be a flaring main sequence star rather than a CV.	MS Star
210241.09-004408.3	Thorstensen & Skinner (2012) determined that the spectrum was not that of a CV.	MS Star or subdwarf?

5.4 Discussion

5.4.1 Distribution of periods

We have assembled periods for over half of the CVs in SDSS I to IV, either from the literature or from our analysis of the ZTF data. The main reasons why the remaining systems have no period measurements are either a low inclination (which will reduce the amplitude of any orbital modulation), faintness (i.e. low signal-to-noise ratio of the time-series photometry or spectroscopy), or sparse sampling of the available time-series data. With the possible exception of low \dot{M} short-period CVs (which do not have much orbital modulation from the hot spot and are inherently fainter) these factors are not likely to correlate with the period. The distribution of the SDSS CV periods is therefore assumed to be relatively unbiased, which we compare in Fig. 5.15 with that of version 7.24 (December 2015) of the [Ritter & Kolb \(2003\)](#) catalogue of CVs (hereafter R&K). This final version of the R&K catalogue lists 1429 CVs (including some from SDSS I to IV); however it focuses on well-studied CVs, many of which were discovered by virtue of their outbursts.

Interestingly the period gap is clearly evident in the period distribution of CVs from the R&K catalogue but is not so evident in the SDSS I to IV sample. The proportion of SDSS CVs with periods below three hours is also greater than in the R&K catalogue, presumably due to spectroscopic identification of CVs with infrequent outbursts as reported by [Gänsicke et al. \(2009\)](#), and the fact that the SDSS CV sample reaches, on average, fainter apparent magnitudes than the R&K sample (19.7 and 18.1 respectively). This is consistent with the results obtained by [Pala et al. \(2020\)](#) and [Inight et al. \(2021\)](#). Figure 5.15 highlights that selection effects have to be taken carefully into account when constructing observed CV samples to develop, support, or disprove theories of CV evolution, such as the canonical ‘disrupted magnetic braking framework’ ([Rappaport et al., 1983](#); [Knigge et al., 2011](#)) as well as suggestions that the structure of the donor star may have no strong dependence upon the efficiency of magnetic braking ([Andronov et al., 2003](#); [El-Badry et al., 2022](#)).

The orbital period distribution broken down by CV-sub-type is shown in Fig. 5.16. From the top panel it can be seen that U Gem CVs typically have periods above the period gap whilst most SU UMa CVs are located below the gap. Later in the evolution process low accretion WZ Sge CVs approach the period minimum and subsequently evolve back towards longer periods as ‘period bouncers’. The CVs below the period minimum have helium-rich donors which were partially evolved before accretion commenced or formed directly from a detached white dwarf/brown dwarf binary ([Kolb & Baraffe, 1999](#); [Littlefair et al., 2007](#); [Podsiadlowski et al., 2003](#)). Polars tend to have shorter periods whilst those of intermediate polars and pre-polars tend to be longer. The ‘period gap’ is not so apparent in magnetic CVs, (see for example [Mason et al. 2019](#)) and

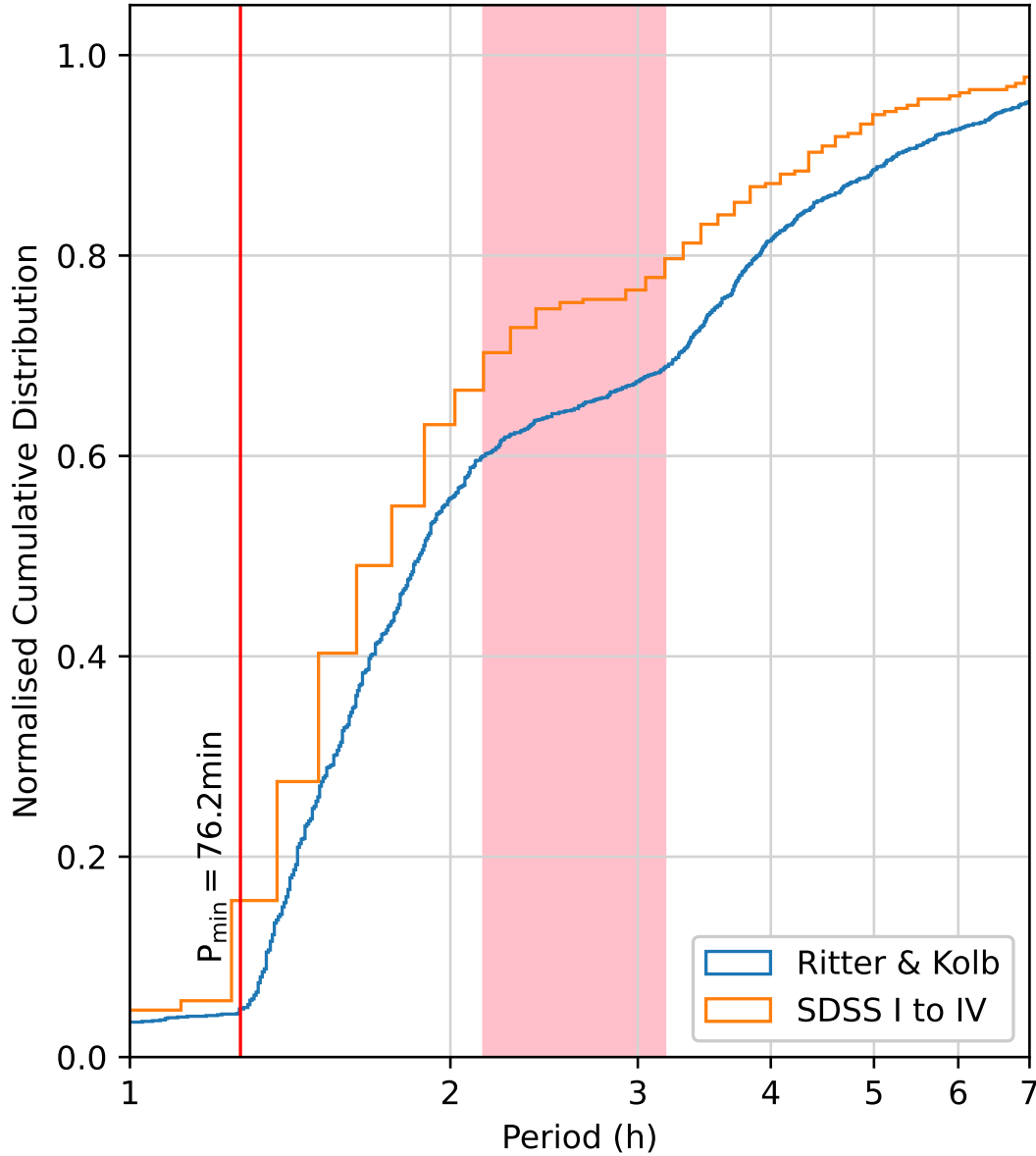


Figure 5.15: Cumulative distribution of the periods of the CVs in SDSS I to IV. The distribution is compared with that of the Ritter and Kolb catalogue (version 7.24, [Ritter & Kolb 2003](#)). The period minimum (red line) and ‘period gap’ (pink rectangle) are identified (see text for details).

may be a result of less efficient magnetic braking due to the white dwarf magnetic field ([Webbink & Wickramasinghe, 2002](#)). Novalike variables congregate above the period gap alongside classical novae. Many classical novae become novalike variables following their eruptions although there are exceptions where they become dwarf novae in the period between eruptions ([Honeycutt et al., 1995](#); [Mróz et al., 2016](#)). Short-period novalike variables are very rare; BK Lyn is the most famous example: [Patterson et al. \(2013\)](#) speculate that this is due to being the result of a relatively recent (~ 2000 yr

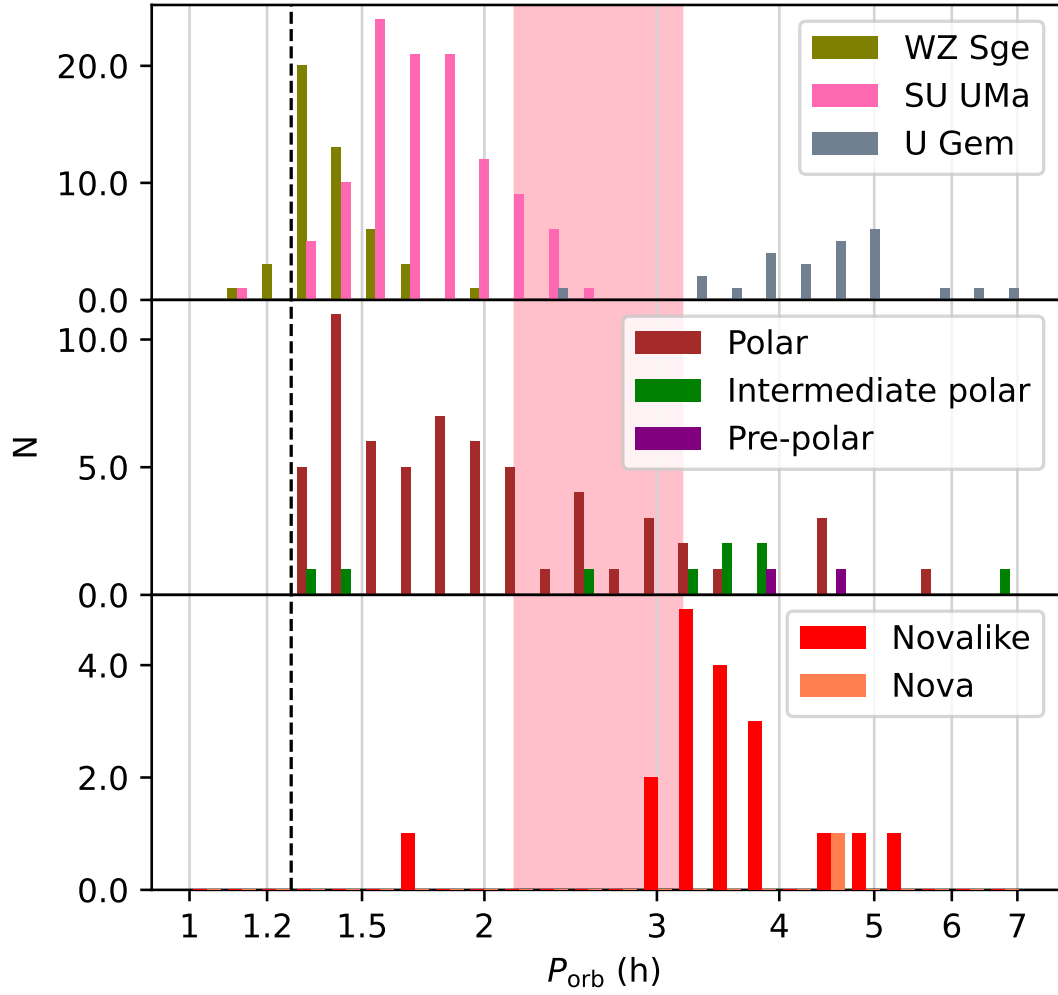


Figure 5.16: Distribution of the periods of the CV sub-types in SDSS I to IV. CVs evolve from right to left past the ‘period gap’ (pink rectangle) to the period minimum (broken black line) and then back out to longer periods. Top panel: U Gem CVs typically have periods above the period gap whilst most SU UMa CVs have shorter periods below the gap. Middle panel: Polars tend to have shorter periods whilst intermediate polars and pre-polars tend to be longer. Bottom panel: Novalike variables congregate above the period gap alongside classical novae.

ago) nova, and it has now morphed into an ER UMa dwarf nova.

The evolution of orbital periods of CVs across the HR diagram is shown in Fig. 5.17. CVs originate in or near the main sequence, with their luminosity dominated either by a luminous accretion disc or donor star, and progressively migrate towards the white dwarf cooling sequence as their donor mass decreases and periods shorten. In most WZ Sge the contribution of the accretion disc to their optical flux is small, and that of their donor stars entirely negligible.

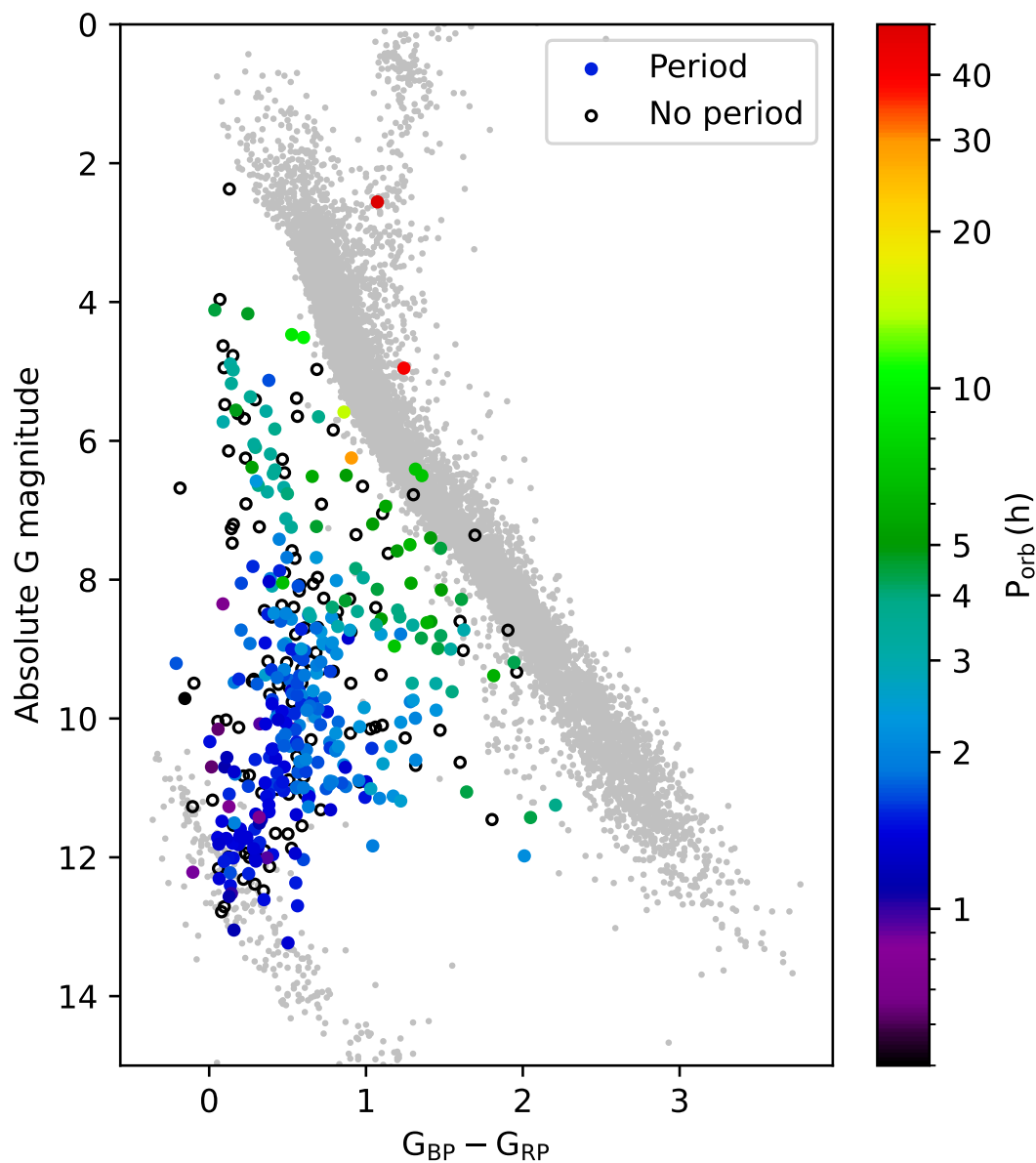


Figure 5.17: HR diagram of the CVs in SDSS I to IV showing the orbital periods where available. CVs without a period are shown as empty black circles. Note that the shortest periods are close to the white dwarf cooling sequence and the longest periods are close to the main sequence.

5.4.2 Distribution of CV sub-types

The distribution of the SDSS I to IV CV sub-types is shown in Fig. 5.18, where we compare it with that of the 150 pc volume-limited sample (Pala et al., 2020) and also with that of the R&K catalogue.

The proportion of magnetic CVs (polars, pre-polars and intermediate polars) in our sample is 20 per cent which is consistent with the 18 per cent found in Ritter & Kolb (2003) but is much lower than the 36 per cent found in Pala et al. (2020)[†]. This may be due to the small sample size (42) in Pala et al. (2020) which has a statistical 2σ

[†]The magnetic CVs in Pala et al. (2020) did not include pre-polars; they excluded a pre-polar (WXLMi) which would have taken the proportion to 37 per cent.

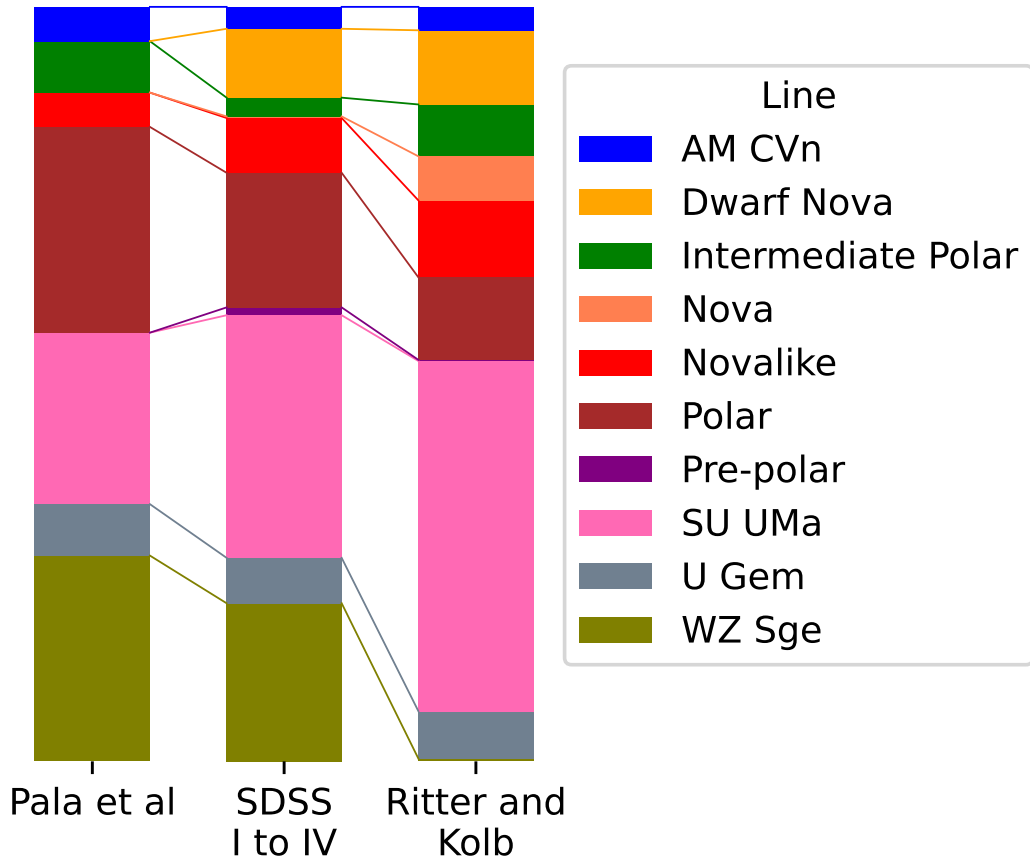


Figure 5.18: Comparison of the distribution of sub-types between a volume-limited 150 pc sample (Pala et al., 2020), the SDSS I to IV sample and the R&K catalogue. Objects identified as either CVs or magnetic CVs (30 out of 507 in SDSS I to IV) without further classification have been omitted in each case. Selection effects are clearly evident with faint and/or non-outbursting sub-types less common in the R&K sample (note that many WZ Sge in the Ritter and Kolb sample are classified as SU UMa). The proportion of magnetic systems is also significantly higher in the 150 pc sample.

uncertainty of ± 19 per cent. By comparison our sample (507) has an uncertainty of ± 3 per cent. Alternatively the difference may be because the absolute luminosity of polars is on average lower than non-magnetic systems causing a selection effect in our magnitude-limited sample.

The proportion of novae and novalikes is lower in Pala et al. (2020) than our sample. This is due to their intrinsic brightness rendering them visible at far greater distances than other CVs and hence there will be a higher proportion in our magnitude-limited sample. The proportion is greater still in Ritter & Kolb (2003) due to historic novae identified by their eruptions.

We found a smaller proportion of WZ Sge CVs than Pala et al. (2020) most probably because they are inherently faint and only observed at relatively short distances. The small proportion of WZ Sge CVs in Ritter & Kolb (2003) is due to inconsistent classification; Ritter & Kolb (2003) classify many WZ Sge CVs simply as SU UMa.

5.4.3 Variability of CVs

The photometric variability of CVs is widely used as a selection criterion when searching for CV candidates. However, different CV sub-types display very different types of variability, both in terms of amplitude and time-scales, and hence specific variability selection methods may introduce strong biases towards (or against) individual sub-types.

To illustrate this point, we computed three variability criteria for the SDSS I to IV CVs: (1) The difference between the maximum and minimum magnitude over the full set of ZTF observations which will be sensitive to outbursts and eclipses, where we only included systems with at least 150 observations. (2) The reduced χ^2 of the ZTF photometry with respect to its median. (3) the *Gaia* EDR3 *G*-band variability defined as (Guidry et al., 2021)

$$G_{\text{var}} = \frac{\text{phot_g_mean_flux_error} \times \sqrt{\text{phot_g_n_obs}}}{\text{phot_g_mean_flux}} \quad (5.1)$$

The distribution of these three types of variability are shown in the *Gaia* HR diagram in Fig. 5.19).

The maximum amplitude of variability in the ZTF light curves (top panel) shows a concentration half-way between the white dwarf cooling track and the main sequence. This reflects the predominant population of SU UMa type CVs in this area of the HR diagram, which have frequent dwarf nova outbursts with amplitudes of $m \simeq 3 - 5$, i.e. it is very likely that ZTF, despite the sparse sampling, will have caught them during an outburst. In contrast, the regions occupied predominantly by novalike variables ($G_{\text{BP}} - G_{\text{RP}} \simeq 0.25$, $G_{\text{abs}} \simeq 6$) and WZ Sge systems ($G_{\text{BP}} - G_{\text{RP}} \simeq 0.25$, $G_{\text{abs}} \simeq 12$) show only relatively small variations between the minimum and maximum brightness detected

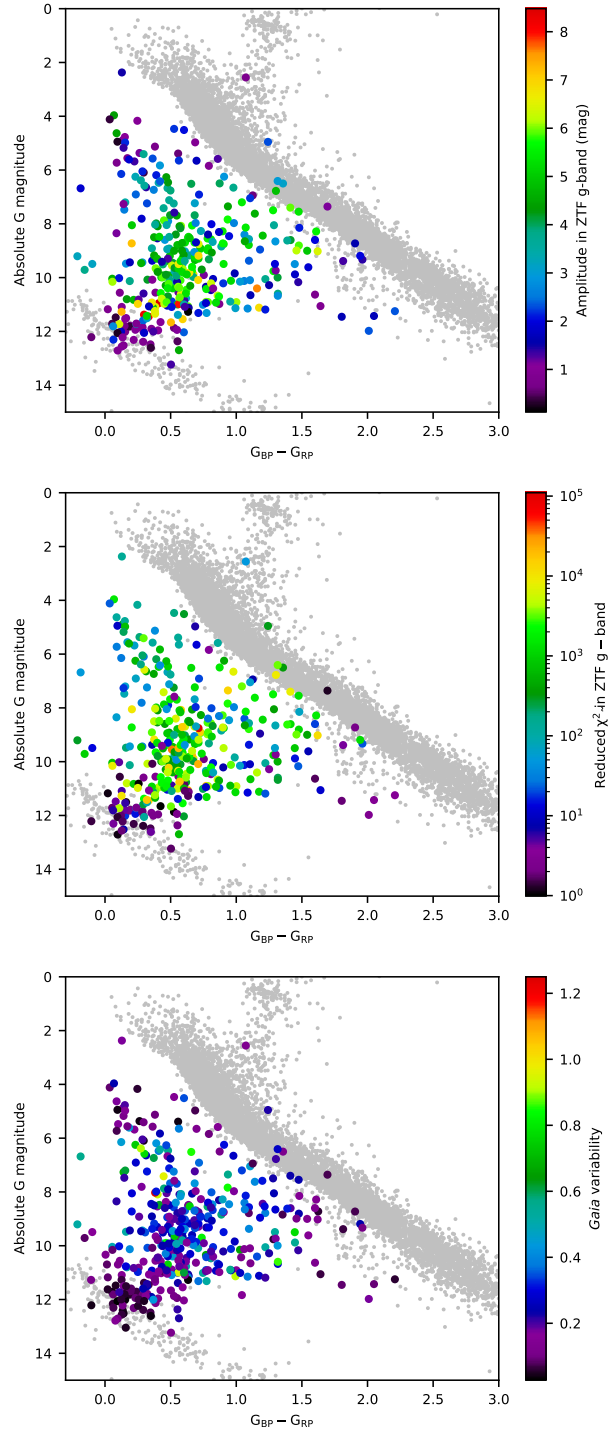


Figure 5.19: Variability of CVs related to position in the HR diagram. In each case older CVs which are approaching the white dwarf cooling sequence show less variability. Top panel: Distribution of maximum variability in the g -band ZTF light curve. Middle panel: Reduced chi-squared of the variability of the g -band ZTF light curve with respect to the median magnitude. Bottom panel: Variability in *Gaia* G -band magnitude (Eq. 5.1).

by ZTF. This is reflected by their stable, hot (novalike variables) or cool (WZ Sge CVs) accretion discs. However, a few systems in the region occupied by WZ Sge CVs show very large amplitude, $\Delta m \simeq 8$, variability, implying that ZTF observed them during one of their rare super-outbursts. The ZTF reduced χ^2 diagram shows overall a similar trend, however, the area occupied by novalike variables exhibits a higher level of variability than in the maximum amplitude diagram, most likely because many of these systems have persistent short-term variability (flickering, Bruch 1992), and on average higher quality ZTF light curves as they are intrinsically bright. Finally, the *Gaia* variability diagram shows again a lack of variability in the area occupied by novalike variables and WZ Sge stars, and overall a lower number of strongly variable systems. This is most likely due to the fact that the *Gaia* data spans a shorter baseline ($\simeq 2.8$ yr), and has on average less data points than the ZTF photometry. Future *Gaia* releases will extend the baseline to at least 5 yr, possibly up to 10 yr, increasing the diagnostic power of the *Gaia* variability index.

5.4.4 Space Density

Measuring the space density of the various CV sub-types is fundamentally important for validating evolutionary models.

Assuming that the Galaxy is axially symmetrical the space density of a class of objects is a function of the height above the Galactic disc and the radial distance from the Galactic centre. Our analysis is sufficiently local that radial variations will be small and we henceforth ignore this factor. We further assume an exponential vertical distribution with scale height h where h is assumed to be dependent upon the typical age of the CV sub-type. The space density at a height z above the plane is therefore:

$$\rho(z) = \rho_0 \times \exp\left(-\frac{|z|}{h}\right) \quad (5.2)$$

Our objective is to estimate the space density of the CV sub-types. Hence if the estimate of the number of a sub-type in a volume V is N_{obs} the space density is given by:

$$\rho_0 = \frac{N_{\text{obs}}}{\int_V \exp\left(-\frac{|z|}{h}\right) dv} \quad (5.3)$$

which for a suitably large sample volume would become a constant dependent only on the choice of h . This poses four challenges which are addressed in the following sections.

(1) some CVs within the SDSS footprint would have been too bright or too faint to be observed by SDSS; (2) an appropriate value of h for each CV sub-type needs to be chosen; (3) SDSS was not complete and did not target a proportion of CVs within its footprint; (4) the SDSS footprint only achieved partial sky coverage and a method of extrapolating the results derived from the SDSS observations is needed.

Table 5.3: Absolute magnitudes and limiting distances of CV sub-types from SDSS I to IV. N is the number of SDSS I to IV objects with reliable distances (see text). μ , σ are the mean and standard deviation of the absolute *Gaia* G magnitudes.

Type	N	μ	σ	R_{lim} (pc)
U Gem	16	7.83	1.13	899
SU UMa	66	9.90	0.94	451
WZ Sge	33	11.77	0.39	412
Polar	39	10.33	1.21	256
Intermediate Polar	7	8.59	1.02	739
Novalike variable	17	5.77	1.03	2676

CV brightness

SDSS I to IV spectroscopy did not target any objects with $g \lesssim 15$, which has been taken into account in section 5.4.4 below. At the faint end it will be apparent from the HR diagram (Fig. 5.17) that some sub-types have a larger intrinsic luminosity than others and will therefore be observable at greater distances by SDSS. We therefore sought to establish for each sub-type a limiting distance ignoring extinction (R_{lim}) within which they would have reliably been detected by SDSS. To derive this we first assume that CVs with $g < 21$ will be reliably detected from inspection of their SDSS spectrum if targeted; this is a conservative assumption as for example Pâris et al. (2017) used $g < 22$. In the following, we decided to use the *Gaia* G -band magnitude rather than SDSS- g , as the multiple observations of *Gaia* more adequately sample the average brightness of an individual system. The two passbands yield very similar apparent magnitudes for a given brightness. We calculated the mean (μ) and standard deviation (σ) of the absolute *Gaia* G magnitude of each sub-type from the SDSS I to IV CVs (ignoring objects where the error in the Bailer-Jones et al. (2018) distance was greater than 20 per cent). By definition for any CV of a given sub-type with apparent magnitude m , absolute magnitude M and distance d there is a 99.7 per cent probability that $M < \mu + 3\sigma$ hence

$$m - 5 \log_{10}(d) + 5 < \mu + 3\sigma \quad (5.4)$$

$$m < \mu + 3\sigma + 5 \log_{10}(d) - 5 \quad (5.5)$$

Now $d < R_{\text{lim}}$ is the largest value of d corresponding to $m = 21$:

$$21 = \mu + 3\sigma + 5 \log_{10}(R_{\text{lim}}) - 5 \quad (5.6)$$

$$5 \log_{10}(R_{\text{lim}}) = 5 + 21 - \mu - 3\sigma \quad (5.7)$$

$$R_{\text{lim}} = 10^{1+0.2(21-\mu-3\sigma)} \quad (5.8)$$

The values of R_{lim} for each sub-type are shown in Table 5.3.

Scale heights of the different CV sub-types

As we shall see the choice of scale height in the model has a significant effect upon the final estimates of the space density. [Patterson \(1984\)](#) used a single scale height of 150 pc for all sub-types in their analysis as did [Duerbeck \(1984\)](#) (who used 125 ± 22 pc). [Pretorius et al. \(2007a\)](#) assumed scale heights of 120, 260 and 450 pc (hereafter the P2007 model) for long- P_{orb} systems ($P_{\text{orb}} > 3$ h), normal short- P_{orb} systems ($P_{\text{orb}} < 3$ h) and period bouncers respectively. This was based on the assumption that these systems had increasing ages and therefore, as a result of scattering with other stars, increased space velocities resulting in higher average heights above the Galactic plane ([Kolb & Stehle, 1996](#)). We have used the assumptions of P2007 in our work. Where systems do not have an observed period we assign them to one of the three scale heights in P2007 based on their sub-type. U Gem CVs, novalike variables and intermediate polars are assumed to be long-period CVs, short-period systems include SU UMa CVs, polars and WZ Sge CVs with the third category reserved for period bouncers. We attempted to analyse the SDSS I to IV data in order to support the scale height assumptions in P2007 but in practice our samples were not complete to a sufficient Galactic height.

Completeness

SDSS I to IV used complex targeting rules focusing largely on quasars and not CVs (e.g. [Richards et al. 2002](#); [Ross et al. 2012](#); [Dwelly et al. 2017](#)). Fortunately CVs have similar colours to quasars and a significant proportion of quasar candidates were observed by SDSS. However, given that CV sub-types occupy different regions of the *Gaia* HR diagram (and in the colour-colour diagrams used by SDSS for their target selection) the proportion of each sub-type observed by SDSS is not the same. Whilst in principle an analysis could estimate the degree of completeness for each sub-type, such an endeavour would be very complex. We have adopted an empirical approach by analysing version 7.24 of the R&K CV catalogue which contains 1429 CVs. We removed the 117 CVs in the R&K catalogue that were originally discovered by SDSS leaving 1312 systems. The apparent magnitude (‘mag1’) of these CVs in their normal state was processed and systems that were too bright ($m < 15$) or too faint ($m > 21$) were also removed[‡]. From this we established that 208 CVs fell within the footprint of SDSS. We then established that 97 of these (46.6 per cent) were re-discovered by SDSS and we assumed that this proportion applies to all CVs and sub-types within the footprint. We then defined a correction factor $C_{\text{orr}} = 2.14$ as the reciprocal of this proportion.

[Pala et al. \(2020\)](#) used a different approach by quantifying the number of *Gaia* objects within the SDSS footprint which fulfilled the quasar colour criteria for SDSS I

[‡]Ideally, this analysis would have been done by sub-type but we discovered that the ‘type1’ and ‘type2’ fields in the R&K catalogue were unreliable; in particular many WZ Sge had been classified as SU UMa

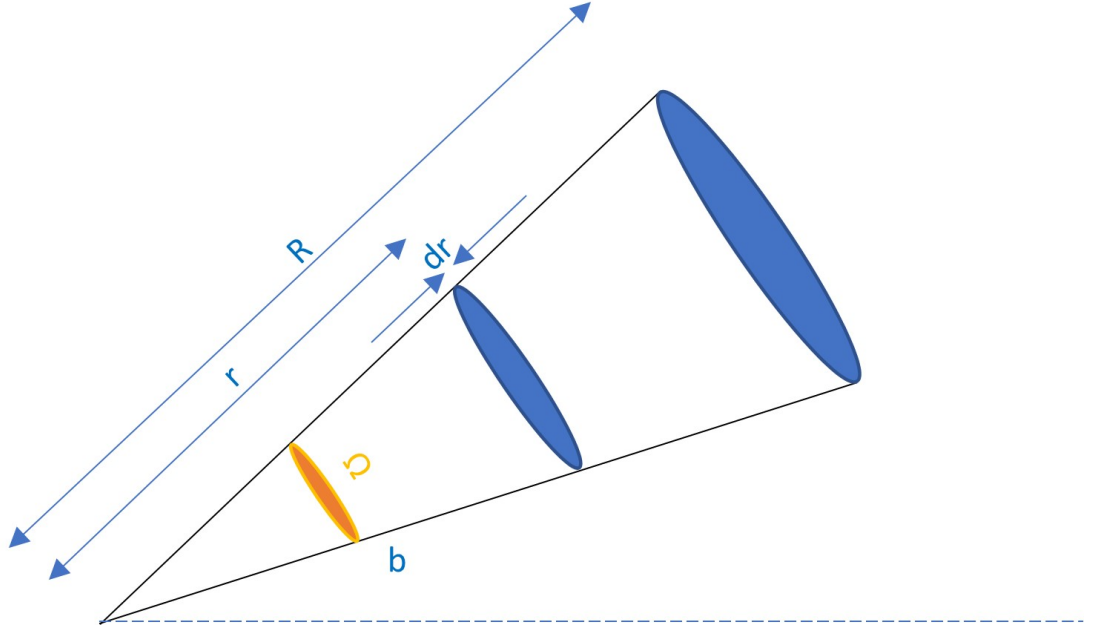


Figure 5.20: Diagram depicting a slice of infinitesimal thickness dr through a cone subtending a solid angle (Ω) at a radial distance (r). The cone represents one HEALPix pixel. The volume of the slice is $r^2\Omega dr$.

and II and did not include any cut in the red colours. This resulted in 5300 objects and Pala et al. 2020 then found the proportion of these objects with an SDSS spectrum (53 per cent) of which ≈ 6 were predicted to be in the sample. Only four were found (three had a spectrum) from which they concluded that the completeness was 71 per cent (i.e. $C_{\text{orr}} = 1.4$). It is unsurprising that the completeness of the full SDSS I to IV sample is lower than that of the nearby, bright 150 pc sample.

SDSS Footprint

The coordinates of the centres of the plates used in the ‘BOSS’, ‘eBOSS’ and ‘SDSS’ surveys, together with their radius (1.49°), define the coverage. However there are two problems to address; firstly the plates overlap and secondly the scale height of each plate will vary.

For convenience we define from the denominator of (5.3) an effective volume for a sphere of radius R with an assumed scale height of h :

$$V_{\text{eff}}(h, R) = \int_{V(R)} \exp\left(-\frac{|z|}{h}\right) dv \quad (5.9)$$

To address the overlap problem we model the celestial sphere using 2^8 ASTROPY HEALPix pixels (Górski et al., 2005). Each HEALPix pixel has the same surface area (Ω steradians) on the unit sphere and can be represented by a cone (Fig. 5.20) with galactic

latitude b . The effective volume of a sphere radius R is therefore the sum of the volume of the cones:

$$V_{\text{eff}}(h, R) = \sum_{\text{All pixels}} \int_0^R \exp\left(-\left(\frac{|r \sin(b)|}{h}\right)\right) (r^2 \Omega dr) \quad (5.10)$$

The following substitutions are used:

$$A = \frac{|R \sin(b)|}{h} \quad (5.11)$$

and

$$x = \left(\frac{rA}{R}\right) \quad (5.12)$$

We then compared the coordinates (ra,dec) of each HealPix pixel with the coordinates of the centre of each plate to identify whether that pixel was covered by that plate. We then defined SDSS_{pix} as the de-duplicated set of HEALPix pixels that lay within the coverage of one or more plates. The effective volume of the SDSS sample is therefore:

$$\begin{aligned} V_{\text{eff}}(h, R) &= \sum_{\text{SDSS}_{\text{pix}}} \int_0^A \exp(-x) \left(\left(\frac{Rx}{A}\right)^2 \Omega \left(\frac{Rdx}{A}\right) \right) \\ &= \Omega R^3 \sum_{\text{SDSS}_{\text{pix}}} \left(\frac{1}{A^3} \right) \int_0^A x^2 \exp(-x) dx \end{aligned} \quad (5.13)$$

Solving the integral analytically yields

$$V_{\text{eff}}(h, R) = \Omega R^3 \sum_{\text{SDSS}_{\text{pix}}} \left(\frac{1}{A^3} \right) (2 - (A^2 + 2A + 2) \exp(-A)) \quad (5.14)$$

which can be computed numerically for a given h and R .

Estimates of space density

Bringing the preceding sections together the three estimates of the space density (for $h = 120, 260, 450$ pc) are calculated from

$$\rho_0 = \frac{N_{\text{obs}} \times C_{\text{corr}}}{V_{\text{eff}}(h, R_{\text{lim}})} \quad (5.15)$$

and the results are listed in Table 5.4.

Next, we need to discuss the accuracy of these results. From equation (5.15) the primary sources of error in ρ_0 are in the correction factor and the scale height. The true scale height in each case will very likely lie between the two extreme values that we adopted, i.e. $h = 120$ pc and $h = 450$ pc (Table 5.4) and so a reasonable estimate for ρ_0 (excepting possibly old WZ Sge systems) is $\rho_0(260$ pc) with the extreme values forming a notional 3σ error estimate. We have avoided quoting any statistical uncertainties on our space density estimates as the true uncertainties are likely to be dominated by the assumptions on the scale height.

It is interesting to compare these estimates with the those based on different approaches used in previous works (Fig. 5.21) noting that the assumed scale heights have to be comparable.

Section 9.5 in Warner (1995) proposed $\rho_0(103 \text{ pc}) = 0.4 \times 10^{-6} \text{ pc}^{-3}$ for U Gem type systems and $\rho_0(176 \text{ pc}) = 0.25 \times 10^{-6} \text{ pc}^{-3}$ for SU UMa systems. Both values are lower than contemporary estimates presumably as earlier CV discoveries were primarily the result of following up transients and limited to brighter targets.

Table 5.4: Analysis of the space density of CV sub-types for different assumptions of scale height. ρ_0 (P2007) assumes the scale heights from Pretorius et al. (2007a). N is the number of SDSS I to IV objects that are closer than the limiting distance. Note that the values of ρ_0 for individual sub-types are slightly understated ($\simeq 6$ per cent) due to the remaining unclassified CVs and dwarf novae. This does not apply to the ‘All CVs’ values which have been calculated for 150 pc and 300 pc limiting distances to enable comparison with Pala et al. (2020) and Inight et al. (2021) respectively.

Type	Limiting distance (pc)	N	Space Density (10^{-6} pc^{-3})			
			$\rho_0(120)$	$\rho_0(260)$	$\rho_0(450)$	$\rho_0(P2007)$
U Gem	899	10	0.68	0.16	0.09	0.63
SU UMa	451	30	4.21	1.71	1.19	1.88
WZ Sge	412	38	6.24	2.72	1.96	2.52
Polar	256	8	3.25	1.89	1.53	1.84
Intermediate polar	739	6	0.50	0.14	0.08	0.32
Novalike	2676	23	1.01	0.12	0.04	0.97
All CVs	150	7	8.21	5.78	5.07	5.68
All CVs	300	52	13.92	7.23	5.61	7.92

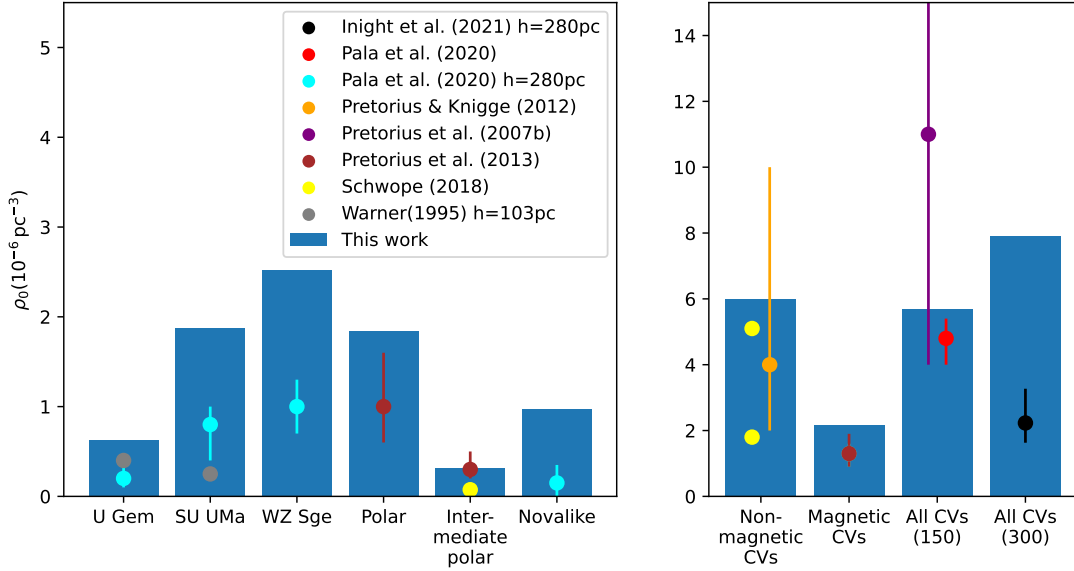


Figure 5.21: Comparison of the space density estimates for CVs from this work (bar chart) and published values. All estimates use the P2007 assumptions for scale height h unless otherwise stated. Left panel: Estimates for individual sub-types. Note that [Pala et al. \(2020\)](#) are understated as they do not take account of completeness. Right panel: Composite estimates. [Knight et al. \(2021\)](#) specifically excluded selection effects.

[Pretorius et al. \(2007b\)](#) estimated $\rho_0(120 \text{ pc}) = (15^{+25}_{-8}) \times 10^{-6} \text{ pc}^{-3}$ for all non-magnetic CVs based on a very small sample of four systems. Our results are towards the lower end of this range.

[Pretorius & Knigge \(2012\)](#) estimated a density of $\rho_0(260 \text{ pc}) = (3.8^{+5.3}_{-1.9}) \times 10^{-6} \text{ pc}^{-3}$ for non-magnetic CVs which compares with our value of $\rho_0(260 \text{ pc}) = (4.29) \times 10^{-6} \text{ pc}^{-3}$ (by adding the individual estimates from Table 5.4).

[Pretorius et al. \(2013\)](#) estimated $\rho_0 = (1.3^{+0.6}_{-0.4}) \times 10^{-6} \text{ pc}^{-3}$ for magnetic CVs, based upon a scale height of 120 pc for long period systems and 260 pc for short period systems, which is consistent with our estimates. They also estimated values for polars and intermediate polars which are consistent with this work.

[Schwöpe \(2018\)](#) estimated $\rho_0(120 \text{ pc}) = 0.13 \times 10^{-6} \text{ pc}^{-3}$ for intermediate polars. This is significantly lower than our estimate.

[Pala et al. \(2020\)](#) estimated a composite $\rho_0(280 \text{ pc}) = (4.8^{+0.6}_{-0.8}) \times 10^{-6} \text{ pc}^{-3}$ for all CVs and our $\rho_0(260 \text{ pc}) = 5.78 \times 10^{-6} \text{ pc}^{-3}$ is consistent with this noting that we use a larger correction factor (2.1 compared with 1.4 in [Pala et al. \(2020\)](#)). [Pala et al. \(2020\)](#) also provided incomplete (their footnote 9 states that they were unable to estimate the completeness of individual sub-types) estimates for $\rho_0(260 \text{ pc})$ for five sub-types. These values are lower than our estimates – partly due to (in)completeness but also because we use a larger correction factor (2.1 compared with 1.4 in [Pala et al. \(2020\)](#)). Our larger sample size may also have had an effect brought about by the effectiveness of SDSS in

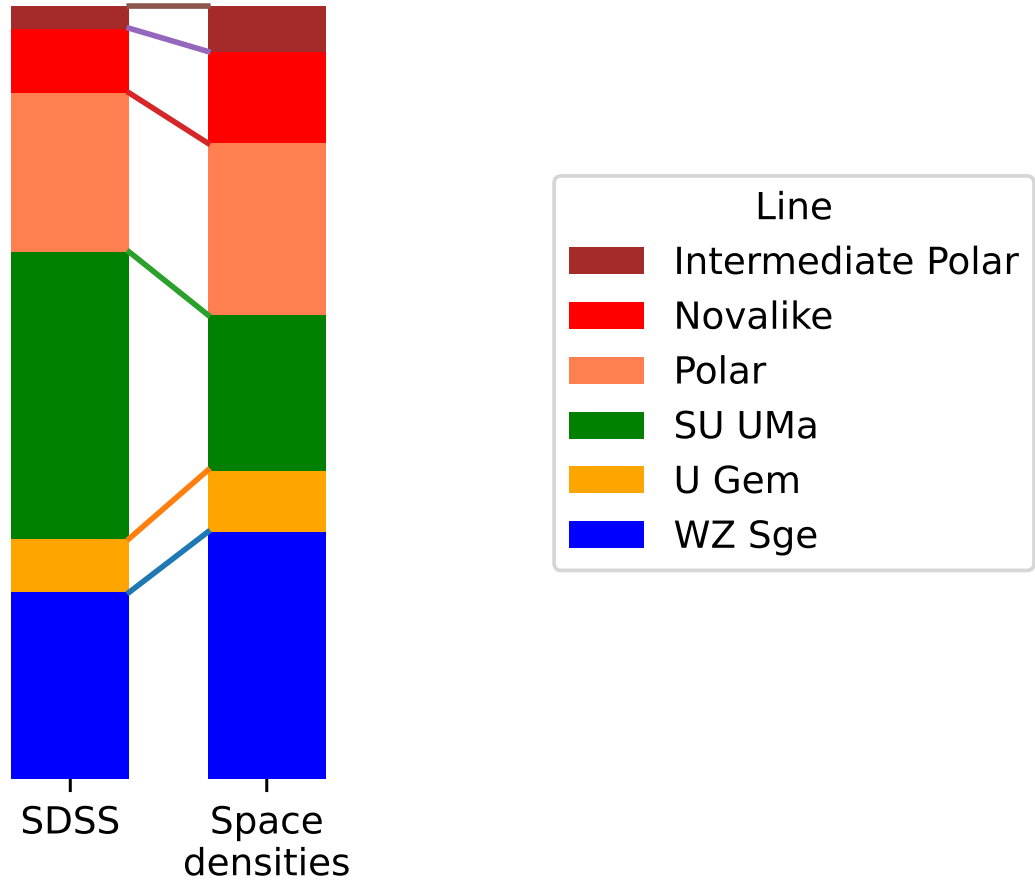


Figure 5.22: Comparison of the distribution of sub-types between the SDSS I to IV sample and our predicted space densities using the P2007 scale height assumptions. This plot ignores sub-types for which we have not estimated a space density.

discovering short-period systems.

[Inight et al. \(2021\)](#) estimated $\rho_0 = (2.23^{+1.04}_{-0.6}) \times 10^{-6} \text{ pc}^{-3}$ for their Gold Sample of 201 systems. The Gold Sample is a reliable subset of the known CVs (at least 305) within 300 pc and their estimate is therefore a lower limit for the true space density.

In principle, the fractions of sub-types from our space density estimates should reflect the true fractions in the underlying population without selection effects – as opposed to the number ratios in the magnitude limited SDSS I to IV sample. We therefore compared these fractions with those from the SDSS I to IV sample (Fig. 5.22), where the main difference is the larger proportion of WZ Sge stars and a lower fraction of SU UMa CVs when looking at the space density results. This is partly a consequence of the assumption regarding scale height and is in line with the expectation that low-luminosity WZ Sge stars should be under-represented in a magnitude limited sample. Whilst demonstrating that the SDSS I to IV sample is subject to some selection effects,

we also caution not to over-interpret the space density ratios because of the significant effect of scale height assumptions.

In summary, the long-standing discussion of the CV space density seems to converge to a value of $\simeq 5 \times 10^{-6} \text{pc}^{-3}$ [§] However, the uncertainties in scale heights continue to limit the accuracy of any estimates of space density. We have calculated space densities for six sub-types and Fig. 5.21 demonstrates that these estimates are consistent with other work.

5.4.5 Low accretion rate systems

Period bouncers are CVs where the mass of the donor has shrunk below the level needed to sustain hydrogen fusion in the core ($\simeq 0.061 M_{\odot}$) and the donor has evolved to a brown dwarf. A consequence of this is that the orbital separation of the CV increases and P_{orb} evolves back from the period minimum (often taken as ~ 76.2 min, Knigge 2006) towards longer periods. Patterson (2011) identified a total of 22 candidate period bouncers, eight of which are in our sample (Table 5.5). Together with one polar, the 13 non-magnetic period-bouncers in Table 5.5 represent 14 per cent of the WZ Sge CVs and 2.6 per cent of our complete sample. The two new candidates from this work

[§]This compares with a thin disk space density for all stars of $6.966 \times 10^{-3} \text{pc}^{-3}$ (Vieira et al., 2023). Assuming similar average masses CVs therefore account for $\simeq 0.07$ per cent of the total stellar mass.

Table 5.5: Period bouncers within the coverage of SDSS I to IV. Candidate systems are shown in italics. The donor mass of J0058-0107 and J2304+0625 was calculated by first finding the mass ratio using the method from Kato & Osaki (2013) and then assuming an average white dwarf mass of $0.83 M_{\odot}$. J1212+0136 is an interesting system as it was initially assumed to be a detached system with a white dwarf and low mass companion. It was only recognised as an accreting system from the detection of cyclotron emissions and an X-ray observation which also confirmed its type.

SDSS name	CV type	Reference	P_{orb} (h)	$M_{\text{donor}}(M_{\odot})$
<i>J0058-0107</i>	WZ Sge	Kato et al. (2017)	1.559	0.066
J0804+5103	WZ Sge	Amantayeva et al. (2021)	1.433	0.042
J0843+2751	WZ Sge	Patterson et al. (1998)	1.439	0.02
<i>J0904+4402</i>	WZ Sge:	This work	1.674	
J1035+0551	WZ Sge:	Littlefair et al. (2006)	1.368	0.06
J1057+2759	WZ Sge:	McAllister et al. (2017)	1.507	0.044
<i>J1212+0136</i>	Polar	Farihi et al. (2008)	1.474	
J1216+0520	WZ Sge:	Southworth et al. (2006)	1.646	<.04
J1255+2642	WZ Sge	Patterson et al. (2005a)	1.992	<.05
J1433+1011	WZ Sge	Savory et al. (2011)	1.302	0.0571
J1435+2336	WZ Sge:	Pala et al. (2022)	1.296	
J1507+5230	WZ Sge	Littlefair et al. (2007)	1.11	0.056
<i>J2131-0039</i>	WZ Sge:	This work	1.67	
J2304+0625	WZ Sge	Nakata et al. (2014)	1.616	0.044

(J0904+4402 and J2131–0039) were identified because of their spectra (white dwarf visible and donor not apparent) and an orbital period significantly larger than the period minimum. We estimated the space density of period bouncers using 14 per cent of the space density of WZ Sge from Table 5.4 to be $\rho_0(450) = 0.27 \times 10^{-6} \text{pc}^{-3}$. Comparing this with $\rho_0(P2007) = 7.92 \times 10^{-6} \text{pc}^{-3}$ implies that only 3.4 per cent of CVs are period bouncers which is a long way from the 70 per cent of all CVs predicted by Kolb (1993). Goliash & Nelson (2015) modelled CV evolution to predict the intrinsic proportion of period bouncers as being 38 – 60 per cent of all CVs and the observed proportion (taking account of selection effects) as 2.5 – 11.2 per cent. Although period bouncers are intrinsically faint any observational bias is unlikely to fully account for this difference. As long as period bouncers maintain a minimum amount of mass transfer, and associated Balmer emission lines, SDSS spectroscopy is extremely efficient at identifying WZ Sge CVs, independent of their orbital period and their outburst frequency. The lack of observed period bouncers remains puzzling, and could be due to the donors in period bouncers either becoming detached or merging with the white dwarfs.

5.4.6 Unusual state changes

In contrast to dwarf novae, which undergo quasi-regular outbursts because of thermal instabilities in their accretion discs, novalike variables are known to exhibit state changes due to sustained changes in \dot{M} (Shafter et al., 1985; Leach et al., 1999; Rodríguez-Gil et al., 2007b). Polars are also known to undergo state changes on a timescale of months to years (Kafka & Honeycutt, 2005; Ramsay et al., 2004; Šimon, 2016), and low states have been observed occasionally in a small number of dwarf novae (Wood et al., 1995; Schreiber et al., 2002). The cause of the high/low state transitions is still debated, but a likely contender is star spots near the inner Lagrangian point (Livio & Pringle, 1994; King & Cannizzo, 1998; Hessman et al., 2000).

Serendipitously whilst reviewing the ZTF light curves we have identified eight CVs (Figure 5.23) within the SDSS I to IV sample that display erratic light curve morphologies, neither displaying disc outbursts, nor clearly identifiable state changes – and which have spectra that are inconsistent with being either magnetic CVs or novalike variables. These systems defy the standard CV classification scheme outlined in section 2.2. These eight examples of systems exhibit significant brightness changes on timescales that indicate the cause is a change to \dot{M} rather than instabilities of their discs. Below, we discuss the properties of these systems.

J0838+4910 is below the period gap with $P_{\text{orb}} = 1.69 \text{ h}$. Thorstensen et al. (2015) rightly concluded that this was an SU UMa based on the measured orbital period and the CRTS light curve. The SDSS spectrum is consistent with an SU UMa classification. However the ZTF data is contradictory – showing no outbursts and two long-lasting faint states.

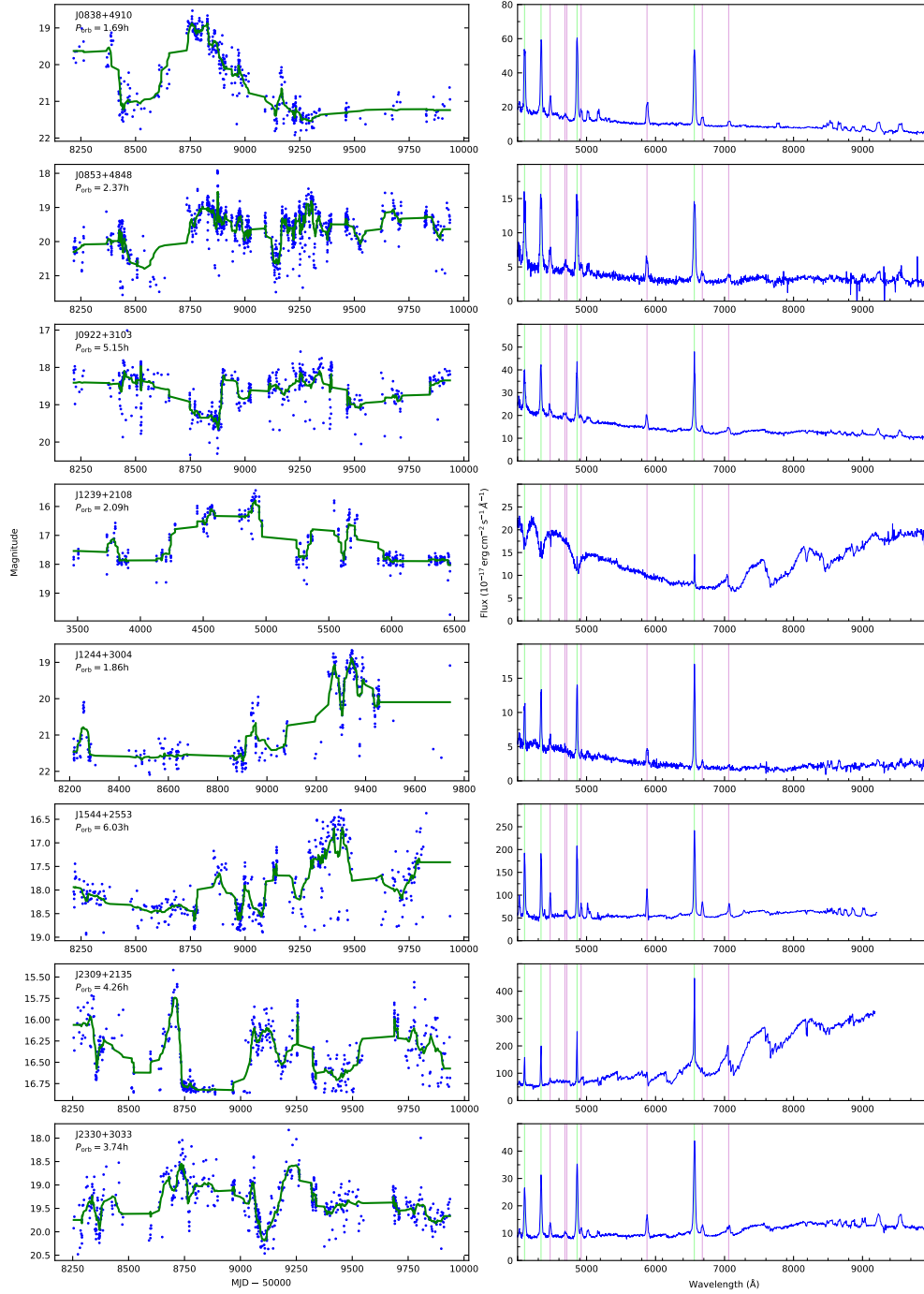


Figure 5.23: We identified eight CVs with substantial and erratic changes in apparent magnitude over periods of months or years – suggesting commensurate changes in accretion rate. The light curves shown are the merged r - and g -band data from ZTF, with the exception of J1239+2108 for which we show the CRTS data. The green lines show the trend using five point boxcar smoothing. The changes are atypical as the spectra of these systems are inconsistent with either a magnetic CV or novalike variable classification.

J0853+4848 has a spectrum that shows Balmer, He I and weak He II emission lines. The white dwarf is not visible but the M-type donor is detected in the red part of the spectrum. The system has been brighter since the SDSS spectrum was obtained. There is no CRTS data and the ZTF data shows one small outburst but also state changes of up to two magnitudes. The period is 2.36 h which is in the period gap.

J0922+3103 (AR Cnc) and J1544+2553 have periods of 5.15 h and 6.03 h respectively and spectra which resemble U Gem CVs with double-peaked Balmer and helium lines, and clear signatures of their M-dwarf donors. However their light curves more closely resemble those of polars and they exhibit no outbursts. This ambiguity prevents any further classification beyond that of a CV. Palaversa et al. (2013) classified J1544+2553 as a novalike using an automated process but this is not consistent with the strong lines in the spectrum, the detection of the donor and the position in the HR diagram.

J1239+2108 (IR Com) has previously been identified as a CV with erratic brightness changes (Richter et al., 1997), and SDSS obtained a spectrum when accretion had virtually ceased for an extended period (Manser & Gansicke, 2014), revealing both the white dwarf and the donor star. It is on the lower edge of the period gap with $P_{\text{orb}} = 2.09$ h.

J1244+3004 (CSS 080427:124418+300401) was found in a bright state within the CRTS light curve for about ten years, albeit exhibiting outbursts (Thorstensen et al., 2015). The ZTF light curve (Fig. 5.23) shows a prolonged drop of $m \simeq 2$. Its period of $P_{\text{orb}} = 1.86$ h places it below the period gap.

J2309+2135 (V405 Peg) was identified by Schwöpe et al. (2002c) as the counterpart of a *ROSAT* X-ray source, and based on the detection of the donor star, and the apparent magnitude, the authors speculated that V405 Peg may be as close as $\simeq 30$ pc. Thorstensen et al. (2009) determined the period to be 4.26 h, and measured a parallax of $\simeq 150$ pc – superseded by the *Gaia* parallax of $\simeq 173$ pc. Schwöpe et al. (2014) obtained deep X-ray observations, revealing a relatively low X-ray luminosity, and the authors noted that the system displays characteristics of both magnetic and non-magnetic CVs. The SDSS spectrum very clearly reveals the M-type donor star, with little contribution from either an accretion disc or the white dwarf.

J2330+3033 has a spectrum showing both Balmer and He I emission lines, the donor is clearly visible. It is eclipsing and Hardy et al. (2017) found $P_{\text{orb}} = 3.74$ h. The CRTS and ZTF light curves show variability but no outbursts.

We note that the periods of these systems cluster both near the lower edge of the period gap, and in the $\simeq 4 - 6$ h range, indicating widely varying evolutionary stages. The lack of outbursts is indicative of a low \dot{M} . A low \dot{M} is corroborated by the detection of the donor stars in the short-period systems, as non-magnetic CVs within this period range are typically SU UMa systems with accretion disc dominated spectra. The long-

period systems coincide with the period range where dwarf novae are usually found (we encourage the reader to inspect section 7.2 of [Knigge et al. 2011](#) for a discussion of the inconsistency between the CV sub-type distribution in the 3 – 6 h period range and the theoretical predictions of \dot{M} and the critical accretion rate for disc instabilities to (not) occur). We speculate that these eight systems may either contain weakly magnetic white dwarfs, with fields that are sufficiently low so that they do not develop the hallmarks of polars or intermediate polars, but strong enough to affect the structure of the disc. However, we also note that a number of intermediate polars exhibit dwarf nova outbursts – so the tentative suggestion of weak fields does not explain the absence of outbursts. An alternative idea is that these systems are undergoing some type of state change in their donor stars, as possibly suggested by their location near the lower edge of the period gap, and in the range where dwarf novae and novalike overlap above the period gap.

Table 5.6: Tertiary systems identified in SDSS I to IV. μ_{RA} and μ_{Dec} are the components of proper motion and a is the projected separation. In each case the calculated binding energy $-E_{\text{bind}}$ (see text for details) is typical of a bound system as shown in fig.6b of Burgasser et al. (2007).

System	<i>Gaia</i> EDR3 source_id	P_{orb} (h)	Distance (pc)	μ_{RA} (mas yr ⁻¹)	μ_{Dec} (mas yr ⁻¹)	a (au)	$-E_{\text{bind}}$ (10 ⁴¹ erg)
J0801+2103	670872860843747072		816 ± 106	-9.22	-17.26	12682 ± 2720	7 ± 1.6
	670872860843744768		1597 ± 608	-8.97	-17.20		
J0803+2516	681813727390427136	2.2	1016 ± 130	-7.63	-7.52	4922 ± 976	22 ± 4.3
	681813723094550144		1042 ± 72	-7.80	-7.22		
J0840+0455	582480170443653376		1466 ± 104	-3.92	-11.11	862 ± 106	142 ± 17.5
	582480166148927744		1441 ± 120	-3.88	-11.00		
J1014+0638	3873721404734233344	1.4	192 ± 5	-62.27	-34.29	1680 ± 80	56 ± 2.7
	3873721409029428352		185 ± 1	-62.89	-34.03		
J1131+4322	772038105376131456	1.5	328 ± 6	-12.78	11.70	1745 ± 65	54 ± 2.0
	772038105376626432		361 ± 5	-12.66	11.94		
J1206+5100	1548430890981046272	3.8	302 ± 8	0.46	-28.23	2080 ± 112	39 ± 2.1
	1548430886684193152		317 ± 49	-0.48	-28.00		
J1702+2235	4571234234022916992	1.6	3237 ± 1269	4.42	-6.84	1447 ± 847	63 ± 36.9
	4571234234022916864		1605 ± 1238	4.40	-6.74		
J2205+1155	2728239161441977216	1.4	1004 ± 451	15.91	-9.58	18470 ± 11519	5 ± 2.9
	2728239200096378368		544 ± 42	16.67	-9.42		

5.4.7 Tertiary systems

Raghavan et al. (2010) suggest that around eight per cent of close binaries are part of a triple system and have a distant companion. They are significant as the distant star can influence the evolution of the inner binary through Kozai cycles (Fabrycky & Tremaine, 2007). We searched *Gaia* EDR3 for such systems by identifying candidate stars within 30 arcsec of each of the CVs in our sample. Potential companions can be expected to have similar proper motions. However proper motions, and hence differences between them, will scale inversely with distance. We therefore adopted the following metric where the denominator is a proxy for distance:

$$\sqrt{\frac{(\text{pmra}_{\text{cv}} - \text{pmra}_{\text{cand}})^2 + (\text{pmdec}_{\text{cv}} - \text{pmdec}_{\text{cand}})^2}{\text{pmra}_{\text{cv}}^2 + \text{pmdec}_{\text{cv}}^2}} < 0.05 \quad (5.16)$$

resulting in the eight systems in Table 5.6.

The projected separations, a , were calculated by multiplying the angular separation by the Bailer-Jones et al. (2018) distance; the errors on the Bailer-Jones et al. (2018) distances are too large to estimate the radial separation. Estimating the binding energy is a useful test of whether these systems are gravitationally bound to the CV or not:

$$-E_{\text{bind}} = G \frac{(M_{\text{WD}} + M_{\text{d}})M_3}{a} \quad (5.17)$$

A rough estimate is sufficient for this purpose and so we assume typical values of $M_{\text{WD}} = 0.83 M_{\odot}$ and a donor of mass $M_{\text{d}} = 0.14 M_{\odot}$. We estimate M_3 from the position of the star in the *Gaia* HR diagram; and find that the CV companion in seven of the tertiaries is on the main sequence; the companion to J1206+5100 is a white dwarf. The calculated values shown in Table 5.6, when compared with fig 6b of Burgasser et al. (2007) show clearly that these eight CVs are tertiary systems. These eight are only 1.6 per cent of our sample and should be considered a lower limit on the fraction of CVs in triple systems. Our search is likely to be incomplete at larger distances where *Gaia* may not resolve close tertiaries or not detect them because they are too faint; in particular tertiaries with very low-mass or cool white dwarf companions would be hard to identify.

5.5 Summary

We have reviewed the spectra of CVs observed by SDSS I to IV and publish 178 for the first time along with 59 new periods. We discovered 70 completely new CVs and classified or updated 262. These 70 new CVs from SDSS III and IV augment the 282 previously identified in SDSS I and II. This total is remarkably consistent with the early prediction of 400 from [Szkody et al. \(2002b\)](#). We have analysed the results and position the different CV sub-types in evolutionary terms together with revised estimates of space density. The period bouncers and tertiary systems within our sample have been identified and the abundances compared with previous estimates.

Chapter 6

Cataclysmic variables from the SDSS-V plate survey

6.1 Introduction

In Chapter 5 we showed how the Sloan Digital Sky Survey (SDSS) ([York et al., 2000](#)) has proven to be an important tool for identifying CVs spectroscopically with the total number of CVs observed by SDSS I to IV standing at 507. The SDSS spectroscopy led, in particular, to the discovery of a large number of CVs with no history of outbursts; analysis of these systems confirmed the long-standing prediction of a pile-up of CVs near the minimum orbital period of about 80 min ([Gänsicke et al., 2009](#)).

During the commissioning of SDSS [Raymond et al. \(2003\)](#) developed a targeting strategy for CVs in *ugriz* colour space, which however proved to be more effective in identifying detached white dwarf plus M-dwarf binaries. As remarkable as the impact of SDSS has been on the research of CVs, most of the SDSS CVs were observed serendipitously in a much larger pool of objects targeted for spectroscopy for a wide range of reasons, e.g. as quasar candidates or blue excess objects ([Strauss et al., 2002](#)) or because of their variability ([Morganson et al., 2015](#)).

SDSS has now entered its fifth phase (SDSS-V, [Kollmeier et al. 2017](#)), which will extend multi-object spectroscopy across the entire sky by operating robotic fibre positioners on the 2.5 m SDSS telescope at Apache Point Observatory (APO) and at the 2.5 m Dupont telescope at Las Campanas Observatory. SDSS-V differs from its predecessors in that it contains a program to deliberately target white dwarfs and CVs. Although most of SDSS-V will be carried out with robotic positioners, the first eight months of SDSS-V observations at APO followed the approach using fibres positioned in the focal plane with drilled plates ([Blanton et al., 2003](#)) to feed a spectrograph, as used in the earlier phases of SDSS.

We report here on the 118 CVs observed in the first eight months of SDSS-V as part of the dedicated white dwarf binary targeting strategy. We describe the identification of new CVs, the spectral confirmation of candidate CVs and new observations of previously known CVs. We report new orbital periods for 21 of these CVs obtained by combining radial velocity data from SDSS with light curves from the Zwicky Transient Facility (ZTF, [Bellm et al. 2019](#)) and other follow-up observations. The remainder of this chapter is organised as follows. We describe the target strategy in Section 6.2 and our observations in Section 6.3. We describe how we analyse and classify the spectra and light curves in Section 6.4, report our results in Section 6.5 and discuss our findings in Section 6.6. Finally, we summarise our results in Section 6.7. A full set of spectra and light curves is provided in Appendix C

6.2 Target selection

Whereas the previous generations of the SDSS surveys were prolific in identifying new CVs, the vast majority of these systems were observed serendipitously, many of them because they overlap in colour space with quasars (see for example [Richards et al., 2002](#); [Gänsicke et al., 2009](#)). SDSS I to IV preceded *Gaia* ([Gaia Collaboration et al., 2018](#)), therefore parallaxes, and hence absolute magnitudes were not available, and the only dedicated target selection for CVs relied on rather crude colour-colour cuts, which were in fact more successful in identifying detached white dwarf plus M-dwarf binaries ([Raymond et al., 2003](#)). The CVs within SDSS I to IV were identified by visual inspection of the SDSS spectroscopy, sometimes aided by various techniques filtering the entire SDSS data set into shortlists of candidate objects to be inspected (e.g. [Szkody et al., 2002b, 2003a, 2004a, 2005, 2006](#); [Carter et al., 2014](#); [Gentile Fusillo et al., 2015](#); [Kepler et al., 2019, 2021](#); [Inight et al., 2023b](#)).

SDSS-V provided the first opportunity to define dedicated target selections aimed at white dwarfs and CVs that made use of the *Gaia* astrometry. These target selections are defined using ‘cartons’, most of which use a set of algorithmic rules, filtering large catalogues of objects, to produce the target lists for SDSS-V (see Table 2 in [Almeida et al. 2023](#) and the description of the [compact binary](#) and [white dwarf cartons](#)). We defined eight cartons using a range of criteria to target white dwarfs, both single and in binaries: `mwm_wd_core` is based on the *Gaia* white dwarf candidate catalogue of [Gentile Fusillo et al. \(2019\)](#) *, whereas `mwm_cb_gaiagalex`, `mwm_cb_uvex1`, `mwm_cb_uvex2`, `mwm_cb_uvex3`, `mwm_cb_uvex4` and `mwm_cb_uvex5` leverage the fact that both single white dwarfs and those in binaries (detached and CVs) have an ultraviolet excess. These ultraviolet-excess cartons are based on cross-matching *Gaia* with

*`mwm_wd_core` was defined in 2019 in anticipation of SDSS-V and before *Gaia* EDR3 and [Gentile Fusillo et al. \(2021b\)](#) were available

ultraviolet surveys including *GALEX* (Morrissey et al., 2007), the ultraviolet observations obtained by the Optical Monitor of *XMM-Newton* (Mason et al., 2001; Page et al., 2012) and the UVOT instrument onboard *SWIFT* (Gehrels et al., 2004; Roming et al., 2005). These ultraviolet-excess cartons contain a substantial proportion of, but not all, the CVs in the observable SDSS-V footprint. Finally, we defined a carton, `mwm_cb_cvcandidates` that contains a collection of published CVs and CV candidates (potential CVs that have typically been identified by an outburst and need confirmation with a spectrum). Full details of the target selection rules will be provided in a forthcoming publication. These eight cartons were then assigned priorities for the SDSS-V observations that were above most of the other stellar and extragalactic cartons, ensuring a high completeness of the spectroscopic follow-up. One important fact to bear in mind in the analysis of the SDSS-V results is that a given target can be selected by multiple cartons.

When referring to individual systems, we abbreviate their SDSS designations to four digits in each of RA and Dec, e.g. SDSS J062429.71+002105.8 is referred to as J0624+0021. The full designations are listed in Table 6.3.

6.3 Observations

6.3.1 SDSS Spectroscopy

The SDSS BOSS spectrograph (Smee et al., 2013; Dawson et al., 2013) covers the range $3600 - 10\,400 \text{ \AA}$. The data analysed here was processed with v6_0_4 of the SDSS-V pipeline (Almeida et al., 2023), which performed sky subtraction together with flux and wavelength calibration of each exposure. Based upon our analysis the SDSS-V spectroscopy can be used to measure radial velocities from narrow spectral lines with an accuracy of up to 20 km s^{-1} . SDSS-V differs from the preceding surveys in that it expanded the coverage to include the Galactic disc, which introduces new challenges; in particular the reddening effect of interstellar dust has impacted the flux calibration of a number of spectra.

SDSS-V spectroscopy of the cartons described in Sect. 6.2 was carried out on 236 individual plates, where each plate covers seven square degrees of the sky. Sixteen pairs of plates had identical plate centre coordinates. The number of targets per carton, observed targets per carton, spectroscopic completeness, and the number of CVs identified per carton are reported in Table 6.1. The exposure time for each plate observation was 900 s. A number of exposures were taken which were often, but not always, contiguous. The pipeline collects all the exposures of a given plate within 2 – 3 d (a ‘plate-epoch’ hereafter referred to as an epoch) and co-adds the individual spectra for each target (see Fig. 6.1). We use the co-added spectrum for our spectral classification identification as it will have a higher signal-to-noise ratio (SNR) than the individual 900 s spectra. We use the individual spectra to probe for variations in radial velocity. The plate observations of SDSS-V collected 27 191 co-added spectra of 11 384 individual targets that fall

Table 6.1: Target cartons observed by SDSS-V and used for the analysis in this paper showing the completeness. The numbers observed per carton refer to the 236 plates observed as part of SDSS-V in which these cartons were implemented in the observing strategy. Many targets are present in multiple cartons.

Carton	Targets	Number observed	per cent complete	CVs found
mwm_cb_gaiagalex	7773	4050	52	26
mwm_cb_uvex1	3281	2488	76	27
mwm_cb_uvex2	8040	5802	72	44
mwm_cb_uvex3	29	24	83	0
mwm_cb_uvex4	179	144	80	2
mwm_cb_uvex5	282	27	10	0
mwm_wd	6229	5781	93	18
mwm_cb_cvcandidates	141	124	88	101

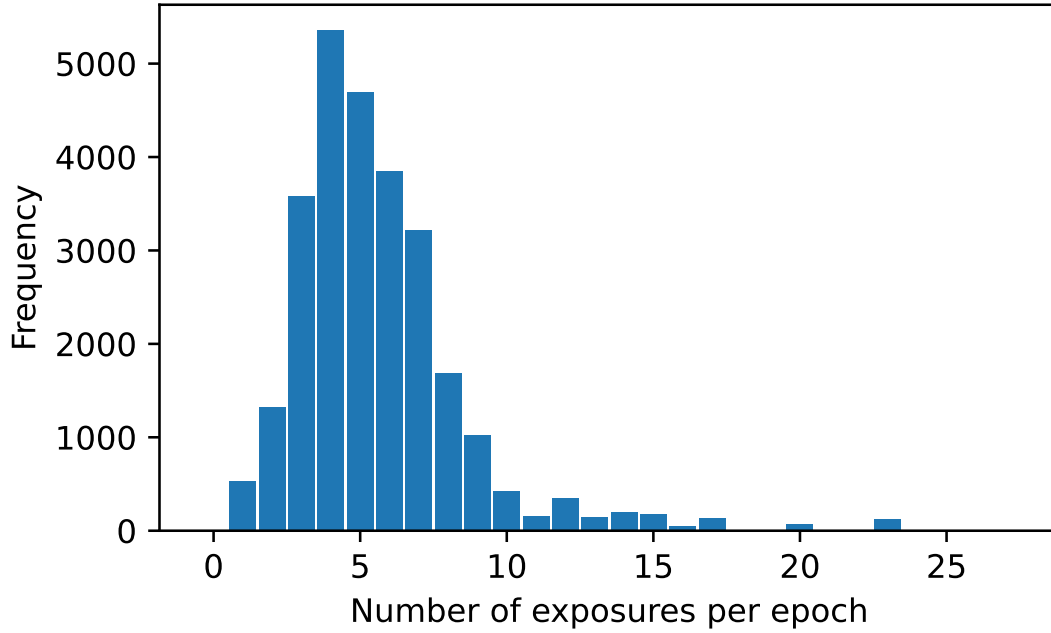


Figure 6.1: Distribution of the number of 900 s exposures used to form each of the 27191 co-added spectra. The exposures were often contiguous but always obtained within a 2–3 day epoch. Where an object was observed in more than one epoch a separate co-added spectrum was produced for each epoch

within our cartons (many plates were observed at different epochs, separated by weeks to months, resulting in multiple co-added spectra of a substantial number of targets).

The CV sample presented in this paper is therefore not complete within the SDSS-V plate program and is limited to the systems targeted in the cartons described above – additional CVs may emerge from the extragalactic programs, although these are most likely to be too faint to have a *Gaia* counterpart.

6.3.2 Photometric survey data

We retrieved archival light curves from the Catalina Real-Time Transient Survey (CRTS, [Djorgovski et al. 2011](#)), Zwicky Transient Facility (ZTF, [Bellm et al. 2019](#)) and the Transiting Exoplanet Survey Satellite (*TESS*, [Ricker et al. 2015](#)). We reviewed these primarily for historical outbursts. The ZTF and *TESS* light curves are shown alongside the spectra in Figs. 1 to 13 in the supplementary material.

6.3.3 Follow-up observations

Photometry

We obtained follow-up photometry using the 2 m Liverpool Telescope (LT, [Steele et al. 2004](#), see Table 6.2 for details) of two particularly interesting CVs: J0624+0021, which

Table 6.2: The journal of the Liverpool Telescope observations.

Date	UTC (start)	<i>N</i> (obs)	Duration (minutes)
J0624+0021			
2021 Dec 29	22:27:40	120	218
2022 Jan 05	22:40:53	90	162
J1740+0258			
2022 Jun 03	23:09:51	180	325
2022 Jun 20	22:41:14	200	262

is located in the period gap (Sect. 6.5.2) and J1740+0258 which exhibits unusual state changes (Sect. 6.5.2). Both systems were identified as potentially eclipsing systems from their SDSS spectra where the higher Balmer lines exhibit deep central absorption dips that go down to, or even below the continuum. Both targets were observed twice. The length of the initial observation was chosen to exceed the likely orbital period so that at least one eclipse would be observed. In both cases, the first observation covered two eclipses, from which we estimated the orbital period, and then scheduled a second observation a few days later to provide a more accurate period measurement. Each LT observation consisted of a sequence of 90 s exposures with the IO:O imager using a Bessel-*V* filter. The standard LT pipeline was then used to provide bias subtraction and flat fielding. Differential photometry was obtained with the SEXTRACTOR package (Bertin & Arnouts, 1996), using *Gaia* EDR3 3120280993084993792 as comparison star for J0624+0021 and *Gaia* EDR3 4376322089783941120 for J1740+0258.

Spectroscopy

Prior to SDSS-*V*, one of the authors (JRT) obtained time-resolved spectroscopy using the 2.4 m Hiltner telescope of the MDM observatory at Kitt Peak (see Thorstensen 2020 for more details on the instrument and data reduction techniques) of the CV candidate J0418+5107 (NS Per) because it appeared to be suitable for a radial-velocity based period determination. We present here the so far unpublished results of these observations (Sect. 6.5.3).

6.4 Analysis

6.4.1 Classification

Classification consists of firstly identifying the CVs among the 27 191 SDSS-V co-added spectra and then determining the sub-type of each CV.

CV identification

We initially scanned each spectrum by eye for indications of a CV nature – typically the presence of emission lines but see Section 2.2 for a full description of the spectral characteristics of CVs. Although in theory this process could be automated there was a risk that some important exotic object could be missed (such as novalike variables and dwarf novae observed during outburst, which have disc-dominated spectra with, in some cases, very weak absorption lines). In addition some plates near the Galactic plane that were subject to substantial amounts of reddening had very poor flux calibrations, and CV spectra obtained on those plates would very likely have been missed in any automated search.

The list of CVs obtained from this visual inspection was then compared with CV catalogues (Ritter & Kolb, 2003; Watson et al., 2017) to identify previously known CVs and then subjected to more detailed scrutiny using the available archival information (light curves, astrometric and photometric data). New CVs identified in SDSS-V and systems where the SDSS-V spectra refute previously published CV classifications are discussed in Sect. 6.5, detailed notes on previously known CVs where the SDSS-V spectra confirms their classification are given in Attachment 6.5.2 and Attachment 6.5.3 includes notes on a selection of well known CVs where SDSS-V has revealed new information.

Several CVs were observed at different epochs by SDSS-V and the resulting co-added spectra were compared and merged where appropriate. As part of this process we found four CVs (J0528–0333, J0808+3550, J0926+0345, J1830+2655) that were observed in both outburst and quiescence and these are shown separately in Fig. 13 in the supplementary material.

The final list of CVs (Table 6.3) was then subjected to a rigorous search of the literature to find references both for the initial claim of a CV nature, the first published spectrum, and the most accurate measurement of the orbital period.

CV sub-types

CVs are categorised into a number of sub-types based on their observed characteristics, with the sub-types often being named after a prototype CV that exemplifies particular characteristics. In this paper we have used the classifications from the literature where available, making additions and corrections where appropriate.

In Section 2.2 we describe the taxonomy of CVs and summarise the salient stages of CV evolution. The following is a highly simplified overview:

Non-magnetic CVs ($B \lesssim 1$ MG) that exhibit disc outbursts are dwarf novae, those with steady hot discs are novalike variables. Dwarf novae are further sub-classified into SU UMa CVs (typically short-period, $P_{\text{orb}} \lesssim 3$ h, that have relatively frequent outbursts, interspersed by longer and brighter superoutbursts), ER UMa CVs (systems with very short superoutburst recurrence times), WZ Sge CVs (which only have rare superoutbursts), U Gem CVs (typically long-period, $P_{\text{orb}} \gtrsim 3$ h, dwarf novae that do not show superoutbursts), and Z Cam CVs (that switch between outburst states and ‘stand-still’ periods of constant brightness). CVs with highly magnetic white dwarfs (MCVs) consist of polars (which typically have $B \gtrsim 10$ MG and the white dwarf spin period synchronised with the orbital period, $P_{\text{spin}} = P_{\text{orb}}$) and intermediate polars (IPs, with $10 \gtrsim B \gtrsim 1$ MG, and $P_{\text{spin}} < P_{\text{orb}}$). Finally, AM CVn CVs are ultra-short period ($P_{\text{orb}} \lesssim 60$ min) hydrogen-deficient CVs.

We classified all SDSS-V CVs by considering all available data. This includes not only the spectrum but also CRTS, ZTF and *TESS* light curves, spectral energy distributions (SED) based on the available broad-band photometry, Hertzsprung-Russell diagrams based on the *Gaia* astrometry and photometry, and Pan-STARRS images. CVs for which we were unable to determine a sub-type are simply classified ‘CV’.

6.4.2 Orbital Periods

We use a combination of spectroscopically derived radial velocities (SDSS and the MDM Observatory) and photometric light curves (ZTF) to estimate orbital periods.

Radial velocities from SDSS-V

The measurement of radial velocities from the Doppler shifts of emission lines, and their variation over an orbital period, has a long history of determining the period of a CV (Merrill, 1923). The emission lines are assumed to arise from the accretion disc around the white dwarf and to track the orbit of the white dwarf around the centre of gravity of the CV. The observed velocity is smaller than the Keplerian velocity of the white dwarf, $v_{\text{obs}} = \sin i \times v_{\text{wd}}$ with i the inclination of the binary, which implies that orbital periods for low inclination systems may be difficult to impossible to measure.

The spectroscopy of the CVs in SDSS-V consists of one or more epochs in each of which multiple 900 s exposures were obtained (see Fig. 6.1). In contrast to the co-added identification spectra shown in Sect. 6.5 and the supplementary material, many of the individual 900 s exposures have low SNR, and some of them are affected with cosmic ray artefacts that had to be manually identified and removed. In order to measure radial velocities from these individual spectra, we developed a two-step procedure simultaneously fitting two Gaussians (to model double-peaked emission lines) to each of the

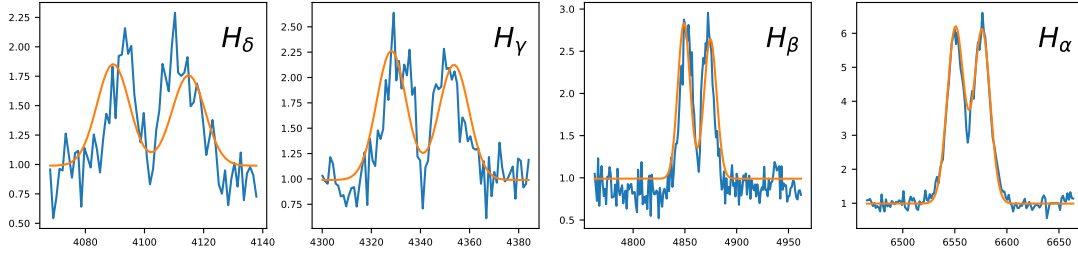


Figure 6.2: Example of extracting radial velocities by fitting a template of four double-Gaussian profiles (orange) to an individual 900s spectrum of J0633+0303 (blue). The observed spectrum and the template are both normalised to unity individually for each Balmer line. The radial velocity of the CV is measured by fitting all four Balmer lines simultaneously with a single free parameter for the velocity.

first four Balmer lines, $H\alpha$ to $H\delta$, using the same radial velocity (Fig. 6.2). The LMFIT package provides a straightforward way to achieve this in PYTHON. Prior to fitting we normalised the continuum around each of the four Balmer lines in each exposure to unity by means of a first-order polynomial fit.

In the first step we notice that a Gaussian has three free parameters – central wavelength (μ), width (σ) and amplitude (A):

$$f(\lambda; A, \mu, \sigma) = \frac{A}{\sigma\sqrt{2\pi}} \exp\left(-\frac{1}{2} \left(\frac{\lambda - \mu}{\sigma}\right)^2\right) \quad (6.1)$$

For this step we created an LMFIT (Newville et al., 2016) model of the form:

$$C + \sum_{i \in \{\alpha, \beta, \gamma, \delta\}} \left(f(\lambda; A_{i,1}, \lambda_i - s/2, \sigma_{i,1}) + f(\lambda; A_{i,2}, \lambda_i + s/2, \sigma_{i,2}) \right) \quad (6.2)$$

where

$$\lambda_i = \mu_i + \sqrt{\frac{1 - v/c}{1 + v/c}} \quad (6.3)$$

Here μ_i is the central wavelength of the i (th) Balmer line, s is the difference in wavelength between the centres of the two Gaussians and v is the radial velocity causing the Doppler shift; C is a constant. This model is fitted to each exposure in turn allowing all the free parameters to vary. In a few cases where the spectrum shows a steep Balmer decrement and the higher order lines are not visible we limit the process to $H\alpha$ and $H\beta$.

For the second step a template model of the form (6.2) is formed by averaging the values of each of the free parameters derived in the first step over the exposures. The template model is then fitted to each exposure with only v being allowed to vary.

With a set of measured radial velocities in hand, the next step is to estimate the period. This is inherently difficult because the dataset is sparse and so we use a

two (three) pronged approach, based on sine fits to the radial velocities, the use of the PYTHON package called THE JOKER (Price-Whelan et al., 2017) and ZTF periodograms where available. We consider a period trustworthy where the approaches give consistent results. To fit a sine wave we use LMFIT to fit an equation of the form:

$$g(t; K, P, \phi, v_{\text{sys}}) = K \sin\left(\frac{2\pi t}{P} + \phi\right) + v_{\text{sys}} \quad (6.4)$$

where K , P and ϕ are the amplitude, period, and phase of the radial velocity variation, and v_{sys} is the systemic velocity. Unfortunately when seeking the optimal values of the four free variables LMFIT is very sensitive to the initial values with which it is seeded and will select a solution giving a local minimum for χ^2 which will not always be the correct one. To address this problem, we used an existing published value or a photometric estimate (e.g. from ZTF) where available to seed the process.

We also used THE JOKER to help identify the correct alias. THE JOKER makes prior assumptions about the distribution of six parameters – namely orbital period, eccentricity[†], pericenter phase and argument, velocity semi-amplitude and the barycenter velocity. These distributions are used to create a large set of samples which are then compared with the observed data to obtain posterior distributions and hence the most likely alias. The accuracy of a period derived from radial velocities depends heavily upon the SNR of the data, the number of exposures and the number of epochs.

[†]For the purpose of our analysis, we assume that the orbit is circular and that any small ellipticity can be ignored.

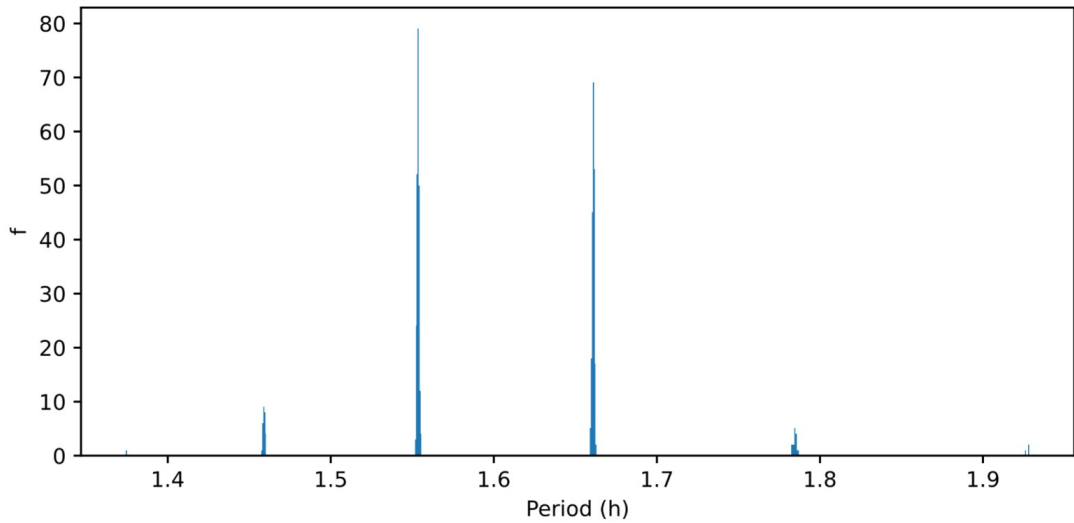


Figure 6.3: Plot of the output from THE JOKER for J0210+5711

Light curves from ZTF

The plate survey of SDSS-V and ZTF have similar coverage in the northern sky, so most of our CVs and CV candidates have ZTF data. ZTF saw first light in November 2017 and is designed to survey the sky every $\simeq 3$ d, although some areas are observed more frequently in the search for extragalactic transients (Bellm et al., 2019). The number of ZTF photometric data points varies with the location on the sky with median values

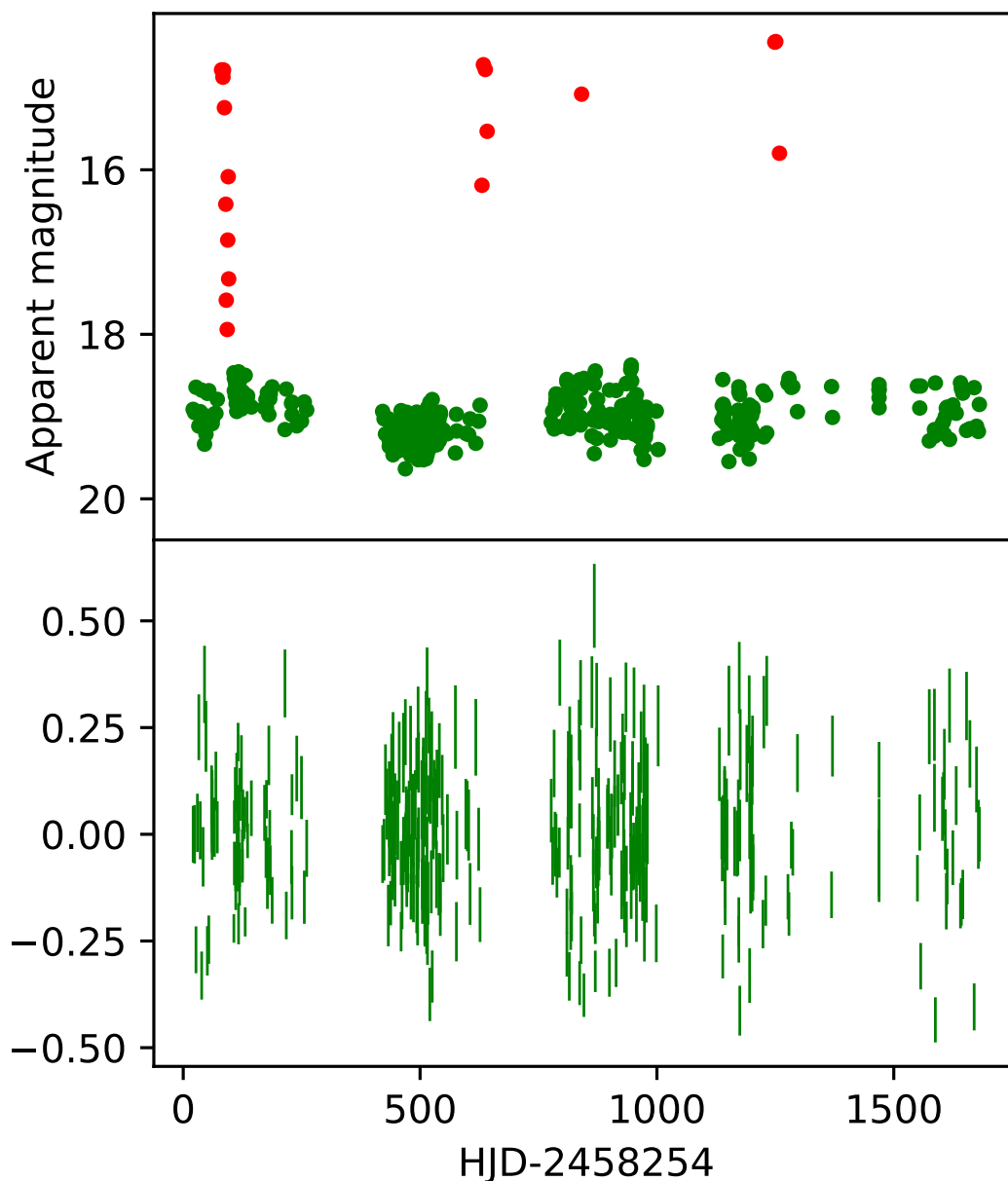


Figure 6.4: Top panel: ZTF light curve of J0038+2509 showing the outbursts in red. Bottom panel: The same light curve, clipped to remove the outbursts and with long-term trends removed.

of 260 and 482 for the g and r -band, respectively. Some objects additionally have a few nights of high cadence (with images obtained typically every few minutes for several hours) observations, which are particularly useful for measuring orbital periods. Before searching for periodic behaviour it is necessary to remove outbursts and also remove any long term trends (see Fig. 6.4). We defined a threshold for each object to clip outbursts and used a polynomial filter to remove trends. The filter spans a longer time than any potential orbital period. We then computed a periodogram (see Fig. 6.5) using two techniques: a Fourier analysis (Deeming, 1975) and the ‘Multi-harmonic Analysis of Variance’ (AOV) algorithm (Schwarzenberg-Czerny, 1989). The Fourier analysis works well for sinusoidal light curves whilst the AOV is superior for light curves with more complex structures, e.g. cyclotron beaming or eclipses. For the 66 systems studied here that had no period measurement, ZTF periodograms provide a unique reliable period in only eight cases (typically where there is high cadence data) but they also help to identify the correct alias from periods derived from radial velocities. Depending on the physical origin of the photometric modulation, the strongest signal in the ZTF periodograms could be equal to the orbital period (e.g. for eclipsing CVs) or half the orbital period (e.g. for systems where the donor contributes significant amounts of light, resulting in ellipsoidal modulation, or cyclotron beaming in a polar), so care has to be taken in the interpretation of photometric periods.

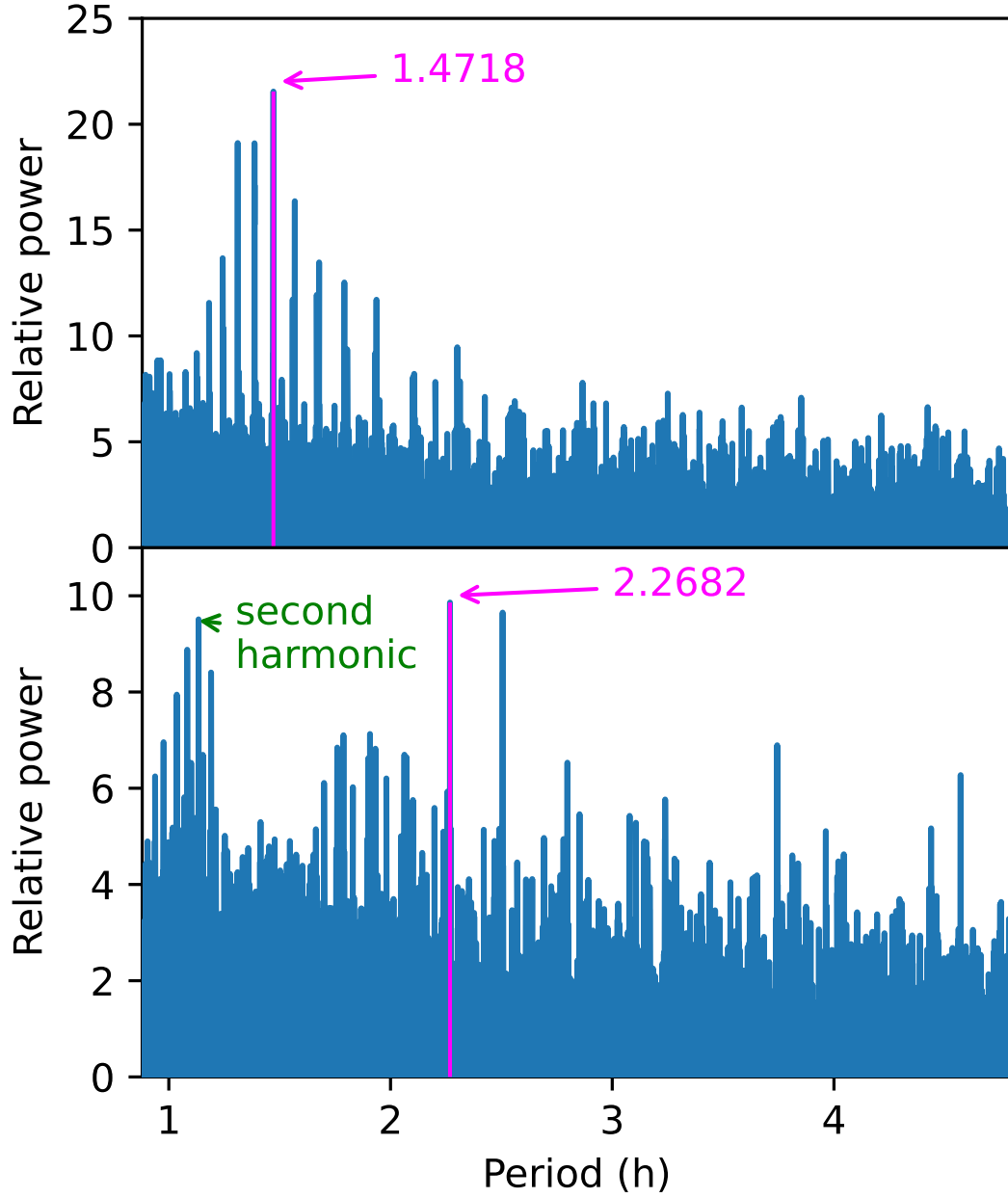


Figure 6.5: Top panel: The ZTF power spectrum of J0635+0303. The strongest signal is likely to be the orbital period and was used to seed the analysis of the radial velocity variations. Bottom panel: The ZTF power spectrum of J0038+2509, showing the strongest signal at 2.26 h, and a slightly weaker signal at the second harmonic. The strongest signal is consistent with the superhump period of 2.33 h found by [Kato et al. \(2012a\)](#) and is therefore the orbital period.

Eclipses from the Liverpool Telescope

We measured the eclipse timings of J0624+0021 and J1740+0258 from the LT light curves (Fig. 6.7 and Fig. 6.9) by fitting a Gaussian to the eclipse profiles. In each case, two eclipses were covered by the initial LT observation, and accurate periods were then determined from this estimate combined with the second sets of LT data, and the periodogram calculated from the ZTF data.

6.5 Results

Details of all 118 CVs observed in SDSS-V are listed in Table 6.3. We identified eight new CVs, obtained the first spectrum for 45 previously known CVs and CV candidates, and disproved the published CV classification of eleven systems. The co-added spectra and light curves for the eight new CVs are shown in Fig. 6.6 and the properties of these systems are discussed in Sect. 6.5.1. The spectra and light curves of 110 previously known CVs and candidate CVs are shown in Figs. 1 to 13 in the supplementary material and any new information on these systems is discussed in Attachments 6.5.2 and 6.5.3. The spectra and light curves of the eleven non-CVs are shown in Fig. 6.10, and we discuss the likely nature of these systems in Sect. 6.5.4. Lastly, an additional 13 published CV candidates were observed by SDSS-V, but their spectra were unusable (Table 6.5).

Table 6.3: CVs from the Plate Survey. Distances are from [Bailer-Jones et al. \(2021\)](#) and variable types from [Watson et al. \(2006\)](#) unless indicated in blue. The references for the initial discovery, spectrum and period (where known) are also shown. New discoveries, orbital periods and identifications are shown in blue. Suffixes to the classifications : Tentative values, * Superhump periods, † Low accretion SU UMa, ‡ CVs with unusual state changes, § Period bouncers, +E Eclipsing.

SDSS	Name	Gaia EDR3 source_id	Period (h)	Gaia <i>G</i> (mag)	Distance (pc)	Variable Type	Cartons	References		
								Disc	Sp	P
J000600.15+012129.8		2738755406045571968	1.52(10)	19.57	352	WZ Sge §	gg,u2,wd	1	1	1
J003827.05+250925.0	1RXS J003828.7+250920	2806802123399581056	2.26826(2)	18.63	503	SU UMa	cv,gg,u1,u2	105	54	72
J003941.08+005427.5	SDSS J003941.06+005427.5	2543387617312121216	1.523(2)	20.76	1078	WZ Sge:	cv,u1,u2,u4	39	39	81
J004335.16-003729.7	SDSS J004335.14-003729.8	2530961280492678528	1.3721(14)	19.85	447	WZ Sge :	cv,gg,u2,wd	33	33	40
J014227.07+001729.8		2510205490257050496	1.88(4)	19.89	697	Polar:	cv,u1,u2	103	103	1
J015543.47+002807.4	FL Cet	2507796391561705728	1.452389(1)	18.65	317	Polar+E	cv,gg,u1,u2	67	67	37
J020712.72-014116.3	SDSSJ020712.71-014116.2	2494386992562185088	1.55(15)	20.27		Polar:	cv	89	89	1
J020809.57+565239.7		505110900157013376		18.77	2961	CV	u4	82	1	
J021008.33+571121.0	UV Per	457106501671769472	1.557(3)	17.75	250	SU UMa	cv	46	46	101
J021315.48+533822.9	MASTER OT J021315.37+533822.7	455380951309048320	2.549(7)*	20.05	3224	SU UMa	cv	42	1	111
J022102.79+732245.0	ASASSN-14jq	546910213373341184	1.32427(31)*	19.94	425	WZ Sge	cv,gg,wd	102	1	73
J022623.34+711831.5	AM Cas	545338083544363392	3.9576(3)	14.37	420	U Gem	cv,gg,u1,u2			
J023322.61+005059.4	HP Cet	2500552912036565120	1.601(2)	20.12	683	WZ Sge:§	cv	67	60	60
J024131.07+593630.5	ASASSN-16jv	464373929923792384		19.84	607	U Gem	cv	102	1	
J040834.99+511448.2	FO Per	250700853140894976	4.126(12)	16.15	587	U Gem	cv	76	5	115
J041844.44+510731.2	NS Per	271562333932151040	6.296(1)	17.43	1076	U Gem	cv	79	5	1
J042609.34+354144.5	MASTER OT J042609.34+354144.8	176429285061830144	1.5720(7)	16.14	184	SU UMa	cv,gg,u1,u2	8	50	87
J043127.01+352713.0	ASASSN-16og	174868189003974016		20.37	1677	SU UMa	cv	102	1	
J044321.37+472125.8	V0392 Per	254361745823908736	1.5841(4)	16.17	3453	Nova	cv	34		92
J050503.07+222529.8	ASASSN-15su	3418268607216934016	1.608(7)*	19.12	588	SU UMa	cv	102	1	68
J052433.47-070527.9	CSS 101108:052433-070528	3207332631484540416		20.59	1538	SU UMa:	cv	58	1	
J052834.08+331821.7	QZ Aur	3449050362952844288	8.579910(1)	16.87	2528	Nova	cv			49
J052859.54-033352.4	V1159 Ori	3210749947983249408	1.49272(3)	14.28	351	ER UMa	cv	108	108	53
J061204.48+252832.6	HQ Gem	3426743917723751680		19.31	3838	U Gem	cv		1	
J062157.13+404236.1	ASASSN-18bz	956899025419314816		19.9	3324	U Gem	cv	109	1	
J062406.13+400743.8		956670430081266176		18.54	1728	NL	u1,u2	1	1	
J062429.71+002105.8	ASASSN-15cu	3120280997380365824	2.429755(4)	18.86	468	SU UMa	cv	97	1	1
J062601.53-035523.0	Gaia17cdo	3116642228070616192		19.19	1184	DN	cv	13	1	
J062724.39+161329.6	Gaia18atj	3369335048381292032	10.428	18.15	3919	U Gem	cv			
J062953.89-033508.4	1RXS J062954.6-033520	3105034928633782400	9.12	13.53	652	Z Cam	cv	56	1	84
J063047.05+023931.2	ASASSN-16ow	3124075927403447936	2.1425(13)*	20.57	3374	SU UMa	cv	32	1	111
J063301.11+030334.1		3130088774241620608		18.3	242	WZ Sge :	wd	1	1	
J063304.77+032422.8	Gaia17ber	3130133544980839680		19.1	2548	U Gem	cv	99	1	
J063516.63+030313.6		3130064176963184896	1.4717(2)	18.95	643	Polar :	wd	1	1	1
J063844.17+181611.4	UV Gem	3371136087085232128	2.226(5)*	18.81	722	SU UMa	cv		1	57
J070533.79-125004.7		3044836838812715264		18.7	246	CV :	wd	1	1	

SDSS	Name	Gaia EDR3 source_id	Period (h)	Gaia G (mag)	Distance (pc)	Variable Type	Cartons	References		
								Disc	Sp	P
J070816.61-124544.8	ASASSN-16an	3044908474565329280		19.16	2071	U Gem	cv	100	1	
J073339.29+212200.8	CSS 091111:073339+212201	865345406593708160		19.37	1961	U Gem	cv	61	61	
J073758.55+205544.6	SDSS J073758.55+205544.5	673118544624392576		19.79	974	SU UMa:	cv	26	1	
J073817.74+285519.7	SDSS J073817.75+285519.7	878597549661945984	5.555(1)	18.46	1204	U Gem+E	cv,gg,u1,u2	48	48	1
J074222.55+172806.7	MLS 110309:074223+172807	671077782322909696		20.04	1828	U Gem	cv	58	30	
J074419.74+325448.2	CSS 091029:074420+325448	881969129052843520	0.55	19.83		AM CVn	cv	58	61	63
J074859.55+312512.5	SDSS J074859.55+312512.6	880821067114616832	1.39946616(2)	18.37	542	SU UMa+E	cv,gg,u1,u2,wd	26	112	110
J074917.11+365427.9	SDSSJ074917.11+365428.0	919046658301858048	1.3401(1)	19.17	820	Polar:	cv	89	89	89
J075107.51+300628.3	SDSS J075107.50+300628.4	878968875354903040	1.3918(3)*	19.68	1366	SU UMa	cv,u1,u2,wd	26	1	66
J075233.17+294339.5		875941782403757056	1.4455(1)	18.5	702	DN	gg,u1,u2	91	1	1
J075240.45+362823.2	EU Lyn	918840426857988736		20.0	631	Polar+E	cv	48	48	15
J075331.99+375800.7	CSS 100407:075332+375801	919213474830239616	1.5363(1)	19.21	1699	MCV:	cv,u1,u2	58	61	1
J075540.64+264618.1	V0516 Gem	874545471356863104	1.4883(1)	18.74	359	Polar:	cv	9	1	1
J080538.98+354054.9	CSS 170417:080539+354055	906152376204919040	5.2069(1)	20.69	1770	U Gem	cv	93	1	1
J080853.73+355053.6	CSS 080416:080854+355053	906214223733883264		19.98	1807	U Gem	cv,u2	22	88	
J081931.24+213338.0	MLS 151206:081931+213338	676203568093232512		19.46	2768	IP:	cv,u2	114	14	
J082253.13+231300.6	SDSS J082253.12+231300.6	678153002209054336		19.8	3077	CV:	cv	90	90	
J083619.15+212105.2	CC Cnc	664787098343076992	1.764(12)	17.45	493	SU UMa	cv,gg,u1,u2	113	113	4
J084400.09+023919.2	V0495 Hya	3079207606650040320	4.9708(6)	18.42	1467	U Gem	cv	48	48	1
J084413.66-012807.9	CSS 090331:084414-012807	3072558340145828864		20.37	2153	AM CVn	cv,u1,u2	61	61	
J084555.06+033929.3	V0498 Hya	581352651334960512	1.4536(14)*	20.72	1635	WZ Sge:§:	cv	57	61	57
J085107.39+030834.5	CT Hya	581110831791334400	1.59612(3)*	18.54	579	SU UMa	cv	76	48	51
J090246.54-014201.9	ASASSN-15gv	5764187028557281280	2.04(10):	20.58	1734	SU UMa:	cv	102	1	1
J090344.25-013326.1		5764195103095781120		19.53	278	AM CVn	gg,u2,wd	16	1	
J090403.48+035501.2	SDSS J090403.48+035501.2	579909164365936512	1.4336(1)	19.31	295	WZ Sge:	cv,gg,u1,u2,wd	33	33	41
J091410.72+013732.9	ASASSN-16as	3843535378146405888	6.043(7)	17.69	1016	U Gem	cv	78	94	94
J092614.30+010557.4		3844016380122912640	1.4723(1)	19.47	385	Polar	gg,u1,u2,wd	44	44	1
J092620.42+034542.3	GUVV J092620.4+034541.8	3845719592354419712		19.7	933	SU UMa	cv,u1,u2	18	1	
J093205.24+034332.5	ASASSN-17od	3850925956004914816		17.75	633	SU UMa:	cv	102	1	
J093238.20+010902.5	SDSS J093238.21+010902.5	3841337699215167232		19.4	3145	Polar:	cv	48	48	
J104245.16+371819.9	SDSS J104245.15+371819.8	751777469035821312	1.82(4)	19.84	507	Polar	gg,u2	89	89	1
J112332.03+431717.5	CSS 090602:112332+431717	783809506927814912		19.65	1261	SU UMa:	cv,u1,u2	85	61	
J113122.38+432238.7	MR UMa	772038105376131456	1.518(3)	17.92	328	SU UMa	cv,gg,u1,u2	7	25	69
J115419.06+575750.8	SDSS J115419.06+575750.9	845441772229861760		20.42	1144	ER UMa	cv	89	89	
J121913.06+204937.6	SDSS J121913.04+204938.3	3952276665815698560	1.3018(1)	19.19	274	WZ Sge	cv,gg,u2,wd	27	27	1
J122740.86+513924.8	GP CVn	1571768231438756864	1.510810(2)	18.74	390	SU UMa	cv,gg,u1,u2,wd	25	25	98
J130514.73+582856.2	SDSS J130514.73+582856.3	1578672472969644288		19.23	3911	DN	cv,u2	33	33	
J133309.19+143706.9	SDSS J133309.19+143706.9	3741755132951336192	2.1148(1)	19.55	2028	Polar	cv	90	90	1
J133941.08+484727.6	V0355 UMa	1558322303741820928	1.3754(4)	17.37	150	WZ Sge	cv,wd	39	39	86
J134052.05+151340.9	CSS 100531:134052+151341	3742038776886730368	2.45	17.94	822	U Gem	cv,u2	55		
J135218.95+280917.1	CSS 090705:135219+280917	1451958950484177280		20.1	2263	U Gem	cv	61	61	
J135642.39+613024.4	V0427 UMa	1661194359687172480		20.47	2330	SU UMa:	cv	24	1	
J142953.55+073231.3	SDSS J142953.56+073231.2	1172464842754767488		20.23	1348	U Gem	cv,u2	26	1	
J143317.77+101122.7	SDSS J143317.78+101123.3	1176468611268115200	1.30177630(5)	18.55	232	WZ Sge	cv,gg,u1,u2,wd	38	38	98
J143435.36+334050.1		1287753107989718784		20.03	363	WZ Sge:§	u2	1	1	
J150240.90+333423.4	NZ Boo	1289860214647954816	1.413831(1)	17.26	184	SU UMa+E	cv,gg,u1,u2,wd	25	25	72

SDSS	Name	Gaia EDR3 source_id	Period (h)	Gaia <i>G</i> (mag)	Distance (pc)	Variable Type	Cartons	References		
								Disc	Sp	P
J160809.54+542131.4	ELAISN1 MOS15-02	1429001113336695168	1.4646(5)	19.43	1168	ER UMa	cv	3	1	1
J161935.78+524631.7	DDE 32	1425200578380530048	1.675066(5)	19.28	449	Polar	cv	80	80	80
J163722.21-001957.1	V2690 Oph	4383291477376259968	1.61736(3)	19.99	1254	SU UMa	cv,u2	67	67	40
J165127.25-131809.2	SSS 130510:165127-131809	4332792802397772672		19.91		U Gem	cv	114	1	
J165244.83+333925.5	SDSS J165244.84+333925.4	1314596271336013824	1.67:	20.74	3281	SU UMa	cv,u2	39	39	1
J165930.37-125327.2	V0841 Oph	4333061392472253440	14.4313(2)	13.65	815	Nova	cv	59	59	45
J170515.34+724403.3	MASTER OT J170515.37+724402.5	1655084339211334016		19.41	2686	SU UMa	cv	43	1	
J171752.03-070654.2	MASTER OT J171752.02-070654.6	4360435241974939392		20.52	3089	U Gem	cv	117	1	
J172148.84-051713.2	CSS 120611:172149-051713	4362925292215906176		20.12	3942	U Gem	cv	58	1	
J172805.34+775117.4		1705302990918074880		20.62	974	WZ Sge:§	u2	1	1	
J173924.38+050049.7	ASASSN-15mk	4473606466292898688		20.54		DN	cv	102	1	
J174045.86+060350.5	PBC J1740.7+0603	4485786821746343680	1.6826(50)	15.84	232	Polar:	cv	29	29	29
J174056.31+025831.6	MG1 995493	4376325246582929920	4.143(3):	17.81	928	U Gem†	cv,gg,u1,u2	124	1	1
J174759.88+032859.7	ASASSN-15fm	4472400370757130496		20.07	957	DN	cv	118	1	
J181111.75+124301.7		4496951052360182656		19.79	689	SU UMa:	wd	1	1	
J182122.51+614855.2	ASASSN-13at	2159834324676298880	1.901(5)	19.46	764	SU UMa	cv,gg,u1,u2	106	74	74
J182138.61+615904.0	ASASSN-14gg	2159842815827966720	1.44(3)*	19.78	722	SU UMa	cv,wd	35	1	77
J182205.84+270849.8	MASTER OT J182205.85+270849.7	4585224931075337216		20.66	1772	SU UMa	cv	62	1	
J182643.55+613816.5		2159773512236202624	2.0654	20.62	2118	SU UMa	cv	121	1	1
J183052.72+265514.9	MGAB-V733	4585376839774011520		18.79	1175	SU UMa	u2	23	1	
J183211.36+615505.9	ASASSN-13ah	2159698023890909184	1.5874(3)*	20.47	960	SU UMa	cv	52		68
J192914.75+202759.5	NQ Vul	2017742684676480896	3.516(2)	17.29	1170	Nova	cv	119	119	75
J192927.83+202035.0	1RXS J192926.6+202038	2017736641707652608	3.89(3)	17.58	567	U Gem	cv	122	94	94
J195837.08+164128.4	AW Sge	1820137772050526464	1.788(5)*	19.29	604	SU UMa	cv	17	1	19
J200318.50+170251.4	RZ Sge	1820209309009288960	1.63872	18.29		SU UMa	cv	17	17	83
J200611.52+334237.6	V1363 Cyg	2058291887543939968	2.42(14):	16.28	1641	U Gem	cv	20	65	120
J200934.41+550525.7		2185841249306525696		16.52	1707	NL	gg	12	1	
J202812.47+414836.3	V2467 Cyg	2068080976989664768	3.83	18.04	1847	IP:	cv	47	10	
J204638.68+603803.0	V0713 Cep	2194206707428148480	2.0500424(1)	18.35	319	SU UMa+E	cv	71	1	6
J205423.76+601706.7	V0962 Cep	2194035978188297728		19.28	3095	Nova	cv	36	1	
J212654.54-012054.3	CRTS J212654.5-012054	2686013551247649152		19.06	1676	Polar	cv,u2	58	58	
J213432.34-012040.5	CSS 081120:213432-012040	2686614060690086016		18.59		U Gem	cv	58	1	
J221832.75+192520.2	Swift J2218.5+1925	1777232423131443840	2.159(24)	17.31	240	Polar	cv,gg,u1,u2	104	95	95
J221900.24+201831.2	SDSS J221900.24+201831.1	1778468682222798080	3.36(1)	18.23	821	DN	gg,u1,u2	89	89	89
J222117.33+194817.6	ASASSN-19wi	1777640754262037248		18.77	708	DN	gg,u1,u2	102	1	
J234440.54-001206.1	MLS 100904:234441-001206	2642699218384434432	1.8411(7)*	20.07	668	SU UMa	cv,u2	114	61	51

Cartons: cv mwm_cb_cvcandidates, gg mwm_cb_gaiagalex, u1 mwm_cb_uvex1, u2 mwm_cb_uvex2, u4 mwm_cb_uvex4, wd mwm_wd

References: 1 This work, 2 Bruch et al. (1987), 3 Gezari et al. (2013), 4 Thorstensen (1997), 5 Bruch (1989), 6 Boyd et al. (2011), 7 Wei et al. (1997), 8 Denisenko et al. (2012a), 9 Morokuma et al. (2014), 10 Poggiani (2009), 11 Fremling et al. (2018), 12 Heinze et al. (2018),

13 Delgado et al. (2017c), 14 Szkody et al. (2020), 15 Homer et al. (2005), 16 Carter et al. (2013a), 17 Vogt & Bateson (1982), 18 Welsh et al. (2005), 19 Shears et al. (2008), 20 Miller (1971), 21 Liu & Hu (2000), 22 Drake et al. (2009a), 23 MGAB Variable Star Catalog, 24 Stanek et al. (2013), 25 Szkody et al. (2006), 26 Wils et al. (2010), 27 Szkody et al. (2011), 28 Richter et al. (1988), 29 Halpern & Thorstensen (2015), 30 Oliveira et al. (2020), 31 Thorstensen (2013), 32 Siviero & Munari (2016), 33 Szkody et al. (2004a), 34 Richter (1970), 35 Delgado et al. (2018a), 36 Srivastava et al. (2015), 37 Schmidt et al. (2005a), 38 Szkody et al. (2007), 39 Szkody et al. (2005), 40 Southworth et al. (2008b), 41 Hameury & Lasota (2005), 42 Yecheistov et al. (2013), 43 Balanutsa et al. (2013), 44 Rodriguez et al. (2023), 45 Peters & Thorstensen (2006), 46 Szkody (1985), 47 Nakano et al. (2007), 48 Szkody et al. (2003a), 49 Schaefer et al. (2019), 50 Hou et al. (2020), 51 Kato et al. (2010), 52 Shappee et al. (2013), 53 Thorstensen et al. (1997), 54 Szkody et al. (2018), 55 Thorstensen & Skinner (2012), 56 Ritter & Kolb (2003), 57 Kato et al. (2009), 58 Drake et al. (2014b), 59 Williams (1983), 60 Southworth et al. (2006), 61 Breedt et al. (2014), 62 Denisenko et al. (2014), 63 Ramsay et al. (2018), 64 Chen et al. (2020), 65 Bruch & Schimpke (1992), 66 vsnet 15408, 67 Szkody et al. (2002b), 68 Kato et al. (2016b), 69 Thorstensen et al. (2015), 70 Delgado et al. (2018c), 71 Antipin & Kroll (2003), 72 Inight et al. in prep, 73 Kato et al. (2015), 74 Thorstensen (2020), 75 Schaefer (2021), 76 Petit (1960), 77 vsnet 20079, 78 VSNET 19440, 79 Hoffmeister (1966), 80 Denisenko & Martinelli (2016), 81 Southworth et al. (2010), 82 Mowlavi et al. (2021), 83 Kato et al. (2014b), 84 Arjyotha et al. (2009), 85 Drake et al. (2009c), 86 Gänsicke et al. (2006), 87 Kato et al. (2014a), 88 Wright et al. (2012), 89 Inight et al. (2023a), 90 Szkody et al. (2009), 91 VSNET 7967, 92 Schmidt (2020), 93 Hodgkin et al. (2020), 94 Thorstensen et al. (2017), 95 Thorstensen & Halpern (2013), 96 Campbell & Shafter (1995), 97 Delgado et al. (2017b), 98 Littlefair et al. (2008), 99 Delgado et al. (2017a), 100 Delgado et al. (2019), 101 Thorstensen & Taylor (1997), 102 ASAS-SN CV candidate, 103 Carbon et al. (2017), 104 Thorstensen & Halpern (2009), 105 VSNET 12318, 106 Garnavich & Deal (2013), 107 Taylor & Thorstensen (1996), 108 Jablonski & Cieslinski (1992), 109 Jayasinghe et al. (2018), 110 vsnet 19297, 111 Kato et al. (2017), 112 Lamost 8/1/2016, 113 Munari et al. (1990), 114 CRTS candidate CV, 115 Sheets et al. (2007), 116 Swierczynski et al. (2010), 117 Vladimirov et al. (2017), 118 Paterson et al. (2019), 119 Cordoni et al. (1977), 120 vsnet 13294, 121 Malkova et al. (2016), 122 Denisenko & Sokolovsky (2011), 123 Szkody & Ingram (1994), 124 Kraus et al. (2007)

6.5.1 New CVs

Inspection of Fig. 6.6 shows that amongst the ZTF light curves of the eight new CVs there is only one outburst (J0635+0303) which is very likely a reason why these systems have so far escaped attention.

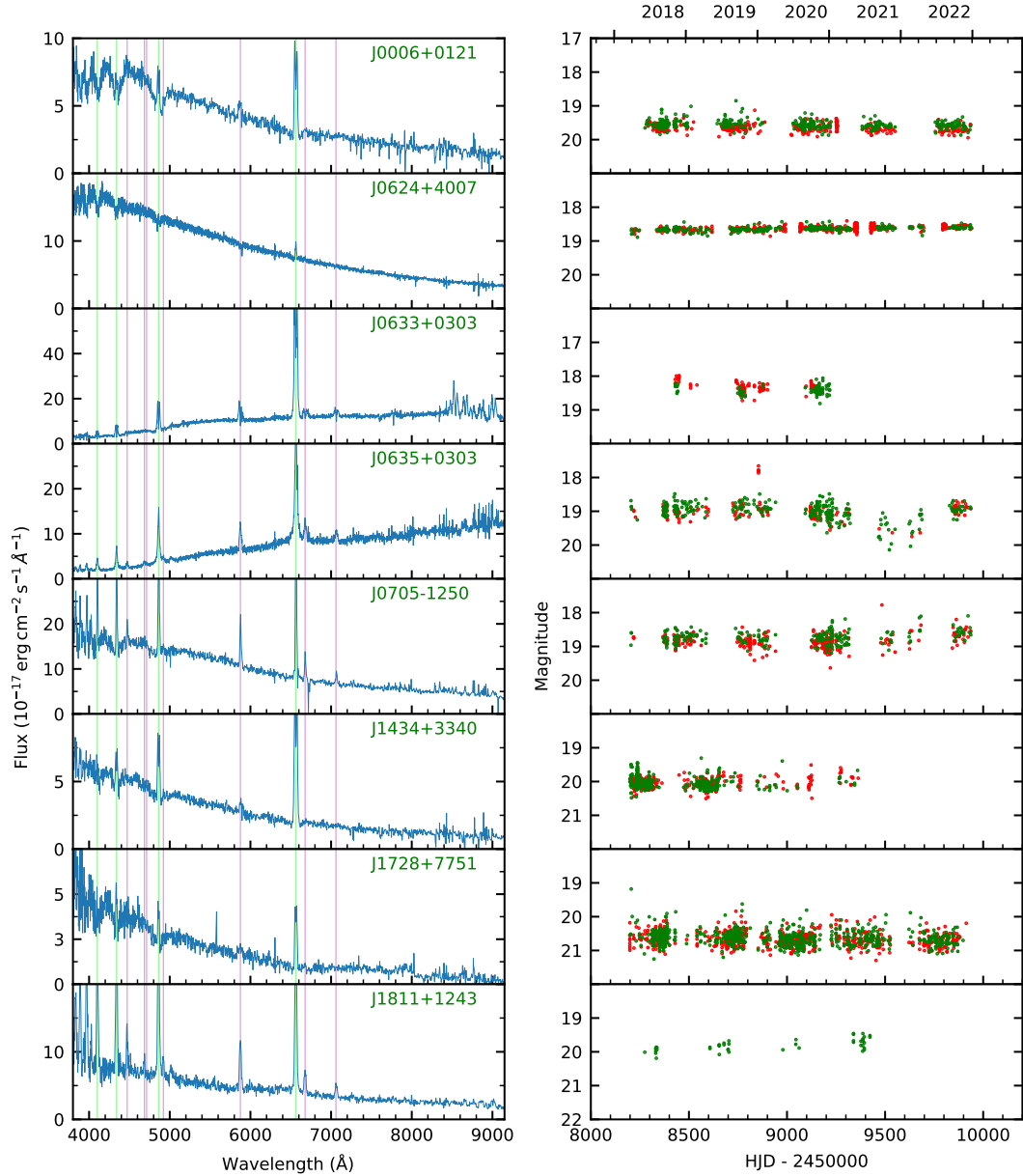


Figure 6.6: Left panels: Spectra of the eight new CVs discovered by SDSS-V. Right panels: ZTF light curves (r - and g -band) of the eight new CVs.

J0006+0121

The spectrum shows strong $H\alpha$ emission, and a steep decrement in the higher lines of the Balmer series. The double-peaked morphology of $H\alpha$ is evidence of an accretion disc seen at moderately high orbital inclination. The continuum rises towards the blue which, together with the broad $H\gamma$ and $H\delta$ absorption lines, is interpreted as being dominated by the emission of the white dwarf. This assumption is consistent with the location of J0006+0121 within the white dwarf cooling sequence. The fact that the white dwarf is visible, combined with the absence of outbursts in the CRTS and ZTF light curves, indicates a low mass transfer rate. No spectroscopic features of the donor star are detected in the red part of the spectrum and the weak infrared peak in the SED plot is suggestive of a brown dwarf companion. We classify this as a WZ Sge.

A periodogram computed from the radial velocities measured from the eight individual SDSS spectra displays a number of possible periods separated by one-day aliases. Whereas the SDSS spectroscopy is not sufficient to unambiguously identify the orbital period, the most likely values from THE JOKER periodogram are 1.434(3) h, 1.525(4) h, and 1.628(4) h, where the uncertainties have been determined from sine fits to the data. We were unable to obtain a period from either the CRTS or ZTF data. If either of the two longer periods represent the true orbital period, this system would likely be a ‘period bouncer’.

J0624+4007

The spectrum exhibits a steep blue continuum and weak, narrow $H\alpha$ emission line. The higher Balmer lines display narrow absorption profiles (with a hint of an emission core in $H\beta$). The ZTF light curve shows the system at constant brightness. With $G_{\text{abs}} = 7.35$ and $G_{\text{BP}} - G_{\text{RP}} = 0.39$ this CV is located near the bottom of the area of the HR diagram populated by novalike variables (see Fig. 6 in [Inight et al. 2022](#)). Combining all observational evidence suggests that J0624+4007 is a novalike. The relatively faint absolute magnitude suggests that it is either a high-inclination system (i.e. nearly edge-on) or, taking into account the absence of eclipses, one with a relatively low mass transfer rate, or both. We were unable to obtain an orbital period from either the radial velocities or the ZTF photometry.

J0633+0303

The spectrum shows strong double-peaked Balmer and He I emission lines on a red continuum. However, the flux calibration of this spectrum is problematic (see Sect. 6.3.1), as the system is located in the Galactic plane ($b = -2.7^\circ$) with a maximum reddening of $E(B - V) \simeq 1.1$ along this line of sight ([Schlafly & Finkbeiner, 2011](#)). However, with a distance of $\simeq 242$ pc, the system is in front of most of the dust ([Lallement et al.,](#)

2019), and inspecting the SED plot of J0633+0303 reveals that it is a blue object. With that knowledge in mind, the spectrum reveals broad depressions suggesting that the white dwarf dominates the emission, which is consistent with the position near the white dwarf cooling sequence in the *Gaia* HR diagram, and is indicative of a low level of accretion. The ZTF light curve is relatively sparse, and contains no outbursts. The very deep central absorption in the Balmer lines suggests a high inclination, and possibly eclipsing nature of J0633+0303. Based on the spectroscopic appearance, period and absence of outbursts, it is most likely a WZSge dwarf nova.

J0635+0303

The spectrum shows strong Balmer and He I emission lines. The He II line is very weak. The asymmetric morphology of the emission lines, and their very broad wings suggest that J0635+0303 is a magnetic CV, although the spectrum does not reveal any cyclotron humps. J0635+0303 is located in the Galactic plane ($b = -2.2^\circ$) with a maximum reddening of $E(B - V) \simeq 1.5$ resulting in bad flux calibration of the SDSS spectrum. However, with a distance of $\simeq 643$ pc, the CV will only be reddened by $E(B - V) \simeq 0.1$ and, as is evident from the the broad-band photometry, it is intrinsically blue. J0635+0303 has been detected as an X-ray source in a 1.4 ksec exposure (Evans et al., 2020). The ZTF light curve contains a $\Delta m \simeq 1.3$ outburst at MJD = 58 854, and a dip in its brightness between MJD $\simeq 59\,200$ and 59 800. The ZTF power analysis shows a strong peak at 1.47 h. There are three epochs of good spectroscopic data and using the photometric period as a seed resulted in a period of 1.4717 h. Visual inspection confirms that $P_{\text{orb}} = 1.4717(2)$ h is the most likely orbital period. We conclude that J0635+0303 is probably a polar.

J0705–1250

The spectrum shows strong Balmer and He I emission lines and broad Balmer absorption lines from the white dwarf, but no sign of the donor. The emission lines are narrow indicating a low inclination. The ZTF light curve does not contain any outbursts. Although there are *Swift* X-ray detections this system is close (246 pc) and so the detection of X-rays is not necessarily suggestive of it being a magnetic CV. J0705–1250 is located on the white dwarf cooling sequence in the HR diagram. Analysis of the radial velocities measured from five epochs of reasonably good radial velocity data reveals a best-fit period of 1.4986(1) h. This value is, however, not consistent with ZTF periodograms which reveal potential periods of 2.34 h and 2.13 h. Given the somewhat mixed set of characteristics, we classify J0705–1250 as a generic CV, and we encourage follow-up studies of this system to accurately determine the orbital period, and stringently rule out a magnetic nature of the white dwarf.

J1434+3340

This object was identified as an optical counterpart to *Chandra* CXOXB J143435.3+334048 by [Brand et al. \(2006\)](#) who were searching for AGNs. It has double peaked Balmer and He I lines but no evidence of He II at 4686 Å. The white dwarf absorption lines are visible, but there is no signature of the donor in either the spectrum or the SED. J1434+3340 sits on the white dwarf cooling sequence in the HR diagram. We could not recover any radial velocity variation. There are no outbursts in the CRTS and ZTF light curves, and the photometric data does not reveal any periodicity. We conclude that this is a WZ Sge and would expect it to have a period close to the period minimum.

J1728+7751

The spectrum shows double-peaked Balmer and He I emission lines on top of a blue continuum. The white dwarf absorption lines are visible but there is no spectroscopic detection of the donor. The ZTF light curve shows a single bright outlier which seems insufficient to qualify as an outburst detection. We could neither recover any radial velocity variations from the SDSS-V spectra, nor could we derive a period from the ZTF data. J1728+7751 is located close to the white dwarf cooling sequence in the HR diagram, and it is probably a WZ Sge.

J1811+1243

The spectrum shows strong Balmer, He II and He I emission lines, and there is no sign of either the white dwarf or the donor. The absence of a spectroscopic signature of the donor suggests that the system is below the period gap. J1811+1243 is closer to the white dwarf cooling sequence than the main sequence in the HR diagram, indicating a relatively low accretion rate. The ZTF light curve contains only 32 observations; there are no CRTS observations. We have seven radial velocity measurements over three epochs of varying SNR but cannot derive a reliable period. We conclude that this is probably a SU UMa.

6.5.2 Spectral confirmation of previously known systems

The spectra and light curves of the following objects are shown in the supplementary material. We note below any new information; we have not commented on well-studied systems where we have nothing new to add.

J0213+5338

The spectrum shows Balmer emission lines. Together with the frequent outbursts and superoutbursts in the ZTF light curve this is consistent with the previous classification of SU UMa and a period of 2.549 h.

J0221+7322

The white dwarf is visible in the spectrum and there is a double peaked H α line. This combination is confirmation of the WZ Sge classification.

J0241+5936

The spectrum is reddened by 0.39 mag due to being in the Galactic plane. It shows Balmer emission lines. There is an outburst in the ZTF light curve and this, together with its position in the HR diagram, confirms that this is a U Gem.

J0431+3527

Although the spectrum of this object has a relatively low SNR, it reveals a strong double-peaked H α emission line. There are four outbursts apparent in the ZTF light curve including at least one superoutburst – confirming the existing classification of SU UMa.

J0505+2225

The spectrum shows Balmer and He I emission lines. The ZTF light curve shows dwarf nova outbursts confirming the previous classification of SU UMa.

J0524–0705

Despite poor flux calibration, the Balmer, He II and He I emission lines are visible in the spectrum. The ZTF light curve shows seven outbursts two of which appear to be superoutbursts with superhumps visible. We classify this as a probable SU UMa.

J0612+2528

This is HQ Gem and is positioned on the edge of the main sequence in the HR diagram. The spectrum shows Balmer and He I emission lines. The light curve shows multiple outbursts, confirming that this is a U Gem.

J0621+4042

This is positioned on the edge of the main sequence in the HR diagram. Lines from the donor are visible in the spectrum as well as Balmer emission lines which confirm the classification of U Gem.

J0624+0021

We obtained photometric light curves (Fig. 6.7) which show a deep eclipse. These curves were combined with ZTF data to determine the correct alias resulting in the ephemeris $\text{HJD}(\phi = 0) 2\,459\,578.48972(7) + N \times 0.101240(1)$. Lines from the donor are visible in the spectrum, along with Balmer emission lines from the accretion disc. The ZTF light curves show outbursts and at least one superoutburst causing us to classify this as a SU UMa in the period gap.

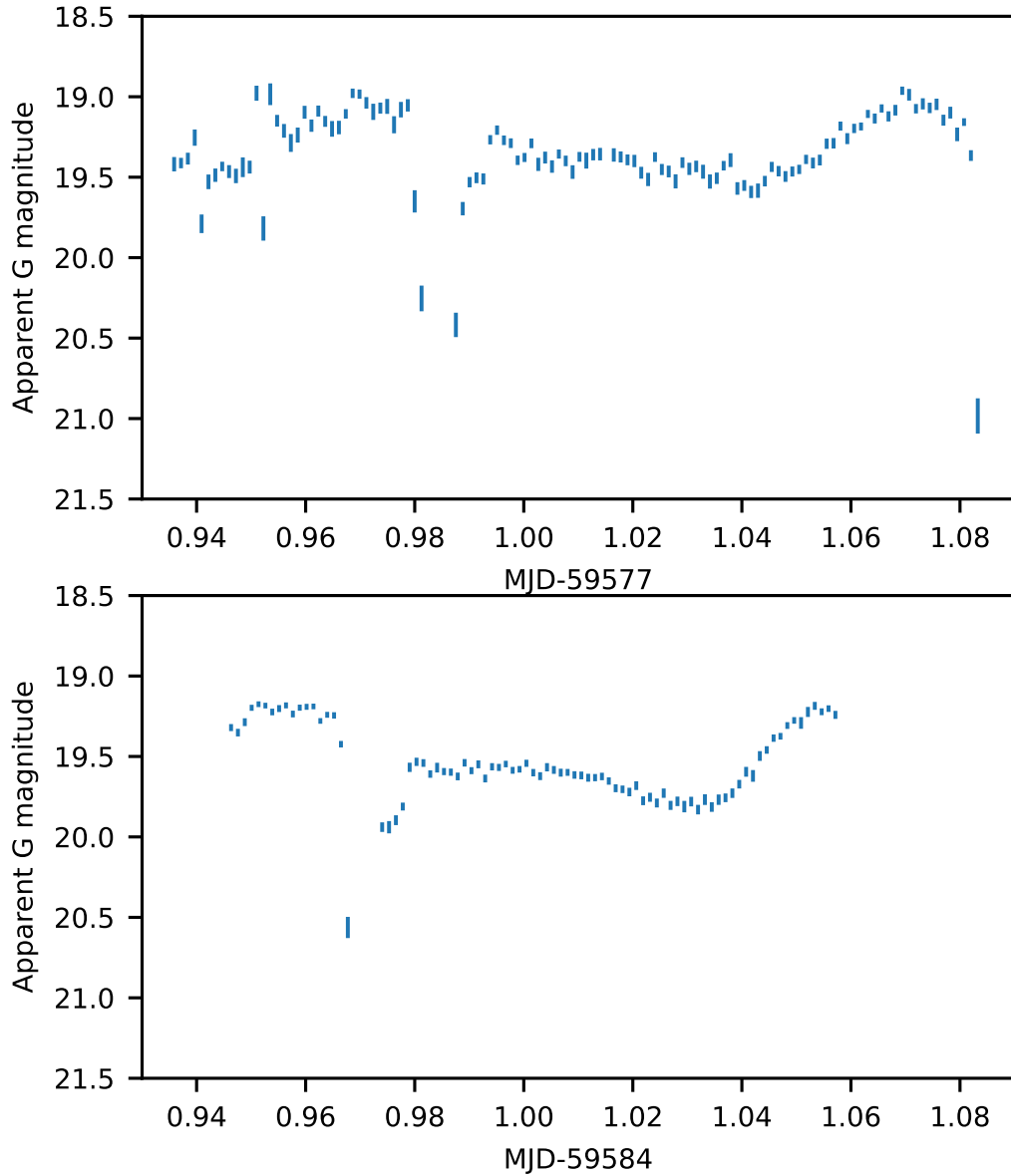


Figure 6.7: Photometric observations of J0624+0021 using the Liverpool Telescope. Top panel: 2021 December 02 showing a clear eclipse and the start of a second. Bottom panel: 2022 January 05 showing a single eclipse.

J0626–0355

The spectrum shows Balmer, He II and He I emission lines which, together with the outbursts in the ZTF light curves, confirm the classification as a dwarf nova.

J0629–0335

The spectrum shows Balmer emission lines albeit with poor calibration which confirm the classification in [Arjyotha et al. \(2009\)](#) of a Z Cam.

J0630+0239

The spectrum shows single-peaked Balmer emission lines as well as absorption lines from the donor although the flux calibration is poor. These characteristics are consistent with the classification of [Kato et al. \(2017\)](#) that this is a low-inclination SU UMa.

J0633+0324

Double-peaked Balmer emission lines from an accretion disc as well as absorption lines from the donor are visible in the spectrum. It is very close to the main sequence in the HR diagram and the SED indicates a mid-K type donor. The donor characteristics together with the outbursts visible in the ZTF light curves lead us to the classification of U Gem.

J0708–1245

This is ASASSN-16an. It is close to the galactic plane ($b = -2.1$) and significantly reddened with $E(B - V) \simeq 0.7$. The spectrum shows Balmer and He I emission lines together with absorption lines from the donor. The ZTF light curve shows multiple outbursts. Taken together this confirms the U Gem classification.

J0737+2055

The spectrum shows narrow Balmer and He I emission lines indicating a low inclination system. There is a single five-magnitude outburst in the ZTF light curve, however there are too few data points to confirm whether or not this is a superoutburst. It is closer to the white dwarf cooling sequence than the main sequence in the HR diagram. This is probably a SU UMa.

0751+3006

The spectrum shows strong Balmer and He I emission lines. The spectrum together with the light curve outbursts and known period of 1.3918 h confirm the SU UMa classification.

J0752+2943

The spectrum shows Balmer and He I emission lines and also emission of He II at 4686 Å. The CRTS light curve shows a ~ 3 magnitude variation over a five year period with a 1.5 magnitude outburst on MJD = 55 211 whilst the ZTF light curve shows a 1.5 mag outburst on MJD = 58 511. Curiously the long term light curve shows a smooth change not typical of a high-low switch. We checked nearby objects in CRTS and they did not show this type of variation. There is ellipsoidal modulation in the ZTF light curve at a period of 1.1445(7) h implying an orbital period of 2.289(2) h. Together with the outbursts this confirms the classification of a dwarf nova.

J0753+2943

The spectrum shows strong Balmer and He I emission lines and J0753+2943 is located between the main sequence and the white dwarf cooling sequence in the HR diagram. There are two outbursts visible in the ZTF light curve. A periodogram of the ZTF light curve shows a reliable period of 1.4455(1) h.

J0755+2646

We have 25 radial velocity measurements with moderate SNR over five epochs spanning 86 days. We find a period of 1.4883(1) h. The spectrum shows Zeeman splitting around weak H α , H β and H γ lines (see Fig. 6.8). This is therefore a magnetic white dwarf and not a U Gem dwarf nova; the field strength of $B \simeq 7$ MG suggests an intermediate polar although polars can have magnetic fields as weak as this (Ferrario et al., 1995). There is slight contamination in the spectrum from a background galaxy. It is currently in a low state (*Gaia* EDR3 $m_G = 18.74$) but previously it has been in a high state (Pan-STARRS $m_g = 16.6$ and *Gaia* DR2 $m_G = 16.82$). The transient reported by Morokuma et al. (2014) is the same magnitude as the high states reported by Pan-STARRS and *Gaia* DR2. The magnitude reported by *Gaia* DR2 is based on 160 observations which would suggest a prolonged high state rather than transient behaviour. This system might also be a low accretion rate polar with the white dwarf accreting material from the donor's wind rather than Roche-lobe overflow (Breedt et al., 2012a). We tentatively classify this as a polar.

J0805+3540

The spectrum shows Balmer, He II and He I emission lines. The spectrum has the appearance of a K-star while an absorption dip just over 5000 Å is reminiscent of QZ Per (Thorstensen et al., 2002b). A periodogram of the ZTF light curve shows ellipsoidal modulation with an orbital period of 5.2 h. This is a U Gem and may have an evolved donor.

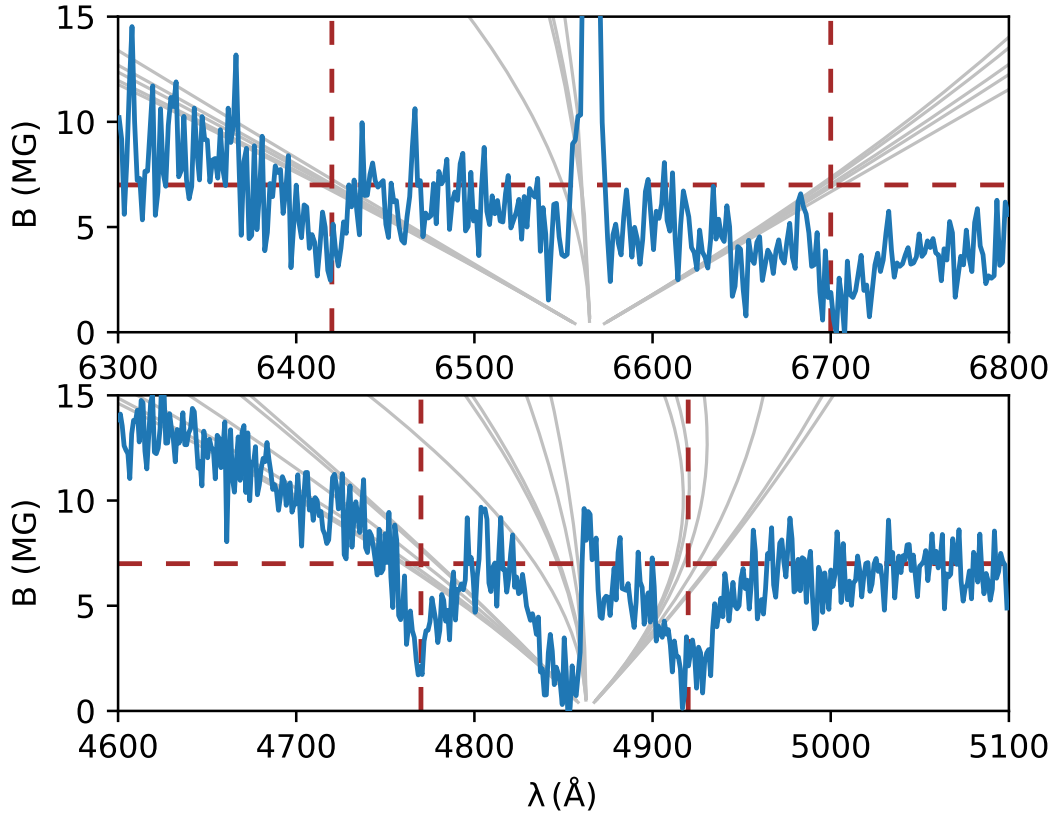


Figure 6.8: Spectra of $H\alpha$ and $H\beta$ lines of J0755+2646 showing the Zeeman splitting lines (Schimeczek & Wunner, 2014). The lines coincide with absorption lines for a magnetic field of $B \simeq 7$ MG.

J0902–0142

The spectrum shows double peaked Balmer and He I emission lines. There are hints of TiO absorption lines from the donor – consistent with the spectral energy distribution. We have a tentative period from the radial velocities of 2.04(10) h. The ZTF light curve shows outbursts; taken together with the tentative period this is probably a SU UMa.

J0903–0133

The spectrum shows strong Helium emission and no hydrogen lines. This confirms that this object is an AM CVn as suggested by Carter et al. (2014).

J0926+0345

J0926+0345 was in outburst during one of the spectra (see Fig. 13 in the supplementary material). The quiescent spectrum shows strong Balmer and He I emission lines. The ZTF light curve shows numerous outbursts and at least one superoutburst. It is nearer

the white dwarf cooling sequence than the main sequence in the HR diagram. We therefore classify this as a SU UMa.

J0932+0343

The spectrum shows strong Balmer and He I emission lines. TiO and Na absorption lines from the donor are visible and also absorption lines from the white dwarf indicating a low accretion rate. The ZTF light curve shows frequent outbursts with the hint of a superoutburst. This is probably a SU UMa.

J1356+6130

The spectrum shows weak double peaked Balmer and He I emission lines. The white dwarf and the donor are both visible in the spectrum indicating a low accretion rate. The photometry is dominated in the red by the bright donor. The ZTF light curve shows six outbursts including a superoutburst. This confirms that this is a SU UMa.

J1429+0732

The spectrum shows double peaked Balmer and He I emission lines. The donor is very visible. The ZTF light curve shows ten outbursts consistent with the classification of U Gem.

J1608+5421

We have twelve usable radial velocities in three epochs. The tallest peak in the THE JOKER periodogram is at $\simeq 1.4646$ h and the amplitude of the periodogram falls off sharply after the two adjacent aliases. The ZTF light curve shows at least ten outbursts (actually probably superoutbursts) with a quiescent magnitude $m \simeq 22.5$. Analysis of the light curve between 19 and 20 magnitude and $58\,376 < \text{MJD} < 58\,390$ shows superhumps with a period of $\simeq 1.506$ h which confirms that $\simeq 1.4646$ h is the correct alias. We therefore estimate the period to be $1.4646(5)$ h. The frequent superhumps in the light curve suggest that this is a ER UMa type system ([Robertson et al., 1995](#); [Kato et al., 2013a](#)) – a sub-type of SU UMa.

J1651–1318

Balmer emission lines are visible despite poor SNR and flux calibration. The ZTF light curve shows four outbursts whilst the quiescent magnitude is at least 21 and so the *Gaia* and Pan-STARRS magnitudes (19.9 and 19.5 respectively) are based on the magnitude of the outbursts. The outbursts and emission lines confirm the classification of U Gem.

J1705+7244

The spectrum shows strong Balmer and He I emission lines with neither the donor nor the white dwarf visible. The ZTF light curve shows frequent outbursts and at least two superoutbursts. We therefore classify this as a SU UMa.

J1717–0706

The spectrum shows Balmer and He I emission lines with neither the donor nor the white dwarf visible. It is next to the main sequence on the HR diagram and the donor is clearly visible in the SED. It is very faint – *Gaia* DR3 reports $m_G = 20.52$. There is no ZTF data although the CRTS data shows two outbursts reaching $m \simeq 16.5$. The emission lines and outbursts confirm that this is a U Gem.

J1721–0517

The spectrum shows strong Balmer, Paschen and He I emission lines with a very red continuum from the donor. It is close to the main sequence in the HR diagram. The ZTF light curve shows three outbursts of $\Delta m \simeq 4.5$. We therefore confirm that it is a U Gem.

J1739+0500

The spectrum shows Balmer and He I emission lines with neither the donor nor the white dwarf visible. The system is faint ($m_G = 20.48$) and the spectrum has a poor SNR. The ZTF light curves show three outbursts and we conclude that this is a dwarf nova.

J1740+0258

The spectrum shows Balmer and He I emission lines. TiO and Na 8194 Å absorption lines from the donor are visible. The ZTF light curve showed two outbursts with unusual state changes and J1740+0258 also appeared to be eclipsing. We therefore obtained LT photometry (see Fig. 6.9) which confirmed that J1740+0258 was eclipsing with ephemeris $\text{HJD}(\phi = 0) 2\,459\,734.5074(2) + N \times 0.172724(2)$. This is therefore a U Gem.

J1747+0328

The spectrum shows a CV in outburst with a synthetic magnitude $m_G = 17.5$ consistent with the outbursts in the ZTF light curve. This confirms the classification of dwarf nova.

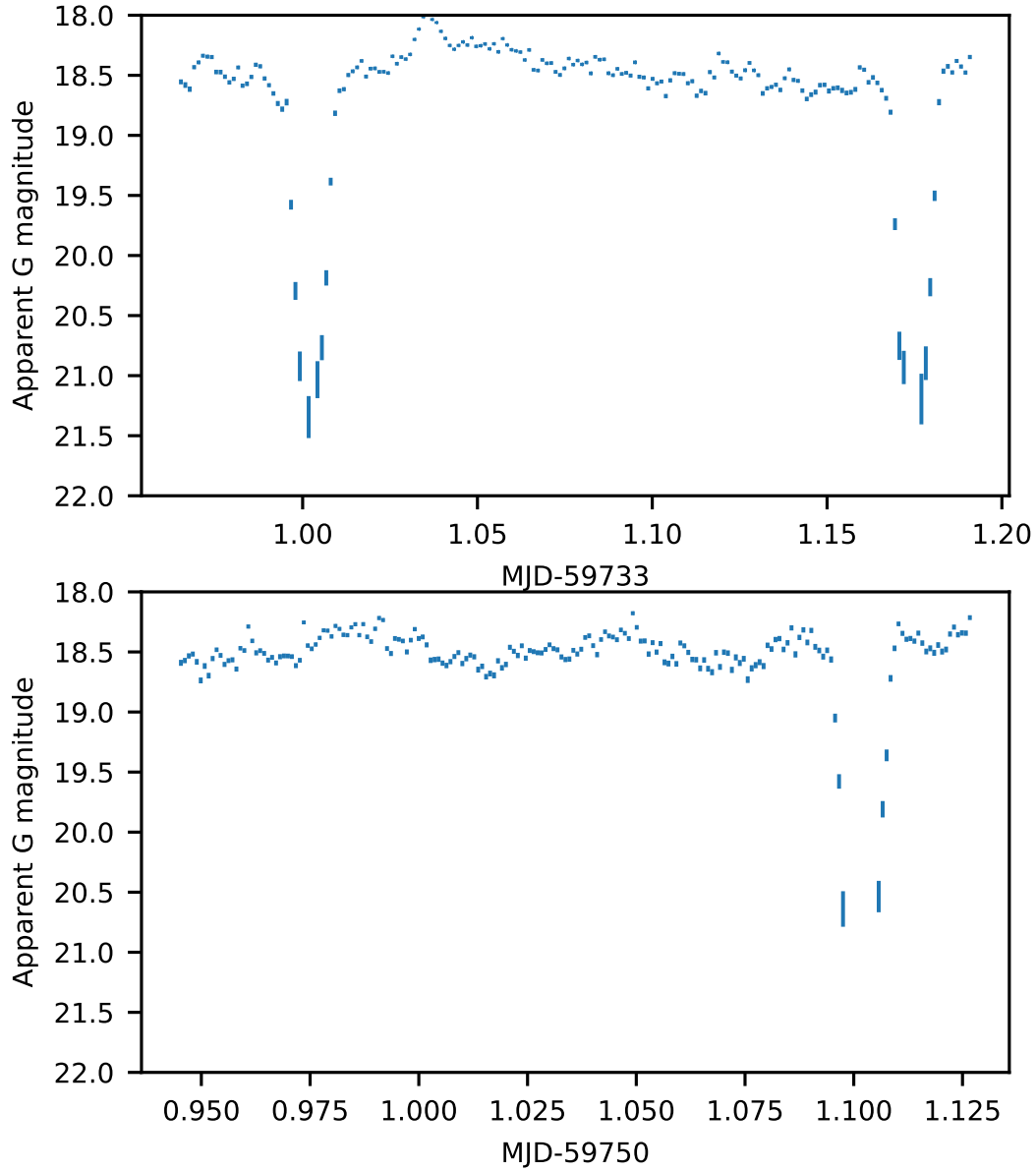


Figure 6.9: Photometric observations of J1740+0258 using the Liverpool Telescope. Top panel: 2022 June 03 showing two clear eclipses. Bottom panel: 2022 June 20 showing a single eclipse.

J1821+6159

The spectrum shows strong Balmer, Paschen and He I emission lines with neither the donor nor the white dwarf visible. The ZTF light curve shows seven outbursts consistent with the published classification of SU UMa and superhump period of 1.44 h.

J1822+2708

The spectrum shows strong double-peaked Balmer, Paschen, He I and Ca emission lines. It is midway between the main sequence and the white dwarf cooling sequence in the HR diagram. The ZTF light curve shows three outbursts including a superoutburst. This is a SU UMa.

J1826+6138

The spectrum shows weak double-peaked Balmer emission lines. The ZTF light curve shows frequent outbursts and also five superoutbursts leading to a classification of SU UMa. We find a period of 2.0654 h from the ZTF periodogram.

J1830+2655

We have both outburst and quiescent spectra (see Fig. 13 in the supplementary material). The quiescent spectrum shows strong Balmer, Paschen and He I emission lines with neither the donor nor the white dwarf visible. The ZTF light curve shows frequent short outbursts and at least one superoutburst resulting in our classification of SU UMa. The light curve is unusual as the quiescent magnitude appears to fall by over a magnitude between MJD = 58800 and MJD = 59000.

J1958+1641

The spectrum shows double-peaked Balmer emission lines. The ZTF light curve shows seven outbursts including at least one superoutburst. A periodogram of the ZTF light curve yields an orbital period of 1.723023(5) h which is consistent with the published superhump period of 1.735(16) h.

J2009+5505

The spectrum appears to be either that of a novalike or a dwarf nova in outburst. However the light curve shows no signs of an outburst and its position in the *Gaia* HR diagram is consistent with a novalike. This object was classified as a subdwarf in [Geier et al. \(2017\)](#) however the spectrum shows H α and H β emission lines and that, together with the position on the HR diagram leads us to classify it as a novalike. The light curve also shows an unusual long term trend of increasing magnitude.

J2054+6017

This is a classical nova that erupted in 2014 ([Srivastava et al., 2015](#)). It is now very faint (synthetic magnitude $m_G = 20.6$) leading to the poor SNR in the spectrum, inconsistent with the *Gaia* magnitude ($m_G = 19.3$).

J2134–0120

This system was identified as a transient by CRTS (CSS 081120:213432–012040) and is classified as a U Gem by VSX. [Drake et al. \(2014b\)](#) considered it a CV based on its CRTS light curve and photometry, however, [Coppejans et al. \(2016\)](#) decided against a dwarf nova classification based on the same CRTS light curve. The archival photometry available shows large-amplitude ($\simeq 2$ mag) variability on time scales of months to years, with no clear periodicity. When non-detections are accounted for the ZTF photometry appears to show the outbursts of a dwarf nova. The system is very blue, and also varies in the far-ultraviolet, with three separate *GALEX* detections ($m_{\text{FUV}} = 18.6, 20.0, 23.5$). The SDSS-V spectrum reveals a blue continuum with weak Balmer absorption lines, and no noticeable emission lines. The spectrum was obtained close to peak brightness and is consistent with a dwarf nova in outburst. *Gaia* has not obtained a parallax for this object and hence we cannot position it on the HR diagram. We therefore classify it as a U Gem.

J2221+1948

The spectrum shows strong Balmer, Paschen, Ca (H and K) and He I emission lines with neither the donor nor the white dwarf visible. The ZTF light curve does not show outbursts and the CRTS light curve shows only one outburst from which we make a classification of dwarf nova.

6.5.3 Well known systems

The following well-studied systems have previously published spectra. We include their spectra and light curves in Appendix C and note below any new information.

J0142+0017

We obtained 16 high SNR radial velocities over 3 epochs. The sine fit yielded an estimated period of 1.8777(1) h whilst THE JOKER identified 1.914 h. We therefore estimate the period as 1.88(4) h. This is consistent with the previous classification of a polar.

J0155+0028

This is FL Cet — a known eclipsing polar. This spectrum is that of a polar in a low state exhibiting cyclotron humps and Zeeman splitting. It contrasts with a previous SDSS spectrum (Szkody et al., 2002b) when it was in a high state.

J0207–0141

We obtained 18 high SNR radial velocities over 3 epochs. A sine fit yields an estimated period of 1.5515(1) h. THE JOKER identified 1.400 h. We therefore estimate the period as 1.55(15) h. The spectrum shows strong Balmer, He II and He I emission lines consistent with the previous classification of a polar.

J0233+0050

The spectrum and ZTF light curve confirm the previous classification of WZ Sge. However the long period (1.6 h) and absence of the donor in the spectrum and SED indicate that this is probably a period bouncer.

J0418+5107

Our MDM campaign on this object started with the modular spectrograph in 2018 November, and continued with the Ohio State Multi-Object Spectrometer (OSMOS; Martini et al. 2011) in 2018 December and 2019 January. We obtained 40 usable velocities of H α emission; the spectrum also showed a contribution from a late-type secondary, and in 33 spectra we were able to measure usable absorption-line velocities by cross-correlating portions of the spectrum with a zero-velocity late-type template spectrum. The periods from the emission velocities and absorption velocities agreed within the uncertainties, with a weighted mean of 6.296(1) h. This is consistent with the U Gem classification — a long period with frequent outbursts. There is some reddening due to its proximity to the Galactic Plane.

J0426+3541

Our spectrum shows double peaked Balmer and He I emission lines. The ZTF light curve shows outbursts and, intriguingly, variations in the quiescent level. It is a non-magnetic system with high inclination consistent with the previous SU UMa classification.

J0443+4721

This is an old nova which erupted in 2018 whose decline can be seen in the ZTF light curve. Comparing the spectrum with the SED shows that J0443+4721 is still in a high state compared with its historical luminosity. It has an unusually long period of 3.4118 d (Munari et al., 2020).

J0627+1613

J0627+1613 was initially identified from a transient by Gaia Alerts (Delgado et al., 2018c). ZTF light curves show two transients $\Delta m \sim 2$ each with a duration of $\simeq 15$ d. Unusually J0627+1613 is positioned slightly above the main sequence in the HR diagram. The SED is essentially a blackbody with a surface temperature $\simeq 3000$ K. The spectrum is consistent with this and suggests that this is a CV with a $\sim K0$ donor which would explain the position in the HR diagram. We confirmed that the orbital period, estimated using the ZTF photometry by Chen et al. (2020), to be 10.428 h, is correct. This period is also consistent with a CV having a high-mass donor at an early stage in its evolution.

J0738+2855

The spectrum shows Balmer and He I emission lines together with absorption lines from the donor. The ZTF light curve suggests that it is eclipsing; there are also at least seven outbursts. Szkody et al. (2003a) found a period of 2.1 h which is not consistent with the donor presence in the spectrum – a short period system would have a dim donor. The ZTF periodogram shows a period of 5.555(1) h. The *TESS* periodogram shows a period of 5.55(2) h.

J0753+3758

The spectrum shows strong Balmer, He II and He I lines. The ZTF light curve shows variability but no outbursts. We have 21 radial velocities with high SNR over four epochs spanning 84 days from which we find a period of 1.5363(1) h. This period is consistent with THE JOKER. This is probably a magnetic CV as previously reported.

J0805+3540

There are three spectra; two in a quiescent state and one during outburst. The outburst state (shown in Fig. 5 in the supplementary material) differs from the quiescent spectra by having a very strong He II emission line. There is the suspicion of TiO absorption lines from the M-dwarf in the quiescent spectra. It is located towards the white dwarf sequence in the HR diagram. The ZTF light curves show outbursts and we derive a period of 5.2069(2) h from a ZTF periodogram.. This is a U Gem and likely to have an evolved donor which would explain the helium emission and the short period for a relatively high mass donor.

J0808+3550

We have two spectra, one in quiescence and one in outburst (see Fig. 13 in the supplementary material). The previously published spectrum (Wright et al., 2012) was taken during an outburst. Our quiescent spectrum has strong double-peaked Balmer and He I emission lines. There are frequent outbursts visible in the ZTF light curves all consistent with the dwarf nova classification.

J0819+2133

The spectrum shows strong Balmer and He I emission lines and also TiO absorption lines from the donor. However the unusually variable ZTF light curve shows apparent changes in state over a period of ~ 1 y indicating a potentially magnetic system. The synthetic *Gaia* G-band magnitude of our spectrum is 21.5 and so our observation was taken during a low state. This is probably an intermediate polar.

J0822+2313

This was identified by Szkody et al. (2009) as a CV based on a strong, broad H α emission line in five exposures taken between 2004 November 05 and 2004 November 08. We have 29 exposures taken between 2020 Nov 11 and 2021 March 08 which show an M-dwarf profile but no sign of H α emission. There are no ultraviolet or X-ray observations shown in VizieR nor evidence of outbursts in ZTF (although CRTS shows some transients). In the absence of other evidence we can only consider this to be a Candidate CV.

J0836+2121

This is CC Cnc which has a known period of 1.764(12) h and is in the Ritter & Kolb catalog (Ritter & Kolb, 2003). The ZTF light curve shows short outbursts but also apparent changes of state of magnitude $\Delta m \simeq 1.5$.

J0844+0239

This is V495 Hya. We measured a period using radial velocities of 4.9708(6) h which is consistent with, and improves upon, the period of 4.968(17) h reported by [Thorstensen et al. \(2015\)](#).

J0845+0339

This is V498 Hya. The spectrum shows double peaked Balmer emission lines. There are clear absorption lines from the white dwarf but no evidence of the donor. Assuming the [Bailer-Jones et al. \(2021\)](#) distance of 1635 pc is correct then V498 Hya is located above the white dwarf cooling sequence on the HR diagram; however this distance is not consistent with the parallax nor the earlier [Bailer-Jones et al. \(2018\)](#) estimate of 302 pc both of which would place V498 Hya on the white dwarf cooling sequence. The period is 1.4256 h from [Kato et al. \(2009\)](#) based on a seven magnitude superoutburst in January 2008. The ZTF light curves do not show any outbursts. From the size of the 2008 outburst and the absence of subsequent observed outbursts we conclude that it is probably a WZ Sge and also a period bouncer.

J0851+0308

This is a well studied system called CTHya. In passing we note that the ZTF light curve shows an apparent brightening over a period of $\simeq 1$ yr of $\Delta m \simeq 0.5$.

J0926+0105

In addition to asymmetric Balmer and He I emission lines the SDSS spectrum contains He II at 4686 Å. Both the donor and the white dwarf are visible in the form of broad Balmer absorption lines and an upturn at the red end of the SDSS spectrum, respectively. Currently *Gaia* EDR3 has $m_G = 19.4$, however the SED plot shows a sequence of detections several magnitudes brighter suggesting that there has been a state change at some point. The ZTF light curve shows considerable variability, and from it, we obtain a period that is consistent with our spectroscopic period of 1.47234(1) h. This is more accurate than the period of 1.48 h reported by [Rodriguez et al. \(2023\)](#).

J0932+0109

This is a bright, distant (3145 pc) object that was identified as a novalike or potential polar in ([Szkody et al., 2003a](#)). The spectrum shows strong Balmer, He II and He I emission lines. The emission lines are asymmetric which, together with the He II are consistent with being a polar. The ZTF data shows variations of $\Delta m \sim 1$ over a six minute interval which we presume is due to cyclotron beaming. We therefore classify this as a polar.

J1042+3718

The spectrum shows distinct signs of cyclotron humps consistent with the previous classification of a polar. We have five high SNR radial velocities in one epoch. We estimate the period to be 1.82(4) h which is consistent with THE JOKER.

J1123+4317

(Breedt et al., 2014) obtained a spectrum and classified this as a dwarf nova. Our ZTF light curve shows a single superoutburst with clearly visible superhumps. We therefore classify this as a SU UMa.

J1219+2049

We have 10 moderate SNR radial velocities in three epochs and estimate the period to be 1.3018(1) h. The white dwarf absorption lines are clearly visible in the spectrum implying that this is a low accretion rate CV – consistent with a short period. It is located in the white dwarf cooling sequence in the HR diagram and taking account of the period and low accretion rate we classify this as a WZ Sge.

J1333+1437

We have 13 RV data points in 3 epochs. We have improved upon the period of 2.2 ± 0.1 h from Schmidt et al. (2008). Our best fit is 2.1148(1) h which is consistent with the earlier observation and takes advantage of the longer baseline (59 days) of our observations. It is also consistent with a periodogram from the ZTF light curve. The spectrum shows strong Balmer, He II and He I emission lines. The ZTF light curve, though sparse, shows evidence of a low state of $m \sim 21$ and a high state of $m \sim 20$. This, together with the He II emission lines, are confirmation of the previous classification of a polar.

J1652+3339

The spectrum shows strong double-peaked Balmer and He I emission lines with both the donor and the white dwarf visible. The ZTF and CRTS light curves show frequent outbursts and at least two superoutbursts. Analysing the radial velocities using THE JOKER suggests that the orbital period may be $\simeq 1.67$ h. This is an SU UMa,

J1740+0258

We obtained a period of 4.143(3) h from LT photometry (Fig. 6.9). The ZTF light curve also shows a significant state change reminiscent of the unusual CVs identified in Section 5.4.6.

J1740+0603

The spectrum shows strong Balmer, Paschen, He II and He I emission lines with neither the donor nor the white dwarf visible. The emission lines are asymmetric and, combined with the He II emission lines, cause us to classify this a probable polar.

J2006+3342

The ZTF light curve shows two ‘outbursts’ with very long (months) decay times. [Sahman et al. \(2015\)](#) report that this CV is surrounded by a faint nova shell which may account for this unusual behaviour.

J2126–0120

The quiescent spectrum shows strong Balmer, Paschen, He II and He I emission lines with the donor but not the white dwarf visible. The emission lines appear to be asymmetric and there are cyclotron humps and these, together with the He II emission imply that this is magnetic and we therefore classify this as a polar.

J2219+2018

The spectrum shows strong Balmer, Paschen, He II and He I emission lines with the donor but not the white dwarf visible. The ZTF light curve shows frequent outbursts together with an apparent standstill between $\text{MJD} \simeq 58\,970$ and $\text{MJD} \simeq 59\,250$. We therefore classify this as a dwarf nova.

6.5.4 Misclassified systems

Analysis of the SDSS-V spectra, ancillary data, and the literature demonstrates that eleven systems were previously misclassified as CVs or CV candidates (Table 6.4). Their SDSS-V spectra and ZTF light curves are shown in Fig. 6.10, and we briefly discuss their most likely nature below.

J0121+1437

This system was detected as a transient by CRTS (MLS 160708:012156+143737). The spectrum shows a broad emission line typical of a quasar and is likely to be $\text{Ly}\alpha$ at $z \simeq 3.5$.

J0430+3603

This object was identified as a transient by MASTER (OT J043017.84+360326.9, [Shurpakov et al. 2014](#)) and subsequently categorised as a U Gem dwarf nova by VSX ([Watson et al., 2017](#)). The SDSS-V spectrum reveals a very red slope with strong TiO absorption bands, characteristic of an M-dwarf. The available broad-band photometry is very red and J0430+3603 is located above the location of single low-mass main-sequence stars in the HR diagram. J0430+3603 has a *Spitzer* detection which was categorised as a young stellar object (YSO) in [Broekhoven-Fiene et al. \(2014\)](#), which appears consistent with its location in the HR diagram. This object was in the footprint of *GALEX* but was not detected in the ultraviolet. We conclude that J0430+3603 is a single star, and the transient detected by MASTER was very likely a flare.

Table 6.4: Previously known CVs and CV candidates which have been misclassified in the literature.

SDSS name	Alternative name	New category
SDSS J012156.25+143737.2	MLS160708:012156+143737	Extra-galactic
SDSS J043017.85+360326.6	MASTER OT J043017.84+360326.9	YSO
SDSS J061043.98+251031.0	NSV 2853	Star
SDSS J064939.16−060005.0	BEST-II lra2b_01098	Detached binary
SDSS J071844.74−242546.3	Gaia18ajg	YSO:
SDSS J080826.00+314125.3	MASTER OT J080826.00+314125.6	Extra-galactic
SDSS J121929.32+471522.9	SDSS J121929.46+471522.8	White dwarf
SDSS J132444.33−142335.7	Gaia17aoi	White dwarf
SDSS J162450.04+654101.1	Gaia16aat	Quasar
SDSS J165449.45+350803.7	MLS160613:165449+350804	Extra-galactic
SDSS J195919.93+162440.3	Gaia17bqf	Star

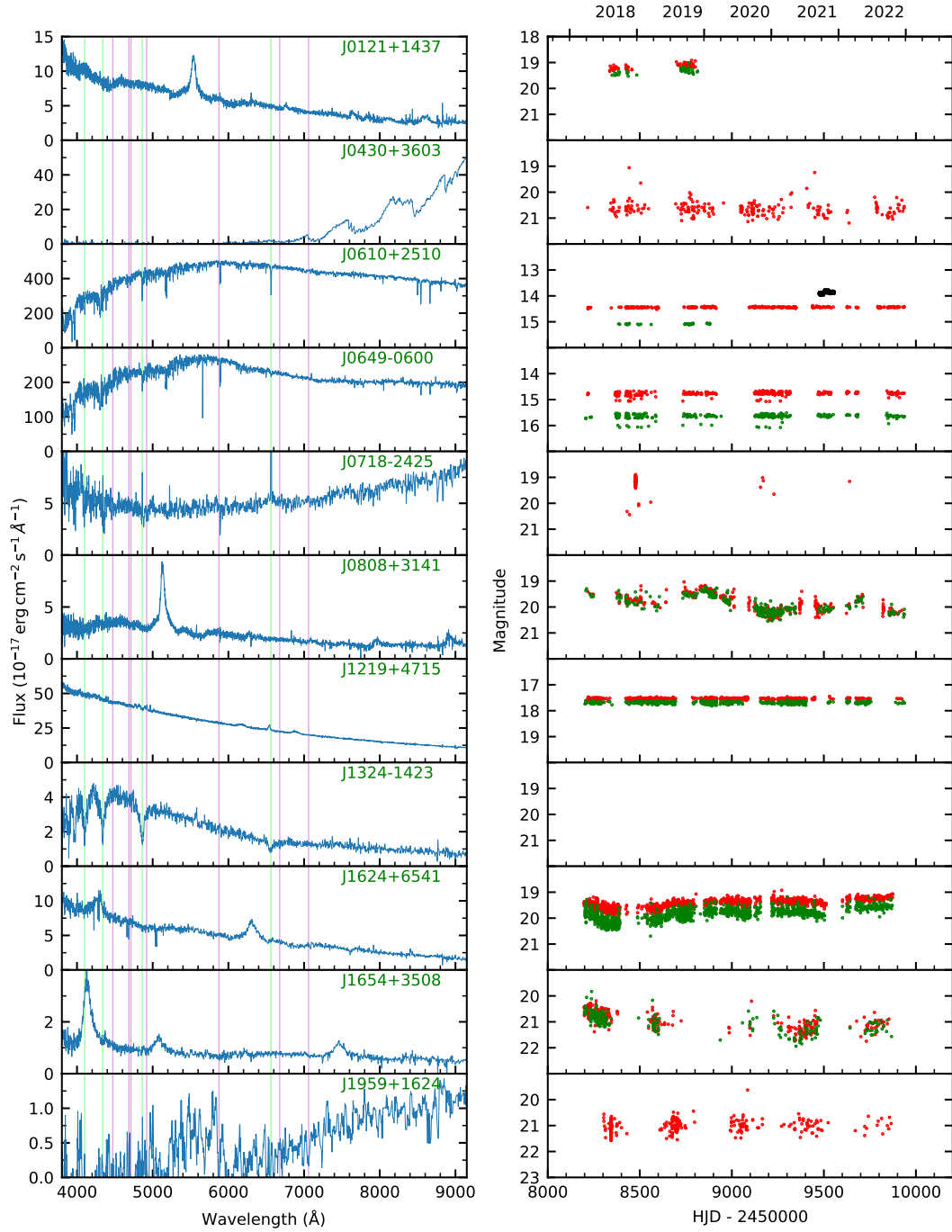


Figure 6.10: SDSS-V Spectra (left) and (r - and g -band) ZTF light curves (right) of systems misclassified in the literature as CVs and CV candidates.

J0610+2510

This object was first identified as a short period variable (NSV 2853) in 1949, and it is classified in VSX as a U Gem dwarf nova. [Haefner et al. \(1996\)](#) obtained CCD photometry for two hours and concluded that it was not a CV. [Liu & Hu \(2000\)](#) also

obtained photometry and concluded that it was a late G-type star – which is consistent with its position on the HR diagram. The ZTF and *TESS* light curves do not show outbursts and we concur with [Liu & Hu \(2000\)](#) that it is not a CV. The reason why it was classified as a variable star in the first place remains unclear.

J0649–0600

This object, BEST-II Ira2b_01098, was found to be variable by [Kabath et al. \(2009\)](#), and it is classified in VSX as a δ Cepheid type star or a CV. The SDSS-V spectrum of J0649–0600 resembles a G/K-spectral type, and does not contain any emission lines. Within the *Gaia* HR diagram, J0649–0600 is located in the sub-giant branch. The ZTF light curve exhibits 0.4 mag peak-to-peak variability, and an AOV analysis of the ZTF data reveals this system to be an eclipsing binary with a period of 9.8 d. We conclude that J0649–0600 is not a CV.

J0718–2425

This object was identified as a *Gaia* alert (Gaia18ajg, [Hodgkin et al. 2021](#)) and classified as a U Gem type by VSX. The system is relatively red ($G_{BP} - G_{RP} \simeq 2$), is located slightly above the main sequence in the HR diagram, exhibits a strong infrared excess, and the SDSS spectrum displays very narrow emission lines. All the observational evidence suggests that J0718–2425 is not a CV, and that it may be a YSO.

J0808+3141

This object was identified as a transient by MASTER (OT J080826.00+314125.6, [Balanutsa et al. 2015](#)) and subsequently categorised as a CV by VSX. The spectrum shows a broad emission line typical of a quasar and is likely to be Ly α at $z \simeq 3.2$.

J1219+4715

This object was classified as a CV candidate based on earlier SDSS spectroscopy ([Szkody et al., 2006](#)) because of its weak H α emission and blue continuum, characteristics of a CV in outburst or a novalike. However, [Gänsicke et al. \(2020\)](#) subsequently classified J1219+4715 as a single magnetic white dwarf with Zeeman-split Balmer emission lines, similar to the enigmatic white dwarf GD356 ([Greenstein & McCarthy, 1985](#)).

J1324–1423

This object was identified by a transient in *Gaia* alerts as Gaia17aoi, and has been categorised by VSX as a U Gem. [Pala et al. \(2020\)](#) raised concerns about the astrometry. The spectrum resembles that of a white dwarf, with no emission lines, which is consistent with its position in the HR diagram. The SED shows no evidence of a red component

and we conclude that this is not a CV but a single white dwarf, and that the nature of the transient detected by *Gaia* remains elusive.

J1624+6541

Gaia identified this system as a transient, Gaia16aat, which was subsequently classified as a CV by VSX. The spectrum shows a broad emission line typical of a quasar, which is likely to be Ly α at $z \simeq 4.2$.

J1654+3508

This was identified as a transient by CRTS (MLS 160613:165449+350804); no follow-up studies are reported in the literature. The spectrum shows a broad emission line typical of a quasar, which is likely to be Ly α at $z \simeq 2.4$. We note that this quasar has a large positive parallax, albeit with a large uncertainty.

J1959+1624

This object was identified as a *Gaia* alert (Gaia17bqf) and classified as a U Gem dwarf nova by VSX. All other *Gaia* observations were non-detections. It is located near the region of the main-sequence occupied by M0 types in the *Gaia* HR diagram. The SDSS-V spectrum is very noisy, and shows no indication of emission lines. The available broadband photometry is consistent with a single cool stellar object without any ultraviolet excess. We conclude that J1654+3508 is not a CV, and that the brightening detected by *Gaia* was most likely due to a stellar flare.

6.5.5 Unusable observations

Table 6.5: The twelve CVs and CV candidates listed below were observed by SDSS-V, however, the quality of their spectra was too low to draw any conclusions.

SDSS name	Alternative name
SDSS J021229.78+570519.4	UW Per
SDSS J062632.18+161622.9	Gaia17cxa
SDSS J074121.62+313821.0	ASASSN-15dx
SDSS J074813.35+290512.0	V434 Gem
SDSS J085228.73+020102.5	CSS 160419:085229+020103
SDSS J142936.25+322629.2	CSS 140607:142936+322630
SDSS J185234.98−001842.4	V1724 Aql
SDSS J200130.23+184255.6	
SDSS J200214.34+313634.7	ASASSN-17eo
SDSS J200504.93+322122.5	V550 Cyg
SDSS J201222.34+325927.5	
SDSS J201649.48+382109.3	V1377 Cyg

6.6 Discussion

6.6.1 Period Bouncers

The standard evolutionary model of CVs (see Section 1.4) predicts that nuclear burning in the donor star stops once mass transfer has eroded its mass to $\simeq 0.06M_{\odot}$, at which point the star’s structure becomes dominated by electron degeneracy, and it becomes a brown dwarf. As a consequence of the now inverted mass-radius relation, the orbital separations and periods increase as they continue their evolution. CVs that have passed the period minimum are colloquially referred to as ‘period bouncers’. QZ Lib is an excellent example of a period bouncer, having an orbital period of 92.7 min, but a very cool ($\lesssim 1700$ K) donor star (Pala et al., 2018). The evolution of CVs near the period minimum has been one of the areas where theory and observations show the largest discrepancies:

(1) The predicted location of the period minimum fell short of the observed value by about ten per cent (Kolb & Baraffe, 1999). Assuming some amount of angular momentum loss in addition to gravitational wave radiation removes that discrepancy (Patterson, 1998; Knigge et al., 2011), and this is the currently favoured solution.

(2) As the evolution of CVs not only slows down towards the period minimum, but also subsequently reverses towards longer periods, an accumulation of systems near the period minimum, the so-called ‘period minimum spike’ has been a firm prediction of all CV population models. Yet observed CV samples consistently fail to exhibit this feature (e.g. King et al., 2002), and it was only the SDSS CV sample that confirmed the existence of the period minimum spike (Gänsicke et al., 2009). The key conclusion was that the earlier CV samples were too shallow to capture a sufficiently large number of the faint population of period-minimum CVs.

(3) Evolutionary models predict that a large proportion of CVs are period bouncers: Kolb (1993) suggested that 70 per cent of all CVs are period bouncers whilst Goliashch & Nelson (2015) predicted 38–60 per cent and Table 1 in Belloni et al. (2018) suggests 75 per cent. Despite much observational effort, the roster of known period bouncers remains small: Patterson (2011) discussed 22 candidates among the known CVs; Pala et al. (2020) estimated a period bouncer fraction of 7 – 14 per cent within the 150 pc CV sample, and Section 5.4.5 concluded that only 0.7 per cent of all the CVs observed by SDSS I to IV were period bouncers. Hernández Santisteban et al. (2018) used the SDSS Stripe 82 and Palomar Transient Factory photometry for an unbiased search of eclipsing period bouncers, and derived an upper limit on their space density of $\lesssim 2 \times 10^{-5} \text{ pc}^{-3}$.

The dedicated spectroscopic follow-up of CV candidates carried out by SDSS-V obtained nearly-complete spectroscopy of period-bounce candidate systems, which we use below to derive a more stringent estimate on the space density of period bouncers.

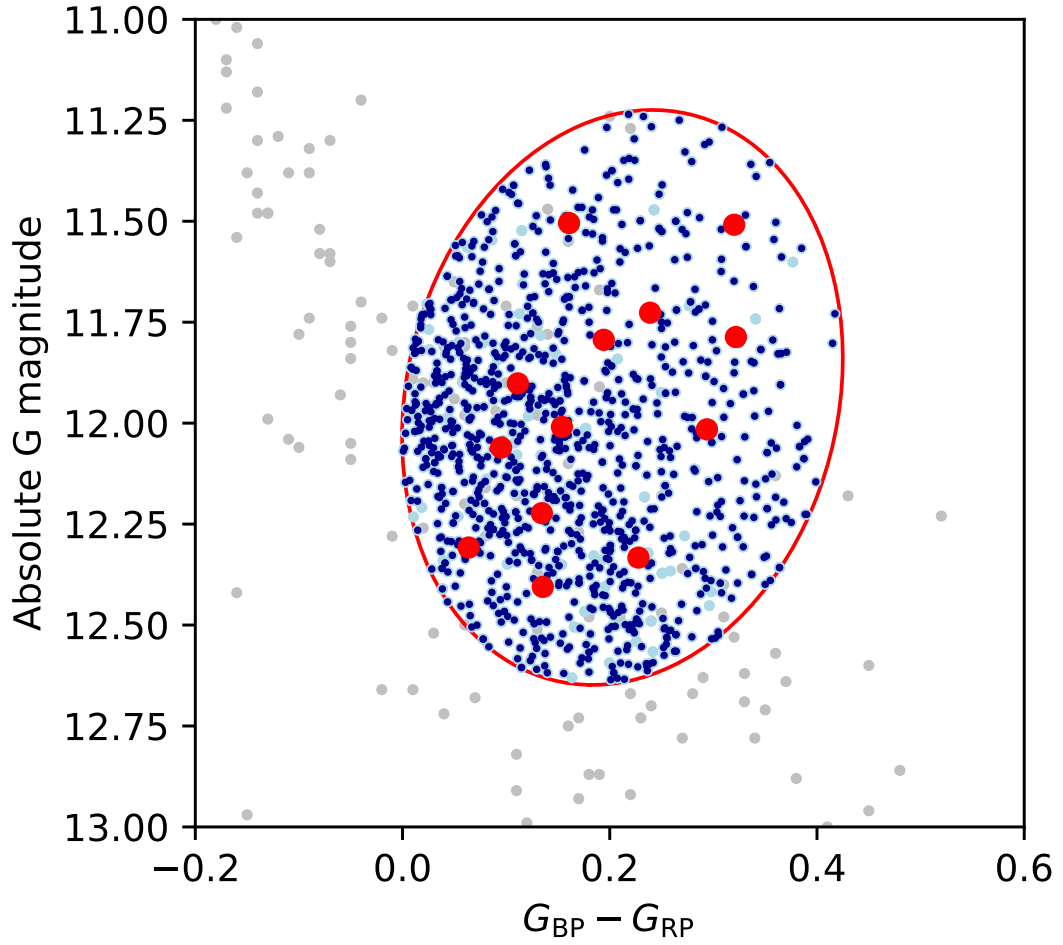


Figure 6.11: Hertzsprung-Russell (HR) diagram of period bouncers (red dots) with reliable parallaxes ($\Delta\varpi < 0.2 \times \varpi$) taken from Tables 5.5 and 6.6. The red contour shows the minimal enclosing ellipse (centred on $G_{\text{BP}} - G_{\text{RP}} = 0.193$, $G_{\text{abs}} = 11.921$ with semi major and minor axes of 0.574 and 0.1159 and rotated by 96.70°) containing the known period bouncers, allowing for 1σ uncertainties in their *Gaia* parameters. The grey dots are an astrometrically clean sample of *Gaia* objects chosen to outline the white dwarf cooling sequence. The light blue dots show the targets of the *mwm_wd* carton within the footprint of the 236 SDSS-V plates analysed here that are contained within the ellipse whilst the dark blue dots show the subset of these targets that were actually observed.

We collected a sample of confirmed and high-confidence period bouncers (Table 6.6) and used their *Gaia* astrometry and photometry to identify their location within the HR diagram. We found that period bouncers are closely clustered near the cooling sequence of single white dwarfs (Fig. 6.11), which is unsurprising as their optical spectra are dominated by the flux from the white dwarf, with only small contributions from the accretion discs and negligible amounts of light from the brown dwarf donors. A number of the systems in Table 6.6 stood out as outliers from this clustering. Upon closer

inspection, we found that these outliers have poor *Gaia* astrometry, and consequently, we removed all period bouncers with $\Delta\varpi/\varpi \geq 0.2$ from the definition of the location of period bouncers in the HR diagram. We then computed the minimal enclosing ellipse (Welzl, 1991) that contains the known period bouncers, where we accounted for the observed uncertainties by displacing each system within its 1σ errors. We then assume that hitherto undiscovered period bouncers have similar absolute magnitudes and colours to the ones that are known already. We believe that this is a reasonable assumption as the white dwarf temperature is set by the accretion rate (Townesley & Gänsicke, 2009), and there is so far no known CV with a quiescent white dwarf temperature $\lesssim 9500$ K (Sion & Godon, 2015). Theoretical models predict that the accretion rate should rapidly decrease as systems evolve back from the period minimum, and hence longer period period bouncers should have significantly cooler white dwarfs. However no such system is known, which means that if they exist, they are undetectable by photometric variability (including outbursts or eclipses), X-ray emission, or emission lines, as plenty of data is available to find at least a handful of these hypothetical systems.

Next, we analysed the number of targets within the `mwm_wd` carton that fall within this ellipse, and the number of spectroscopic observations of these targets carried

Table 6.6: Period bouncers and candidates from SDSS I to IV and SDSS-V. These were used (excluding those with bad astrometry) to characterise the location of period bouncers in the HR diagram (Fig. 6.11)

SDSS name	Other name	<i>Gaia</i> <i>G</i>	Distance) (pc)	Bad astrometry
J0006+0121		19.64	352	
J0233+0050	HP Cet	20.16	683	*
J0845+0339	V0498 Hya	20.83	1635	*
J1434+3340		20.14	363	
J1728+7751		20.7	974	*
J0058-0107	ASASSN-16iw			*
J0804+5103	EZ Lyn	17.79	143	
J0843+2751	EG Cnc	18.77	187	
J0904+4402	FV Lyn	19.42	335	
J1035+0551		18.78	196	
J1057+2759		19.54	355	
J1212+0136	V0379 Vir	17.98	152	
J1216+0520		20.11	377	
J1255+2642	MT Com	19.21	347	
J1433+1011		18.55	232	
J1435+2336		18.62	209	
J1507+5230	OV Boo	18.15	212	
J2131-0039	QZ Aqr			*
J2304+0625	KX Psc	20.91		*

out by SDSS-V. We made use of only the `mwm_wd` carton as it provides good coverage of the HR diagram location occupied by period bouncers, has the cleanest selection rules, homogeneously covers the entire SDSS-V footprint, and has a well-defined ($G \leq 20$ mag) magnitude limit with a completeness of 85 per cent (Gentile Fusillo et al., 2019). We found 1256 `mwm_wd` targets within the ellipse defined by the known period bouncers, of which 1132 were observed during the SDSS-V plate program, i.e. the correction factor to account for the incompleteness of the spectroscopic observations is $C_{\text{corr}} = 1256/(1132 * 0.85) = 1.31$. Amongst these 1132 observed targets, we identify only one candidate period bouncer: J0006+0121 with a period of 91 min ($N_{\text{obs}} = 1$)[‡]

We estimated the space density of period bouncers using the technique described in Section 5.4.4. We first concluded from inspection of Fig. 6.11 that all period bouncers would have an absolute magnitude $G_{\text{abs}} \leq 12.25$, yielding a limiting distance of $R_{\text{lim}} = 355$ pc (based on a reliable detection limit of $G < 21$). As in Section 5.4.4 we assumed a scale height of 450 pc as period bouncers are an old population. Next, we determined the SDSS-V sky coverage from the 236 plates on which the 1132 `mwm_wd` targets were observed. HEALpix were then used to find the sky coverage of these 236 plates by accounting for overlaps and hence the effective volume of the magnitude limited `mwm_wd` sample contained within the ellipse defined by the known period bouncers.

Taken together, these assumptions yielded a space density $\rho_0 \simeq 0.2 \times 10^{-6} \text{ pc}^{-3}$ for period bouncers. Estimates for the composite space density of all sub-types of CVs range from $\rho_0 = 4.8 \times 10^{-6} \text{ pc}^{-3}$ (Pala et al., 2020) to $\rho_0 = 7.8 \times 10^{-6} \text{ pc}^{-3}$ (Section 5.4.5) implying that accreting [§] period bouncers only account for about three per cent of CVs.

From the above analysis, we can only conclude that the large number of period bouncers predicted by CV models either do not exist, or that the majority of them look so distinctly different from the small sample of known period bouncers that they escape spectroscopic (our analysis) and photometric (Hernández Santisteban et al., 2018) detections. Our conclusions echo those of Patterson (1998), ‘*It is probably necessary to have some means of destroying CVs before they reach the predicted very high space densities.*’ Possible scenarios to ‘destroy’ CVs include either a merger, maybe as a result of a final classical nova eruption (e.g. via consequential angular momentum loss, Schreiber et al. 2016; Nelemans et al. 2016), or the secondary contracting within its Roche lobe, thereby terminating mass transfer. The latter option was suggested by Patterson (1998), arguing that the final state of CVs may be white dwarfs with detached, planet-like companions – and the ultimate test of that hypothesis would be a more sensitive survey for apparently single white dwarfs eclipsed by their (at optical

[‡]The plate program obtained spectroscopy of four additional confirmed or candidate period bouncers, J0233+0050 ($P_{\text{orb}} = 96$ min), J0845+0339 with a period of 87 min, J1434+3340 (no P_{orb}) and J1728+7751 (no P_{orb}), which are however all too faint to be included in the `mwm_wd` carton.

[§]We assume that the presence, or otherwise of emission lines in a spectra is a sensitive test for accretion.

wavelengths) invisible ultra-low-mass companions.

6.6.2 Orbital period distribution

We have obtained periods for 72 of the 118 CVs in the SDSS-V plate survey. The main reasons why the remaining systems have no period measurements are due to either a low inclination (which will reduce the amplitude of any orbital modulation), faintness (i.e. low signal-to-noise ratio of the time-series photometry or spectroscopy), or sparse sampling of the available time-series data. With the possible exception of low \dot{M} short-period CVs (which do not have much orbital modulation from the hot spot and are inherently fainter) these factors are not likely to correlate with the period. Systems with longer periods have smaller variations in radial velocity making them harder to detect using spectroscopy, however photometry does not suffer the same bias.

The orbital period distribution of the SDSS-V CVs is shown in Fig. 6.12 where it is compared to that of the [Ritter & Kolb \(2003\)](#) sample, which is a very heterogeneous collection of CVs, and the 150 pc volume-limited sample of ([Pala et al., 2020](#)). The period gap, which has been a defining feature of the observed period distribution of CVs and motivated the widely accepted idea ‘disrupted magnetic braking’ ([Rappaport et al., 1983](#); [Howell et al., 2001](#); [Schreiber et al., 2010](#)), is at best marginally detected in the SDSS-V sample (and not at all in the 150 pc sample) which is in clear contrast with the period distribution of the CVs from the Ritter and Kolb catalogue.

The SDSS-V period distribution also shows a slight flattening between $\simeq 3$ h and $\simeq 5$ h which is consistent with the predictions of [Schreiber et al. \(2021\)](#) for CVs where the formation of magnetic white dwarfs undergoes a detached phase within that period range, resulting in a decrease in the number of accreting CVs.

The orbital periods of the new CVs, where we were able to obtain unambiguous measurements, are all below 94 min, which is typical of old, low accretion rate systems. This reinforces the findings of [Gänsicke et al. \(2009\)](#) and suggests that SDSS-V will continue to increase the proportion of short-period CVs among the known CV population.

6.6.3 CV sub-types

The distribution of the new and previously known CVs is given in Table 6.7. Taken in conjunction with their distribution in the HR diagram (Fig. 6.13) we notice that the new discoveries include a novalike variable in the expected area (see Fig. 4.7). All of the other new discoveries are close to the white dwarf cooling sequence, i.e. the area associated with short-period CVs with low accretion rates, experiencing infrequent outbursts. This demonstrates the importance of a spectroscopic survey that compensates for the traditional bias of CV searches based on large-amplitude photometric variability. In passing, we note that there are 17 magnetic CVs (14 per cent of the total) in the

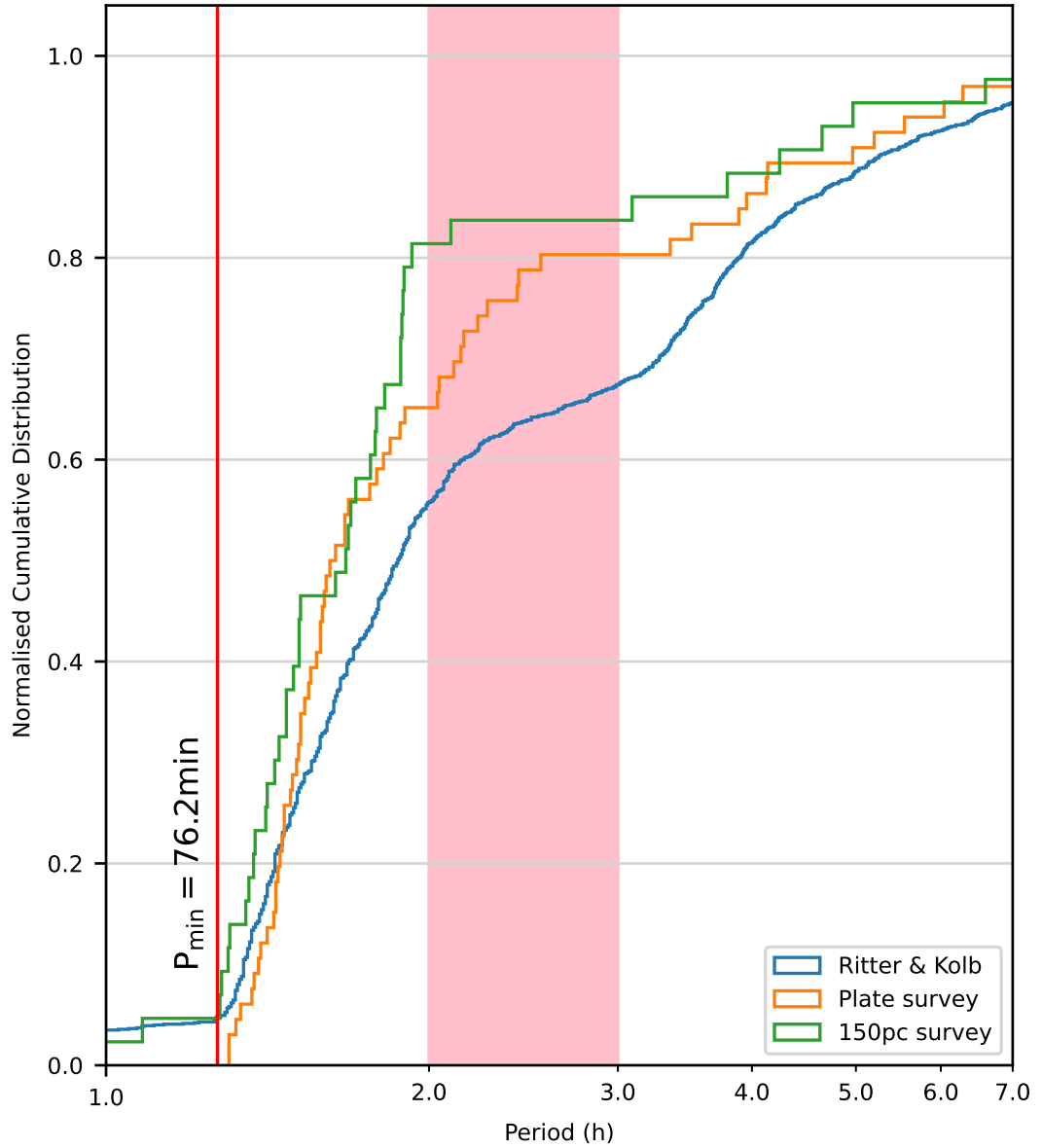


Figure 6.12: Cumulative distribution of the orbital periods of the CVs observed by SDSS-V (orange), compared to those of the [Ritter & Kolb \(2003\)](#) catalogue of CVs (blue) and of the 150pc volume-limited survey ([Pala et al. 2020](#), green). The period minimum (red line) and ‘period gap’ (pink rectangle) are indicated (see text for details).

SDSS-V CV sample, which is similar to the fraction found in the SDSS I to IV sample (Section 5.4.2), but lower than in the volume-limited 150pc sample, probably due to the, on average, lower accretion rates in polars when compared to non-magnetic CVs ([Webbink & Wickramasinghe, 2002](#); [Araujo-Betancor et al., 2005b](#)).

Table 6.7: The CV sub-types of the new and previously known systems

CV type	Previously known	New	Total
U Gem	26	0	26
ER UMa	3	0	3
SU UMa	36	1	37
WZ Sge	9	4	13
Z Cam	1	0	1
AM CVn	3	0	3
Nova	5	0	5
Novalike	1	1	2
Polar - AM Her	14	1	15
Intermediate polar - DQ Her	2	0	2
Magnetic CV	1	0	1
Dwarf nova	7	0	7
Unclassified	2	1	3
Total	110	8	118

6.7 Summary

SDSS-V is, for the first time, carrying out a dedicated survey of white dwarfs, both single and in binaries. We have analysed the SDSS-V spectra of CVs and CV candidates observed as part of the final plug-plate operations of SDSS, and we discovered eight new CVs. None of the new CVs displays noticeable changes in brightness in their ZTF light curves, underlining the selection effects in existing CV samples that are largely based on photometric variability, and hence the importance of unbiased spectroscopic surveys. We did not discover any new CVs within 150 pc which is consistent with the relatively high completeness of this volume-limited sample (Pala et al., 2020).

SDSS-V also observed 110 previously known CVs and CV candidates, for 53 of these, the SDSS data represents the first spectroscopic confirmation of their CV nature. Vice versa, the SDSS-V spectroscopy disproves the CV nature of eleven systems that were previously classified as CVs or CV candidates.

We measured 21 new orbital periods from the analysis of radial velocities and time-series photometry. The period distribution of the SDSS-V CV sample does not provide strong evidence for a period gap, which contrasts strongly with the orbital period distribution of the large, but very heterogeneous (Ritter & Kolb, 2003) sample. We suggest that future modelling of the CV population should aim to reproduce the period distribution of well-defined samples.

Lastly, but most importantly, we demonstrate that there is no large population of period bounce CVs awaiting discovery, which represents a major challenge to CV evolution theory. The implications are, most likely, that CVs that evolve past the period minimum either get destroyed (e.g. by a merger) or become detached and therefore

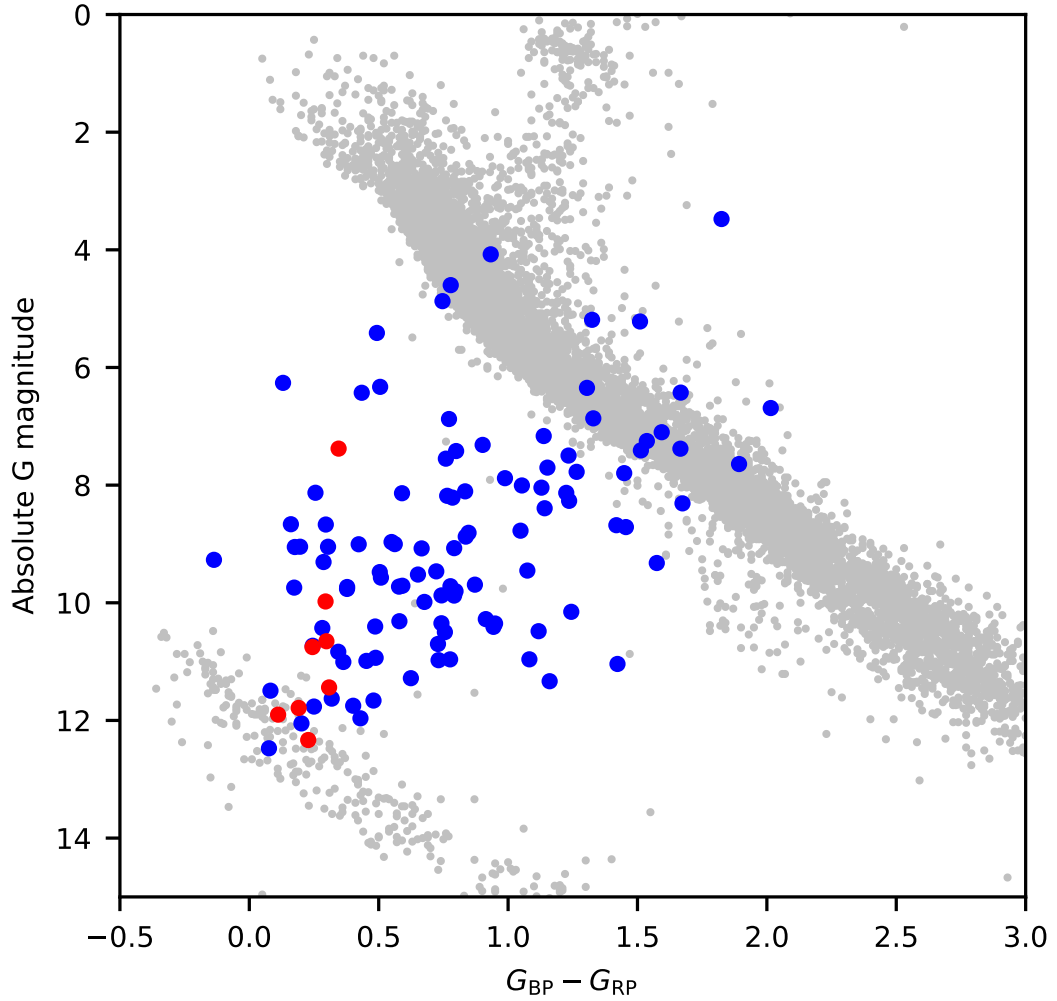


Figure 6.13: HR diagram showing the 110 previously known CVs in blue and the eight new discoveries in red. The grey dots are an astrometrically clean sample of *Gaia* objects chosen to outline the main sequence and the white dwarf cooling sequence

very difficult to detect. The Legacy Survey of Space and Time survey will provide an opportunity to search for a population of cool white dwarfs that are eclipsed by planet-mass and size objects with periods of $\sim 80 - 120$ min.

SDSS-V will continue to survey both the northern and southern hemisphere for single and binary white dwarfs, and the growing sky coverage will provide increasingly stronger constraints on the intrinsic properties of the Galactic CV population.

Chapter 7

Conclusion

The evolution of CVs has been discussed for over three decades and documented extensively in the literature. However there remain substantive gaps in our understanding and with the benefit of new data some previously settled concepts are having to be updated.

The work leading up to this thesis is both foundational and investigative.

The analysis of ASAS J071404+7004.3 spectroscopy yielded unplanned insights into disc winds from novalikes. By using the PYTHON simulation package we were able to show that the Balmer emission lines could originate entirely in the wind far from the CV. This offers an intriguing alternative explanation to an open question; why the Balmer emission lines in SW Sex novalikes are single-peaked even when they are highly inclined. Confirmation of this will require further observations. ASAS J071404+7004.3 has unusually strong winds as evidenced by the infrequently-seen P Cygni He 5876Å optical line. Winds are more commonly traced using He, C, N, and Si lines in the ultraviolet and this naturally suggests that future observations should use the *HST* STIS spectrograph together with simultaneous ground-based optical observations to derive accurate phasing. PYTHON could then be used to constrain the structure, geometry, and driving mechanism of the wind. HST Cycle 31 proposal 4020 has been submitted to address this.

The Gold Samples defined in chapter 4 have already been used to inform the targeting of SDSS-V and will be used in future spectroscopic surveys. The overall effort to deliver a complete 300 pc volume-limited sample of CVs has been hampered by implementation delays in spectroscopic surveys but the next few years can be expected to deliver survey data from the southern hemisphere in particular including the implementation of SDSS-V robotic fibre positioners at the Las Campanas observatory in

Chile and 4MOST. A key finding from the volumetric approach was the greatly reduced prominence of the period gap suggesting that selection effects have been a major cause of this observed phenomenon. This is important as a large part of CV evolution theory has been based upon the existence of a period gap and the concept of ‘disrupted magnetic braking’ but this is not universally accepted ([Andronov et al., 2003](#)).

The SDSS data analysed in Chapter 5 provides a large, *consistently classified*, data set of CVs. Existing classifications such as those in the widely-used Ritter and Kolb sample are not suitable for evolutionary analysis – most WZ Sge CVs being classified as SU UMa for example. In addition we obtained and confirmed many orbital periods – the most important observable parameter when studying CV evolution. We used this data set to estimate the space density of each CV sub-type. Estimating space densities is difficult and subject to multiple assumptions but our findings clearly show a greater density of older CVs than previous studies. Improving upon these estimates will require more complete coverage, improved targeting and greater depth. A number of multi-object all-sky spectroscopic surveys are in progress; SDSS-V will extend its coverage into the southern hemisphere whilst targeting white dwarfs, DESI uses a 4 m telescope to probe deeper as will WEAVE on the 4.2 m William Herschel Telescope (expected to complete commissioning in summer 2023) and 4MOST on the 4 m VISTA telescope. *Gaia* DR3 has also released low resolution spectra for brighter stars that have already enabled the identification of some new CVs. DR4 (in 2025) can be expected to increase the number and SNR of such spectra.

Targeting CVs and white dwarfs generally is dependent upon archive *GALEX* ultraviolet observations with partial sky coverage to a limited depth. To date there has been no successor to *GALEX* but a NASA proposal to launch *UVEX* in 2028 would deliver an all-sky survey with 50 – 100 times the depth of *GALEX*.

ZTF light curves have proved invaluable when classifying CVs but they are limited in coverage (being based in the northern hemisphere) and depth. The Vera Rubin Telescope, based in Chile, will not only complete the sky coverage but also provide much greater depth (~ 24 mag per image compared with ~ 21 mag) albeit at a smaller cadence (100 visits per year spread over six filters compared with 300 per year spread over three filters [Graham et al. 2019](#)).

Whilst analysing the ZTF light curves of SDSS-identified CVs a small number stood out because of their unusual state changes. Whereas novalike variables and polars are known to exhibit state changes due to sustained changes in \dot{M} other types are generally expected to remain at a relatively constant level unless undergoing an outburst arising from disc instability. We found seven examples of systems that exhibit significant state changes on timescales that indicate the cause is a change in \dot{M} rather than storage in the disc. This phenomenon is most unexpected and further investigation is needed. In the first instance spectroscopy in different states is needed to establish the size of the

disc and also the relative proportions of line-based and continuum emission. Liverpool Telescope time has been allocated for this purpose (PL23A08).

The analysis of SDSS-V data in Chapter 6 broke new ground as it was the first multi-object spectroscopic survey systematically targeting white dwarfs. This yielded a high proportion of older (short-period) systems with the period gap again not very conspicuous. The targeted nature of the survey has enabled us to put an upper limit on the space density of *accreting* period bouncers. This is an important result providing input to the long running debate regarding the ultimate fate of CVs. This leads to the key question regarding AML and whether other factors than gravitational wave radiation are at work. Observations to date have been hampered by the low mass of the donor in period bouncers which can only realistically be observed in the infrared. The James Webb Space Telescope (*JWST*) provides a wonderful opportunity to observe a sample of known period bouncers and establish their evolutionary history. *JWST* Cycle 2 proposal 3579 was submitted to address this; it was not approved and will be re-submitted in Cycle 3.

At a more fundamental level our knowledge of CV accretion discs is incomplete. In section 1.3.2 we discuss the conventional model for the behaviour of CV accretion disks and the assumption that the source of viscosity is magnetic turbulence. However this does not correctly account for the temperature profile of a quiescent CV disc - proposing $T(r) \propto r^{-3/4}$ when observations show a flat temperature distribution (Mason et al., 2000). The fundamental obstacle to resolving this and other concerns is the fact that the *thermal* emission of the quiescent disks has never been detected – existing observations only probe the emission of an optically thin, warm layer on top of the disks. Hence, predictions of the rates of AML and \dot{M} (both of which correlate with temperature) within these quiescent disks are largely unconstrained. The temperature of quiescent disks is sufficiently low that their emissions peak in the mid-infrared and again *JWST* offers a potential solution. *JWST* Cycle 2 proposal 3506 was submitted to address this. It was placed in the second quintile but was not approved and will be re-submitted in Cycle 3.

Bibliography

- Abazajian K., et al., 2003, [AJ](#), **126**, 2081
- Abazajian K. N., et al., 2009, [ApJS](#), **182**, 543
- Abbott B. P., et al., 2016, [Phys. Rev. Lett.](#), **116**, 061102
- Abril J., Schmidtbreick L., Ederoclite A., López-Sanjuan C., 2020, [MNRAS](#), **492**, L40
- Adelman-McCarthy J. K., et al., 2008, [ApJS](#), **175**, 297
- Aguado D. S., et al., 2019, [ApJS](#), **240**, 23
- Ahn C. P., et al., 2012, [ApJS](#), **203**, 21
- Ahumada R., et al., 2020, [ApJS](#), **249**, 3
- Aihara H., et al., 2011, [ApJS](#), **193**, 29
- Allard F., Homeier D., Freytag B., 2012, [Philosophical Transactions of the Royal Society of London Series A](#), **370**, 2765
- Allen M. G., Ochsenbein F., Derriere S., Boch T., Fernique P., Landais G., 2014, in Manset N., Forshay P., eds, *Astronomical Society of the Pacific Conference Series Vol. 485, Astronomical Data Analysis Software and Systems XXIII*. p. 219
- Almeida A., et al., 2023, [arXiv e-prints](#), p. [arXiv:2301.07688](#)
- Altan M., et al., 2019, [MNRAS](#), **489**, 1451
- Althaus L. G., Córscico A. H., Isern J., García-Berro E., 2010, [A&A Rev.](#), **18**, 471
- Álvarez-Hernández A., et al., 2021, [MNRAS](#), **507**, 5805
- Amantayeva A., Zharikov S., Page K. L., Pavlenko E., Sosnovskij A., Khokhlov S., Ibraimov M., 2021, [ApJ](#), **918**, 58
- Amaro-Seoane P., et al., 2017, [arXiv e-prints](#), p. [arXiv:1702.00786](#)
- Anderson S. F., et al., 2005, [AJ](#), **130**, 2230
- Anderson S. F., et al., 2008, [AJ](#), **135**, 2108
- Andronov N., Pinsonneault M., Sills A., 2003, [ApJ](#), **582**, 358
- Antipin S. V., 1998, *Information Bulletin on Variable Stars*, **4578**, 1
- Antipin S. V., Kroll P., 2003, *Information Bulletin on Variable Stars*, **5461**, 1
- Antoja T., et al., 2018, *Gaia DR2 documentation Chapter 10: Catalogue validation*, Gaia DR2 documentation, European Space Agency; Gaia Data Processing and Analysis Consortium.
- Araujo-Betancor S., et al., 2003, [ApJ](#), **583**, 437
- Araujo-Betancor S., et al., 2005a, [A&A](#), **430**, 629
- Araujo-Betancor S., Gänsicke B. T., Long K. S., Beuermann K., de Martino D., Sion E. M., Szkody P., 2005b, [ApJ](#), **622**, 589
- Arenas J., Mennickent R. E., 1998, [A&A](#), **337**, 472

- Arévalo P., Uttley P., 2006, [MNRAS](#), **367**, 801
- Arjyotha S., Aungwerojwit A., Gänsicke B. T., Marsh T., Rodríguez-Gil P. R., 2009, in Murphy S. J., Bessell M. S., eds, *Astronomical Society of the Pacific Conference Series Vol. 404, The Eighth Pacific Rim Conference on Stellar Astrophysics: A Tribute to Kam-Ching Leung*, p. 272
- Armstrong E., et al., 2013, [MNRAS](#), **435**, 707
- Ashley R. P., Farihi J., Marsh T. R., Wilson D. J., Gänsicke B. T., 2019, [MNRAS](#), **484**, 5362
- Auddy S., Basu S., Valluri S. R., 2016, [Advances in Astronomy](#), **2016**, 574327
- Augusteijn T., Tappert C., Dall T., Maza J., 2010, [MNRAS](#), **405**, 621
- Aungwerojwit A., et al., 2006, [A&A](#), **455**, 659
- Bade N., et al., 1998, [A&AS](#), **127**, 145
- Badenes C., Mullally F., Thompson S. E., Lupton R. H., 2009, [ApJ](#), **707**, 971
- Bailer-Jones C. A. L., 2015, [PASP](#), **127**, 994
- Bailer-Jones C. A. L., Rybizki J., Fouesneau M., Mantelet G., Andrae R., 2018, [AJ](#), **156**, 58
- Bailer-Jones C. A. L., Rybizki J., Fouesneau M., Demleitner M., Andrae R., 2021, [AJ](#), **161**, 147
- Bailey J., Ferrario L., Wickramasinghe D. T., 1991, [MNRAS](#), **251**, 37P
- Balanutsa P., et al., 2013, *The Astronomer's Telegram*, **5676**, 1
- Balanutsa P., et al., 2015, *The Astronomer's Telegram*, **8426**, 1
- Balbus S. A., Hawley J. F., 1998, [Reviews of Modern Physics](#), **70**, 1
- Balman S., Godon P., Sion E. M., 2014, [ApJ](#), **794**, 84
- Bao Supernova Survey Esamdin A., Dong X., Zhao Y., 1997, *IAU Circ.*, **6763**, 2
- Baptista R., Steiner J. E., Cieslinski D., 1994, [ApJ](#), **433**, 332
- Barrett P. E., Dieck C., Beasley A. J., Singh K. P., Mason P. A., 2017, [AJ](#), **154**, 252
- Barrett P., Dieck C., Beasley A. J., Mason P. A., Singh K. P., 2020, [Advances in Space Research](#), **66**, 1226
- Baskill D. S., Wheatley P. J., Osborne J. P., 2005, [MNRAS](#), **357**, 626
- Bauer A., et al., 2009, [ApJ](#), **705**, 46
- Bédard A., Bergeron P., Brassard P., Fontaine G., 2020, [ApJ](#), **901**, 93
- Belle K., Nguyen Q., Fabian D., Sion E. M., Huang M., 1998, [PASP](#), **110**, 47
- Bellm E. C., et al., 2019, [PASP](#), **131**, 018002
- Belloni D., Schreiber M. R., 2020, [MNRAS](#), **492**, 1523
- Belloni D., Schreiber M. R., 2023, [arXiv e-prints](#), p. [arXiv:2303.08997](#)
- Belloni D., Schreiber M. R., Zorotovic M., Ilkiewicz K., Hurley J. R., Giersz M., Lagos F., 2018, [MNRAS](#), **478**, 5626
- Belloni D., Schreiber M. R., Pala A. F., Gänsicke B. T., Zorotovic M., Rodrigues C. V., 2020, [MNRAS](#), **491**, 5717
- Belokurov V., et al., 2020, [MNRAS](#), **496**, 1922
- Bergeron P., Greenstein J. L., Liebert J., 1990, [ApJ](#), **361**, 190
- Bergeron P., et al., 2011, [ApJ](#), **737**, 28
- Bernardini F., de Martino D., Mukai K., Falanga M., 2014, [MNRAS](#), **445**, 1403
- Bertin E., Arnouts S., 1996, [A&AS](#), **117**, 393
- Beuermann K., Stasiewski U., Schwöpe A. D., 1992, [A&A](#), **256**, 433
- Bíró I. B., 2000, [A&A](#), **364**, 573
- Blanton M. R., Lin H., Lupton R. H., Maley F. M., Young N., Zehavi I., Loveday J., 2003, [AJ](#),

- 125, 2276
- Blanton M. R., et al., 2017, [AJ](#), **154**, 28
- Bleach J. N., Wood J. H., Catalán M. S., Welsh W. F., Robinson E. L., Skidmore W., 2000, [MNRAS](#), **312**, 70
- Bode M. F., Evans A., 2012, *Classical Novae*. Cambridge University Press
- Bours M. C. P., et al., 2015, [MNRAS](#), **450**, 3966
- Boyd D., Denisenko D., Koff R., Miller I., Staels B., 2011, [Journal of the British Astronomical Association](#), **121**, 233
- Brady S., Thorstensen J. R., Koppelman M. D., Prieto J. L., Garnavich P. M., Hirschauer A., Florack M., 2008, [PASP](#), **120**, 301
- Brand K., et al., 2006, [ApJ](#), **641**, 140
- Breedt E., Gänsicke B. T., Girven J., Drake A. J., Copperwheat C. M., Parsons S. G., Marsh T. R., 2012a, [MNRAS](#), **423**, 1437
- Breedt E., Gänsicke B. T., Marsh T. R., Steeghs D., Drake A. J., Copperwheat C. M., 2012b, [MNRAS](#), **425**, 2548
- Breedt E., et al., 2014, [MNRAS](#), **443**, 3174
- Broekhoven-Fiene H., et al., 2014, [ApJ](#), **786**, 37
- Brown W. R., Kilic M., Allende Prieto C., Kenyon S. J., 2010, [ApJ](#), **723**, 1072
- Brown J. M., Kilic M., Brown W. R., Kenyon S. J., 2011, [ApJ](#), **730**, 67
- Brown W. R., Kilic M., Allende Prieto C., Gianninas A., Kenyon S. J., 2013, [ApJ](#), **769**, 66
- Brown W. R., et al., 2020, [ApJ](#), **889**, 49
- Bruch A., 1989, *A&AS*, **78**, 145
- Bruch A., 1992, *A&A*, **266**, 237
- Bruch A., 2017, [New Astronomy](#), **57**, 51
- Bruch A., 2019, [MNRAS](#), **489**, 2961
- Bruch A., Schimpke T., 1992, *A&AS*, **93**, 419
- Bruch A., Fischer F. J., Wilmsen U., 1987, *A&AS*, **70**, 481
- Buat-Ménard V., Hameury J. M., 2002, [A&A](#), **386**, 891
- Buat-Ménard V., Hameury J. M., Lasota J. P., 2001, [A&A](#), **369**, 925
- Burgasser A. J., Reid I. N., Siegler N., Close L., Allen P., Lowrance P., Gizis J., 2007, in Reipurth B., Jewitt D., Keil K., eds, *Protostars and Planets V*. p. 427 ([arXiv:astro-ph/0602122](#)), doi:10.48550/arXiv.astro-ph/0602122
- Burleigh M. R., Hogan E., Dobbie P. D., Napiwotzki R., Maxted P. F. L., 2006a, [MNRAS](#), **373**, L55
- Burleigh M. R., et al., 2006b, [MNRAS](#), **373**, 1416
- Burrows D. N., et al., 2005, [Space Sci. Rev.](#), **120**, 165
- Burwitz V., et al., 1998, *A&A*, **331**, 262
- Byckling K., Mukai K., Thorstensen J. R., Osborne J. P., 2010, [MNRAS](#), **408**, 2298
- Campbell C. G., 1984, [MNRAS](#), **211**, 69
- Campbell C. G., Schwope A. D., 1999, *A&A*, **343**, 132
- Campbell R. D., Shafter A. W., 1995, [ApJ](#), **440**, 336
- Cannizzo J. K., Shafter A. W., Wheeler J. C., 1988, [ApJ](#), **333**, 227
- Carbon D. F., Henze C., Nelson B. C., 2017, [ApJS](#), **228**, 19
- Carter P. J., et al., 2013a, [MNRAS](#), **429**, 2143

- Carter P. J., et al., 2013b, *MNRAS*, **431**, 372
- Carter P. J., et al., 2014, *MNRAS*, **439**, 2848
- Casares J., Mouchet M., Martinez-Pais I. G., Harlaftis E. T., 1996, *MNRAS*, **282**, 182
- Casewell S. L., Littlefair S. P., Parsons S. G., Marsh T. R., Fortney J. J., Marley M. S., 2018, *MNRAS*, **481**, 5216
- Castelli F., Kurucz R. L., 2003, in Piskunov N., Weiss W. W., Gray D. F., eds, IAU SYM-POSIUM Vol. 210, Modelling of Stellar Atmospheres. p. A20 ([arXiv:astro-ph/0405087](#)), [doi:10.48550/arXiv.astro-ph/0405087](#)
- Castro Segura N., et al., 2021, *MNRAS*, **501**, 1951
- Chambers K. C., et al., 2016, *arXiv e-prints*, p. [arXiv:1612.05560](#)
- Chau W. Y., 1978, *ApJ*, **219**, 1038
- Chen X., Maxted P. F. L., Li J., Han Z., 2017, *MNRAS*, **467**, 1874
- Chen X., Wang S., Deng L., de Grijs R., Yang M., Tian H., 2020, *ApJS*, **249**, 18
- Cieslinski D., Steiner J. E., 1997, *MNRAS*, **291**, 321
- Claeys J. S. W., Pols O. R., Izzard R. G., Vink J., Verbunt F. W. M., 2014, *A&A*, **563**, A83
- Clark D. H., Stephenson F. R., 1976, *QJRAS*, **17**, 290
- Clark D. H., Stephenson F. R., 1977, The historical supernovae. Pergamon, Oxford
- Clark D. H., Parkinson J. H., Stephenson F. R., 1977, *QJRAS*, **18**, 443
- Coppejans D. L., K rding E. G., Knigge C., Pretorius M. L., Woudt P. A., Groot P. J., Van Eck C. L., Drake A. J., 2016, *MNRAS*, **456**, 4441
- Cordoni J. P., Gleizes F., Jasniewicz G., 1977, *A&A*, **55**, 307
- Cropper M., 1987, *MNRAS*, **228**, 389
- Cropper M., 1990, *Space Sci. Rev.*, **54**, 195
- Cutri R. M., et al., 2003, VizieR Online Data Catalog, p. [II/246](#)
- Cutri R. M., et al., 2021, VizieR Online Data Catalog, p. [II/328](#)
- D’Antona F., Mazzitelli I., Ritter H., 1989, *A&A*, **225**, 391
- DESI Collaboration et al., 2016a, *arXiv e-prints*, p. [arXiv:1611.00036](#)
- DESI Collaboration et al., 2016b, *arXiv e-prints*, p. [arXiv:1611.00037](#)
- Dalton G., et al., 2012, in McLean I. S., Ramsay S. K., Takami H., eds, Society of Photo-Optical Instrumentation Engineers (SPIE) Conference Series Vol. 8446, Ground-based and Airborne Instrumentation for Astronomy IV. p. 84460P, [doi:10.1117/12.925950](#)
- Danzmann K., LISA Study Team 1996, *Classical and Quantum Gravity*, **13**, A247
- Darnley M. J., Ribeiro V. A. R. M., Bode M. F., Hounsell R. A., Williams R. P., 2012, *ApJ*, **746**, 61
- Davis P. J., Kolb U., Willems B., G nsicke B. T., 2008, *MNRAS*, **389**, 1563
- Davis A. B., et al., 2014, The Astronomer’s Telegram, **6455**, 1
- Dawson K. S., et al., 2013, *AJ*, **145**, 10
- Dawson K. S., et al., 2016, *AJ*, **151**, 44
- Debes J. H., 2006, *ApJ*, **652**, 636
- Debes J. H., Kilic M., Tremblay P.-E., L pez-Morales M., Anglada-Escude G., Napiwotzki R., Osip D., Weinberger A., 2015, *AJ*, **149**, 176
- Deeming T. J., 1975, *Ap&SS*, **36**, 137
- Delgado A., Harrison D., Hodgkin S., Leeuwen M. V., Rixon G., Yoldas A., 2016, Transient Name Server Discovery Report, **2016-481**, 1

- Delgado A., Harrison D., Hodgkin S., Leeuwen M. V., Rixon G., Yoldas A., 2017a, Transient Name Server Discovery Report, [2017-547](#), 1
- Delgado A., Harrison D., Hodgkin S., Leeuwen M. V., Rixon G., Yoldas A., 2017b, Transient Name Server Discovery Report, [2017-925](#), 1
- Delgado A., Harrison D., Hodgkin S., Leeuwen M. V., Rixon G., Yoldas A., 2017c, Transient Name Server Discovery Report, [2017-933](#), 1
- Delgado A., Harrison D., Hodgkin S., Leeuwen M. V., Rixon G., Yoldas A., 2018a, Transient Name Server Discovery Report, [2018-1819](#), 1
- Delgado A., Harrison D., Hodgkin S., Leeuwen M. V., Rixon G., Yoldas A., 2018b, Transient Name Server Discovery Report, [2018-337](#), 1
- Delgado A., Harrison D., Hodgkin S., Leeuwen M. V., Rixon G., Yoldas A., 2018c, Transient Name Server Discovery Report, [2018-423](#), 1
- Delgado A., Harrison D., Hodgkin S., Leeuwen M. V., Rixon G., Yoldas A., 2019, Transient Name Server Discovery Report, [2019-241](#), 1
- Deloye C. J., Taam R. E., Winisdoerffer C., Chabrier G., 2007, *MNRAS*, **381**, 525
- Denisenko D. V., Martinelli F., 2016, *arXiv e-prints*, p. [arXiv:1609.08511](#)
- Denisenko D. V., Sokolovsky K. V., 2011, *Astronomy Letters*, **37**, 91
- Denisenko D., et al., 2012a, The Astronomer's Telegram, [4441](#), 1
- Denisenko D., et al., 2012b, The Astronomer's Telegram, [4475](#), 1
- Denisenko D., et al., 2014, The Astronomer's Telegram, [6049](#), 1
- Dhillon V. S., 1996, in Evans A., Wood J. H., eds, *Astrophysics and Space Science Library* Vol. 208, IAU Colloq. 158: Cataclysmic Variables and Related Objects. p. 3 ([arXiv:astro-ph/9509156](#)), [doi:10.1007/978-94-009-0325-8_1](#)
- Dhillon V. S., Jones D. H. P., Marsh T. R., Smith R. C., 1992, *MNRAS*, **258**, 225
- Dhillon V. S., Littlefair S. P., Howell S. B., Ciardi D. R., Harrop-Allin M. K., Marsh T. R., 2000, *MNRAS*, **314**, 826
- Dhillon V. S., et al., 2007, *MNRAS*, **378**, 825
- Dhillon V. S., Smith D. A., Marsh T. R., 2013, *MNRAS*, **428**, 3559
- Dhillon V. S., et al., 2014, *MNRAS*, **444**, 4009
- Dilday B., et al., 2005, in *American Astronomical Society Meeting Abstracts*. p. 180.05
- Dillon M., et al., 2008, *MNRAS*, **386**, 1568
- Djorgovski S. G., et al., 2011, *arXiv e-prints*, p. [arXiv:1102.5004](#)
- Downes R. A., Shara M. M., 1993, *PASP*, **105**, 127
- Downes R. A., Szkody P., 1989, *AJ*, **97**, 1729
- Downes R. A., Webbink R. F., Shara M. M., Ritter H., Kolb U., Duerbeck H. W., 2001, *PASP*, **113**, 764
- Drake A. J., et al., 2009a, *ApJ*, **696**, 870
- Drake A. J., et al., 2009b, The Astronomer's Telegram, [2057](#), 1
- Drake A. J., et al., 2009c, The Astronomer's Telegram, [2086](#), 1
- Drake A. J., et al., 2009d, The Astronomer's Telegram, [2266](#), 1
- Drake A. J., et al., 2014a, *ApJS*, **213**, 9
- Drake A. J., et al., 2014b, *MNRAS*, **441**, 1186
- Drew J. E., Kley W., 1993, in , Vol. 9, *Accretion Disks in Compact Stellar Systems*. World Scientific Publishing Co Pte Ltd, p. 212, [doi:10.1142/9789814350976_0008](#)

- Duerbeck H. W., 1984, [Ap&SS](#), **99**, 363
- Duffy C., et al., 2022, [MNRAS](#), **510**, 1002
- Dupke R. A., 1992, Information Bulletin on Variable Stars, **3749**, 1
- Duszanowicz G., Huchra J., 2008, Central Bureau Electronic Telegrams, **1574**, 1
- Dwelly T., et al., 2017, [MNRAS](#), **469**, 1065
- Eggleton P. P., 1983, [ApJ](#), **268**, 368
- Eggleton P. P., Tokovinin A. A., 2008, [MNRAS](#), **389**, 869
- Einstein A., 1916, [Annalen der Physik](#), **354**, 769
- Eisenstein D. J., et al., 2011, [AJ](#), **142**, 72
- El-Badry K., Rix H.-W., Quataert E., Kupfer T., Shen K. J., 2021, [MNRAS](#), **508**, 4106
- El-Badry K., Conroy C., Fuller J., Kiman R., van Roestel J., Rodriguez A. C., Burdge K. B., 2022, [MNRAS](#), **517**, 4916
- Esamdin A., Qui Y., Li W., Qiao Q., Wei J., Li C., Hu J., 1998, Acta Astrophysica Sinica, **18**, 214
- Evans P. A., et al., 2009, [MNRAS](#), **397**, 1177
- Evans P. A., et al., 2020, [ApJS](#), **247**, 54
- Eyres S. P. S., et al., 2018, [MNRAS](#), **481**, 4931
- Fabricius C., Makarov V. V., Knude J., Wycoff G. L., 2002, [A&A](#), **386**, 709
- Fabrycky D., Tremaine S., 2007, [ApJ](#), **669**, 1298
- Faherty J. K., Burgasser A. J., Bochanski J. J., Looper D. L., West A. A., van der Blik N. S., 2011, [AJ](#), **141**, 71
- Farihi J., Zuckerman B., Becklin E. E., 2005a, [AJ](#), **130**, 2237
- Farihi J., Becklin E. E., Zuckerman B., 2005b, [ApJS](#), **161**, 394
- Farihi J., Hoard D. W., Wachter S., 2006, [ApJ](#), **646**, 480
- Farihi J., Burleigh M. R., Hoard D. W., 2008, [ApJ](#), **674**, 421
- Farihi J., Hoard D. W., Wachter S., 2010, [ApJS](#), **190**, 275
- Faulkner J., Flannery B. P., Warner B., 1972, [ApJ](#), **175**, L79
- Feline W. J., Dhillon V. S., Marsh T. R., Stevenson M. J., Watson C. A., Brinkworth C. S., 2004a, [MNRAS](#), **347**, 1173
- Feline W. J., Dhillon V. S., Marsh T. R., Brinkworth C. S., 2004b, [MNRAS](#), **355**, 1
- Feline W. J., Dhillon V. S., Marsh T. R., Watson C. A., Littlefair S. P., 2005, [MNRAS](#), **364**, 1158
- Ferland G. J., Langer S. H., MacDonald J., Pepper G. H., Shaviv G., Truran J. W., 1982, [ApJ](#), **262**, L53
- Ferrario L., Wickramasinghe D., Bailey J., Buckley D., 1995, [MNRAS](#), **273**, 17
- Ferrario L., de Martino D., Gänsicke B. T., 2015, [Space Sci. Rev.](#), **191**, 111
- Ferrario L., Wickramasinghe D., Kawka A., 2020, [Advances in Space Research](#), **66**, 1025
- Flannery B. P., 1975, [MNRAS](#), **170**, 325
- Flewelling H. A., et al., 2020, [ApJS](#), **251**, 7
- Fontaine G., Brassard P., Bergeron P., 2001, [PASP](#), **113**, 409
- Fouesneau M., et al., 2022, [arXiv e-prints](#), p. [arXiv:2206.05992](#)
- Frank J., King A., Raine D., 1992, Accretion power in astrophysics.. Cambridge astrophysics series Vol. 21, Cambridge University Press
- Fremling C., Blagorodnova N., Kupfer T., Neill J. D., Walters R., Cannella C. B., Kulkarni

- S. R., 2018, The Astronomer’s Telegram, [11512](#), [1](#)
- Fried R. E., Kemp J., Patterson J., Skillman D. R., Retter A., Leibowitz E., Pavlenko E., 1999, [PASP](#), [111](#), [1275](#)
- Fujimoto M. Y., 1982, [ApJ](#), [257](#), [767](#)
- Gaia Collaboration 2020, VizieR Online Data Catalog, [p. I/350](#)
- Gaia Collaboration et al., 2016, [A&A](#), [595](#), [A1](#)
- Gaia Collaboration et al., 2018, [A&A](#), [616](#), [A1](#)
- Gaia Collaboration et al., 2021, [A&A](#), [649](#), [A1](#)
- Gänsicke B. T., 2004, in Tovmassian G., Sion E., eds, Revista Mexicana de Astronomia y Astrofisica Conference Series Vol. 20, Revista Mexicana de Astronomia y Astrofisica Conference Series. pp 152–154 ([arXiv:astro-ph/0402125](#)), [doi:10.48550/arXiv.astro-ph/0402125](#)
- Gänsicke B. T., 2005, in Hameury J. M., Lasota J. P., eds, Astronomical Society of the Pacific Conference Series Vol. 330, The Astrophysics of Cataclysmic Variables and Related Objects. p. 3 ([arXiv:astro-ph/0410412](#)), [doi:10.48550/arXiv.astro-ph/0410412](#)
- Gänsicke B. T., Sion E. M., Beuermann K., Fabian D., Cheng F. H., Krautter J., 1999, [A&A](#), [347](#), [178](#)
- Gänsicke B. T., Fried R. E., Hagen H. J., Beuermann K., Engels D., Hessman F. V., Nogami D., Reinsch K., 2000, [A&A](#), [356](#), [L79](#)
- Gänsicke B. T., Schmidt G. D., Jordan S., Szkody P., 2001, [ApJ](#), [555](#), [380](#)
- Gänsicke B. T., et al., 2003, [ApJ](#), [594](#), [443](#)
- Gänsicke B. T., et al., 2005a, [MNRAS](#), [361](#), [141](#)
- Gänsicke B. T., Szkody P., Howell S. B., Sion E. M., 2005b, [ApJ](#), [629](#), [451](#)
- Gänsicke B. T., et al., 2006, [MNRAS](#), [365](#), [969](#)
- Gänsicke B. T., et al., 2009, [MNRAS](#), [397](#), [2170](#)
- Gänsicke B. T., Rodríguez-Gil P., Gentile Fusillo N. P., Inight K., Schreiber M. R., Pala A. F., Tremblay P.-E., 2020, [MNRAS](#), [499](#), [2564](#)
- Garnavich P., Deal S., 2013, The Astronomer’s Telegram, [5178](#), [1](#)
- Gehrels N., et al., 2004, [ApJ](#), [611](#), [1005](#)
- Geier S., 2020, [A&A](#), [635](#), [A193](#)
- Geier S., Østensen R. H., Nemeth P., Gentile Fusillo N. P., Gänsicke B. T., Telting J. H., Green E. M., Schaffenroth J., 2017, [A&A](#), [600](#), [A50](#)
- Geier S., Raddi R., Gentile Fusillo N. P., Marsh T. R., 2019, [A&A](#), [621](#), [A38](#)
- Genest-Beaulieu C., Bergeron P., 2019, [ApJ](#), [882](#), [106](#)
- Gentile Fusillo N. P., Gänsicke B. T., Greiss S., 2015, [MNRAS](#), [448](#), [2260](#)
- Gentile Fusillo N. P., et al., 2019, [MNRAS](#), [482](#), [4570](#)
- Gentile Fusillo N. P., et al., 2021a, VizieR Online Data Catalog, [p. J/MNRAS/508/3877](#)
- Gentile Fusillo N. P., et al., 2021b, [MNRAS](#), [508](#), [3877](#)
- Gezari S., et al., 2013, [ApJ](#), [766](#), [60](#)
- Giammichele N., Bergeron P., Dufour P., 2012, [ApJS](#), [199](#), [29](#)
- Gilliland R. L., et al., 1991, [AJ](#), [101](#), [541](#)
- Girven J., Gänsicke B. T., Steeghs D., Koester D., 2011, [MNRAS](#), [417](#), [1210](#)
- Godon P., et al., 2016, [ApJ](#), [833](#), [146](#)
- Godon P., Sion E. M., Balman Ş., Blair W. P., 2017, [ApJ](#), [846](#), [52](#)
- Goliasch J., Nelson L., 2015, [ApJ](#), [809](#), [80](#)

- Golysheva P., Shugarov S., Katysheva N., Khruzina T., 2015, in Rucinski S. M., Torres G., Zejda M., eds, *Astronomical Society of the Pacific Conference Series Vol. 496, Living Together: Planets, Host Stars and Binaries*. pp 231–235
- González-Buitrago D., Tovmassian G., Zharikov S., Yungelson L., Miyaji T., Echevarría J., Aviles A., Valyavin G., 2013, *A&A*, **553**, [A28](#)
- González Martínez-País I., Shahbaz T., Casares Velázquez J., 2014, *Accretion Processes in Astrophysics*. Cambridge University Press
- Górski K. M., Hivon E., Banday A. J., Wandelt B. D., Hansen F. K., Reinecke M., Bartelmann M., 2005, *ApJ*, **622**, [759](#)
- Graham M. J., et al., 2019, *PASP*, **131**, [078001](#)
- Green R. F., Schmidt M., Liebert J., 1986, *ApJS*, **61**, [305](#)
- Green M. J., et al., 2020, *MNRAS*, **496**, [1243](#)
- Greenstein J. L., McCarthy J. K., 1985, *ApJ*, **289**, [732](#)
- Groot P. J., Rutten R. G. M., van Paradijs J., 2001, *A&A*, **368**, [183](#)
- Guidry J. A., et al., 2021, *ApJ*, **912**, [125](#)
- Gülsecen H., Esenoglu H., 2014, *New Astronomy*, **28**, [49](#)
- Gunn J. E., et al., 1998, *AJ*, **116**, [3040](#)
- Haefner R., Fiedler A., Rau S., 1996, *Information Bulletin on Variable Stars*, **4366**, [1](#)
- Hakala P., Parsons S. G., Marsh T. R., Gänsicke B. T., Ramsay G., Schwobe A., Hermes J. J., 2022, *MNRAS*, **513**, [3858](#)
- Halpern J. P., Thorstensen J. R., 2015, *AJ*, **150**, [170](#)
- Hameury J. M., Lasota J. P., eds, 2005, *The Astrophysics of Cataclysmic Variables and Related Objects* *Astronomical Society of the Pacific Conference Series Vol. 330*
- Hameury J. M., Lasota J. P., 2014, *A&A*, **569**, [A48](#)
- Hameury J. M., Lasota J. P., 2017, *A&A*, **602**, [A102](#)
- Hamilton R. T., Harrison T. E., Tappert C., Howell S. B., 2011, *ApJ*, **728**, [16](#)
- Hardy L. K., et al., 2017, *MNRAS*, **465**, [4968](#)
- Harper W. E., 1928, *Publications of the Dominion Astrophysical Observatory Victoria*, **4**, [171](#)
- Harrison T. E., 2018, *ApJ*, **861**, [102](#)
- Harrop-Allin M. K., Warner B., 1996, *MNRAS*, **279**, [219](#)
- Hartley L. E., Drew J. E., Long K. S., Knigge C., Proga D., 2002, *MNRAS*, **332**, [127](#)
- Hastings N. C., Szkody P., Hoard D. W., Fried R., Vanmunster T., Pray D., Kowalski R. A., 1999, *PASP*, **111**, [177](#)
- Haug K., Drechsel H., 1985, *A&A*, **151**, [157](#)
- Hawley J. F., Balbus S. A., 1998, in Howell S., Kuulkers E., Woodward C., eds, *Astronomical Society of the Pacific Conference Series Vol. 137, Wild Stars in the Old West*. p. 273
- He B., Fan D., Cui C., Li S., Li C., Mi L., 2017, in Lorente N. P. F., Shortridge K., Wayth R., eds, *Astronomical Society of the Pacific Conference Series Vol. 512, Astronomical Data Analysis Software and Systems XXV*. p. 153 ([arXiv:1601.02334](#)), [doi:10.48550/arXiv.1601.02334](#)
- Heinze A. N., et al., 2018, *AJ*, **156**, [241](#)
- Hellier C., 2001, *Cataclysmic Variable Stars*. Springer
- Hellier C., Cropper M., Mason K. O., 1991, *MNRAS*, **248**, [233](#)
- Henden A. A., Munari U., Sumner B., 2001, *Information Bulletin on Variable Stars*, **5140**, [1](#)
- Henden A. A., Levine S., Terrell D., Welch D. L., 2015, in *American Astronomical Society*

- Meeting Abstracts #225. p. 336.16
- Hermes J. J., et al., 2014, [MNRAS](#), **444**, 1674
- Hernández Santisteban J. V., et al., 2016, [Nature](#), **533**, 366
- Hernández Santisteban J. V., Knigge C., Pretorius M. L., Sullivan M., Warner B., 2018, [MNRAS](#), **473**, 3241
- Hernandez M. S., et al., 2021a, [MNRAS](#), **501**, 1677
- Hernández M. S., Tovmassian G., Zharikov S., Gänsicke B. T., Steeghs D., Aungwerojwit A., Rodríguez-Gil P., 2021b, [MNRAS](#), **503**, 1431
- Hertfelder M., Kley W., Suleimanov V., Werner K., 2013, [A&A](#), **560**, A56
- Hessman F. V., Gänsicke B. T., Mattei J. A., 2000, [A&A](#), **361**, 952
- Hewitt D. M., et al., 2020, [MNRAS](#), **496**, 2542
- Hillebrandt W., Niemeyer J. C., 2000, [ARA&A](#), **38**, 191
- Hillwig T. C., Gale A. A., Honeycutt R. K., Rengstorf A. W., 2002, [PASP](#), **114**, 756
- Hilton E. J., Szkody P., Mukadam A., Henden A., Dillon W., Schmidt G. D., 2009, [AJ](#), **137**, 3606
- Hiroi K., et al., 2009, [PASJ](#), **61**, 697
- Hirose M., Osaki Y., 1990, [PASJ](#), **42**, 135
- Hjellming M. S., 1989, PhD thesis, University of Illinois, Urbana-Champaign
- Hoard D. W., Szkody P., Linnell A., Long K., Sion E. M., Hubeny I., Knigge C., 2002, in American Astronomical Society Meeting Abstracts. p. 33.04
- Hoard D. W., Linnell A. P., Szkody P., Fried R. E., Sion E. M., Hubeny I., Wolfe M. A., 2004, [ApJ](#), **604**, 346
- Hoard D., Brinkworth C., Howell S., Wachter S., 2007, Circumbinary Dust in Magnetic Cataclysmic Variables - Bright State of AM Her, Spitzer Proposal ID 299
- Hoard D. W., et al., 2009, [ApJ](#), **693**, 236
- Hoard D. W., et al., 2014, [ApJ](#), **786**, 68
- Hodgkin S. T., Wyrzykowski L., Blagorodnova N., Koposov S., 2013, [Philosophical Transactions of the Royal Society of London Series A](#), **371**, 20120239
- Hodgkin S. T., et al., 2019, Transient Name Server Discovery Report, [2019-1818](#), 1
- Hodgkin S. T., et al., 2020, Transient Name Server Discovery Report, [2020-768](#), 1
- Hodgkin S. T., et al., 2021, [A&A](#), **652**, A76
- Hoffmeister C., 1966, [Astronomische Nachrichten](#), **289**, 1
- Holberg J. B., Bergeron P., 2006, [AJ](#), **132**, 1221
- Holberg J. B., Saffer R. A., Tweedy R. W., Barstow M. A., 1995, [ApJ](#), **452**, L133
- Holberg J. B., Oswalt T. D., Sion E. M., McCook G. P., 2016, [MNRAS](#), **462**, 2295
- Hollands M. A., Tremblay P. E., Gänsicke B. T., Gentile-Fusillo N. P., Toonen S., 2018, [MNRAS](#), **480**, 3942
- Homer L., et al., 2005, [ApJ](#), **620**, 929
- Homer L., Szkody P., Chen B., Henden A., Schmidt G., Anderson S. F., Silvestri N. M., Brinkmann J., 2006a, [AJ](#), **131**, 562
- Homer L., Szkody P., Henden A., Chen B., Schmidt G. D., Fraser O. J., West A. A., 2006b, [AJ](#), **132**, 2743
- Honeycutt R. K., 2001, [PASP](#), **113**, 473
- Honeycutt R. K., Kafka S., 2004, [AJ](#), **128**, 1279

- Honeycutt R. K., Robertson J. W., Turner G. W., 1995, [ApJ](#), **446**, 838
- Honeycutt R. K., Robertson J. W., Turner G. W., 1998, [AJ](#), **115**, 2527
- Honeycutt R. K., Kafka S., Robertson J. W., 2013, [AJ](#), **145**, 45
- Horne K., Marsh T. R., 1986, [MNRAS](#), **218**, 761
- Hou W., Luo A. l., Li Y.-B., Qin L., 2020, [AJ](#), **159**, 43
- Houk N., Swift C., 1999, Michigan Spectral Survey, **5**, 0
- Howarth I. D., 1975, Journal of the British Astronomical Association, **85**, 271
- Howarth I. D., 1983, [MNRAS](#), **203**, 301
- Howell S. B., Mason E., 2018, [AJ](#), **156**, 198
- Howell S., Szkody P., 1988, [PASP](#), **100**, 224
- Howell S. B., Szkody P., Kreidl T. J., Mason K. O., Puchnarewicz E. M., 1990, [PASP](#), **102**, 758
- Howell S. B., Nelson L. A., Rappaport S., 2001, [ApJ](#), **550**, 897
- Howell S. B., Harrison T. E., Huber M. E., Szkody P., Walter F. M., Harbeck D., 2008, [AJ](#), **136**, 2541
- Huggins W., 1866, [MNRAS](#), **26**, 275
- Hulse R. A., Taylor J. H., 1975, [ApJ](#), **195**, L51
- Huruhata M., 1983, Information Bulletin on Variable Stars, **2401**, 1
- Husser T. O., Wende-von Berg S., Dreizler S., Homeier D., Reiners A., Barman T., Hauschildt P. H., 2013, [A&A](#), **553**, A6
- Ibeling D., Heger A., 2013, [ApJ](#), **765**, L43
- Iben I. J., 1982, [ApJ](#), **259**, 244
- Iben Icko J., Livio M., 1993, [PASP](#), **105**, 1373
- Iben Icko J., Ritossa C., García-Berro E., 1997, [ApJ](#), **489**, 772
- Ingram A., Done C., 2011, [MNRAS](#), **415**, 2323
- Ingram A., Done C., 2012, [MNRAS](#), **419**, 2369
- Ingram A., van der Klis M., 2013, [MNRAS](#), **434**, 1476
- Inight K., Gänsicke B. T., Breedt E., Marsh T. R., Pala A. F., Raddi R., 2021, [MNRAS](#), **504**, 2420
- Inight K., et al., 2022, [MNRAS](#), **510**, 3605
- Inight K., et al., 2023a, [arXiv e-prints](#), p. [arXiv:2304.06749](#)
- Inight K., et al., 2023b, [MNRAS](#), **524**, 4867
- Ishioka R., et al., 2001, [PASJ](#), **53**, 905
- Isogai K., et al., 2019a, [PASJ](#), **71**, 22
- Isogai K., Kawabata M., Maeda K., 2019b, The Astronomer’s Telegram, **13277**, 1
- Ivanova N., et al., 2013, [A&A Rev.](#), **21**, 59
- Ivezić Ž., et al., 2007, [AJ](#), **134**, 973
- Jablonski F. J., Cieslinski D., 1992, [A&A](#), **259**, 198
- Jayasinghe T., et al., 2018, [MNRAS](#), **477**, 3145
- Jayasinghe T., et al., 2019, [MNRAS](#), **485**, 961
- Jurdana-Šepić R., Poljančič Beljan I., 2015, Central European Astrophysical Bulletin, **39**, 161
- Kabath P., et al., 2009, [A&A](#), **506**, 569
- Kafka S., Honeycutt R. K., 2004, [AJ](#), **128**, 2420
- Kafka S., Honeycutt R. K., 2005, [AJ](#), **130**, 742
- Kafka S., Hoard D. W., Honeycutt R. K., Deliyannis C. P., 2009, [AJ](#), **137**, 197

- Kahabka P., van den Heuvel E. P. J., 1997, [ARA&A](#), **35**, 69
- Kamiński K. Z., et al., 2007, [AJ](#), **134**, 1206
- Kaplan D. L., et al., 2014, [ApJ](#), **780**, 167
- Karachentsev I. D., et al., 2003, [A&A](#), **398**, 467
- Karl C. A., Napiwotzki R., Nelemans G., Christlieb N., Koester D., Heber U., Reimers D., 2003, [A&A](#), **410**, 663
- Kato T., 2015, [PASJ](#), **67**, 108
- Kato T., 2019, [PASJ](#), **71**, 20
- Kato T., Osaki Y., 2013, [PASJ](#), **65**, 115
- Kato T., Uemura M., 2000, *Information Bulletin on Variable Stars*, **4902**, 1
- Kato T., Yamaoka H., 2002, *Information Bulletin on Variable Stars*, **5334**, 1
- Kato T., Nogami D., Baba H., 1996, [PASJ](#), **48**, L93
- Kato T., Uemura M., Ishioka R., Matsumoto K., Tanabe K., 2002, *Information Bulletin on Variable Stars*, **5284**, 1
- Kato T., Nogami D., Matsumoto K., Baba H., 2004, [PASJ](#), **56**, S109
- Kato T., et al., 2009, [PASJ](#), **61**, S395
- Kato T., et al., 2010, [PASJ](#), **62**, 1525
- Kato T., et al., 2012a, [PASJ](#), **64**, 21
- Kato T., Maehara H., Uemura M., 2012b, [PASJ](#), **64**, 63
- Kato T., Nogami D., Baba H., Masuda S., Matsumoto K., Kunjaya C., 2013a, [arXiv e-prints](#), p. [arXiv:1301.3202](#)
- Kato T., et al., 2013b, [PASJ](#), **65**, 23
- Kato T., et al., 2014a, [PASJ](#), **66**, 30
- Kato T., et al., 2014b, [PASJ](#), **66**, 90
- Kato T., et al., 2015, [PASJ](#), **67**, 105
- Kato T., et al., 2016a, [PASJ](#), **68**, 49
- Kato T., et al., 2016b, [PASJ](#), **68**, 65
- Kato T., et al., 2017, [PASJ](#), **69**, 75
- Kato T., et al., 2020, [PASJ](#), **72**, 14
- Kato T., et al., 2021, [PASJ](#), **73**, 1280
- Katysheva N. A., Pavlenko E. P., 2003, [Astrophysics](#), **46**, 114
- Kawka A., Vennes S., 2003, [AJ](#), **125**, 1444
- Kawka A., Vennes S., Dupuis J., Chayer P., Lanz T., 2008, [ApJ](#), **675**, 1518
- Kawka A., Vennes S., Vaccaro T. R., 2010, [A&A](#), **516**, L7
- Kazarovets E. V., Samus N. N., Durlevich O. V., Kireeva N. N., Pastukhova E. N., 2013, *Information Bulletin on Variable Stars*, **6052**, 1
- Kennedy M. R., et al., 2016, [AJ](#), **152**, 27
- Kennedy M. R., Callanan P., Garnavich P. M., Fausnaugh M., Zinn J. C., 2017, [MNRAS](#), **466**, 2202
- Kepler S. O., Kleinman S. J., Nitta A., Koester D., Castanheira B. G., Giovannini O., Costa A. F. M., Althaus L., 2007, [MNRAS](#), **375**, 1315
- Kepler S. O., et al., 2015, [MNRAS](#), **446**, 4078
- Kepler S. O., et al., 2016, [MNRAS](#), **455**, 3413
- Kepler S. O., et al., 2019, [MNRAS](#), **486**, 2169

- Kepler S. O., Koester D., Pelisoli I., Romero A. D., Ourique G., 2021, *MNRAS*, **507**, 4646
- Kesseli A. Y., West A. A., Veyette M., Harrison B., Feldman D., Bochanski J. J., 2017, *ApJS*, **230**, 16
- Kholopov P. N., Samus' N. N., Kukarkina N. P., Medvedeva G. I., Perova N. B., 1981, *Information Bulletin on Variable Stars*, **2042**, 1
- Kiman R., Schmidt S. J., Angus R., Cruz K. L., Faherty J. K., Rice E., 2019, *AJ*, **157**, 231
- King A. R., 1988, *QJRAS*, **29**, 1
- King A. R., Cannizzo J. K., 1998, *ApJ*, **499**, 348
- King A. R., Kolb U., 1995, *ApJ*, **439**, 330
- King A. R., Schenker K., Hameury J. M., 2002, *MNRAS*, **335**, 513
- Kippenhahn R., Weigert A., Weiss A., 2013, *Stellar Structure and Evolution*. Springer, doi:10.1007/978-3-642-30304-3
- Kiraga M., Stepień K., 2013, *Acta Astronomica*, **63**, 53
- Kleinman S. J., et al., 2013, *ApJS*, **204**, 5
- Knigge C., 2006, *MNRAS*, **373**, 484
- Knigge C., Long K. S., Wade R. A., Baptista R., Horne K., Hubeny I., Rutten R. G. M., 1998, *ApJ*, **499**, 414
- Knigge C., Baraffe I., Patterson J., 2011, *ApJS*, **194**, 28
- Koester D., Voss B., Napiwotzki R., Christlieb N., Homeier D., Lisker T., Reimers D., Heber U., 2009, *A&A*, **505**, 441
- Kolb U., 1993, *A&A*, **271**, 149
- Kolb U., Baraffe I., 1999, *MNRAS*, **309**, 1034
- Kolb U., Stehle R., 1996, *MNRAS*, **282**, 1454
- Kolbin A. I., Serebryakova N. A., Gabdeev M. M., Borisov N. V., 2019, *Astrophysical Bulletin*, **74**, 80
- Kollmeier J. A., et al., 2017, *arXiv e-prints*, p. arXiv:1711.03234
- Kong X., Luo A. L., Li X.-R., Wang Y.-F., Li Y.-B., Zhao J.-K., 2018, *PASP*, **130**, 084203
- Kosakowski A., Kilic M., Brown W. R., Gianninas A., 2020, *ApJ*, **894**, 53
- Kowalski P. M., Saumon D., 2006, *ApJ*, **651**, L137
- Krajci T., Wils P., 2010, *AAVSO*, **38**, 33
- Kraus A. L., Craine E. R., Giampapa M. S., Scharlach W. W. G., Tucker R. A., 2007, *AJ*, **134**, 1488
- Kreiner J. M., 2004, *Acta Astronomica*, **54**, 207
- Kroupa P., Tout C. A., Gilmore G., 1993, *MNRAS*, **262**, 545
- Kruse E., Agol E., 2014, *Science*, **344**, 275
- Krushinsky V., et al., 2020, *MNRAS*, **493**, 5208
- Kube J., Gänsicke B. T., Beuermann K., 2000, *A&A*, **356**, 490
- Kukarkin B. V., Parenago P. P., 1949, English version of introduction and remarks from The general catalogue of variable stars. USSR Academy of Sciences, Moscow
- Kupfer T., Groot P. J., Levitan D., Steeghs D., Marsh T. R., Rutten R. G. M., Nelemans G., 2013, *MNRAS*, **432**, 2048
- Kupfer T., Breedt E., Ramsay G., Hodgkin S., Marsh T., 2019, *The Astronomer's Telegram*, **12558**, 1
- Kuulkers E., Page K. L., Knigge C., Marsh T. R., Osborne J. P., Sivakoff G. R., 2013, *The*

- Astronomer's Telegram, [4716](#), 1
- Lagos F., et al., 2020a, [MNRAS](#), **494**, 915
- Lagos F., Schreiber M. R., Parsons S. G., Gänsicke B. T., Godoy N., 2020b, [MNRAS](#), **499**, L121
- Lallement R., Babusiaux C., Vergely J. L., Katz D., Arenou F., Valette B., Hottier C., Capitanio L., 2019, [A&A](#), **625**, A135
- Landi R., Bassani L., Dean A. J., Bird A. J., Fiocchi M., Bazzano A., Nousek J. A., Osborne J. P., 2009, [MNRAS](#), **392**, 630
- Leach R., Hessman F. V., King A. R., Stehle R., Mattei J., 1999, [MNRAS](#), **305**, 225
- Lehtinen J. J., Spada F., Käpylä M. J., Olsper N., Käpylä P. J., 2020, [Nature Astronomy](#), **4**, 658
- Liaw A., Wiener M., 2001, *Forest*, 23
- Lightkurve Collaboration et al., 2018, Lightkurve: Kepler and TESS time series analysis in Python, Astrophysics Source Code Library, record ascl:1812.013 (ascl:1812.013)
- Lindgren L., 2018, Re-normalising the astrometric chi-square in Gaia DR2, GAIA-C3-TN-LU-LL-124, http://www.rssd.esa.int/doc_fetch.php?id=3757412
- Lindgren L., et al., 2018, [A&A](#), **616**, A2
- Littlefair S. P., Dhillon V. S., Marsh T. R., Gänsicke B. T., Southworth J., Watson C. A., 2006, [Science](#), **314**, 1578
- Littlefair S. P., Dhillon V. S., Marsh T. R., Gänsicke B. T., Baraffe I., Watson C. A., 2007, [MNRAS](#), **381**, 827
- Littlefair S. P., Dhillon V. S., Marsh T. R., Gänsicke B. T., Southworth J., Baraffe I., Watson C. A., Copperwheat C., 2008, [MNRAS](#), **388**, 1582
- Littlefield C., Garnavich P., Magno K., Murison M., Deal S., McClelland C., Rose B., 2015, [Information Bulletin on Variable Stars](#), **6129**, 1
- Littlefield C., et al., 2023a, [AJ](#), **165**, 43
- Littlefield C., et al., 2023b, [ApJ](#), **943**, L24
- Liu W., Hu J. Y., 2000, [ApJS](#), **128**, 387
- Liu W.-M., Jiang L., Chen W.-C., 2021, [ApJ](#), **910**, 22
- Livio M., Pringle J. E., 1994, [ApJ](#), **427**, 956
- Lohmann W., 1949, [Astronomische Nachrichten](#), **277**, 37
- Long K. S., Knigge C., 2002, [ApJ](#), **579**, 725
- Long K. S., Mauche C. W., Raymond J. C., Szkody P., Mattei J. A., 1996, [ApJ](#), **469**, 841
- Lyubarskii Y. E., 1997, [MNRAS](#), **292**, 679
- Maccarone T. J., Kupfer T., Najera Casarrubias E., Rivera Sandoval L., Shaw A., Britt C., van Roestel J., Zurek D., 2023, [arXiv e-prints](#), p. [arXiv:2302.12318](#)
- Magnier E. A., et al., 2013, [ApJS](#), **205**, 20
- Malkova A., et al., 2016, The Astronomer's Telegram, [8956](#), 1
- Manser C. J., Gänsicke B. T., 2014, [MNRAS](#), **442**, L23
- Margon B., Levitan D., Prince T. A., Hallinan G., PTF Collaboration 2014, in Woudt P. A., Ribeiro V. A. R. M., eds, *Astronomical Society of the Pacific Conference Series Vol. 490, Stellar Novae: Past and Future Decades*. p. 389 ([arXiv:1304.4585](#)), [doi:10.48550/arXiv.1304.4585](#)
- Marsh T. R., 1989, [PASP](#), **101**, 1032

- Marsh T. R., 1990, [ApJ](#), **357**, 621
- Marsh T. R., 1995, [MNRAS](#), **275**, L1
- Marsh T. R., 1999, [MNRAS](#), **304**, 443
- Marsh T., 2019, molly: 1D astronomical spectra analyzer, Astrophysics Source Code Library, record ascl:1907.012 (ascl:1907.012)
- Marsh T. R., Dhillon V. S., Duck S. R., 1995, [MNRAS](#), **275**, 828
- Marsh T. R., et al., 2002, in Gänsicke B. T., Beuermann K., Reinsch K., eds, *Astronomical Society of the Pacific Conference Series Vol. 261, The Physics of Cataclysmic Variables and Related Objects*. p. 200 ([arXiv:astro-ph/0108334](#)), doi:10.48550/arXiv.astro-ph/0108334
- Marsh T. R., et al., 2016, [Nature](#), **537**, 374
- Martínez-Pais I. G., Martín-Hernández N. L., Casares J., Rodríguez-Gil P., 2000, [ApJ](#), **538**, 315
- Martini P., et al., 2011, [PASP](#), **123**, 187
- Masci F. J., et al., 2019, [PASP](#), **131**, 018003
- Mason E., Skidmore W., Howell S. B., Ciardi D. R., Littlefair S., Dhillon V. S., 2000, [MNRAS](#), **318**, 440
- Mason K. O., et al., 2001, [A&A](#), **365**, L36
- Mason P. A., Wells N. K., Motsoaledi M., Szkody P., Gonzalez E., 2019, [MNRAS](#), **488**, 2881
- Mattei J. A., Cook L. M., McMahon A. T. P., Foster R. M., 1986, *AAVSO*, **15**, 3
- Matthews J. H., Knigge C., Long K. S., Sim S. A., Higginbottom N., 2015, [MNRAS](#), **450**, 3331
- Mauche C. W., Mukai K., 2002, [ApJ](#), **566**, L33
- Maxted P. F. L., Marsh T. R., Moran C., Dhillon V. S., Hilditch R. W., 1998, [MNRAS](#), **300**, 1225
- Maxted P. F. L., Marsh T. R., Moran C. K. J., Han Z., 2000a, [MNRAS](#), **314**, 334
- Maxted P. F. L., Marsh T. R., Moran C. K. J., 2000b, [MNRAS](#), **319**, 305
- Maxted P. F. L., Marsh T. R., Moran C. K. J., 2002a, [MNRAS](#), **332**, 745
- Maxted P. F. L., Burleigh M. R., Marsh T. R., Bannister N. P., 2002b, [MNRAS](#), **334**, 833
- Maxted P. F. L., Napiwotzki R., Marsh T. R., Burleigh M. R., Dobbie P. D., Hogan E., Nelemans G., 2007, in Napiwotzki R., Burleigh M. R., eds, *Astronomical Society of the Pacific Conference Series Vol. 372, 15th European Workshop on White Dwarfs*. p. 471
- Maxted P. F. L., et al., 2014, [MNRAS](#), **437**, 1681
- McAllister M. J., et al., 2015, [MNRAS](#), **451**, 114
- McAllister M. J., et al., 2017, [MNRAS](#), **467**, 1024
- McAllister M., et al., 2019, [MNRAS](#), **486**, 5535
- McCleery J., et al., 2020, [MNRAS](#), **499**, 1890
- Mennickent R. E., Nogami D., Kato T., Worraker W., 1996, [A&A](#), **315**, 493
- Mennickent R. E., Diaz M., Skidmore W., Sterken C., 2001, [A&A](#), **376**, 448
- Merc J., et al., 2021, [MNRAS](#), **506**, 4151
- Merrill P. W., 1923, [ApJ](#), **58**, 215
- Meyer F., Meyer-Hofmeister E., 1979, [A&A](#), **78**, 167
- Meyer F., Meyer-Hofmeister E., 1981, [A&A](#), **104**, L10
- Meyer F., Meyer-Hofmeister E., 1984, [A&A](#), **132**, 143
- Meyer F., Meyer-Hofmeister E., 1994, [A&A](#), **288**, 175
- Miller W. J., 1971, *Ricerche Astronomiche*, **8**, 167

- Mittaz J. P. D., Rosen S. R., Mason K. O., Howell S. B., 1992, *MNRAS*, **258**, 277
- Monard L. A. G., Africa S., 2005, *IAU Circ.*, **8540**, 3
- Morales-Rueda L., Marsh T. R., Maxted P. F. L., Nelemans G., Karl C., Napiwotzki R., Moran C. K. J., 2005, *MNRAS*, **359**, 648
- Moran C., Marsh T. R., Bragaglia A., 1997, *MNRAS*, **288**, 538
- Morganson E., et al., 2015, *ApJ*, **806**, 244
- Morokuma T., Tominaga N., Matsumoto E., Shibata T., Yamanaka M., Tanaka M., 2014, *Central Bureau Electronic Telegrams*, **4013**, 1
- Morrissey P., et al., 2007, *ApJS*, **173**, 682
- Mowlavi N., et al., 2021, *A&A*, **648**, A44
- Mróz P., et al., 2015, *Acta Astronomica*, **65**, 313
- Mróz P., et al., 2016, *Nature*, **537**, 649
- Mukadam A. S., Gänsicke B. T., Szkody P., Aungwerojwit A., Howell S. B., Fraser O. J., Silvestri N. M., 2007, *ApJ*, **667**, 433
- Mukai K., 2017, *PASP*, **129**, 062001
- Mukai K., et al., 1990, *MNRAS*, **245**, 385
- Mukai K., Baumgartner W., Tueller J., Mushotzky R., Kennea J., Cenko B., Rau A., Markwardt C., 2007, *The Astronomer's Telegram*, **1309**, 1
- Munari U., Bianchini A., Claudi R., 1990, *IAU Circ.*, **5024**, 2
- Munari U., Valisa P., Marinelli M., Dallaporta S., Skiff B., 2011, *Central Bureau Electronic Telegrams*, **2617**, 1
- Munari U., Mason E., Valisa P., 2014, *A&A*, **564**, A76
- Munari U., Jurdana-Šepić R., Ochner P., Cherini G., 2015, *A&A*, **584**, A12
- Munari U., Moretti S., Maitan A., 2020, *A&A*, **639**, L10
- Nakano S., Tago A., Nishiyama K., Sakamoto T., 2007, *IAU Circ.*, **8821**, 1
- Nakata C., et al., 2013, *PASJ*, **65**, 117
- Nakata C., et al., 2014, *PASJ*, **66**, 116
- Napiwotzki R., et al., 2002, *A&A*, **386**, 957
- Napiwotzki R., et al., 2020, *A&A*, **638**, A131
- National Astronomical Observatories C. A. o. S., 2019, LAMOST DR5 Spectra Web Interface, VO resource provided by the GAVO Data Center, <https://dc.zah.uni-heidelberg.de/lamost5/q/web/info>
- Nebot Gómez-Morán A., et al., 2011, *A&A*, **536**, A43
- Nelemans G., Yungelson L. R., Portegies Zwart S. F., 2004, *MNRAS*, **349**, 181
- Nelemans G., et al., 2005, *A&A*, **440**, 1087
- Nelemans G., Siess L., Repetto S., Toonen S., Phinney E. S., 2016, *ApJ*, **817**, 69
- Nelson B., Young A., 1970, *PASP*, **82**, 699
- Neustroev V. V., Suleimanov V. F., Borisov N. V., Belyakov K. V., Shearer A., 2011, *MNRAS*, **410**, 963
- Neustroev V. V., et al., 2017, *MNRAS*, **467**, 597
- Newville M., Stensitzki T., Allen D. B., Rawlik M., Ingargiola A., Nelson A., 2016, *Lmfit: Non-Linear Least-Square Minimization and Curve-Fitting for Python*, Astrophysics Source Code Library, record ascl:1606.014 (ascl:1606.014)
- Nixon C. J., Pringle J. E., 2019, *A&A*, **628**, A121

- Noebauer U. M., Long K. S., Sim S. A., Knigge C., 2010, *ApJ*, **719**, 1932
- Nogami D., Kato T., Baba H., Masuda S., 1998, *PASJ*, **50**, L1
- Nogami D., et al., 2004a, *PASJ*, **56**, S99
- Nogami D., Uemura M., Ishioka R., Kato T., Pietz J., 2004b, *PASJ*, **56**, S155
- Norton A. J., Wynn G. A., Somerscales R. V., 2004, *ApJ*, **614**, 349
- Norton A. J., Butters O. W., Parker T. L., Wynn G. A., 2008, *ApJ*, **672**, 524
- Nucita A. A., De Paolis F., Licchelli D., Strafella F., Ingrosso G., Maiorano M., 2021, *ApJ*, **906**, 134
- O’Brien M. S., Bond H. E., Sion E. M., 2001, *ApJ*, **563**, 971
- O’Donoghue D., Kilkenny D., Chen A., Stobie R. S., Koen C., Warner B., Lawson W. A., 1994, *MNRAS*, **271**, 910
- Olech A., Rutkowski A., Schwarzenberg-Czerny A., 2009, *MNRAS*, **399**, 465
- Olech A., et al., 2011, *A&A*, **532**, A64
- Oliveira A. S., Rodrigues C. V., Cieslinski D., Jablonski F. J., Silva K. M. G., Almeida L. A., Rodríguez-Ardila A., Palhares M. S., 2017, *AJ*, **153**, 144
- Oliveira A. S., Rodrigues C. V., Martins M., Palhares M. S., Silva K. M. G., Lima I. J., Jablonski F. J., 2020, *AJ*, **159**, 114
- Oppenheimer B. R., Kulkarni S. R., Stauffer J. R., 1998, *arXiv e-prints*, pp astro-ph/9812091
- Osaki Y., 1974, *PASJ*, **26**, 429
- Osaki Y., 1989, *PASJ*, **41**, 1005
- Osaki Y., 1996, *PASP*, **108**, 39
- Osborne J. P., Beardmore A. P., Wheatley P. J., Hakala P., Watson M. G., Mason K. O., Hassall B. J. M., King A. R., 1994, *MNRAS*, **270**, 650
- Ovcharov E., Kurtenkov A., Enikova P., Ganchev G., Bozhilov V., Tsvetkov T., Genkova T., 2013, *The Astronomer’s Telegram*, **5564**, 1
- Paczyński B., 1967, *Acta Astronomica*, **17**, 287
- Paczyński B., 1971, *ARA&A*, **9**, 183
- Paczynski B., 1976, in Eggleton P., Mitton S., Whelan J., eds, *IAU SYMPOSIUM Vol. 73, Structure and Evolution of Close Binary Systems*. p. 75
- Paczynski B., Schwarzenberg-Czerny A., 1980, *Acta Astronomica*, **30**, 127
- Page M. J., et al., 2012, *MNRAS*, **426**, 903
- Page M. J., et al., 2013, *MNRAS*, **436**, 1684
- Pala A. F., et al., 2017, *MNRAS*, **466**, 2855
- Pala A. F., Schmidtobreick L., Tappert C., Gänsicke B. T., Mehner A., 2018, *MNRAS*, **481**, 2523
- Pala A. F., et al., 2019, *MNRAS*, **483**, 1080
- Pala A. F., et al., 2020, *MNRAS*, **494**, 3799
- Pala A. F., et al., 2022, *MNRAS*, **510**, 6110
- Palaversa L., et al., 2013, *AJ*, **146**, 101
- Pâris I., et al., 2017, *A&A*, **597**, A79
- Parisi P., et al., 2014, *A&A*, **561**, A67
- Parsons S. G., et al., 2012, *MNRAS*, **426**, 1950
- Parsons S. G., et al., 2013a, *MNRAS*, **429**, 256
- Parsons S. G., Marsh T. R., Gänsicke B. T., Schreiber M. R., Bours M. C. P., Dhillon V. S.,

- Littlefair S. P., 2013b, *MNRAS*, **436**, 241
- Parsons S. G., et al., 2015a, *MNRAS*, **449**, 2194
- Parsons S. G., et al., 2015b, *MNRAS*, **452**, 1754
- Parsons S. G., Rebassa-Mansergas A., Schreiber M. R., Gänsicke B. T., Zorotovic M., Ren J. J., 2016, *MNRAS*, **463**, 2125
- Parsons S. G., Gänsicke B. T., Schreiber M. R., Marsh T. R., Ashley R. P., Breedt E., Littlefair S. P., Meusinger H., 2021, *MNRAS*, **502**, 4305
- Parsons S. G., et al., 2023, *MNRAS*, **518**, 4579
- Paterson K., Woudt P. A., Warner B., Breytenbach H., Gilligan C. K., Motsoaledi M., Thorstensen J. R., Worters H. L., 2019, *MNRAS*, **486**, 2422
- Patterson J., 1984, *ApJS*, **54**, 443
- Patterson J., 1994, *PASP*, **106**, 209
- Patterson J., 1998, *PASP*, **110**, 1132
- Patterson J., 2011, *MNRAS*, **411**, 2695
- Patterson J., et al., 1998, *PASP*, **110**, 1290
- Patterson J., et al., 2002, *PASP*, **114**, 721
- Patterson J., et al., 2003, *PASP*, **115**, 1308
- Patterson J., Thorstensen J. R., Kemp J., 2005a, *PASP*, **117**, 427
- Patterson J., et al., 2005b, *PASP*, **117**, 1204
- Patterson J., et al., 2013, *MNRAS*, **434**, 1902
- Pavlenko E., et al., 2007, in Napiwotzki R., Burleigh M. R., eds, *Astronomical Society of the Pacific Conference Series Vol. 372, 15th European Workshop on White Dwarfs*. p. 511 ([arXiv:0712.1956](https://arxiv.org/abs/0712.1956)), [doi:10.48550/arXiv.0712.1956](https://doi.org/10.48550/arXiv.0712.1956)
- Pavlenko E. P., et al., 2018, *MNRAS*, **479**, 341
- Perlmutter S., 2003, *Physics Today*, **56**, 53
- Peters P. C., 1964, *Physical Review*, **136**, 1224
- Peters C. S., Thorstensen J. R., 2005, *PASP*, **117**, 1386
- Peters C. S., Thorstensen J. R., 2006, *PASP*, **118**, 687
- Petit M., 1960, *Journal des Observateurs*, **43**, 17
- Pickering E. C., Fleming W. P., 1896, *ApJ*, **4**, 369
- Podsiadlowski P., Han Z., Rappaport S., 2003, *MNRAS*, **340**, 1214
- Poggiani R., 2009, *Astronomische Nachrichten*, **330**, 77
- Pogson N., 1857, *MNRAS*, **17**, 200
- Politano M., 1996, *ApJ*, **465**, 338
- Potter S. B., 2016, in Boffin H. M. J., Hussain G., Berger J.-P., Schmidtbreick L., eds, *Astrophysics and Space Science Library Vol. 439, Astronomy at High Angular Resolution*. p. 179, [doi:10.1007/978-3-319-39739-9_10](https://doi.org/10.1007/978-3-319-39739-9_10)
- Pretorius M. L., Knigge C., 2012, *MNRAS*, **419**, 1442
- Pretorius M. L., Woudt P. A., Warner B., Bolt G., Patterson J., Armstrong E., 2004, *MNRAS*, **352**, 1056
- Pretorius M. L., Knigge C., Kolb U., 2007a, *MNRAS*, **374**, 1495
- Pretorius M. L., Knigge C., O'Donoghue D., Henry J. P., Gioia I. M., Mullis C. R., 2007b, *MNRAS*, **382**, 1279
- Pretorius M. L., Knigge C., Schwöpe A. D., 2013, *MNRAS*, **432**, 570

- Price-Whelan A. M., Hogg D. W., Foreman-Mackey D., Rix H.-W., 2017, [ApJ](#), **837**, 20
- Prieto J. L., et al., 2013, The Astronomer’s Telegram, [5102](#), 1
- Pringle J. E., 1981, [ARA&A](#), **19**, 137
- Proga D., Stone J. M., Drew J. E., 1998, [MNRAS](#), **295**, 595
- Puebla R. E., Diaz M. P., Hubeny I., 2007, [AJ](#), **134**, 1923
- Pyrzas S., et al., 2012, [MNRAS](#), **419**, 817
- Quimby R., Mondol P., 2006, The Astronomer’s Telegram, [787](#), 1
- Raghavan D., et al., 2010, [ApJS](#), **190**, 1
- Ramsay G., Potter S. B., Buckley D. A. H., Wheatley P. J., 1999, [MNRAS](#), **306**, 809
- Ramsay G., Cropper M., Wu K., Mason K. O., Córdova F. A., Friedhorsky W., 2004, [MNRAS](#), **350**, 1373
- Ramsay G., Wheatley P. J., Norton A. J., Hakala P., Baskill D., 2008, [MNRAS](#), **387**, 1157
- Ramsay G., et al., 2018, [A&A](#), **620**, A141
- Rappaport S., Verbunt F., Joss P. C., 1983, [ApJ](#), **275**, 713
- Raymond S. N., et al., 2003, [AJ](#), **125**, 2621
- Rebassa-Mansergas A., Gänsicke B. T., Rodríguez-Gil P., Schreiber M. R., Koester D., 2007, [MNRAS](#), **382**, 1377
- Rebassa-Mansergas A., Gänsicke B. T., Schreiber M. R., Koester D., Rodríguez-Gil P., 2010, [MNRAS](#), **402**, 620
- Rebassa-Mansergas A., Nebot Gómez-Morán A., Schreiber M. R., Girven J., Gänsicke B. T., 2011, [MNRAS](#), **413**, 1121
- Rebassa-Mansergas A., Nebot Gómez-Morán A., Schreiber M. R., Gänsicke B. T., Schwöpe A., Gallardo J., Koester D., 2012a, [MNRAS](#), **419**, 806
- Rebassa-Mansergas A., et al., 2012b, [MNRAS](#), **423**, 320
- Rebassa-Mansergas A., Agurto-Gangas C., Schreiber M. R., Gänsicke B. T., Koester D., 2013, [MNRAS](#), **433**, 3398
- Rebassa-Mansergas A., Parsons S. G., Copperwheat C. M., Justham S., Gänsicke B. T., Schreiber M. R., Marsh T. R., Dhillon V. S., 2014, [ApJ](#), **790**, 28
- Rebassa-Mansergas A., Ren J. J., Parsons S. G., Gänsicke B. T., Schreiber M. R., García-Berro E., Liu X. W., Koester D., 2016, [MNRAS](#), **458**, 3808
- Rebassa-Mansergas A., Parsons S. G., García-Berro E., Gänsicke B. T., Schreiber M. R., Rybicka M., Koester D., 2017a, [MNRAS](#), **466**, 1575
- Rebassa-Mansergas A., et al., 2017b, [MNRAS](#), **472**, 4193
- Rebull L., et al., 2019, in Molinaro M., Shortridge K., Pasian F., eds, Astronomical Society of the Pacific Conference Series Vol. 521, Astronomical Data Analysis Software and Systems XXVI. p. 36
- Reimers D., Hagen H. J., 2000, [A&A](#), **358**, L45
- Reimers D., Hagen H. J., Hopp U., 1999, [A&A](#), **343**, 157
- Reis R. C., Wheatley P. J., Gänsicke B. T., Osborne J. P., 2013, [MNRAS](#), **430**, 1994
- Ren J. J., et al., 2020, [ApJ](#), **905**, 38
- Ribeiro F. M. A., Diaz M. P., 2007, [AJ](#), **133**, 2659
- Richards G. T., et al., 2002, [AJ](#), **123**, 2945
- Richter G. A., 1970, Zentralinstitut fuer Astrophysik Sternwarte Sonneberg Mitteilungen ueber Veraenderliche Sterne, **5**, 99

- Richter G. A., Notni P., Borngen F., Afanas'ev V. L., Karachentsev I. D., Kopylov A., 1981, [Astronomische Nachrichten](#), **302**, 211
- Richter G. A., Notni P., Tiersch H., 1988, [Astronomische Nachrichten](#), **309**, 91
- Richter G. A., Kroll P., Greiner J., Wenzel W., Luthardt R., Schwarz R., 1997, [A&A](#), **325**, 994
- Ricker G. R., et al., 2015, [Journal of Astronomical Telescopes, Instruments, and Systems](#), **1**, 014003
- Riess A. G., et al., 1998, [AJ](#), **116**, 1009
- Ringwald F. A., Chase D. W., Reynolds D. S., 2005, [PASP](#), **117**, 1223
- Ringwald F. A., Rude G. D., Roveto J. J., Khamvongsa K. S., 2012, [New Astronomy](#), **17**, 570
- Ritter H., Kolb U., 1998, [A&AS](#), **129**, 83
- Ritter H., Kolb U., 2003, [A&A](#), **404**, 301
- Robertson J. W., Honeycutt R. K., Turner G. W., 1995, [PASP](#), **107**, 443
- Robertson J. W., Honeycutt R. K., Henden A. A., Campbell R. T., 2018, [AJ](#), **155**, 61
- Rodrigues C. V., Jablonski F. J., D'Amico F., Cieslinski D., Steiner J. E., Diaz M. P., Hickel G. R., 2006, [MNRAS](#), **369**, 1972
- Rodríguez-Gil P., Gänsicke B. T., Araujo-Betancor S., Casares J., 2004, [MNRAS](#), **349**, 367
- Rodríguez-Gil P., Gänsicke B. T., Hagen H. J., Marsh T. R., Harlaftis E. T., Kitsionas S., Engels D., 2005a, [A&A](#), **431**, 269
- Rodríguez-Gil P., et al., 2005b, [A&A](#), **440**, 701
- Rodríguez-Gil P., Schmidtobreick L., Gänsicke B. T., 2007a, [MNRAS](#), **374**, 1359
- Rodríguez-Gil P., et al., 2007b, [MNRAS](#), **377**, 1747
- Rodríguez A. C., et al., 2023, [ApJ](#), **945**, 141
- Roelofs G. H. A., Groot P. J., Marsh T. R., Steeghs D., Barros S. C. C., Nelemans G., 2005, [MNRAS](#), **361**, 487
- Roelofs G. H. A., Groot P. J., Steeghs D., Marsh T. R., Nelemans G., 2007, [MNRAS](#), **382**, 1643
- Roelofs G. H. A., et al., 2009, [MNRAS](#), **394**, 367
- Roming P. W. A., et al., 2005, [Space Sci. Rev.](#), **120**, 95
- Rosino L., Romano G., Marziani P., 1993, [PASP](#), **105**, 51
- Ross N. P., et al., 2012, [ApJS](#), **199**, 3
- Ruiz M. T., Rojo P. M., Garay G., Maza J., 2001, [ApJ](#), **552**, 679
- Rutkowski A., Olech A., Wiśniewski M., Pietrukowicz P., Pala J., Poleski R., 2009, [A&A](#), **497**, 437
- Rutkowski A., Olech A., Poleski R., Sobolewska M., Kankiewicz P., Ak T., Boyd D., 2010, [Acta Astronomica](#), **60**, 337
- Rykoff E. S., et al., 2004, [Information Bulletin on Variable Stars](#), **5559**, 1
- Ryu K., et al., 2006, [ApJ](#), **644**, L185
- Sahman D. I., Dhillon V. S., 2022, [MNRAS](#), **510**, 4180
- Sahman D. I., Dhillon V. S., Knigge C., Marsh T. R., 2015, [MNRAS](#), **451**, 2863
- Savonije G. J., de Kool M., van den Heuvel E. P. J., 1986, [A&A](#), **155**, 51
- Savoury C. D. J., et al., 2011, [MNRAS](#), **415**, 2025
- Scaringi S., 2014, [MNRAS](#), **438**, 1233
- Scaringi S., et al., 2010, [MNRAS](#), **401**, 2207
- Scaringi S., KÖrding E., Uttley P., Knigge C., Groot P. J., Still M., 2012, [MNRAS](#), **421**, 2854
- Scaringi S., Groot P. J., Verbeek K., Greiss S., Knigge C., KÖrding E., 2013, [MNRAS](#), **428**,

2207

- Scaringi S., et al., 2015, *Science Advances*, **1**, e1500686
- Schaefer B. E., 2021, *Research Notes of the American Astronomical Society*, **5**, 150
- Schaefer B. E., et al., 2019, *MNRAS*, **487**, 1120
- Schenker K., Kolb U., Ritter H., 1998, *MNRAS*, **297**, 633
- Schimeczek C., Wunner G., 2014, *ApJS*, **212**, 26
- Schlafly E. F., Finkbeiner D. P., 2011, *ApJ*, **737**, 103
- Schlegel E. M., Honeycutt R. K., 2019, *ApJ*, **876**, 152
- Schlindwein W., Baptista R., 2018, *MNRAS*, **478**, 3841
- Schmadel L. D., Schmeer P., Börngen F., 1996, *A&A*, **312**, 496
- Schmidt R. E., 2020, *AAVSO*, **48**, 53
- Schmidt G. D., et al., 2003, *ApJ*, **595**, 1101
- Schmidt G. D., et al., 2005a, *ApJ*, **620**, 422
- Schmidt G. D., et al., 2005b, *ApJ*, **630**, 1037
- Schmidt G. D., Smith P. S., Szkody P., Anderson S. F., 2008, *PASP*, **120**, 160
- Schmidtobreick L., 2017, *arXiv e-prints*, p. arXiv:1705.09332
- Schmidtobreick L., Mason E., Howell S. B., Long K. S., Pala A. F., Points S., Walter F. M., 2018, *A&A*, **617**, A16
- Schmitt J. H. M. M., Fleming T. A., Giampapa M. S., 1995, *ApJ*, **450**, 392
- Schreiber M. R., Gänsicke B. T., 2003, *A&A*, **406**, 305
- Schreiber M. R., Gänsicke B. T., Mattei J. A., 2002, *A&A*, **384**, L6
- Schreiber M. R., et al., 2010, *A&A*, **513**, L7
- Schreiber M. R., Zorotovic M., Wijnen T. P. G., 2016, *MNRAS*, **455**, L16
- Schreiber M. R., Belloni D., Gänsicke B. T., Parsons S. G., Zorotovic M., 2021, *Nature Astronomy*, **5**, 648
- Schwarz R., et al., 1998, *A&A*, **338**, 465
- Schwarzenberg-Czerny A., 1989, *MNRAS*, **241**, 153
- Schwarzenberg-Czerny A., 1996, *ApJ*, **460**, L107
- Schwöpe A. D., 2018, *A&A*, **619**, A62
- Schwöpe A. D., Beuermann K., Jordan S., Thomas H. C., 1993, *A&A*, **278**, 487
- Schwöpe A. D., Brunner H., Hambaryan V., Schwarz R., 2002a, in Gänsicke B. T., Beuermann K., Reinsch K., eds, *Astronomical Society of the Pacific Conference Series Vol. 261, The Physics of Cataclysmic Variables and Related Objects*. p. 102
- Schwöpe A. D., Hambaryan V., Schwarz R., Kanbach G., Gänsicke B. T., 2002b, *A&A*, **392**, 541
- Schwöpe A. D., Brunner H., Buckley D., Greiner J., Heyden K. v. d., Neizvestny S., Potter S., Schwarz R., 2002c, *A&A*, **396**, 895
- Schwöpe A. D., Nebot Gomez-Moran A., Schreiber M. R., Gänsicke B. T., 2009, *A&A*, **500**, 867
- Schwöpe A. D., Scipione V., Traulsen I., Schwarz R., Granzer T., Pires A. M., Thorstensen J. R., 2014, *A&A*, **561**, A121
- Segura Montero O., Ramírez S. H., Echevarría J., 2020, *MNRAS*, **494**, 4110
- Sekiguchi K., 1992, *Nature*, **358**, 563
- Shafter A. W., Szkody P., 1984, *ApJ*, **276**, 305

- Shafter A. W., Szkody P., Liebert J., Penning W. R., Bond H. E., Grauer A. D., 1985, [ApJ](#), **290**, 707
- Shafter A. W., Wheeler J. C., Cannizzo J. K., 1986, [ApJ](#), **305**, 261
- Shafter A. W., Davenport J. R. A., Güth T., Kattner S., Marin E., Sreenivasamurthy N., 2008, [PASP](#), **120**, 374
- Shahbaz T., 2019, in Mignani R., Shearer A., Słowikowska A., Zane S., eds, *Astrophysics and Space Science Library* Vol. 460, *Astronomical Polarisation from the Infrared to Gamma Rays*. p. 247 ([arXiv:1909.02316](#)), doi:10.1007/978-3-030-19715-5_10
- Shakura N. I., Sunyaev R. A., 1973, [A&A](#), **24**, 337
- Shappee B. J., et al., 2013, *The Astronomer’s Telegram*, **5052**, 1
- Shappee B. J., et al., 2014, [ApJ](#), **788**, 48
- Shears J., 2015, [Journal of the British Astronomical Association](#), **125**, 358
- Shears J., Pickard R., Krajci T., Poyner G., 2008, [Journal of the British Astronomical Association](#), **118**, 145
- Shears J., Brady S., Koff R., Goff W., Boyd D., 2012a, [Journal of the British Astronomical Association](#), **122**, 49
- Shears J., et al., 2012b, [Journal of the British Astronomical Association](#), **122**, 237
- Sheets H. A., Thorstensen J. R., Peters C. J., Kapusta A. B., Taylor C. J., 2007, [PASP](#), **119**, 494
- Shen K. J., Quataert E., 2022, [ApJ](#), **938**, 31
- Shlosman I., Vitello P., 1993, [ApJ](#), **409**, 372
- Shugarov S., Malashevich S., 2021, *Peremennye Zvezdy*, **41**, 6
- Shurpakov S., et al., 2014, *The Astronomer’s Telegram*, **5732**, 1
- Silber A. D., 1992, PhD thesis, Massachusetts Institute of Technology
- Silvestri N. M., et al., 2007, [AJ](#), **134**, 741
- Simonsen M., et al., 2014, [AAVSO](#), **42**, 177
- Sion E. M., Godon P., 2015, [Acta Polytechnica CTU Proceedings](#), **2**, 35
- Siviero A., Munari U., 2016, *The Astronomer’s Telegram*, **9862**, 1
- Skumanich A., 1972, [ApJ](#), **171**, 565
- Smak J., 2019, [Acta Astronomica](#), **69**, 79
- Smee S. A., et al., 2013, [AJ](#), **146**, 32
- Smith R. K., Brickhouse N. S., Liedahl D. A., Raymond J. C., 2001, [ApJ](#), **556**, L91
- Sokolovsky K., et al., 2019, *The Astronomer’s Telegram*, **12947**, 1
- Solheim J. E., 2010, [PASP](#), **122**, 1133
- Southworth J., Gänsicke B. T., Marsh T. R., de Martino D., Hakala P., Littlefair S., Rodríguez-Gil P., Szkody P., 2006, [MNRAS](#), **373**, 687
- Southworth J., Gänsicke B. T., Marsh T. R., de Martino D., Aungwerojwit A., 2007a, [MNRAS](#), **378**, 635
- Southworth J., Marsh T. R., Gänsicke B. T., Aungwerojwit A., Hakala P., de Martino D., Lehto H., 2007b, [MNRAS](#), **382**, 1145
- Southworth J., Townsley D. M., Gänsicke B. T., 2008a, [MNRAS](#), **388**, 709
- Southworth J., et al., 2008b, [MNRAS](#), **391**, 591
- Southworth J., Marsh T. R., Gänsicke B. T., Steeghs D., Copperwheat C. M., 2010, [A&A](#), **524**, A86

- Southworth J., Gänsicke B. T., Breedt E., 2012, in Richards M. T., Hubeny I., eds, Proceedings IAU Symposium Vol. 282, From Interacting Binaries to Exoplanets: Essential Modeling Tools. pp 123–124, [doi:10.1017/S174392131102713X](https://doi.org/10.1017/S174392131102713X)
- Southworth J., Tappert C., Gänsicke B. T., Copperwheat C. M., 2015, [A&A](#), **573**, A61
- Spruit H. C., Taam R. E., 2001, [ApJ](#), **548**, 900
- Srivastava M. K., Ashok N. M., Banerjee D. P. K., Sand D., 2015, [MNRAS](#), **454**, 1297
- Stanek K. Z., et al., 2013, The Astronomer’s Telegram, **5118**, 1
- Stanishev V., Kraicheva Z., Genkov V., 2006, [A&A](#), **455**, 223
- Stark M. A., Wade R. A., Thorstensen J. R., Peters C. S., Smith H. A., Miller R. D., Green E. M., 2008, [AJ](#), **135**, 991
- Steele I. A., et al., 2004, in Oschmann Jacobus M. J., ed., Society of Photo-Optical Instrumentation Engineers (SPIE) Conference Series Vol. 5489, Ground-based Telescopes. pp 679–692, [doi:10.1117/12.551456](https://doi.org/10.1117/12.551456)
- Steele P. R., et al., 2013, [MNRAS](#), **429**, 3492
- Steinfadt J. D. R., Kaplan D. L., Shporer A., Bildsten L., Howell S. B., 2010, [ApJ](#), **716**, L146
- Stepanyan D. A., 1982, *Peremennye Zvezdy*, **21**, 691
- Stockman H. S., Schmidt G. D., Lamb D. Q., 1988, [ApJ](#), **332**, 282
- Strauss M. A., et al., 2002, [AJ](#), **124**, 1810
- Suleimanov V. F., Neustroev V. V., Borisov N. V., Fioktistova I. S., 2004, in Tovmassian G., Sion E., eds, *Revista Mexicana de Astronomia y Astrofisica Conference Series Vol. 20*, *Revista Mexicana de Astronomia y Astrofisica Conference Series*. pp 270–270
- Sun M., Arras P., 2018, [ApJ](#), **858**, 14
- Swierczynski E., et al., 2010, in Prša A., Zejda M., eds, *Astronomical Society of the Pacific Conference Series Vol. 435*, *Binaries - Key to Comprehension of the Universe*. p. 297 ([arXiv:0909.5149](https://arxiv.org/abs/0909.5149)), [doi:10.48550/arXiv.0909.5149](https://doi.org/10.48550/arXiv.0909.5149)
- Szkody P., 1985, [AJ](#), **90**, 1837
- Szkody P., 1988, [PASP](#), **100**, 791
- Szkody P., Howell S. B., 1987, in *Bulletin of the American Astronomical Society*. p. 1058
- Szkody P., Howell S. B., 1992, [ApJS](#), **78**, 537
- Szkody P., Ingram D., 1994, [ApJ](#), **420**, 830
- Szkody P., Wade R. A., 1981, [ApJ](#), **251**, 201
- Szkody P., Nishikida K., Long K. S., Fried R., 2001, [AJ](#), **121**, 2761
- Szkody P., et al., 2002a, [AJ](#), **123**, 413
- Szkody P., et al., 2002b, [AJ](#), **123**, 430
- Szkody P., et al., 2003a, [AJ](#), **126**, 1499
- Szkody P., et al., 2003b, [ApJ](#), **583**, 902
- Szkody P., et al., 2004a, [AJ](#), **128**, 1882
- Szkody P., et al., 2004b, [AJ](#), **128**, 2443
- Szkody P., et al., 2005, [AJ](#), **129**, 2386
- Szkody P., et al., 2006, [AJ](#), **131**, 973
- Szkody P., et al., 2007, [AJ](#), **134**, 185
- Szkody P., Linnell A. P., Campbell R. K., Plotkin R. M., Harrison T. E., Holtzman J., Seibert M., Howell S. B., 2008, [ApJ](#), **683**, 967
- Szkody P., et al., 2009, [AJ](#), **137**, 4011

- Szkody P., et al., 2011, [AJ](#), **142**, 181
- Szkody P., et al., 2013, [PASP](#), **125**, 1421
- Szkody P., Everett M. E., Howell S. B., Landolt A. U., Bond H. E., Silva D. R., Vasquez-Soltero S., 2014, [AJ](#), **148**, 63
- Szkody P., Everett M. E., Dai Z., Serna-Grey D., 2018, [AJ](#), **155**, 28
- Szkody P., et al., 2020, [AJ](#), **159**, 198
- Tampo Y., et al., 2021, [PASJ](#), **73**, 753
- Tappert C., Gänsicke B. T., Schmidtobreick L., Aungwerojwit A., Mennickent R. E., Koester D., 2007, [A&A](#), **474**, 205
- Tappert C., Gänsicke B. T., Zorotovic M., Toledo I., Southworth J., Papadaki C., Mennickent R. E., 2009, [A&A](#), **504**, 491
- Tappert C., Gänsicke B. T., Rebassa-Mansergas A., Schmidtobreick L., Schreiber M. R., 2011, [A&A](#), **531**, A113
- Taylor C. J., Thorstensen J. R., 1996, [PASP](#), **108**, 894
- Teyssier F., 2019, The Astronomer's Telegram, [12936](#), 1
- Thomas H. C., Beuermann K., Schwobe A. D., Burwitz V., 1996, [A&A](#), **313**, 833
- Thomas H. C., Beuermann K., Burwitz V., Reinsch K., Schwobe A. D., 2000, [A&A](#), **353**, 646
- Thoroughgood T. D., Dhillon V. S., Watson C. A., Buckley D. A. H., Steeghs D., Stevenson M. J., 2004, [MNRAS](#), **353**, 1135
- Thorstensen J. R., 1997, [PASP](#), **109**, 1241
- Thorstensen J. R., 2013, [PASP](#), **125**, 506
- Thorstensen J., 2016, The Astronomer's Telegram, [9141](#), 1
- Thorstensen J. R., 2020, [AJ](#), **160**, 6
- Thorstensen J. R., Fenton W. H., 2002, [PASP](#), **114**, 74
- Thorstensen J. R., Fenton W. H., 2003, [PASP](#), **115**, 37
- Thorstensen J. R., Halpern J. P., 2009, The Astronomer's Telegram, [2177](#), 1
- Thorstensen J. R., Halpern J., 2013, [AJ](#), **146**, 107
- Thorstensen J. R., Skinner J. N., 2012, [AJ](#), **144**, 81
- Thorstensen J. R., Taylor C. J., 1997, [PASP](#), **109**, 1359
- Thorstensen J. R., Taylor C. J., 2001, [MNRAS](#), **326**, 1235
- Thorstensen J. R., Ringwald F. A., Wade R. A., Schmidt G. D., Norsworthy J. E., 1991a, [AJ](#), **102**, 272
- Thorstensen J. R., Davis M. K., Ringwald F. A., 1991b, [AJ](#), **102**, 683
- Thorstensen J. R., Patterson J. O., Shambrook A., Thomas G., 1996, [PASP](#), **108**, 73
- Thorstensen J. R., Taylor C. J., Becker C. M., Remillard R. A., 1997, [PASP](#), **109**, 477
- Thorstensen J. R., Patterson J., Kemp J., Vennes S., 2002a, [PASP](#), **114**, 1108
- Thorstensen J. R., Fenton W. H., Patterson J., Kemp J., Halpern J., Baraffe I., 2002b, [PASP](#), **114**, 1117
- Thorstensen J. R., Fenton W. H., Patterson J. O., Kemp J., Krajci T., Baraffe I., 2002c, [ApJ](#), **567**, L49
- Thorstensen J. R., Fenton W. H., Taylor C. J., 2004, [PASP](#), **116**, 300
- Thorstensen J. R., Schwarz R., Schwobe A. D., Staude A., Vogel J., Krumpe M., Kohnert J., Nebot Gómez-Morán A., 2009, [PASP](#), **121**, 465
- Thorstensen J. R., Peters C. S., Skinner J. N., 2010, [PASP](#), **122**, 1285

- Thorstensen J. R., Taylor C. J., Peters C. S., Skinner J. N., Southworth J., Gänsicke B. T., 2015, [AJ](#), **149**, 128
- Thorstensen J. R., Alper E. H., Weil K. E., 2016, [AJ](#), **152**, 226
- Thorstensen J. R., Ringwald F. A., Taylor C. J., Sheets H. A., Peters C. S., Skinner J. N., Alper E. H., Weil K. E., 2017, [Research Notes of the American Astronomical Society](#), **1**, 29
- Thorstensen J. R., Motsoaledi M., Woudt P. A., Buckley D. A. H., Warner B., 2020, [AJ](#), **160**, 70
- Tokovinin A., Thomas S., Sterzik M., Udry S., 2006, [A&A](#), **450**, 681
- Toloza O., et al., 2019, [BAAS](#), **51**, 168
- Tonry J. L., et al., 2018, [ApJ](#), **867**, 105
- Tonry J. L., et al., 2021, VizieR Online Data Catalog, [p. J/ApJ/867/105](#)
- Toonen S., Hamers A., Portegies Zwart S., 2016, [Computational Astrophysics and Cosmology](#), **3**, 6
- Toonen S., Hollands M., Gänsicke B. T., Boekholt T., 2017, [A&A](#), **602**, A16
- Tovmassian G. H., Greiner J., Zharikov S. V., Echevarría J., Kniazev A., 2001, [A&A](#), **380**, 504
- Tovmassian G., Stephania Hernandez M., González-Buitrago D., Zharikov S., García-Díaz M. T., 2014, [AJ](#), **147**, 68
- Townsley D. M., Bildsten L., 2003, [ApJ](#), **596**, L227
- Townsley D. M., Bildsten L., 2005, [ApJ](#), **628**, 395
- Townsley D. M., Gänsicke B. T., 2009, [ApJ](#), **693**, 1007
- Traulsen I., Reinsch K., Schwope A. D., Burwitz V., Dreizler S., Schwarz R., Walter F. M., 2011, [A&A](#), **529**, A116
- Tremblay P. E., Bergeron P., Gianninas A., 2011, [ApJ](#), **730**, 128
- Unda-Sanzana E., et al., 2008, [MNRAS](#), **388**, 889
- Uthas H., Knigge C., Long K. S., Patterson J., Thorstensen J., 2011, [MNRAS](#), **414**, L85
- Uthas H., et al., 2012, [MNRAS](#), **420**, 379
- Vanmunster T., Velthuis F., McCormick J., 2000, Information Bulletin on Variable Stars, [4955](#), 1
- Vennes S., Thorstensen J. R., 1996, [AJ](#), **112**, 284
- Vennes S., Thorstensen J. R., Thejll P., Shipman H. L., 1991, [ApJ](#), **372**, L37
- Vennes S., Thorstensen J. R., Polonski E. F., 1999, [ApJ](#), **523**, 386
- Vennes S., Polonski E. F., Lanz T., Thorstensen J. R., Chayer P., Gull T. R., 2000, [ApJ](#), **544**, 423
- Vennes S., Kawka A., Hughes S. L., Németh P., 2010, in Prša A., Zejda M., eds, *Astronomical Society of the Pacific Conference Series Vol. 435, Binaries - Key to Comprehension of the Universe*. p. 183
- Vennes S., et al., 2011, [ApJ](#), **737**, L16
- Vernet J., et al., 2011, [A&A](#), **536**, A105
- Vieira K., Korchagin V., Carraro G., Lutsenko A., 2023, [Galaxies](#), **11**, 77
- Vladimirov V., et al., 2017, *The Astronomer's Telegram*, [10415](#), 1
- Vogel J., Schwope A. D., Gänsicke B. T., 2007, [A&A](#), **464**, 647
- Vogel J., Byckling K., Schwope A., Osborne J. P., Schwarz R., Watson M. G., 2008, [A&A](#), **485**, 787
- Voges W., et al., 1999, [A&A](#), **349**, 389

- Vogt N., Bateson F. M., 1982, *A&AS*, **48**, 383
- Wade R. A., 1988, *ApJ*, **335**, 394
- Wagner R. M., et al., 1998, *AJ*, **115**, 787
- Wang Z., Archibald A. M., Thorstensen J. R., Kaspi V. M., Lorimer D. R., Stairs I., Ransom S. M., 2009, *ApJ*, **703**, 2017
- Warner B., 1987, *MNRAS*, **227**, 23
- Warner B., 1995, *Cataclysmic variable stars*. Cambridge astrophysics series Vol. 28, Cambridge University Press
- Warner B., 2003, *Cataclysmic Variable Stars*. Cambridge University Press, doi:10.1017/CBO9780511586491
- Warner B., Woudt P. A., 2002, *MNRAS*, **335**, 84
- Watkins L. L., et al., 2009, *MNRAS*, **398**, 1757
- Watson C. L., Henden A. A., Price A., 2006, Society for Astronomical Sciences Annual Symposium, **25**, 47
- Watson C., Henden A. A., Price A., 2017, VizieR Online Data Catalog, [p. B/vsx](#)
- Weaver B. A., Blanton M. R., Brinkmann J., Brownstein J. R., Stauffer F., 2015, *PASP*, **127**, 397
- Webb N. A., et al., 2020, *A&A*, **641**, A136
- Webbink R. F., 1984, *ApJ*, **277**, 355
- Webbink R. F., Wickramasinghe D. T., 2002, *MNRAS*, **335**, 1
- Wei J., Li C., Xu D., Hu J., Li Q., 1997, *Acta Astrophysica Sinica*, **17**, 107
- Welsh B. Y., et al., 2005, *AJ*, **130**, 825
- Welzl E., 1991, in Maurer H., ed., *New Results and New Trends in Computer Science*. Springer Berlin Heidelberg, Berlin, Heidelberg, pp 359–370
- Wenger M., et al., 2000, *A&AS*, **143**, 9
- Werner K., Reindl N., Löbbling L., Pelisoli I., Schaffenroth V., Rebassa-Mansergas A., Irawati P., Ren J., 2020, *A&A*, **642**, A228
- Wheatley P. J., Burleigh M. R., Watson M. G., 2000, *MNRAS*, **317**, 343
- Whyte C. A., Eggleton P. P., 1980, *MNRAS*, **190**, 801
- Wickramasinghe D. T., 1988, in Coyne G. V., Magalhaes A. M., Moffat A. F., Schulte-Ladbeck R. E., Tapia S., eds., *Polarized Radiation of Circumstellar Origin*. University of Arizona Press, pp 199–236
- Wickramasinghe D. T., Ferrario L., 2005, *MNRAS*, **356**, 1576
- Wickramasinghe D. T., Wu K., 1994, *MNRAS*, **266**, L1
- Wickramasinghe D. T., Tout C. A., Ferrario L., 2014, *MNRAS*, **437**, 675
- Willems B., Kolb U., 2004, *A&A*, **419**, 1057
- Willems B., Kolb U., Sandquist E. L., Taam R. E., Dubus G., 2005, *ApJ*, **635**, 1263
- Williams G., 1983, *ApJS*, **53**, 523
- Williams K. A., Howell S. B., Liebert J., Smith P. S., Bellini A., Rubin K. H. R., Bolte M., 2013, *AJ*, **145**, 129
- Wils P., Gänsicke B. T., Drake A. J., Southworth J., 2010, *MNRAS*, **402**, 436
- Wilson D. J., Toloza O., Landstreet J. D., Gänsicke B. T., Drake J. J., Hermes J. J., Koester D., 2021, *MNRAS*, **508**, 561
- Wolfe M. A., Szkody P., Fraser O. J., Homer L., Skinner S., Silvestri N. M., 2003, *PASP*, **115**,

- Wonnacott D., Kellett B. J., Stickland D. J., 1993, *MNRAS*, **262**, 277
- Wood J. H., Naylor T., Hassall B. J. M., Ramseyer T. F., 1995, *MNRAS*, **273**, 772
- Woudt P. A., Warner B., 2004, *MNRAS*, **348**, 599
- Woudt P. A., Warner B., 2010, *MNRAS*, **403**, 398
- Woudt P. A., Warner B., Pretorius M. L., Dale D., 2005, in Hameury J. M., Lasota J. P., eds, *Astronomical Society of the Pacific Conference Series Vol. 330, The Astrophysics of Cataclysmic Variables and Related Objects*. p. 325
- Wright A. E., Cropper M., Stewart R. T., Nelson G. J., Slee O. B., 1988, *MNRAS*, **231**, 319
- Wright D., et al., 2012, *The Astronomer's Telegram*, **4516**, 1
- Wu K., 2000, *Space Sci. Rev.*, **93**, 611
- Wyrzykowski Ł., Hodgkin S., Blogorodnova N., Koposov S., Burgon R., 2012, in 2nd Gaia Follow-up Network for Solar System Objects. p. 21 ([arXiv:1210.5007](https://arxiv.org/abs/1210.5007)), [doi:10.48550/arXiv.1210.5007](https://doi.org/10.48550/arXiv.1210.5007)
- Yamaoka H., Itagaki K., 2009, *Central Bureau Electronic Telegrams*, **1644**, 1
- Yamaoka H., Itagaki K., Miyashita A., Koff R. A., 2008, *Central Bureau Electronic Telegrams*, **1631**, 1
- Yamaoka H., Itagaki K., Martignoni M., Koff R. A., 2012, *Central Bureau Electronic Telegrams*, **3228**, 1
- Yanny B., et al., 2009, *AJ*, **137**, 4377
- Yecheistov V., et al., 2013, *The Astronomer's Telegram*, **5536**, 1
- York D. G., et al., 2000, *AJ*, **120**, 1579
- Yu Z., et al., 2019, *MNRAS*, **489**, 1023
- Yungelson L. R., 2008, *Astronomy Letters*, **34**, 620
- Zengin Çamurdan D., İbanoglu C., Çamurdan C. M., 2010, *New Astronomy*, **15**, 476
- Zhao G., Zhao Y., Chu Y., Jing Y., Deng L., 2012, *arXiv e-prints*, p. [arXiv:1206.3569](https://arxiv.org/abs/1206.3569)
- Zharikov S. V., et al., 2008, *A&A*, **486**, 505
- Zorotovic M., Schreiber M. R., 2013, *A&A*, **549**, A95
- Zorotovic M., Schreiber M., 2022, *MNRAS*, **513**, 3587
- Zorotovic M., Schreiber M. R., Gänsicke B. T., Nebot Gómez-Morán A., 2010, *A&A*, **520**, A86
- Zorotovic M., Schreiber M. R., Gänsicke B. T., 2011, *A&A*, **536**, A42
- Zorotovic M., Schreiber M. R., Parsons S. G., 2014, *A&A*, **568**, L9
- Zorotovic M., et al., 2016, *MNRAS*, **457**, 3867
- Zwitter T., Munari U., 1994, *A&AS*, **107**, 503
- de Jong R. S., et al., 2016, in Evans C. J., Simard L., Takami H., eds, *Society of Photo-Optical Instrumentation Engineers (SPIE) Conference Series Vol. 9908, Ground-based and Airborne Instrumentation for Astronomy VI*. p. 99081O, [doi:10.1117/12.2232832](https://doi.org/10.1117/12.2232832)
- Šimon V., 2016, *MNRAS*, **463**, 1342
- van Roestel J., et al., 2018, *MNRAS*, **475**, 2560
- van Roestel J., et al., 2022, *MNRAS*, **512**, 5440
- van Teeseling A., Drake J. J., Drew J. E., Hoare M. G., Verbunt F., 1995, *A&A*, **300**, 808
- van den Besselaar E. J. M., et al., 2007, in Hartkopf W. I., Harmanec P., Guinan E. F., eds, *Proceedings IAU Symposium Vol. 240, Binary Stars as Critical Tools & Tests in Contemporary Astrophysics*. pp 105–108, [doi:10.1017/S1743921307003882](https://doi.org/10.1017/S1743921307003882)

Appendix A

Supplementary Material - Chapter 4

A.1 List of WD+M

Table A.1: The WD+M 300pc Gold sample. We provide the geometric distances from [Bailer-Jones et al. \(2018\)](#) and types according to the definitions in Chapter 4. .

Name	<i>Gaia</i> DR2 source_id	Period (h)	phot_g_mean_mag (mag)	Distance (pc)	Type	Teff WD (K)	logg	Reference
SDSS J011009.09+132616.1	2584756467429594880	7.98	16.73	275	DA+M	25167	7.54	8
SDSS J013851.54-001621.6	2509786614982022016	1.75	16.39	49	WD+M			19
SDSS J015225.38-005808.5	2506120327818999936	2.15	17.31	112	DA+M	8773	8.19	2
SDSS J022503.02+005456.2	2501315732588500224	21.86	19.01	231	WD+M			2
SDSS J023804.39-000545.7	2498742463062264192	5.08	18.21	248	DA+M	20566	7.72	2
SDSS J030308.35+005444.1	155649614856576	3.23	17.38	122	PREP			8
SDSS J030607.18-003114.4	3266296412128039424		15.64	144	DA+M	19193	7.9	4
SDSS J032038.72-063822.9	5169658173472195072	3.38	18.85	278	DA+M	11173	8.3	2
SDSS J074730.57+430403.6	925792948115904256		17.89	282	DA+M	16336	8.41	4
SDSS J075919.41+321948.4	881086019353249280		15.59	90	DA+M	14065	7.42	29
SDSS J082022.02+431411.0	916277400827964544		15.81	125	DA+M	20568	7.79	4
SDSS J084307.27+122610.1	602243853298434176		18.56	242	DA+M	10073	8.55	35
SDSS J084841.17+232051.7	689473234627550080		17.08	279	WD+M			35
SDSS J085253.22+272620.9	692776579874699008		16.25	175	DA+M	14065	8.32	35
SDSS J091809.57+175216.2	632169192552095360		18.55	268	DA+M	12250	7.52	4
SDSS J092452.39+002449.0	3840862774616739328	57.7	17.93	272	DA+M	19193	7.81	2
SDSS J100609.18+004417.0	3834915417437497088	6.73	17.51	80	DA+M	7819	8.42	2

Name	<i>Gaia</i> DR2 source_id	Period (h)	phot_g_mean_mag (mag)	Distance (pc)	Type	Teff WD (K)	logg	Reference
SDSS J104012.99+252559.9	724616061496025984		17.95	198	DA+M	10073	8.11	35
SDSS J105133.35+663401.0	1059664849644881152		17.13	219	DA+M	19416	7.64	29
SDSS J105421.97+512254.2	836369328128006144		15.81	224	DA+M	23863	8.15	35
SDSS J111715.70+110737.7	3963435334447992576		18.31	263	DA+M	15071	7.84	4
SDSS J112909.50+663704.3	1057463111970047488		17.39	281	DA+M	15964	7.67	4
SDSS J113655.17+040952.6	3800979880104156032		16.9	130	DA+M	11699	7.99	35
SDSS J114312.57+000926.5	3795834474923972096	9.27	17.84	276	DA+M	16719	7.813	2
SDSS J115156.94-000725.4	3795157381919461504	3.4	17.94	211	DA+M	10428	7.995	23
SDSS J115236.99+002141.8	3795245828182343296		17.22	148	DA+M	10367	7.97	29
SDSS J121010.13+334722.9	4028597414327329664	2.99	15.52	46	WD+M			8
SDSS J121258.25-012310.2	3697668912861183872	8.06	16.66	207	DA+M	17304	7.52	29
SDSS J121928.05+161158.7	3945572123083449984		16.92	74	DA+M	7131	8.61	29
SDSS J122339.61-005631.1	3695073893620867584	2.16	17.84	247	DA+M	11908	7.64	35
SDSS J122630.86+303852.5	4012093916593061120		16.07	290	DA+M	30071	7.41	8
SDSS J123139.80-031000.3	3681534232558058368	5.85	17.66	262	DA+M	20331	7.35	2
SDSS J124525.34+343346.9	1515333976075216640		17.89	292	WD+M			35
SDSS J124935.08+375132.8	1520611490154087936		18.01	247	DA+M	8875	8.46	35
SDSS J134208.94+044852.7	3714154470515963520		17.86	234	DA+M	14065	7.53	4
SDSS J143443.24+533521.2	1606753179605063936	104.56	16.0	145	DA+M	21785	7.74	2
SDSS J143547.87+373338.5	1486587588165368576	3.02	17.04	182	DA+M	12392	7.59	8
SDSS J143809.13+330905.0	1287480463466590848		17.12	247	DA+M	21785	7.82	4
SDSS J144921.19+352430.9	1293077557469962112		18.21	222	DA+M	12976	7.83	4
SDSS J145331.70+405844.2	1489086739439384576		17.17	187	DA+M	17505	7.77	4

Name	<i>Gaia</i> DR2 source_id	Period (h)	phot_g_mean_mag (mag)	Distance (pc)	Type	Teff WD (K)	logg	Reference
SDSS J151921.72+353625.8	1291066348840336128	32.81	16.8	171	DA+M	19416	7.9	2
SDSS J152359.22+460448.9	1395677046202567296	9.93	17.45	108	DA+M	8378	8.28	2
SDSS J152425.21+504009.7	1595543929141360000	14.15	16.92	224	DA+M	20098	8.14	2
SDSS J152933.25+002031.2	4417363143698091136	3.96	18.04	297	DA+M	13986	7.54	4
SDSS J154843.79+372749.7	1376105769292093184		18.16	158	DA+M	8977	8.37	9
SDSS J160821.47+085149.9	4451708691493927808	9.94	18.36	178	DA+M	9844	8.6	2
SDSS J161113.13+464044.2	1386934206479083904	1.98	17.55	173	DA+M	10307	8.04	2
SDSS J161145.88+010327.8	4411458392598114432	7.29	18.21	244	DA+M	10189	7.81	2
SDSS J161931.74+005730.9	4408582856156349696		18.47	200	DA+M	9081	7.87	35
SDSS J200537.68+775415.9	2291355809647561600		18.8	286	DA+M			35
SDSS J211205.31+101427.9	1744641455375760256	2.22	18.15	217	DA+M	19868	8.73	2
SDSS J212051.92-005827.3	2686185285515993984	10.78	17.37	228	DA+M	16336	8.04	2
SDSS J221616.59+010205.6	2679389410302604544	5.05	17.81	264	DA+M	12536	7.62	2
SDSS J224038.37-093541.4	2608898409880983808	6.25	17.29	205	DA+M	13300	7.615	2
SDSS J234312.95+154106.4	2771402315752426240		17.25	204	DA+M	26801	7.92	35
SDSS J234638.76+434041.7	1925542316791165952		17.63	236	WD+M			18
SDSS J130733.49+215636.7	3943463122342099456	5.19	16.76	105	DC+M			8
SDSS J135931.90+054420.6	3672474909579800320		15.81	134	DA+M	15782	7.6	9
SDSS J145238.12+204511.8	1238124314206289536		17.91	127	DC+M			9
SDSS J153924.25+013537.3	4423688874610759808		19.07	210	DA+M	8673	8.02	9
SDSS J162552.91+640024.9	1629033335337458048	5.24	18.58	184	DA+M	8773	8.3	35
SDSS J000531.09-054343.2	2444337223266568064		16.18	136	DA+M	13279	7.98	2
SDSS J030138.24+050218.9	3787061643780608	12.94	17.71	201	DA+M	11109	8.43	2

Name	<i>Gaia</i> DR2 source_id	Period (h)	phot_g_mean_mag (mag)	Distance (pc)	Type	Teff WD (K)	logg	Reference
SDSS J073003.86+405450.0	900613070984335232		16.88	137	WD+M			35
SDSS J073455.91+410537.4	924450105117580928		16.78	249	DA+M	19416	7.96	27
SDSS J085336.03+072033.5	584688088576825088	3.61	18.05	256	DC+M			2
SDSS J102857.78+093129.8	3876099549601111040	5.64	15.24	174	DA+M	15782	8.34	8
SDSS J105526.23+472923.0	831399531274288512		16.66	275	DA+M	26801	8.26	35
SDSS J110517.60+385125.7	764867636000984576	8.27	17.75	217	DA+M	10548	8.17	2
SDSS J112308.40-115559.3	3565412778028357888		16.88	157	DA+M	10073	9.12	35
SDSS J130012.49+190857.4	3941505918629413248	7.39	18.2	246	DA+M	8673	8.81	2
SDSS J131632.04-003758.0	3686708461263474816	9.66	17.69	179	DC+M			2
SDSS J134841.61+183410.5	1245093255125979904	5.96	16.81	163	DA+M	15071	7.96	8
SDSS J143642.01+574146.3	1611031615570789760	20.74	18.07	251	WD+M			2
SDSS J162354.45+630640.4	1628922185879538304	53.56	18.01	223	DA+M	9731	8.64	4
SDSS J184412.58+412029.4	2098661762613244160	5.42	16.05	64	DA+M	7554	7.49	2
SDSS J224307.59+312239.1	1888922223031933568	2.87	17.9	166	DC+M			2
SDSS J013532.97+144555.9	2588874825669925504	1.7	16.92	77	DA+BD	8032	8.06	7
SDSS J102627.48+384502.4	755705822218381184		16.34	98	PREP			13
WD 0023+388	379359102453525376	15.4	15.8	63	DA	10980		26
WD 0354+463	245807579721338752	3.96	15.42	43	DA	8230		26
WD 0752-146	5725503293214289280	25.26	13.57	39	DA	19440		26
WD 1333+487	1552488776081383040	42.14	14.09	36	DB	14676		26
WD 1436-216	6278962983814509184	48.43	15.5	175	DA	23690		26
WD 1504+546	1600249121650105472	22.34	15.97	188	DA	23120		26
WD 2257+162	2828888597582293760	7.74	15.99	199	DA	25450		26

Name	<i>Gaia</i> DR2 source_id	Period (h)	phot_g_mean_mag (mag)	Distance (pc)	Type	Teff WD (K)	logg	Reference
WD 0137-349	5012047927570807552		15.37	101	DA+BD			17
GD 448	1112171030998592256	2.47	15.02	99	DA	19000		25
LTT 560	5034416735723964800	3.55	15.32	44	DA	7500		32
CC Cet	15207693216816512	6.82	15.17	120	DA	26200		16
EC 12477-1738	3522398478696160512	8.69	15.78	133	DA	17718		5
V* DE CVn	1550299304833675392	8.74	11.98	30	DA	8000		24
V* EG UMa	1548104507825815296	16.03	12.58	28	DA	13100		16
WD 2237+819	2062408081119518592	16.94	13.9	107	DA	49000		1
RE J1016-052	3779037205721914240	18.94	14.06	112	DA	55000		1
IN CMa	5604890028746727552	30.24	14.58	180	DA	52400		3
Feige 24	2503828498910129664	101.57	12.22	78	DA	57000		20
SDSS J214952.27-071756.9	2667019698331625856	15.45	15.59	155	DA+M			2
SDSS J154057.27+370543.4	1376209093321219456	6.27	16.31	203	DA+M			34
BPM 71214	5165151485764431360	4.84	12.71	56	DA+M			15
WD 2237+819"	2287248210301342336	2.97	15.41	78	DA+M			6
WD 1333+005	3662988495054111232	2.93	16.71	93	DA+M			33
SDSS J141126.20+200911.1	1246281350455075840	2.03	17.92	176	DA+BD			22
WD 2147-140	6840346923439592064	35.93	15.2	145	DA+M			30
WD 2009+62	2243943635605220736	17.79	15.15	113	DA+M			12
WD 2154+408	1959593642149299968	6.43	14.89	139	DA+M			31
KIC 11548140	2132027576829358208	33.09	15.35	176	DA+M			34
WD 2123-447	6576232101460909056	20.4	15.18	93	DA+M			11
WD 0416+701	499960104796222976		14.78	55				14

Name	<i>Gaia</i> DR2 source_id	Period	phot_g_mean_mag	Distance	Type	Teff WD	logg	Reference
		(h)	(mag)	(pc)		(K)		
V* HK Cet	5135466183642594304	9.98	15.23	46	DA+BD			10
WD 1319-288	6182278665776280320	21.02	15.35	77	DA+M			11
PTF1 J015256.60+384413.4	343212249668886144	9.27	16.47	230	DA+M			34
MQ Dra	1597621426298361216		17.35	185	PREP			21
HS0922+1333	594162958230409088		16.48	162	PREP			28

References: 1 [Vennes et al. \(1999\)](#), 2 [Nebot Gómez-Morán et al. \(2011\)](#), 3 [Vennes & Thorstensen \(1996\)](#), 4 [Rebassa-Mansergas et al. \(2011\)](#), 5 [Tappert et al. \(2009\)](#), 6 [Tappert et al. \(2011\)](#), 7 [Steele et al. \(2013\)](#), 8 [Parsons et al. \(2013a\)](#), 9 [Rebassa-Mansergas et al. \(2012a\)](#), 10 [Farihi et al. \(2005a\)](#), 11 [Maxted et al. \(2007\)](#), 12 [Morales-Rueda et al. \(2005\)](#), 13 [Vogel et al. \(2007\)](#), 14 [Maxted et al. \(2000b\)](#), 15 [Kawka & Vennes \(2003\)](#), 16 [Bleach et al. \(2000\)](#), 17 [Zorotovic et al. \(2010\)](#), 18 [Rebassa-Mansergas et al. \(2010\)](#), 19 [Parsons et al. \(2012\)](#), 20 [Vennes et al. \(1991\)](#), 21 [Szkody et al. \(2008\)](#), 22 [Casewell et al. \(2018\)](#), 23 [Rebassa-Mansergas et al. \(2007\)](#), 24 [van den Besselaar et al. \(2007\)](#), 25 [Maxted et al. \(1998\)](#), 26 [Ashley et al. \(2019\)](#), 27 [Rebassa-Mansergas et al. \(2016\)](#), 28 [Reimers & Hagen \(2000\)](#), 29 [Silvestri et al. \(2007\)](#), 30 [Koester et al. \(2009\)](#), 31 [Hillwig et al. \(2002\)](#), 32 [Tappert et al. \(2007\)](#), 33 [Zorotovic & Schreiber \(2013\)](#), 34 [Parsons et al. \(2015a\)](#), 35 [Schreiber et al. \(2010\)](#)

A.2 List of WD+AFGK

Table A.2: The WD+AFGK 300pc Gold sample. We provide the geometric distances from [Bailer-Jones et al. \(2018\)](#).

Name	<i>Gaia</i> DR2 source_id	Period (h)	phot_g_mean_mag (mag)	Distance (pc)	Teff (K)	Reference
TYC 110-755-1	3240025986963617792		10.3	135	5664	6
TYC 1380-957-1	668982117457244800		10.53	162	5773	6
TYC 1655-707-1	1813628457037321216		10.8	190	5872	6
TYC 278-239-1	3909860363370059392		6.82	158	4975	6
TYC 3104-932-1	2108688277865923328		10.23	164	5823	6
TYC 4564-627-1	1724905874492270336		10.25	187	6021	6
TYC 4700-815-1	5187257579357136896		8.79	165	6203	6
TYC 4717-255-1	3250948264892822272		6.97	299	4764	6
TYC 5523-324-1	3573364278618188544		10.84	123	5226	6
TYC 8873-148-1	4672702561514172544		10.95	205	5754	6
TYC 4962-1205-1	3635396697431775104	30.72	8.81	76	5392	3
TYC 6760-497-1	6211996983310161664	11.97	11.09	282	6136	1
V471 Tau	43789772861265792		9.2	47	4993	2
GPX-TF16E-48	531486745299867904		14.06	193	4157	5
EL CVn	1549628911977705856	19.1	9.41	264	8172	4

References: 1 [Parsons et al. \(2015b\)](#), 2 [Vennes et al. \(2010\)](#), 3 [Hernandez et al. \(2021a\)](#), 4 [Ritter & Kolb \(2003\)](#), 5 [Krushinsky et al. \(2020\)](#), 6 [Ren et al. \(2020\)](#)

A.3 List of CVs

Table A.3: The CV 300pc Gold sample. We provide the geometric distances from [Bailer-Jones et al. \(2018\)](#) and types according to the definitions in Chapter 4.

Name	<i>Gaia</i> DR2 source_id	Period (h)	phot_g_mean_mag (mag)	Distance (pc)	CV Type	References
1RXS J203242.4+104937	1754525270341133312		17.45	297	CV	
AM CVn	1519860699806445184	0.29	14.08	295	AM CVn	
UX UMa	1559987685901122304		12.97	295	Novalike	68
KIS J192703.08+421131.7	2101752244981853440		19.22	298	CV	75
V1239 Her	1313538545446290688	2.4	17.91	292	SU UMa	22,1
V0844 Her	1332378466733219456	1.31	17.49	291	SU UMa	12
ASASSN-14cv	1368447331503747968	1.44	19.0	290	WZ Sge	11
V1129 Cen	6132314520950881664	21.43	9.54	288	U Gem	
V0453 Nor	5984221987022142464	1.52	16.08	286	SU UMa	24
LS Peg	1768858645653683200	4.19	12.31	285	Novalike	18
KIS J192651.94+503301.7	2130112326354193024		19.16	286	CV	75
EQ Cet	5041907811522399488	1.55	17.34	282	Magnetic	66
ASASSN-14jv	2104562321825510400	1.31	18.7	283	WZ Sge	3
V0342 Cam	550106214500410112	1.81	17.65	281	SU UMa	11
V0393 Pav	6447773336193467520	1.65	18.74	282	Magnetic	78
DT Oct	6347097928386163072	1.74	16.22	279	SU UMa	11
DH Aql	4200218019655998720	1.92	17.97	280	SU UMa	8

Name	<i>Gaia</i> DR2 source_id	Period (h)	phot_g_mean_mag (mag)	Distance (pc)	CV Type	References
RZ Leo	3799290858445023488	1.82	18.24	280	WZ Sge	
GZ Cet	2465053942183130240	1.33	18.37	279	SU UMa	57
TU Men	4625018043590839424	2.81	17.08	275	SU UMa	8
PNV J05580574-0011155	3218565547214437632		17.84	276	WZ Sge	20
RU Peg	2727974767550030080	8.99	12.27	274	U Gem	60
HP Lib	6265476408553544320	0.31	13.62	273	AM CVn	76
ASASSN-15oq	5057652062118956672	1.41	16.33	272	Magnetic	49
BS Tri	107522105369340800	1.6	17.97	271	Magnetic	66
BY Cam	283187642167998720	3.35	14.99	270	Magnetic	31
CRTS CSS100615 J215815+094709	2725645692684615168	1.86	17.49	268	SU UMa	69
CTCV J2118-3412	6782793537041886464	1.8	15.59	266	U Gem	45
MASTER OT J064725.70+491543.9	990916128476988928	1.57	17.37	266	SU UMa	58
IR Gem	3386289728137230976	1.64	15.96	264	SU UMa	8
OGLE BLG-DN-0254	4040721003309923840	1.73	18.09	264	SU UMa	88
1SWASP J162117.36+441254.2	1382549392763335936	4.99	15.03	263	U Gem	5
GY Cnc	635508894697188864	4.21	16.06	262	U Gem	70
WX Cet	2355217815809560192	1.4	18.14	262	SU UMa	8
CTCV J2056-3014	6794414550313352448	1.76	16.99	261	SU UMa	
CRTS CSS160906 J160346+193540	1203263915795342336	1.37	18.99	260	Magnetic	38
ASASSN-14cl	1796893134146598144	1.4	18.19	259	WZ Sge	3
TY Psc	316447594027782912	1.64	16.87	259	SU UMa	8
SS Aur	968824328534823936	4.39	14.46	257	U Gem	15
SDSS J075507.70+143547.6	654539826068054400	1.41	18.64	259	WZ Sge	9,66

Name	<i>Gaia</i> DR2 source_id	Period (h)	phot_g_mean_mag (mag)	Distance (pc)	CV Type	References
KIC 11390659	2132186284460008832	1.78	16.37	256	U Gem	32
TT Ari	78395045917118976	3.3	10.92	255	Novalike	47
PM J03338+3320	220706553887988864	1.6	17.93	256	SU UMa	26
TCP J05002724+1334199	3391618889196357248	3.71	16.76	253	U Gem	58
ASASSN-15pq	3417582928575520768	1.92	16.94	252	U Gem	32
VZ Pyx	5652773897568243072	1.76	15.32	249	SU UMa	8
V1024 Per	230780309488710016	1.69	17.06	249	SU UMa	11
UV Per	457106501671769472	1.56	17.93	249	SU UMa	11
FT Cam	463350318963210624	1.8	17.45	247	U Gem	43
ASASSN-14mv	3367007627080317824		18.01	244	AM CVn	4
PHL 1445	5171137394568701184	1.27	17.52	243	U Gem	85
V1033 Cen	5332776117932015104	3.16	17.98	243	Magnetic	29
Gaia19bbb	462713869228951424		18.17	243	U Gem	
PNV J03093063+2638031	112541169793045120	1.35	18.65	244	WZ Sge	2,65
PBC J1740.7+0603	4485786821746343680	1.68	15.84	239	CV	23,82
V0386 Ser	4406459119386466176	1.34	19.04	242	WZ Sge	
Swift J2218.5+1925	1777232423131443840	2.16	17.26	237	Magnetic	21
RW Sex	3769067109159364608	5.88	10.63	235	Novalike	25
CRTS SSS130101 J122222-311525	3469884768265773824	1.82	18.85	236	WZ Sge	39
PBC J0325.6-0820	5168129581727355008	2.09	18.08	227	Magnetic	56
Gaia19cwm	4433651721269127552	1.44	18.83	226	WZ Sge	
SDSS J143317.78+101123.3	1176468611268115200	1.3	18.59	223	Period bouncer	72
IR Com	3955313418148878080	2.09	16.72	219	U Gem	19,46

Name	<i>Gaia</i> DR2 source_id	Period (h)	phot_g_mean_mag (mag)	Distance (pc)	CV Type	References
SU UMa	1091051096255456384	1.83	15.29	219	SU UMa	
AX J1853.3-0128	4265216749035591808	1.45	17.47	218	Magnetic	27
V0808 Aur	950114317120915840	1.95	17.4	215	Magnetic	52
V0624 Peg	1759156585115470976	1.41	18.42	215	WZ Sge	3
CP Tuc	6492236727426610304	1.48	19.15	214	Magnetic	40
ASAS J071404+7004.3	1109608206832496512	5.95	11.98	212	U Gem	
SDSS J143544.02+233638.7	1242828982729309952		18.63	212	U Gem	80
PM J07068+0324	3116059834803771904		17.18	210	Magnetic	23
OV Boo	1593140224924964864	1.12	18.23	210	Period bouncer	86
LS IV -08 3	4339398736975240192	4.69	11.32	209	Novalike	77
RX J0502.8+1624	3393408546234335488		18.88	211	Magnetic	7
SDSS J113826.73+061919.5	3909559715659399808		18.56	210	CV	80,66,61
SDSS J103533.03+055158.4	3859020040917830400	1.37	18.82	209	Period bouncer	64
AP CrB	1223491257550872192	2.53	17.15	207	Magnetic	66
DW Cnc	667150159287327360	1.44	15.52	207	Magnetic	37
1RXS J023238.8-371812	4953766320874344704		18.67	206	WZ Sge	3
SDSS J113732.32+405458.3	767756877680612864	0.99	19.16	206	AM CVn	14
CC Scl	6557154200328277120	1.41	16.88	203	SU UMa	11
TCP J21290156+3631056	1951666884868218112		17.31	201	U Gem	
V1838 Aql	4306244746253355776	1.37	17.87	201	WZ Sge	3
SDSS J120841.96+355025.2	4029844634175275136	0.88	18.87	200	AM CVn	14
DO Dra	1074721664954807040	3.97	15.16	196	Magnetic	48
V1025 Cen	6153373329716524800	1.41	17.12	192	Magnetic	63

Name	<i>Gaia</i> DR2 source_id	Period (h)	phot_g_mean_mag (mag)	Distance (pc)	CV Type	References
V0426 Oph	4471872295941149056	6.85	12.37	191	Magnetic	41,66
V0521 Peg	1776946133496845440	1.44	17.04	190	SU UMa	62
IM Eri	5091939988633728640	3.49	11.76	190	Novalike	44
LV Cnc	587578670286348160	1.36	18.34	190	WZ Sge	55,66
MASTER OT J042609.34+354144.8	176429285061830144	1.57	16.21	186	SU UMa	57
QZ Lib	6318149711371454464	1.54	18.88	187	Period bouncer	30
QS Tel	6684490840966796928	2.33	16.88	186	Magnetic	16
NZ Boo	1289860214647954816	1.41	17.34	185	SU UMa	71
TY PsA	6610409767574182912	2.02	15.8	183	SU UMa	8
EG Cnc	703580960947960576	1.44	18.81	183	WZ Sge	54
SDSS J101421.55+063857.7	3873721404734233344		18.25	183	WZ Sge	
NSV 4618	5665509162794290944	1.58	16.85	182	SU UMa	11
Gaia18dwy	6185371175372936064		17.9	180	U Gem	
IY UMa	855167540988615296	1.77	17.44	177	SU UMa	8
ASASSN-14ag	3071240270519385856	1.45	16.18	176	SU UMa	11
PNV J17144255-2943481	4107290939047483008	1.43	17.16	176	WZ Sge	3
V0405 Peg	2838503311371673472	4.26	15.28	172	Magnetic	34,66
V1043 Cen	6179636986011888512	4.19	15.11	171	Magnetic	66
V0406 Vir	3681313024562519552		17.72	168	WZ Sge	67
V5662 Sgr	6749618724313541760	1.51	17.97	168	Novalike	
V0391 Cam	IBVS 6052	1.35	15.53	163	SU UMa	35
PU CMa	286497000368243200	1.36	15.25	162	SU UMa	8
SW UMa	2923643719394227328	1.36	16.58	161	SU UMa	8

Name	<i>Gaia</i> DR2 source_id	Period (h)	phot_g_mean_mag (mag)	Distance (pc)	CV Type	References
EF Eri	1030279027003254784		18.21	159	Magnetic	66
CU Vel	5099482805904892288	1.88	16.71	158	SU UMa	8
SDSS J150551.58+065948.7	5524430207364715520		19.12	159	AM CVn	14
V0436 Cen	1160374338017986688	1.5	16.32	156	SU UMa	33
FL Psc	5397102019219938944	1.35	17.53	152	WZ Sge	3
EI Psc	2754909740118313344	1.07	15.91	151	SU UMa	74
BZ UMa	2757417008882236672	1.63	16.21	151	SU UMa	8
V0355 UMa	1037411284055821568	1.37	17.38	149	WZ Sge	3
V0379 Vir	1558322303741820928	1.47	18.01	149	Magnetic	6
EZ Lyn	3699606286708406912	1.42	17.81	145	WZ Sge	36
SDSSJ102905.21+485515.2	935056333580267392		18.16	143	Period bouncer	58
HT Cas	834947865750806272	1.77	16.35	140	SU UMa	8
VY Aqr	426306363477869696	1.51	16.86	137	SU UMa	8
VV Pup	6896767366186700416	1.67	15.93	136	Magnetic	66
Gaia J154008.36-392917.58	5719598950133755392		17.36	133	SU UMa	50
V3885 Sgr	6008982469163902464	4.97	10.25	132	Novalike	83
MR Ser	6688624794231054976		16.23	131	Magnetic	66
BL Hyi	1203639265875666304	1.89	17.25	130	Magnetic	73
SDSS J125044.42+154957.3	4697621824327141248		18.22	128	Magnetic	10
V1040 Cen	3934459045528378368		14.04	127	SU UMa	8
QZ Vir	5343601913741261312	1.41	16.06	127	SU UMa	11
V0893 Sco	3800596876396315648	1.82	14.65	123	SU UMa	
Gaia J051903.96+630339.67	6039131391540808832	2.1	15.17	116	SU UMa	50

Name	<i>Gaia</i> DR2 source_id	Period (h)	phot_g_mean_mag (mag)	Distance (pc)	CV Type	References
V0884 Her	285957277597658240	1.88	13.49	114	Magnetic	51
GW Lib	4503256687122329088		16.49	112	WZ Sge	17
V0834 Cen	6226943645600487552	1.69	16.66	112	Magnetic	84
V2051 Oph	6096905573613586944	1.5	15.37	111	SU UMa	8
TCPJ21040470+4631129	4111991385628196224	1.28	17.77	109	WZ Sge	42
1RXS J105010.3-140431	2163612727665972096	1.48	17.17	109	Period bouncer	13
AR UMa	3750072904055666176	1.93	16.26	101	Magnetic	66
V627 Peg	783921244796958208	1.31	15.67	99	WZ Sge	11
BW Scl	1800384942558699008	1.3	16.26	94	WZ Sge	22
V0396 Hya	2307289214897332480		17.66	93	AM CVn	28
AE Aqr	3503987633230546688	9.88	10.95	90	Magnetic	79
IX Vel	4226332451596335616	4.65	9.32	90	Novalike	53
ASASSN-14dx	5515820034889610112	1.38	14.96	80	WZ Sge	65
NSV 25966	2488974302977323008	1.71	16.46	80	WZ Sge	87
V0455 And	2208124536065383424	1.35	16.06	75	WZ Sge	3,59
GP Com	1920126431748251776		15.95	72	AM CVn	14
VW Hyi	3938156295111047680	1.78	13.84	53	SU UMa	11
WZ Sge	4653893040002306432	1.36	15.21	45	WZ Sge	
WDJ194125.05+152255.30.	1809844934461976832		16.82	215	Magnetic	
WDJ194125.05+152255.30.	4318508939464901760		16.96	215	Magnetic	

References: 1 [Kazarovets et al. \(2013\)](#), 2 [Munari et al. \(2015\)](#), 3 [Kato \(2015\)](#), 4 [Green et al. \(2020\)](#), 5 [Thorstensen \(2016\)](#), 6 [Burleigh et al. \(2006b\)](#), 7 [Howell et al. \(2008\)](#), 8 [Kato et al. \(2009\)](#), 9 [Pala et al. \(2017\)](#), 10 [Breedt et al. \(2012a\)](#), 11 [Kato et al. \(2015\)](#), 12 [Coppejans](#)

et al. (2016), 13 Mennickent et al. (2001), 14 Ramsay et al. (2018), 15 Mattei et al. (1986), 16 Traulsen et al. (2011), 17 Hiroi et al. (2009), 18 Hoard et al. (2002), 19 Szkody et al. (2011), 20 vsnet-alert 21627, 21 Bernardini et al. (2014), 22 Kato et al. (2013b), 23 Halpern & Thorstensen (2015), 24 Monard & Africa (2005), 25 Godon et al. (2016), 26 Kato et al. (2016a), 27 Thorstensen & Halpern (2013), 28 Ruiz et al. (2001), 29 Cieslinski & Steiner (1997), 30 Pala et al. (2018), 31 Scaringi et al. (2010), 32 Thorstensen (2020), 33 Hamilton et al. (2011), 34 Thorstensen et al. (2009), 35 Rutkowski et al. (2010), 36 Zharikov et al. (2008), 37 Segura Montero et al. (2020), 38 Oliveira et al. (2020), 39 Kuulkers et al. (2013), 40 Ramsay et al. (1999), 41 Ramsay et al. (2008), 42 Sokolovsky et al. (2019), 43 Thorstensen & Fenton (2003), 44 Armstrong et al. (2013), 45 Augusteijn et al. (2010), 46 Manser & Gansicke (2014), 47 Bruch (2019), 48 Szkody et al. (2002a), 49 vsnet-alert 19045, 50 Pala et al. (2020), 51 Hastings et al. (1999), 52 Kolbin et al. (2019), 53 van Teeseling et al. (1995), 54 Kato et al. (2004), 55 Thorstensen et al. (2015), 56 Parisi et al. (2014), 57 Kato et al. (2017), 58 Thorstensen et al. (2016), 59 Araujo-Betancor et al. (2005a), 60 Howarth (1975), 61 Szkody et al. (2006), 62 Rodríguez-Gil et al. (2005a), 63 Gänsicke et al. (2005a), 64 Littlefair et al. (2006), 65 Isogai et al. (2019a), 66 Barrett et al. (2020), 67 Pala et al. (2019), 68 Knigge et al. (1998), 69 Kato et al. (2010), 70 Gänsicke et al. (2000), 71 Nakata et al. (2013), 72 Hernández Santisteban et al. (2016), 73 Cropper (1987), 74 Thorstensen et al. (2002c), 75 Scaringi et al. (2013), 76 O'Donoghue et al. (1994), 77 Stark et al. (2008), 78 Thomas et al. (1996), 79 Casares et al. (1996), 80 Thorstensen & Skinner (2012), 81 Bruch (2017), 82 Barrett et al. (2020), 83 Ribeiro & Diaz (2007), 84 Wright et al. (1988), 85 McAllister et al. (2015), 86 Uthas et al. (2011), 87 Jurdana-Šepić & Poljančič Beljan (2015), 88 Ritter & Kolb (2003)

A.4 List of CVs with data quality issues

Table A.4: CVs within 300pc that were omitted from the Gold sample due to data quality issues. We provide the geometric distances from [Bailer-Jones et al. \(2018\)](#).

Name	<i>Gaia</i> DR2 source_id	Distance (pc)
Gaia19eem	6237062584251753472	246
MASTER OTJ231437.93-405351.7	6548343809360111744	234
WX Hyi	4701058897674276736	232
CSS 111021:220328+141059	1768390043246037120	271
Gaia19ewe	2660838205305484672	110
ASASSN-16jg	6105337384683991552	156
BPM 18764	5512466799298330240	108
V1454 Cyg	2035604633348389504	104
V0348 Pav	6443663915781143296	153
Gaia16bvf	4308267336592964480	103
U Gem	674214551557961984	93
OY Car	5242787486412627072	90
AM Her	2123837555230207744	87
MASTER OT J085945.08+753627.8	1125344790910293504	230
MASTER OTJ194753.58-475722.9	6671305080912878976	90
MASTER OTJ020836.79-104018.8	2461410645980184704	81
CSS 131106:032129+180827	56061898877135872	78
Z Cam	1123169888190445568	223
EX Hya	6185040879503491584	56
OGLE-BLG-DN-0128	4041521619610315520	56
MASTER OTJ015119.13-643046.6	4699355032608266496	39
V1108 Her	4538504384210935424	151
ASASSN-13cv	1898408805059830400	234
IPHAS J052832.69+283837.6	3445477328117272576	222
V2301 Oph	4476137370261520000	120
ASASSN-16ee	5640533756172726528	268
OGLE-BLG-DN-0824	4050525898398798208	244
IGR J14536-5522	5893562752211667328	217
WW Cet	2427474150870397056	216
Gaia17aoi	3608370667261082368	234
OGLE-BLG-DN-0460	4042926554954231808	221
MASTER OT J202151.88-455950.3	6669764085302140160	221

Name	<i>Gaia</i> DR2 source_id	Distance (pc)
1RXS J174320.1-042953	4176399299256927488	212
V1235 Oph	4127952132584502144	212
SSS_J155147.2-211323	6240789280132901632	144
MASTER OTJ143453.02+023616.1	3656050538028470144	119
SDSS J053553.55-004003.9	3217759570831525120	213
IP Peg	2824150286583562496	140
ASASSN-14ib	3204003344636046336	157
ASASSN-17rc	5070939380966139776	299
TCP J18001854-3533149	4041983178121844224	206
MASTER OT J012303.34-492007.7	4929599428958427008	204
SDSS J225831.18-094931.7	2606580678024447104	294
V0347 Pup	5553468275089335040	293
MASTER OTJ175847.37+253624.2	4582541366791136512	295
ASASSN-15bu	109693846992684544	291
J194827-131733	4188707163699348992	288
UW Pic	4798833587650467200	288
ASASSN-14ip	6481531817797462272	223
RX And	374510294830244992	197
OGLE-BLG-DN-0924	4050692890856193152	297
Z Cha	5210507882302442368	115
V2779 Oph	4482863941883637632	283
HU Aqr	6911950900211768704	191
SDSS J121913.04+204938.3	3952276665815698560	281
V0379 Tel	6658737220627065984	130
PT Per	454808969042727168	183
UZ Boo	1241536747327175936	287
Gaia19abb	111944405560751488	132
ASASSN-17eo	2030910474596086528	133
ASASSN-18bh	401703515191891968	247
Gaia17bhj	5870181328169203840	297
SDSS J001912.58+220733.0	2800340564145444352	276
J1514+0744	1163569523103341568	181
ASASSN-13cg	6916720061963174016	269
SDSS J090403.48+035501.2	579909164365936512	277
MASTEROTJ020404.19+741804.6	558705666741812096	200
Gaia17bzq	6721443743158616960	296
SS Cyg	1972957892448494592	114
USNO-B1.0 0886-0475568	4262279021472873856	265

Name	<i>Gaia</i> DR2 source_id	Distance (pc)
GG Leo	3876618514794039040	262
OGLE-BLG-DN-0742	4063038340493742208	266
MASTER OTJ120525.84+621743.3	1582897002802390400	175
SSS 120411:103035-315419	5448901107220447488	278
ST LMi	3996419759863758592	112
ASASSN-14cn	1629388752470472704	256
MASTER OTJ140957.49+290922.7	1453003417810298496	173
IGR J19552+0044	4240284979281473920	170
UU Aqr	2675351827511262720	254
RX J0131.4+3602	319016667370280064	258
OGLE-BLG-DN-0347	4043251254487758976	277
ASAS J102522-1542.4	3749056714792756352	260
ASASSN-14ei	4752105374261391360	253
EF Peg	1759321791032618624	258
SDSSJ111823.91+620817.4	862126311425005056	258
ASASSN-17mj	6762473973752036096	252
SDSS J214140.43+050730.0	2698490156365025536	257
PQ And	337940224558062080	254
SSS_J035055.8-204817	5093945085525624448	124
SDSS J125641.29-015852.0	3688476819557779712	281
MACHO 401.48296.2600	4062767070547321984	184
NSV 35	4706297108508032128	245
NSV 18024	5529197346190132480	171
EX Dra	2258357545848389888	244
CD Ind	6453536224527716224	242
MLS 120517:152507-032655	4413778946245759360	242
KT Per	405873692214746368	240
MASTER OTJ012916.47+321859.0	315797744000875904	171
UZ For	5084805635638179584	238
YZ Cnc	683908812437792000	237
MASTER OTJ231033.30-335509.7	6556126324459834752	240
V0347 Pav	6414928454268212352	160
CSS 091027:222548+252511	1879049845562942592	242
OGLE-BLG-DN-0428	4062261157598683392	169

A.5 List of Double White Dwarfs

Table A.5: The Double White Dwarf 300pc Gold sample. We provide the geometric distances from [Bailer-Jones et al. \(2018\)](#).

Name	<i>Gaia</i> DR2 source_id	Period (h)	phot_g_mean_mag (mag)	Distance (pc)	Reference
WD0028-474	4978793541987799040	9.35	15.18	96	2
EGGR 561	2542961560852591744		14.87	54	22
WD0136+768	560568793490187264	33.77	14.92	74	19
HE0205-2945	5020319141229055360		15.92	100	15
HE0225-1912	5131327656235273088		16.01	155	15
HE0315-0118	3262674487682440448	45.91	14.73	69	2
HE0320-1917	5104856776357892480	20.76	15.92	113	21
HE0324-1942	5101782335688104960		16.07	138	15
HE0325-4033	4849811172961336960		16.27	104	15
WD0341+021	3270918350990573184	43.7	15.46	144	10
NLTT11748	44582933060466560	5.65	16.64	181	3
WD0344+073	3277341526122556160		16.62	140	15
HE0410-1137	3189613692364776576	12.21	15.93	104	2
WD0455-282	4876689387538123008	8.6	15.03	97	15
HE 0455-5315	4782942513595999872		16.81	239	15
EQ J0755+4800	933556290482790528	13.11	16.22	181	12
WD 0920+306	700346923589710080	1.08	15.94	297	14
WD0957-666	5245683698817306624	1.46	14.5	162	6

Name	<i>Gaia</i> DR2 source_id	Period (h)	phot_g_mean_mag (mag)	Distance (pc)	Reference
WD1013-010	3830623164560911872	10.48	15.3	46	21
WD1022+050	3860381618565361024	27.77	14.23	39	9
WD 1101+364	762814371050472448	3.47	14.58	88	25
EQ J1104+0918	3866880552624195584	13.28	16.83	189	12
PG1114+224	3991120727998388864	7.68	16.35	264	18
PG1115+166	3970767638191849984	722.11	15.11	90	1
WD1202+608	1582231699483080192	35.83	13.52	198	7
WD1210+140	3920848710779658880	15.41	14.69	207	21
WD 1241-010	3683519503881169920	80.34	14.01	83	23
WD1242-105	3530399693530713344	2.85	14.66	40	8
SDSS J125733.63+542850.5	1570271658673389568	4.55	16.7	119	17
HS1334+0701	3718352444565698432		15.42	106	15
WD1349+144	3728966476985207936	53.03	15.27	116	13
HE1414-0848	3638957019161984640	12.43	15.91	81	4
WD1428+373	1481311753417900160	27.76	15.49	97	9
HE1511-0448	6335184655474717312	77.33	15.35	284	21
PG1519+500	1595402921071043584	20.65	16.5	295	18
EQ J1557+2823	1319676603468508544	9.78	17.88	250	12
WD 1704+481	1408135749896104192	3.47	14.4	39	16
GD 360	1334770870892758912	27.06	14.47	89	23
GALEX J171708.5+675712	1637422647712544512	5.91	13.32	177	11
WD2020-425	6679362959252072832	7.2	14.85	99	15
WD 2032+188	1815657193425348096	122.03	15.42	109	23

Name	<i>Gaia</i> DR2 source_id	Period (h)	phot_g_mean_mag (mag)	Distance (pc)	Reference
WD2200-136	2612442135856683648	15.8	15.4	138	15
HE2209-1444	2600033326799287296	6.65	15.01	37	20
HS 2216+1551	2735823425146356224		15.98	129	15
WD2330-212	2388953031573382784		16.72	254	15
GD 251	2869402611769740544	4.0	15.72	248	23
WD2336-187	2393875961742886656		15.51	37	15
WD 2345-481	6524412152806190336		15.89	251	22
WD0135-052	2480523216087975040		12.76	12	5
WD0121-429	4983839647522981504		14.71	18	5
WD0233-242	5125186299678747008		15.69	18	5
WD2048+263	1844125748497557632		15.4	19	5
J053620.21+412955.62	194394347281717504	3.48	14.66	32	24
J094846.64+242125.88	643183348419998336		14.27	36	24
J012924.26+102301.34	2585189473147457408	35304.0	14.37	29	24
J134532.97+420043.66	1500607765872799616		17.06	37	24
J163441.85+173634.09	4466388790929771904		13.16	25	24
J000754.11+394732.18	383108338321272448		16.58	34	24
J002215.19+423642.15	385105360675267840		16.38	34	24
J020847.22+251409.97	104648944047154432		13.25	39	24
J054457.66+260300.14	3429296884940000000		16.9	36	24
J111536.96+003317.11	3810099989754827136		17.29	39	24
J214913.61+041550.35	2696628687474414208		16.66	35	24

References: 1 [Maxted et al. \(2002b\)](#), 2 [Rebassa-Mansergas et al. \(2017a\)](#), 3 [Steinfadt et al. \(2010\)](#), 4 [Napiwotzki et al. \(2002\)](#), 5 [Hollands et al. \(2018\)](#), 6 [Moran et al. \(1997\)](#), 7 [Holberg et al. \(1995\)](#), 8 [Debes et al. \(2015\)](#), 9 [Morales-Rueda et al. \(2005\)](#), 10 [Maxted et al. \(2000b\)](#), 11 [Vennes et al. \(2011\)](#), 12 [Brown et al. \(2013\)](#), 13 [Farihi et al. \(2005b\)](#), 14 [Brown et al. \(2010\)](#), 15 [Napiwotzki et al. \(2020\)](#), 16 [Maxted et al. \(2000a\)](#), 17 [Badenes et al. \(2009\)](#), 18 [Brown et al. \(2011\)](#), 19 [Maxted et al. \(2002a\)](#), 20 [Karl et al. \(2003\)](#), 21 [Nelemans et al. \(2005\)](#), 22 [Koester et al. \(2009\)](#), 23 [Marsh et al. \(1995\)](#), 24 [McCleery et al. \(2020\)](#), 25 [Marsh \(1995\)](#)

Appendix B

Supplementary Material - Chapter 5

B.1 Introduction

We include here all of the data supporting Chapter 5.

In section [B.2](#) we list the full set of all CVs (new and rediscovered) together with pertinent attributes and references. In section [B.3](#) we discuss individual CV classifications and other relevant discoveries. In section [B.4](#) we list the spectra and light curves for all the CVs. In section [B.5](#) we list the plate, MJD and fibre for each CV in the paper.

We have included some unpublished spectroscopic periods that were derived from observations at the MDM observatory and photometric periods obtained from photometry using ULTRACAM ([Dhillon et al., 2007](#)) and ULTRASPEC ([Dhillon et al., 2014](#)) at the Thai National Telescope.

B.2 List of CVs

Table B.1: CVs from SDSS I to IV. We provide the geometric distances from [Bailer-Jones et al. \(2021\)](#) and CV sub-types according to the definitions in Sect. 3 in [5](#). SDSS g -band magnitudes are from data release 7 ([Abazajian et al., 2009](#)). The references for the initial discovery (ID), spectrum (Sp) and orbital and superhump periods (P – where known) are also shown. New discoveries, orbital periods and sub-type identifications are shown in blue. Sub-type identifications in black are from VSX ([Watson et al., 2017](#)). : Tentative values,

* Superhump periods, † low accretion SU UMa, ‡ CVs with unusual state changes, § period bouncers.

SDSS	Name	Gaia EDR3 source_id	Period (days)	SDSS g (mag)	Distance (pc)	Variable Sub-type	References		
							ID	Sp	P
J000014.74+255603.1				22.17		CV:	1	1	
J000720.77+200721.6	CSS 110921:000721+200722			21.48		WZ Sge:	91	1	
J000844.32-014014.6	Gaia15abi	2544817841421994624		17.93	1236^{+220}_{-230}	NL:/Polar	91	1	
J001107.26+303235.9	V0402 And	2861506395998660096	0.063499(3)*	20.4	793^{+434}_{-225}	SU UMa	59	1	42
J001153.08-064739.2	SDSS J001153.08-064739.1	2443219535337313280	0.10028081(8)	17.83	477^{+29}_{-19}	U Gem	94	94	94
J001158.28+315543.7	CSS 101111:001158+315544	2861949606559861120	0.0554(1):	21.85		SU UMa	91	1	1
J001231.54+280011.1		2859847683924640384		20.98		WZ Sge:	1	1	
J001538.25+263656.7	CSS 090918:001538+263657	2856493142666940544	0.10150(6)	17.92	557^{+36}_{-34}	SU UMa	91	206	206
J001856.92+345444.2	V0479 And	2876157251000218496	0.594093(4)	17.46	2027^{+408}_{-259}	Polar:	21	21	165
J002049.51+280020.2	MASTER OT J002049.54+280020.5	2857063063352792320	0.05658(1)	19.64	347^{+59}_{-45}	WZ Sge:	99	1	1
J002243.55+061002.7	MGAB-V295	2747622177049417344	0.079(1):	19.88	2113^{+1596}_{-715}	SU UMa	76	1	1
J002500.17+073349.2	CSS 081123:002500+073350	2748173586426407424		19.68	1484^{+412}_{-306}	DN/IP:	91	1	
J002637.05+242915.6	CSS 091026:002637+242916	2807191999055199232	0.08533(1)	18.75	588^{+100}_{-87}	Polar	91	1	1
J002728.00-010828.5	EN Cet	2541910801397761152	0.05933(5)	20.78	1218^{+461}_{-547}	WZ Sge	95	21	170
J002842.53+311819.4		2859593555004235520	1.217(1)	18.59	3642^{+1152}_{-985}	NL	47	47	1
J002910.96+324125.8				22.12		DN	1	1	
J003151.76+202051.0	MGAB-V534	2796463449923353856	0.080871025(2)	18.06	368^{+19}_{-16}	SU UMa†	76	1	227
J003153.46+084118.5	ASASSN-17kg	2749846901389046656	0.0585(3)*	19.15	283^{+24}_{-17}	WZ Sge	210	1	93
J003203.62+314510.4	CSS 091220:003204+314510	2859621764350006784		19.1	960^{+335}_{-184}	SU UMa	91	1	
J003459.90+273619.0	CSS 081031:003460+273620	2857545615813275136	0.07337(1)	21.12	1349^{+828}_{-462}	SU UMa	91	1	1
J003640.29+230831.3	ASASSN-14dr	2805913271327662976	0.06655(9)	18.4	495^{+49}_{-38}	SU UMa:	126	206	206
J003827.05+250924.9	1RXS J003828.7+250920	2806802123399581056	0.094511(1)	18.86	503^{+64}_{-38}	SU UMa	7	199	1
J003941.06+005427.4	SDSS J003941.06+005427.5	2543387617312121216	0.06347(6)	20.5	1078^{+468}_{-414}	WZ Sge:	21	21	180
J004213.04+073137.8	PB 6108	2557191783935736448	0.1070(1)	18.27	680^{+67}_{-58}	IP:	149	47	1
J004335.13-003729.8	SDSS J004335.14-003729.8	2530961280492678528	0.05791(6)	19.81	447^{+91}_{-75}	WZ Sge:	72	72	12

SDSS	Name	Gaia EDR3 source_id	Period (days)	SDSS g (mag)	Distance (pc)	Variable Sub-type	References		
							ID	Sp	P
J004500.31+222707.2	CSS 081102:004500+222708	2802955963006146176	0.07042(1):	20.47	782 ⁺⁵⁸⁵ ₋₂₀₁	SU UMa	62	1	1
J004849.86+332832.9		361363704879572736		20.61	763 ⁺³⁵⁸ ₋₂₃₀	SU UMa:	1	1	
J004902.10+074726.8	CSS 090204:004902+074726			21.51		WZ Sge:	91	1	
J004924.50+222617.9		2802295461460467072	0.24652(1)	19.45	671 ⁺¹³² ₋₉₄	Polar	137	137	1
J005050.87+000912.7	GS Cet	2537078211571341568	0.0558(1)	20.4	308 ⁺¹²⁴ ₋₈₁	WZ Sge	21	21	124
J005217.22+315938.5		360893388779827456		21.5	1493 ⁺⁸³³ ₋₅₉₁	Polar	132	132	
J005421.90+334815.7				22.12		WZ Sge:	1	1	
J005657.57+320621.7	MGAB-V3456	312918810242506624	0.06614875(2)	20.11	606 ⁺¹⁵² ₋₁₁₆	Polar	76	1	1
J005811.09-010750.8	ASASSN-16iw		0.06495(4)	22.06		WZ Sge§:	171	1	171
J010340.75+200525.9		2788762156951156864	0.158(1):	21.45		IP:	1	1	1
J010411.63-031342.3	CSS 091009:010412-031341	2531434796342548224		19.54	1096 ⁺³⁶⁷ ₋₂₃₆	SU UMa:	97	226	
J010844.12+022638.9	MGAB-V3459	2538720705848262912	0.05372(1)	18.62		Polar:	76	137	1
J011011.29+033234.6	XY Psc	2539642959880875136	0.06067(5)*	21.13	1455 ⁺²⁵⁵⁸ ₋₇₃₂	SU UMa	183	1	13
J011331.69-033233.5		2483547933921120768	0.183133(1)	20.46	381 ⁺⁶⁴ ₋₄₀	Polar	137	137	137
J011516.54+245530.2	CSS 101008:011517+245530	294125858715647360	0.0731(6)*	21.24	951 ⁺⁷³¹ ₋₂₉₅	SU UMa	91	1	17
J011712.94+175527.0	ASASSN-20pq	2785769840349672960	0.0612(1))	20.5	318 ⁺¹⁹¹ ₋₇₅	SU UMa:	126	1	1
J012008.20+185715.5		2785962113150663424		19.95	426 ⁺⁹² ₋₉₀	WZ Sge:	99	1	
J012212.21+075546.8		2578454444735885056		20.33	343 ⁺¹¹⁹ ₋₇₈	WZ Sge:	1	1	
J012402.25+211359.7		289388711652054912	0.083475(1)	21.38	688 ⁺³⁵⁷ ₋₂₄₁	Polar	1	1	1
J012838.37+184535.6	CSS 100114:012838+184536			21.67		CV	91	1	
J012842.13+113050.4	CSS 141018:012842+113051	2585586186391694592		20.89	1660 ⁺⁶⁸¹ ₋₅₂₉	DN	91	1	
J012940.05+384210.4	V0744 And	323321873867827968	0.026080*	19.8	700 ⁺²⁷³ ₋₁₉₉	AM CVn	191	191	129
J013132.38-090122.2	GY Cet	2477023401857408640	0.05663(9)	18.3	267 ⁺¹⁵ ₋₁₂	WZ Sge	130	130	124
J013421.83+042200.0				21.41		Polar:	1	1	
J013540.99+340132.9		316371177970255232		22.42		Polar:	1	1	
J013701.06-091234.8	GZ Cet	2465053942183130240	0.055343(7)	18.99	297 ⁺¹³ ₋₁₄	SU UMa†	130	130	197
J013737.20+300248.6	TX Tri	303093922229116160		17.49	1164 ⁺¹¹⁵ ₋₈₆	U Gem	40	121	
J014121.21+062007.6		2562434457240098432		20.77		WZ Sge:	1	1	
J014227.07+001729.8	SDSS J014227.07+001729.8	2510205490257050496		20.82	697 ⁺²⁶¹ ₋₁₅₉	Polar:	134	1	
J014245.89+232339.8	ASASSN-18ad	290720529470734592	0.0712(6):	21.27		SU UMa:	126	1	1
J014732.85+144443.3		2588313902941290112		22.38	907 ⁺⁷²² ₋₃₁₀	Polar	1	1	
J015051.52+332621.8	CSS 111006:015052+332622	305760371070111872	.072706(32)*	18.21	719 ⁺⁷⁹ ₋₅₈	SU UMa	203	199	33
J015151.86+140047.1	BG Ari	2576029647934945792	0.08242(2)	20.28	576 ⁺²²⁰ ₋₁₂₄	SU UMa	32	32	170
J015253.39-004350.4				20.81		SU UMa:	1	1	
J015543.39+002807.1	FL Cet	2507796391561705728	0.06051621(4)	19.32	317 ⁺¹³ ₋₁₂	Polar	32	32	85
J015712.18+224402.6	CSS 130916:015712+224402			21.9		SU UMa:	91	1	
J015803.40+282303.6		298356019250182016	0.0888104(1)	20.37	254 ⁺²⁰ ₋₁₆	DN	1	1	1

SDSS	Name	Gaia EDR3 source_id	Period (days)	SDSS g (mag)	Distance (pc)	Variable Sub-type	References		
							ID	Sp	P
J020348.61+295925.7	AI Tri	300427537812198656	0.1917448(7)	16.84	513^{+13}_{-10}	Polar	138	138	138
J020537.55+264304.1	ASASSN-13dh	105746011838379392	0.091322(56)*	19.37	492^{+104}_{-82}	SU UMa	126	1	13
J020712.71-014116.2		2494386992562185088		21.43		Polar:	1	1	
J021107.98+305406.7	Gaia18aot	300540061660343040	0.078830(2)	19.15	517^{+76}_{-56}	Polar	26	174	174
J022319.71-052002.3		2489505809474839680		19.85	300^{+80}_{-43}	WZ Sge:	132	1	
J022940.29-030620.8	CSS 130930:022940-030620	2496208333573924352		20.77		DN	91	1	
J023003.79+260440.3	SDSS J023003.79+260440.3	103226927620025472		20.18	557^{+98}_{-62}	CV	185	185	
J023046.26-004531.1				21.68		WZ Sge:	1	1	
J023151.47-000511.4				20.79		SU UMa:	132	1	
J023322.60+005059.5	HP Cet	2500552912036565120	0.06672(6)	20.06	683^{+429}_{-175}	WZ Sge	32	32	214
J024215.05-011054.4				22.3		CV:	1	1	
J025214.63+002010.6	ASASSN-21rq			22.57		WZ Sge:	126	1	
J031051.66-075500.2	KY Eri	5167772343527624576	0.068636(37)*	15.48		SU UMa	130	130	24
J032651.73+011513.3	CSS 100219:032652+011513			22.67		DN	91	1	
J032855.00+052254.1	SDSS J032855.00+052254.2	3275721498815710464	0.0847(1)	18.97	968^{+447}_{-346}	Polar	196	196	196
J033710.91-065059.4	SDSS J033710.91-065059.4			19.58		SU UMa:	196	196	
J035747.16-063850.7		3244886171956393600		19.99	386^{+64}_{-54}	WZ Sge:	99	1	
J040714.78-064425.1	LT Eri	3197024400735832832	0.17020393(2)	17.76	683^{+24}_{-21}	U Gem	130	130	84
J072827.34+330741.6				21.94		WZ Sge:	1	1	
J072910.68+365838.2	V0654 Aur	898787739946740096	0.104(4)	20.39	1344^{+776}_{-456}	Polar	102	32	147
J073208.11+413008.7	SDSS J073208.11+413008.7	924670003146928640	.079571(21)*	16.2		SU UMa	103	103	17
J073605.07+182709.8		672172522242684800		21.83		Polar	1	1	
J073648.03+200959.7				22.0		CV	1	1	
J073817.74+285519.6	SDSS J073817.75+285519.7	878597549661945984	0.231475(10)	19.3	1204^{+318}_{-187}	U Gem	130	130	130
J074355.55+183834.8	SDSS J074355.56+183834.8			20.1		CV	63	63	
J074431.43+482630.4	ASASSN-16cz	933777159176254208		21.6		SU UMa:	126	1	
J074531.91+453829.3	EQ Lyn	927255749553754880	0.0528(1)	19.04	314^{+28}_{-19}	WZ Sge	63	63	193
J074640.62+173412.8	SDSS J074640.62+173412.8	668162873918693504	0.0649(14)	19.78	672^{+327}_{-217}	SU UMa	63	63	193
J074716.79+424849.0	SDSS J074716.81+424849.0	924287789712940800		17.11	8724^{+5928}_{-3094}	NL:	32	32	
J074813.54+290509.0	V0434 Gem	878801779650368256		18.52	2701^{+756}_{-800}	NL:	102	72	
J074917.11+365428.0	MGAB-V3545	919046658301858048	.0558(1)	18.96	820^{+188}_{-129}	Polar:	76	1	1
J075059.97+141150.1	SDSS J075059.97+141150.1	3164517889217942016	0.093165496(2)	19.08	825^{+162}_{-106}	SU UMa:	196	196	84
J075240.44+362823.2	EU Lyn	918840426857988736	0.114(2)	17.64	631^{+224}_{-186}	Polar	130	130	147
J075331.98+375800.6	CSS 100407:075332+375801	919213474830239616		21.37	1699^{+1379}_{-612}	MCV:	91	1	
J075414.49+313215.7	CSS 110414:075414+313216	880693906019213824	0.0615(5)	19.66	532^{+41}_{-38}	SU UMa	91	72	22
J075443.00+500729.2	EV Lyn	934203971550630656	0.14303(1)	17.27	1812^{+399}_{-250}	NL	63	63	124
J075507.69+143547.4	SDSS J075507.70+143547.6	654539826068054400	0.05886(4)	18.21	240^{+12}_{-11}	WZ Sge:	196	196	193

SDSS	Name	Gaia EDR3 source_id	Period (days)	SDSS g (mag)	Distance (pc)	Variable Sub-type	References		
							ID	Sp	P
J075648.04+305805.0	CSS 080406:075648+305805	877602521701648768		20.87		SU UMa:	91	103	
J075653.11+085831.8	SDSS J075653.11+085831.8	3146975005100167296	0.1369745(4)	16.26	1070^{+87}_{-67}	NL	103	103	105
J075808.81+104345.5	SDSS J075808.81+104345.5	3147451888206160896	0.199(1)	16.96	1907^{+241}_{-222}	NL	185	185	1
J075853.03+161645.1	DW Cnc	667150159287327360	0.05979(4)	15.33	203^{+1}_{-2}	IP	80	63	228
J075939.78+191417.2	SDSS J075939.79+191417.3	670122409797824000	0.1309337(8)	18.1	1754^{+608}_{-382}	NL	63	63	1
J080142.36+210345.6	SDSS J080142.37+210345.8	670872860843747072		18.86	815^{+213}_{-137}	Polar	21	21	
J080215.39+401047.1	SDSS J080215.39+401047.2	921311411737108480	0.15390(3)	16.68	1284^{+89}_{-77}	NL	102	130	193
J080249.06+363716.4				21.9		WZ Sge:	1	1	
J080303.90+251626.9	SDSS J080303.90+251627.0	681813727390427136	.0919(1)*	19.58	1015^{+261}_{-142}	SU UMa	21	21	17
J080434.13+510349.2	EZ Lyn	935056333580267392	0.059713(7)*	17.85	143^{+2}_{-3}	WZ Sge§	63	63	135
J080449.49+161624.8	SDSS J080449.49+161624.8	655188018235294208	0.03090(7)	18.14	998^{+186}_{-133}	AM CVn	48	48	48
J080534.49+072029.1	SDSS J080534.49+072029.1	3097732002461148672	0.228711(1)	18.65	1542^{+280}_{-272}	CV	196	196	1
J080625.73+343244.4			0.0637(1):	21.46		SU UMa:	1	1	1
J080701.10+554739.0	CSS 140311:080701+554739	1033373117151731840		20.62	661^{+143}_{-101}	SU UMa:	91	1	
J080710.33+485259.6	SDSS J080710.33+485259.6	934578664497649280	0.0370(2)	20.41	1276^{+968}_{-553}	AM CVn	116	1	14
J080846.19+313105.9	SDSS J080846.19+313106.0	877832117769627904	0.2059(5)	19.43	1778^{+559}_{-405}	U Gem	72	72	193
J080853.71+355053.7	CSS 080416:080854+355053	906214223733883264		19.66	1807^{+1555}_{-822}	DN	91	101	
J080908.39+381406.2	SDSS J080908.39+381406.2	908714959852556672	0.133616(2)	15.61	1172^{+44}_{-42}	NL	102	130	46
J081017.41+262238.3				21.31		SU UMa:	1	1	
J081207.63+131824.4	LX Cnc	650594709629698304	0.08432(1)*	19.26	865^{+238}_{-172}	SU UMa	196	196	24
J081256.84+191157.8	NS Cnc	669503831427966080	0.160151(79)	16.1	773^{+31}_{-26}	NL	63	63	159
J081321.91+452809.3	FH Lyn	928715626116734976	0.2890(4)	18.26	1693^{+321}_{-285}	U Gem	32	32	200
J081352.02+281317.2	SDSS J081352.02+281317.3	684088337774683520	0.1220(4)	17.16	1085^{+156}_{-129}	NL	21	21	46
J081425.38+202125.1	CSS 150222:081425+202126			22.1		SU UMa:	91	1	
J081520.83+335634.1				21.6		WZ Sge:	1	1	
J081610.83+453010.1	SDSS J081610.84+453010.2	928798016474365952	0.2096(4)	20.05	2436^{+1470}_{-792}	U Gem	32	32	169
J082019.39+474731.2	CSS 091213:082019+474732	930544698069767296		21.37	1712^{+1196}_{-541}	SU UMa	62	22	
J082051.06+493432.1	EG Lyn	931911249288264576	0.06901(2)	19.54	870^{+391}_{-241}	Polar	222	1	222
J082123.73+454135.4	CSS 090224:082124+454135	930082250350668928		19.48	1494^{+483}_{-312}	U Gem	91	1	
J082236.05+510524.5	BH Lyn	1028258463932870656	0.155875577(14)	15.35	736^{+17}_{-21}	NL	207	207	30
J082253.12+231300.7	SDSS J082253.12+231300.6	678153002209054336		21.82	3077^{+2946}_{-1397}	CV:	185	185	
J082409.72+493124.4	FL Lyn	931852494135604736	0.0660(2)	19.24	1478^{+677}_{-431}	SU UMa	32	32	170
J082457.15+073702.4	SDSS J082457.15+073702.4			18.58		DN	63	63	
J082809.87+222004.2		665816516105274496		20.79		CV:	1	1	
J083038.51+404739.0	Gaia19ebs	914867444668112256	0.0731(1)	21.3		Polar	69	1	1
J083404.24+185416.8		662643501643372544		19.23	1634^{+726}_{-438}	Polar	1	1	
J083549.86+292636.9	ZTF18aalmddl	704773999783239808		19.88	1244^{+657}_{-442}	Polar	1	1	

SDSS	Name	Gaia EDR3 source_id	Period (days)	SDSS g (mag)	Distance (pc)	Variable Sub-type	References		
							ID	Sp	P
J083619.14+212105.3	CC Cnc	664787098343076992	0.07352(5)	16.78	493^{+20}_{-24}	SU UMa	100	100	145
J083642.74+532838.0	SW UMa	1030279027003254784	0.05681500(7)	16.89	160^{+1}_{-1}	SU UMa	96	96	193
J083744.34+413338.7		911972671070820352		20.39	642^{+268}_{-187}	WZ Sge:	99	1	
J083750.99+383012.4	SDSS J083751.00+383012.5	910285126880014720	.125(4)	19.18	1066^{+238}_{-173}	Polar	21	21	173
J083754.64+564506.7	SDSS J083754.64+564506.7	1034202286353947776		18.98		WZ Sge:	196	196	
J083845.21+491055.3	SDSS J083845.23+491055.5	1014962001098647680	0.07034(19)	19.59	708^{+102}_{-70}	SU UMa†‡	32	32	46
J083931.35+282823.9	SDSS J083931.35+282824.0	704464491556726912	0.078423(7)*	20.23	928^{+1038}_{-398}	SU UMa	21	21	65
J084026.16+220446.4	SDSS J084026.16+220446.6	665231545856102400	0.06092(1)	19.62	438^{+64}_{-63}	Polar	63	63	1
J084054.15+045519.1	SDSS J084054.15+045519.2	582480170443653376		15.68	1465^{+208}_{-152}	NL	63	63	
J084127.37+210053.5	CSS 090525:084127+210054	664538372493738752	0.0877(3)*	20.61	727^{+359}_{-235}	SU UMa	140	1	17
J084228.13+462334.4				22.17		CV	1	1	
J084303.98+275149.6	EG Cnc	703580960947960576	0.05997(5)	18.86	187^{+7}_{-6}	WZ Sge§	81	21	24
J084358.08+425036.6	CSS 080309:084358+425037	913594794319130368		19.91	2107^{+2584}_{-1361}	SU UMa:	91	1	
J084400.10+023919.3	V0495 Hya	3079207606650040320	0.2070(7)	18.33	1467^{+674}_{-344}	U Gem	130	130	46
J084617.11+245344.0	SDSS J084617.12+245344.1	690436235014785024	.193:	19.88	1232^{+796}_{-285}	Polar	63	63	125
J085107.38+030834.3	CT Hya	581110831791334400	0.066505(1)*	18.78	579^{+35}_{-35}	SU UMa	218	130	65
J085117.04+184249.4	ASASSN-15fq	660056209046609152		19.81	1579^{+975}_{-593}	SU UMa:	126	1	
J085127.17+114656.9	EU Cnc	604917354477205120	0.08712(1)	99.0	2358^{+1456}_{-1714}	Polar	157	150	157
J085228.72+020102.6	CSS 160419:085229+020103	577877683490889728		21.64		Polar:	91	1	
J085300.56+020424.7	CSS 131207:085301+020425			15.0		WZ Sge:	91	1	
J085332.82+484847.7	ZTF18aabjfue	1014328888559622784	0.0986(10)	18.94	1626^{+754}_{-449}	SU UMa†‡	199	199	199
J085344.17+574840.6	BZ UMa	1037411284055821568	0.06799(7)	16.4	154^{+1}_{-1}	SU UMa	209	209	193
J085409.42+201338.9	CSS 080506:085409+201339	660872630790269056		20.89	1224^{+926}_{-463}	SU UMa:	91	1	
J085414.02+390537.2	FR Lyn	719893044876142848	0.07865(2)	19.13	478^{+48}_{-42}	Polar	102	21	170
J085521.17+111815.3	AK Cnc	604649859617712384	0.0651(2)	18.81	557^{+40}_{-35}	SU UMa	205	20	20
J085603.78+322109.2	CSS 100508:085604+322109	712763536603376512		19.64	1378^{+522}_{-442}	SU UMa	91	1	
J085623.00+310833.9	SDSS J085623.00+310834.1	711875745387165696		20.06	621^{+412}_{-175}	WZ Sge:	102	21	
J085909.18+053654.5	SDSS J085909.18+053654.5	583340808875713280	0.09986	18.59	440^{+22}_{-20}	Polar	21	21	193
J090016.55+430118.1	SDSS J090016.56+430118.2	1008926403817205888	0.20937(5)	18.88	851^{+88}_{-75}	U Gem	72	72	193
J090016.66+343927.6	CSS 110512:090017+343928	713695132190090112		20.67	2164^{+1414}_{-714}	SU UMa:	91	1	
J090103.93+480911.1	PU UMa	1012556991212091008	0.0778805326(6)	19.25	636^{+205}_{-139}	SU UMa	130	130	84
J090113.51+144704.6	SDSS J090113.51+144704.6	610249401755733376	0.14633(2)	16.23	1401^{+99}_{-85}	NL	185	185	1
J090350.72+330036.1	SDSS J090350.73+330036.1	712480889099565696	0.059073525(4)	18.84	331^{+35}_{-29}	SU UMa	21	21	65
J090403.48+035501.2	SDSS J090403.48+035501.2	579909164365936512	0.05972325(50)	19.31	295^{+42}_{-36}	WZ Sge:	72	72	10
J090452.08+440255.4	FV Lyn	1009443620958770048	0.06977*	19.39	335^{+43}_{-31}	WZ Sge:§:	72	72	33
J090628.25+052656.9	SDSS J090628.25+052656.9	580320897110564480		18.77	1568^{+230}_{-174}	DN	21	21	
J090744.63+463050.4		1011418309482280704		19.99	1074^{+1677}_{-436}	CV	99	1	

SDSS	Name	Gaia EDR3 source_id	Period (days)	SDSS g (mag)	Distance (pc)	Variable Sub-type	References		
							ID	Sp	P
J090947.82+110637.0		592059145810439808		20.83	601^{+631}_{-232}	WZ Sge:	1	1	
J090950.53+184947.4	GY Cnc	635508894697188864	0.1754424988(21)	16.05	271^{+4}_{-4}	U Gem	23	23	187
J091001.63+164820.0	SDSS J091001.63+164820.0	610980332174389632	0.0734(2)*	18.86	554^{+82}_{-61}	SU UMa	185	185	171
J091107.84+260617.3				21.53		SU UMa:	1	1	
J091127.35+084140.7	SDSS J091127.36+084140.7	590408469622313344	0.2054(2)	19.74	1324^{+943}_{-369}	U Gem	21	21	214
J091216.20+505353.8	DI UMa	1013298268207936128	0.054579	17.92	705^{+32}_{-36}	ER UMa	189	189	60
J091242.18+620940.1	SDSS J091242.18+620940.1	1040150781699159680	0.08013(9)	18.83	298^{+17}_{-17}	SU UMa:	103	103	46
J091425.64+540311.0	ZTF19aaqxclz	1022872716679007488		20.97	849^{+527}_{-256}	SU UMa	74	1	
J091650.76+284943.1	HH Cnc	698627557985830912	0.1846(40)	19.18	965^{+353}_{-259}	U Gem	102	196	46
J091709.89+314307.6	CSS 110430:091710+314309	701449321434522624	0.0541437(1)	20.49	1292^{+694}_{-465}	Polar	91	1	1
J091935.65+502825.2	SDSS J091935.66+502825.1	1019022222662292864		19.86	1551^{+445}_{-300}	DN	21	21	
J091945.10+085710.0	LV Cnc	587578670286348160	0.05647(12)	18.2	196^{+5}_{-6}	WZ Sge:	21	21	46
J092009.54+004244.8	V0524 Hya	3844106127759399808	0.147875676(6)	17.56	1165^{+176}_{-141}	U Gem:	130	130	84
J092122.84+203857.1	SDSS J092122.84+203857.1	637583290886543104	0.058500(3)	19.84	705^{+784}_{-243}	Polar	185	185	166
J092207.56+310314.3	AR Cnc	700436735649429376	0.2146	18.54	871^{+107}_{-112}	CV‡	66	50	189
J092219.55+421256.7	SDSS J092219.55+421256.7	817424772844576768		19.9	397^{+110}_{-57}	WZ Sge:	21	21	
J092229.25+330743.6	SDSS J092229.26+330743.6	702007319289982336	0.0656(2)	18.45	684^{+141}_{-108}	SU UMa	102	21	46
J092444.48+080150.9	HU Leo	587316166180416640	0.09114108(31)	17.9	550^{+103}_{-85}	Polar:	21	21	166
J092638.71+362402.4	YZ LMi	798764346831516032	0.01966127289(2)	18.97	815^{+179}_{-121}	AM CVn	191	191	146
J092809.84+071130.5	SDSS J092809.84+071130.5			15.32		WZ Sge:	103	103	
J092918.90+622346.2	SDSS J092918.90+622346.2	1064002487440866688		18.71	4940^{+1641}_{-1376}	MCV:	103	103	
J093130.75+335651.2		797435239135183744	0.0799(2):	20.44	797^{+990}_{-248}	SU UMa	1	1	1
J093214.82+495054.7	QS UMa	1018018235403653504	0.4183737(3)	17.49	2465^{+320}_{-223}	NL	90	63	193
J093220.93+133122.2	SDSS J093220.92+133122.2	617344855231732096		18.02	712^{+196}_{-124}	NL:	103	103	
J093238.21+010902.5	SDSS J093238.21+010902.5	3841337699215167232		20.28	3145^{+1300}_{-1259}	Polar:	130	130	
J093249.56+472522.9	SDSS J093249.57+472523.0	825341673177429376	0.066303254(8)	17.78	733^{+225}_{-105}	SU UMa	102	72	144
J093423.39+403808.9	NSV 18230	813335929619062272		20.15	1449^{+586}_{-346}	SU UMa:	102	1	
J093537.46+161950.8	SDSS J093537.46+161950.8	619153448780495872	0.0640591(53)	18.81	1525^{+504}_{-281}	CV	185	185	166
J093836.98+071455.1	HM Leo	3854288674880283264	0.1868(3)	18.34	506^{+19}_{-20}	U Gem	153	153	193
J093839.25+534403.8	SDSS J093839.25+534403.8	1021254918466332160		19.18	3920^{+2164}_{-1161}	MCV	185	185	
J093946.04+065209.4	SDSS J093946.03+065209.4			17.3		DN	77	77	
J094002.56+274942.0	SDSS J094002.56+274942.0	647867748990767616	0.16352	19.1	791^{+87}_{-72}	U Gem	196	196	164
J094302.75+275807.5	TCP J09430280+2758080	648047068170272256	0.1815698	19.31	841^{+138}_{-111}	U Gem:	11	1	142
J094325.89+520128.6	SDSS J094325.90+520128.8	1020121493772472704		18.37	908^{+166}_{-144}	SU UMa	72	72	
J094431.70+035805.5	VZ Sex	3848210123629587072	0.1489(1)	16.79		IP	130	130	112
J094558.25+292253.2	SDSS J094558.24+292252.2	648437669676020352	0.0639(2)	19.09	378^{+46}_{-35}	MCV	196	196	46
J094634.46+135057.8	HY Leo	614650192750888320		17.11	1261^{+139}_{-115}	IP	152	103	152

SDSS	Name	Gaia EDR3 source_id	Period (days)	SDSS g (mag)	Distance (pc)	Variable Sub-type	References		
							ID	Sp	P
J094636.59+444644.7	DV UMa	820959638305816448	0.0858526521(14)	19.36	387^{+34}_{-26}	SU UMa	102	21	115
J094741.69+452415.7		821368171297757952	0.056235(1)	22.08	554^{+244}_{-129}	DN	99	1	1
J095135.20+602939.6	SDSS J095135.21+602939.6	1050668027031809280		20.0	460^{+135}_{-110}	WZ Sge:	72	72	
J095151.79+471008.7	SDSS J095151.79+471008.7	821807975948772608		20.33	862^{+822}_{-315}	WZ Sge:	103	103	
J095835.92+281054.7	CSS 140505:095836+281054	743252856601141888		21.61	1651^{+700}_{-628}	SU UMa:	91	1	
J100041.43+385303.0		803113190198180352		19.63	282^{+45}_{-30}	WZ Sge:	99	1	
J100515.36+191107.8	SDSS J100515.38+191107.9	626719772406892288	.075(2)	18.2	340^{+19}_{-17}	SU UMa	185	185	24
J100516.61+694136.5	SDSS J100516.61+694136.5	1070597495622821376	0.1518(3)	19.42	1122^{+167}_{-137}	Polar:	103	103	174
J100658.40+233724.4	SDSS J100658.40+233724.4	630384204143715328	0.18591303(2)	18.33	965^{+264}_{-155}	U Gem	196	196	84
J101037.05+024914.9	SDSS J101037.05+024915.0			20.72		DN:	130	130	
J101323.63+455858.9	SDSS J101323.64+455858.9	810195694346871808	0.08204(13)	18.84	752^{+143}_{-107}	SU UMa	102	72	46
J101335.56+393826.3		802734507224071936		20.78	882^{+741}_{-316}	WZ Sge:	1	1	
J101421.46+063857.0	SDSS J101421.55+063857.7	3873721404734233344	0.05914(7):	18.52	191^{+10}_{-8}	WZ Sge:	99	1	1
J101534.65+090441.9	GG Leo	3876618514794039040	0.05547185(5)	17.26	258^{+11}_{-10}	Polar	131	21	193
J101723.18+375343.4	ZTF19acymwir	754291266149306496		21.65		SU UMa	1	1	
J101947.26+335753.6	AC LMi	752316642050644992	0.07915(14)	18.4	621^{+69}_{-53}	SU UMa:	53	196	46
J102026.48+530433.1	KS UMa	851753282506891776	0.0680(1)	17.42	350^{+5}_{-4}	SU UMa	102	72	34
J102320.26+440509.8	NSV 4838	806057025204204032	0.0679(3)	18.85	640^{+61}_{-53}	SU UMa	21	21	46
J102402.70+480851.1	TCP J10240289+4808512	834525820788839680		19.51	356^{+40}_{-28}	WZ Sge:	99	1	
J102517.94+430221.2	SDSS J102517.94+430221.2	805007163398959360		19.93	334^{+86}_{-55}	WZ Sge:	102	21	
J102637.04+475426.4	V0375 UMa	834461538014044288	0.0667(5)	20.16	632^{+116}_{-94}	SU UMa	82	1	22
J102800.08+214813.5	MV Leo	721859001729641216	0.14606(17)	16.03	999^{+61}_{-62}	Z Cam	102	185	46
J102905.21+485515.2	SDSS J102905.24+485515.2	834947865750806272	0.063421(8)	17.98	149^{+2}_{-3}	WZ Sge:	206	206	206
J103100.54+202831.9	IL Leo	720694618916104576	0.0578(16)	18.25	524^{+54}_{-56}	Polar	193	185	193
J103147.98+085224.3	SDSS J103147.99+085224.3	3863986985912225280		18.81	1001^{+229}_{-198}	SU UMa:	21	21	
J103533.01+055158.7	SDSS J103533.03+055158.4	3859020040917830400	0.0570067(2)	18.82	196^{+11}_{-12}	WZ Sge:§	63	63	75
J104051.24+151133.7	DO Leo	3886153548349816576	0.2345148(2)	17.96	1178^{+102}_{-94}	Z Cam	103	103	120
J104245.15+371819.8		751777469035821312		19.7	507^{+95}_{-91}	Polar	1	1	
J104356.65+580731.5	IY UMa	855167540988615296	0.0739089285(3)	17.54	181^{+2}_{-2}	SU UMa	102	185	84
J104521.19+362433.0				21.44		WZ Sge:	1	1	
J105135.09+540435.6	EK UMa	849625139095603072	.0795(1)	18.4	753^{+129}_{-114}	Polar	102	21	193
J105430.43+300610.1	SX LMi	733329416268149376	0.0672(1)	16.76	312^{+8}_{-6}	SU UMa	189	189	55
J105507.00+365945.2	EL UMa	774791621794667648	0.06045(6)*	20.29	475^{+272}_{-137}	WZ Sge	102	1	65
J105550.08+095620.4	CSS 080130:105550+095621	3867869700772424960	0.1624(5)	19.24	801^{+90}_{-68}	U Gem	103	103	206
J105656.96+494118.3	CY UMa	832942871937909632	0.06957(4)	17.78	307^{+6}_{-7}	SU UMa	90	21	175
J105754.25+275947.5	SDSS J105754.25+275947.5	730651486979234560	0.0627919557(6)	19.6	355^{+52}_{-37}	WZ Sge:§	185	185	1
J105905.06+272755.4	SDSS J105905.07+272755.5	730389322175845248		22.1	895^{+415}_{-339}	PREP	185	185	

SDSS	Name	Gaia EDR3 source_id	Period (days)	SDSS g (mag)	Distance (pc)	Variable Sub-type	References		
							ID	Sp	P
J110014.72+131552.0	SDSS J110014.72+131552.1	3968038512892514048	0.0656(1)	18.68	552 ⁺⁵⁴ ₋₃₈	SU UMa	63	63	193
J110425.64+450313.9	AN UMa	782275761222286720	0.07975274(4)	15.78	333 ⁺⁵ ₋₆	Polar	51	63	193
J110539.76+250628.6	ST LMi	3996419759863758592	0.0790890(7)	17.57	114 ⁺¹ ₋₁	Polar	185	185	193
J110706.75+340527.0	SDSS J110706.76+340526.8	761302194669760256		19.48	1947 ⁺⁷⁴⁴ ₋₃₇₄	DN:	196	196	
J111126.82+571238.9	CSS 120422:111127+571239	856604632750452736	0.038449(6)*	19.23	569 ⁺⁴² ₋₂₇	SU UMa	91	35	17
J111544.50+425822.4	AR UMa	783921244796958208	0.08050074(2)	15.56	98 ⁺¹ ₋₁	Polar	102	63	193
J111715.90+175741.7	DP Leo	3971777500966832384	0.0623628369(7)	99.0	320 ⁺³¹ ₋₂₅	Polar	41	1	41
J111721.92+520501.0	CSS_J111721.9+520500	839265785353309056		19.49	3429 ⁺³⁵⁹⁰ ₋₁₃₀₆	DN	91	1	
J112003.39+663632.4	SDSS J112003.40+663632.4	1057589384008637312		15.64	1678 ⁺²¹⁹² ₋₇₇₈	SU UMa	103	103	
J112253.32-111037.5	CSS 100603:112253-111037	3589668932249752064	0.04530(1)	20.45	832 ⁺⁴⁹⁸ ₋₃₃₂	SU UMa/AM CVn	91	103	179
J113122.39+432238.5	MR UMa	772038105376131456	0.06325(10)	16.18	328 ⁺¹² ₋₁₂	SU UMa	102	63	46
J113215.49+624900.4	SDSS J113215.50+624900.4	862957679655169536	0.0689(2)	18.39	1327 ⁺³²¹ ₋₁₉₁	SU UMa	102	72	46
J113551.09+532246.1	SDSS J113551.09+532246.2	841085507160031232	.0966(1)*	20.81	1982 ⁺⁷⁴⁶ ₋₅₃₄	SU UMa	5	1	171
J113722.20+014858.7	RZ Leo	3799290858445023488	0.0760383(7)	18.73	278 ⁺¹³ ₋₁₂	SU UMa:†	71	189	34
J113732.34+405458.0	SDSS J113732.32+405458.3	767756877680612864	0.0414	19.02	209 ⁺⁹ ₋₁₀	AM CVn	83	83	83
J113826.69+061919.4	SDSS J113826.73+061919.5	3909559715659399808		18.9	208 ⁺⁸ ₋₈	WZ Sge:	63	63	
J113826.82+032207.0	QZ Vir	3800596876396315648	0.058820(5)	14.89	125 ⁺¹ ₋₁	SU UMa	49	64	123
J113950.57+455817.7	NSV 5285	785986539950983296	0.0843(6)	19.64	580 ⁺⁹³ ₋₇₇	SU UMa	9	1	22
J114628.80+675909.6	SDSS J114628.80+675909.7	1058116114501904384	0.0615(8)*	18.75	678 ⁺⁴⁹ ₋₄₈	SU UMa	130	130	224
J114955.68+284507.2	EU UMa	4019704731785215360	0.06262(1)	17.61	286 ⁺¹⁶ ₋₁₄	Polar	211	185	193
J115030.59+404151.8		768134186262349568		21.9	1273 ⁺⁵⁴⁹ ₋₄₅₁	Polar	1	1	
J115207.00+404947.6	SDSS J115207.00+404947.8	768139576446752000	0.0677497017(2)	19.26	639 ⁺¹⁴⁹ ₋₁₁₉	SU UMa	196	196	84
J115215.80+491441.7	BC UMa	787683052032971904	0.06261(8)	18.51	294 ⁺¹⁰ ₋₁₀	SU UMa:†	50	50	34
J115330.25+315835.9	CSS 080201:115330+315836			20.11		SU UMa:	22	22	
J115419.05+575751.1	SDSS J115419.06+575750.9	845441772229861760		20.62	1144 ⁺⁴⁴⁹ ₋₃₅₂	ER UMa	1	1	
J115639.47+630907.7	SDSS J115639.48+630907.7	860177774958213632		20.72	795 ⁺²³⁴ ₋₁₃₁	Polar	102	72	
J120231.00+450349.0	SDSS J120231.01+450349.1	1539493368978351104	0.059801(42)*	19.95	498 ⁺⁶⁵ ₋₄₈	SU UMa	63	63	56
J120615.73+510047.0		1548430890981046272	0.16(3)	19.91	301 ⁺¹⁷ ₋₁₅	PREP	19	19	19
J120724.69+223529.8	SDSS J120724.69+223529.8		0.058542(3)	19.97		Polar	103	103	1
J120841.91+355024.8	SDSS J120841.96+355025.2	4029844634175275136	0.0368(3)	18.79	210 ⁺¹³ ₋₁₂	AM CVn	117	117	44
J121015.61+351334.4		4029016667559886080		19.38	356 ⁺⁶⁴ ₋₅₈	WZ Sge:	1	1	
J121209.31+013627.7	V0379 Vir	3699606286708406912	0.061408(7)	18.0	152 ⁺³ ₋₂	Polar§:	118	118	193
J121607.03+052013.9	SDSS J121607.03+052013.9	3894428163622866304	0.0686(1)	20.15	377 ⁺¹⁰¹ ₋₇₁	WZ Sge:§	72	72	214
J121913.04+204938.3	SDSS J121913.04+204938.3	3952276665815698560		19.17	274 ⁺²⁵ ₋₂₄	WZ Sge:	103	103	
J122021.17+565456.7	MGAB-V359	1574499830637256448	0.070356(1)	18.46	995 ⁺³⁵⁸ ₋₁₉₈	Polar	76	1	1
J122405.58+184102.7	SDSS J122405.58+184102.7	3947303029263219712		16.04	2621 ⁺³⁹⁶ ₋₂₃₀	NL	103	103	
J122740.83+513924.9	GP CVn	1571768231438756864	0.062959041(7)	19.08	390 ⁺²⁷ ₋₁₈	SU UMa	63	63	75

SDSS	Name	Gaia EDR3 source_id	Period (days)	SDSS g (mag)	Distance (pc)	Variable Sub-type	References		
							ID	Sp	P
J122808.73+454516.3		1541836947948009472	0.07829(1):	21.66	1599^{+778}_{-608}	Polar	1	1	1
J123255.10+222209.4	SDSS J123255.11+222209.4	3958687059123923584	0.12781(1)	17.71	2389^{+1114}_{-596}	NL	103	103	1
J123717.98+365535.2		1519559914656417920		21.22		WZ Sge:	1	1	
J123813.73-033932.9	V0406 Vir	3681313024562519552	0.055917(1)	17.82		WZ Sge	130	130	215
J123931.98+210806.2	IR Com	3955313418148878080	0.0870386279(2)	18.32	216^{+3}_{-2}	DN‡	103	103	187
J124058.02-015919.2	SDSS J124058.03-015919.2	3683277061567168000	0.025941(2)	19.58	764^{+594}_{-220}	AM CVn	156	156	156
J124325.92+025547.4	NSV 19466	3703726255561754880	0.071733(2)	17.73	598^{+38}_{-38}	DN	130	130	1
J124413.48+593610.2	Gaia16adi	1578229644661071360	0.0728975(1)	20.6	812^{+261}_{-172}	SU UMa:	192	1	1
J124417.87+300400.8	CSS 080427:124418+300401	4011210252842172672	0.07744(9)	18.59	579^{+95}_{-71}	SU UMa‡	185	185	46
J124426.25+613514.6	V0351 UMa	1580508421164776064	0.09924(14)	18.76	676^{+55}_{-42}	DN	72	72	170
J125023.79+665525.5	OV Dra	1679210927155357952	0.0587356818(6)	18.67	488^{+23}_{-21}	SU UMa	130	130	84
J125044.42+154957.3		3934459045528378368	0.05995(1)	18.26	131^{+2}_{-3}	Polar	109	109	109
J125510.54+264226.4	MT Com	3958622291017334400	0.08298(12)	19.14	347^{+44}_{-37}	WZ Sge§	8	1	87
J125609.82+623704.5	ASASSN-16da	1676508087056380544	0.0562(2)*	21.56		WZ Sge	126	1	58
J125637.10+263643.2	GO Com	3958581402928688768	0.0659	17.96	440^{+30}_{-25}	SU UMa	161	185	193
J125641.29-015851.9	SDSS J125641.29-015852.0	3688476819557779712		20.12	350^{+163}_{-90}	WZ Sge:	32	32	
J125716.08+582501.5		1578799436498250368		20.13	953^{+109}_{-99}	CV	1	1	
J125834.73+640823.0	SDSS J125834.74+640823.1	1677083161701552000		20.18	2020^{+690}_{-586}	DN:	130	130	
J125834.76+663551.5	SDSS J125834.77+663551.6	1678957558444645376	0.05973	20.55	2389^{+1137}_{-836}	SU UMa	130	130	151
J130147.97+434549.4		1529416619788906624		21.44	501^{+99}_{-86}	PREP:	137	137	
J130514.72+582856.2	SDSS J130514.73+582856.3	1578672472969644288		19.28	3911^{+2790}_{-1431}	DN	72	72	
J130527.72+390927.5	ASASSN-17eg	1523605151079140224	0.15719(1)	18.8	3609^{+1937}_{-1698}	U Gem	126	1	1
J130542.26+180104.0	GP Com	3938156295111047680	0.032339(2)	15.91	72^{+1}_{-1}	AM CVn	51	51	114
J130753.86+535130.5	EV UMa	1563999425873420800	0.05533887(2)	16.54	673^{+60}_{-49}	Polar	89	89	193
J131223.48+173659.1	2XMMp J131223.4+173659	3937217307886601088	0.06378527(1)	19.94	830^{+220}_{-176}	Polar	212	212	212
J131908.88+315832.0	ASASSN-14mr	1463559824653584512	0.135179(3)	19.93	1006^{+364}_{-225}	U Gem	126	1	1
J131954.47+591514.8	SDSS J131954.50+591514.5	1566956008344163456	0.0456	19.1	203^{+9}_{-6}	AM CVn	132	132	61
J132104.01+560958.2	V0496 UMa	1565395908719728384	0.06323501(7)	21.75	758^{+33}_{-34}	Polar	91	182	182
J132411.57+032050.5	PZ Vir	3712647349312292864	0.11022(6)	22.1	782^{+901}_{-330}	Polar	52	72	166
J132715.28+425932.8	GUVV J132715.2+425932.1	1549364994827244032		20.82	1849^{+1256}_{-811}	DN	77	1	
J132723.38+652854.2	OZ Dra	1666187138909384448	0.13665(6)	17.73	1756^{+508}_{-296}	NL	154	130	193
J133309.19+143706.9	SDSS J133309.19+143706.9	3741755132951336192	0.092	18.51	2028^{+1277}_{-534}	Polar	185	185	166
J133540.75+050722.5	SDSS J133540.76+050722.7	3714792599576481024		18.56	2028^{+1031}_{-602}	Z Cam	72	72	
J133615.76+380933.4	MGAB-V701	1475606486364775552		19.39	2783^{+2390}_{-954}	DN	76	1	
J133816.44+371639.8				21.66		WZ Sge:	1	1	
J133940.98+484727.9	V0355 UMa	1558322303741820928	0.05729(2)	17.67	150^{+2}_{-1}	WZ Sge	21	21	158
J134323.16+150916.8	HW Boo	3741979368899159552	0.0644(1)	17.97	429^{+23}_{-22}	SU UMa	193	185	193

SDSS	Name	Gaia EDR3 source_id	Period (days)	SDSS g (mag)	Distance (pc)	Variable Sub-type	References		
							ID	Sp	P
J134441.83+204408.4	SDSS J134441.83+204408.3	1249384550225817856	0.070592(4)	17.18	598^{+53}_{-45}	Polar	103	103	174
J140203.08+461333.8	ASASSN-16fy	1508860876245585920	0.049238(63)*	19.51	603^{+74}_{-62}	WZ Sge:	213	1	213
J140429.36+172359.5	RX J1404.4+1723	1245262790370992256		17.55	511^{+22}_{-21}	IP:	168	1	
J140430.98+525811.1				21.93		CV	1	1	
J140430.98+552558.5		1609460864427043072		21.48	1413^{+776}_{-636}	DN	1	1	
J141118.31+481257.6	SDSS J141118.31+481257.6	1507944978763511936	0.032(1)	19.38	452^{+50}_{-55}	AM CVn	191	191	191
J142256.31-022108.0	SDSS J142256.31-022108.1	3646450942524067072	0.1404	21.58	1676^{+1088}_{-495}	Polar	72	72	188
J142955.86+414516.8	SDSS J142955.86+414516.8		0.0637(1)	17.73		Polar	21	21	1
J143209.77+191403.4	SDSS J143209.78+191403.5	1239185510431005440	0.1171	18.4	1815^{+632}_{-353}	NL	139	199	1
J143317.77+101122.8	SDSS J143317.78+101123.3	1176468611268115200	0.054240679(2)	18.56	232^{+8}_{-8}	WZ Sge§	196	196	75
J143500.22-004606.3	OU Vir	3650020648757787008	0.072706113(5)	18.59	485^{+44}_{-41}	SU UMa	45	32	225
J143544.02+233638.7	SDSS J143544.02+233638.7	1242828982729309952	0.054(5)	18.21	209^{+7}_{-7}	WZ Sge:§	196	196	217
J144659.95+025330.3	SDSS J144659.95+025330.3	1157501971264781824	0.165(15)	17.71	1619^{+625}_{-375}	IP	130	130	127
J145003.12+584501.8	SDSS J145003.12+584501.9			20.8		WZ Sge:	130	130	
J145744.75+404340.6	TT Boo	1296877675817415680	0.07593962(7)	19.36	682^{+43}_{-43}	SU UMa	38	151	151
J145758.18+514808.1	SDSS J145758.21+514807.9	1593786703401901952	0.054087(6)	19.56	587^{+80}_{-58}	WZ Sge	21	21	219
J150137.18+550122.4	SDSS J150137.22+550123.4	1612331959869359872	0.0568412(2)	19.38	320^{+24}_{-22}	WZ Sge:	72	72	75
J150240.97+333423.8	NZ Boo	1289860214647954816	0.05890961(5)	17.54	184^{+3}_{-1}	SU UMa	63	63	1
J150441.76+084752.6	SDSS J150441.76+084752.6	1167630942962176512	0.08089(18)	19.13	923^{+220}_{-172}	CV	185	185	46
J150551.60+065948.5	SDSS J150551.58+065948.7	1160374338017986688	0.047(2)	19.11	160^{+8}_{-7}	AM CVn	83	83	86
J150722.15+523040.2	OV Boo	1593140224924964864	0.0462583290(7)	18.34	212^{+4}_{-4}	WZ Sge§	21	21	181
J150903.71+465056.6	CSS 130324:150904+465057	1587913868200450048	0.068440(8)	21.0	838^{+397}_{-258}	SU UMa	91	1	1
J151302.29+231508.4	NY Ser	1263484034505616256	0.0975(2)	16.08	808^{+24}_{-20}	SU UMa+Z Cam	6	185	193
J151413.71+454911.8	PP Boo	1587569038162292736		19.7	315^{+31}_{-23}	WZ Sge:	21	21	
J151415.60+074445.9		1163569523103341568	0.061610(1)	18.86	181^{+9}_{-6}	Polar	109	109	109
J151915.85+064529.0	SDSS J151915.86+064529.1	1163201663448924544		16.59	2685^{+649}_{-397}	NL	103	103	
J152020.40-000948.3		4418752449654921088		16.54	2018^{+337}_{-249}	NL	104	1	
J152212.20+080340.9	SDSS J152212.20+080340.9	1163743344724940160	0.068(1)	19.0	888^{+291}_{-179}	SU UMa	185	185	201
J152238.83+391352.3	CSS_J152238.7+391351	1388827294919788032	10.768609(0.004)	17.12	6347^{+1960}_{-1309}	CV	54	1	1
J152419.31+220920.2	SDSS J152419.33+220920.0	1214663721071751296	0.0653187310(8)	19.05	523^{+55}_{-47}	SU UMa	185	185	84
J152603.67+382216.4				21.35		WZ Sge:	1	1	
J152613.96+081802.3	QW Ser	1163811724898541440	0.07453(10)	17.8	296^{+5}_{-5}	SU UMa	216	185	34
J152717.96+543724.9	SDSS J152717.96+543724.9	1599597141318244992		20.32	612^{+185}_{-118}	IP:	196	196	
J152857.86+034911.7	SDSS J152857.86+034911.7	4428174160497320832	0.063(2)*	19.53	1774^{+1935}_{-659}	SU UMa	130	130	162
J153015.04+094946.3	SDSS J153015.04+094946.3	1165571939936731264	0.0753(2)*	18.88	1356^{+350}_{-227}	SU UMa	185	185	13
J153023.63+220646.3	CSS 110920:153024+220646	1214510510998076288		19.07	330^{+23}_{-21}	Polar	22	22	
J153213.67+370104.8	SDSS J153213.68+370104.9	1375610271801084032		17.39	2500^{+479}_{-380}	NL	63	63	

SDSS	Name	Gaia EDR3 source_id	Period (days)	SDSS g (mag)	Distance (pc)	Variable Sub-type	References		
							ID	Sp	P
J153412.17+594832.0	DM Dra	1603228248405352064	0.0734(30)*	20.31	1019 ⁺⁴⁴⁸ ₋₂₃₃	SU UMa	57	57	43
J153634.42+332851.9	SDSS J153634.42+332851.9	1370642265950491776	0.0921(2)	19.21	760 ⁺⁸⁵ ₋₇₆	SU UMa	21	21	46
J153817.34+512338.0	SDSS J153817.35+512338.0	1595085299649674240	0.06466(6)	18.57	613 ⁺³⁴ ₋₄₀	Polar	72	72	193
J154104.67+360252.8	BM CrB	1374430388449392000	0.0585(2)	19.69	423 ⁺¹⁴ ₋₁₆	Polar	21	21	193
J154453.60+255348.8	SDSS J154453.60+255348.8	1222867765738898560	0.25128168(2)	16.58	486 ⁺¹⁵ ₋₁₂	CV†	185	185	36
J154459.80+464835.3	SDSS J154459.80+464835.4	1398189185457847680	0.056422(1)	19.18	314 ⁺¹⁸ ₋₂₁	WZ Sge:	91	1	
J154539.08+142231.4	CT Ser	1192697922589844352	0.195(2)	16.33	3089 ⁺⁵⁷⁵ ₋₄₈₅	Nova	220	103	195
J154544.88+442830.0	CSS 110428:154545+442830	1396642623570704384	0.0742(5)	20.95	2316 ⁺¹⁶²⁸ ₋₉₈₃	SU UMa	42	22	22
J154953.41+173938.9	SDSS J154953.41+173939.0	1196777901001463296		19.44	3312 ⁺¹²⁹⁹ ₋₈₈₄	NL:	185	185	
J155037.27+405439.9	SDSS J155037.27+405440.0	1383764490550797824	0.27766(1)	18.55	1083 ⁺¹³³ ₋₁₁₃	IP	72	72	
J155247.18+185629.1	MR Ser	1203639265875666304	0.07879785(7)	17.25	131 ⁺¹ ₋₁	Polar	136	136	193
J155252.48+320150.9	SDSS J155252.48+320150.9	1369702252228215168	0.039078(4)	20.22	422 ⁺⁵⁹ ₋₅₃	AM CVn	191	191	128
J155331.11+551614.4	MQ Dra	1597621426298361216	0.18298(4)	18.51	180 ⁺² ₋₂	PREP:	172	172	172
J155412.33+272152.4	AP CrB	1223491257550872192	0.105462(6)	17.51	199 ⁺² ₋₂	Polar	221	221	177
J155531.98-001054.9	V0489 Ser	4409578051617714688	0.0788455518(3)	19.33	675 ⁺¹⁴⁵ ₋₁₀₉	SU UMa:	124	124	84
J155538.12+380250.5		1373544697473750272	0.104(1)	20.39	486 ⁺⁴⁶ ₋₄₉	Polar	1	1	1
J155644.23-000950.2	V0493 Ser	4409581010854168064	0.08012(8)	18.27	292 ⁺¹¹ ₋₁₃	SU UMa	32	32	46
J155654.47+210718.9	QZ Ser	1204588041329337600	0.083161(2)	17.92	317 ⁺⁸ ₋₇	SU UMa	73	73	73
J155656.91+352336.6	BT CrB	1371889764970726144	0.088091490(4)	18.95	1167 ⁺²³⁵ ₋₁₈₆	SU UMa	63	63	84
J155720.75+180720.2	SDSS J155720.75+180720.2	1202680251217734400	0.0810(2)	18.65	692 ⁺⁸⁵ ₋₁₀₀	SU UMa	185	185	151
J160003.70+331113.8	VW CrB	1323332342191466112	0.0705(5)	19.88	785 ⁺¹⁹⁴ ₋₁₂₅	SU UMa	3	22	22
J160111.53+091712.6	SDSS J160111.53+091712.6	4454748295687814528		20.63	2680 ⁺²⁹⁹⁸ ₋₁₄₉₅	DN:	63	63	
J160232.13+161731.7	CSS 080424:160232+161732			21.95		DN	22	22	
J160419.02+161548.5	SDSS J160419.02+161548.5	1199129584573929984		19.09	850 ⁺²⁵⁴ ₋₁₃₀	SU UMa	185	185	
J160450.18+414328.5	SDSS J160450.16+414328.6	1383342720466698240		17.67	4506 ⁺¹⁴⁹³ ₋₉₇₇	NL	21	21	
J160501.35+203056.9	SDSS J160501.35+203056.9	1205022962601053312	0.05666:	19.9	379 ⁺⁸⁴ ₋₄₆	WZ Sge	185	185	42
J160712.11+392450.6		1379871940214896640	0.08071(1)	21.57		Polar	1	1	1
J160745.02+362320.5	CH CrB	1378159038537517312	0.14549982(2)	18.07	2683 ⁺⁹²⁵ ₋₆₆₄	NL	63	63	92
J160813.59+301952.2				21.46		WZ Sge:	1	1	
J160932.67+055044.6	SDSS J160932.67+055044.6	4449776402888284288		18.75	3854 ⁺¹⁹⁵⁷ ₋₁₁₉₇	NL	185	185	
J161007.50+035232.7	V0519 Ser	4413231423818141568	0.13232(4)	17.38	339 ⁺¹¹ ₋₁₀	Polar	31	185	31
J161012.52+222110.8	SDSS J161012.52+222110.8	1205683464147877120		17.41	2326 ⁺³⁵⁶ ₋₃₂₁	NL	196	196	
J161027.61+090738.4	SDSS J161027.61+090738.4	4453218973793773824	0.05695(1)*	20.12	412 ⁺¹²³ ₋₇₆	WZ Sge	77	103	65
J161030.34+445901.7	SDSS J161030.35+445901.7	1386167468917461376		19.8	428 ⁺⁴⁹ ₋₄₉	WZ Sge:	72	72	
J161033.63-010223.2	V0386 Ser	4406459119386466176	0.05592(6)	19.06	244 ⁺¹⁷ ₋₁₅	WZ Sge	32	32	133
J161332.55-000331.0	SDSS J161332.56-000331.0	4408131270415770496		18.61	1308 ⁺¹⁰⁹ ₋₈₉	U Gem	32	32	
J161853.16+303845.5		1319026547281204480		20.69	1822 ⁺¹⁴⁰⁴ ₋₉₂₂	WZ Sge:	1	1	

SDSS	Name	Gaia EDR3 source_id	Period (days)	SDSS g (mag)	Distance (pc)	Variable Sub-type	References		
							ID	Sp	P
J161909.10+135145.5	SDSS J161909.10+135145.5	4463547515444791168	0.2865(5)	18.51	1720 ⁺¹⁷⁴ ₋₁₅₇	Z Cam	185	185	46
J161935.76+524631.8	DDE 32	1425200578380530048	0.0697944(2)	19.0	449 ⁺³⁶ ₋₂₉	Polar	27	27	27
J162207.15+192236.6	V0589 Her	1201107636054271744	0.09090(1)*	19.16	1096 ⁺²³⁸ ₋₁₅₁	SU UMa	189	189	202
J162209.63+360418.1	CSS 111019:162210+360419	1329525856830867712	0.0601(8)*	20.16	779 ⁺²²¹ ₋₁₃₈	WZ Sge:	91	1	208
J162212.44+341147.3	CY CrB	1328757431346007680	0.0650(1)	19.13	437 ⁺³¹ ₋₃₁	SU UMa	72	72	1
J162450.82+451806.8	MGAB-V3563	1409634075007666048	0.09554(1)	19.8		CV	76	1	1
J162501.74+390926.3	V0844 Her	1332378466733219456	0.054643(7)	17.23	304 ⁺⁶ ₋₅	SU UMa	141	21	18
J162520.29+120308.7	SDSS J162520.29+120308.7	4459922356886052992	0.09111(15)	18.54	440 ⁺³⁷ ₋₃₀	SU UMa	103	103	113
J162558.18+364200.6	SDSS J162558.18+364200.6	1329615982424327936		21.69		SU UMa:	77	1	
J162608.15+332827.7	SDSS J162608.16+332827.8	1325655193647771008		18.67	2429 ⁺¹³²¹ ₋₆₆₄	AM CVn	72	72	
J162718.38+120434.9	SDSS J162718.39+120435.0	4459936440084462464	0.104(2)*	19.24	1122 ⁺³⁴⁰ ₋₂₄₃	SU UMa	185	185	193
J162830.89+240259.1	SDSS J162830.89+240259.1	1299245787639918080	0.071(1):*	20.01	687 ⁺¹²⁴ ₋₇₅	SU UMa	63	63	167
J162936.53+263519.5	V1189 Her	1304296149486147584	0.093(2)	19.27	714 ⁺¹²¹ ₋₇₉	Polar	21	21	193
J163545.72+112458.0	V0849 Her	4459185168703405568	0.1414(30)	15.2	1117 ⁺³⁷ ₋₃₂	Z Cam	106	103	88
J163605.01+465204.5	SDSS J163605.01+465204.5	1407217451528505728		16.69	1618 ⁺¹⁰⁴ ₋₁₀₅	Z Cam	130	130	
J163620.62+472442.4		1410251583929439744		20.59	708 ⁺³¹⁸ ₋₂₂₇	WZ Sge:	1	1	
J163722.21-001957.1	V2690 Oph	4383291477376259968	0.06739(1)	16.65	1254 ⁺⁹³³ ₋₄₆₂	SU UMa	32	32	12
J164248.52+134751.4	SDSS J164248.52+134751.4	4461280391188698368	0.07889 (11)	17.91	531 ⁺²⁵ ₋₂₂	SU UMa	196	196	12
J164624.78+180808.9	CSS 100616:164625+180808			21.09		DN	22	22	
J165244.83+333925.3	SDSS J165244.84+333925.4	1314596271336013824		20.86	3281 ⁺²⁵⁴⁹ ₋₁₆₆₁	SU UMa	21	21	
J165359.05+201010.4	V1227 Her	4564460623922361472	0.06310(9)	18.68	754 ⁺³³ ₋₃₂	SU UMa	63	63	46
J165658.12+212139.3	V1229 Her	4565045873343899136	0.06733(14)	18.5	547 ⁺²⁶ ₋₂₉	SU UMa:	21	21	46
J165837.70+184727.4	SDSS J165837.70+184727.4	4561074914085742592	0.06806(4)	20.08	386 ⁺⁵³ ₋₃₆	CV	63	63	12
J165951.68+192745.6	SDSS J165951.69+192745.6	4561245342686490496	0.141(2)	17.01	1572 ⁺¹⁴⁹ ₋₁₃₁	NL	63	63	46
J170053.29+400357.6	V1237 Her	1353646217070728704	0.08080175(8)	20.09	522 ⁺³¹ ₋₂₅	Polar	130	130	147
J170213.25+322954.1	V1239 Her	1313538545446290688	0.100082222(1)	17.9	300 ⁺⁶ ₋₆	SU UMa	72	72	78
J170244.09+223547.9	V1240 Her	4571234234022916992	0.068596(1)	17.37	3237 ⁺²⁵³⁷ ₋₁₂₄₅	NL:	63	63	1
J170324.08+320953.1	SDSS J170324.09+320953.2	1310490286897519360	0.261(1)	18.14	1109 ⁺¹³¹ ₋₁₀₄	U Gem	72	72	1
J170542.53+313240.7	SDSS J170542.54+313240.8	1310224819268701696	0.1854(1)	19.66	2341 ⁺¹⁷⁶⁷ ₋₁₁₂₈	U Gem	72	72	1
J171016.94+403127.5				22.08		WZ Sge:	1	1	
J171145.08+301319.9	V1247 Her	1309111357581001088	0.05580(4)	20.22	439 ⁺⁹² ₋₅₈	WZ Sge:	72	72	170
J171222.06+321856.2	CSS_ J171222.0+321856	1334339278219282944	0.37333(1)	18.91	3183 ⁺⁷²⁵ ₋₄₃₆	NL	91	1	1
J171247.70+604603.2	SDSS J171247.71+604603.3	1437612007369245696	0.16310(1)	20.0	687 ⁺⁷⁸ ₋₆₉	U Gem:	32	32	1
J172325.99+330414.1	ASASSN-14gz		0.0592*	22.07		WZ Sge:	204	1	29
J172601.95+543230.7	SDSS J172601.96+543230.8	1419437320680556544	0.636596(3)	20.56		CV	32	32	1
J173008.39+624754.6	SDSS J173008.38+624754.7	1440078211950524544	0.07657(16)	14.07	530 ⁺⁹ ₋₈	SU UMa	32	32	46
J173102.22+342633.2	ASASSN-15cm	1335522795110752384	0.208466(2)	19.11	2713 ⁺⁸⁵⁶ ₋₅₆₄	U Gem	126	206	206

SDSS	Name	Gaia EDR3 source_id	Period (days)	SDSS g (mag)	Distance (pc)	Variable Sub-type	References		
							ID	Sp	P
J183131.63+420220.2		2111270034246759424		16.9	1490^{+162}_{-155}	AM CVn:	1	1	
J204448.91-045928.8	V0485 Aqr	6914363228723335296	1.68(1)	16.86	1948^{+238}_{-198}	U Gem	130	130	98
J204720.76+000007.6	SDSS J204720.76+000007.7	4227956460334694272		19.38	824^{+412}_{-226}	DN	72	72	
J204817.84-061044.8	SDSS J204817.85-061044.8	6913162042334862720	0.060597(2)	19.36	565^{+122}_{-86}	WZ Sge:	130	130	68
J204827.90+005008.9	SDSS J204827.91+005008.9	4228442478834563712	0.175	19.53	612^{+69}_{-57}	PREP	63	63	176
J205017.83-053626.8	PW Aqr		0.06542463(1)	18.15		Polar	130	130	127
J205914.87-061220.4	QT Aqr	6910341691929801856	0.074665(10)	18.38	1123^{+427}_{-244}	SU UMa	130	130	124
J210014.11+004445.9	QU Aqr	1729491319015998208	0.083304(6)	18.07	851^{+87}_{-79}	SU UMa	72	72	194
J210131.26+105251.5	SDSS J210131.26+105251.5	1756642208180119040	0.074	18.53	1660^{+972}_{-821}	MCV	130	130	127
J210449.94+010545.8	QV Aqr	1729567357118146304	0.07196(8)	16.64	1306^{+365}_{-226}	SU UMa	63	63	124
J210842.62+084429.9	MGAB-V3716	1743295309545913728		21.43		SU UMa:	76	1	
J211605.42+113407.4	VV Equ		0.0557(2)	15.32		DN	72	72	170
J211652.28+014144.3		2692060074926640000		20.43	2752^{+2087}_{-1558}	SU UMa:	1	1	
J211936.95+033211.8	CSS 150520:211937+033212	2692906015980924544	0.0988429(3)	20.18	796^{+139}_{-111}	CV	91	1	1
J212406.75+010029.8		2691114426208274176		20.84		WZ Sge:	1	1	
J213040.11-001319.1				22.34		WZ Sge:	1	1	
J213122.40-003937.0	QZ Aqr		0.0696(2)*	21.56		WZ Sge:§:	4	1	25
J213503.93-004129.6	ASASSN-16ep			22.36		DN:	126	1	
J214140.43+050729.9	SDSS J214140.43+050730.0	2698490156365025536	0.05467(3)	18.87	274^{+18}_{-17}	WZ Sge:	107	107	1
J214354.60+124457.9	SDSS J214354.60+124458.0	1767199173369655424	0.126	15.16	1110^{+61}_{-46}	Z Cam	21	21	37
J215411.12-090121.6	DM Cap	2618370049719441920	0.222(2)	19.19	3488^{+1704}_{-1188}	NL	130	130	170
J220553.97+115553.6	SDSS J220553.98+115553.7	2728239161441977216	0.0575175(62)	20.04	1003^{+902}_{-350}	WZ Sge	130	130	15
J220818.52+135330.0				21.33		WZ Sge	1	1	
J220935.78-001332.5		2678822818216797056		21.8		WZ Sge:	1	1	
J221009.93+185418.1	CSS 111227:221010+185418	1778078561752634624	0.17077(1)	19.83	1392^{+584}_{-493}	U Gem	91	1	1
J221159.03+302835.1	ASASSN-13am			21.89		WZ Sge:	190	1	
J221333.38+245059.3				21.94		WZ Sge:	1	1	
J221519.79-003257.1	V0344 Aqr			17.41		SU UMa:	70	22	
J221814.05-005848.8	SDSS J221814.06-005849.2	2677830440253389824	0.0583(3)*	20.27	595^{+289}_{-197}	WZ Sge	223	1	160
J221832.76+192520.2	Swift J2218.5+1925	1777232423131443840	0.08996(9)	17.63	240^{+6}_{-6}	Polar	229	111	111
J221900.24+201831.1		177846868222798080	0.140(1)	19.85	821^{+124}_{-98}	DN	1	1	1
J222144.78+184008.2	V0521 Peg	1776946133496845440	0.0599	17.55	189^{+2}_{-3}	SU UMa	2	2	2
J222334.17+074518.8	1RXS J222335.6+074515	2710544484592654464		18.64	936^{+219}_{-123}	SU UMa:	122	226	
J222724.50+284403.5	CSS 090531:222724+284404	1882329723109880576	0.09101(18)	18.56	737^{+91}_{-70}	SU UMa	62	206	206
J223212.79+260725.1		1880505014843117696		22.26		Polar	1	1	
J223233.67+185037.0	CSS 100520:223234+185036	2738094943157120512		20.58	1169^{+937}_{-370}	DN	91	1	
J223252.34+140352.9	SDSS J223252.35+140353.0			22.49		DN	72	72	

SDSS	Name	Gaia EDR3 source_id	Period (days)	SDSS g (mag)	Distance (pc)	Variable Sub-type	References		
							ID	Sp	P
J223352.56+225913.4		1875338547143938944		19.89	1294^{+491}_{-329}	Polar	1	1	
J223439.92+004127.2	SDSS J223439.93+004127.2	2654255639643078528	0.088396(17)	18.62	510^{+24}_{-24}	DN	130	130	193
J223606.51+291559.9		1888191490179330304		20.8	1555^{+740}_{-462}	Polar:	137	137	
J223623.52+323913.1				21.02		WZ Sge:	1	1	
J223843.83+010820.6	V0349 Aqr	2654647748682905600	0.134932(11)	18.34	3591^{+7386}_{-1258}	IP	130	130	12
J223909.83+250331.1	CSS 100521:223910+250331	1877138512102151424	0.0761141(1)	19.17	910^{+201}_{-143}	SU UMa	91	1	1
J224303.82+221456.0	SDSS J224303.82+221456.0	2836524396600372352	0.1870(1)	17.02	3844^{+1409}_{-939}	NL	196	196	1
J224736.37+250436.3	CSS 120616:224736+250436		0.056673(20)*	21.81		SU UMa	91	1	17
J225417.52+074227.1	PQ J225417.5+074227	2712901249112064384		18.78	415^{+62}_{-38}	CV	39	39	
J225613.53+191132.9				22.12		WZ Sge:	1	1	
J225831.18-094931.6	SDSS J225831.18-094931.7	2606580678024447104	0.08257(1)	15.63	293^{+3}_{-2}	SU UMa	130	130	193
J225926.51+223902.4				21.81		WZ Sge:	1	1	
J230319.85+274736.0				22.43		DN:	1	1	
J230351.64+010651.0	HY Psc	2652196593667289856	0.076743(17)	18.3	571^{+48}_{-47}	SU UMa	32	32	193
J230425.88+062545.6	KX Psc	2663767755253693568	0.067317(35)*	21.11		WZ Sge§	108	1	119
J230641.47+244055.8	ZTF J230641.45+244055.7	2842721961392797312	0.2911640	20.29	1524^{+1653}_{-516}	CV:	198	1	198
J230813.57+254341.0	CSS 130916:230814+254341	2843638610493150976		19.82	1316^{+824}_{-461}	SU UMa:	91	1	
J230949.12+213516.7	V0405 Peg	2838503311371673472	0.1776464(2)	16.79	171^{+2}_{-1}	CV‡	67	103	36
J231110.88+013002.7	USNO-B1.0 0915-0569037		0.05161(20)*	21.68		WZ Sge	184	1	143
J231552.35+271037.3	CSS 100610:231552+271037	2844956207676441728		20.64	1325^{+658}_{-422}	SU UMa	62	1	
J231643.23+011640.2	Karachurin 15	2657363477979129984	0.145(1)	19.02	710^{+15}_{-13}	NL	91	1	1
J231909.18+331539.6	CSS 111021:231909+331540	1910583495451438720	0.14616(19)	17.79	603^{+46}_{-46}	IP	62	206	206
J231930.43+261518.6	Swift J2319.4+2619	2844608590203675136	0.12544(3)	17.35	512^{+18}_{-20}	Polar	186	1	163
J232113.45+251822.3		2841125848466425856		20.96	1189^{+715}_{-482}	WZ Sge:	1	1	
J232553.47+011527.3				21.39		WZ Sge:	1	1	
J232619.40+282649.7	CSS 080930:232619+282650	2868928481740258176	0.067917(1)	20.92	2801^{+1555}_{-1362}	SU UMa	91	1	1
J232727.14+085538.6	V0681 Peg		0.05339(4) *	21.86		WZ Sge	155	1	148
J233003.03+303300.4	CSS 111101:233003+303301	2869854820286374016	0.1559784(6)	19.5	846^{+173}_{-99}	DN‡	84	1	84
J233325.92+152222.1	V0598 Peg	2819557935751631744	0.0577(1)	18.77	609^{+79}_{-67}	IP	178	21	178
J233705.01+314149.4		2871487075361158400		19.64	2574^{+939}_{-1150}	SU UMa:	1	1	
J234226.21+324819.8	ASASSN-15nv	2871939764914510976	0.134825922(6)	17.57	567^{+32}_{-24}	U Gem	126	36	79
J234401.83+002116.6	MLS 120926:234402+002117			21.65		SU UMa	91	1	
J234440.53-001205.8	MLS 100904:234441-001206	2642699218384434432	0.076711(30)*	21.15	668^{+235}_{-176}	SU UMa	91	22	65
J234502.47+342923.9	1RXS J234500.2+342913	2878205989054948864	0.1300(1)	24.64	927^{+124}_{-99}	Polar	76	1	1
J234814.69+181219.6	CSS 110115:234815+181220	2821834126683649280		18.01	906^{+1008}_{-411}	DN	62	1	
J234843.14+250249.9	MASTER OT J234843.23+250250.4	2852495455827670400	0.032(1)*	20.27	538^{+128}_{-92}	SU UMa	110	16	28
J235131.68+270907.7		2854471033409793024		21.9	1089^{+467}_{-451}	DN:	1	1	

SDSS	Name	Gaia EDR3	Period	SDSS g	Distance	Variable	References		
		source_id	(days)	(mag)	(pc)	Sub-type	ID	Sp	P
	J235603.71+001833.3			21.45		WZ Sge:	1	1	

References: 1 This work, 2 Rodríguez-Gil et al. (2005a), 3 Nogami et al. (2004b), 4 Yamaoka et al. (2008), 5 Quimby & Mondol (2006), 6 Nogami et al. (1998), 7 VSNET12318, 8 Wheatley et al. (2000), 9 Duszanowicz & Huchra (2008), 10 Hameury & Lasota (2005), 11 VSNET 25916, 12 Southworth et al. (2008b), 13 Kato et al. (2020), 14 Kupfer et al. (2019), 15 Southworth et al. (2008a), 16 Isogai et al. (2019b), 17 Kato et al. (2013b), 18 Thorstensen et al. (2002a), 19 Schwöpe et al. (2009), 20 Arenas & Mennickent (1998), 21 Szkody et al. (2005), 22 Breedt et al. (2014), 23 Gänsicke et al. (2000), 24 Kato et al. (2009), 25 VSNET10830, 26 Delgado et al. (2018b), 27 Denisenko & Martinelli (2016), 28 Tampo et al. (2021), 29 Kato (2015), 30 Stanishev et al. (2006), 31 Rodrigues et al. (2006), 32 Szkody et al. (2002b), 33 Kato et al. (2014a), 34 Patterson et al. (2003), 35 Carter et al. (2013b), 36 Thorstensen et al. (2017), 37 Altan et al. (2019), 38 Howell & Szkody (1988), 39 Carter et al. (2013a), 40 Richter et al. (1981), 41 Schwöpe et al. (2002b), 42 Kato et al. (2012a), 43 Kato et al. (2002), 44 Kupfer et al. (2013), 45 Vanmunster et al. (2000), 46 Thorstensen et al. (2015), 47 Hou et al. (2020), 48 Roelofs et al. (2009), 49 Belle et al. (1998), 50 Mukai et al. (1990), 51 Williams (1983), 52 Szkody et al. (2004b), 53 Aungwerojwit et al. (2006), 54 Drake et al. (2014a), 55 Wagner et al. (1998), 56 Kato et al. (2015), 57 Stepanyan (1982), 58 VSNET19579, 59 Antipin (1998), 60 Rutkowski et al. (2009), 61 Ramsay et al. (2018), 62 Drake et al. (2014b), 63 Szkody et al. (2006), 64 Szkody et al. (2001), 65 Kato et al. (2010), 66 Bruch et al. (1987), 67 Kato & Yamaoka (2002), 68 Woudt & Warner (2010), 69 Hodgkin et al. (2019), 70 Rykoff et al. (2004), 71 Szkody & Howell (1987), 72 Szkody et al. (2004a), 73 Thorstensen et al. (2002b), 74 ZTF, 75 Littlefair et al. (2008), 76 MGAB catalog, 77 Wils et al. (2010), 78 Golysheva et al. (2015), 79 VSNET18954, 80 Kholopov et al. (1981), 81 Huruata (1983), 82 Yamaoka & Itagaki (2009), 83 Carter et al. (2014), 84 Hardy et al. (2017), 85 Schmidt et al. (2005a), 86 Green et al. (2020), 87 Patterson et al. (2005a), 88 Ringwald et al. (2012), 89 Osborne et al. (1994), 90 Downes & Shara (1993), 91 CRTS candidate CV, 92 Zengin Çamurdan et al. (2010), 93 VSNET21317, 94 Rebassa-Mansergas et al. (2014), 95 Esamdin et al. (1998), 96 Dhillon et al. (2000), 97 Drake et al. (2009d), 98 Peters & Thorstensen (2005), 99 Gentile Fusillo et al. (2019), 100 Munari et al. (1990), 101 Wright et al. (2012), 102 Downes et al. (2001), 103 Szkody et al. (2011), 104 Gentile Fusillo et al. (2015), 105 Tovmassian et al. (2014), 106 Green et al. (1986), 107 Szkody et al. (2014), 108 Munari et al. (2011), 109 Breedt et al. (2012a), 110 Ovcharov et al. (2013), 111 Thorstensen & Halpern (2013), 112 Thorstensen et al. (2010), 113 Olech et al. (2011), 114 Marsh (1999), 115 Feline et al. (2004b), 116 Kong et al. (2018), 117 Anderson et al. (2008), 118 Schmidt et al. (2003), 119 Nakata et al. (2014), 120 Kreiner (2004), 121 Liu & Hu (2000), 122 Denisenko & Sokolovsky (2011), 123 Shafter & Szkody (1984), 124 Southworth et al. (2007b), 125 Littlefield et al. (2023a), 126 ASAS-SN CV candidate, 127 Homer et al. (2006b), 128 Roelofs et al. (2007), 129 Shears et al. (2012a), 130 Szkody et al. (2003a), 131 Burwitz et al. (1998), 132 Kepler et al. (2016), 133 Woudt & Warner (2004), 134 Watkins et al. (2009), 135 Pavlenko et al. (2007), 136 Szkody (1988), 137 Parsons et al. (2021), 138 Schwarz et al. (1998), 139 Southworth et al. (2012), 140 Drake et al. (2009b), 141 Kato & Uemura (2000), 142 VSNET25917, 143 Shugarov & Malashevich (2021), 144 Homer et al. (2006a), 145 Thorstensen (1997), 146 Schlindwein & Baptista (2018), 147 Homer et al. (2005), 148 VSNET14952, 149 Bauer et al. (2009), 150 Williams et al. (2013), 151 Thorstensen (2020), 152 Rodríguez-Gil et al. (2005b), 153 Thorstensen & Taylor (2001), 154 Wolfe et al. (2003), 155 Yamaoka et al. (2012), 156 Roelofs et al. (2005), 157 Gilliland et al. (1991), 158 Gänsicke et al. (2006), 159 Gülsecen & Esenoğlu (2014), 160 VSNET23496, 161 Howell et al. (1990), 162 VSNET21056, 163 Shafter et al. (2008), 164 Krajci & Wils (2010), 165 González-Buitrago et al. (2013), 166 Southworth et al. (2015), 167 VSNET13491, 168 Bade et al. (1998), 169 Shears et al. (2012b), 170 Dillon et al. (2008), 171 Kato et al. (2017), 172 Szkody et al. (2003b), 173 Hilton et al. (2009), 174 Thorstensen et al. (2020), 175 Thorstensen et al. (1996), 176 Schmidt et al. (2005b), 177 Thorstensen & Fenton (2002), 178 Southworth et al. (2007a), 179 Breedt et al. (2012b), 180 Southworth et al. (2010), 181 Littlefair et al. (2007), 182 Littlefield et al. (2015), 183 Henden et al. (2001), 184 VSNET-OUTBURST-8239, 185 Szkody et al. (2009), 186 Mukai et al. (2007), 187 Feline et al. (2005), 188 Marsh et al. (2002), 189 Szkody & Howell (1992), 190 Prieto et al. (2013), 191 Anderson et al. (2005), 192 Delgado et al. (2016), 193 Gänsicke et al. (2009), 194 Olech et al. (2009), 195 Ringwald et al. (2005), 196 Szkody et al. (2007), 197 Pretorius et al. (2004), 198 Chen et al. (2020), 199 Szkody et al. (2018), 200 Thorstensen et al. (2004), 201 Kato et al. (2012b), 202 Katysheva & Pavlenko (2003), 203 Denisenko et al. (2012b), 204 Davis et al. (2014), 205 Mennickent et al. (1996), 206 Thorstensen et al. (2016), 207 Thorstensen et al. (1991b), 208 VSNET25759, 209 Bruch (1989), 210 Kepler et al. (2015), 211 Mittaz et al. (1992), 212 Vogel et al. (2008), 213 VSNET 19922, 214 Southworth et al. (2006), 215 Pala et al. (2019), 216 Nogami et al. (2004a), 217 Pala et al. (2017), 218 Petit (1960), 219 Uthas et al. (2012), 220 Lohmann (1949), 221 Tovmassian et al. (2001), 222 Schwöpe et al. (2002c), 223 Ivezić et al. (2007), 224 VSNET 12567, 225 Feline et al. (2004a), 226 Oliveira et al. (2017), 227 VSNET23583, 228 Rodríguez-Gil et al. (2004), 229 Thorstensen & Halpern (2009)

B.3 Details

Specific Details are presented below. For simplicity the system names are abbreviated by omitting arc seconds – thus for example SDSS J000600.15+012129.8 becomes J0006+0121.

B.3.1 New systems

J0000+2556

Balmer emission lines are detected in the noisy spectrum. The ZTF light curves are sparse and appear to show outburst magnitudes with the quiescent level too faint to observe. We cannot classify this beyond recognising that the system is most probably a CV.

J0012+2800

The spectrum shows strong Balmer emission lines together with broad absorption lines from the white dwarf; the donor signature is not visible. The system is too faint in quiescence for a *Gaia* parallax measurement, but it is located close to the white dwarf cooling sequence in an SDSS u-g/g-r colour-colour diagram. The visibility of the white dwarf implies a low accretion rate which, together with the absence of outbursts in the ZTF light curve, suggests that this is likely to be a WZ Sge.

J0029+3241

The spectrum shows slightly double-peaked Balmer lines. The line at $\approx 5890\text{\AA}$ is an artefact and not a He line. The signal-to-noise ratio (SNR) is poor (1.9) but the higher Balmer emission lines appear to sit in broader absorption lines which would be evidence of the white dwarf. There is one possible outburst of $\Delta m \approx 1.5$ in the ZTF light curve although all of the other ZTF observations are comparable with the Pan-STARRS magnitude $m = 22.03$. This is possibly a WZ Sge.

J0048+3328

The spectrum shows strong double-peaked Balmer and He I 5876 emission lines and the Balmer jump is also visible. There is no signature of the donor visible. The position in the HR diagram suggests a short period CV. There are no outbursts in either the ZTF or CRTS light curves. The spectrum is reminiscent of SU UMa CVs such as QZ Vir and, combined with the HR position, leads to a tentative classification of SU UMa.

J0054+3348

There is a strong double-peaked $H\alpha$ emission line and apparent white dwarf $H\beta$ and $H\gamma$ absorption lines. The signal-to-noise ratio is poor (1.6) and there is no evidence of the donor; also there is no *Gaia* parallax. The ZTF light curve is sparse with no outbursts. This would appear to be a low-accretion rate CV and we tentatively classify it as a WZ Sge.

J0103+2005

The spectrum shows both Balmer and strong He II 4686 emission lines – possibly double-peaked. The signal-to-noise ratio is only 2.7 and there is no *Gaia* parallax. The ZTF light curves are sparse and show no outbursts although there are variations of $\Delta m < 1$. We obtained tentative periods of 3.79h and 47m from the ZTF light curve. Together these suggest that this is probably an intermediate polar CV.

J0122+0755

The spectrum shows strong, double-peaked $H\alpha$ emission with other Balmer emission lines sitting in broad absorption lines from the white dwarf. The system is on the white dwarf cooling sequence in the HR diagram implying a short period. There are no outbursts in the ZTF and CRTS light curves. We suspect that this is a WZ Sge.

J0124+2113

The spectrum shows Balmer, He I and He II asymmetric emission lines. There is no donor signature but the SDSS photometry in the g,r and i bands appears to form a broad cyclotron hump. We obtained a strong periodic signal from the ZTF light curve at 1.002h and a weaker one at 2.004h which we interpret as cyclotron beaming with two peaks per orbital cycle. We therefore conclude that this is a polar CV with $P_{\text{orb}} = 2.0034(1)$ h.

J0134+0422

The spectrum shows narrow, single-peaked Balmer, He I and weak He II asymmetric emission lines. ZTF shows brightening of $\Delta m = 1$ over a period of around one year consistent with the Spectral Energy Distribution (SED) which shows the spectrum was taken when the system was in a low state. The system appears to be a polar.

J0135+3401

Balmer and double-peaked He I and He II emission lines are detected in the spectrum together with broad Balmer absorption troughs. The SED shows that at the time of

the SDSS spectrum it was in a low state and has had a high state previously. This is consistent with the CRTS light curve which shows changes of $\Delta m \sim 2$ as well as a long term reduction in brightness. The state changes suggest that this either a polar or a novalike but there is not enough data to say which and so the classification is just a CV.

J0141+0620

The spectrum exhibits strong double-peaked Balmer emission lines and absorption lines from the white dwarf are also visible. There is no sign of the donor in the spectrum. There are no outbursts in the ZTF and CRTS light curves. This is likely to be a WZ Sge.

J0147+1444

The spectrum shows narrow Balmer, He I and He II emission lines. An M-dwarf is visible in the spectrum as well as cyclotron humps. The variability with no outbursts in the ZTF and CRTS light curves is consistent with the classification of a polar CV.

J0152–0043

The spectrum shows strong single-peaked Balmer and He I emission lines with the Balmer jump visible in emission. No donor signature is visible. The ZTF data shows no outbursts but is very sparse. The absence of donor and white dwarf signatures is suggestive of an SU UMa sub-type.

J0158+2823

Strong Balmer and weak He I emission lines as well as the signature of an M-dwarf donor are clearly visible in the spectrum. The ZTF and CRTS light curves show variability and eclipses but no outbursts. The ZTF light curve shows periodic behaviour at 1.0657h which we interpret as ellipsoidal modulation implying $P_{\text{orb}} = 2.13145(1)\text{h}$. This is within the period gap. The system is positioned between the main sequence and the white dwarf cooling sequence in the HR diagram. Despite the lack of outbursts this is probably an SU UMa.

J0207–0141

The spectrum shows Balmer, He I and He II asymmetric emission lines. Comparison between SDSS photometry and the SED suggests a cyclotron hump in the red. There is considerable variability in the ZTF light curve and a gradual brightening trend ($\Delta m = 2$ in two years). We conclude that this is a polar.

J0230–0045

The spectrum shows double-peaked Balmer and He I emission lines with no sign of the donor. The spectrum also shows broad absorption lines from the white dwarf. There are only three ZTF data points and no CRTS data. This is likely to be a WZ Sge.

J0242–0110

The signal-to-noise ratio of the spectrum is very poor. The presence of H α emission suggests that it may well be a CV.

J0728+3307

The spectrum shows broad double-peaked Balmer and He I emission lines and absorption lines from the white dwarf. There is no signature of the donor and there is only a small amount of ZTF photometry. The system is likely to be a WZ Sge.

J0736+1827

The spectrum shows double-peaked Balmer, He I, strong He II and Ca asymmetric emission lines. There is no sign of the donor or white dwarf in the spectrum although we tentatively identify cyclotron humps. The spectrum is brighter than the SED and inconsistent with the SDSS photometry suggesting that there have been state changes – one of which can be seen in the ZTF light curve. We conclude that this is a polar.

J0736+2009

The spectrum shows double-peaked Balmer and He I emission lines. The SED shows that it has been much brighter in the past suggesting at least one state change. There are only 8 ZTF data points and no CRTS data. The system is therefore a CV and possibly a polar.

J0802+3637

This object is faint (SDSS $m_g = 22$). The spectrum shows double-peaked Balmer emission lines in absorption troughs from the white dwarf with no sign of the donor. The ZTF light curve shows no outbursts. This is likely to be a WZ Sge.

J0806+3432

The spectrum shows strong Balmer and He I emission lines with no sign of the white dwarf or donor. There is a suggestion of He II emission. The ZTF light curve is highly variable with no outbursts. It includes six minute cadence data on three nights with a tentative period of 1.53h. This is likely to be an SU UMa.

J0810+2622

The spectrum shows strong Balmer, He I and He II emission lines with no sign of the white dwarf or donor. The ZTF light curve includes 6m cadence data on three nights with no outbursts. This is likely to be an SU UMa.

J0815+3356

The spectrum shows single-peaked Balmer emission lines with absorption lines from the white dwarf. There is no sign of the donor. The sparse ZTF data shows no outbursts. This is likely to be a WZ Sge.

J0828+2220

The spectrum shows narrow single-peaked Balmer emission lines and white dwarf absorption lines with no sign of the donor. The ZTF and CRTS light curves show short term variability with a constant mean magnitude and no outbursts (except for a single ZTF observation that appears to be an artefact). We find a period of 1.62h from the ZTF light curve. The SDSS photometry is not consistent with the spectrum in r,i,z filters; one possible explanation is that it was eclipsing. However the narrow lines are also indicative of a detached system with the line emissions arising from light reprocessed by the donor. Without further data this can only be classified as a candidate CV.

J0834+1854

There are two spectra (MJD = 57805, 59083). In both cases the spectrum shows strong and broad Balmer, He I and He II asymmetric emission lines with no sign of the white dwarf or donor. The second spectrum shows a cyclotron hump in the red. There is an *XMM* X-ray detection. The ZTF light curve is highly variable with a low to high state change. This is a polar CV.

J0835+2926

There are two spectra (MJD = 58464, 55544). In both cases the spectrum shows strong and broad Balmer, He I and He II asymmetric emission lines with no sign of the white dwarf or donor. Cyclotron humps are visible in both spectra. The SDSS photometry is not consistent with the spectra suggesting orbital variability. The ZTF light curve is highly variable with low and high states visible. This is a polar CV.

J0842+4623

There are two spectra (MJD = 55889, 56722) with a factor of five difference in flux. Both spectra show strong double-peaked Balmer and He I emission lines with no evidence

of the white dwarf or donor. The SED shows evidence of historical state changes. The CRTS and ZTF light curves show considerable variability and a state change but no outbursts. There is no HR diagram positional information as there is no *Gaia* counterpart. The system is clearly a CV but no further classification is possible.

J0909+1106

The spectrum shows strong double-peaked Balmer and He I emission lines with no evidence of the donor. There are deep central absorption dips suggesting that the system is eclipsing. The spectrum shows Balmer absorption lines from the white dwarf. J0909+1106 is located close to the white dwarf cooling sequence in the HR diagram. The ZTF light curve shows variability but no outbursts. This is likely to be a WZ Sge.

J0911+2606

The spectrum shows strong Balmer, Paschen, He I and weak He II emission lines. There is no sign of the donor. The ZTF light curve is sparse with no evidence of outbursts. This is likely to be an SU UMa.

J0931+3356

The spectrum shows double-peaked Balmer and He I emission lines with deep absorption cores indicating potential eclipsing. The donor is evident with the Na absorption doublet at 8183Å and 8194Å visible in the spectrum. The ZTF light curve shows one $\Delta m \sim 5$ outburst (MJD = 59105, duration $\simeq 10$ d) and one shorter outburst (MJD = 59338, duration < 2 d). We obtained a tentative period of 1.918(2) h. This is an SU UMa.

J1013+3938

The spectrum shows double-peaked Balmer and He I emission lines. The white dwarf is evident in the broad Balmer absorption lines; the donor is not visible. The ZTF light curves show significant variability but no outbursts. This is probably a WZ Sge.

J1017+3753

The spectrum shows double-peaked Balmer and He I emission lines. The emission lines have deep central absorption suggesting that J1017+3753 may be eclipsing. Neither the white dwarf nor the donor are visible. The system is faint with no *Gaia* parallax. The ZTF light curves show two outbursts. This is an SU UMa.

J1042+3718

The spectrum shows strong Balmer, He I and He II asymmetric single-peaked emission lines. The donor is visible in the spectrum as well as the Na doublet at 8183Å and 8194Å. There is a possible cyclotron hump between 4400Å and 5000Å. The ZTF light curve shows strong variability but no outbursts. This is a polar.

J1045+3624

This is a faint system with a noisy spectrum ($SNR = 1.5$), and no *Gaia* parallax or photometry. Nevertheless a double-peaked H α emission line is visible in the spectrum together with white dwarf absorption lines. The ZTF light curves show variability but no outbursts. This is likely to be a WZ Sge.

J1150+4041

See Chapter 5.

J1154+5757

The spectrum is noisy (SNR 2.6) but nevertheless shows strong Balmer and weak He I emission lines. The Balmer jump is visible in emission and there is no signature of the white dwarf. The SED shows that it has historically been much brighter suggesting there has been a state change. The ZTF light curve shows variability and frequent low-amplitude ($\Delta m \sim 2$ outbursts and superoutbursts. The system is close to the white dwarf cooling sequence in the HR diagram. This is probably an ER UMa.

J1210+3513

The spectrum shows strong double-peaked Balmer emission lines sitting in absorption lines from the white dwarf. The donor is not visible. The system sits on the white dwarf cooling curve in the HR diagram. There are no ZTF or CRTS light curve observations. This is probably a WZ Sge.

J1228+4545

The spectrum shows strong single-peaked Balmer and weak He I and He II emission lines. Comparison with historical SDSS photometry shows a broad cyclotron hump in the red. Neither the white dwarf nor the donor are visible. There are sparse ZTF observations showing variability but no outbursts. We have a tentative period of 1.879h from the ZTF light curve. We conclude that this is a polar.

J1237+3655

The spectrum shows strong double-peaked $H\alpha$ and $H\beta$ emission lines with absorption lines from the white dwarf. The spectrum also shows deep absorption dips within the emission lines indicating potential eclipsing. There is no signature of the donor. The spectrum is noisy ($SNR \simeq 3.5$) and there is no *Gaia* parallax for this faint ($m = 20.87$) object. The ZTF light curves show variability but no outbursts. This is probably a WZ Sge.

J1257+5825

There are two nearly identical spectra. They show strong single-peaked Balmer, He I and Ca emission lines as well as the Balmer jump. The spectrum shows absorption lines including the Na doublet which confirm that the donor is visible. There is no X-ray data. The system is located close to the main sequence on the HR diagram. The CRTS and ZTF light curves show variability over a range of 1.5 magnitudes but no outbursts. There is an unusual oscillation around MJD = 58780 of period $\simeq 20$ d in the ZTF light curve. This would seem to be a long-period dwarf nova but the absence of outbursts is not consistent with this. It has a similar low accretion rate and other similarities with V405 Peg (Thorstensen et al., 2009; Schwöpe et al., 2014, 2002c) which is most likely to be magnetic. We can only reliably classify this as a candidate CV.

J1338+3716

The spectrum shows strong double-peaked Balmer and He I emission lines. This is a faint system ($m = 21.64$) with no *Gaia* counterpart. The ZTF light curve shows variability but no outbursts. The spectrum is noisy ($SNR = 1.7$) but there appears to be an excess in the ultraviolet (consistent with the SED) and also the suggestion of wide Balmer absorption lines. This is probably a WZ Sge.

J1404+5258

The spectrum shows double-peaked Balmer and He I emission lines. This is a faint system ($m = 21.93$) with no *Gaia* counterpart. There is no ZTF or CRTS data. The spectrum is noisy ($SNR = 0.9$) but there appears to be an excess in the ultraviolet and also the suggestion of wide Balmer absorption lines. This is a CV but we cannot reliably classify it further.

J1404+5525

The spectrum shows double-peaked Balmer emission lines. This is a faint system ($m = 20.84$) located half way between the main sequence and white dwarf cooling sequence

in the HR diagram. The spectrum is noisy ($SNR = 3.5$) with no indications of either the white dwarf or donor. The ZTF light curve shows variability with one outburst. This is a dwarf nova.

J1526+3822

The spectrum shows strong double-peaked Balmer and He I emission lines. This is a faint system ($m = 21.35$) with no *Gaia* counterpart. The ZTF light curve shows variability but no outbursts. The spectrum is noisy ($SNR = 1.9$) but there appears to be an excess in the ultraviolet (the SED has a UV observation) and also the suggestion of wide Balmer absorption lines. This is probably a WZ Sge.

J1555+3802

The spectrum has a very small H α emission line and no others. The absorption lines from the donor are clearly visible. There are also cyclotron humps consistent with a magnetic field of $B \simeq 13.5$. The ZTF light curve shows variability but no outbursts. The ZTF data yields a period of 2.506(1) h with the phase-folded light curve showing a "top hat" profile. This is a polar.

J1607+3924

The spectrum shows slightly double-peaked Balmer and He II emission lines. The spectrum is noisy ($SNR = 1.4$) and there are no visible indications of either the white dwarf or the donor. The SED, and also SDSS photometry, shows that it was historically much brighter implying there has been a state change or frequent outbursts. The system is faint ($m = 20.95$) and there is no *Gaia* parallax. The ZTF light curve shows variability but no outbursts. The ZTF data yields a period of 0.9686h implying $P_{\text{orb}} = 1.937(1)$ h. This is likely to be a polar.

J1608+3019

The noisy ($SNR = 2.9$) spectrum shows double-peaked Balmer lines with absorption lines from the white dwarf. This is a faint system (PanSTARRS $m = 21.5$) with no *Gaia* counterpart. The ZTF light curve has a single data point indicating either a small ($\Delta m \simeq 2$) outburst or more likely an artefact. This is likely to be a WZ Sge.

J1618+3038

The spectrum shows strong double-peaked Balmer emission lines sitting in absorption lines from the white dwarf. The donor is not visible. The system is located just above the white dwarf cooling sequence in the HR diagram; the distance derived from the *Gaia*

parallax is unreliable and a realistic distance would place this on the cooling sequence. The ZTF light curve shows variability. This is likely to be a WZ Sge.

J1636+4724

The spectrum shows strong Balmer and He I emission lines. The white dwarf is visible as a slight excess at the blue end and also from H γ and H δ absorption lines. The system is located just above the white dwarf cooling sequence in the HR diagram. The ZTF light curve shows variability but no outbursts. This is likely to be a WZ Sge.

J1710+4031

The spectrum is noisy ($SNR = 0.9$) but double-peaked Balmer emission lines are visible. There appears to be an absorption line from the white dwarf at H γ . The system is faint ($m = 22.08$) and has no *Gaia* counterpart. There is no ZTF or CRTS data. This is likely to be a WZ Sge.

J1831+4202

See Chapter 5.

J2116+0141

The spectrum shows strong Balmer, Paschen, He I and He II emission lines and the Balmer jump is visible in emission. The white dwarf and donor are not visible. There are only five ZTF observations. The system is located between the main sequence and white dwarf cooling sequence in the HR diagram. This is likely to be a SU UMa.

J2124+0100

The spectrum is noisy ($SNR = 2.4$) and the flux calibration is faulty at the red end. Nevertheless double-peaked Balmer emission lines are detected and the higher Balmer lines appear sit within absorption lines from the white dwarf. There is no *Gaia* parallax. The system is positioned in the white dwarf cooling sequence in the SDSS $u - g/g - r$ diagram. There is no sign of the donor. The ZTF light curve shows variability but no outbursts. This is likely to be a WZ Sge.

J2130–0013

The spectrum is noisy ($SNR = 2.4$) but shows double-peaked Balmer emission lines together with a suggestion of absorption lines from the white dwarf. There is no *Gaia* counterpart. The ZTF light curve is sparse and shows variability but no outbursts. This is likely to be a WZ Sge.

J2208+1353

The spectrum is noisy ($SNR = 1.8$). Nevertheless double-peaked Balmer emission lines are detected together with $H\beta$ and $H\gamma$ absorption lines. There is no *Gaia* counterpart. The ZTF light curve is sparse and shows variability and an outburst. This is a WZ Sge.

J2209–0013

The spectrum is noisy ($SNR = 2.5$). Nevertheless double-peaked Balmer and He I emission lines are detected. $H\beta$ and $H\gamma$ absorption lines from the white dwarf are also apparent. There is no *Gaia* parallax. The ZTF light curve shows variability but no outbursts. This is likely to be a WZ Sge.

J2213+2450

The spectrum is noisy ($SNR = 2.0$) and the flux calibration is faulty at the red end. Nevertheless double-peaked Balmer emission lines are detected. There is no *Gaia* counterpart. The ZTF light curve shows variability but no outbursts. This is likely to be a WZ Sge.

J2219+2018

The spectrum shows strong Balmer and He I emission lines. The Na absorption doublet at 8183Å and 8194Å from the donor is visible. The system is close to the main sequence in the HR diagram. The ZTF light curve shows variability and multiple outbursts. We find a period of 3.36 h in the ZTF light curve. This is a dwarf nova.

J2232+2607

The spectrum shows strong asymmetric Balmer, He I and He II emission lines. There is no *Gaia* parallax. The current magnitude ($m = 20.2$) is brighter than it was in 2009 ($m = 22.9$) (Ahn et al., 2012), suggesting that the system is currently in a high state. The ZTF light curve shows variability but no outbursts. This is a polar CV.

J2233+2259

The spectrum shows strong narrow Balmer, Ca, He I and He II emission lines. The white dwarf and donor are not visible. There is a *GALEX* FUV observation. This is probably the counterpart to the *ROSAT* source 2RXS J223351.7+225905. The system is located between the main sequence and the white dwarf cooling sequence in the HR diagram. The ZTF light curve shows variability in the range $18.5 < m < 20.3$ with four short drop-outs to $m \simeq 21.4$; it does not appear to be eclipsing. This is a polar CV.

J2236+3239

The spectrum shows strong Balmer and weak He I double-peaked emission lines. There is no *Gaia* counterpart. The spectrum is noisy ($SNR = 3.2$) but there appear to be absorption lines from the white dwarf. The donor is not apparent. The ZTF light curve shows variability but no outbursts. This is probably a WZ Sge.

J2256+1911

The spectrum shows strong Balmer double-peaked emission lines and there is the suggestion of absorption lines from the white dwarf. The donor is not visible. There is no *Gaia* counterpart. The ZTF light curve is sparse and shows variability but no outbursts. This is probably a WZ Sge.

J2259+2239

The spectrum shows strong Balmer double-peaked emission lines. The spectrum is noisy ($SNR = 1.9$) but absorption lines from the white dwarf are discernible and the continuum rises steeply in the blue. The donor is not visible. There is no *Gaia* counterpart. The ZTF light curve is sparse and shows variability but no outbursts. This is probably a WZ Sge.

J2303+2747

The spectrum shows Balmer and weak He I double-peaked emission lines. The white dwarf is not visible. The continuum rises in the red and there is a hint of the donor signature. There is no *Gaia* counterpart. There is no ZTF or CRTS data available. The system is probably a dwarf nova.

J2321+2518

The spectrum shows Balmer double-peaked emission lines with no sign of the white dwarf or donor. There is deep central absorption in the emission lines suggesting that J2321+2518 may be eclipsing. The system is positioned between the main sequence and the white dwarf cooling sequence in the HR diagram. The ZTF light curve shows variability but no outbursts. We found a period of 1.615(1) h from the ZTF light curve. The system is therefore likely to be a WZ Sge.

J2325+0115

The spectrum shows strong Balmer double-peaked emission lines. There is deep central absorption in the emission lines suggesting that J2325+0115 may be eclipsing. The spectrum is noisy ($SNR = 2.9$) and the flux calibration is faulty at the red end however

the white dwarf and donor are not apparent. There is no *Gaia* counterpart. The ZTF light curve shows variability but no outbursts. This is probably a WZ Sge.

J2337+3141

The spectrum shows strong broad Balmer and double-peaked He I emission lines and a weaker He II emission line. The Balmer jump is visible in emission. The white dwarf and donor are not visible. There is a nearby Swift detection (2SXPS J233705.0+314150). The system is located between the white dwarf cooling sequence and the main sequence. The ZTF light curve shows variability but no outbursts. This is probably an SU UMa.

J2351+2709

The spectrum shows strong Balmer, He I and He II asymmetric emission lines. The white dwarf is not visible. TiO lines from the donor are clearly visible suggesting a mid-M dwarf. The system is located between the white dwarf cooling sequence and the main sequence. The ZTF light curve shows variability but no outbursts whilst the CRTS data shows a possible outburst. This is probably a dwarf nova.

J2356+0018

There are three very similar spectra. The spectra show strong Balmer and weak He I emission lines. Absorption lines from the white dwarf are visible. The flux calibration at the red end is faulty but there is no evidence of the donor. The ZTF light curve shows a large outburst. This is a WZ Sge.

B.3.2 Previously known systems

J0007+2007

The noisy spectrum shows double-peaked Balmer emission lines above a blue continuum. There is a suggestion of the donor spectrum. There is no *Gaia* counterpart. The object is on the white dwarf cooling sequence in the u-g/g-r diagram. The ZTF light curve shows one outburst of over $\Delta m > 5$ with a long (over 15 days) decline. This is a superoutburst and so this is probably either an SU UMa or more likely a WZ Sge.

J0008-0140

This is Gaia15abi. The spectrum shows strong single-peaked Balmer and He I emission lines above a blue continuum with the Balmer jump visible in emission. There is no sign of the white dwarf or the donor. The system is located nearer the main sequence than the white dwarf cooling sequence in the HR diagram. ZTF shows an interesting long-term light curve with outbursts, but also quite a large amount of variability in the

quiescent level. This is not a typical dwarf nova. We were unable to find a reliable period from either the ZTF or *TESS* light curves. This is probably a novalike although it might be a polar.

J0011+3155

The spectrum shows double-peaked Balmer and He I emission lines. The Balmer jump is visible in emission as well as TiO absorption lines from the donor. The ZTF light curve shows four outbursts including two superoutbursts. We obtained a tentative period of 1.33h from the ZTF light curve. This is an SU UMa.

J0020+2800

The transient was originally detected as MASTER OT J002049.54+280020.5. The CRTS and ZTF light curves show variability without outbursts. The spectrum shows dual peaked Balmer emission lines with H β , H γ and H δ set in absorption lines from the white dwarf. The H α emission line has a deep absorption core suggesting that it may be eclipsing. The system is next to the white dwarf cooling sequence in the HR diagram. The light curve shows a signal at 0.679h which we interpret as $P_{\text{orb}} = 1.358(1)$ h. This is probably a WZ Sge.

J0022+0610

The spectrum shows narrow double-peaked Balmer emission lines and He I emission lines and the Balmer jump in emission. There is no sign of the donor in the spectrum. The system is located midway between the main sequence and the white dwarf cooling sequence in the HR diagram. There are outbursts and superoutbursts visible in the ZTF light curve. We find a tentative period of 1.9h in the ZTF light curve. This is an SU UMa.

J0025+0733

The spectrum shows strong narrow Balmer and weak He I and He II emission lines with no sign of the white dwarf or donor. The system is located nearer the main sequence than the white dwarf cooling sequence in the HR diagram. There are 11 outbursts in the ZTF light curve. We find a tentative orbital period of 3.24h. This is a dwarf nova.

J0026+2429

The spectrum shows Balmer and He II emission lines. There are no outbursts in the ZTF Light curves which is consistent with the existing classification of polar (Margon et al., 2014). Additionally we obtained a period of $P_{\text{orb}} = 2.048(1)$ h. The phase-folded light curve is double-peaked which we interpret as being due to cyclotron beaming .

J0027–0108

This is EN Cet. The spectrum shows double-peaked Balmer emission lines with absorption lines from the white dwarf visible. There appears to be a red excess. The system is close to the white dwarf cooling sequence in the HR diagram. There is one recorded outburst of $\Delta m \simeq 6$ in 1997 ([Bao Supernova Survey et al., 1997](#)) but no other outbursts in ZTF or CRTS. It has a known period of 84m. It has previously been classified as a U Gem but we classify it as a WZ Sge.

J0028+3118

See Chapter [5](#).

J0031+0841

This is ASASSN-17kg. The spectrum shows double-peaked Balmer emission lines with absorption lines from the white dwarf visible. The system is close to the white dwarf cooling sequence in the HR diagram. It has a period of 84m. There is one recorded outburst of $\Delta m \simeq 6$ on 2017-08-1. This has been classified as an SU UMa but is actually a WZ Sge.

J0031+2020

This is MGAB-V534. The spectrum shows double-peaked Balmer, He I and He II emission lines. The white dwarf and donor are visible. The system is eclipsing and the known period is 1.94h; close to the period gap. There have been two recorded outbursts; one on 2018:08:16 by ZTF and one on 2019:09:27 (VSNET 23583) by ASAS-SN. In each case the amplitude was $\Delta m \simeq 4.3$. This is a low accretion rate SU UMa.

J0032+3145

The spectrum shows slightly double-peaked Balmer, He I, He II and Ca emission lines as well as the Balmer jump in emission. There is no sign of the donor. The system is located midway between the main sequence and the white dwarf cooling sequence in the HR diagram. ZTF shows four outbursts and one superoutburst. Superhumps are visible but the data are too sparse to get a period. This is a SU UMa.

J0034+2736

The spectrum shows double-peaked Balmer lines. The system is located midway between the main sequence and the white dwarf cooling sequence in the HR diagram. There are at least eight outbursts and one superoutburst (with superhumps) in the

ZTF light curve. The ZTF light curve shows ellipsoidal modulation at a period of 0.8807h and so $P_{\text{orb}} = 1.761(1)$ h. This is an SU UMa.

J0038+2509

The spectrum shows strong double-peaked Balmer and He I 5876 emission lines and the Balmer jump is visible. TiO absorption lines from the donor are visible. The system is midway between the main sequence and the white dwarf cooling sequence in the HR diagram. The ZTF light curve shows multiple outbursts and superoutbursts. [Szkody et al. \(2018\)](#) studied this CV and found a spectroscopic period of 95 minutes derived from radial velocities following two hours of observations. We could not identify this period in the ZTF light curve. We did however find a period of 0.094511(1) d. This is an SU UMa even though it has a period within the period gap.

J0039+0054

The spectrum shows double-peaked Balmer and He I emission lines with absorption lines from the white dwarf visible. The system is close to the white dwarf cooling sequence in the HR diagram. It has a period of 1.52h. The ZTF and CRTS light curves show no signs of outbursts beyond energetic flickering with $\Delta m < 1$. This has been classified as a CV but is probably an WZ Sge and possibly a period bouncer.

J0042+0731

The spectrum shows double peaked Balmer lines, He II and Ca emission lines. The Balmer jump is visible and there is no sign of the white dwarf. The system is located midway between the main sequence and the white dwarf cooling sequence in the HR diagram. The ZTF light curve shows variability and also an apparent state change. There is also one possible small outburst. There is *TESS* light curve data. Both *TESS* and ZTF show signals at 0.9789 h. *TESS* also exhibits a signal at 2.567 h. This is probably an intermediate polar.

J0043–0037

The spectrum shows double-peaked Balmer and He I emission lines with absorption lines from the white dwarf visible. The system is close to the white dwarf cooling sequence in the HR diagram. It has a period of 1.39 h. The ZTF and CRTS light curves show no signs of outbursts beyond energetic flickering of $\Delta m < 1$. This has been classified as a CV but is probably an WZ Sge.

J0045+2227

The spectrum shows double-peaked Balmer and He I emission lines as well as the Balmer jump in emission. The system is closer to the white dwarf cooling sequence than the main sequence in the HR diagram. There are two superoutbursts and one other outburst in the ZTF light curve. We found a tentative period of 1.690(1) h in the ZTF light curve. This is an SU UMa star.

J0049+0747

The spectrum shows double-peaked Balmer and He I emission lines as well as the Balmer jump in emission. Absorption lines from the donor are clearly visible. There is no *Gaia* parallax. The object is close to the white dwarf cooling sequence in the $u - g/g - r$ diagram. The CRTS and ZTF light curves do not show any outbursts. This is probably a WZ Sge.

J0049+2226

This is discussed in Fig. 2.15. The spectrum shows double-peaked Balmer emission lines but no He II. The donor is visible at the red end of the spectrum. This is depicted in Fig. 2.15 where we demonstrate the cyclotron humps and magnetic field strength of $B \simeq 78\text{MG}$. We find a reliable period of 5.9165(1) h from the ZTF light curve which is consistent with the orbital period of 5.916h reported by Parsons et al. (2021). The fact that the donor is visible implies that the accretion rate is low and so this is probably a pre-polar accreting from the donor wind.

J0052+3159

The spectrum shows narrow double-peaked Balmer and He I emission lines as well as the Balmer jump in emission. There is no sign of the donor. The system is located midway between the main sequence and the white dwarf cooling sequence in the HR diagram. The CRTS and ZTF light curves show multiple outbursts but no apparent superoutbursts. This is probably an SU UMa.

J0056+3206

This is MGAB-V3456 which has previously been classified as a novalike of the VY Scl sub-type. (<https://sites.google.com/view/mgab-astronomy/mgab-v3451-v3500>). The system is also probably the *ROSAT* X-ray source 2RXS J005657.9+320612. The spectrum shows strong Balmer, Ca, He I and He II emission lines. The lines have broad bases suggesting that the system is magnetic. The system is located midway between the main sequence and the white dwarf cooling sequence in the HR diagram – not

in the area normally associated with novalikes. ZTF light curves show phase changes of $\Delta m \sim 2$ and the SED confirms that it has historically been much dimmer. We find $P_{\text{orb}} = 1.58757(2)$ h from the ZTF light curve. This is a polar.

J0058–0107

This is ASASSN-16iw. [Kato et al. \(2017\)](#) found a superhump period of 1.56h from a superoutburst on 2016:08:16 and suggested it may be a WZ Sge. There are no other outbursts visible in the ZTF and CRTS light curves. The SED shows no trace of the donor. The system is currently classified as an SU UMa. This is a WZ Sge and probably a period bouncer.

J0104–0313

The spectrum shows strong narrow Balmer, He I emission lines and weak He II lines. There is no sign of the white dwarf or the donor in the spectrum. The system is located midway between the main sequence and the white dwarf cooling sequence in the HR diagram. The ZTF light curve shows at least 11 short outbursts of $\Delta m \sim 5$. This is probably an SU UMa.

J0108+0226

This is MGAB-V3459 which has previously been classified as a polar CV. Our spectrum is noisy but shows two strong cyclotron humps at ~ 4800 and ~ 6250 . This would imply $B \simeq 58$ MG. We find a period of 1.2893h from the ZTF light curve.

J0113–0332

The spectrum is very red with the donor clearly visible. There is a slight $H\alpha$ emission line but overall this would appear to be the spectrum of an M star but for a cyclotron hump at $\simeq 4250\text{\AA}$. The ZTF light curve suggests a period of 4.39552(2) h which is consistent with [Parsons et al. \(2021\)](#). This is a polar.

J0117+1755

This is ASASSN-20pq. The spectrum shows double peaked Balmer emission lines with deep absorption cores. The absorption lines from the white dwarf are visible and the suggestion of the donor. The system is close to the white dwarf cooling sequence in the HR diagram. There are four outbursts in the ZTF light curve at least one of which is a superoutburst. There are also three outbursts in the CRTS light curve. We find a periodic signal in the ZTF light curve around 1.569h; it also appears to be eclipsing. This is probably an SU UMa.

J0120+1857

The spectrum shows Balmer and He I emission lines and also absorption lines from the white dwarf. The CRTS and ZTF light curves do not show any outbursts. The system is close to the white dwarf cooling sequence in the HR diagram. This is probably a WZ Sge.

J0128+1130

The spectrum shows slightly double-peaked Balmer, He I, He II and Ca emission lines as well as the Balmer jump in emission. TiO absorption lines from the donor are also visible. The system is located midway between the main sequence and the white dwarf cooling sequence in the HR diagram. There are four short-lived (a few days) outbursts in the ZTF light curve. No periods are visible in the light curves. This is a dwarf nova.

J0128+1845

This is an *XMM* X-ray source (XMMSL2 J012838.3+184537). The spectrum shows strong narrow single-peaked Balmer and weaker He I emission lines. There is a suggestion of absorption lines from the white dwarf. There is no sign of the donor. There is an outburst in the CRTS light curve which did not decay for over 60 days. There is no *Gaia* counterpart and hence no position in the HR diagram. This is a CV but more data is needed to refine the classification.

J0129+3842

This is V0744 And. It has been classified on VSX as UGSU/IBWD. The spectrum shows helium emission lines and no hydrogen lines. It has a superhump -derived period of 37m. The system is recognised as an AM CVn (see for example [Kato et al. \(2015\)](#)). We therefore classify this as an AM CVn.

J0137–0912

This is GZ Cet. This is an SU UMa where both the donor and the white dwarf are visible in the spectrum. It has an unusually short period of 80m which is inconsistent with a luminous main sequence donor. The spectrum shows strong helium emission lines and therefore this probably has an evolved donor.

J0142+0017

The spectrum shows strong Balmer He I and He II emission lines. The lines are asymmetric which is indicative of a magnetic CV. There appears to be a cyclotron hump at the red end of the spectrum. There is no sign of the white dwarf or donor. The synthetic

magnitude of 18.5 is brighter than the *Gaia* G magnitude of 19.9 suggesting that the system was in a high state consistent with the ZTF light curve which shows at least 3 state changes. This is all consistent with the VSX category of a polar.

J0142+2323

This is ASASSN-18ad. The noisy spectrum shows double-peaked Balmer emission lines with a deep absorption core. There is a suggestion of absorption lines from the white dwarf. There is no *Gaia* parallax data. The ZTF light curve shows four outbursts confirming the classification as dwarf nova. We obtained a tentative period from the ZTF light curve of 1.71(6) h. This is therefore likely to be a SU UMa.

J0157+2244

The spectrum shows double-peaked Balmer and He I emission lines. The white dwarf is apparent at the blue end. There is no *Gaia* parallax data. The $u - g/g - r$ plot places this near the white dwarf cooling sequence. The ZTF light curve shows a superoutburst and two other outbursts. This is probably a SU UMa.

J0223–0520

See Chapter 5.

J0229–0306

The spectrum shows double-peaked Balmer and He I emission lines. The Balmer jump is evident in emission. The donor is not visible. There is no *Gaia* parallax data. The ZTF light curve shows three short-lived outbursts. This is a dwarf nova.

J0230+2604

The spectrum shows double-peaked Balmer and He I emission lines indicating the presence of a disc. The spectrum shows Na absorption lines, presumably from the donor but no TiO absorption lines. The continuum of the spectrum and the SED also suggest the presence of the donor. The HR diagram positions the system close to the main sequence. The CRTS and ZTF light curves show state changes with $\Delta m \sim 1$ but no outbursts. This is a CV but more data is needed to refine the classification.

J0231–0005

The spectrum shows narrow Balmer emission lines and the Balmer jump in emission. There is no *Gaia* parallax data. Neither the white dwarf nor the donor are visible in

the spectrum. The sparse ZTF light curve shows no outbursts. We tentatively classify this as a SU UMa as the donor is not seen.

J0252+0020

This is ASASSN-21rq. The noisy spectrum shows double-peaked Balmer and He I emission lines. There is a suggestion of absorption lines from the white dwarf. There is no *Gaia* parallax data. There are no ZTF or CRTS light curve data. The ASAS-SN light curve has a median magnitude of 16.73 which is the limiting magnitude. The reported outburst of 16.17 magnitude may not be genuine given that this is a very faint system invisible in Pan-STARRS. This is likely to be a WZ Sge.

J0326+0115

J0326+0115 has a very noisy spectrum with weak narrow Balmer emission lines. The SED shows that it has been much brighter in the past although the SED observations were contemporaneous and so they may all have happened during an outburst. There are 2 outbursts visible in the ZTF light curve. This is probably a dwarf nova.

J0337–0650

The noisy spectrum shows narrow single-peaked Balmer emission and strong Ca emission lines. The white dwarf and donor are not visible. There are superoutbursts and outbursts visible in the ZTF light curve. This is probably an SU UMa.

J0357–0638

The spectrum shows strong double-peaked Balmer, He I and Ca emission lines. There is a hint of the white dwarf in the spectrum. The CRTS and ZTF light curves show strong variability but no apparent outbursts and we were not able to identify a period. The system is close to the white dwarf cooling sequence in the HR diagram. This is probably a WZ Sge.

J0738+2855

[Szkody et al. \(2003a\)](#) reported a spectroscopic period of 125-127m for this eclipsing U Gem system. The ZTF light curve yields a reliable double-humped orbital period of 5.5554(1) h.

J0743+1838

The noisy spectrum shows narrow single-peaked Balmer emission lines. The SED shows that it has been brighter in the past – possibly due to an outburst. There is no *Gaia*

counterpart. The u-g/g-r diagram shows that the system is a long way from the white dwarf cooling sequence which would be consistent with J0743+1838 being a dwarf nova or a polar. The ZTF and CRTS light curves show variability but no outbursts. This is a CV but more data is needed to refine the classification further.

J0744+4826

This is ASASSN-16cz. The spectrum shows very broad double-peaked Balmer emission lines with unusual side wings particularly in $H\beta$. There is no *Gaia* parallax data. The donor is not visible. This is a blue object ($BP - RP = 0.4$) and the *GALEX* observation shows that the system is brightest in the FUV. The ZTF light curve shows three outbursts – two of which decline over ~ 20 days with apparent superhumps. This is probably an SU UMa.

J0747+4248

[Szkody et al. \(2002b\)](#) describes this as having the bright blue continuum and weak Balmer emission of an old nova with a high accretion rate. The ZTF light curve shows long term variations and no outbursts consistent with this. The system is in the novalike area of the HR diagram. This is probably a novalike.

J0748+2905

This is V434 Gem – a known novalike ([Dillon et al., 2008](#)). It has not been possible to recover a period from the *TESS* light curve.

J0749+3654

This is MGAB-V3545; Gabriel Murawski classified this as a polar *. The spectrum shows Balmer emission lines. There are no He lines evident although the quality of the spectrum is poor. The synthetic magnitude from the spectrum is 20.3 which is near the historical maximum. There are no X-ray observations. The ZTF light curve shows a gradual increasing trend in luminosity over $\simeq 2$ years but no outbursts. There is high cadence ZTF data which reveals a period of $P_{\text{orb}} = 1.34(1)$ h –. The phase-folded light curve shows two peaks which are probably due to cyclotron beaming. This is probably a polar.

J0750+1411

This has previously been classified as a U Gem. However the ZTF and CRTS light curves show at least one superoutburst and, combined with the short orbital period of 2.2 h, we consider this is probably an SU UMa.

*<https://sites.google.com/view/mgab-astronomy/mgab-v3501-v3550>

J0753+3758

The spectrum shows strong Balmer and weak He I and He II single-peaked emission lines. The Balmer jump is visible in emission. The white dwarf and donor are not visible. The system is located midway between the main sequence and the white dwarf cooling sequence in the HR diagram. The SED shows one set of observations where the system was dimmer than it is now. The ZTF light curve shows considerable variability and two distinct states – reminiscent of a magnetic system. The CRTS light curve also shows variability and a large ($\Delta m > 4$) outburst. Despite the anomalous CRTS outburst this is probably a magnetic CV.

J0754+5007

This has previously been identified as a CV. The spectrum shows a blue continuum with Balmer and He II emission lines. The system is in the novalike area of the HR diagram. There are no outbursts in the ZTF and CRTS light curves. This is a novalike.

J0755+1435

The spectrum shows double-peaked Balmer emission lines with absorption lines from the white dwarf visible. The system is on the white dwarf cooling sequence in the HR diagram. It has a period of 84m. There is one recorded outburst with $\Delta m \simeq 6$ on 2017-08-1. This is probably a WZ Sge.

J0756+3058

The spectrum shows narrow double peaked Balmer and weaker, He I emission lines with no evidence of the white dwarf or donor. The ZTF light curve shows outbursts and at least one superoutburst. The CRTS light curve shows a further outburst. This would appear to be an SU UMa.

J0758+1043

The spectrum shows a strong blue continuum and H α and H β emission lines whilst the other Balmer emission lines sit in absorption troughs. The object is located in the top left of the HR diagram where novalikes are typically found. The *TESS* light curve yields a period of 4.77(5) h. This is a novalike.

J0758+1616

Following [Duffy et al. \(2022\)](#) we classify this as an intermediate polar.

J0759+1914

We have an accurate previously unpublished photometric period of 0.1309337(8) provided by SL based on observations using ULTRACAM.

J0801+2103

The spectrum is noisy but nevertheless it shows Balmer, He I and He II emission lines. The SED shows that it was historically much brighter. The system is positioned in the HR diagram away from the novalikes and so it is unlikely to be a VY Scl. The ZTF light curve shows variability but no outbursts. The CRTS light curve shows a $\Delta m \sim 4$ state change but no outbursts. This is probably a polar.

J0805+0720

This has been well studied and there is a period derived from radial velocities ([Thorstensen et al., 2015](#)). We have been able to derive a period of 0.228711(1) d from the ZTF light curve which we consider to be more accurate.

J0807+5547

The spectrum shows strong Balmer and He I emission lines. The Balmer jump in emission is visible. The system is positioned between the main sequence and white dwarf cooling sequences in the HR diagram. There is a single strong outburst in the ZTF light curve. This is an SU UMa.

J0808+3550

The spectrum shows a strong blue continuum with strong Balmer and He I emission lines. The equivalent width of the He lines compared with the Balmer lines is unusually strong. There are odd thin peaks in the emission lines which may be background emission. Neither the white dwarf nor the donor are visible in the spectrum. There are many outbursts and superoutbursts in the ZTF and CRTS light curves. The spectrum is considerably brighter than the historical observations in the SED suggesting that the observation was taken in the aftermath of an outburst. This is a dwarf nova but more data is needed to refine the classification.

J0814+2021

The spectrum shows strong double-peaked Balmer and weak He I emission lines. The white dwarf and the donor are not visible. There is no *Gaia* counterpart. The ZTF and CRTS light curves show variability but no outbursts. ASAS-SN shows a superoutburst peaking at $m = 14.6$ on MJD = 57066 with a long decay time and evident superhumps.

The quiescent magnitude of this system is over 21 and so this outburst must have been $\delta m \sim 7$. This is probably an SU UMa.

J0820+4747

The spectrum shows double-peaked Balmer and He I emission lines. He II is also present with no sign of the white dwarf or donor. The system is located midway between the main sequence and the white dwarf sequence in the HR diagram. There are multiple outbursts and superoutbursts in the ZTF light curve. This is a SU UMa.

J0821+4541

The spectrum shows double-peaked Balmer and He I emission lines. TiO absorption lines from the donor can also be seen. The system is located midway between the main sequence and the white dwarf sequence in the HR diagram. There are at least three outbursts in the ZTF light curve. This is a U Gem.

J0822+2313

The spectrum shows a strong double-peaked H α emission line and also TiO absorption lines from the donor. The spectrum is reminiscent of an M-dwarf with the exception of the H α line which is too broad to be the result of flaring. The system is located near the main sequence in the HR diagram. The ZTF light curve shows variability but no outbursts. The CRTS light curve also shows variability and possibly several small outbursts. The SED shows no evidence of a white dwarf. Without further data we can only classify this as a candidate CV.

J0824+0737

The noisy spectrum shows double-peaked Balmer emission lines and also TiO absorption lines from the donor. The white dwarf is not visible. There is no *Gaia* counterpart. The quiescent magnitude is about 22 and the ZTF light curve shows outbursts of $\Delta m \simeq 3$. The SED includes a set of historical observations when it was much brighter; these were probably taken during an outburst. The ZTF light curve shows frequent outbursts. This is a dwarf nova.

J0830+4047

This is *Gaia* alerts Gaia19eb5 which is based upon two short transients on 2019-09-03 and 2019-11-24 of $\Delta m \sim 1.5$. The spectrum shows single-peaked Balmer, He I and He II emission lines. The Balmer jump in emission is visible with no sign of the white dwarf or donor. The ZTF light curve shows variability but no outbursts other than those

reported in Gaia19ebs. We find a period of 0.877 h which suggests $P_{\text{orb}} \simeq 1.754$ h. This is probably a polar.

J0837+3830

The spectrum shows narrow weak Balmer emission lines with the donor and the white dwarf clearly visible. [Schmidt et al. \(2005b\)](#) and [Hilton et al. \(2009\)](#) demonstrated that the system is magnetic and suggested that it is a pre-polar. [Parsons et al. \(2021\)](#) suggest that the system is a detached system that was a CV for a while. The ZTF light curve shows a transition into a high state at MJD = 59600 and so we conclude that the system is a polar.

J0837+4133

The spectrum shows double-peaked H α emission and higher Balmer absorption lines from the white dwarf. The system is in the white dwarf cooling sequence in the HR diagram. There are no outbursts in the CRTS and ZTF light curves. This is probably a WZ Sge.

J0837+5645

The spectrum shows double-peaked Balmer and He I emission lines and absorption lines from the white dwarf are also visible. There is no *Gaia* parallax. The system is close to the white dwarf cooling sequence in the u-g/g-r diagram. The ZTF light curve shows a superoutburst with a long (~ 100 d) decay. The SED shows the SDSS photometry apparently occurred during an outburst. This is probably a WZ Sge.

J0838+4910

See Chapter [5](#).

J0840+2204

The spectrum shows narrow, asymmetric Balmer, He I, He II and Ca emission lines as well as the Balmer jump in emission. There is no sign of the donor but there is a probable cyclotron hump at the red end of the spectrum. The system is closer to the white dwarf cooling sequence than the main sequence in the HR diagram. The ZTF and CRTS light curves show variability with a state change and we find a period of 1.462 h from the ZTF light curve. This is probably a polar.

J0840+0455

The spectrum shows weak H α emission with absorption lines reminiscent of a moderately hot star (perhaps a G-type) above a bright blue continuum. The lines are sharp with metal lines (such as Mg at 5167, 5172 and 5183) which are not found in discs and would be smeared in any case. *Gaia* shows that there is another star only 0.25 arcsec away which has very similar parallax, proper motion and colour magnitudes. This triple system accounts for the blended spectrum. As *Gaia* resolves the triple the position in the *Gaia* HR diagram is correct and is consistent with a novalike. The ZTF light curve shows variability of over a magnitude with no outbursts. This is therefore consistent with the conclusion of [Szkody et al. \(2006\)](#) that this is a novalike.

J0840+2204

The spectrum shows narrow, asymmetric Balmer, He I, He II and Ca emission lines as well as the Balmer jump in emission. There is no sign of the donor. The system is closer to the white dwarf cooling sequence than the main sequence in the HR diagram. The ZTF and CRTS light curves show variability with a state change. This is probably a polar.

J0843+4250

The spectrum shows narrow, single-peaked Balmer and He I emission lines as well as the Balmer jump in emission. There is no sign of the donor. The system is located midway between the main sequence and the white dwarf cooling sequence in the HR diagram. The CRTS and ZTF light curves show frequent outbursts and superoutbursts. This is probably an SU UMa.

J0846+2453

This has previously been classified as a CV. The spectrum shows a strong He II emission line indicative of a magnetic CV. We concur with [Littlefield et al. \(2023a\)](#) who concluded that J0846+2453 is an asynchronous polar.

J0851+1842

This is ASASSN-15fq. The spectrum shows narrow, single-peaked Balmer and He I emission lines as well as the Balmer jump in emission. There is no sign of the donor. The system is located midway between the main sequence and the white dwarf cooling sequence in the HR diagram. There is one superoutburst visible in the ZTF light curve and another in the CRTS light curve but no outbursts. This is probably an SU UMa.

J0852+0201

The spectrum shows narrow, single-peaked Balmer and He I emission lines. The higher Balmer emission lines are embedded in absorption lines from the white dwarf. There is a suggestion of cyclotron humps in the red and also of Zeeman splitting in the white dwarf absorption lines. The SED shows that the system has historically been brighter than it is now. There is no sign of the donor. There is no *Gaia* parallax. The system is in the white dwarf cooling sequence in the u-g/g-r diagram. There are no outbursts visible in the CRTS and ZTF light curves. This is probably a polar with a moderate magnetic field.

J0853+0204

The spectrum is noisy with poor flux calibration. Nevertheless double peaked Balmer emission lines are detected and also absorption lines from the white dwarf. There is no sign of the donor. There is no *Gaia* parallax. The system is in the white dwarf cooling sequence in the u-g/g-r diagram. The ZTF light curve shows a superoutburst and a second outburst. This is probably a WZ Sge.

J0853+4848

See Chapter [5](#).

J0854+2013

The spectrum shows narrow, double-peaked Balmer and He I emission lines. There is a hint that the higher Balmer emission lines are surrounded by absorption lines from the white dwarf. The system is closer to the white dwarf cooling sequence than the main sequence in the HR diagram. There are outbursts and at least one superoutburst visible in the ZTF and CRTS light curves. This is probably an SU UMa.

J0856+3108

The spectrum shows double-peaked Balmer and He I emission lines. The higher Balmer emission lines are surrounded by deep absorption lines from the white dwarf. There is no sign of the donor. The system is close to the white dwarf cooling sequence in the HR diagram. The ZTF and CRTS light curves show variability but no outbursts. This is probably a WZ Sge.

J0856+3221

The spectrum shows narrow, double-peaked Balmer and He I emission lines. There is a hint that the higher Balmer emission lines are surrounded by absorption lines from

the white dwarf. The system is located midway between the main sequence and the white dwarf cooling sequence in the HR diagram. There are outbursts and at least one superoutburst visible in the ZTF and CRTS light curves. This is consistent with the existing classification of SU UMa.

J0900+3439

The spectrum shows slightly double-peaked Balmer, He I and He II emission lines. The emission lines are unusually narrow – which implies a very low inclination. The system is closer to the main sequence than the white dwarf cooling sequence in the HR diagram. The spectrum is noisy and it is not possible to determine if the white dwarf and donor are present or not. The ZTF and CRTS light curves show outbursts and at least one superoutburst. This is probably an SU UMa although the spectrum is not typical of this sub-type.

J0901+1447

The spectrum shows a strong blue continuum with an $H\alpha$ emission line whilst the other Balmer emission lines sit in absorption troughs. The object is located in the top left of the HR diagram where novalikes are typically found. The CRTS and ZTF light curves show no outbursts. However the ZTF light curve does show several curious short term drops in amplitude of $\Delta m \simeq 0.8$. The *TESS* light curve does not show such short term drops and yields a period of 3.5120 h. This is a novalike.

J0904+0355

The spectrum shows double-peaked Balmer emission lines with absorption lines from the white dwarf visible. The system is close to the white dwarf cooling sequence in the HR diagram. It has a period of 86m. There are no recorded outbursts in ZTF or CRTS. This is probably a WZ Sge.

J0904+4402

This is FV Lyn. The spectrum shows double-peaked Balmer emission lines with absorption lines from the white dwarf visible. There is no sign of the donor. The system is on the white dwarf cooling sequence in the HR diagram. The CRTS light curve shows no outbursts whilst the ZTF light curve shows one outburst with $\Delta m \simeq 3.5$. [Kato et al. \(2014a\)](#) report that the system is an SU UMa with a superhump period of 0.06977 h. This is probably a WZ Sge and may be a period bouncer.

J0906+0526

There are two spectra; MJD = 52674 was taken when the CV was in a quiescent state whilst MJD = 52649 was taken in outburst. The spectrum from MJD = 52674 shows double-peaked Balmer emission lines. The system is located midway between the main sequence and the white dwarf cooling sequence in the HR diagram. The CRTS and ZTF light curves show frequent outbursts. This is a dwarf nova.

J0907+4630

The spectrum shows strong Balmer and He I asymmetric emission lines and weak He II. The spectrum does not match the SED and so either the flux calibration is faulty or we observed J0907+4630 in a low state. The signal-to-noise ratio is poor (3.6) but there is a hint of the donor spectrum. J0907+4630 is located close to the white dwarf cooling sequence. The ZTF light curve includes data for three nights with a cadence of six minutes; this shows variability of $\Delta m \simeq 1$ in a few minutes which may be due to cyclotron beaming. This is a CV but without more data we cannot classify it further.

J0912+6209

Both the white dwarf and the donor are visible in the spectrum together with Balmer and He I emission lines. There is a spectroscopic period of 1.92 h. The sparse CRTS light curve shows an outburst whilst the sparse ZTF light curve does not show any. This is probably an SU UMa as suggested by [Thorstensen et al. \(2015\)](#).

J0914+5403

The spectrum shows double-peaked Balmer and He I emission lines as well as the Balmer jump in emission. There is no sign of the white dwarf or the donor. There is deep central absorption in the emission lines implying that the system is eclipsing. The system is close to the white dwarf cooling sequence in the HR diagram. The CRTS and ZTF light curves show multiple outbursts and at least two superoutbursts. This is an SU UMa.

J0917+3143

The noisy spectrum shows narrow double-peaked Balmer and He II emission lines. TiO absorption lines from the donor are visible; there is no sign of the white dwarf. The system is located midway between the main sequence and the white dwarf cooling sequence in the HR diagram. The CRTS and ZTF light curves show variability but no outbursts whilst the ZTF light curve shows what appears to be the beginning of a state change. We obtained a period of 0.0541437(1) h from the ZTF light curve which is consistent with our unpublished spectroscopic period of 0.054144 d. This is a polar.

J0919+0857

This is LC Cnc. The white dwarf is visible in the spectrum together with Balmer and He I emission lines. The system is located on the white dwarf cooling sequence in the HR diagram. There is a known period of 81 min. There are no outbursts in the ZTF and CRTS light curves. This is probably a WZ Sge.

J0919+5028

The spectrum shows narrow double-peaked Balmer and He I emission lines. TiO absorption lines from the donor are visible and also absorption lines from the white dwarf. There is potential contamination from another star at a distance of 1.7 arcsec. The other star has a similar proper motion and so this may be a triple system. The CV is located close to the main sequence in the HR diagram. The CRTS and ZTF light curves show multiple outbursts. This is a dwarf nova.

J0920+0042

This is V0524 Hya. The spectrum shows double peaked Balmer and helium lines. The system is located nearer to the main sequence than the white dwarf cooling sequence in the HR diagram. There appear to be small ($\Delta m < 1$) outbursts in the ZTF and CRTS light curves. The VSX period is 3.6 h. This is probably a U Gem.

J0922+3103

See [Chapter 5](#)

J0922+3307

The spectrum shows Balmer, He I and He II emission lines. The system is located midway between the main sequence and the white dwarf cooling sequence in the HR diagram. It has a known period of 1.57 h. The ZTF light curve shows both outbursts and at least one superoutburst. This is a SU UMa.

J0922+4212

The spectrum shows narrow double-peaked Balmer emission lines and absorption lines from the white dwarf. There is a hint of the donor. The system is close to the white dwarf cooling sequence in the HR diagram. There is no ZTF data and the CRTS data does not show outbursts – with one small exception that may be an artefact. This is probably a WZ Sge.

J0928+0711

The spectrum shows wide Balmer absorption lines above a blue continuum. The SED shows that this is much higher than its historical level suggesting that the spectrum (MJD = 54169) occurred during an outburst. By coincidence the SDSS photometry also appears to have occurred during an outburst (MJD = 52921). There is no *Gaia* counterpart and the system is near the white dwarf cooling sequence in the u-g/g-r diagram. There are no normal outbursts in the CRTS and ZTF light curves and a single superoutburst in the ZTF light curve. This is probably a WZ Sge.

J0929+6223

The spectrum shows broad multiple-peaked Balmer, He I, He II and Ca emission lines. There is no sign of the white dwarf or the donor. The system is located next to the main sequence in the HR diagram. The CRTS and ZTF light curves show variability but no outbursts. The ZTF light curve appears to show at least two periods although we have not been able to obtain reliable values for them. This is probably a magnetic CV.

J0932+0109

The spectrum shows strong single-peaked Balmer and weaker He I and He II emission lines as well as the Balmer jump in emission. The white dwarf and donor are not visible. The system is close to the main sequence in the HR diagram. The CRTS and ZTF light curves show variability but no outbursts. We obtained a tentative period of 2.16 h from the CRTS light curve. This is probably a polar.

J0932+1331

The spectrum shows a strong blue continuum with weak double-peaked H α emission and weak absorption for the higher Balmer lines. There is a LAMOST observation ([National Astronomical Observatories, 2019](#)) on 2014-12-17 which shows a similar continuum but much weaker H α emission and stronger absorption for the higher Balmer lines. The system is close to the white dwarf cooling sequence in the HR diagram. However the *Gaia* absolute magnitude is based on the low state and if this is adjusted for the high state then it would reach the novalike area assuming it had a very high inclination (such as Lanning 386). The CRTS light curve shows two distinct states; one at $m \cong 18$ and one at $m \cong 20$. For years it remained at the high level and after MJD = 55250 it has alternated. These two states can also be seen in the *Gaia* epoch photometry. There are no outbursts in the CRTS light curve and there is no ZTF data. The system is close to the white dwarf cooling sequence in the *Gaia* HR diagram. We find a tentative period of 4.62 h from the CRTS light curve. This would appear to be a novalike.

J0932+4725

See Chapter 5

J0934+4038

The spectrum shows double-peaked Balmer and He I emission lines as well as the Balmer jump in emission. There is a small amount of He II emission. The donor is not visible – and is at a low level in the SED. The system is located midway between the main sequence and the white dwarf cooling sequence in the HR diagram. There are multiple outbursts visible in the CRTS and ZTF light curves. This is probably an SU UMa.

J0935+1619

The spectrum shows Balmer, He I and He II double-peaked emission lines above a strong blue continuum. It has a period of 1.54 h. The ZTF light curve shows strong variability together with drop-outs as this system is eclipsing. [Hardy et al. \(2017\)](#) found “a typical polar light curve similar to that seen in HU Aqr”. The period is too short to be a novalike and the disk implied by the spectrum is inconsistent with being a polar. The system is clearly a CV but we cannot classify it further.

J0938+5344

The spectrum shows double-peaked Balmer, He I and He II emission lines. The spectrum also shows Ca and Mg absorption lines. There is no sign of the donor. Its location next to the main sequence in the HR diagram implies a G-type or possibly K-type donor which is not consistent with the existing classification of a polar – an intermediate polar would be more likely. The CRTS and ZTF light curves show variability but no outbursts. This is probably the optical counterpart to *ROSAT* 2RXS J093838.0+534415. Whilst clearly magnetic the data is not sufficient to classify this further.

J0939+0652

The spectrum shows a strong blue continuum with wide Balmer absorption lines and a synthetic magnitude of 17.9. The SED shows that it has historically been much dimmer. There is no *Gaia* counterpart. The CRTS light curve has a few points around $m \sim 22$ and the ZTF light curve is also sparse with a few points $m > 18$. This is probably a dwarf nova with the light curves only detecting outbursts; the spectrum was taken during an outburst.

J0943+5201

The spectrum shows double-peaked Balmer and He I emission lines as well as the Balmer jump in emission. There is no sign of the donor or white dwarf. The system is located midway between the main sequence and the white dwarf cooling sequence in the HR diagram. The CRTS and ZTF light curves show multiple outbursts and at least one superoutburst. This is probably an SU UMa.

J0944+0358

This is VZ Sex. The spectrum shows Balmer and helium emission lines. The CRTS and ZTF light curves show outbursts. There is no *Gaia* parallax. [Nucita et al. \(2021\)](#) used an *XMM* X-ray observation to confirm that this is an intermediate polar.

J0945+2922

The spectrum shows sharp peaked Balmer and helium emission lines. The CRTS and ZTF light curves do not show any outbursts. The system is close to the white dwarf cooling sequence in the HR diagram. [Thorstensen et al. \(2015\)](#) obtained a period of 1.53 h and concluded that it was a magnetic CV.

J0947+4524

See Chapter [5](#)

J0951+4710

The spectrum shows double-peaked Balmer and He I emission lines and absorption lines from the white dwarf are visible. The system is close to the white dwarf cooling sequence in the HR diagram. The CRTS light curve shows one observation that may be part of an outburst or an artefact. The ZTF light curve shows no outbursts. This is probably a WZ Sge.

J0951+6029

The spectrum shows double-peaked Balmer, He I, He II and Ca emission lines as well as the Balmer jump in emission. Absorption lines from the white dwarf are visible. The system is close to the white dwarf cooling sequence in the HR diagram. The CRTS and ZTF light curves do not show any outbursts. This is probably a WZ Sge.

J0958+2810

The spectrum shows single-peaked Balmer, He I, He II and Ca emission lines as well as the Balmer jump in emission. The donor is not visible. The system is located midway

between the main sequence and the white dwarf cooling sequence in the HR diagram. There are at least eight outbursts visible in the ZTF light curve. This is probably an SU UMa.

J1000+3853

The spectrum shows strong, narrow Balmer single-peaked emission lines set in absorption lines from the white dwarf. There is no sign of the donor. The system is located on the white dwarf cooling sequence in the HR diagram. There are no outbursts visible in the ZTF light curve. This is probably a WZ Sge.

J1005+6941

The spectrum shows single-peaked Balmer, He I and strong He II emission lines. The system is located near to the main sequence in the HR diagram. There is strong variability but no outbursts in the CRTS and ZTF light curves. [Thorstensen et al. \(2020\)](#) found a period of 3.64h and concluded that this is probably a polar.

J1010+0249

The spectrum shows double-peaked Balmer and He I, emission lines with no sign of the white dwarf or donor. There is no *Gaia* counterpart. There are very few points on the ZTF light curve and none on the CRTS one. The system is a long way from the white dwarf sequence in the u-g/g-r diagram. This is probably a dwarf nova.

J1013+4558

The spectrum shows Balmer and He I emission lines. The system is located midway between the main sequence and the white dwarf cooling sequence in the HR diagram. It has a period of 1.97h. The ZTF light curve shows two outbursts and one superoutburst. We conclude that this is an SU UMa.

J1014+0638

The H α emission line in the spectrum is double-peaked. The H β and higher emission lines have multiple peaks and are set in wide absorption lines from the white dwarf. There is no sign of the donor. There are also suggestions of He I and He II emission lines. The synthetic magnitude is 19.6 which is $\Delta m \cong 1.5$ dimmer than historical observations. The system is located on the white dwarf sequence in the HR diagram. The CRTS, ZTF and *TESS* light curves do not show any outbursts. We have an unpublished spectroscopically-derived period of 0.05914(7) d where there is a slight possibility that the correct period is 0.05583(7) d due to a possible cycle-count error. This is probably a WZ Sge.

J1019+3357

This is AC LMi. The spectrum shows double-peaked Balmer, He I and He II emission lines. There is no sign of the white dwarf or the donor. The system is closer to the white dwarf cooling sequence than the main sequence in the HR diagram. It has a period of 1.9 h. The CRTS light curve shows two outbursts and the ZTF shows three; one of which at MJD = 58855 appears to be a superoutburst. This is most probably an SU UMa.

J1024+4808

The spectrum shows double-peaked Balmer, He I and Ca emission lines with no sign of the donor. Absorption lines from the white dwarf are visible. The system is close to the white dwarf cooling sequence in the HR diagram. There is a superoutburst in the ZTF light curve but no other outbursts in either the CRTS or ZTF light curves. This is probably a WZ Sge.

J1025+4302

The spectrum shows double-peaked Balmer and He I emission lines with no sign of the donor or the white dwarf. The system is on the white dwarf cooling sequence in the HR diagram. There are several small ($\Delta m \cong 1$) outbursts visible in the CRTS and ZTF light curves. This is probably a WZ Sge.

J1031+0852

The spectrum shows double-peaked Balmer emission lines with no sign of the donor or the white dwarf. The system is located midway between the main sequence and the white dwarf cooling sequence in the HR diagram. There are a large number of outbursts and at least two superoutbursts in the CRTS and ZTF light curves. This is a probably an SU UMa.

J1035+0551

The spectrum shows double-peaked Balmer emission lines superimposed upon absorption lines from the white dwarf. There is no sign of the donor. The system is located on the white dwarf cooling sequence. It has a period of 82 min. The CRTS and ZTF light curves do not show any outbursts. This is probably a WZ Sge.

J1057+2759

The spectrum shows double-peaked Balmer emission lines with no sign of the donor. Absorption lines from the white dwarf are visible. The system is close to the white dwarf

cooling sequence in the HR diagram. The CRTS and ZTF light curves do not show any outbursts. We have an accurate unpublished photometric period of 0.0627919557(6) d provided by SL based on observations using ULTRACAM. This is probably a WZ Sge.

J1107+3405

The spectrum shows double-peaked Balmer, He I, He II and Ca emission lines as well as the Balmer jump in emission. The donor is not visible. The system is located next to the main sequence in the HR diagram. The CRTS and ZTF light curves show considerable short-term variability ($\Delta m \cong 1.5$) and small amplitude ($\Delta m \cong 1$) outbursts. This is probably a dwarf nova.

J1111+5712

The spectrum shows broad Balmer absorption lines on a blue continuum. The synthetic magnitude confirms that it was in outburst at the time of the observation. The system is closer to the white dwarf cooling sequence than the main sequence in the HR diagram. It has a period of 55 min. The ZTF light curve shows outbursts and superoutbursts. [Carter et al. \(2013b\)](#) confirms that this is an SU UMa with an evolved donor which explains the period being below the period minimum.

J1117+5205

The spectrum shows single-peaked Balmer, He I and Ca emission lines as well as the Balmer jump in emission. The donor is not visible. The system is located midway between the main sequence and the white dwarf cooling sequence in the HR diagram. The CRTS and ZTF show frequent outbursts of $\Delta m \cong 2.5$. This is possibly a dwarf nova.

J1120+6636

The spectrum shows double-peaked Balmer, He I and Ca emission lines as well as the Balmer jump in emission. The donor is not visible. The system is located midway between the main sequence and the white dwarf cooling sequence in the HR diagram. There are multiple outbursts including at least one superoutburst in the ZTF light curve. This is an SU UMa.

J1132+6249

The spectrum shows single-peaked Balmer, He I and He II emission lines. The system is located midway between the main sequence and the white dwarf cooling sequence in the

HR diagram. It has a period of 1.65 h. The CRTS light curve does not show any outbursts but the ZTF curve shows nine outbursts at least one of which is a superoutburst. This is therefore an SU UMa with a small inclination.

J1137+0148

This is RZ Leo – a well-studied CV that has been classified as a WZ Sge. Its period is 1.82 h which is unusually long for a WZ Sge and with $q = 0.14$ (Ishioka et al., 2001) it's donor has a relatively high mass of $\simeq 0.112 M_{\odot}$. In view of the high donor mass and long period this is more likely to be an SU UMa which has recently recommenced accretion after transiting the period gap.

J1138+0619

The spectrum shows bright single-peaked Balmer and dimmer He I emission lines. The higher Balmer lines sit in absorption lines from the white dwarf. The donor is not visible. The system is located on the white dwarf sequence. There are two possible small amplitude outbursts in the CRTS and ZTF light curves although they are single data points and may be artefacts. This is probably a WZ Sge.

J1146+6759

See Chapter 5

J1152+4914

This is BC UMa – a well-studied CV. The spectrum shows Balmer and helium emission lines. The white dwarf and donor are visible in the spectrum. This is consistent with Patterson et al. (2003) who inferred that the donor is an M-dwarf. We therefore classify this as an SU UMa rather than a WZ Sge.

J1153+3158

The spectrum shows double-peaked Balmer and He I emission lines together with the Balmer jump in emission above a red continuum. There is no sign of the donor. There is no *Gaia* counterpart. The CRTS and ZTF light curves show multiple outbursts and more than one superoutburst. This is probably an SU UMa.

J1156+6309

The spectrum shows double-peaked Balmer and He I emission lines above a red continuum. Comparison with the SDSS photometry suggests the presence of cyclotron hump(s) – and indeed the red continuum may well be a cyclotron hump. The system

is located midway between the main sequence and the white dwarf cooling sequence in the HR diagram. The CRTS and ZTF light curves show strong variability of $\Delta m < 2$ but no outbursts. We find a reliable period of 1.742 h from the ZTF light curve. The phase folded light curve shows two peaks and the period is likely to be due to cyclotron beaming. This is a polar.

J1538+5123

From the *TESS* light curve we confirmed the orbital period of 0.06466(6) d. We also obtained a period of 0.06869 d with a strong second harmonic which we attribute to the white dwarf spin. This is therefore an asynchronous polar.

J1207+2235

[Szkody et al. \(2011\)](#) identified this object as a candidate polar. The spectrum shows Balmer, He I, He II and Ca emission lines as well as the Balmer jump in emission. Comparison of the spectrum with the SDSS photometry suggests that there was a cyclotron hump when the SDSS photometry was observed. There is no sign of the donor. There is no *Gaia* counterpart. The CRTS and ZTF light curves show at least one state change and considerable variability but no outbursts. The ZTF periodogram shows a short period of 0.7026 h; the phase folded light curve shows two distinct double humps and so $P_{\text{orb}} = 1.4053(3)$ h. This is a polar.

J1216+0520

The spectrum shows double-peaked Balmer and He I emission lines superimposed upon absorption lines from the white dwarf. There is no sign of the donor. The system is located on the white dwarf cooling sequence in the HR diagram. Its period is 1.64 h. There are no outbursts in the CRTS or the ZTF light curves. There is no sign of the donor in either the spectrum or the SED. This is probably a WZ Sge and possibly a period bouncer.

J1219+2049

The spectrum shows bright single-peaked Balmer and dimmer He I emission lines. The higher Balmer lines sit in absorption lines from the white dwarf. The donor is not visible. The system is located on the white dwarf sequence. The CRTS and ZTF light curves show variability but no outbursts. This is probably a WZ Sge.

J1220+5654

This was classified as an AM CVn with a period of 0.03517863 d in the MGAB catalog (MGAB-V359). The spectrum contains Balmer emission lines that are significantly

brighter than the helium lines which is not consistent with being an AM CVn. Comparison with SDSS photometry also suggests the presence of cyclotron humps. The ZTF and CRTS light curves show strong variability $\Delta m \sim 2$ but no outbursts. Folding the ZTF light curve at 0.070356(1) h shows a twin peaked orbital period typical of cyclotron beaming. This appears to be a polar.

J1224+1841

See Chapter 5

J1232+2222

The spectrum shows double-peaked Balmer, He I, He II and Ca emission lines. There is no sign of the white dwarf or donor. The system is in the area of the HR diagram occupied by novalikes. The ZTF and CRTS light curves show variability of $\Delta m \cong 0.5$ with no outbursts. We found a reliable period of 3.0675(1) h from the ZTF light curve. This is a novalike.

J1243+0255

This is NSV 19466 and an X-ray source (1RXS J124326.5+025603). The spectrum shows narrow, single-peaked Balmer, He I, He II and Ca emission lines as well as the Balmer jump in emission. There is no sign of the white dwarf or donor. The system is located midway between the main sequence and the white dwarf cooling sequence in the HR diagram. The ZTF light curve shows two short outbursts. We obtained a period of 1.7218 h from the *TESS* light curve and 1.7214 h from the ZTF light curve. The CRTS light curve shows long term trends in amplitude of $\delta m \sim 0.5$. This is definitely a dwarf nova and most likely an SU UMa. However there are no observed superoutbursts and so it could also possibly be an intermediate polar.

J1244+5936

This is Gaia16adi. There is a double-peaked H α emission line visible in the spectrum and also other Balmer, He I and He II emission lines. There is deep central absorption suggesting that the system is eclipsing. Absorption lines from the white dwarf are also visible together with TiO from the donor. The continuum is not consistent with a spectrum dominated by the white dwarf and donor; there is a hint of cyclotron humps. The system is closer to the white dwarf cooling sequence than the main sequence in the HR diagram. The ZTF and CRTS light curves show ~ 10 outbursts with at least one superoutburst accompanied by superhumps. We obtained a reliable period of 1.74954(1) h from the ZTF light curve and a consistent period from the CRTS light curve. The phase folded light curve shows that the system is eclipsing with a hot spot

just before the eclipse. This is a dwarf nova – the visibility of the donor implies its mass is too great to be a WZ Sge.

J1250+1549

The spectrum shows hydrogen absorption lines with Zeeman splitting. The system is on the white dwarf cooling sequence in the HR diagram. It has a period of 86 min. [Breedt et al. \(2012a\)](#) found that the system is a low accretion rate magnetic binary. This is a polar approaching the period minimum.

J1255+2642

The spectrum shows Balmer emission lines above absorption lines from the white dwarf. The system is next to the white dwarf cooling sequence in the HR diagram. The CRTS light curve shows one outburst whilst the ZTF light curve does not show any. We concur with [Amantayeva et al. \(2021\)](#) that this is a WZ Sge and probably a period bouncer.

J1256–0158

The spectrum shows narrow, double-peaked Balmer and He I emission lines. The system is on the white dwarf cooling sequence in the HR diagram. The ZTF light curve is sparse; there are no outbursts visible in either the ZTF or CRTS light curves. Based on the HR position this is likely to be a WZ Sge.

J1258+6408

The spectrum shows double-peaked Balmer, He I, He II and Ca emission lines and also the Balmer jump in emission. There is no sign of the donor. The synthetic magnitude of the SED (19.2) is brighter than historical photometry suggesting that the spectrum occurred during an outburst. The system is located midway between the main sequence and the white dwarf cooling sequence in the HR diagram. There are no outbursts visible in the CRTS and ZTF light curves although both are sparse. Despite the lack of observed outbursts this is likely to be a dwarf nova.

J1258+6635

The spectrum shows double-peaked Balmer and He I emission lines with no sign of the white dwarf or donor. The system is located midway between the main sequence and the white dwarf cooling sequence in the HR diagram. It has a period of 1.43 h. The ZTF light curve shows multiple outbursts including at least one superoutburst. This is an SU UMa.

J1305+3909

(Chen et al., 2020) found a period of 0.0785972 d from ZTF data. The correct orbital period is twice this; a folded light curve clearly shows a deep eclipse and a shallower one. We therefore find $P_{\text{orb}} = 3.7727(1)$ h.

J1305+5828

The spectrum shows single-peaked Balmer, He I, He II and Ca emission lines. There is no sign of the white dwarf or donor. The system is closer to the main sequence than the white dwarf cooling sequence in the HR diagram. There are multiple outbursts in both the ZTF and CRTS light curves. This is a dwarf nova.

J1319+3158

This is ASASSN-14mr. The spectrum shows slightly double-peaked Balmer, He I, He II and Ca emission lines together with TiO absorption lines. The spectrum of a K9 or M0 star is visible. The system is close to the main sequence in the HR diagram. In addition to the ASAS-SN transient the ZTF light curve shows one outburst and the CRTS light curve shows another. We obtained a reliable period of 1.62215 h suggesting $P_{\text{orb}} = 3.24430(1)$ h. This period is quite short for a such a massive donor – the donor may be evolved. This is a U Gem.

J1327+4259

The spectrum shows Balmer, He I, He II and Ca emission lines together with the Balmer jump in emission. There is no sign of the donor. The system is located midway between the main sequence and the white dwarf cooling sequence in the HR diagram. There are two outbursts visible in the ZTF light curve. This is a dwarf nova.

J1336+3809

The spectrum shows double-peaked Balmer, He I and He II emission lines above a strong blue continuum. There is no sign of the donor. The SED shows that the spectrum was observed when the system was in outburst. The system is located midway between the main sequence and the white dwarf cooling sequence in the HR diagram. The ZTF light curve shows frequent dwarf novae. This is a dwarf nova.

J1344+2044

The spectrum shows single-peaked Balmer emission lines above a blue continuum with at least one cyclotron hump visible. The SED shows that the object has historically been brighter. There is no sign of the donor. The system is just above the top of the

white dwarf cooling sequence in the HR diagram. In line with [Thorstensen et al. \(2020\)](#) and [Littlefield et al. \(2023b\)](#) we classify this as an asynchronous polar.

J1404+1723

This is a *ROSAT* X-ray source with a positive hardness ratio of 0.4. The spectrum shows single-peaked Balmer, He I, He II and Ca emission lines with wide bases indicative of a magnetic CV. The Balmer jump is also visible in emission. The system is located midway between the main sequence and the white dwarf cooling sequence in the HR diagram. The ZTF light curve shows one outburst and [Shears \(2015\)](#) report four previous outbursts. The ZTF light curve shows a sudden drop in level at about MJD = 59000. This is probably an intermediate polar.

J1429+4145

The spectrum shows single-peaked Balmer, He I and strong He II emission lines with wide wings on a blue continuum. There is no *Gaia* counterpart. [Thorstensen et al. \(2015\)](#) found a period of 0.0685(2) d but with the possibility of an incorrect cycle count between observations. The CRTS light curve is two magnitudes brighter than the ZTF light curve indicating a state change; there are no outbursts in either light curve. ([Thorstensen et al., 2015](#)) considered the possibility that this might be an intermediate polar. They also considered that this might be a polar but were concerned that the strength of the He II emission line was insufficient. [Sahman & Dhillon \(2022\)](#) obtained a phase-resolved series of spectra one of which had central absorption in the Balmer lines which might be suggestive of an SW Sex novalike although the period would not be consistent with such a classification. We analysed the ZTF light curve which fortuitously includes some high cadence data from which we could obtain an unambiguous orbital period of 0.0637(1) d. A periodogram of the full ZTF light curve shows a strong secondary period of 0.0543 d which is likely to be the white dwarf spin period. It appears that this is a polar CV at an early stage before it is fully tidally locked.

J1432+1914

We have an unpublished photometric period of 0.1171 d provided by SL based on observations using ULTRACAM.

J1435+2336

The spectrum shows double-peaked Balmer and He I emission lines above a strong blue continuum. The spectrum shows strong Balmer absorption lines from the white dwarf but there is no sign of the donor. It appears to be eclipsing. The system is close to the white dwarf cooling sequence in the HR diagram. The CRTS light curve appears to be

consistently brighter than the ZTF light curve but this is an artefact caused by another object within $\cong 3''$. There are no outbursts in either light curve. [Pala et al. \(2017\)](#) established that this was a WZ Sge by finding the white dwarf effective temperature from *HST* observations. They found a period of 78 min. This is probably a WZ Sge.

J1450+5845

The spectrum shows narrow double-peaked Balmer, He I and Ca emission lines. The Balmer jump in emission is visible. There is no sign of the donor. There is no *Gaia* counterpart. The system is close to the white dwarf cooling sequence in the u-g/g-r diagram. There are no outbursts in the ZTF light curve. This is probably a WZ Sge.

J1501+5501

The spectrum shows double-peaked Balmer emission lines sitting in broad absorption lines from the white dwarf. The system is next to the white dwarf cooling sequence in the HR diagram. It has a period of 82 min. There are no outbursts in either the ZTF or the CRTS light curves. It has previously been classified as an SU UMa however [McAllister et al. \(2017\)](#) identified that it has a very low mass donor and is a potential period bouncer. The system is therefore most probably a WZ Sge.

J1502+3334

We have an accurate unpublished photometric period of 0.05890961(5) d provided by SL based on observations using ULTRACAM.

J1509+4650

We have an accurate unpublished photometric period of 0.068440(8) d provided by SL based on observations using ULTRACAM.

J1514+0744

The noisy spectrum shows weak, narrow, single-peaked Balmer emission lines with evidence of Zeeman splitting. The system is close to the white dwarf cooling sequence in the HR diagram. There are no outbursts in the ZTF and CRTS light curves. It has a period of 88 min. This appears to be a polar approaching the period minimum.

J1514+4549

This is PP Boo. The spectrum shows double-peaked Balmer emission lines and Balmer absorption lines from the white dwarf. There is no sign of the donor. The system is on

the white dwarf cooling sequence in the HR diagram. There are no outbursts visible in the CRTS and ZTF light curves. This is likely to be a WZ Sge.

J1519+0645

The spectrum shows single-peaked Balmer, He I , He II and Ca emission lines above a strong blue continuum. There is no sign of the donor. The system is located in the novalike area of the HR diagram. There are no outbursts in the CRTS and ZTF light curves. This is a novalike.

J1520–0009

There is a single-peaked H α emission line and higher Balmer absorption lines visible in the spectrum above a strong blue continuum. There is no sign of the donor. The system is located in the novalike area of the HR diagram. There are no outbursts in the CRTS and ZTF light curves. The ZTF light curve shows a long term gradual brightening. This is a novalike.

J1522+0803

The spectrum shows double-peaked Balmer, He I , He II and Ca emission lines along with the Balmer jump in emission. There is no sign of the donor. The system is located midway between the main sequence and the white dwarf cooling sequence in the HR diagram. There are two outbursts visible in the ZTF light curve and an additional one in *Gaia* alerts (Gaia20eoa) . Four more outbursts are visible in the ASAS-SN light curve. VSNET 24573 refers to 6 outbursts including two probable superoutbursts lasting $\cong 12$ days. [Kato et al. \(2012b\)](#) estimate $P_{\text{orb}} = 1.632$ or 1.8 h using a neural network methodology. This is an SU UMa.

J1522+3913

See Chapter 5.

J1527+5437

The spectrum shows broad double-peaked Balmer emission lines along with the Balmer jump in emission. There is no sign of the donor. The system is closer to the white dwarf cooling sequence than the main sequence in the HR diagram. There are small ($\Delta m < 1$) transients in the ZTF light curve and a larger outburst at the beginning of the CRTS light curve. We found a reliable period of 36.48 min from the ZTF light curve which does not appear to be ellipsoidal modulation and is likely to be the white dwarf spin period. Although we could not detect an orbital period this is probably an intermediate polar.

J1532+3701

There is a single-peaked $H\alpha$ emission line and higher Balmer absorption lines visible in the spectrum above a strong blue continuum. There is no sign of the donor. The system is located in the novalike area of the HR diagram. There is an *XMM* X-ray observation. There are no outbursts in either the CRTS or ZTF light curves. This is a novalike.

J1544+2553

See Chapter 5.

J1544+4648

The spectrum shows double-peaked Balmer emission lines and Balmer absorption lines from the white dwarf. There is no sign of the donor. The system is on the white dwarf cooling sequence in the HR diagram. There are no outbursts visible in the CRTS and ZTF light curves. We obtained a period of 1.354 h from the ZTF light curve; the folded light curve was double-peaked. This is likely to be a WZ Sge.

J1549+1739

See Chapter 5.

J1550+4054

The spectrum shows double-peaked Balmer, He I, He II and Ca emission lines along with the Balmer jump in emission. There is no sign of the donor. The system is located midway between the main sequence and the white dwarf cooling sequence in the HR diagram. The CRTS and ZTF light curves do not show any outbursts but the ZTF light curve does show a state change. We find two reliable periods from the ZTF light curve – 6.6647 h and 1.259 h. This is an intermediate polar.

J1553+5516

This is MQ Dra. The spectrum shows strong cyclotron humps and weak, narrow Balmer emission lines. The system is located midway between the main sequence and the white dwarf cooling sequence in the HR diagram. The ZTF light curve shows strong variability but no outbursts. It has a period of 4.4 h. [Szkody et al. \(2008\)](#) established that this was a low accretion rate polar. Given its position in the HR diagram this is likely to be a pre-polar.

J1601+0917

The spectrum shows double-peaked Balmer, He I and Ca emission lines along with the Balmer jump in emission. There are also TiO lines from the donor.

The system is located midway between the main sequence and the white dwarf cooling sequence in the HR diagram. There are no outbursts in either the CRTS or the ZTF light curves. Nevertheless this is probably a dwarf nova.

J1602+1617

Balmer emission lines can be discerned in the noisy spectrum. There is no *Gaia* counterpart. Four outbursts are visible in the ZTF light curve. This is a dwarf nova.

J1604+1615

The spectrum shows double-peaked Balmer, He I, He II and Ca emission lines along with the Balmer jump in emission. There is no sign of the donor. The system is located midway between the main sequence and the white dwarf cooling sequence in the HR diagram. The CRTS and ZTF light curves show outbursts and two superoutbursts. This is an SU UMa.

J1604+4143

The spectrum shows single-peaked Balmer emission lines above a strong blue continuum. There is no sign of the white dwarf or the donor. The system is located in the novalike area of the HR diagram. There are no outbursts in the CRTS and ZTF light curves. The ZTF light curve shows a drop of $\delta m \cong 3$ lasting about a year. This is a VY Scl sub-type of novalike as suggested in VSNET 8567.

J1609+0550

The spectrum shows single-peaked Balmer emission lines above a blue continuum. There is no sign of the white dwarf or the donor. The system is located in the novalike area of the HR diagram. The CRTS and ZTF light curves do not show any outbursts. Both curves show short-term drop-outs of $\Delta m \sim 2$. This is a novalike.

J1610+2221

The spectrum shows Balmer absorption lines with embedded emission lines in H α and H β above a strong blue continuum. There is no sign of the white dwarf or the donor. The system is located in the novalike area of the HR diagram. There are no outbursts in the CRTS and ZTF light curves. This is a novalike.

J1610+4459

There are three spectra all showing strong slightly double-peaked Balmer emission lines with the higher Balmer lines sitting in absorption troughs from the white dwarf. There is no sign of the donor. The system is very close to the white dwarf cooling sequence in the HR diagram. There are no outbursts in the CRTS and ZTF light curves. This is probably a WZ Sge.

J1613–0003

The spectrum shows double-peaked Balmer and He I emission lines. There is no sign of the white dwarf whilst the donor is apparent at the red end. The system is located on the edge of the main sequence in the HR diagram. The CRTS and ZTF light curves both show frequent outbursts of $\Delta m \cong 2.5$. This is probably a U Gem with an early M-dwarf donor.

J1622+3411

The spectrum shows very narrow double-peaked Balmer He I, and He II emission lines which implies a low inclination system. The system is midway between the main sequence and the white dwarf cooling sequence in the HR diagram. The CRTS light curve shows outbursts and at least one superoutburst. VSNET 22433 found a superhump-derived period of 0.066(2) d. We have a spectroscopically derived period of 0.0650(1) d.

J1622+3604

The spectrum shows double-peaked Balmer emission lines with the higher Balmer lines sitting in absorption troughs from the white dwarf. There is no sign of the donor. The system is closer to the white dwarf cooling sequence than the main sequence in the HR diagram. There are two outbursts visible in the sparse ZTF data. VSNET 25759 identified this as a SU UMa and found a superhump-derived period of 0.0601(8) d. As the white dwarf is visible in the spectrum this is probably a WZ Sge.

J1624+4518

The spectrum shows slightly double-peaked Balmer, He I, He II and Ca emission lines as well as the Balmer jump in emission. There is no *Gaia* parallax. The system is just above the white dwarf cooling sequence in the u-g/g-r diagram. The CRTS and ZTF light curves show considerable variability but do not show any outbursts. The ZTF light curve shows eclipses and we obtained a period of 2.293 h from it. The double-peaked lines imply the presence of a quiescent disc however the lack of outbursts, coupled with a period in the period gap suggests that this may be a novalike. The classification is

therefore too uncertain to conclude anything more than that the system is definitely a CV.

J1625+3642

The spectrum shows double-peaked Balmer emission lines and the Balmer jump in emission. There is no sign of the donor. The synthetic magnitude (21.6) is not consistent with the *Gaia* magnitude (16.87) and we suspect that this is because *Gaia* only detected outbursts; the *Gaia* magnitude is based on `phot_g_n_obs` = 35. There is no *Gaia* parallax. The sparse ZTF light curve shows two superoutbursts and two possible outbursts. This is probably an SU UMa.

J1626+3328

The spectrum shows single peaked Balmer emission lines above a blue continuum. The Balmer jump is also visible in emission. The He II emission line has a greater equivalent width than $H\beta$. The system is located midway between the main sequence and the white dwarf cooling sequence in the HR diagram. The CRTS and ZTF light curves do not show any outbursts. We were unable to obtain any periods from the ZTF light curve which shows considerable variability. [Thorstensen & Skinner \(2012\)](#) classified this as a novalike whilst subsequently [Barrett et al. \(2017\)](#) classified this as a polar based on finding circular polarisation in radio observations. The radio observations were taken in the k-band (21.1GHz) which would imply a small ($\sim 10KG$) magnetic field. [Szkody et al. \(2018\)](#) obtained a new spectrum which showed a weaker (by a factor of 5) continuum and greatly reduced He II emission which they interpreted as a polar entering a lower state. This is all consistent with the existing classification of a polar.

J1628+2402

The spectrum shows double-peaked Balmer and He I emission lines and the Balmer jump in emission. There is no sign of the donor. The system is closer to the white dwarf cooling sequence than the main sequence in the HR diagram. The CRTS and ZTF light curves show outbursts and superoutbursts. This confirms the VSNET 13491 classification as an SU UMa.

J1635+1124

This is V0849 Her. The spectrum shows a weak $H\alpha$ emission line and remaining Balmer absorption lines above a strong blue continuum. The system is in the novalike area of the HR diagram. The ZTF light curve shows a Z Cam profile with classic outbursts in the range $MJD = 59350 - 59500$. We conclude that this is a Z Cam.

J1636+4652

The spectrum shows single-peaked Balmer, He I, He II and Ca emission lines above a strong blue continuum. The Balmer jump in emission is also visible. There is no sign of the donor. The system is in the novalike area of the HR diagram. The ZTF light curve shows very frequent outbursts and also a "standstill". Although there is a *TESS* light curve we were unable to recover a reliable period. This appears to be a Z Cam sub-type of novalike.

J1646+1808

The noisy spectrum shows Balmer lines in emission. There is no *Gaia* counterpart. There are only 10 points on the ZTF light curve but one appears to show an outburst. [Drake et al. \(2014b\)](#) report an outburst of $m = 17.7$. This is a dwarf nova but in the absence of other data this cannot be classified further.

J1652+3339

The spectrum shows double-peaked Balmer and He I emission lines along with the Balmer jump in emission. There is no sign of the donor. The system is located midway between the main sequence and the white dwarf cooling sequence in the HR diagram. There are frequent outbursts and superoutbursts in both the CRTS and ZTF light curves. This is a SU UMa.

J1658+1847

The Spectrum shows double-peaked Balmer and helium lines. The white dwarf and the donor are not visible. The system is located close to the white dwarf cooling sequence in the HR diagram. It has a period of 1.63 h. The CRTS and ZTF light curves both show unusually shaped "outbursts" with a long rise time (months). This can only be classified as a CV without more data.

J1659+1927

The spectrum shows Balmer and helium double-peaked emission lines above a blue continuum. The SED does not show any sign that there have been any lower states. The system is in the novalike area of the HR diagram. [Thorstensen et al. \(2015\)](#) found a period of 3.38 h. The ZTF light curve shows a temporary drop of $\delta m \simeq 1.5$ for around six months. This is a novalike and probably a VY Scl.

J1702+2235

This is V1240 Her. The spectrum shows weak Balmer emission lines with the higher ones in absorption troughs above a strong blue continuum. The system is in the novalike area of the HR diagram. The ZTF light curve shows variability but no outbursts and a long term drop in luminosity. We obtained a period of 1.64625(35) h from the *TESS* light curve and 1.646296(22) h from the ZTF light curve. These are consistent with the period found by [Szkody et al. \(2006\)](#). This is an unusually short period for a novalike but nevertheless that is the most likely classification.

J1703+3209

The spectrum shows single-peaked Balmer, He I, He II and Ca emission lines as well as the Balmer jump in emission. There is no sign of the donor. The system is close to the main sequence in the HR diagram. The CRTS and ZTF light curves show multiple outbursts. We have an unpublished spectroscopic period of 0.261(1) d; the error is difficult to determine as the period comes from two runs 13 years apart. This is a U Gem with a late k-type donor.

J1705+3132

The spectrum shows single-peaked Balmer, He I, He II and Ca emission lines as well as the Balmer jump in emission. TiO absorption lines from the donor are also visible. The system is close to the main sequence in the HR diagram. The CRTS and ZTF light curves both show outbursts. The system is eclipsing and we obtained a period of 2.225 h from the ZTF light curve implying $P_{\text{orb}} = 4.450(1)$ h. This is a dwarf nova with a M-dwarf donor.

J1711+3013

This is V1247 Her. The spectrum shows double-peaked Balmer emission lines above absorption lines from the white dwarf. The system is next to the white dwarf cooling sequence in the HR diagram. The CRTS and ZTF light curves do not show any outbursts. It has a period of 79 min. This is probably a WZ Sge.

J1712+3218

See Chapter 5.

J1712+6046

The spectrum shows single-peaked Balmer and helium lines above the spectrum of the donor. The white dwarf is not visible. The system is located close to the main sequence.

The ZTF light curve does not show any outbursts. [Chen et al. \(2020\)](#) obtained a period of 0.0815989 d however this is probably due to ellipsoidal modulation resulting in an orbital period of 0.1631978 d which would be consistent with a U Gem.

J1723+3304

The noisy spectrum shows narrow double-peaked Balmer lines with absorption lines from the white dwarf. The SED is contaminated with a red object at 2" distance. There is no *Gaia* counterpart. There is no CRTS light curve and only a sparse ZTF one. The original discovery (ASASSN-14gz) detected an outburst with apparent magnitude of $m = 14.2$. Given the quiescent magnitude of $m \simeq 22$ this appears to be a WZ Sge as suggested in ATEL 6455.

J1726+5432

See Chapter 5.

J2047+0000

The spectrum shows narrow double-peaked Balmer, He I, He II and Ca emission lines as well as the Balmer jump in emission. There is no sign of the donor. The system is located midway between the main sequence and the white dwarf cooling sequence in the HR diagram. The ZTF light curve shows frequent outbursts. This is a dwarf nova.

J2048–0610

The spectrum shows double-peaked Balmer and helium emission lines above absorption lines from the white dwarf. The system is closer to the white dwarf cooling sequence than the main sequence in the HR diagram. Both the ZTF and CRTS light curves show outbursts of $\Delta m > 5$. It has a period of 86 min. This is probably a WZ Sge.

J2101+1052

The spectrum shows single peaked slightly asymmetric Balmer and He I lines. There is also a He II emission line. There is no sign of the white dwarf or the donor. The SED indicates that the spectrum was taken when it was in a high state. The system is between the main sequence and the white dwarf cooling sequence in the HR diagram. The sparse ZTF light curve shows variability. There is an *XMM* X-ray detection. [Homer et al. \(2006b\)](#) did not see variability in the X-ray and so concluded that the system is not magnetic and that it is an SW Sex. However An SW Sex classifications is not consistent with the HR diagram. We classify the system as a magnetic CV based on the shape of the emission lines.

J2059–0612

The spectrum shows double-peaked Balmer and helium lines. There is no sign of the white dwarf or donor. It lies halfway between the white dwarf cooling sequence and the main sequence in the HR diagram. The period is 1.78 h. The ZTF light curve shows superoutbursts and so this is an SU UMa.

J2119+0332

See Chapter 5.

J2131–0039

This is QZ Aqr. The spectrum shows double-peaked Balmer emission lines and the Balmer jump in emission. There is no sign of the donor in either the spectrum or the SED. There is no *Gaia* counterpart. The ZTF light curve is very sparse and there is no CRTS data. VSNET 10830 identified a superoutburst and obtained a period of 0.0696(2) d. The AAVSO light curve does not reveal any subsequent outbursts. This is probably a WZ Sge and if the period is correct it could be a period bouncer.

J2135–0041

This is erroneously recorded in VSX as ASASSN-16eo; it should be ASASSN-16ep. The spectrum shows double-peaked Balmer emission lines and the Balmer jump in emission. There is no sign of the donor. There is a *GALEX* detection but no *Gaia* counterpart. The system is above the white dwarf cooling sequence in the u-g/g-r diagram. There is no CRTS or ZTF data. ASASSN recorded an outburst of magnitude $m = 15.6$ on 2016-04-15. This is probably a dwarf nova.

J2141+0507

The spectrum shows double-peaked Balmer emission lines above absorption lines from the white dwarf. The system is located on the white dwarf cooling sequence in the HR diagram. The CRTS light curves show no outbursts but do show evidence of eclipsing. We have an unpublished photometric period of 0.05467(3) d provided by SL based on observations using ULTRACAM. This is probably a WZ Sge.

J2210+1854

The spectrum shows single-peaked Balmer, He I, He II and Ca emission lines as well as the Balmer jump in emission. There is no sign of the donor. The system is closer to the main sequence than the white dwarf cooling sequence in the HR diagram. There

are three outbursts visible in the CRTS light curve. We obtained an ellipsoidal orbital period of 4.0985(1) h from the CRTS light curve. This is a U Gem.

J2211+3028

The spectrum shows $H\alpha$ in emission and the other Balmer lines in absorption. The Balmer jump is visible in emission. There is no sign of the donor. There is no *Gaia* counterpart. The system is on the white dwarf cooling sequence in the u-g/g-r diagram. There is one possible outburst amongst the sparse ZTF data. This is probably a WZ Sge.

J2215–0032

The spectrum shows double-peaked $H\alpha$ in emission and the other Balmer lines in absorption. The Balmer jump is visible in emission. There is no sign of the donor. There is no *Gaia* counterpart. The system is on the white dwarf cooling sequence in the u-g/g-r diagram. There are multiple outbursts and at least one superoutburst in the ZTF light curve. This is probably an SU UMa.

J2223+0745

This is the X-ray source *ROSAT* 1RXS J222335.6+074515. The spectrum shows double-peaked Balmer, He I, He II and Ca emission lines as well as the Balmer jump in emission. There is no sign of the donor. The system is located midway between the main sequence and the white dwarf cooling sequence in the HR diagram. The CRTS light curve shows no outbursts. The ZTF light curve shows a probable outburst – a single datapoint in the g-band on MJD = 58348 of $\Delta m \cong 0.75$. The light curve also shows a long term drift towards a brighter magnitude. [Denisenko & Sokolovsky \(2011\)](#) recorded two outbursts. This is probably an SU UMa.

J2232+1850

The spectrum shows double-peaked Balmer and He I emission lines as well as the Balmer jump in emission. There is no sign of the donor. The system is closer to the white dwarf cooling sequence than the main sequence. There are multiple outbursts in the CRTS and ZTF light curves. This is a dwarf nova.

J2232+1403

The spectrum shows double-peaked Balmer and He I emission lines as well as the Balmer jump in emission. These lines are set on top of a continuum with both a blue and red excess. The spectrum is noisy but absorption lines from the donor are visible. There is no *Gaia* counterpart. The system is positioned above the white dwarf cooling sequence

in the u-g/g-r diagram. There is one outburst ($\Delta m \sim 5$) in the ZTF light curve. This is a dwarf nova.

J2239+2503

The spectrum shows double-peaked Balmer, He I, He II and Ca emission lines as well as the Balmer jump in emission. There is no sign of the donor. The system is located midway between the main sequence and the white dwarf cooling sequence in the HR diagram. There are multiple outbursts visible in the CRTS and ZTF light curves; the system is also eclipsing. We obtained a reliable period of 1.82674(1) h from the ZTF light curve. Despite the lack of observed superoutbursts this is an SU UMa.

J2243+2214

The spectrum shows weak single-peaked Balmer and He II emission lines above a strong blue continuum. The system is in the novalike area of the HR diagram. There are no outbursts visible in the CRTS and ZTF light curves although there is one anomalous data point in the ZTF light curve; this point has a magnitude of $m = 15.9$ but the previous point is only 76 minutes earlier at the prevailing magnitude of $m = 17.5$. We obtained a tentative period of 4.487(1) h from the ZTF light curve. This is a novalike.

J2254+0742

The spectrum shows narrow, slightly double-peaked, Balmer, He I, He II and Ca emission lines as well as the Balmer jump in emission. The donor is not visible. The system is closer to the white dwarf cooling sequence than the main sequence in the HR diagram. There are no outbursts in either the CRTS or ZTF light curves but the CRTS light curve shows two cases of large ($\Delta m \sim 2$) changes over a period of $\cong 1$ yr. We found a period of 34.67 h from the ZTF light curve which is anomalous. Without further data we can only classify this as a CV.

J2306+2440

The spectrum shows strong, narrow Balmer, helium and calcium emission lines. The donor is visible and appears to be an early m-star. The object is close to the main sequence in the HR diagram. An orbital period of 0.2911640 d derived from ZTF photometry was reported in (Chen et al., 2020) who classified J2306+2440 as a contact binary. The CRTS and ZTF light curves show variability but no outbursts. The blue continuum in the spectrum is not consistent with being a contact binary. The emission lines are also unlikely to be due to reflected light off the donor due to the long orbital period (and hence separation) of the system. This is probably a CV but further classification is not possible without more data.

J2308+2543

The spectrum shows narrow, slightly double-peaked, Balmer, He I, He II and Ca emission lines as well as the Balmer jump in emission. The donor is not visible. The system is located midway between the main sequence and the white dwarf cooling sequence in the HR diagram. The CRTS and ZTF light curves show multiple outbursts. *Gaia* alert Gaia21dij shows two other outbursts. This is likely to be a SU UMa.

J2311+0130

The flux calibration of this spectrum failed. However slightly double-peaked, Balmer and He I emission lines are detected in the spectrum as well as the Balmer jump in emission. There is no *Gaia* counterpart. The system is located on the white dwarf cooling sequence in the u-g/g-r diagram. There is a superoutburst with re-brightening visible in the ZTF light curve and there is an outburst in the CRTS light curve. The first recorded outburst $\Delta m \simeq (6.2)$ was VSNET-OUTBURST-8239 on 2007-11-02. [Shugarov & Malashevich \(2021\)](#) observed the ZTF outburst on 2021-09-08 and found a superhump period of 0.05161(20) d. This is a WZ Sge.

J2315+2710

The spectrum shows slightly double-peaked Balmer, He I and Ca emission lines. There are strong absorption lines from an early m-dwarf and also an absorption line from the white dwarf around $H\beta$. The system is positioned next to the main sequence in the HR diagram. There are multiple outbursts visible in the CRTS and ZTF light curves and at least one superoutburst. As both the donor and the white dwarf are visible the mass transfer rate is low – possibly it may have just passed the period gap and recommenced accretion. This is an SU UMa.

J2316+0116

The spectrum shows single-peaked Balmer, He I, He II and Ca emission lines above a blue continuum. The Balmer jump in emission is also visible. There is no sign of the donor. The system is in the novalike area of the HR diagram. There are frequent outbursts and also a ‘standstill’ visible in the ZTF light curve. The CRTS light curve also shows a sustained (~ 1 yr) $\Delta m = 5$ drop-out. We obtained a tentative period of 3.49(1) h from the *TESS* light curve. This is a VY Scl novalike.

J2326+2826

This has an X-ray observation – 3XMM J232619.3+282649. The spectrum shows double-peaked Balmer, He I, He II and Ca emission lines. The Balmer jump in emission

is also visible. There is no sign of the donor. The system is located midway between the main sequence and the white dwarf cooling sequence in the HR diagram. There are frequent outbursts and superoutbursts in both the CRTS and ZTF light curves. We find a tentative period of 1.6300(1) h in the ZTF light curve. This is an SU UMa.

J2344+0021

This has an X-ray observation – 3XMM J234401.8+002116. The spectrum shows double-peaked Balmer emission lines and absorption lines from the donor. There is no *Gaia* counterpart. The system is located above the white dwarf cooling sequence in the u-g/g-r diagram. There are multiple outbursts in both the CRTS and ZTF light curves and at least one superoutburst. This is a SU UMa.

J2344–0012

This has an X-ray observation – 2SXPS J234440.4–001207. The spectrum shows single-peaked Balmer, He I , He II and Ca emission lines. The Balmer jump in emission is also visible. There is no sign of the donor. The system is located midway between the main sequence and the white dwarf cooling sequence in the HR diagram. There is one outburst ($\Delta m > 6$) in the CRTS light curve; there are no other outbursts in either the CRTS or ZTF light curves. The SDSS spectrum was observed on MJD = 55449, six days after CRTS recorded the outburst on MJD = 55443; the spectrum therefore occurred during the decline of the outburst when the synthetic magnitude (17.8) was between the outburst ($m = 14.2$) and quiescence ($m = 20.0$). It has a period of 109 min. This is an SU UMa.

J2345+3429

This has an X-ray observation – 2RXS J234502.2+342927. The spectrum shows single-peaked Balmer, He I , He II and Ca emission lines. The Balmer jump in emission is also visible. There is no sign of the donor. The system is located midway between the main sequence and the white dwarf cooling sequence in the HR diagram. There are at least four state changes in the ZTF light curve but no outbursts. There is also evidence of two amplitude levels in the CRTS light curve. We find a period of 3.121(1) h in the ZTF light curve. From the strength of the He II line and the absence of outbursts we conclude that this is a polar.

J2348+1812

The spectrum shows single-peaked Balmer, He I , He II and Ca emission lines. The Balmer jump in emission is also visible. There is no sign of the donor. The system is located midway between the main sequence and the white dwarf cooling sequence in the

HR diagram. There are frequent outbursts in the CRTS and ZTF light curves. This is a dwarf nova.

B.4 Spectra and light curves

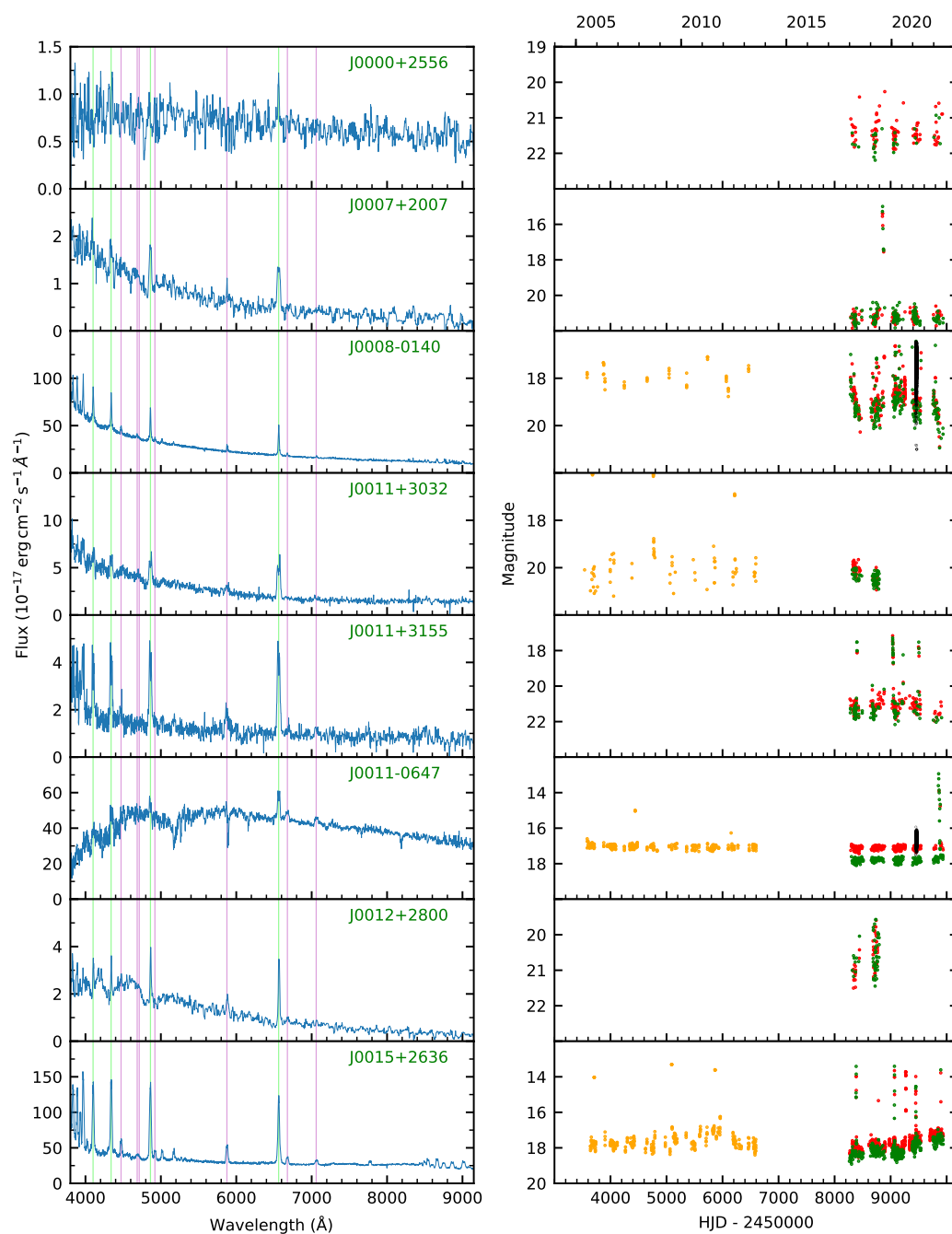


Figure B.1: Left panels: Spectra with H lines shown in green and He in pink. Right panels: Light curves with CRTS shown in orange, ZTF in red and green and *TESS* in black.

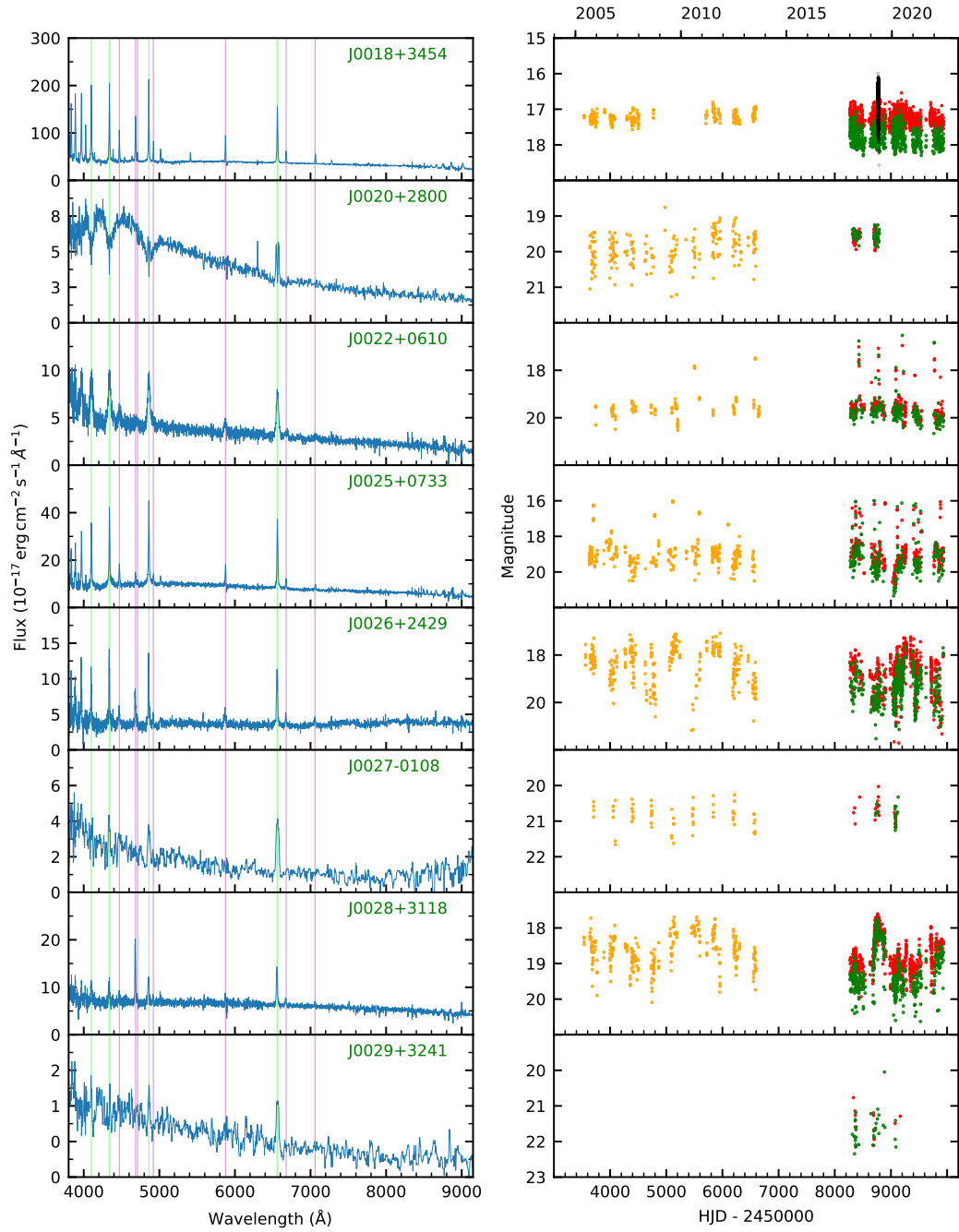


Figure B.2: Left panels: Spectra with H lines shown in green and He in pink. Right panels: Light curves with CRTS shown in orange, ZTF in red and green and *TESS* in black.

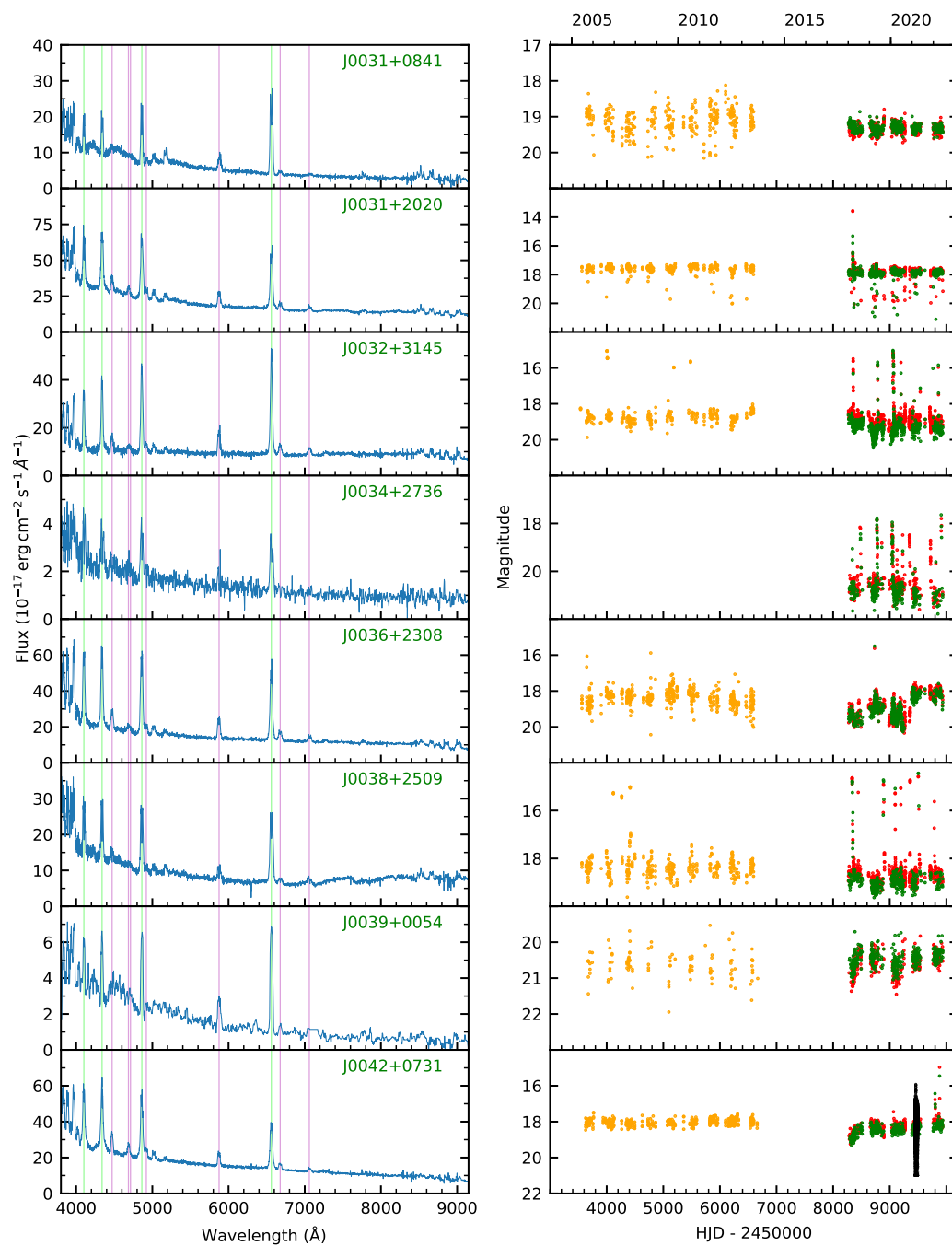


Figure B.3: Left panels: Spectra with H lines shown in green and He in pink. Right panels: Light curves with CRTS shown in orange, ZTF in red and green and *TESS* in black.

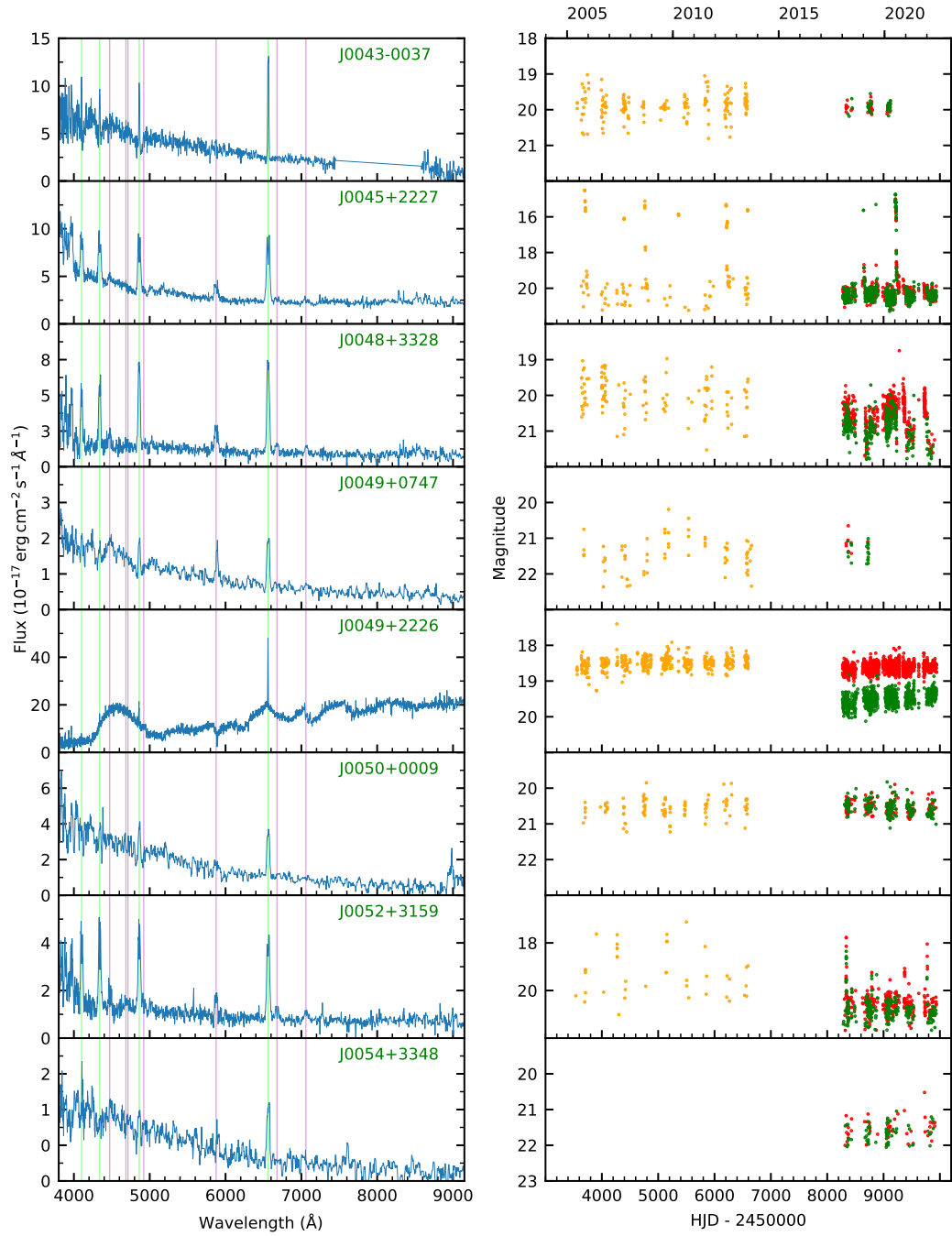


Figure B.4: Left panels: Spectra with H lines shown in green and He in pink. Right panels: Light curves with CRTS shown in orange, ZTF in red and green and *TESS* in black.

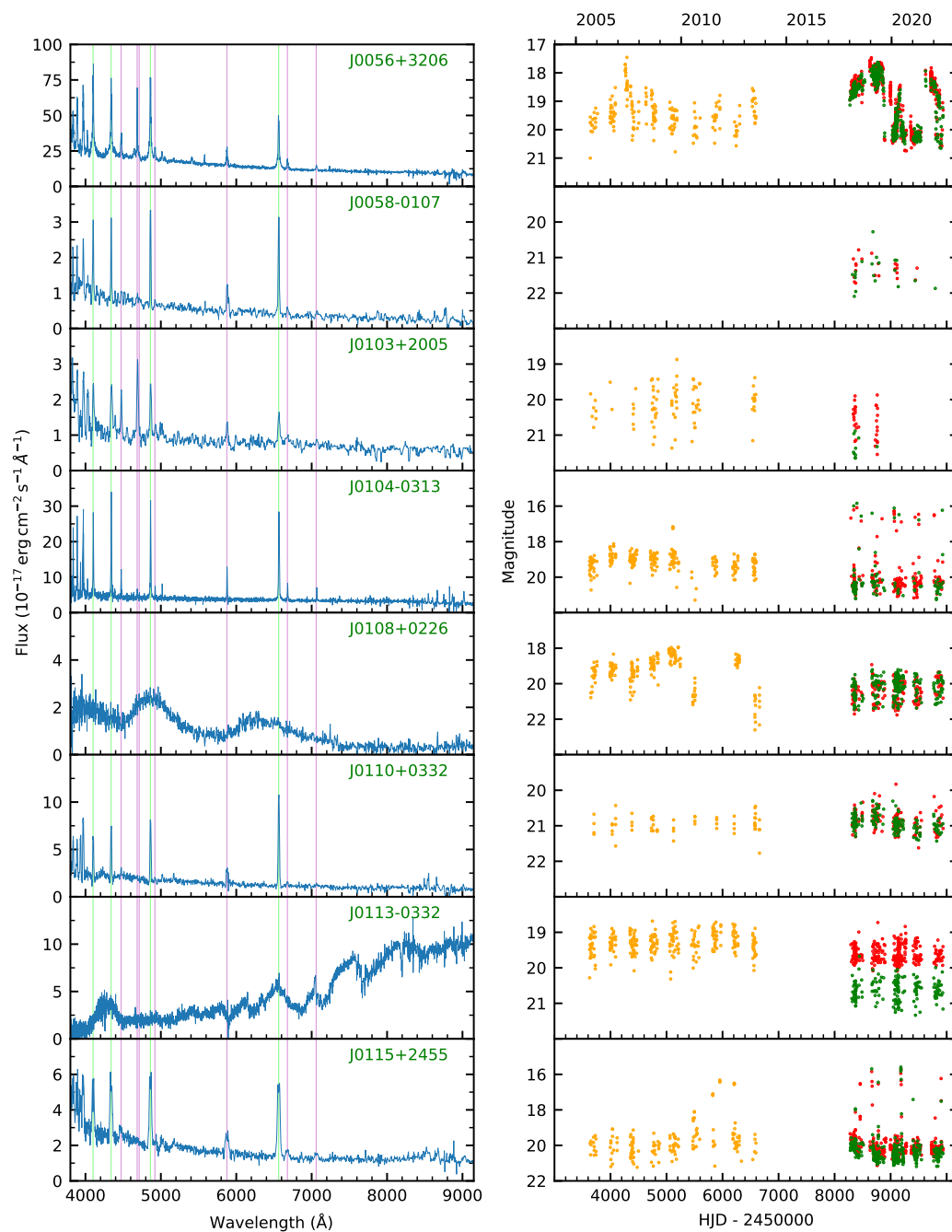


Figure B.5: Left panels: Spectra with H lines shown in green and He in pink. Right panels: Light curves with CRTS shown in orange, ZTF in red and green and *TESS* in black.

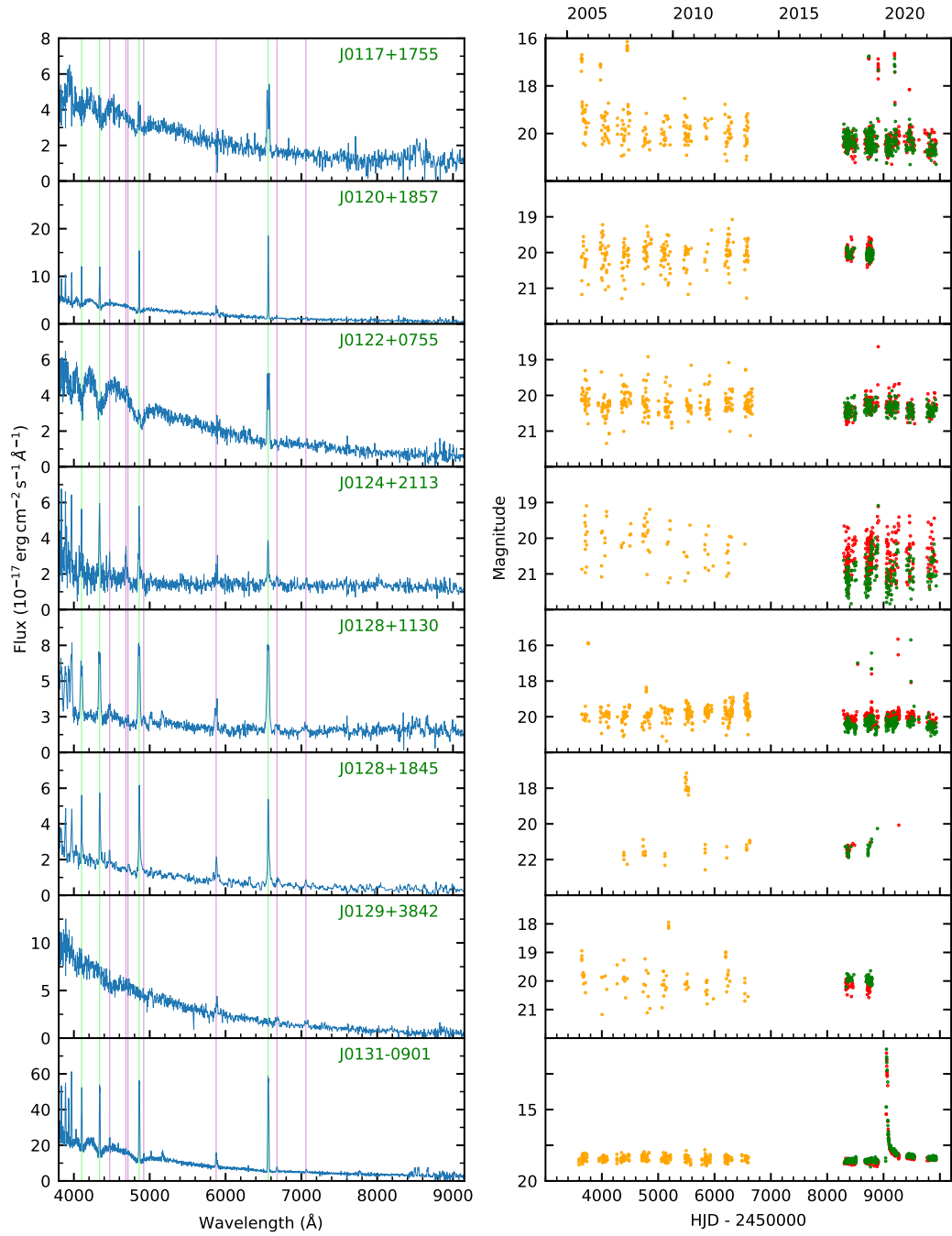


Figure B.6: Left panels: Spectra with H lines shown in green and He in pink. Right panels: Light curves with CRTS shown in orange, ZTF in red and green and *TESS* in black.

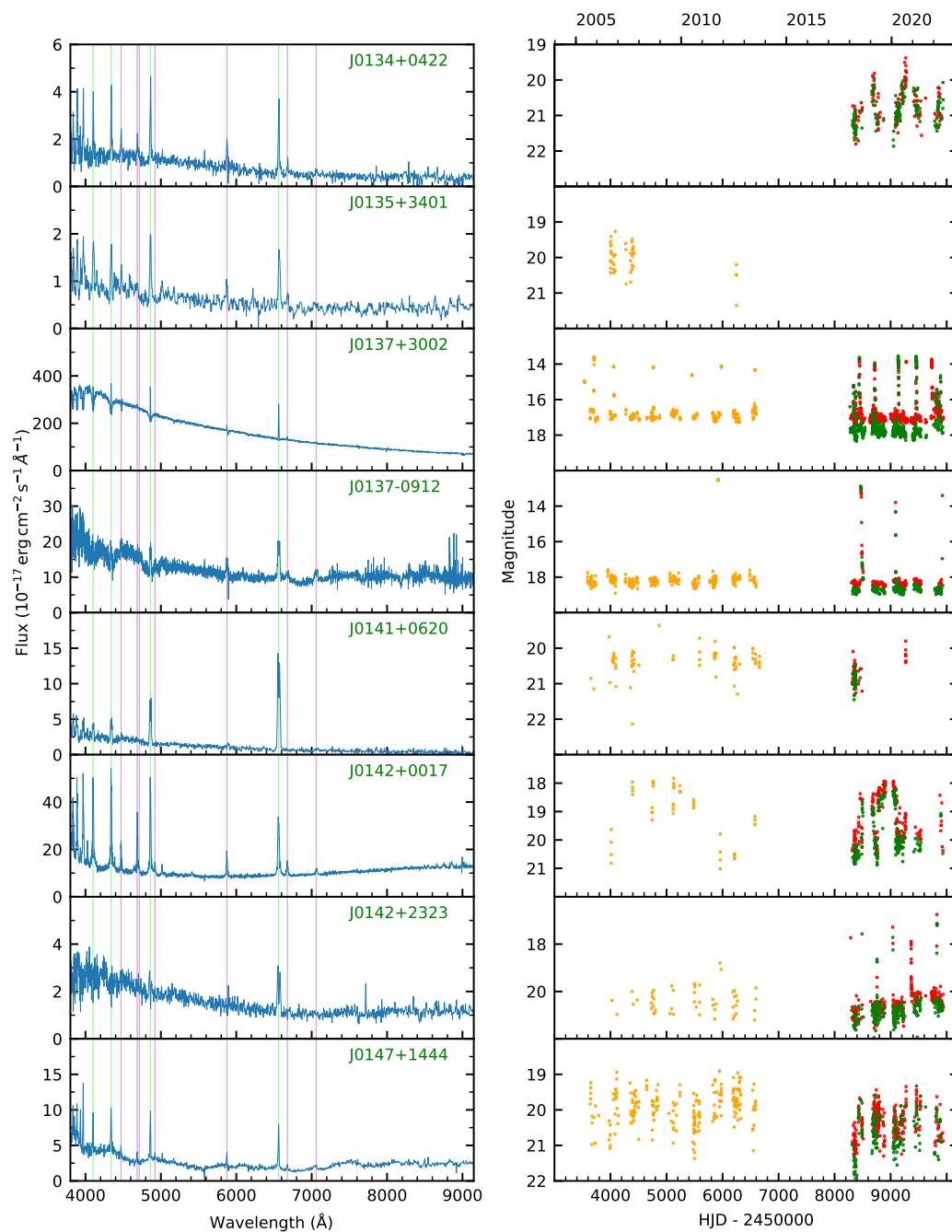


Figure B.7: Left panels: Spectra with H lines shown in green and He in pink. Right panels: Light curves with CRTS shown in orange, ZTF in red and green and *TESS* in black.

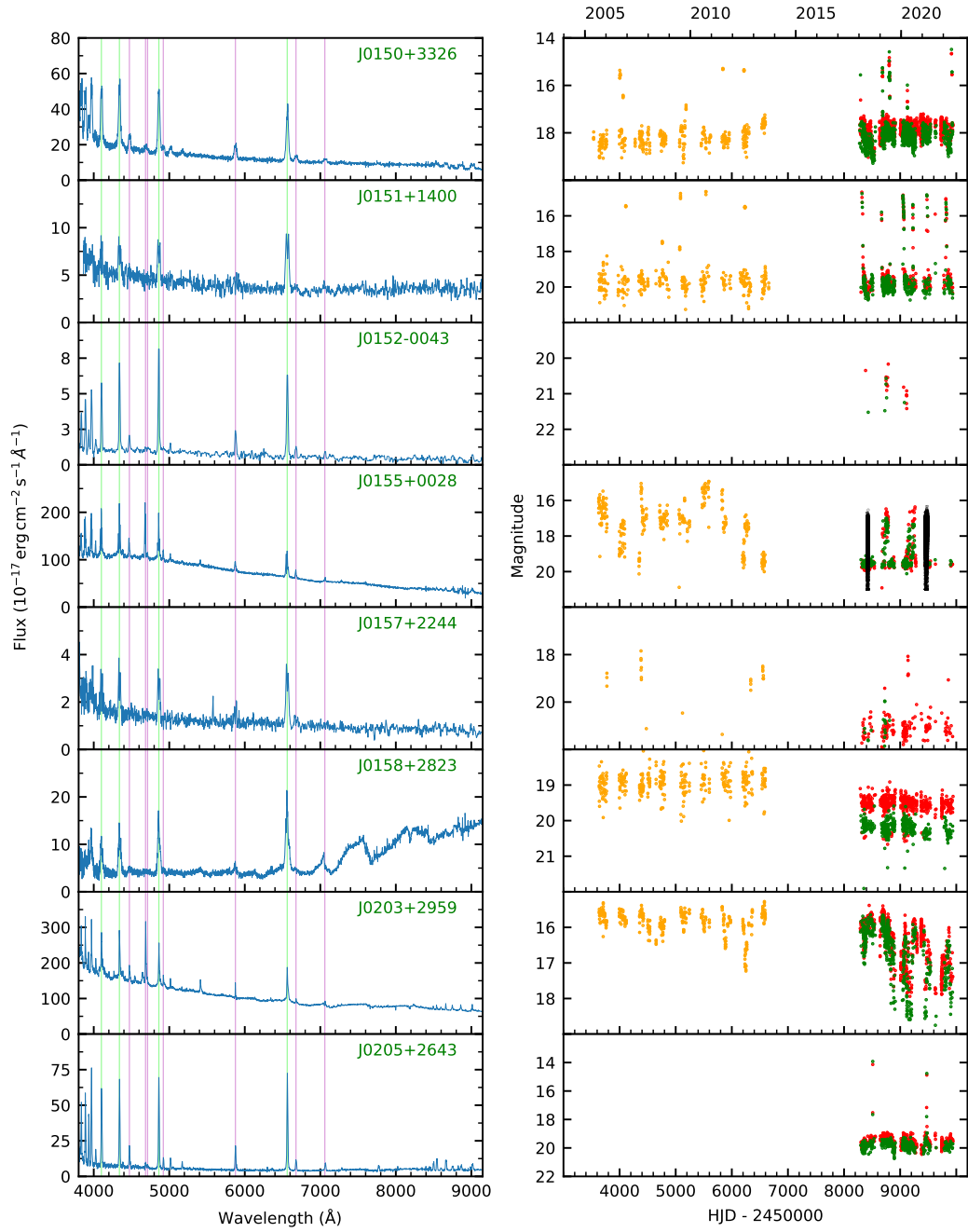


Figure B.8: Left panels: Spectra with H lines shown in green and He in pink. Right panels: Light curves with CRTS shown in orange, ZTF in red and green and *TESS* in black.

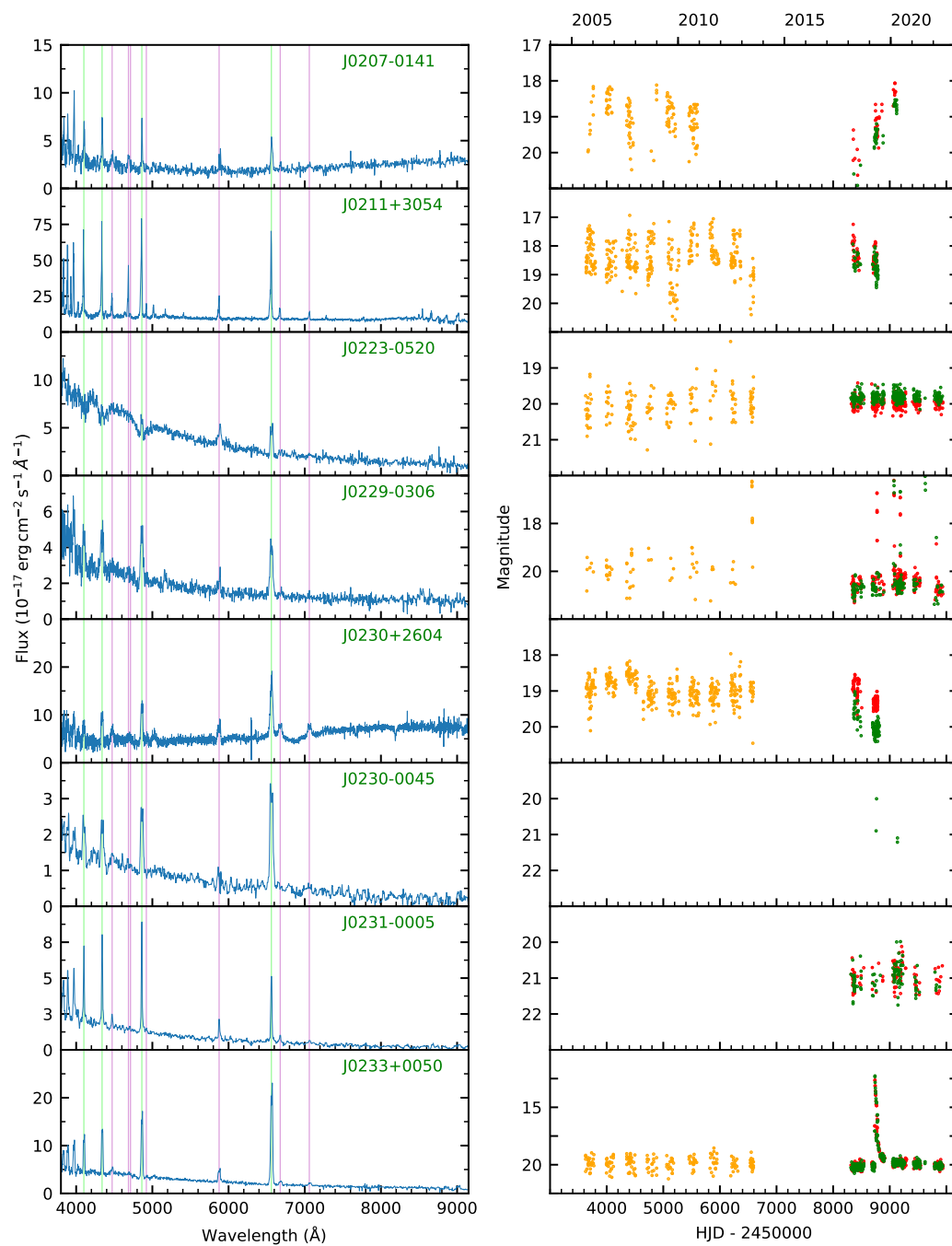


Figure B.9: Left panels: Spectra with H lines shown in green and He in pink. Right panels: Light curves with CRTS shown in orange, ZTF in red and green and *TESS* in black.

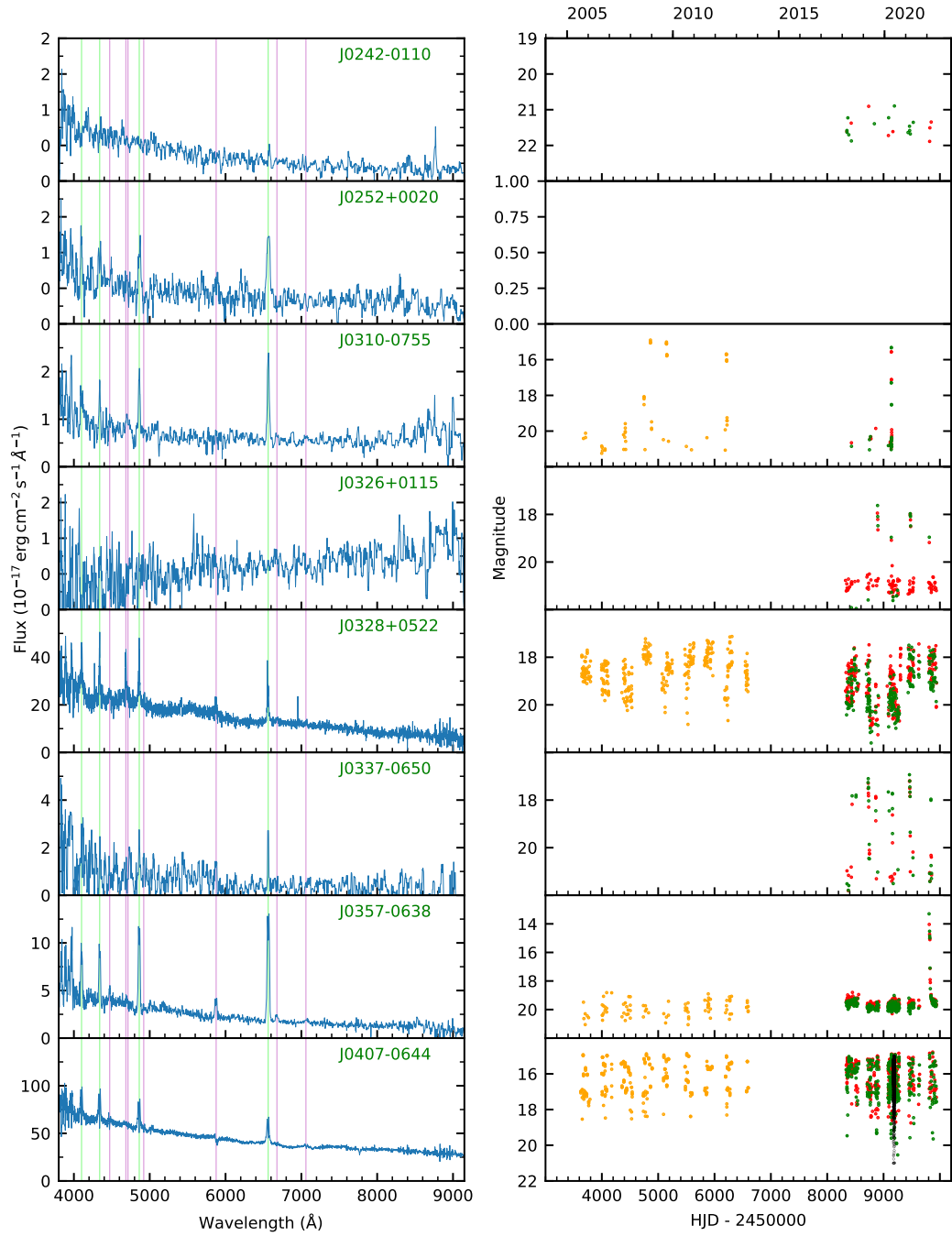


Figure B.10: Left panels: Spectra with H lines shown in green and He in pink. Right panels: Light curves with CRTS shown in orange, ZTF in red and green and *TESS* in black.

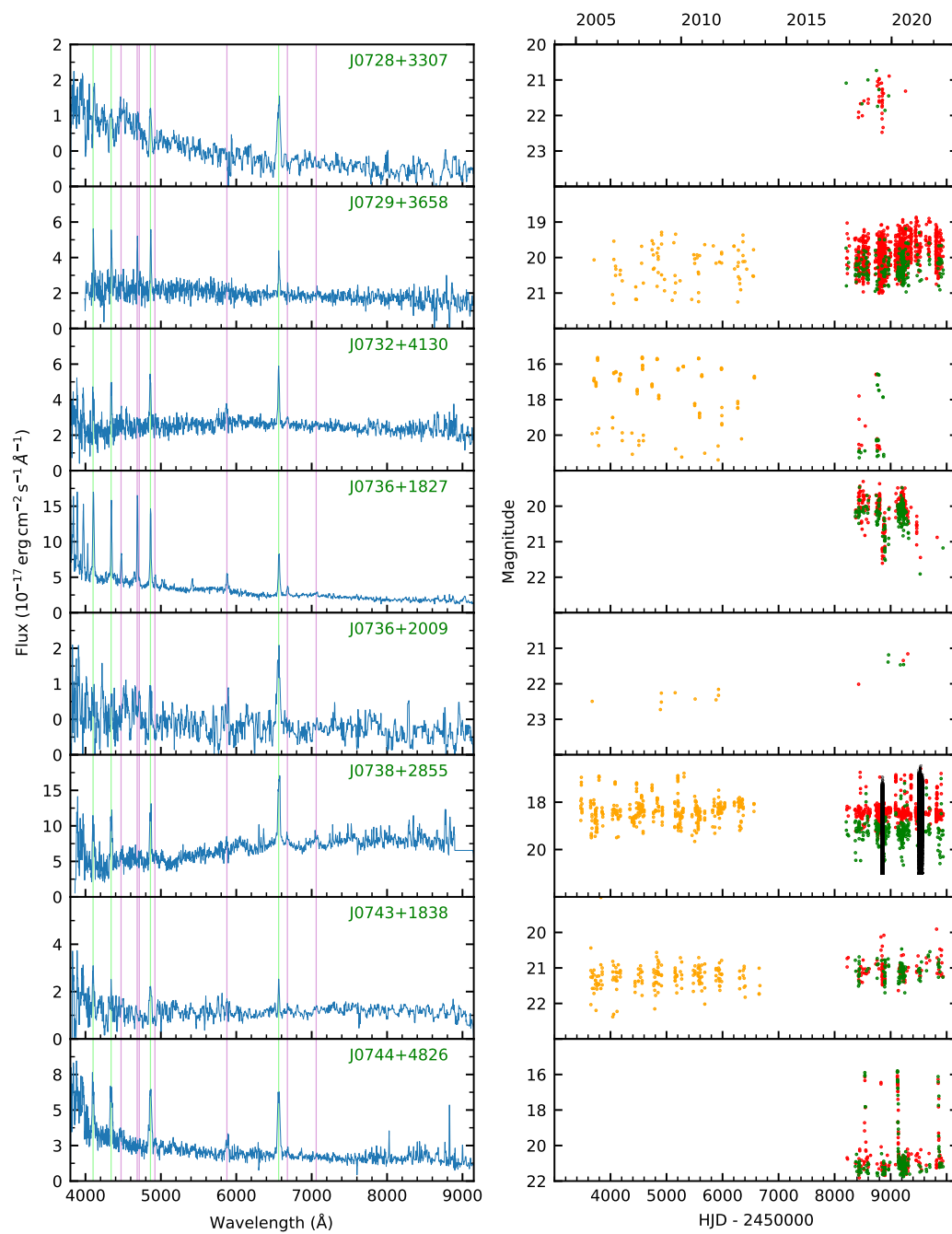


Figure B.11: Left panels: Spectra with H lines shown in green and He in pink. Right panels: Light curves with CRTS shown in orange, ZTF in red and green and *TESS* in black.

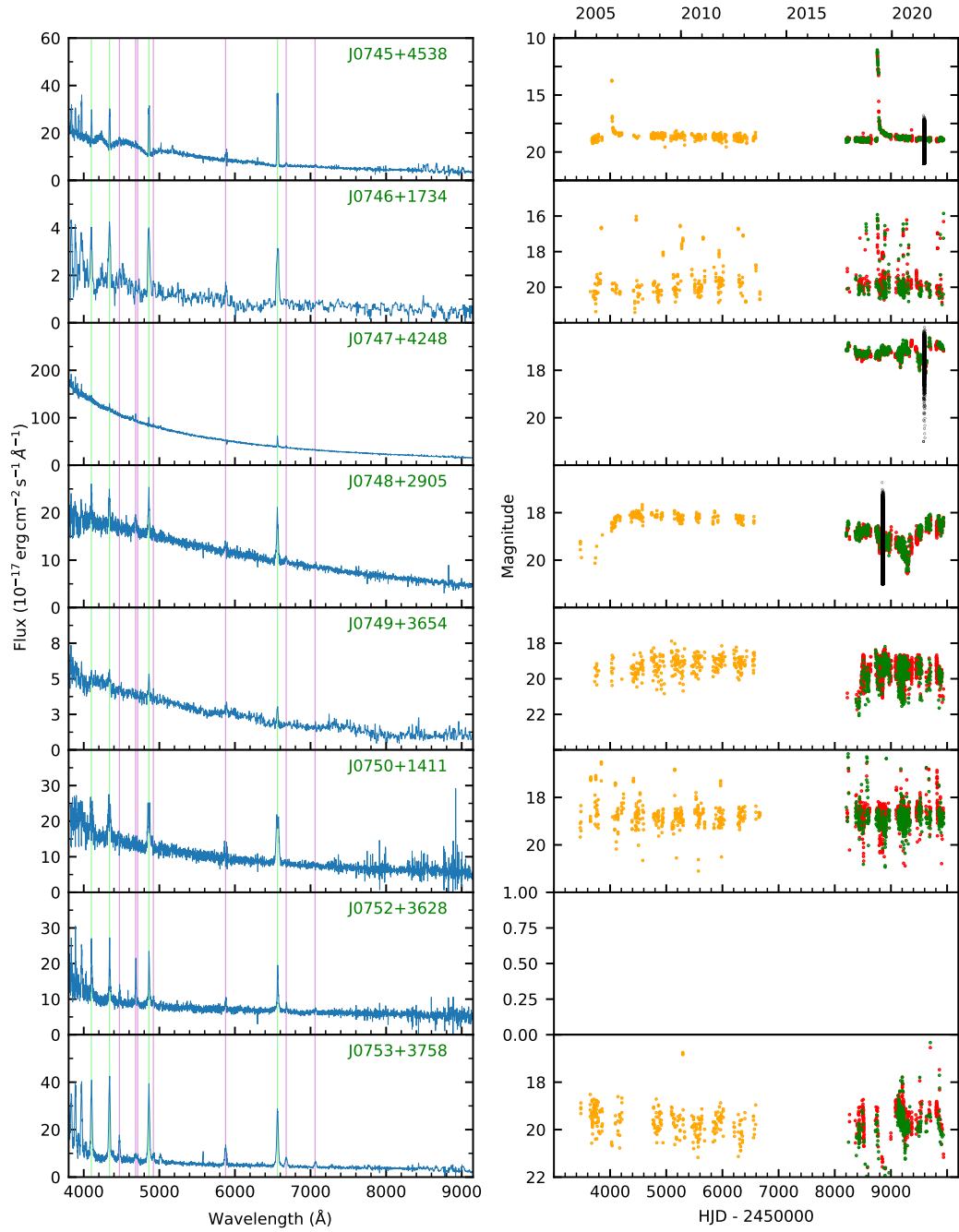


Figure B.12: Left panels: Spectra with H lines shown in green and He in pink. Right panels: Light curves with CRTS shown in orange, ZTF in red and green and *TESS* in black.

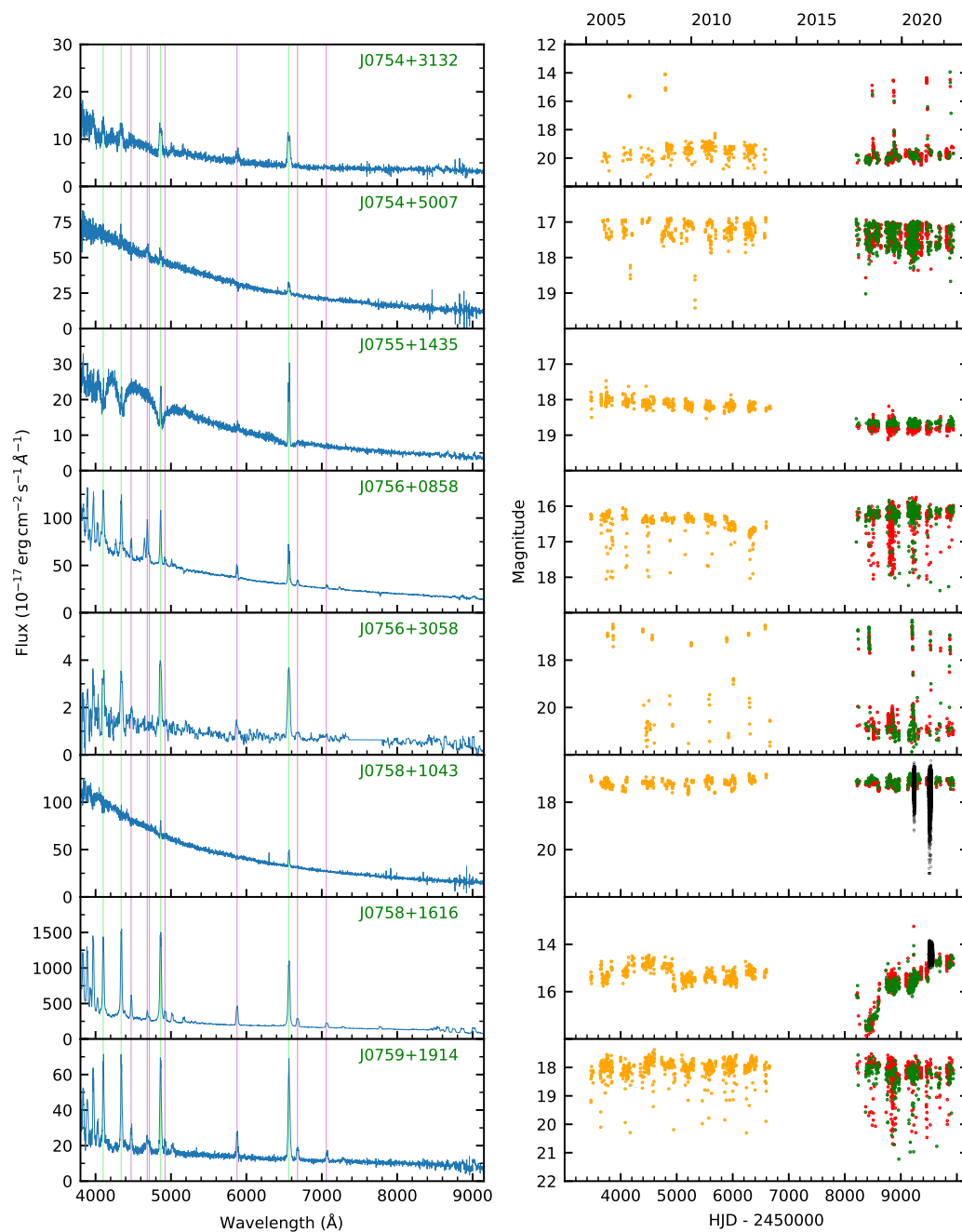


Figure B.13: Left panels: Spectra with H lines shown in green and He in pink. Right panels: Light curves with CRTS shown in orange, ZTF in red and green and *TESS* in black.

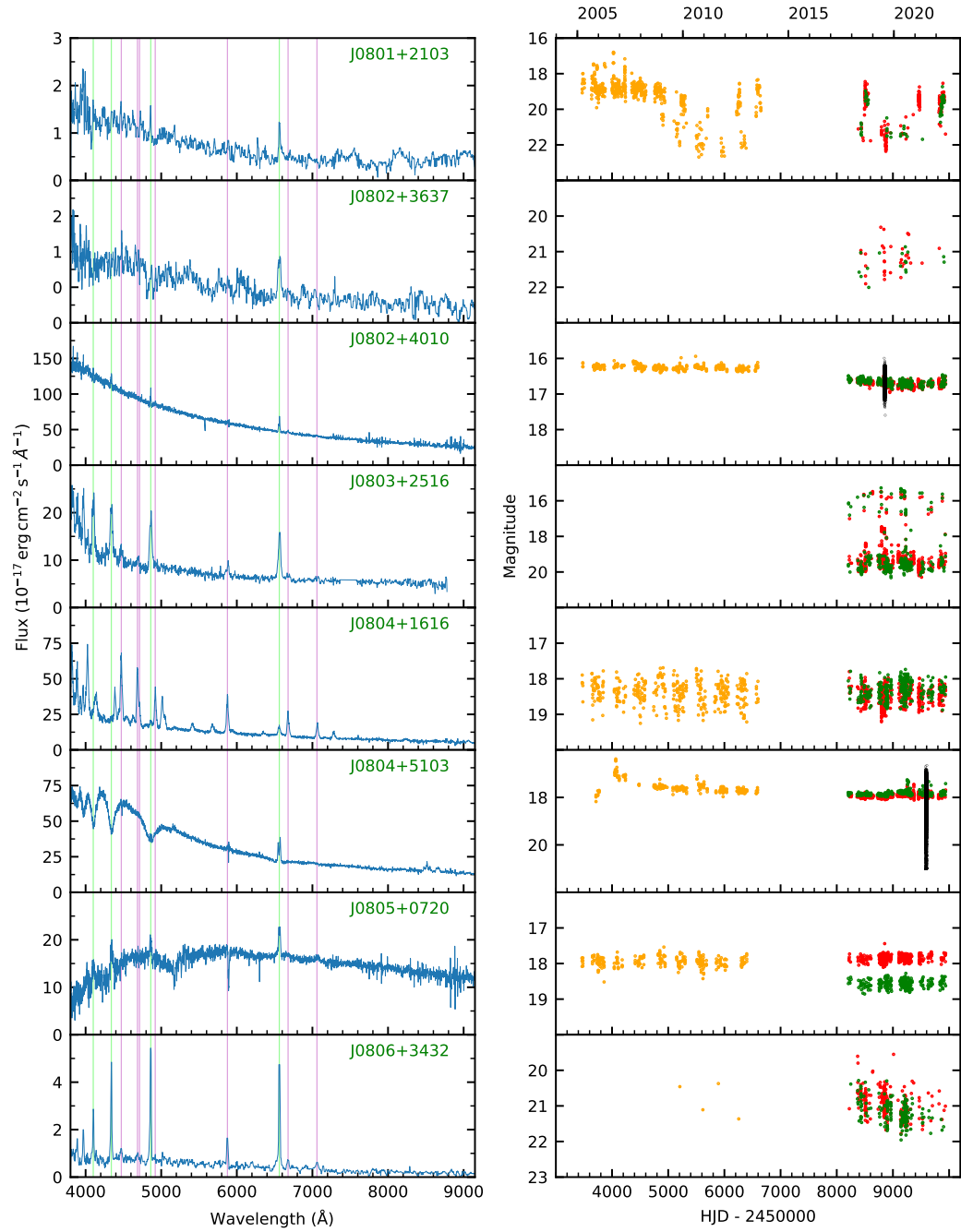


Figure B.14: Left panels: Spectra with H lines shown in green and He in pink. Right panels: Light curves with CRTS shown in orange, ZTF in red and green and *TESS* in black.

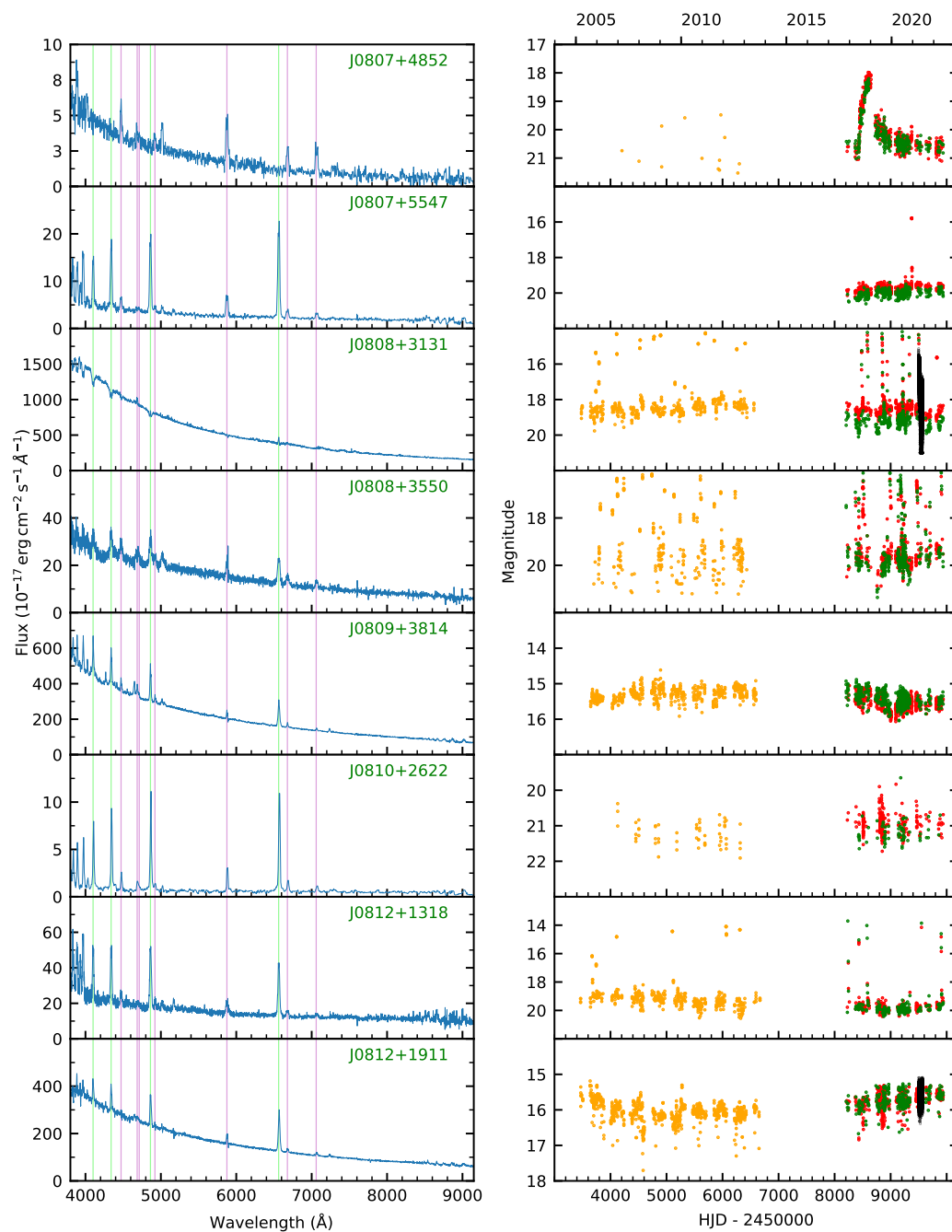


Figure B.15: Left panels: Spectra with H lines shown in green and He in pink. Right panels: Light curves with CRTS shown in orange, ZTF in red and green and *TESS* in black.

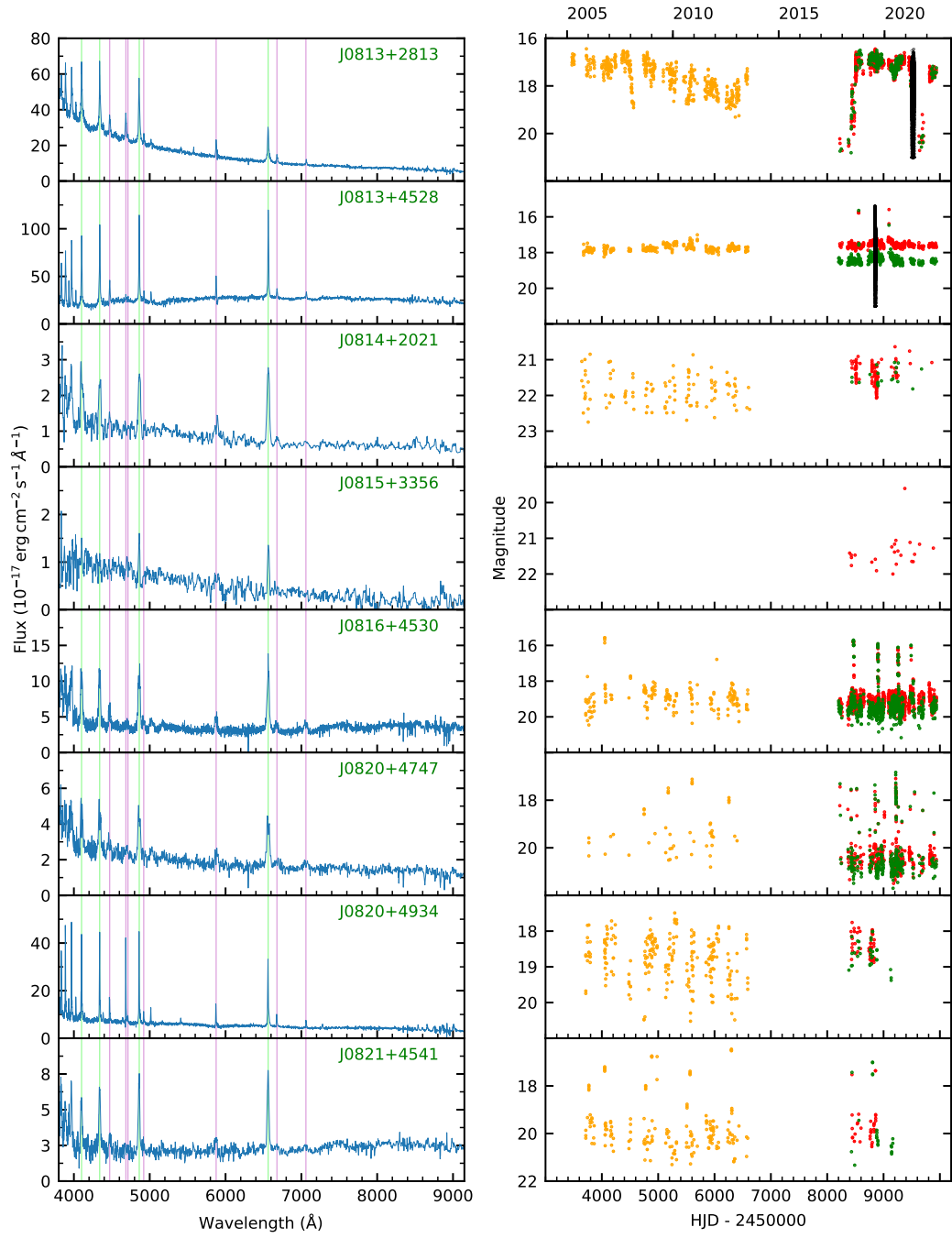


Figure B.16: Left panels: Spectra with H lines shown in green and He in pink. Right panels: Light curves with CRTS shown in orange, ZTF in red and green and *TESS* in black.

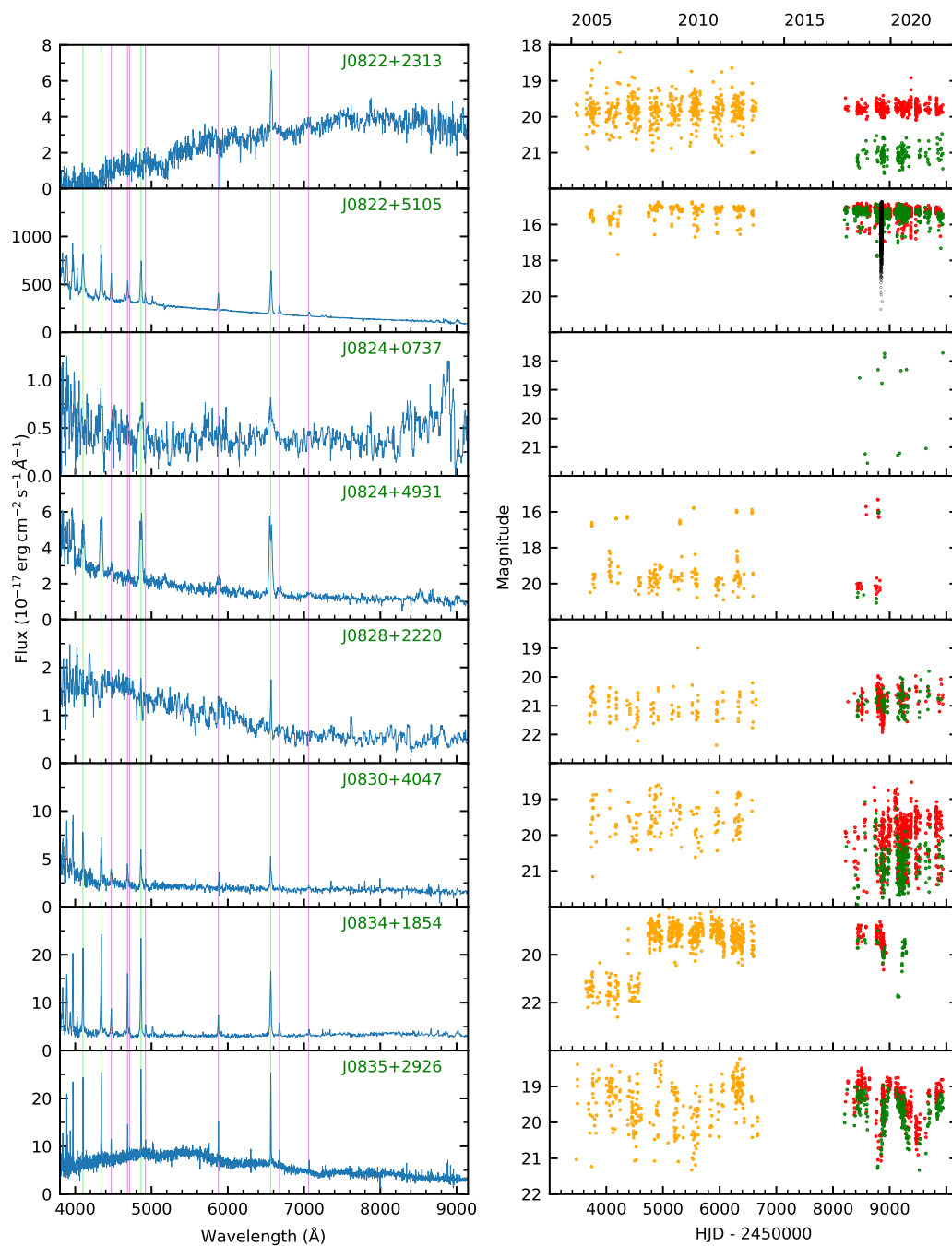


Figure B.17: Left panels: Spectra with H lines shown in green and He in pink. Right panels: Light curves with CRTS shown in orange, ZTF in red and green and *TESS* in black.

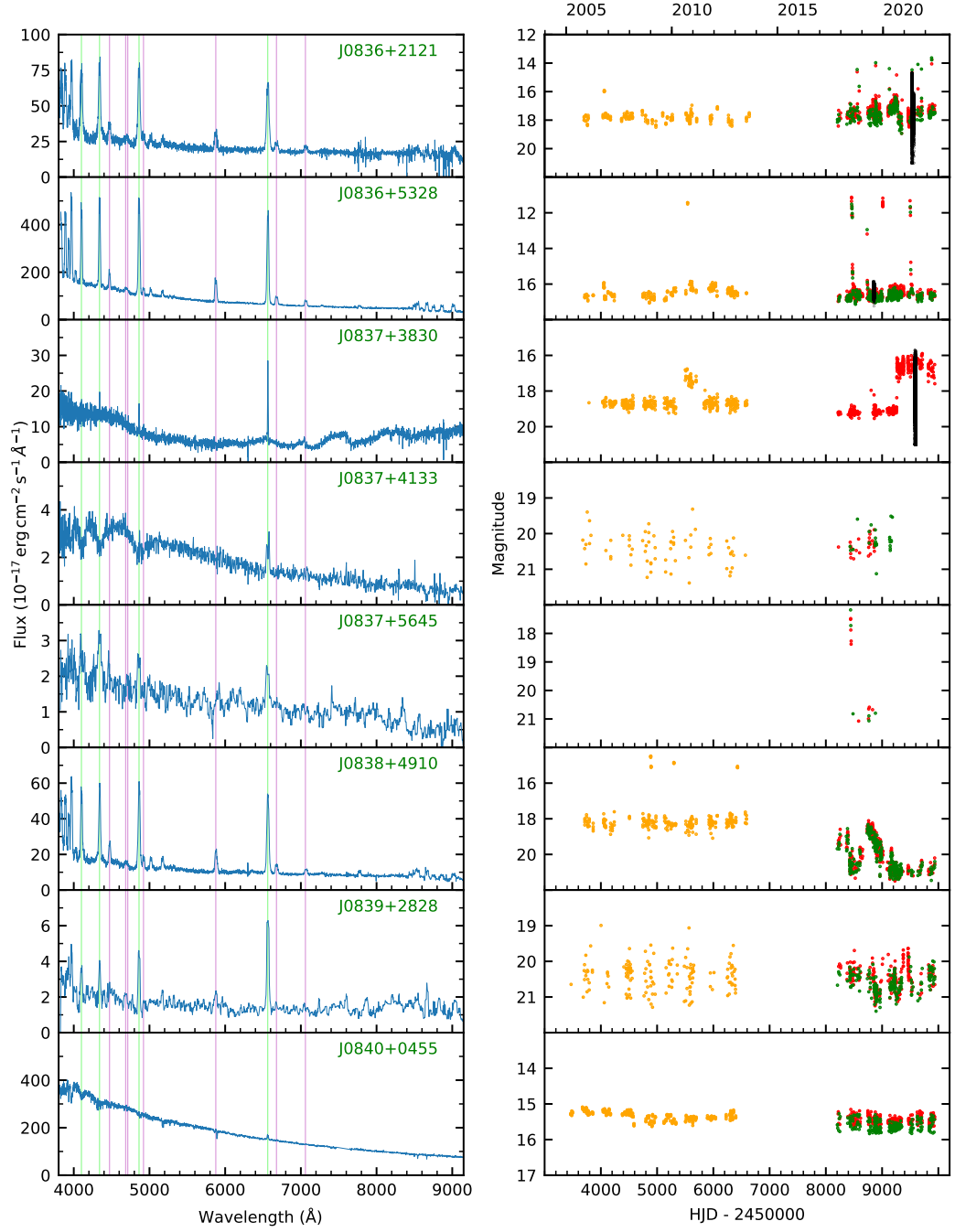


Figure B.18: Left panels: Spectra with H lines shown in green and He in pink. Right panels: Light curves with CRTS shown in orange, ZTF in red and green and *TESS* in black.

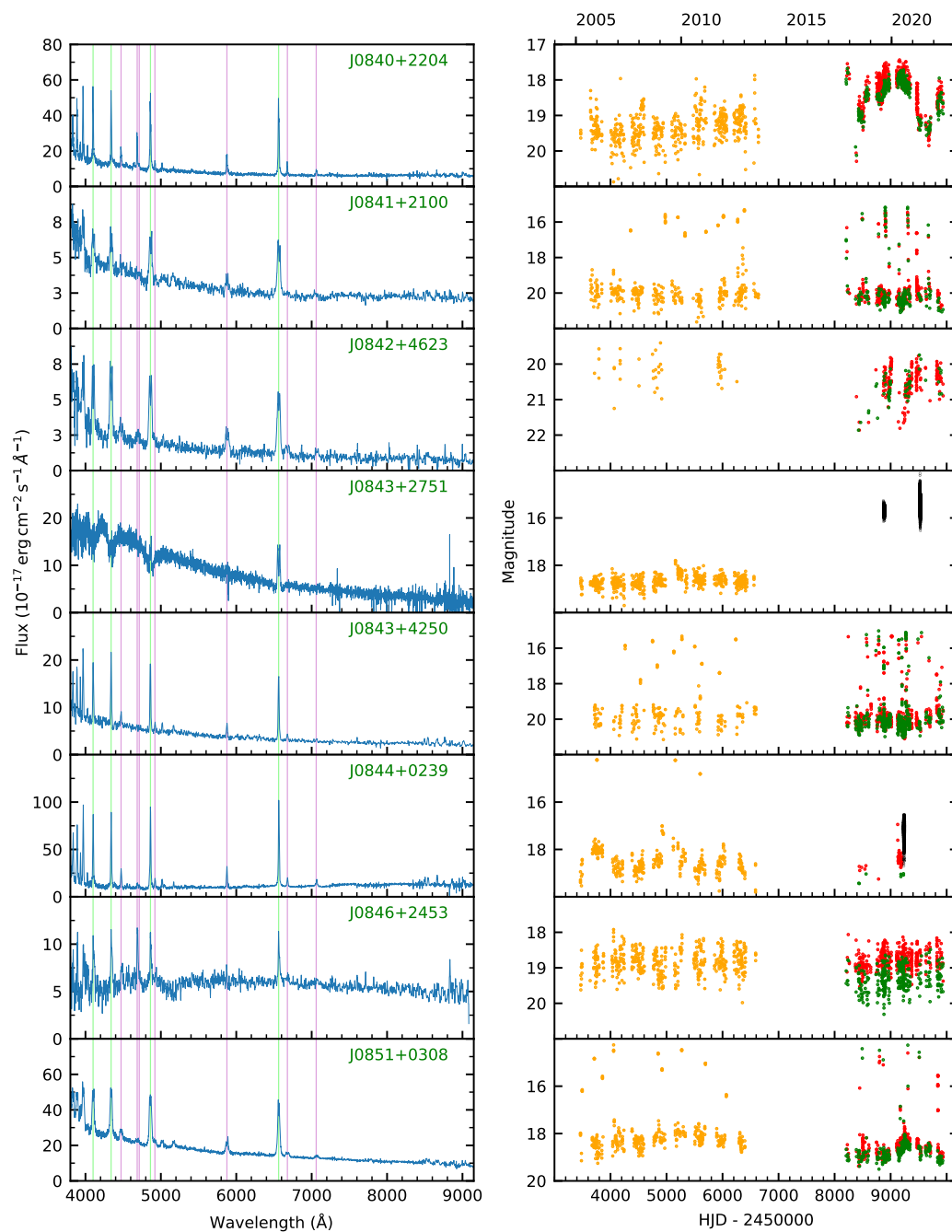


Figure B.19: Left panels: Spectra with H lines shown in green and He in pink. Right panels: Light curves with CRTS shown in orange, ZTF in red and green and *TESS* in black.

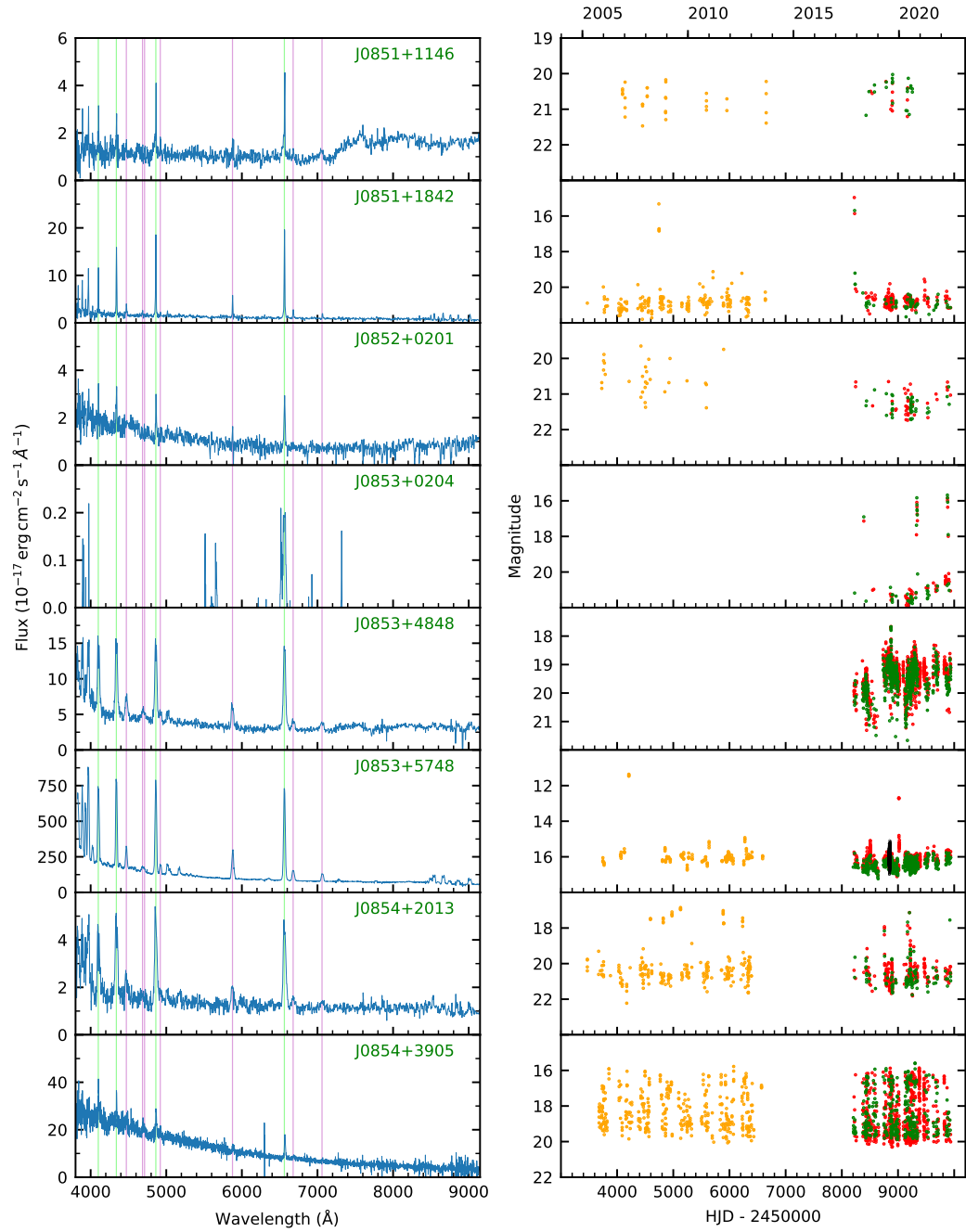


Figure B.20: Left panels: Spectra with H lines shown in green and He in pink. Right panels: Light curves with CRTS shown in orange, ZTF in red and green and *TESS* in black.

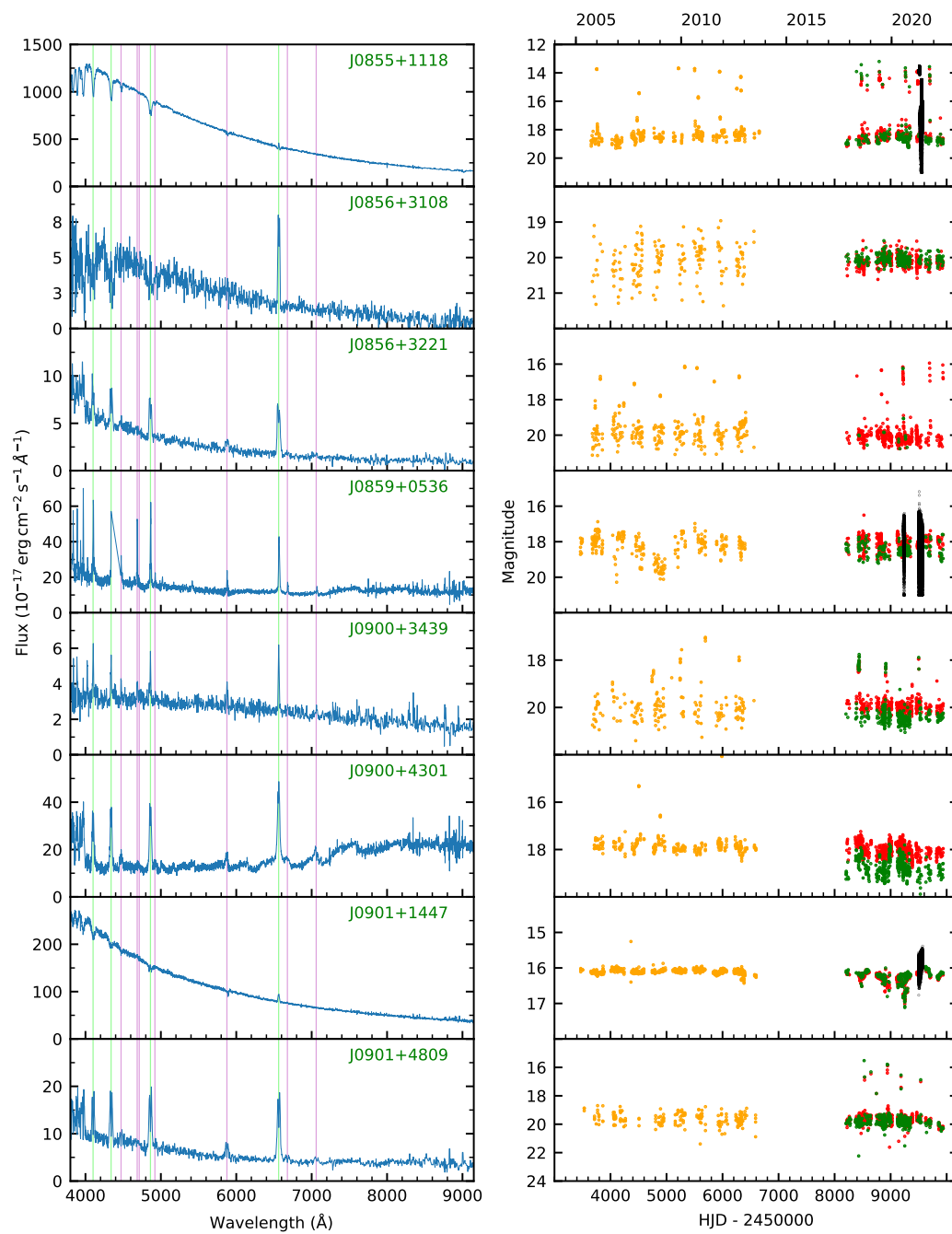


Figure B.21: Left panels: Spectra with H lines shown in green and He in pink. Right panels: Light curves with CRTS shown in orange, ZTF in red and green and *TESS* in black.

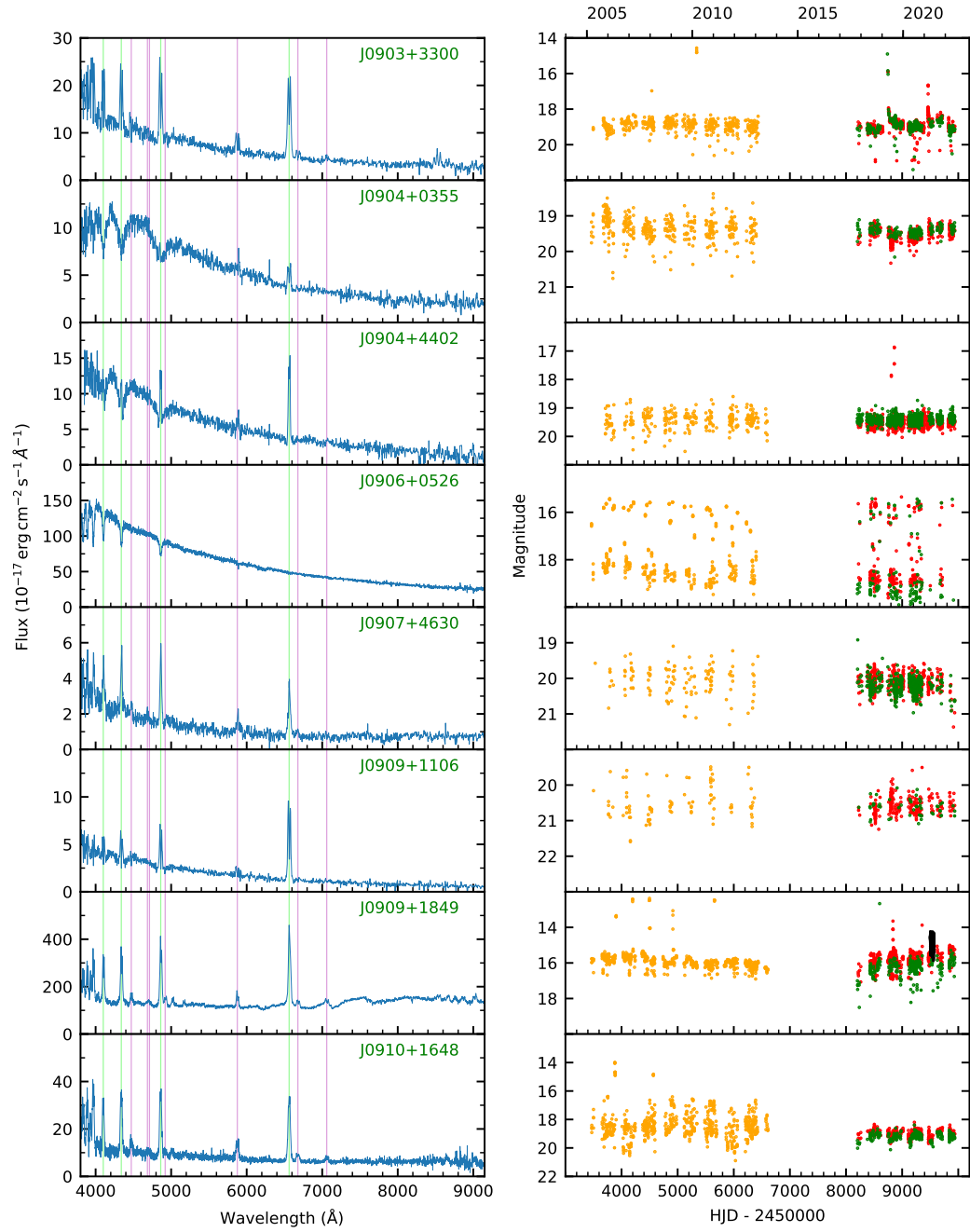


Figure B.22: Left panels: Spectra with H lines shown in green and He in pink. Right panels: Light curves with CRTS shown in orange, ZTF in red and green and *TESS* in black.

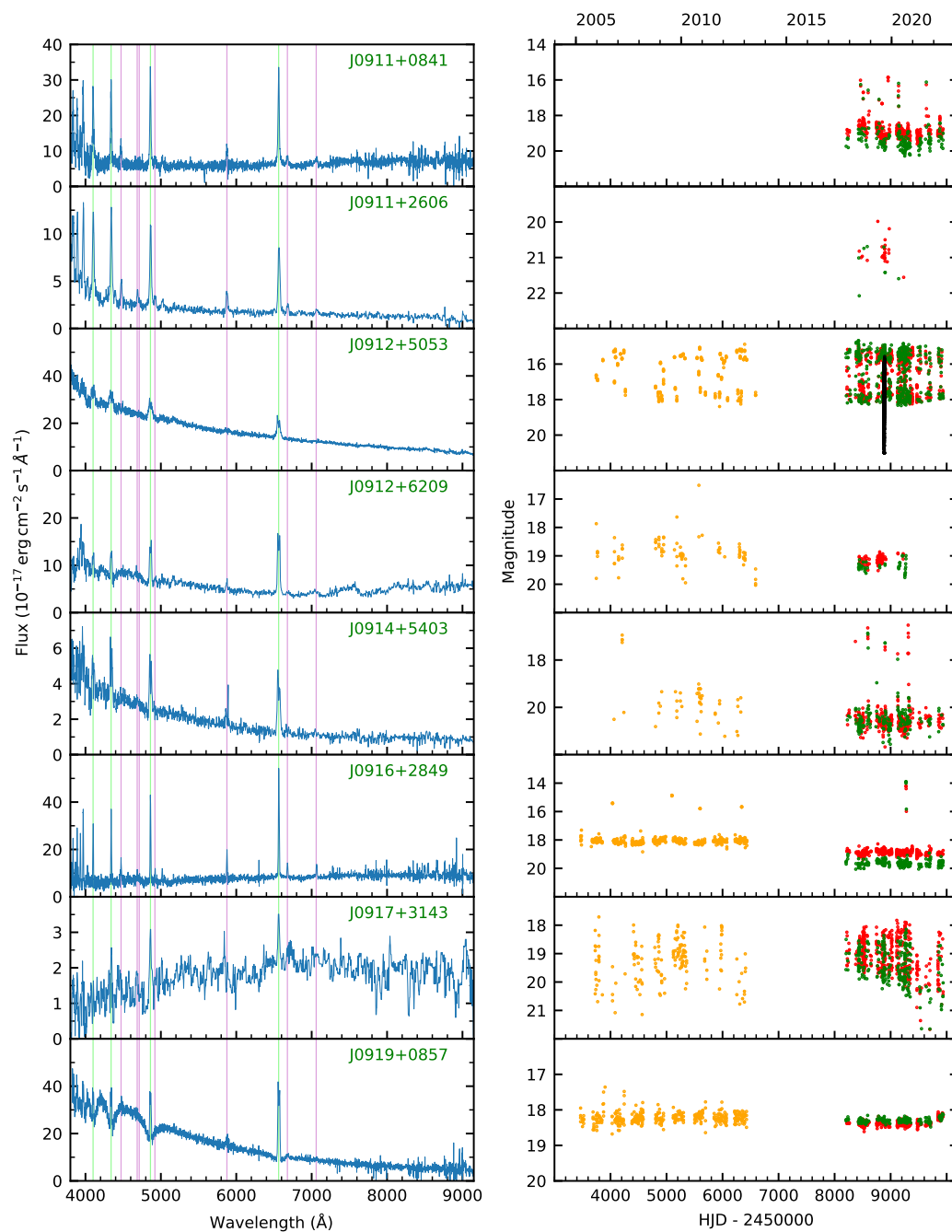


Figure B.23: Left panels: Spectra with H lines shown in green and He in pink. Right panels: Light curves with CRTS shown in orange, ZTF in red and green and *TESS* in black.

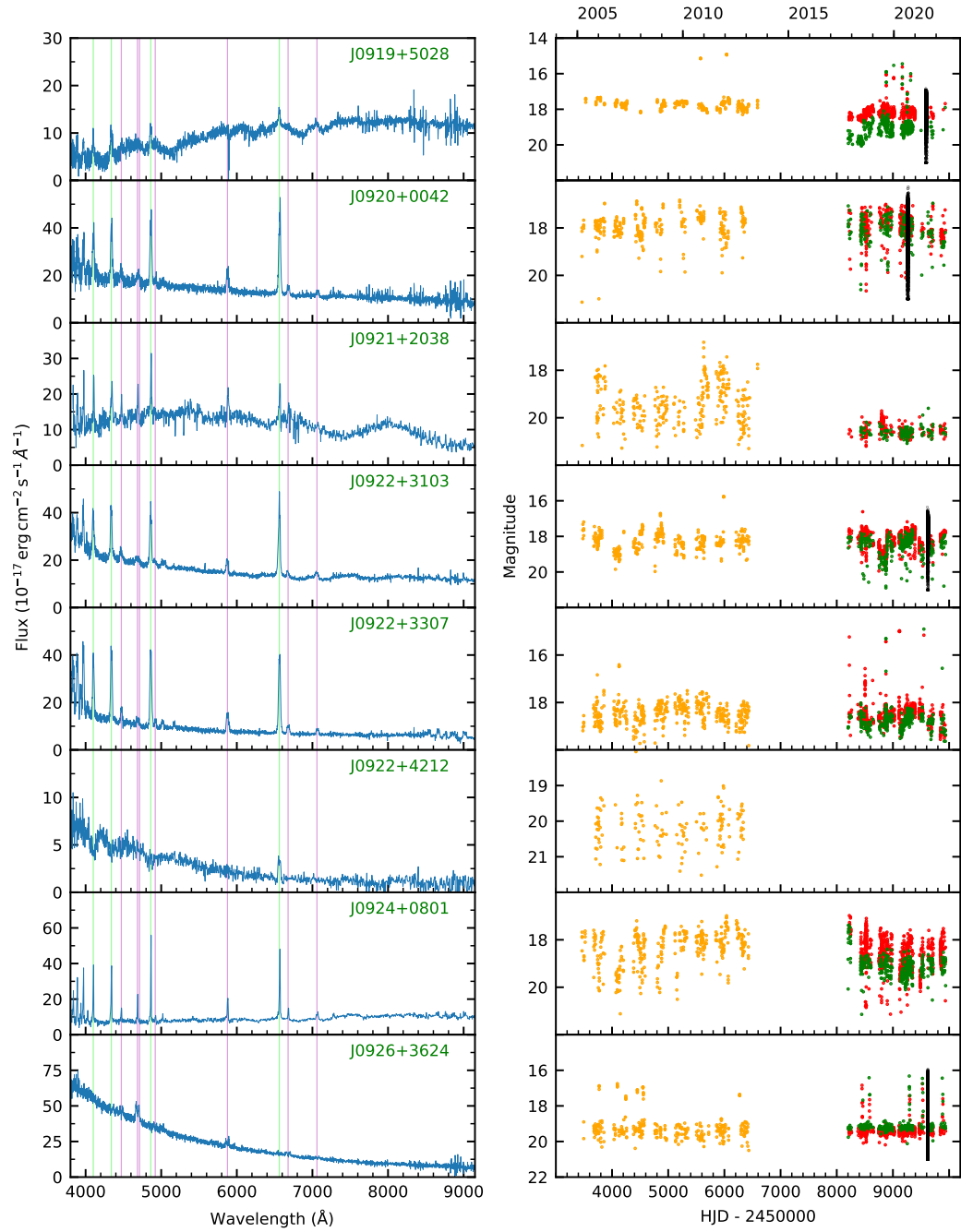


Figure B.24: Left panels: Spectra with H lines shown in green and He in pink. Right panels: Light curves with CRTS shown in orange, ZTF in red and green and *TESS* in black.

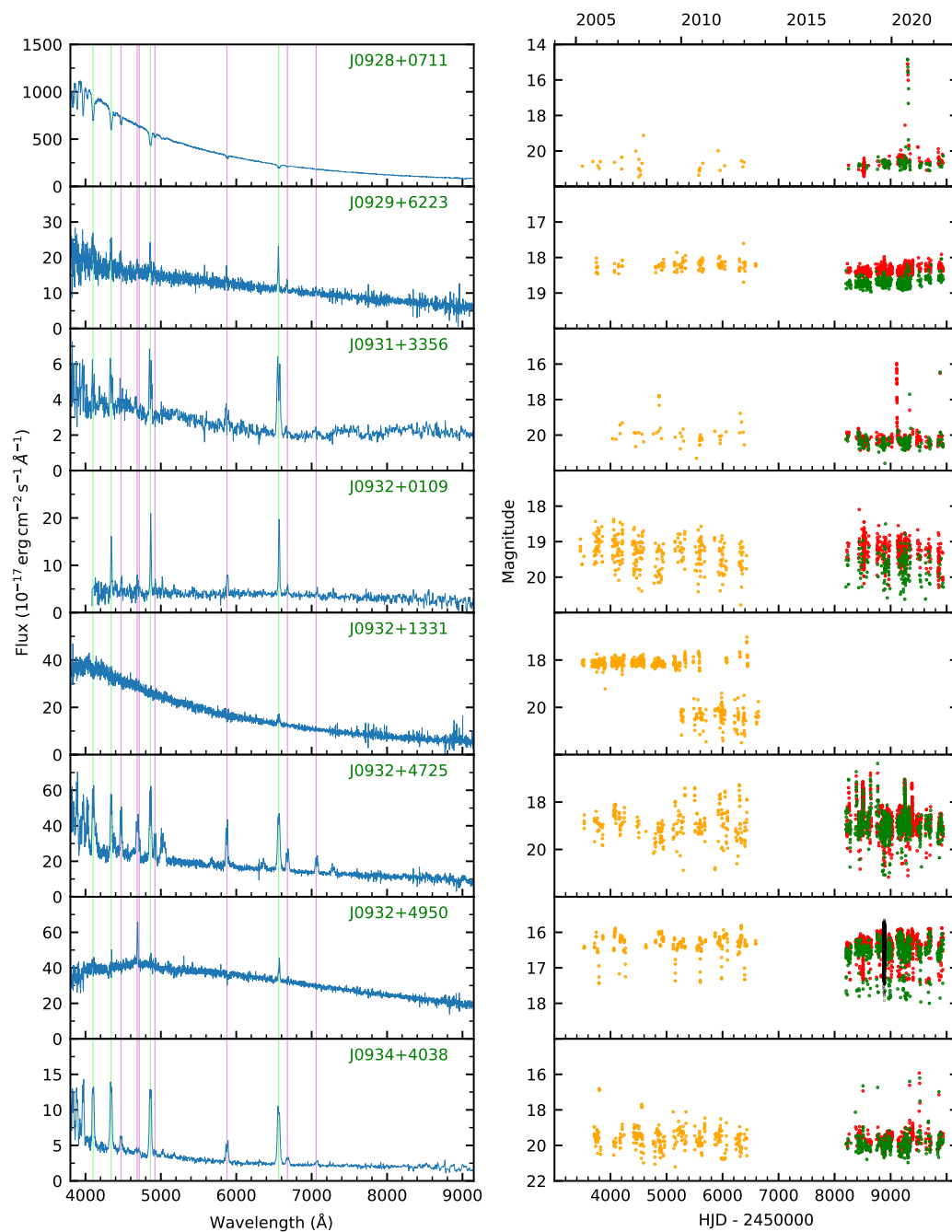


Figure B.25: Left panels: Spectra with H lines shown in green and He in pink. Right panels: Light curves with CRTS shown in orange, ZTF in red and green and *TESS* in black.

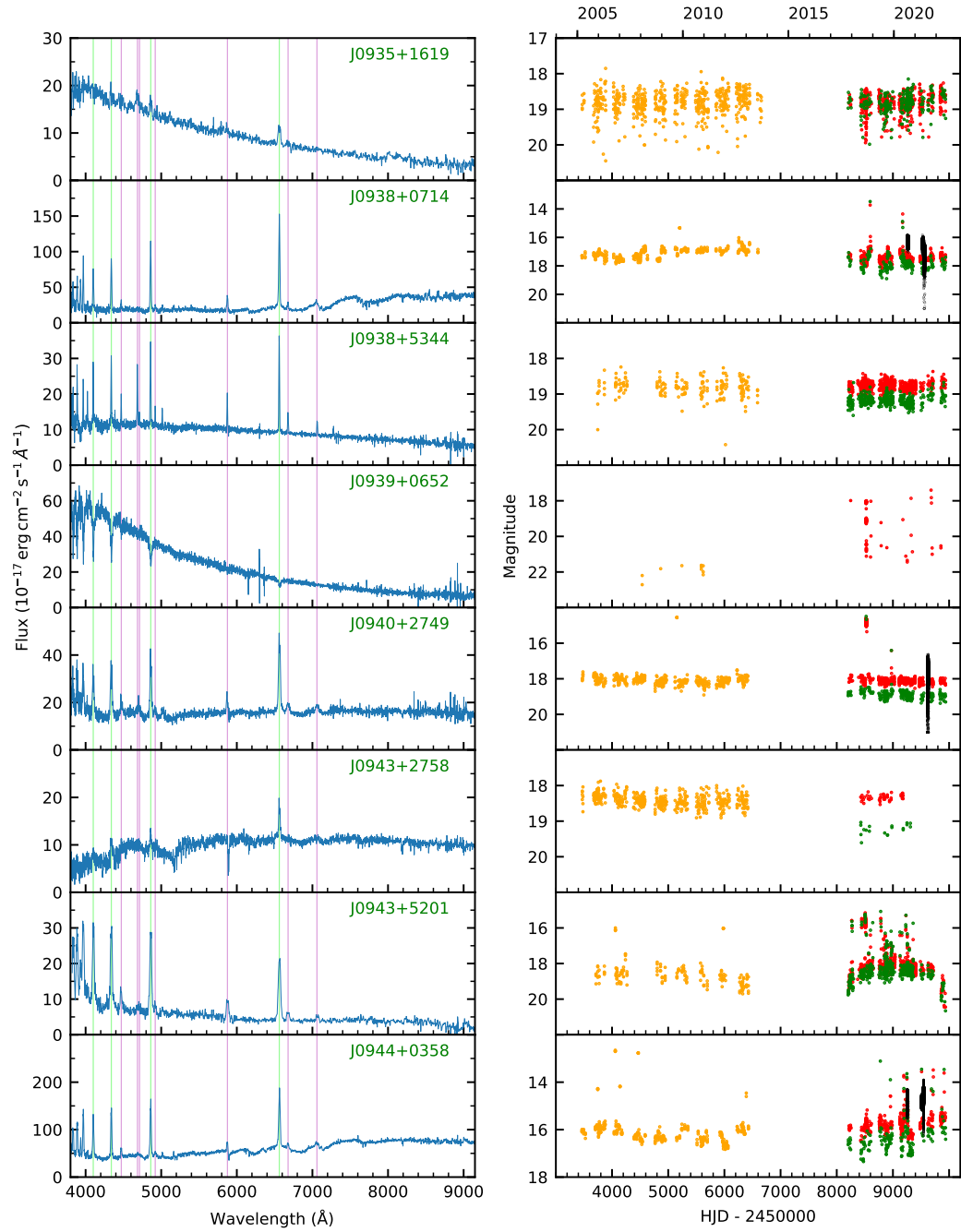


Figure B.26: Left panels: Spectra with H lines shown in green and He in pink. Right panels: Light curves with CRTS shown in orange, ZTF in red and green and *TESS* in black.

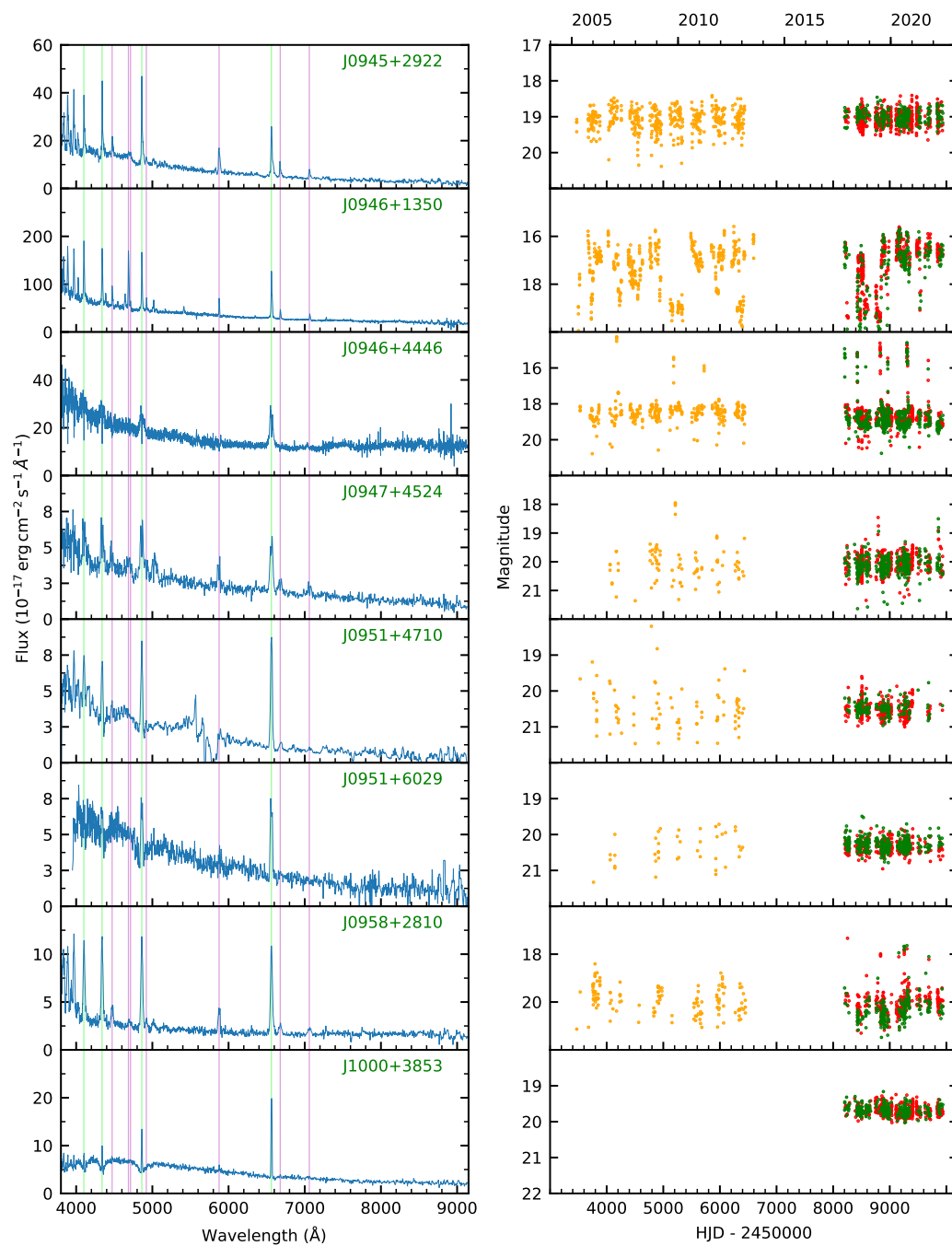


Figure B.27: Left panels: Spectra with H lines shown in green and He in pink. Right panels: Light curves with CRTS shown in orange, ZTF in red and green and *TESS* in black.

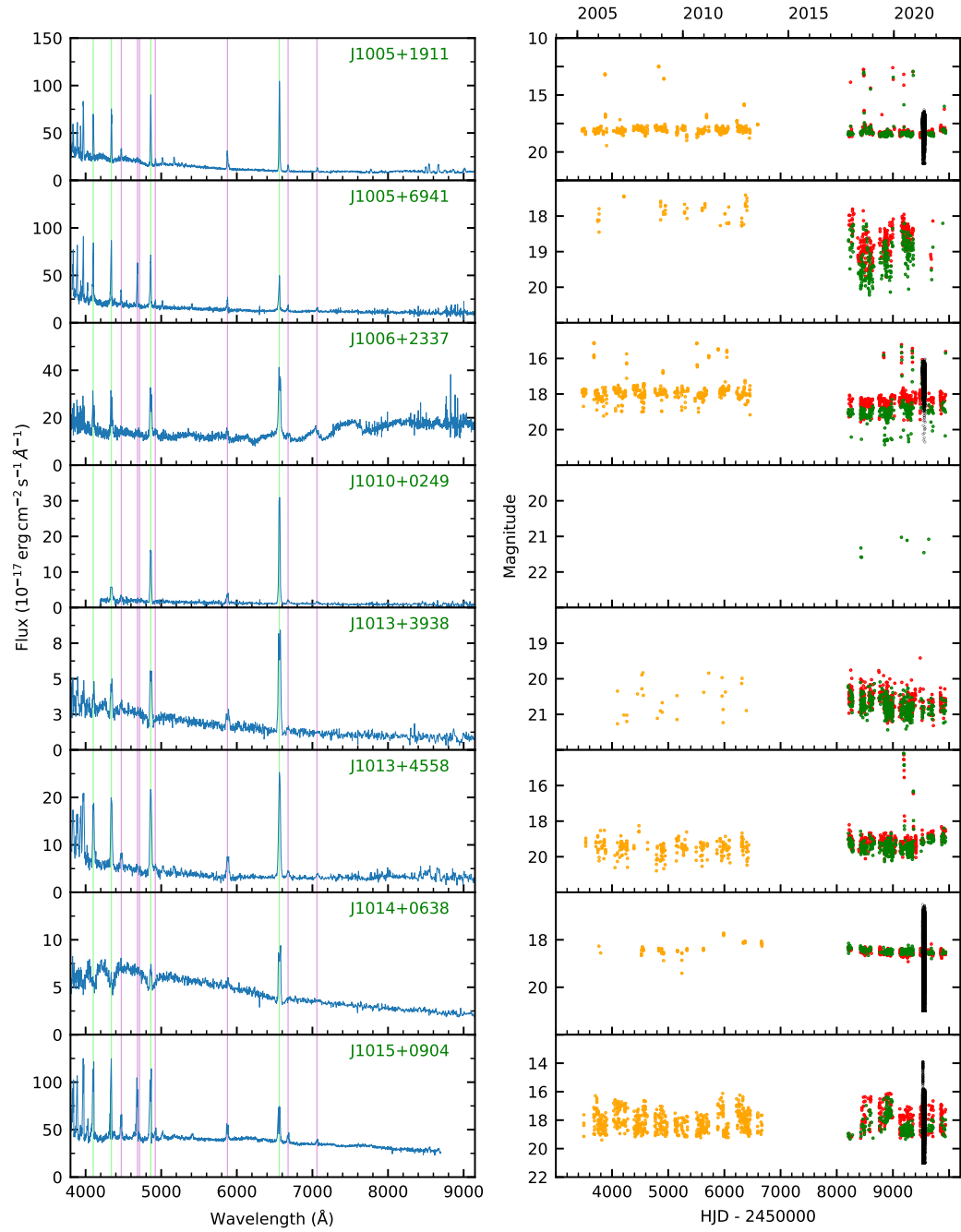


Figure B.28: Left panels: Spectra with H lines shown in green and He in pink. Right panels: Light curves with CRTS shown in orange, ZTF in red and green and *TESS* in black.

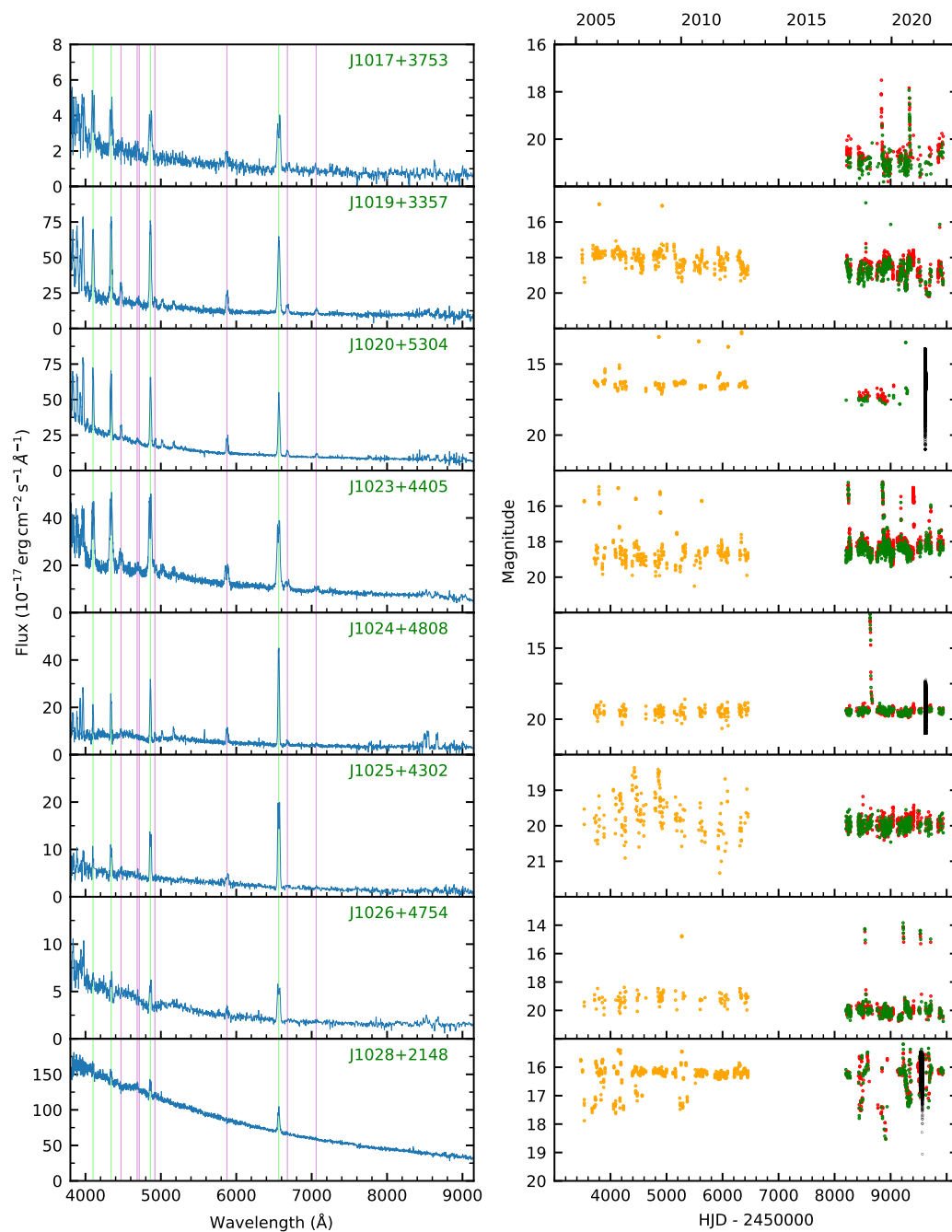


Figure B.29: Left panels: Spectra with H lines shown in green and He in pink. Right panels: Light curves with CRTS shown in orange, ZTF in red and green and *TESS* in black.

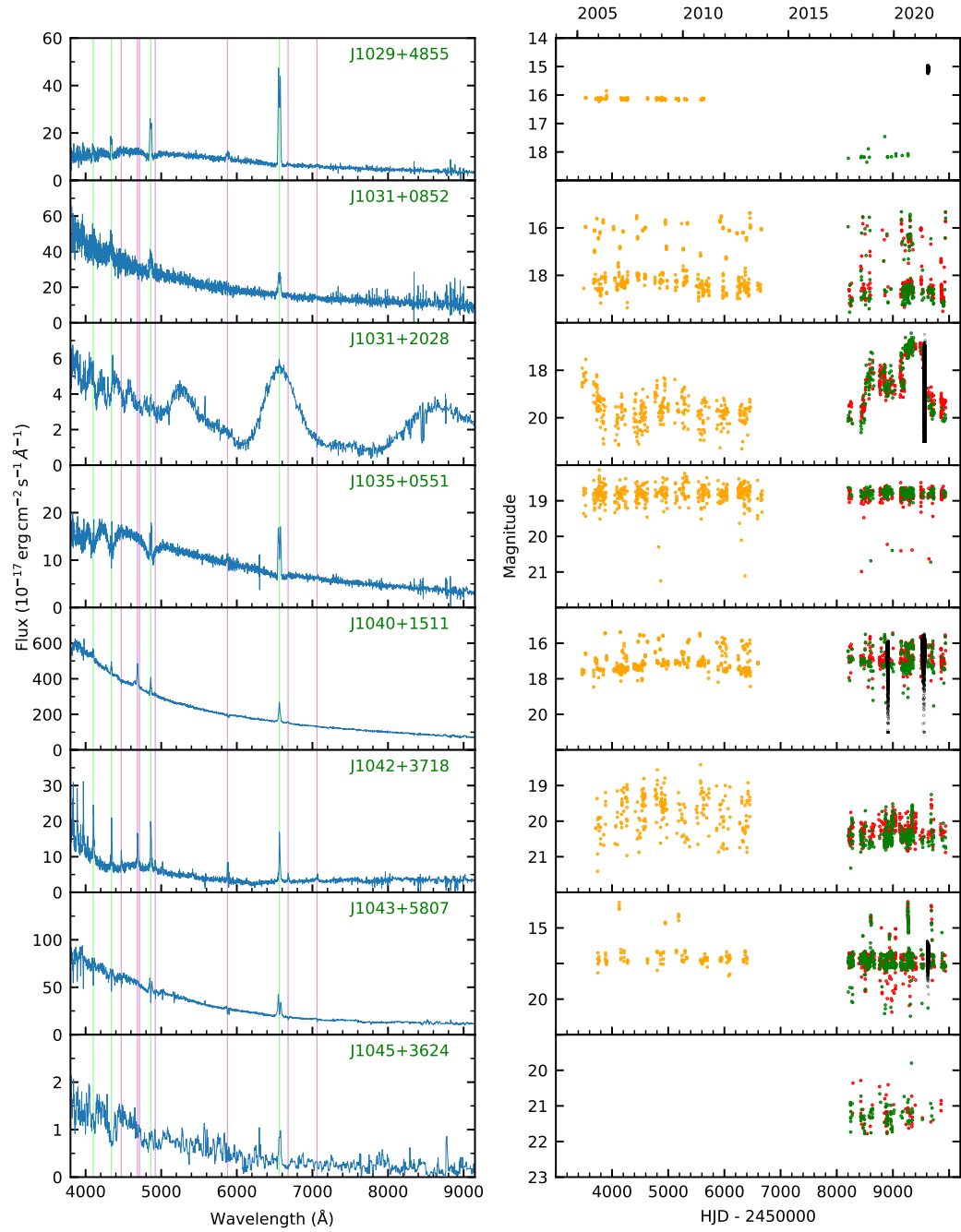


Figure B.30: Left panels: Spectra with H lines shown in green and He in pink. Right panels: Light curves with CRTS shown in orange, ZTF in red and green and *TESS* in black.

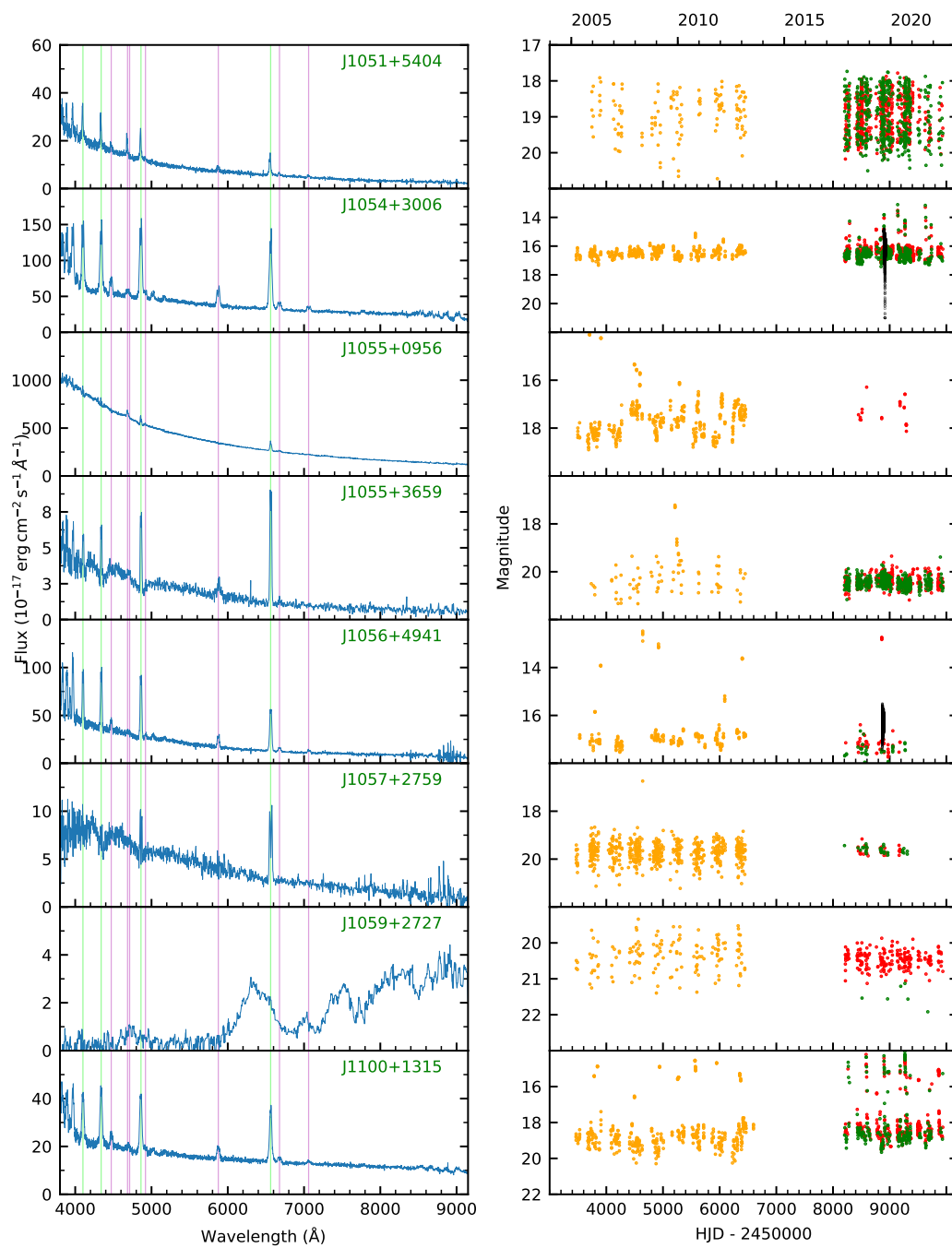


Figure B.31: Left panels: Spectra with H lines shown in green and He in pink. Right panels: Light curves with CRTS shown in orange, ZTF in red and green and *TESS* in black.

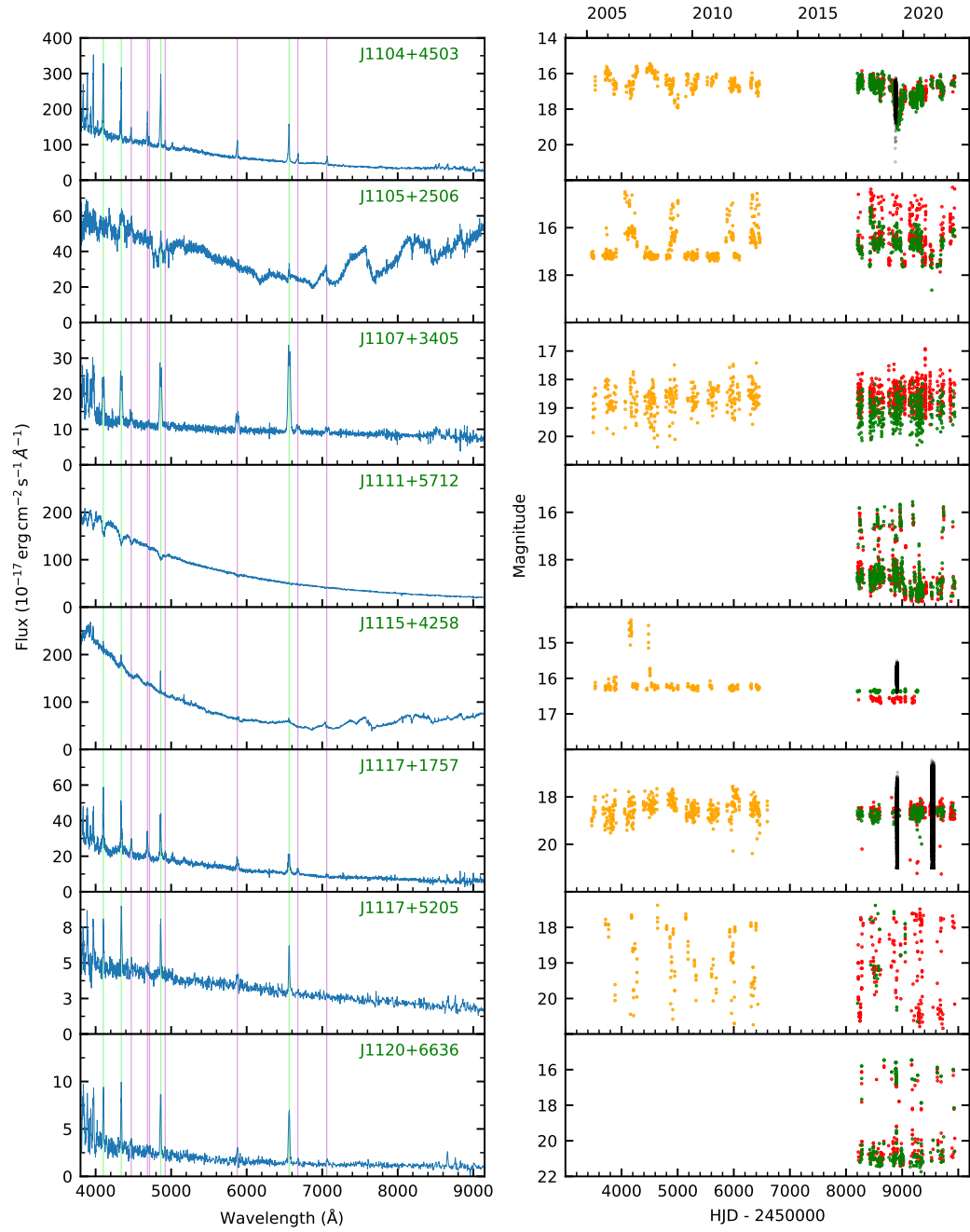


Figure B.32: Left panels: Spectra with H lines shown in green and He in pink. Right panels: Light curves with CRTS shown in orange, ZTF in red and green and *TESS* in black.

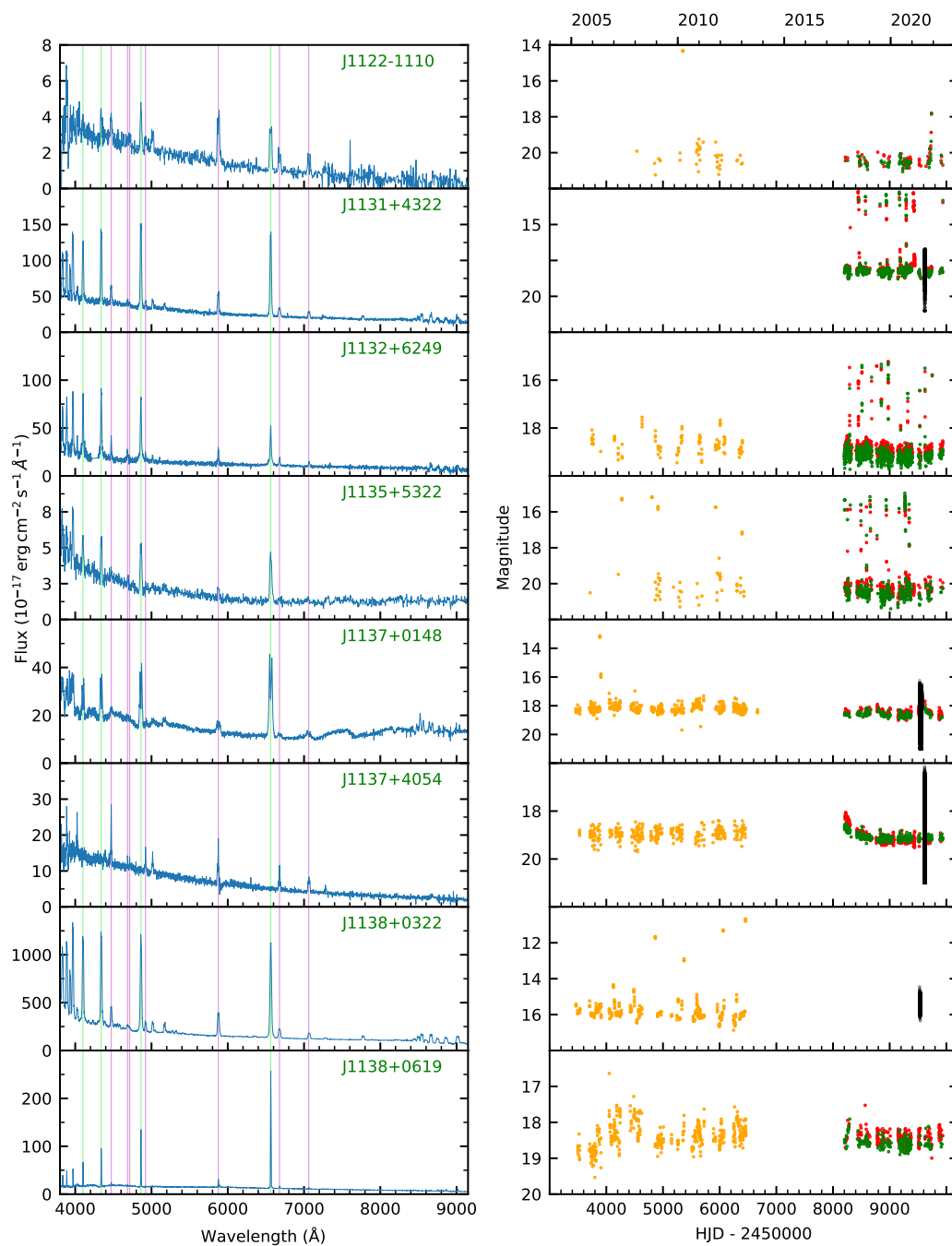


Figure B.33: Left panels: Spectra with H lines shown in green and He in pink. Right panels: Light curves with CRS shown in orange, ZTF in red and green and *TESS* in black.

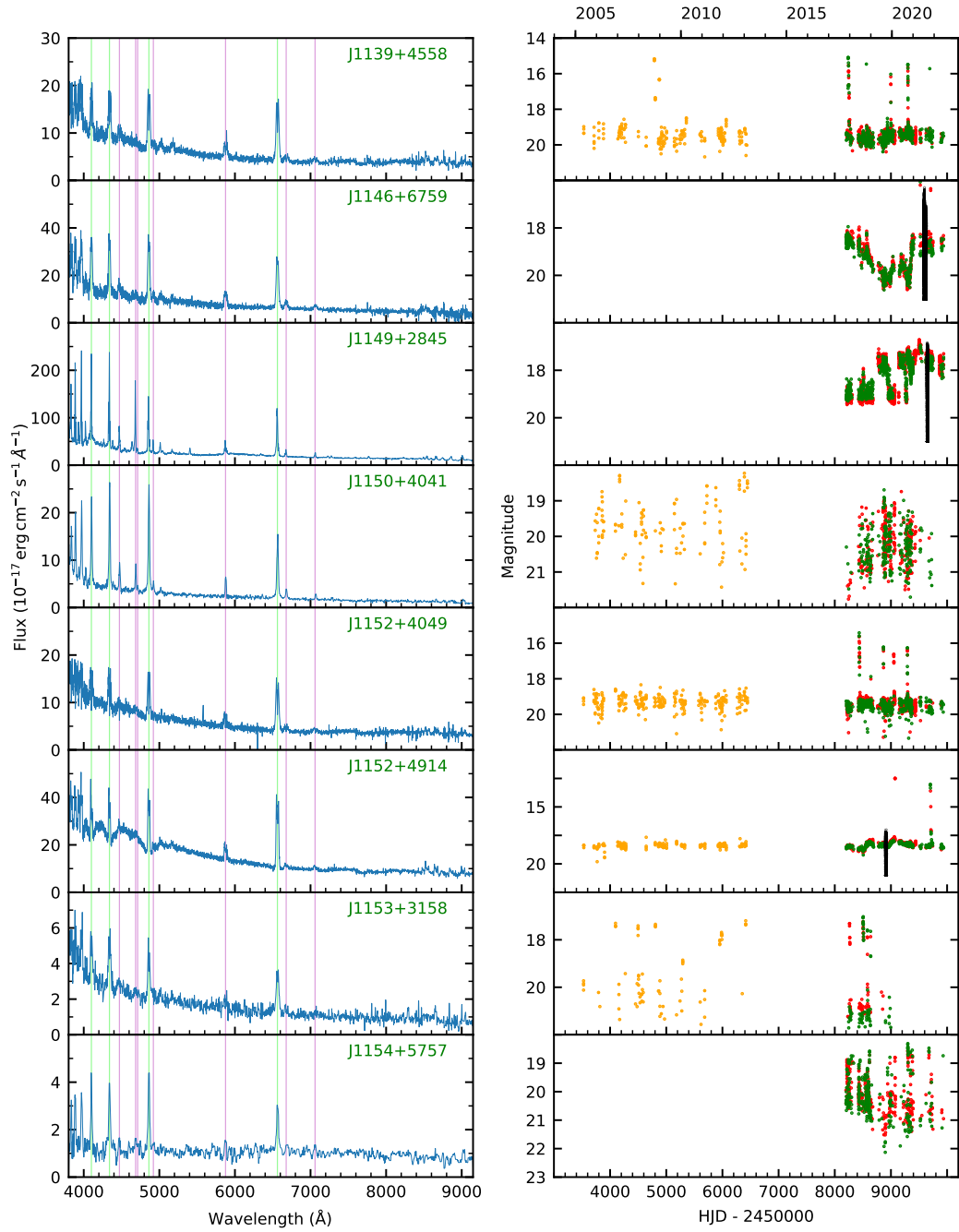


Figure B.34: Left panels: Spectra with H lines shown in green and He in pink. Right panels: Light curves with CRTS shown in orange, ZTF in red and green and *TESS* in black.

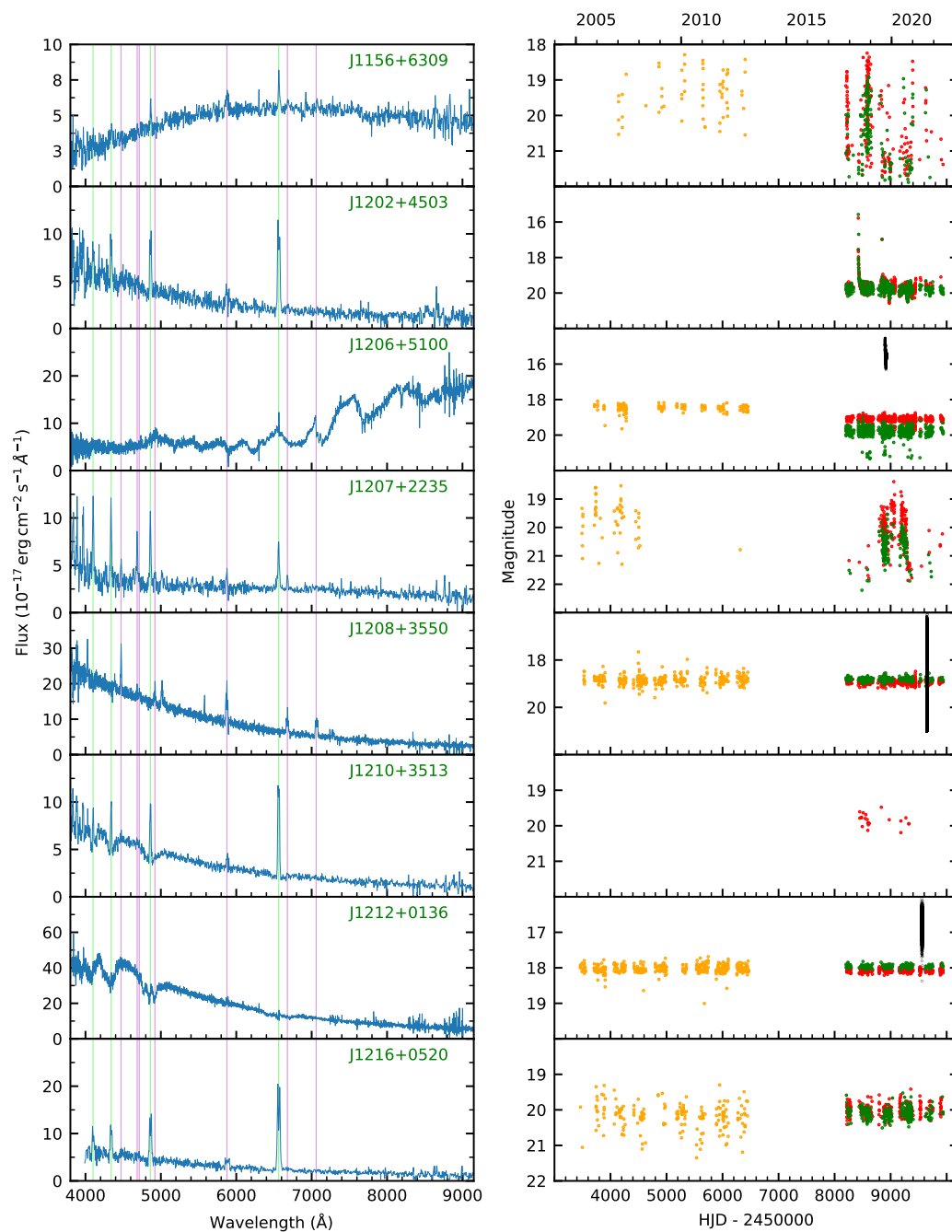


Figure B.35: Left panels: Spectra with H lines shown in green and He in pink. Right panels: Light curves with CRTS shown in orange, ZTF in red and green and *TESS* in black.

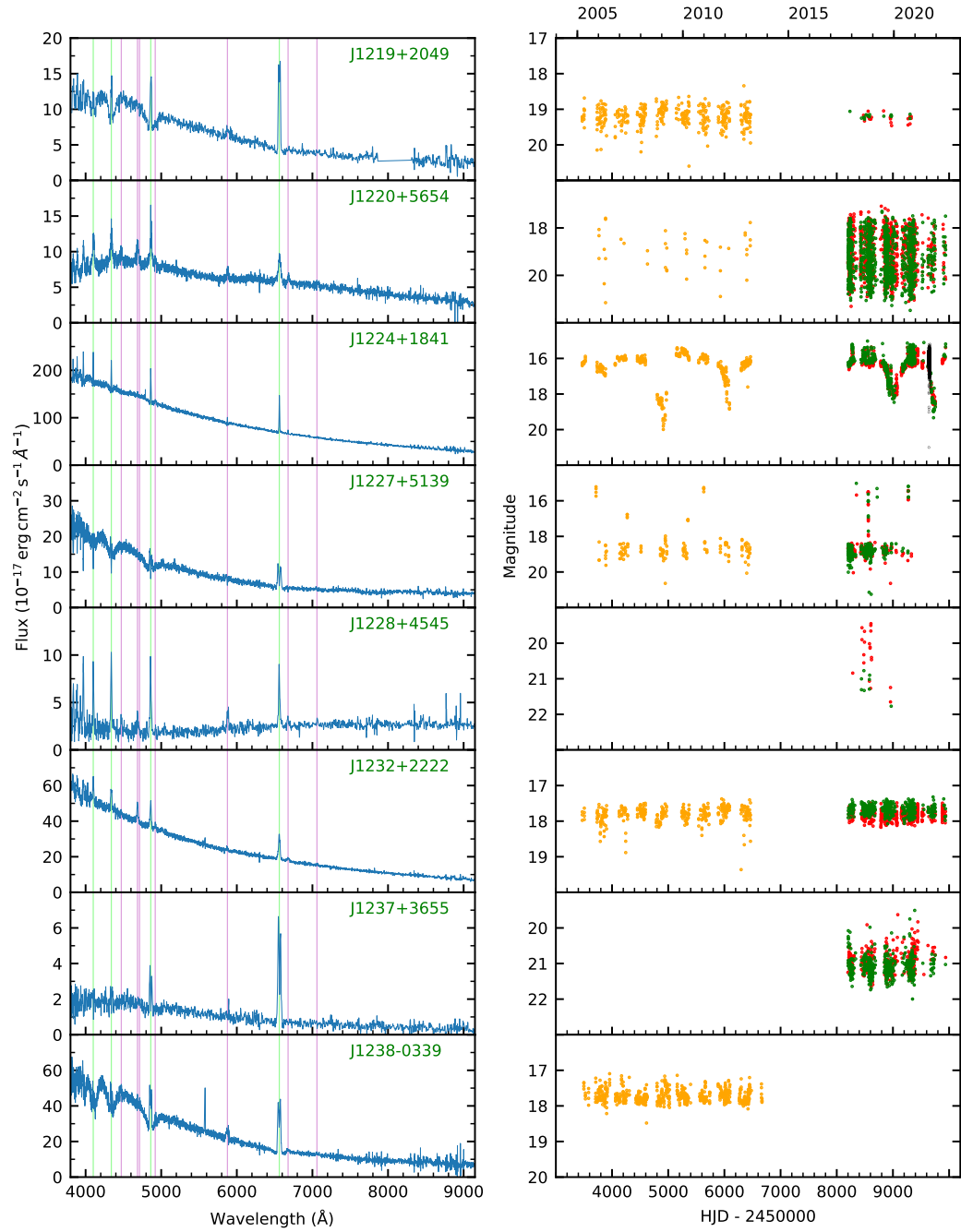


Figure B.36: Left panels: Spectra with H lines shown in green and He in pink. Right panels: Light curves with CRTS shown in orange, ZTF in red and green and *TESS* in black.

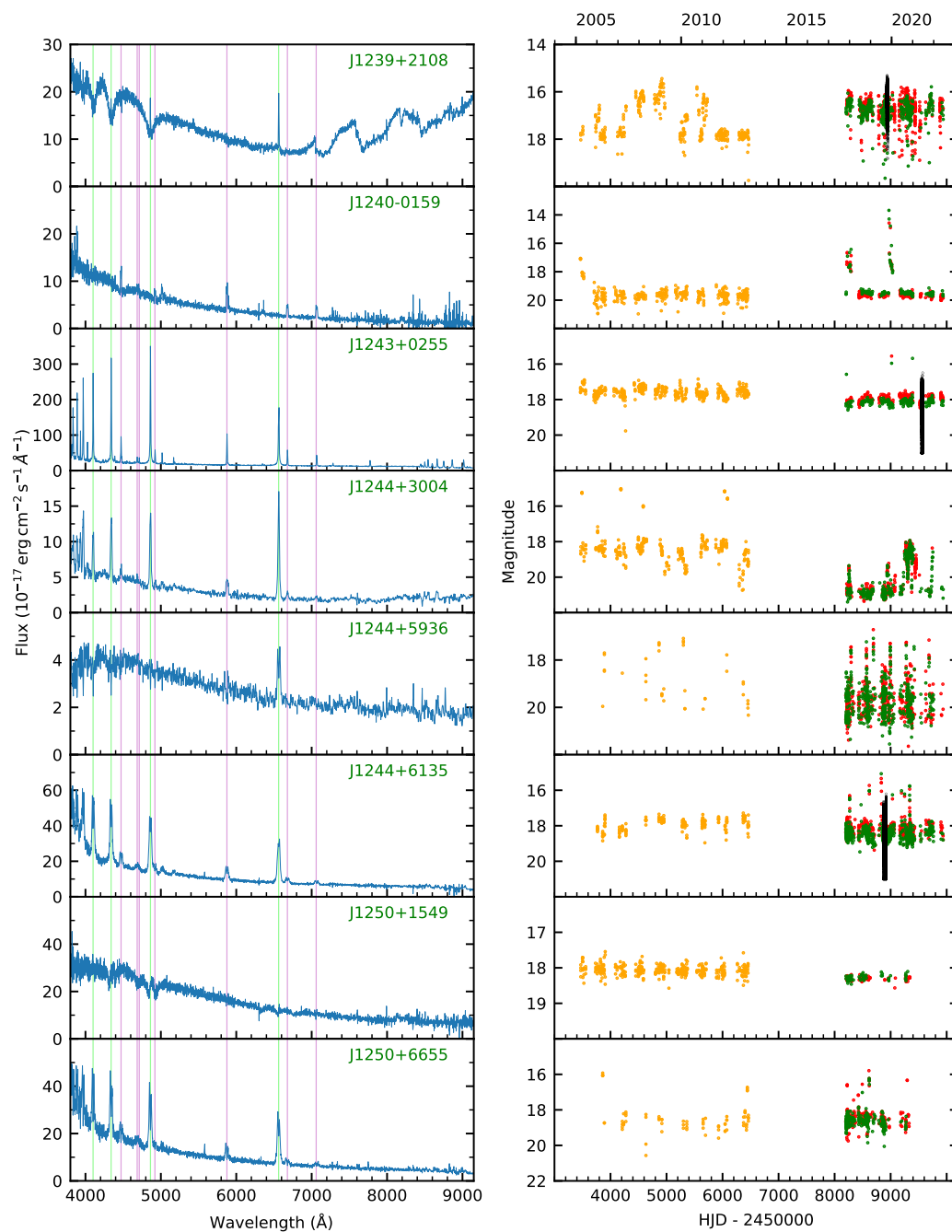


Figure B.37: Left panels: Spectra with H lines shown in green and He in pink. Right panels: Light curves with CRTS shown in orange, ZTF in red and green and *TESS* in black.

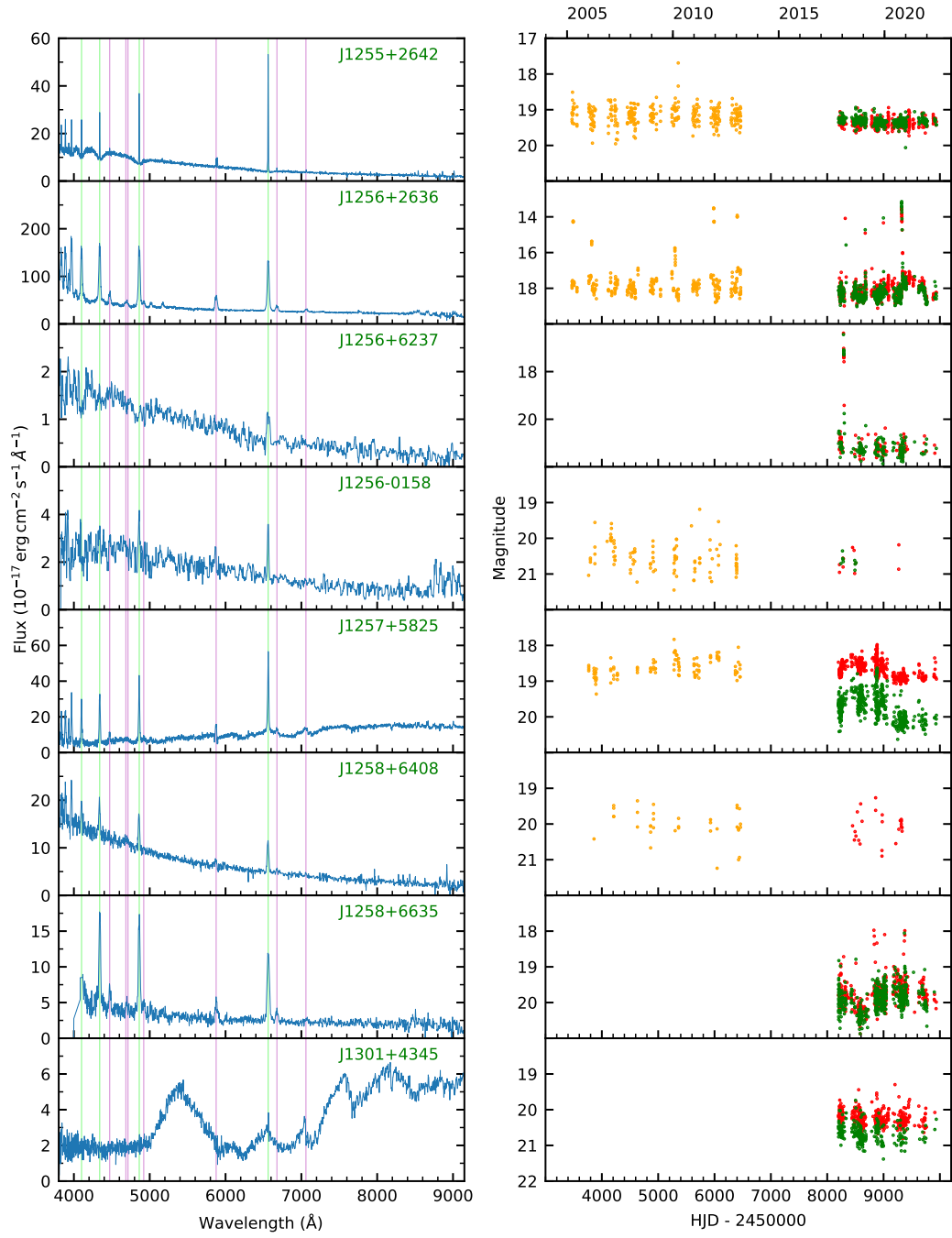


Figure B.38: Left panels: Spectra with H lines shown in green and He in pink. Right panels: Light curves with CRTS shown in orange, ZTF in red and green and *TESS* in black.

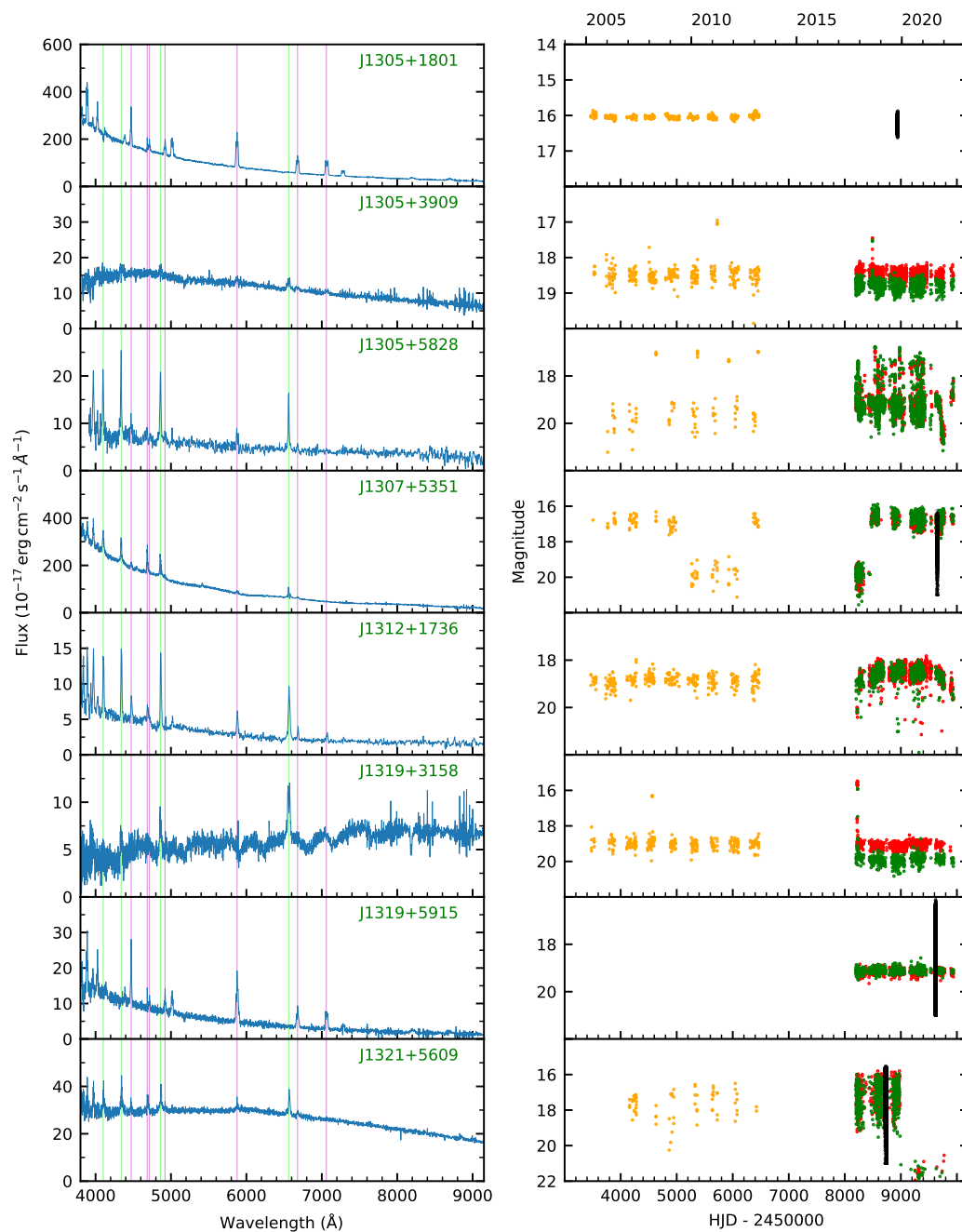


Figure B.39: Left panels: Spectra with H lines shown in green and He in pink. Right panels: Light curves with CRTS shown in orange, ZTF in red and green and *TESS* in black.

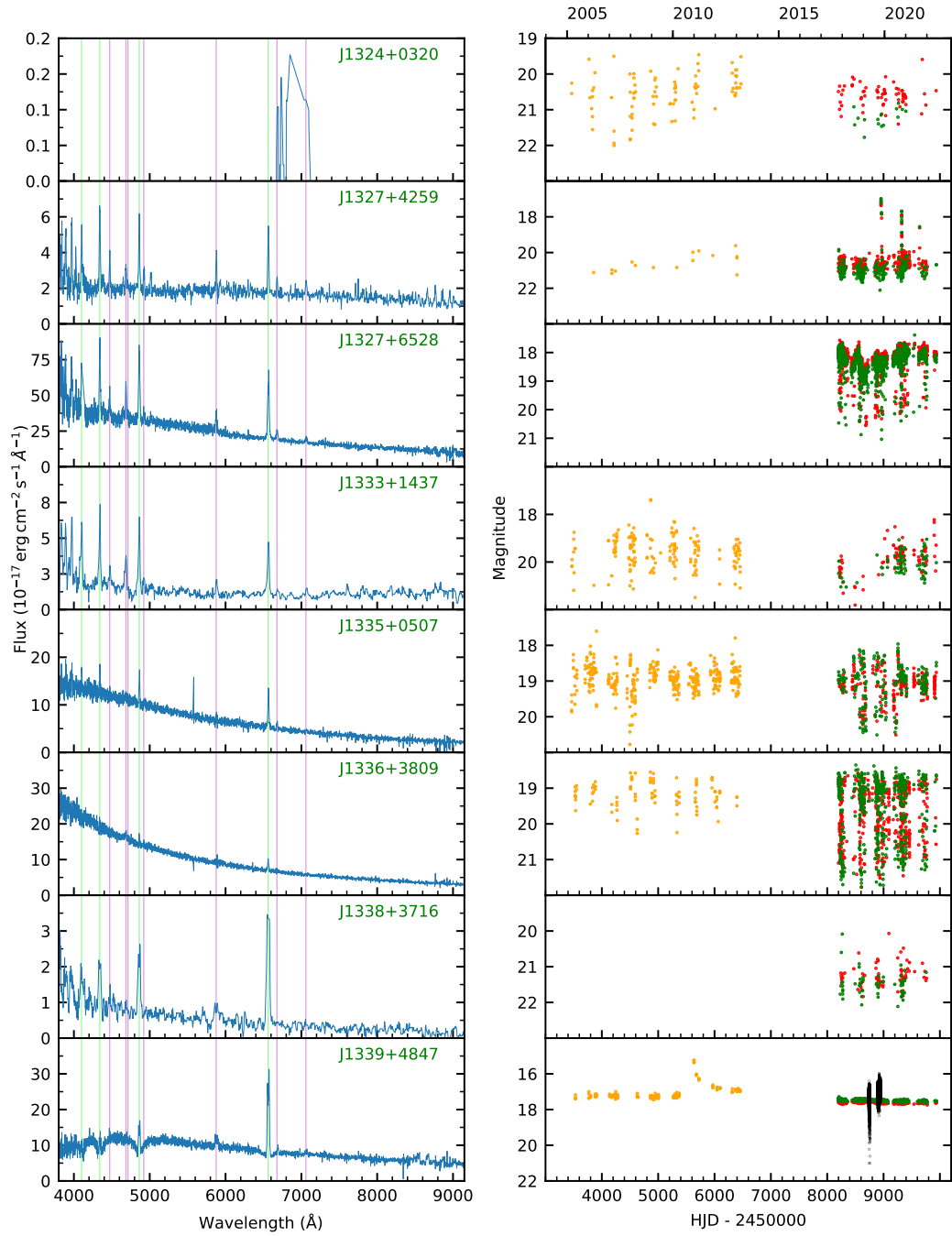


Figure B.40: Left panels: Spectra with H lines shown in green and He in pink. Right panels: Light curves with CRTS shown in orange, ZTF in red and green and *TESS* in black.

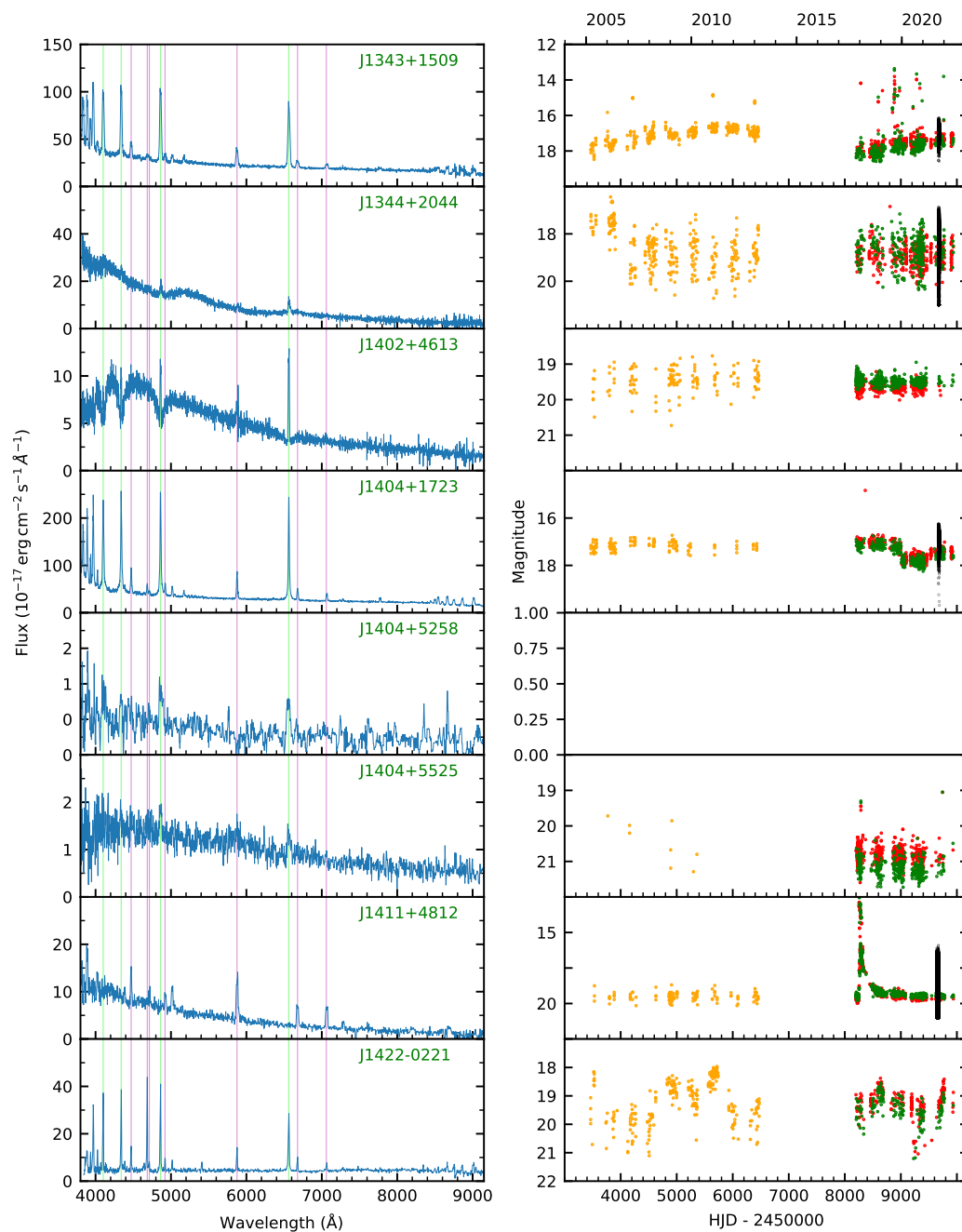


Figure B.41: Left panels: Spectra with H lines shown in green and He in pink. Right panels: Light curves with CRTS shown in orange, ZTF in red and green and *TESS* in black.

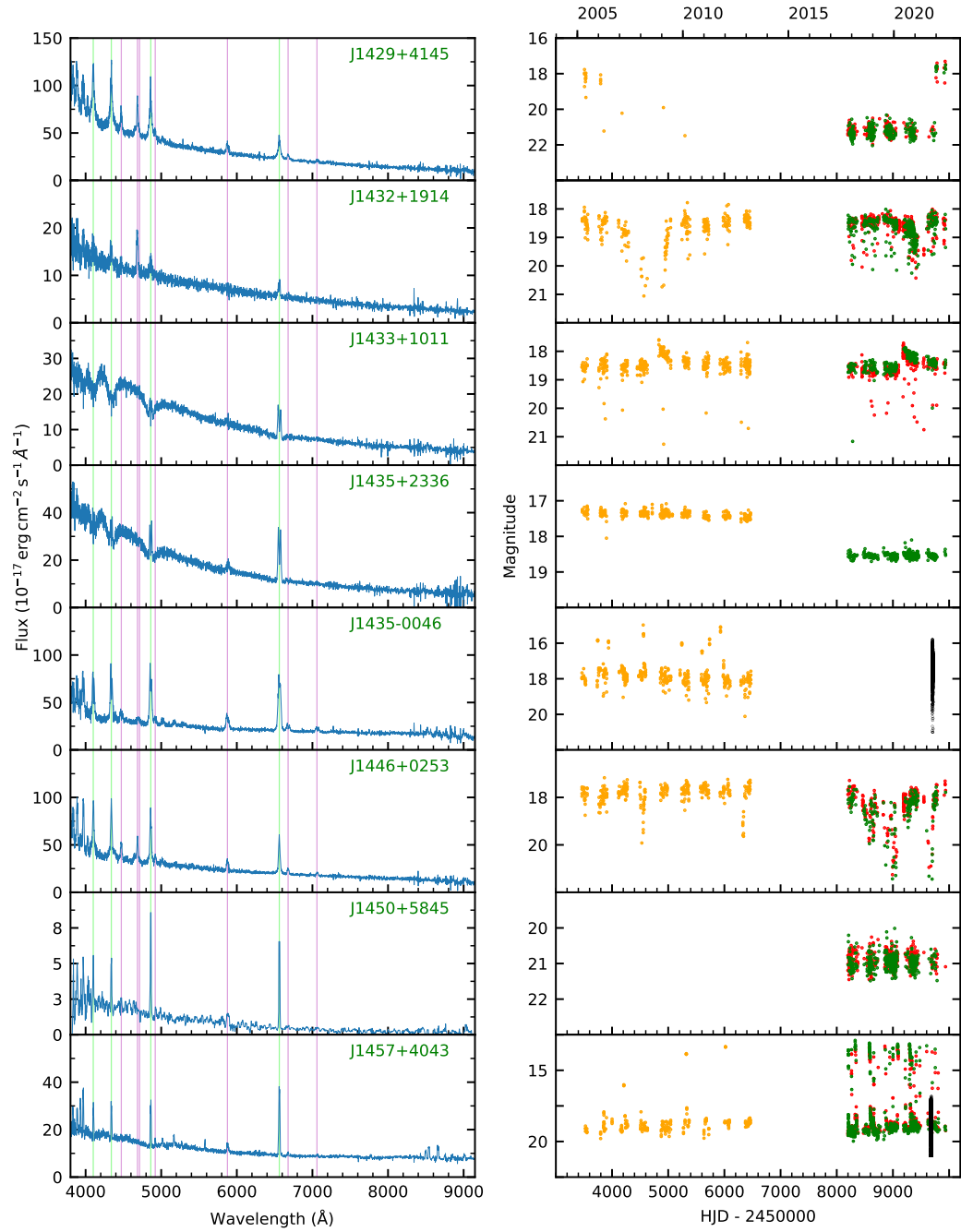


Figure B.42: Left panels: Spectra with H lines shown in green and He in pink. Right panels: Light curves with CRTS shown in orange, ZTF in red and green and *TESS* in black.

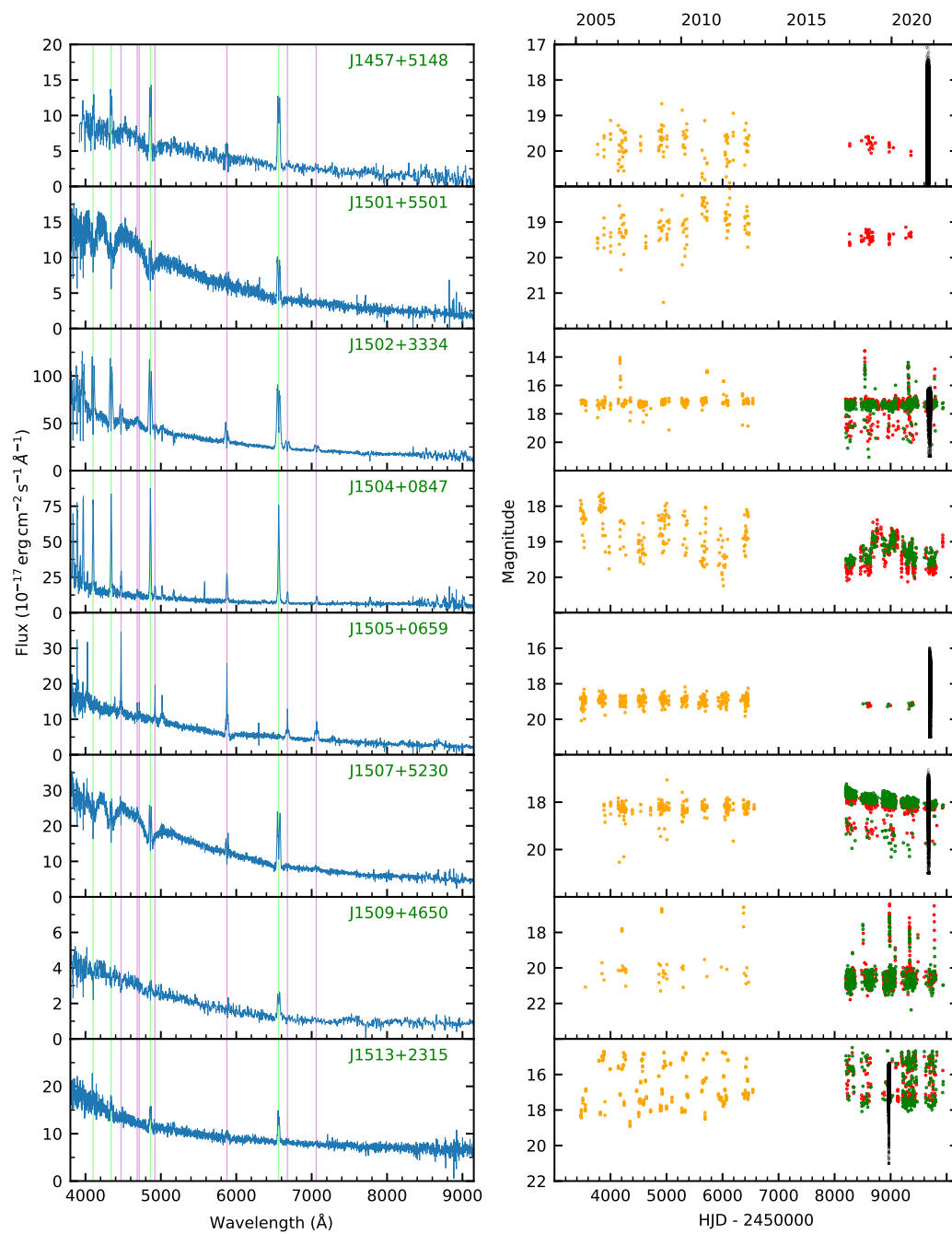


Figure B.43: Left panels: Spectra with H lines shown in green and He in pink. Right panels: Light curves with CRTS shown in orange, ZTF in red and green and *TESS* in black.

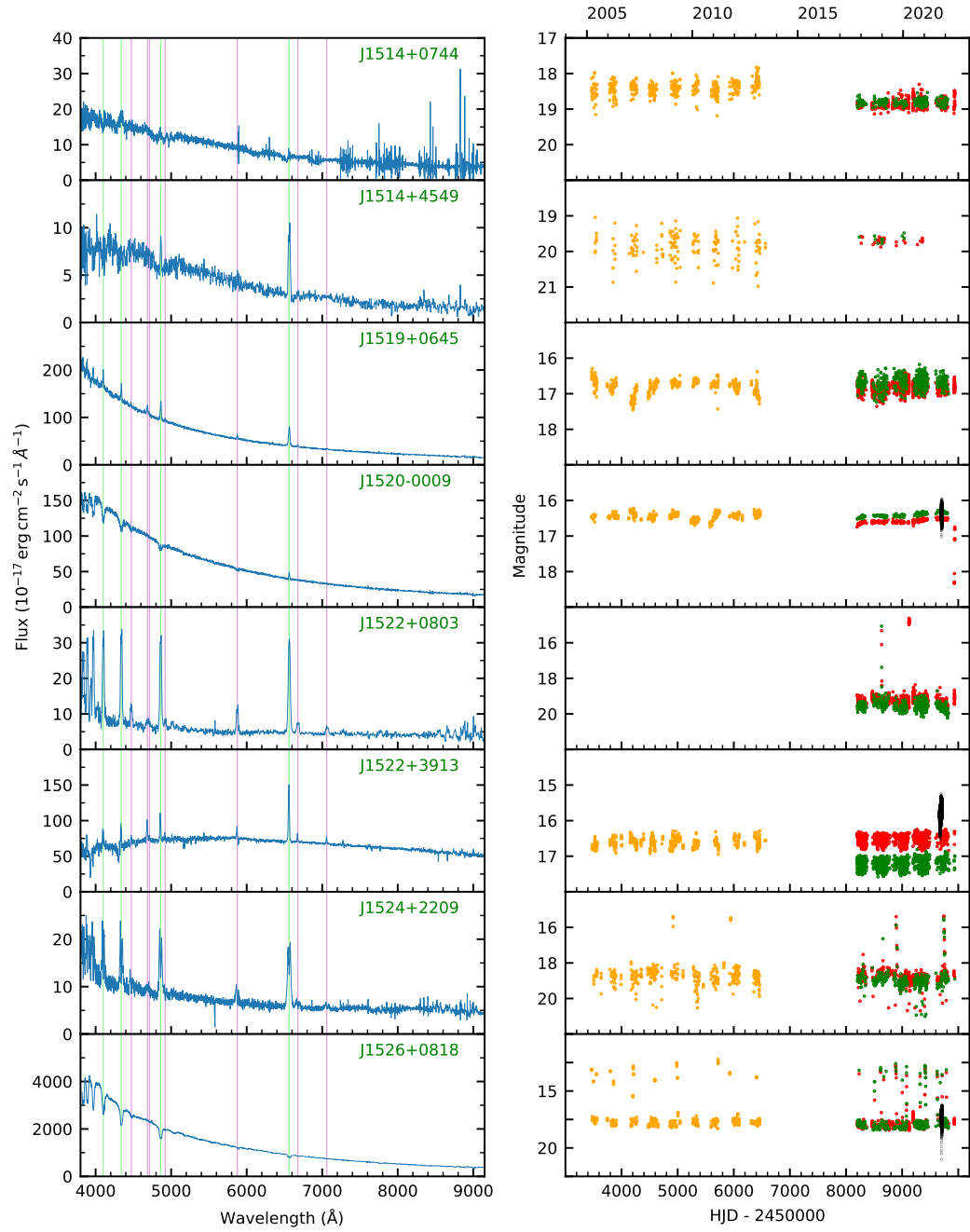


Figure B.44: Left panels: Spectra with H lines shown in green and He in pink. Right panels: Light curves with CRTS shown in orange, ZTF in red and green and *TESS* in black.

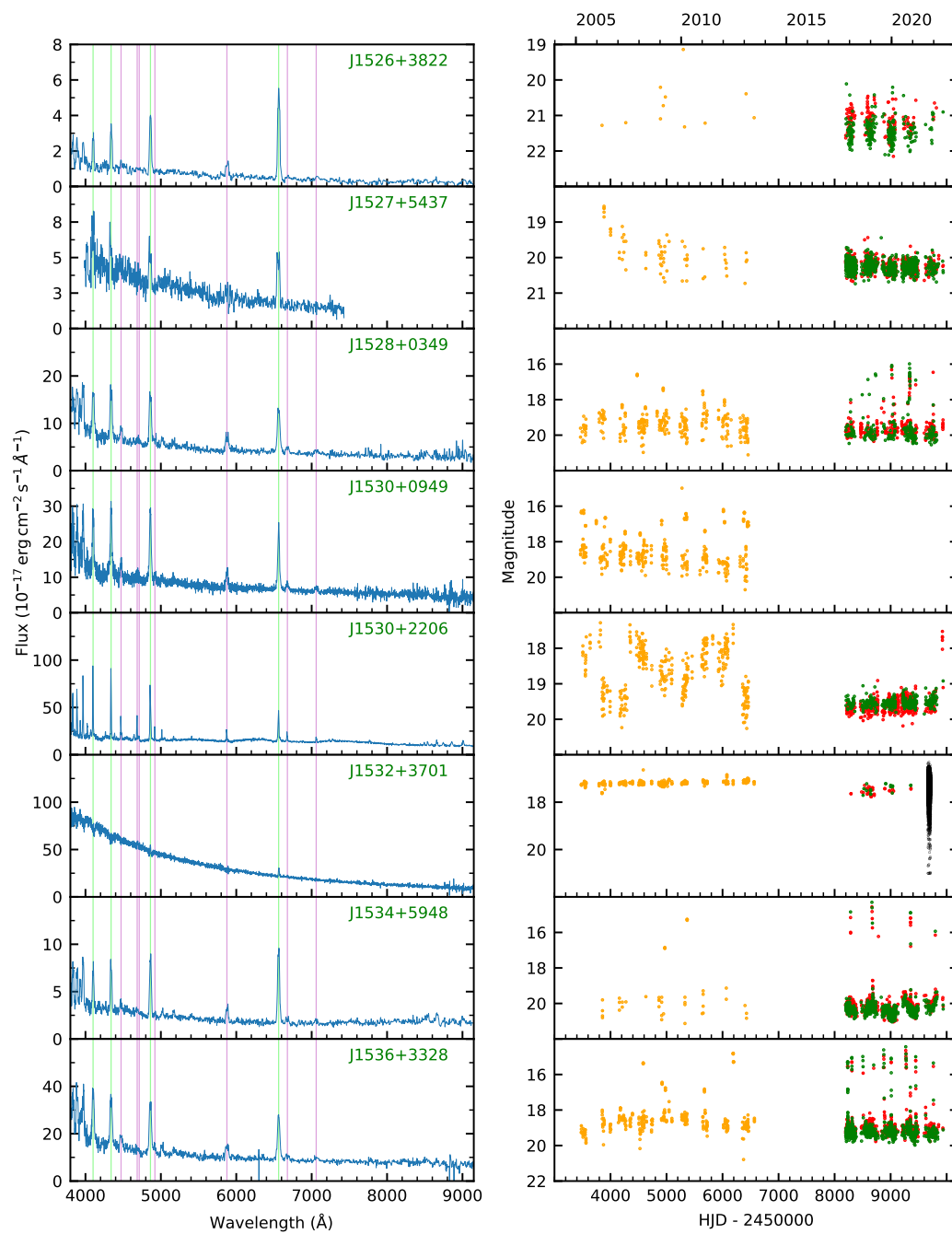


Figure B.45: Left panels: Spectra with H lines shown in green and He in pink. Right panels: Light curves with CRTS shown in orange, ZTF in red and green and *TESS* in black.

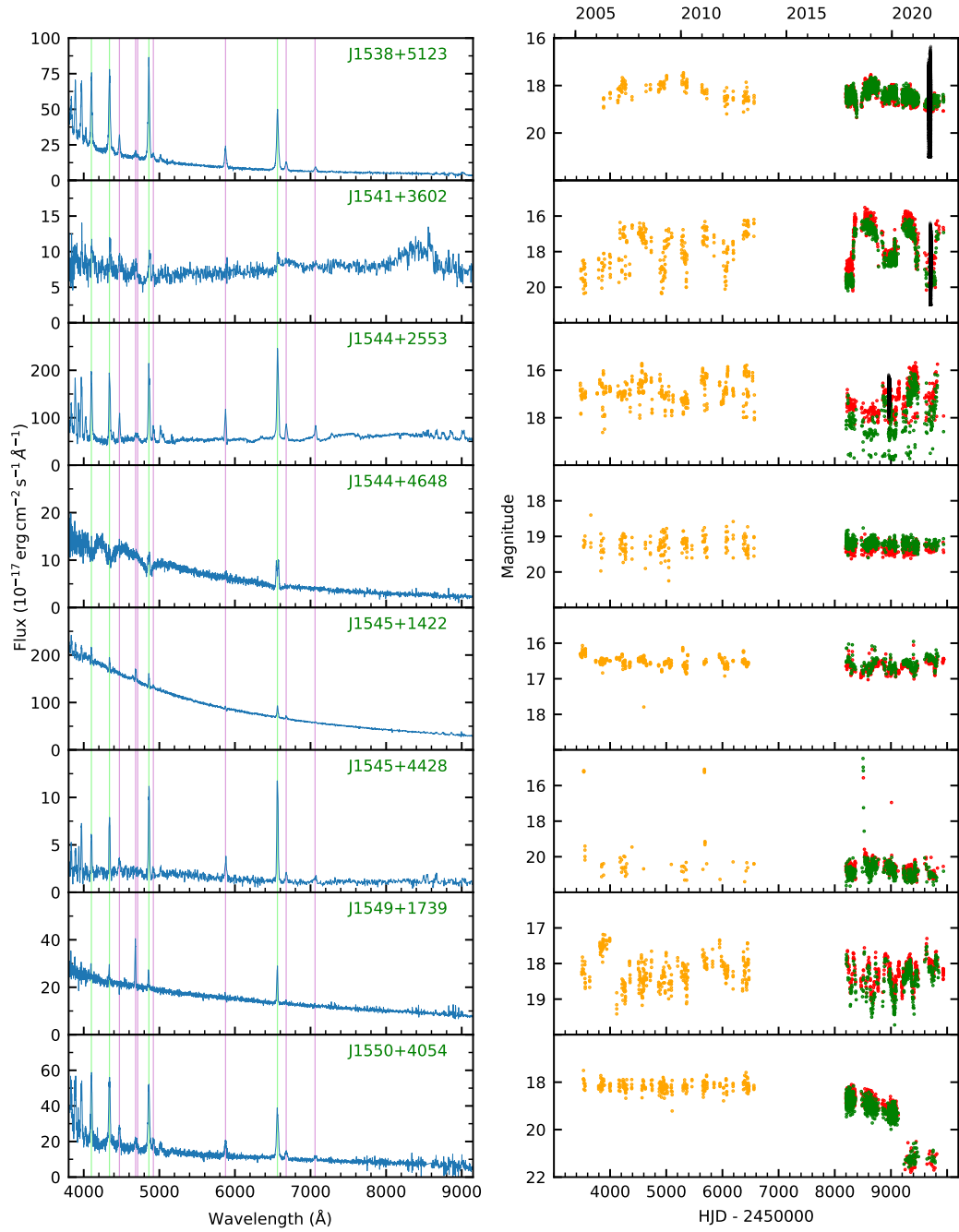


Figure B.46: Left panels: Spectra with H lines shown in green and He in pink. Right panels: Light curves with CRTS shown in orange, ZTF in red and green and *TESS* in black.

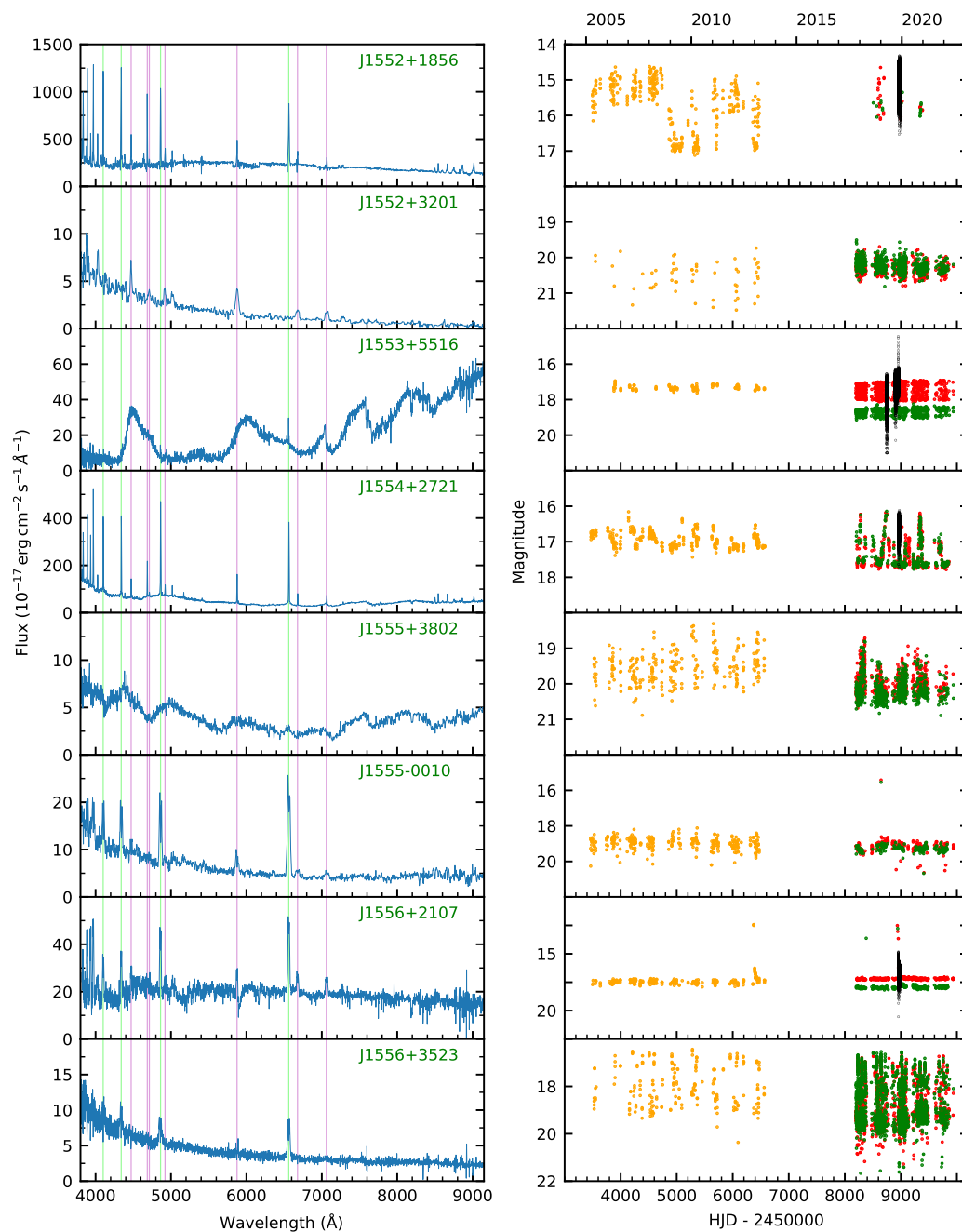


Figure B.47: Left panels: Spectra with H lines shown in green and He in pink. Right panels: Light curves with CRTS shown in orange, ZTF in red and green and *TESS* in black.

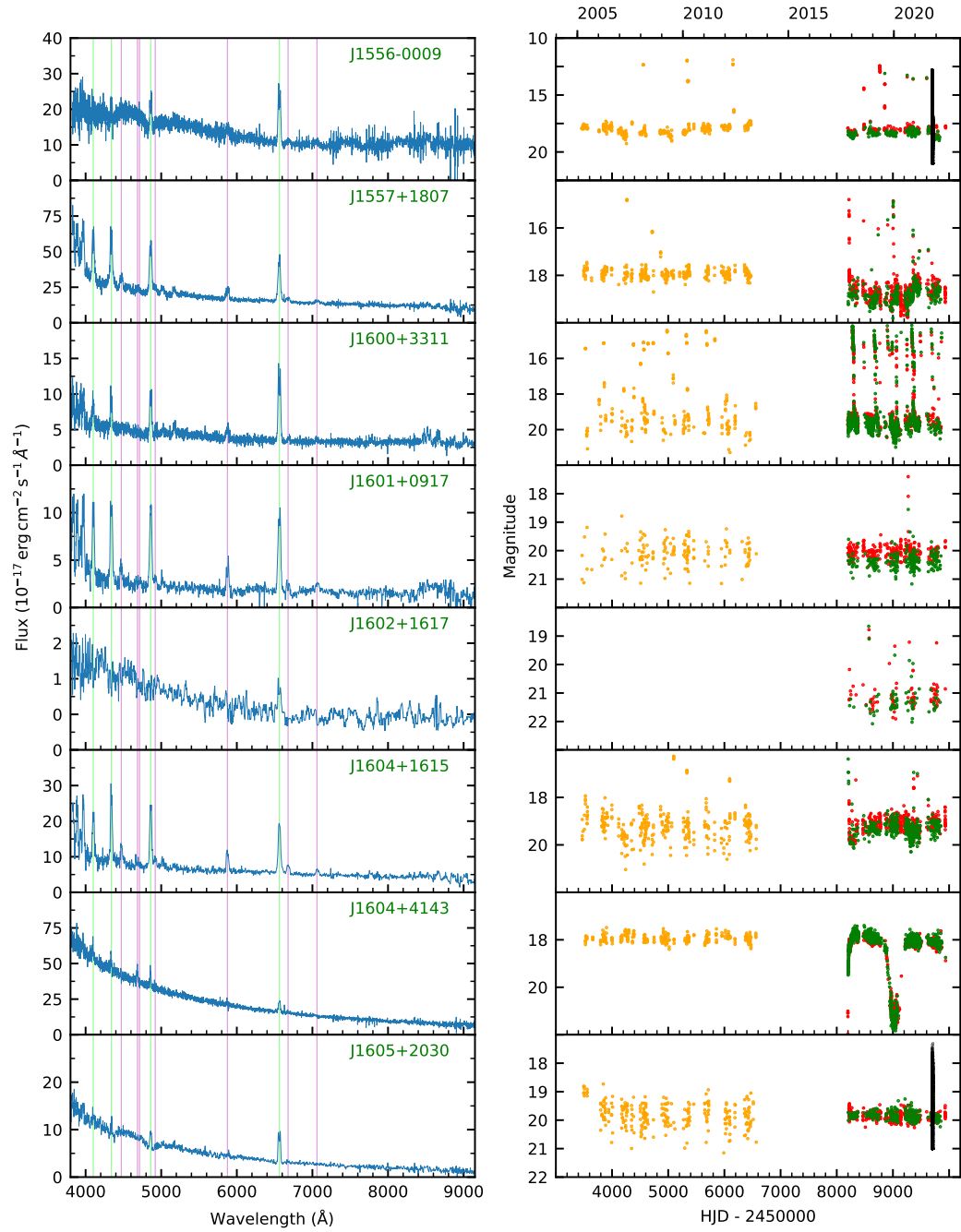


Figure B.48: Left panels: Spectra with H lines shown in green and He in pink. Right panels: Light curves with CRTS shown in orange, ZTF in red and green and *TESS* in black.

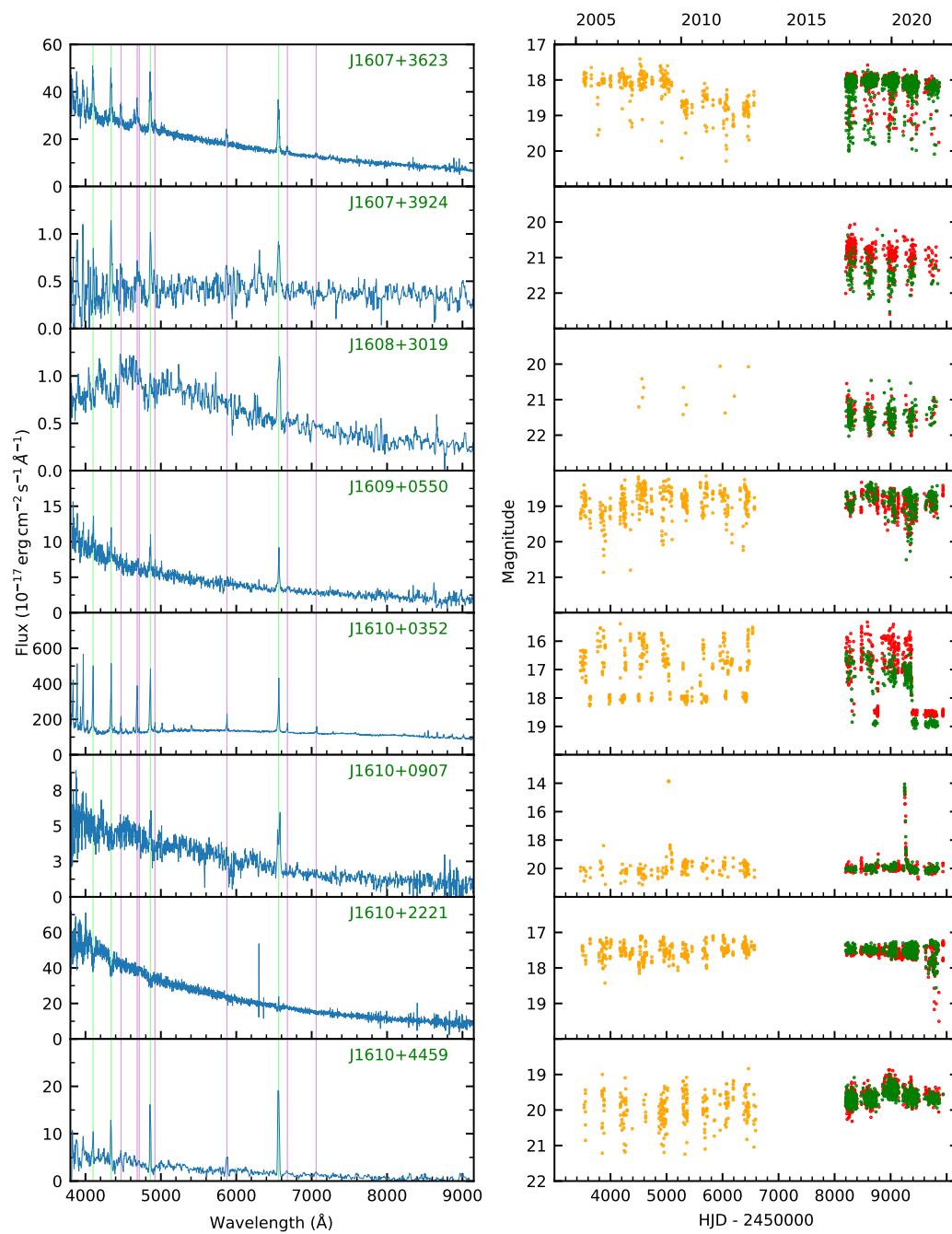


Figure B.49: Left panels: Spectra with H lines shown in green and He in pink. Right panels: Light curves with CRTS shown in orange, ZTF in red and green and *TESS* in black.

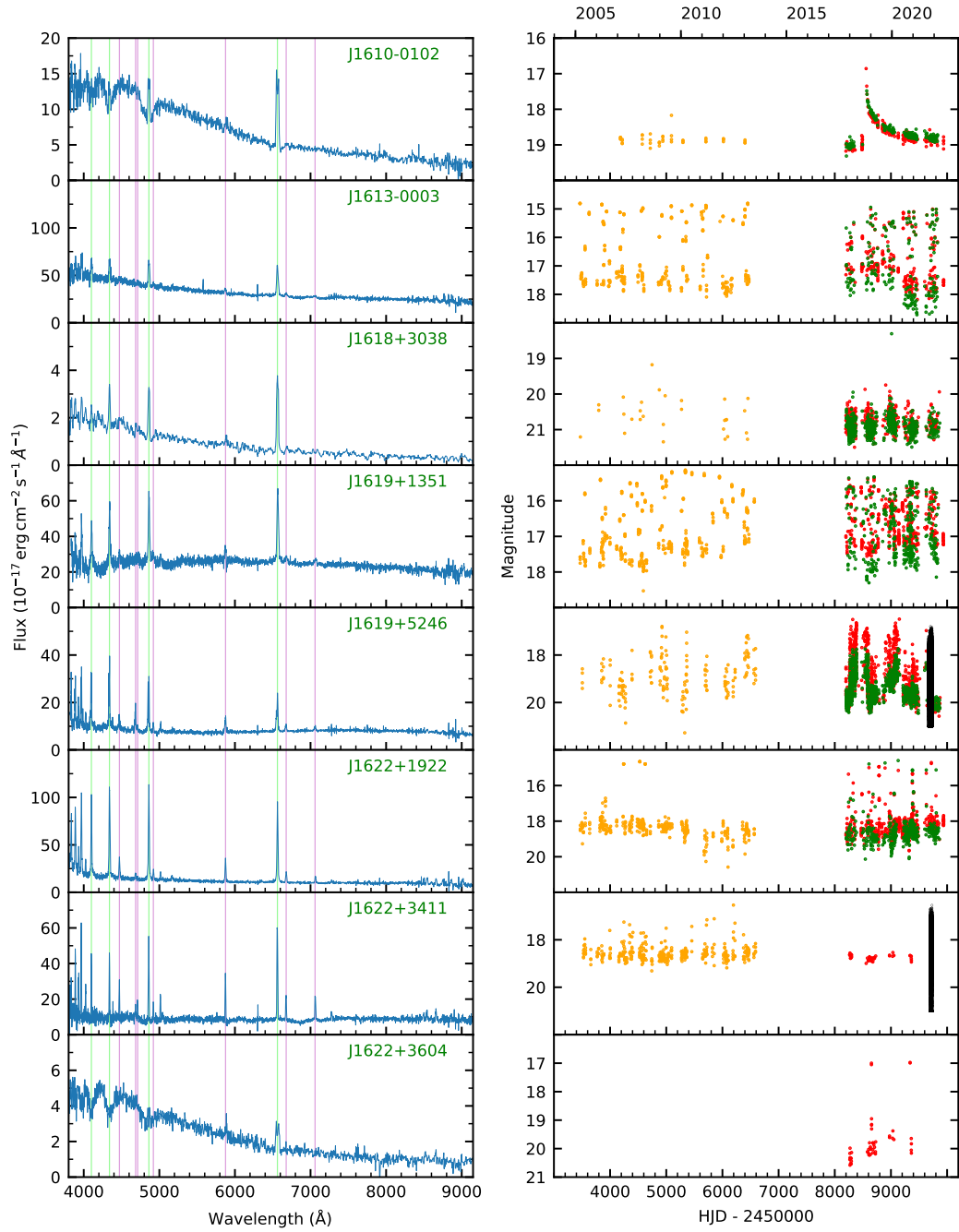


Figure B.50: Left panels: Spectra with H lines shown in green and He in pink. Right panels: Light curves with CRTS shown in orange, ZTF in red and green and *TESS* in black.

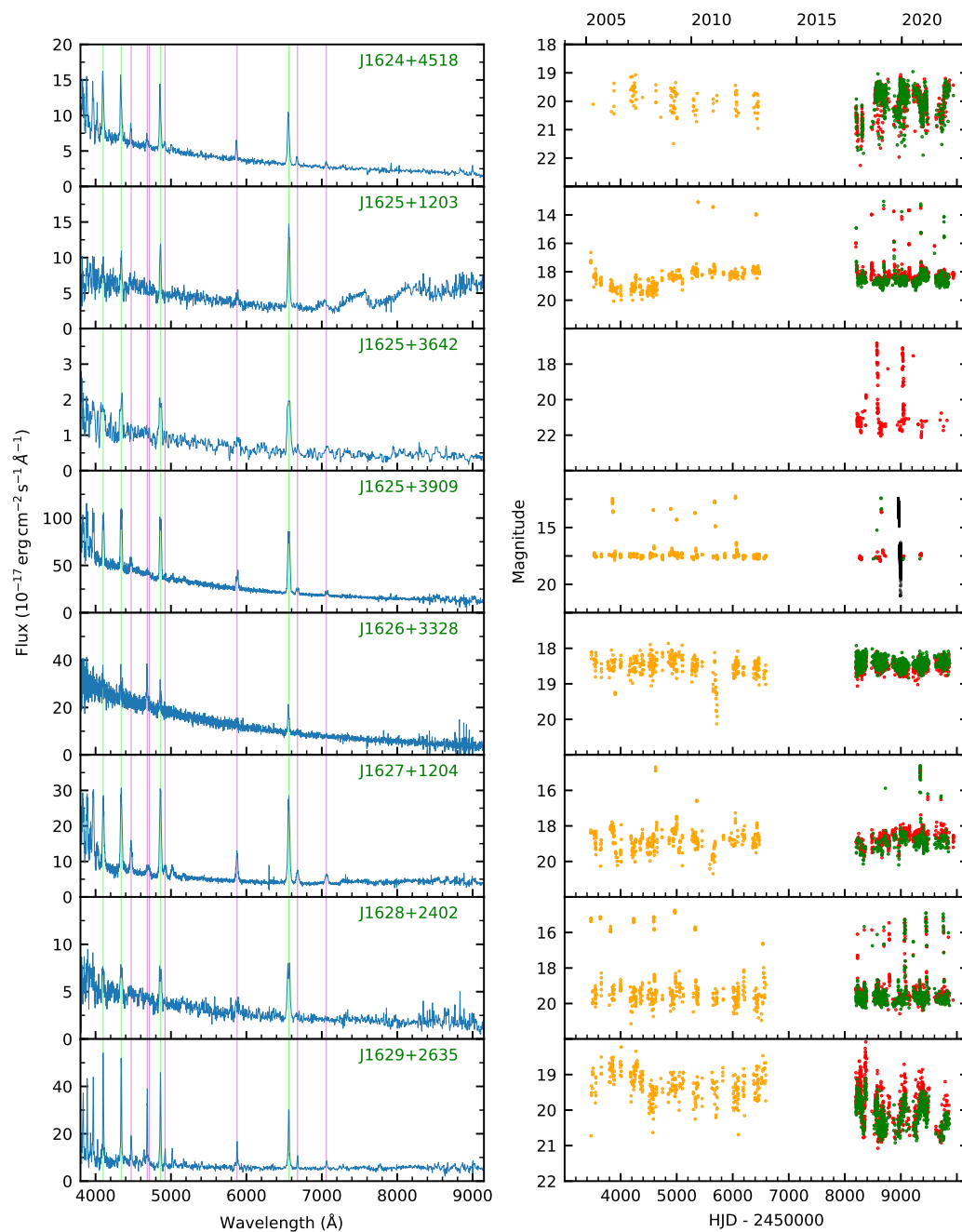


Figure B.51: Left panels: Spectra with H lines shown in green and He in pink. Right panels: Light curves with CRTS shown in orange, ZTF in red and green and *TESS* in black.

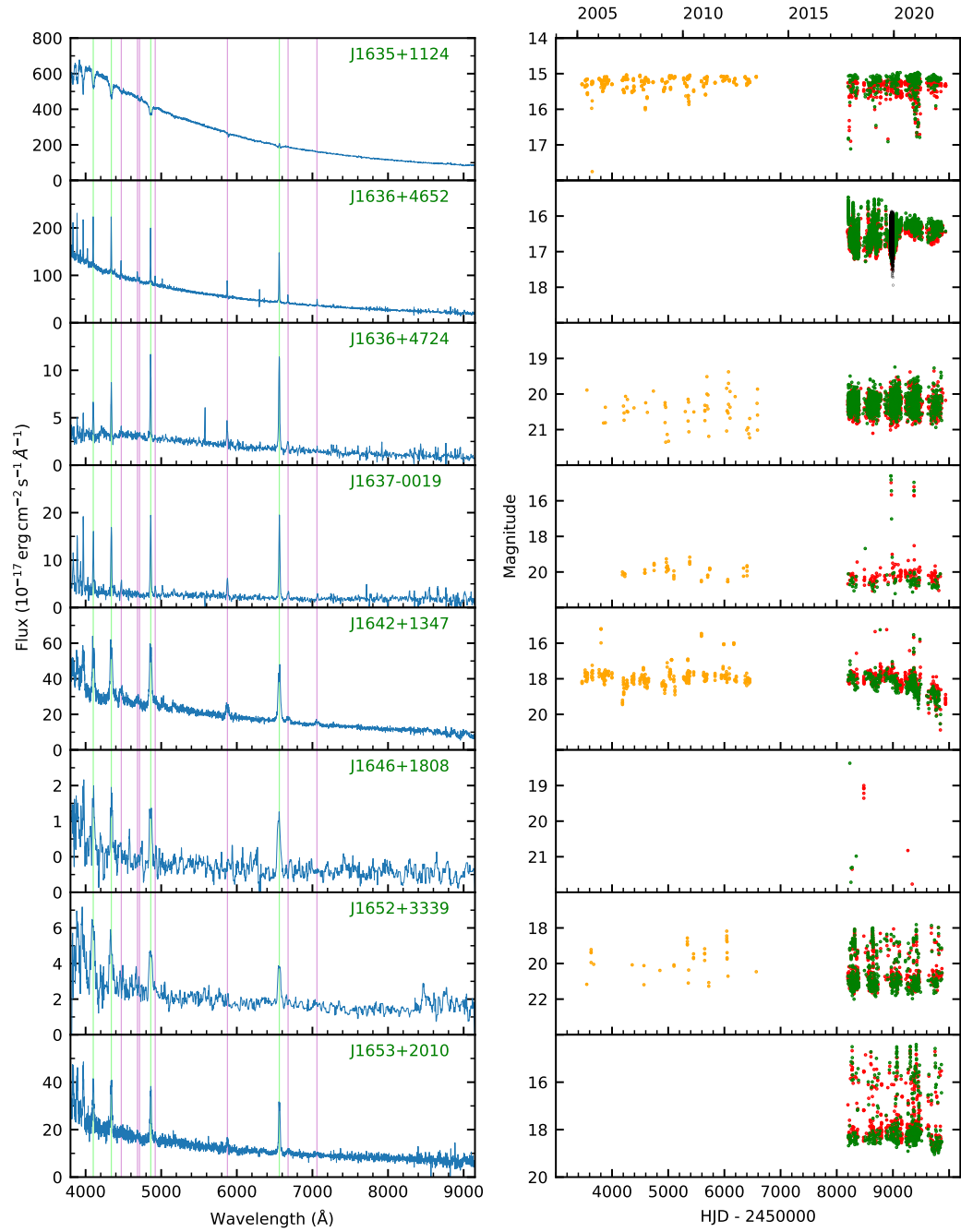


Figure B.52: Left panels: Spectra with H lines shown in green and He in pink. Right panels: Light curves with CRTS shown in orange, ZTF in red and green and *TESS* in black.

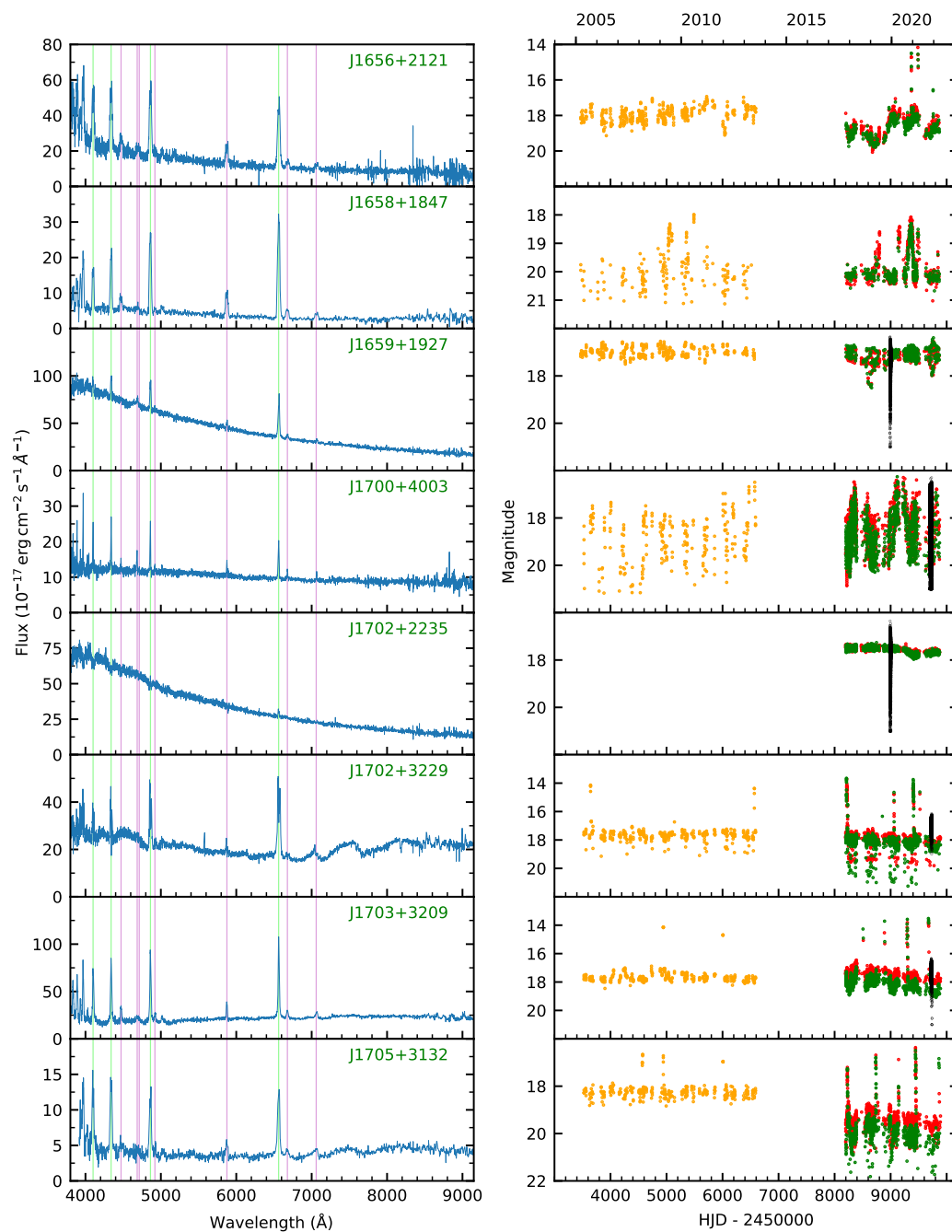


Figure B.53: Left panels: Spectra with H lines shown in green and He in pink. Right panels: Light curves with CRTS shown in orange, ZTF in red and green and *TESS* in black.

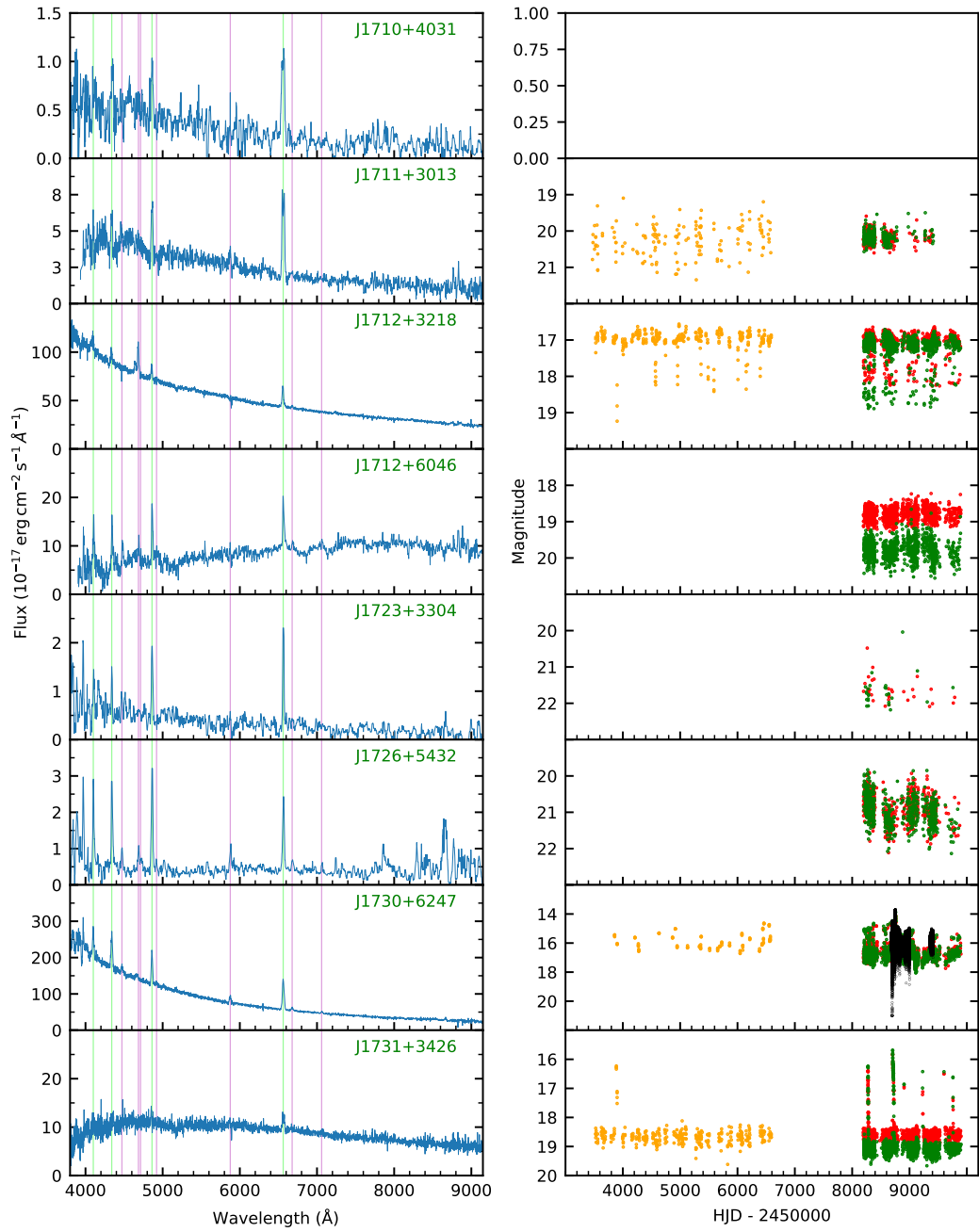


Figure B.54: Left panels: Spectra with H lines shown in green and He in pink. Right panels: Light curves with CRTS shown in orange, ZTF in red and green and *TESS* in black.

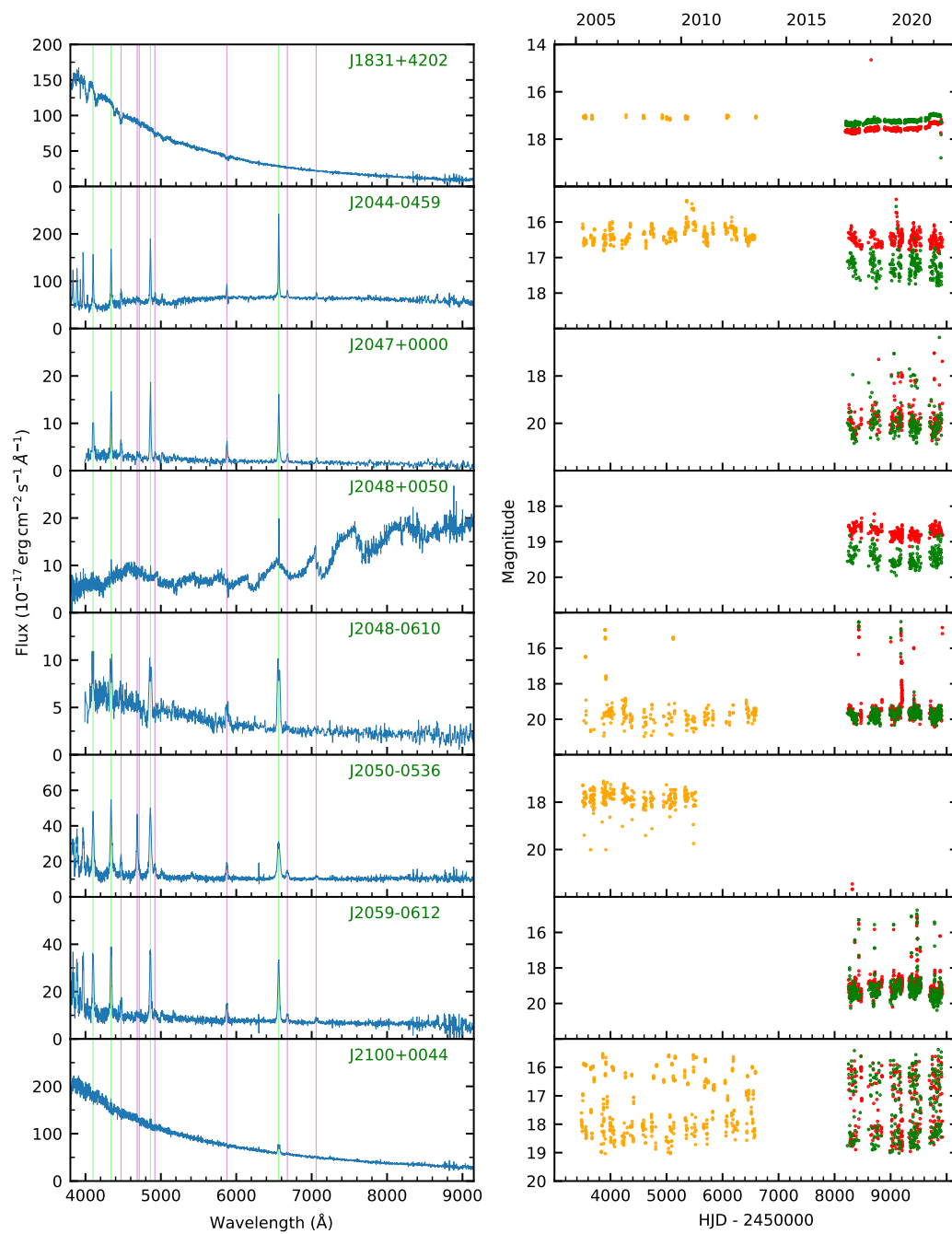


Figure B.55: Left panels: Spectra with H lines shown in green and He in pink. Right panels: Light curves with CRTS shown in orange, ZTF in red and green and *TESS* in black.

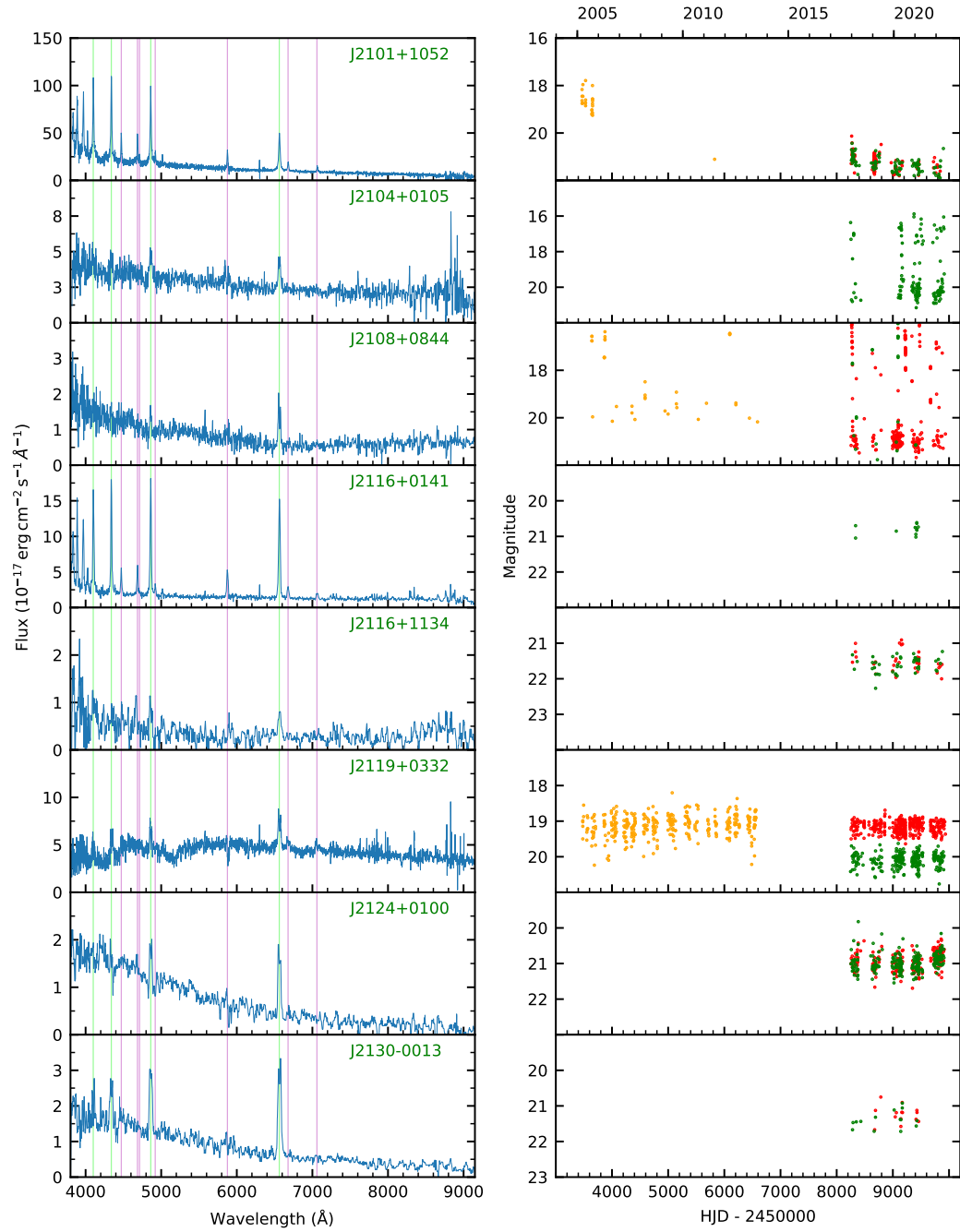


Figure B.56: Left panels: Spectra with H lines shown in green and He in pink. Right panels: Light curves with CRTS shown in orange, ZTF in red and green and *TESS* in black.

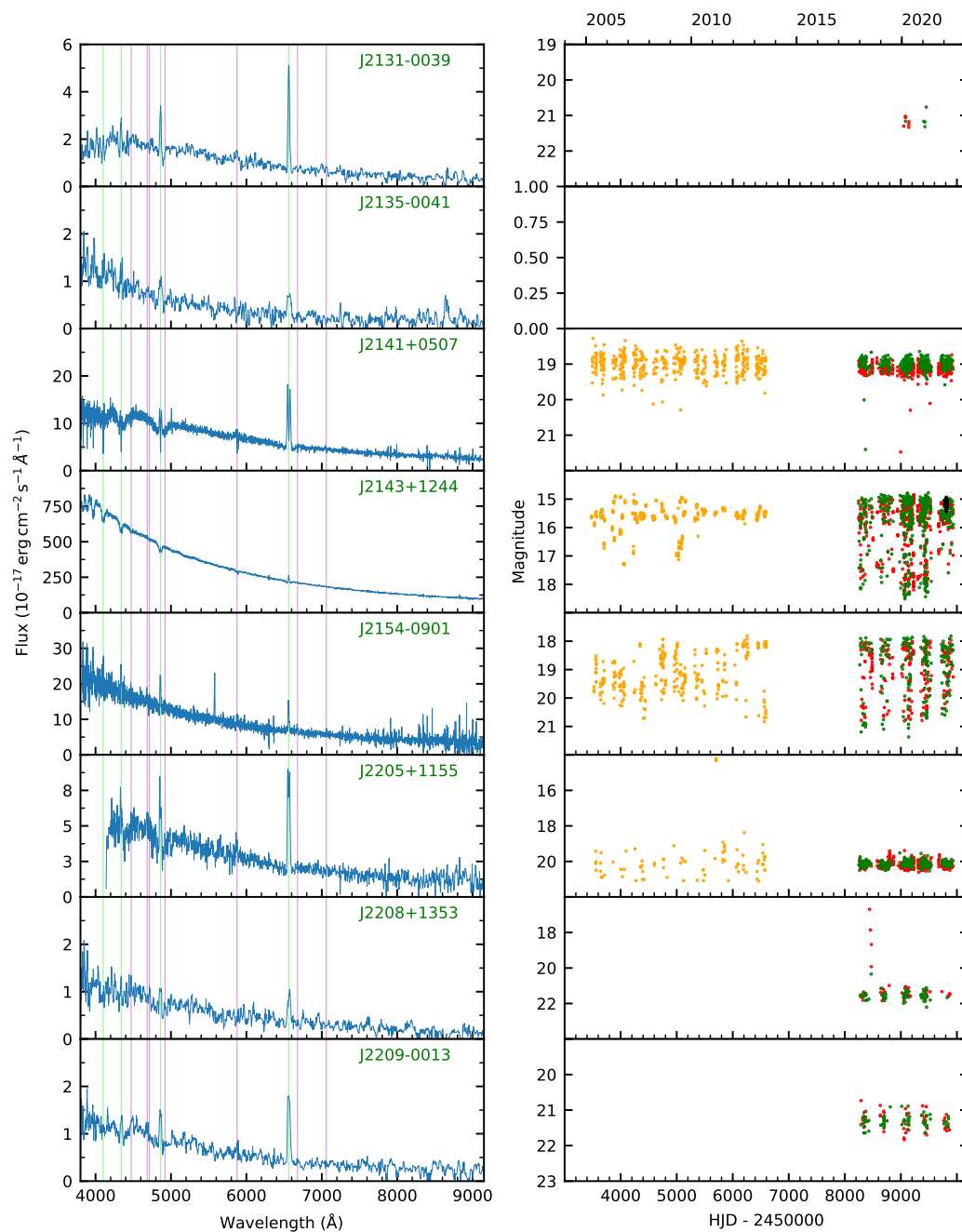


Figure B.57: Left panels: Spectra with H lines shown in green and He in pink. Right panels: Light curves with CRTS shown in orange, ZTF in red and green and *TESS* in black.

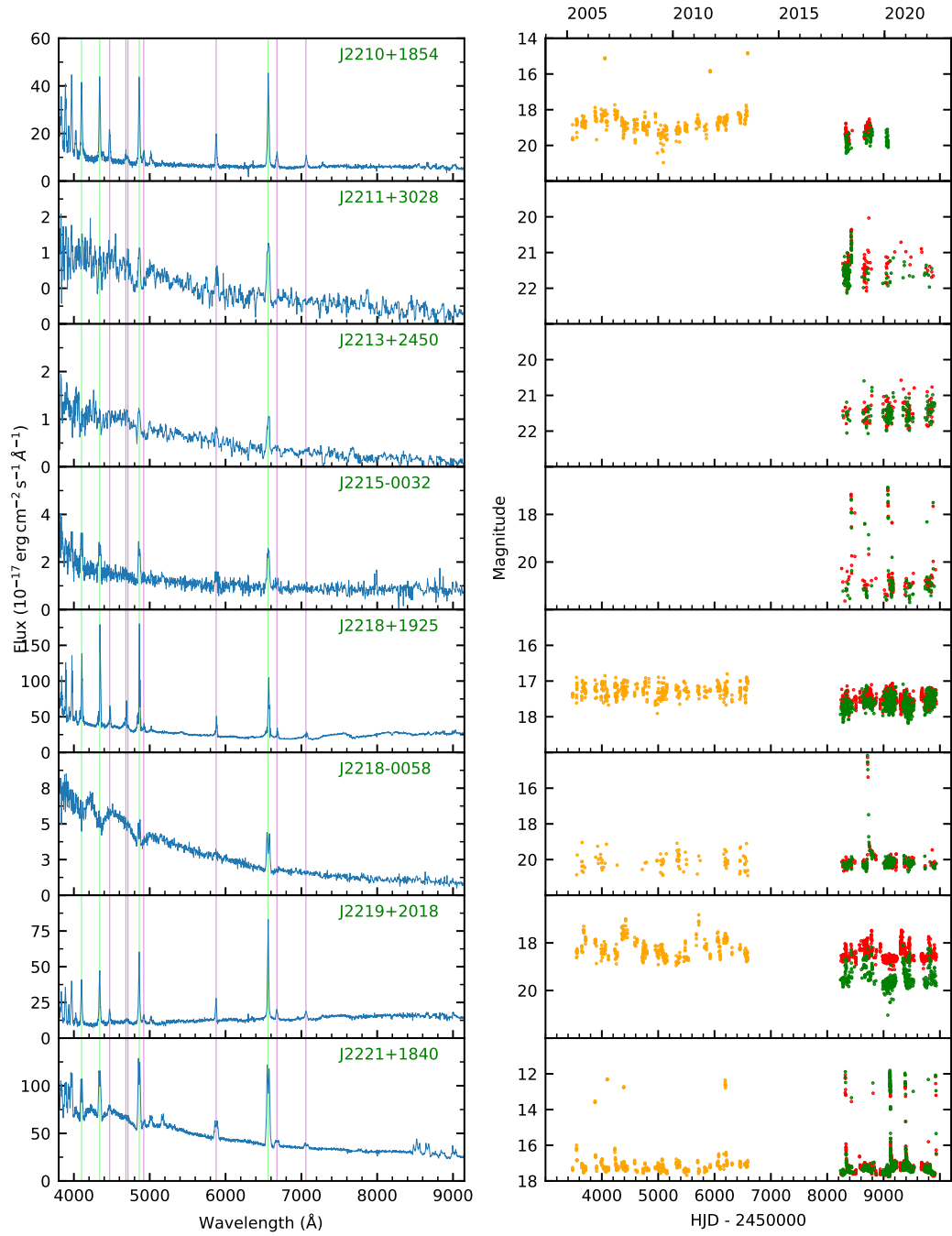


Figure B.58: Left panels: Spectra with H lines shown in green and He in pink. Right panels: Light curves with CRTS shown in orange, ZTF in red and green and *TESS* in black.

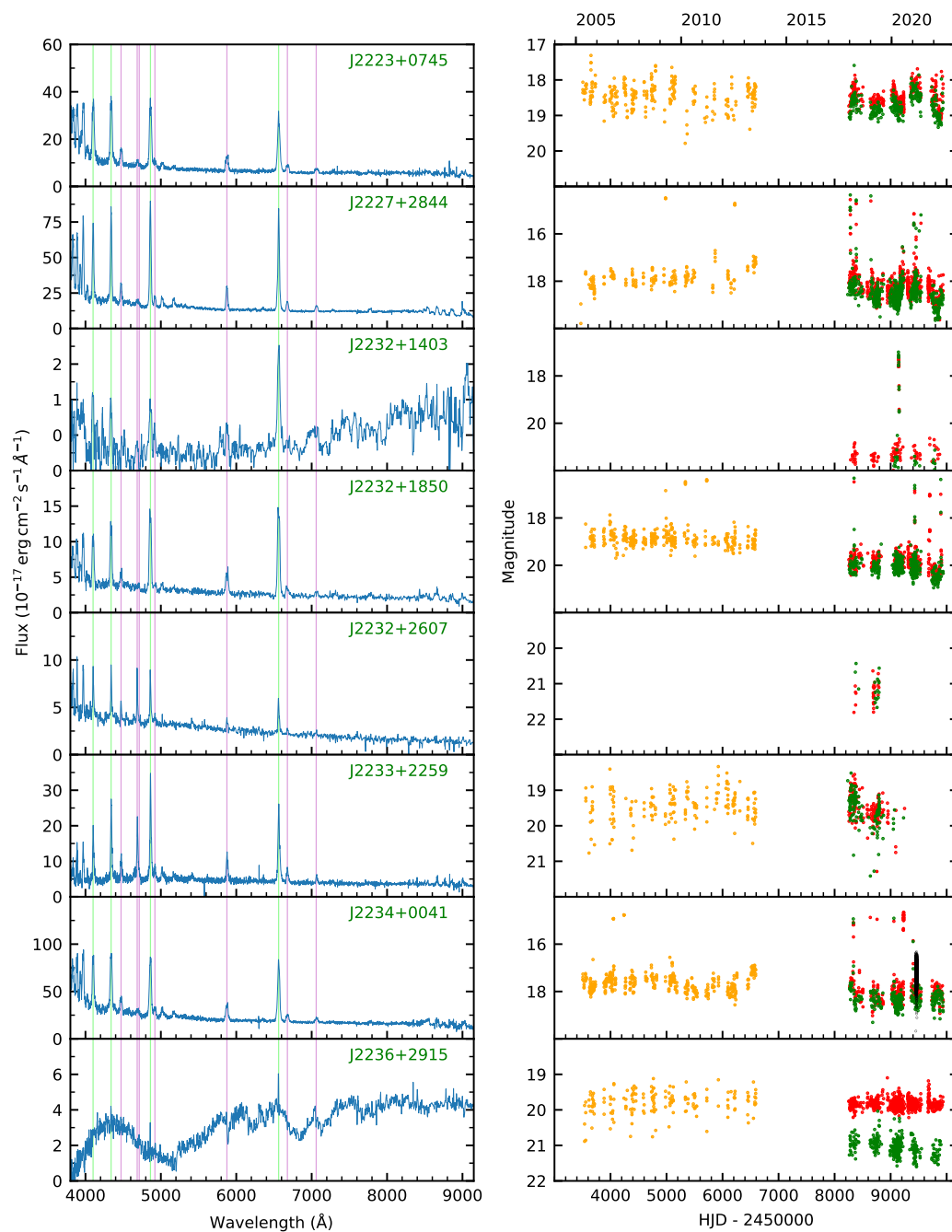


Figure B.59: Left panels: Spectra with H lines shown in green and He in pink. Right panels: Light curves with CRTS shown in orange, ZTF in red and green and *TESS* in black.

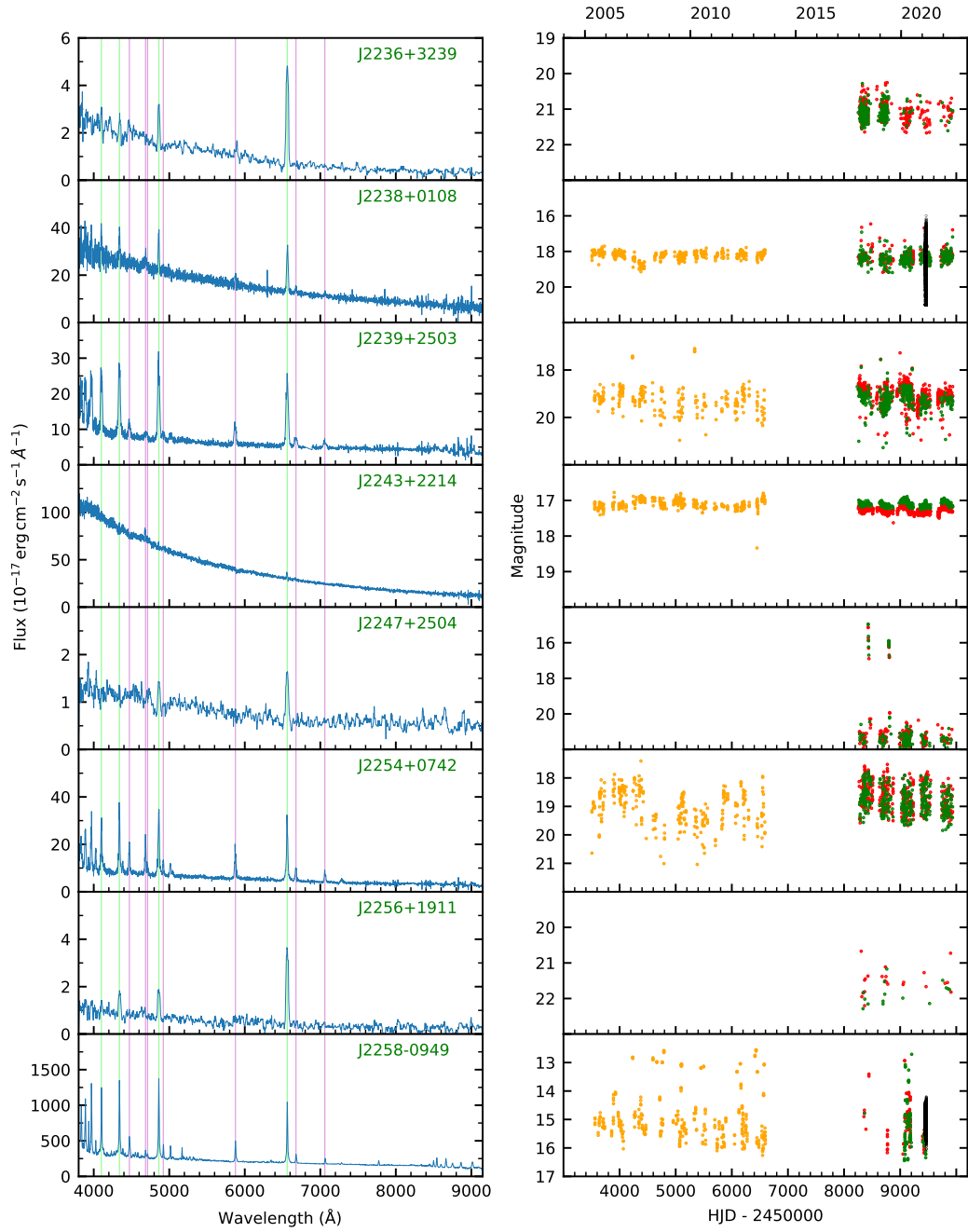


Figure B.60: Left panels: Spectra with H lines shown in green and He in pink. Right panels: Light curves with CRTS shown in orange, ZTF in red and green and *TESS* in black.

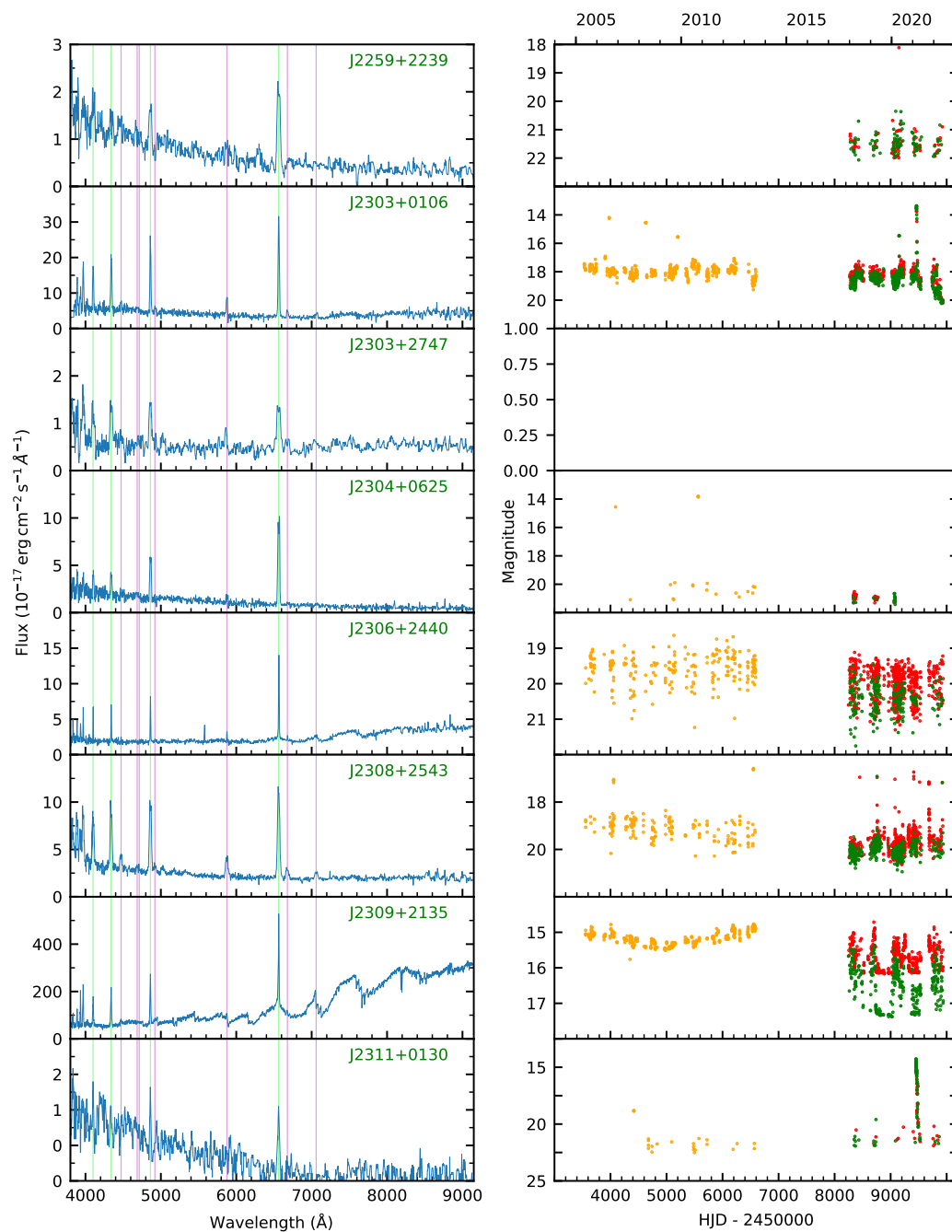


Figure B.61: Left panels: Spectra with H lines shown in green and He in pink. Right panels: Light curves with CRTS shown in orange, ZTF in red and green and *TESS* in black.

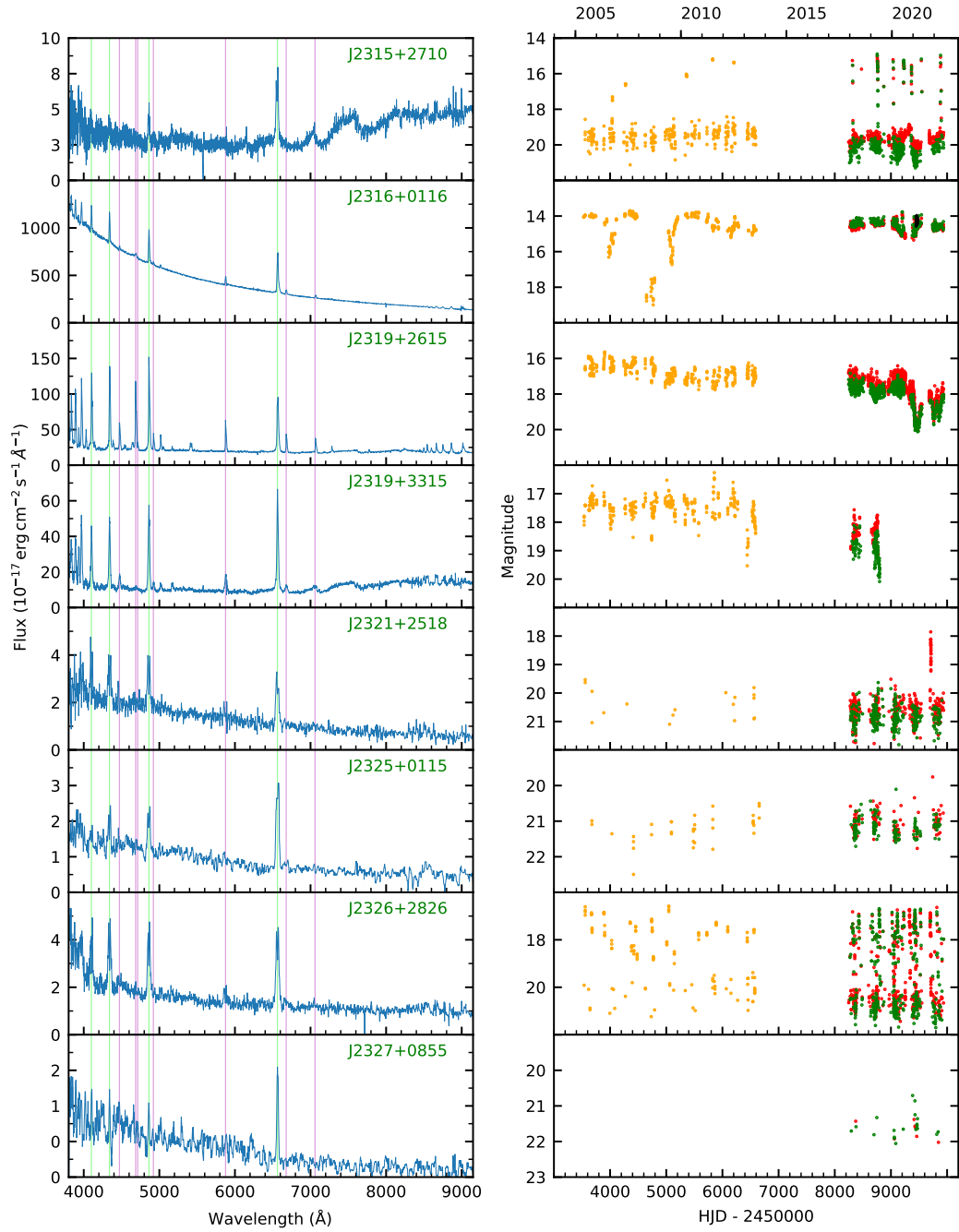


Figure B.62: Left panels: Spectra with H lines shown in green and He in pink. Right panels: Light curves with CRTS shown in orange, ZTF in red and green and *TESS* in black.

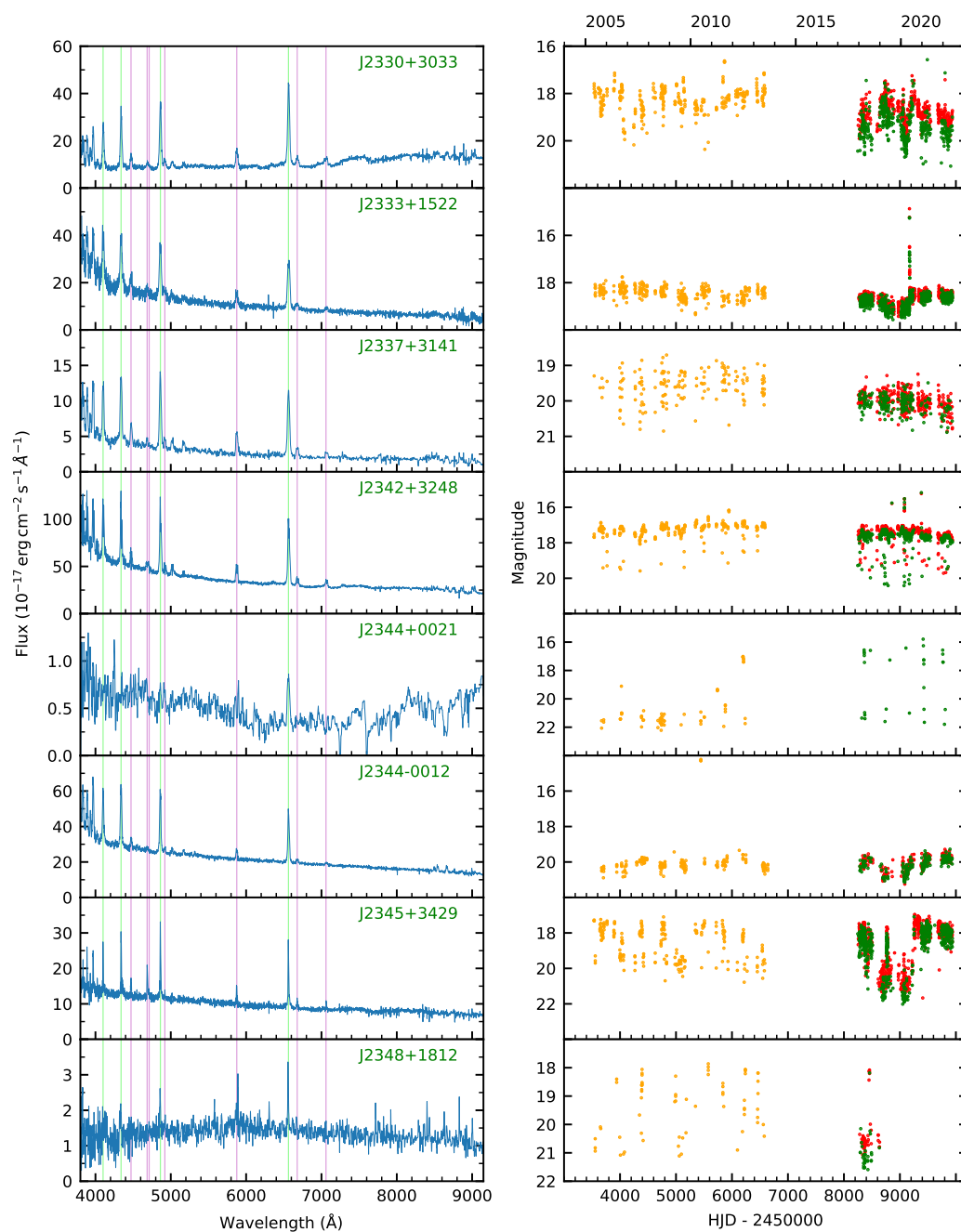


Figure B.63: Left panels: Spectra with H lines shown in green and He in pink. Right panels: Light curves with CRTS shown in orange, ZTF in red and green and *TESS* in black.

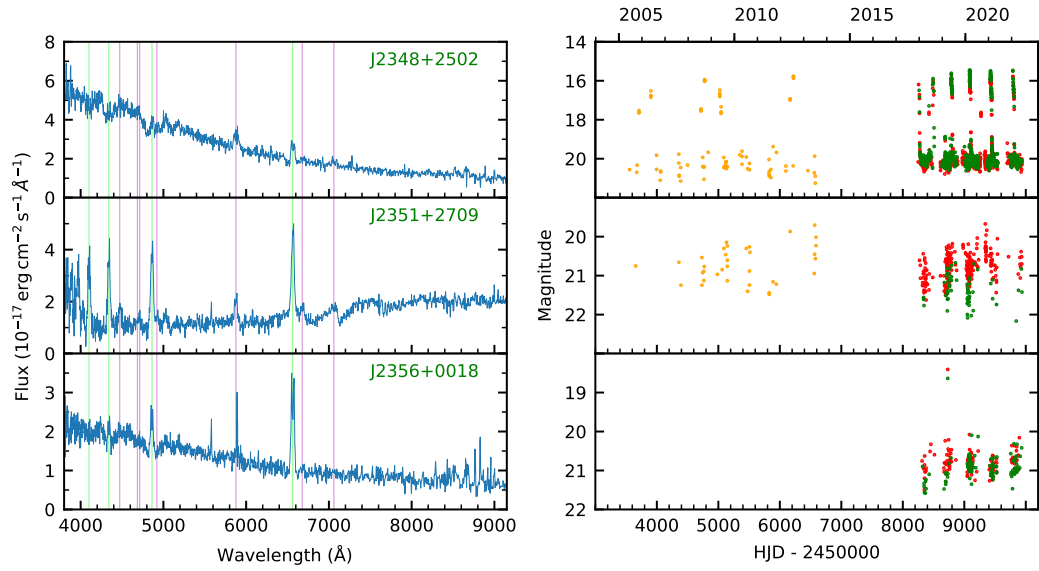


Figure B.64: Left panels: Spectra with H lines shown in green and He in pink. Right panels: Light curves with CRTS shown in orange, ZTF in red and green and *TESS* in black.

B.5 SDSS plate, MJD and fibre list

Table B.2: Plate, MJD and fibre references for CVs in the paper.

SDSS name	Other name	Plate	MJD	Fibre
J000014.74+255603.1		7666	57339	847
J000720.77+200721.6	CSS 110921:000721+200722	6171	56311	312
J000844.32-014014.6	Gaia15abi	7863	56975	619
J001107.26+303235.9	V0402 And	7745	58077	356
J001153.08-064739.2	SDSS J001153.08-064739.1	3134	54806	600
J001158.28+315543.7	CSS 101111:001158+315544	7745	58077	687
J001231.54+280011.1		7694	57359	568
J001538.25+263656.7	CSS 090918:001538+263657	7694	57359	325
J001856.92+345444.2	V0479 And	1468	52999	163
J002049.51+280020.2	MASTER OT J002049.54+280020.5	7694	57359	938
J002243.55+061002.7	MGAB-V295	8746	58396	768
		11313	58426	447
J002500.17+073349.2	CSS 081123:002500+073350	4537	55806	998
		4539	55865	533
		11313	58426	640
J002637.05+242915.6	CSS 091026:002637+242916	7661	57286	736
J002728.00-010828.5	EN Cet	1493	52933	204
J002842.53+311819.4		7741	58078	70
J002910.96+324125.8		6530	56537	324
J003151.76+202051.0	MGAB-V534	7589	56946	200
J003153.46+084118.5	ASASSN-17kg	4540	55863	302
J003203.62+314510.4	CSS 091220:003204+314510	7741	58078	15
J003459.90+273619.0	CSS 081031:003460+273620	7671	57360	492
J003640.29+230831.3	ASASSN-14dr	7615	56977	878
J003827.05+250924.9	1RXS J003828.7+250920	6284	56310	222
		7660	57357	60
J003941.06+005427.4	SDSS J003941.06+005427.5	690	52261	568
J004213.04+073137.8	PB 6108	4543	55888	480
J004335.13-003729.8	SDSS J004335.14-003729.8	1085	52531	175
J004500.31+222707.2	CSS 081102:004500+222708	7617	56949	700
J004849.86+332832.9		7719	58082	621
J004902.10+074726.8	CSS 090204:004902+074726	11054	58424	725
J004924.50+222617.9		5700	56245	516

SDSS name	Other name	Plate	MJD	Fibre
J005050.87+000912.7	GS Cet	1496	52883	493
J005217.22+315938.5		6872	56540	230
J005421.90+334815.7		7720	58101	572
J005657.57+320621.7	MGAB-V3456	7722	58425	504
J005811.09-010750.8	ASASSN-16iw	7872	57279	203
J010340.75+200525.9		7624	57039	223
J010411.63-031342.3	CSS 091009:010412-031341	7915	57309	559
J010844.12+022638.9	MGAB-V3459	7859	57282	723
J011011.29+033234.6	XY Psc	8756	57687	138
J011331.69-033233.5		7914	57331	531
J011516.54+245530.2	CSS 101008:011517+245530	7681	57042	746
J011712.94+175527.0	ASASSN-20pq	7621	56985	340
J012008.20+185715.5		7621	56985	798
J012212.21+075546.8		11077	58433	926
J012402.25+211359.7		7635	56979	481
J012838.37+184535.6	CSS 100114:012838+184536	5135	55862	59
J012842.13+113050.4	CSS 141018:012842+113051	11069	58456	389
J012940.05+384210.4	V0744 And	2062	53381	22
J013132.38-090122.2	GY Cet	662	52147	384
		662	52178	384
		2878	54465	585
J013421.83+042200.0		8759	57700	686
J013540.99+340132.9		7729	58135	854
J013701.06-091234.8	GZ Cet	662	52147	552
		662	52178	541
J013737.20+300248.6	TX Tri	7731	58130	177
J014121.21+062007.6		8755	58138	844
		11071	58429	44
J014227.07+001729.8	SDSS J014227.07+001729.8	4231	55444	808
J014245.89+232339.8	ASASSN-18ad	7638	56981	577
J014732.85+144443.3		4658	55592	862
		11052	58438	886
J015051.52+332621.8	CSS 111006:015052+332622	7735	58136	526
J015151.86+140047.1	BG Ari	430	51877	430
		11045	58485	387
J015253.39-004350.4		7840	57003	295
J015543.39+002807.1	FL Cet	403	51871	423
J015712.18+224402.6	CSS 130916:015712+224402	7637	56933	191

SDSS name	Other name	Plate	MJD	Fibre
J015803.40+282303.6		7691	57040	710
		10000	57346	710
		7691	57360	696
		10000	57716	692
		7691	58124	708
		10000	58141	706
		10000	58462	688
		7691	58487	710
		10000	58514	706
J020348.61+295925.7	AI Tri	7737	57722	164
J020537.55+264304.1	ASASSN-13dh	7659	57060	438
J020712.71-014116.2		4347	55830	930
J021107.98+305406.7	Gaia18aot	7738	58100	351
J022319.71-052002.3		6369	56217	255
		7236	56605	142
J022940.29-030620.8	CSS 130930:022940-030620	7832	56904	52
		7881	57282	757
J023003.79+260440.3	SDSS J023003.79+260440.3	2399	53764	405
J023046.26-004531.1		6370	56238	106
		6780	56267	102
		6780	56577	104
		6780	56605	106
J023151.47-000511.4		6370	56238	79
		6780	56267	73
		6780	56577	73
		6780	56605	77
J023322.60+005059.5	HP Cet	407	51820	592
		6781	56274	599
		6781	56575	579
		6781	56599	575
J024215.05-011054.4		6782	56273	370
		6782	56572	370
		6782	56576	362
		6782	56602	362
J025214.63+002010.6	ASASSN-21rq	7820	56984	538
J031051.66-075500.2	KY Eri	459	51924	222
J032651.73+011513.3	CSS 100219:032652+011513	1064	52577	459
		1516	52933	450

SDSS name	Other name	Plate	MJD	Fibre
J032855.00+052254.1	SDSS J032855.00+052254.2	2334	53713	581
		2334	53730	600
J033710.91-065059.4	SDSS J033710.91-065059.4	2070	53405	320
		2070	53729	320
J035747.16-063850.7		2071	53741	137
J040714.78-064425.1	LT Eri	465	51910	226
J072827.34+330741.6		9364	57699	535
J072910.68+365838.2	V0654 Aur	431	51877	316
J073208.11+413008.7	SDSS J073208.11+413008.7	2701	54154	411
		3658	55205	726
		5941	56193	722
J073605.07+182709.8		11083	58515	578
J073648.03+200959.7		11085	58462	252
J073817.74+285519.6	SDSS J073817.75+285519.7	754	52232	34
		888	52339	378
J074355.55+183834.8	SDSS J074355.56+183834.8	1582	52939	302
J074431.43+482630.4	ASASSN-16cz	8303	57805	506
J074531.91+453829.3	EQ Lyn	1737	53055	253
		3673	55178	372
J074640.62+173412.8	SDSS J074640.62+173412.8	1920	53314	305
J074716.79+424849.0	SDSS J074716.81+424849.0	434	51885	430
		3674	55182	714
		3669	55481	100
J074813.54+290509.0	V0434 Gem	1059	52592	405
		1059	52618	407
		4452	55536	843
J074917.11+365428.0	MGAB-V3545	3791	55501	752
J075059.97+141150.1	SDSS J075059.97+141150.1	2264	53682	352
J075240.44+362823.2	EU Lyn	543	52017	65
J075331.98+375800.6	CSS 100407:075332+375801	9368	57817	999
J075414.49+313215.7	CSS 110414:075414+313216	10292	58113	555
J075443.00+500729.2	EV Lyn	1869	53327	188
J075507.69+143547.4	SDSS J075507.70+143547.6	2264	53682	416
		4501	55590	555
J075648.04+305805.0	CSS 080406:075648+305805	2959	54537	46
J075653.11+085831.8	SDSS J075653.11+085831.8	2945	54505	144
J075808.81+104345.5	SDSS J075808.81+104345.5	2418	53794	278
J075853.03+161645.1	DW Cnc	2080	53350	594

SDSS name	Other name	Plate	MJD	Fibre
J075939.78+191417.2	SDSS J075939.79+191417.3	1922	53315	172
J080142.36+210345.6	SDSS J080142.37+210345.8	1583	52941	595
		4482	55617	964
J080215.39+401047.1	SDSS J080215.39+401047.2	544	52201	523
J080249.06+363716.4		3801	55509	850
J080303.90+251626.9	SDSS J080303.90+251627.0	1205	52670	188
J080434.13+510349.2	EZ Lyn	1780	53090	431
		3699	55517	734
		3700	55542	450
		4528	55559	442
		4527	55590	728
J080449.49+161624.8	SDSS J080449.49+161624.8	4494	55569	72
J080534.49+072029.1	SDSS J080534.49+072029.1	2076	53442	501
		2056	53463	554
J080625.73+343244.4		9355	57814	273
J080701.10+554739.0	CSS 140311:080701+554739	7280	56709	412
J080710.33+485259.6	SDSS J080710.33+485259.6	7324	56935	828
J080846.19+313105.9	SDSS J080846.19+313106.0	861	52318	352
J080853.71+355053.7	CSS 080416:080854+355053	9355	57814	865
		9359	58056	424
J080908.39+381406.2	SDSS J080908.39+381406.2	758	52253	570
J081017.41+262238.3		11121	58438	277
J081207.63+131824.4	LX Cnc	2268	53682	69
J081256.84+191157.8	NS Cnc	2082	53358	344
J081321.91+452809.3	FH Lyn	439	51877	582
		3686	55268	46
J081352.02+281317.2	SDSS J081352.02+281317.3	1206	52670	380
		4457	55858	686
J081425.38+202125.1	CSS 150222:081425+202126	11109	58523	172
J081520.83+335634.1		3759	55236	382
		3758	55506	798
J081610.83+453010.1	SDSS J081610.84+453010.2	439	51877	624
		3691	55274	898
J082019.39+474731.2	CSS 091213:082019+474732	7378	56715	82
J082051.06+493432.1	EG Lyn	3694	55209	356
		7318	56990	711
J082123.73+454135.4	CSS 090224:082124+454135	7325	56717	468
J082236.05+510524.5	BH Lyn	442	51882	494

SDSS name	Other name	Plate	MJD	Fibre
J082253.12+231300.7	SDSS J082253.12+231300.6	1926	53317	544
J082409.72+493124.4	FL Lyn	443	51873	360
		7309	56991	60
J082457.15+073702.4	SDSS J082457.15+073702.4	1758	53084	213
J082809.87+222004.2		11108	58467	951
J083038.51+404739.0	Gaia19ebs	8294	57365	330
J083404.24+185416.8		2275	53709	174
		9559	57805	714
		9566	58083	162
J083549.86+292636.9	ZTF18aalmdcl	4449	55544	98
		10664	58464	328
J083619.14+212105.3	CC Cnc	1929	53349	1
J083642.74+532838.0	SW UMa	444	51883	619
J083744.34+413338.7		8294	57365	80
J083750.99+383012.4	SDSS J083751.00+383012.5	828	52317	49
J083754.64+564506.7	SDSS J083754.64+564506.7	1783	53386	623
J083845.21+491055.3	SDSS J083845.23+491055.5	445	51873	89
		7311	57038	192
J083931.35+282823.9	SDSS J083931.35+282824.0	1588	52965	294
J084026.16+220446.4	SDSS J084026.16+220446.6	2084	53360	172
		9594	58086	200
		9594	58135	194
		11106	58511	376
J084054.15+045519.1	SDSS J084054.15+045519.2	1187	52708	99
J084127.37+210053.5	CSS 090525:084127+210054	11106	58511	241
J084228.13+462334.4		5163	55889	750
		7320	56722	281
J084303.98+275149.6	EG Cnc	1588	52965	278
J084358.08+425036.6	CSS 080309:084358+425037	6783	56284	186
		8295	57401	702
J084400.10+023919.3	V0495 Hya	564	52224	197
J084617.11+245344.0	SDSS J084617.12+245344.1	1931	53358	487
		9599	58131	552
		11115	58514	764
J085107.38+030834.3	CT Hya	565	52225	359
		3813	55532	745
J085117.04+184249.4	ASASSN-15fq	11090	58487	98
J085127.17+114656.9	EU Cnc	5291	55947	661

SDSS name	Other name	Plate	MJD	Fibre
J085228.72+020102.6	CSS 160419:085229+020103	3813	55532	868
J085300.56+020424.7	CSS 131207:085301+020425	2888	54529	252
J085332.82+484847.7	ZTF18aabjfew	7512	56777	103
J085344.17+574840.6	BZ UMa	483	51902	332
		483	51924	348
		483	51942	352
J085409.42+201338.9	CSS 080506:085409+201339	11096	58485	54
J085414.02+390537.2	FR Lyn	1199	52703	286
J085521.17+111815.3	AK Cnc	2575	54085	318
		5293	55953	322
J085603.78+322109.2	CSS 100508:085604+322109	10238	58155	257
J085623.00+310833.9	SDSS J085623.00+310834.1	1271	52974	88
J085909.18+053654.5	SDSS J085909.18+053654.5	1192	52649	343
J090016.55+430118.1	SDSS J090016.56+430118.2	831	52294	435
J090016.66+343927.6	CSS 110512:090017+343928	5812	56354	714
J090103.93+480911.1	PU UMa	764	52238	589
J090113.51+144704.6	SDSS J090113.51+144704.6	2434	53826	400
J090350.72+330036.1	SDSS J090350.73+330036.1	1272	52989	188
		10238	58155	20
J090403.48+035501.2	SDSS J090403.48+035501.2	566	52238	380
J090452.08+440255.4	FV Lyn	831	52294	410
J090628.25+052656.9	SDSS J090628.25+052656.9	1192	52649	543
		1191	52674	7
J090744.63+463050.4		7516	56782	806
J090947.82+110637.0		5302	55896	668
J090950.53+184947.4	GY Cnc	2285	53687	30
		2285	53700	30
J091001.63+164820.0	SDSS J091001.63+164820.0	2435	53828	75
J091107.84+260617.3		11678	58511	972
J091127.35+084140.7	SDSS J091127.36+084140.7	1301	52976	278
J091216.20+505353.8	DI UMa	5730	56607	518
		7295	57067	42
J091242.18+620940.1	SDSS J091242.18+620940.1	1786	54450	573
J091425.64+540311.0	ZTF19aaqxclz	7275	57093	129
J091650.76+284943.1	HH Cnc	1937	53388	416
J091709.89+314307.6	CSS 110430:091710+314309	1592	52990	207
J091935.65+502825.2	SDSS J091935.66+502825.1	766	52247	517
		7297	57040	518

SDSS name	Other name	Plate	MJD	Fibre
J091945.10+085710.0	LV Cnc	1301	52976	624
J092009.54+004244.8	V0524 Hya	473	51929	98
J092122.84+203857.1	SDSS J092122.84+203857.1	2288	53699	635
		2289	53708	316
		9561	57809	438
J092207.56+310314.3	AR Cnc	11376	58430	628
J092219.55+421256.7	SDSS J092219.55+421256.7	1201	52674	75
J092229.25+330743.6	SDSS J092229.26+330743.6	1592	52990	593
		10242	58161	160
J092444.48+080150.9	HU Leo	1195	52724	403
		2402	54176	409
J092638.71+362402.4	YZ LMi	1274	52995	505
J092809.84+071130.5	SDSS J092809.84+071130.5	2382	54169	502
J092918.90+622346.2	SDSS J092918.90+622346.2	1787	54465	52
J093130.75+335651.2		10244	58225	84
J093214.82+495054.7	QS UMa	901	52641	235
J093220.93+133122.2	SDSS J093220.92+133122.2	2578	54093	620
J093238.21+010902.5	SDSS J093238.21+010902.5	475	51965	66
J093249.56+472522.9	SDSS J093249.57+472523.0	834	52316	431
J093423.39+403808.9	NSV 18230	8299	57346	284
J093537.46+161950.8	SDSS J093537.46+161950.8	2581	54085	332
J093836.98+071455.1	HM Leo	1196	52733	26
J093839.25+534403.8	SDSS J093839.25+534403.8	2404	53764	414
J093946.04+065209.4	SDSS J093946.03+065209.4	1234	52724	304
J094002.56+274942.0	SDSS J094002.56+274942.0	1944	53385	190
J094302.75+275807.5	TCP J09430280+2758080	11347	58440	64
J094325.89+520128.6	SDSS J094325.90+520128.8	768	52281	13
		2384	53763	7
J094431.70+035805.5	VZ Sex	570	52266	512
J094558.25+292253.2	SDSS J094558.24+292252.2	1947	53431	400
		10430	58155	271
		11348	58438	594
J094634.46+135057.8	HY Leo	2582	54139	185
J094636.59+444644.7	DV UMa	1202	52672	30
		3321	54924	404
J094741.69+452415.7		7308	56709	285
J095135.20+602939.6	SDSS J095135.21+602939.6	770	52282	358
J095151.79+471008.7	SDSS J095151.79+471008.7	2956	54525	373

SDSS name	Other name	Plate	MJD	Fibre
J095835.92+281054.7	CSS 140505:095836+281054	11349	58441	227
J100041.43+385303.0		8825	57451	536
J100515.36+191107.8	SDSS J100515.38+191107.9	2372	53768	473
		5882	56029	272
		9571	57808	520
J100516.61+694136.5	SDSS J100516.61+694136.5	1879	54478	608
J100658.40+233724.4	SDSS J100658.40+233724.4	2343	53735	493
J101037.05+024914.9	SDSS J101037.05+024915.0	502	51957	444
J101323.63+455858.9	SDSS J101323.64+455858.9	944	52614	397
		7384	56715	818
J101335.56+393826.3		8826	57452	656
J101421.46+063857.0	SDSS J101421.55+063857.7	4876	55679	652
J101534.65+090441.9	GG Leo	1237	52762	510
		5334	55928	884
J101723.18+375343.4	ZTF19acymwir	8855	57780	604
J101947.26+335753.6	AC LMi	1955	53442	529
J102026.48+530433.1	KS UMa	904	52381	147
		6687	56602	108
J102320.26+440509.8	NSV 4838	1429	52990	359
		8357	58157	532
J102402.70+480851.1	TCP J10240289+4808512	7381	56717	8
J102517.94+430221.2	SDSS J102517.94+430221.2	1358	52994	77
J102637.04+475426.4	V0375 UMa	7386	56769	764
J102800.08+214813.5	MV Leo	2366	53741	72
J102905.21+485515.2	SDSS J102905.24+485515.2	6656	56624	533
J103100.54+202831.9	IL Leo	2375	53770	636
		5873	56035	226
J103147.98+085224.3	SDSS J103147.99+085224.3	1239	52760	621
J103533.01+055158.7	SDSS J103533.03+055158.4	999	52636	55
		4852	55689	323
J104051.24+151133.7	DO Leo	2594	54177	26
J104245.15+371819.8		8851	57460	605
J104356.65+580731.5	IY UMa	949	52427	358
		7088	56657	960
J104521.19+362433.0		8851	57460	307
J105135.09+540435.6	EK UMa	1011	52652	345
		6707	56383	384
		8172	57423	387

SDSS name	Other name	Plate	MJD	Fibre
J105430.43+300610.1	SX LMi	1981	53463	66
		6445	56366	172
J105507.00+365945.2	EL UMa	10269	58220	632
J105550.08+095620.4	CSS 080130:105550+095621	2886	54498	504
J105656.96+494118.3	CY UMa	876	52346	104
		876	52669	103
		6700	56384	434
J105754.25+275947.5	SDSS J105754.25+275947.5	2359	53800	102
		2359	53826	105
J105905.06+272755.4	SDSS J105905.07+272755.5	2359	53800	51
		2359	53826	51
		6446	56363	170
J110014.72+131552.0	SDSS J110014.72+131552.1	1750	53358	15
		5357	55956	768
J110425.64+450313.9	AN UMa	1436	53054	57
		6649	56364	388
J110539.76+250628.6	ST LMi	2212	53789	201
J110706.75+340527.0	SDSS J110706.76+340526.8	2034	53466	215
		10266	58462	751
J111126.82+571238.9	CSS 120422:111127+571239	8177	57374	696
J111544.50+425822.4	AR UMa	1364	53061	115
		4686	56013	580
J111715.90+175741.7	DP Leo	3327	54951	337
J111721.92+520501.0	CSS_J111721.9+520500	8160	57071	671
J112003.39+663632.4	SDSS J112003.40+663632.4	2858	54464	228
		2858	54498	239
		7111	56741	72
J112253.32-111037.5	CSS 100603:112253-111037	2874	54561	603
J113122.39+432238.5	MR UMa	1366	53063	231
J113215.49+624900.4	SDSS J113215.50+624900.4	776	52319	381
J113551.09+532246.1	SDSS J113551.09+532246.2	8163	57049	657
J113722.20+014858.7	RZ Leo	513	51989	70
		4740	55651	188
J113732.34+405458.0	SDSS J113732.32+405458.3	4655	55620	930
J113826.69+061919.4	SDSS J113826.73+061919.5	1620	53137	290
		5377	55957	374
J113826.82+032207.0	QZ Vir	513	51989	562
J113950.57+455817.7	NSV 5285	7398	56781	940

SDSS name	Other name	Plate	MJD	Fibre
J114628.80+675909.6	SDSS J114628.80+675909.7	492	51955	454
J114955.68+284507.2	EU UMa	2222	53799	10
		6406	56330	942
J115030.59+404151.8		8381	57512	292
J115207.00+404947.6	SDSS J115207.00+404947.8	1970	53386	541
		8381	57512	216
J115215.80+491441.7	BC UMa	968	52412	280
		6677	56385	612
J115330.25+315835.9	CSS 080201:115330+315836	4614	55604	44
J115419.05+575751.1	SDSS J115419.06+575750.9	8237	58162	443
J115639.47+630907.7	SDSS J115639.48+630907.7	777	52320	574
J120231.00+450349.0	SDSS J120231.01+450349.1	1369	53089	479
J120615.73+510047.0		2919	54537	415
J120724.69+223529.8	SDSS J120724.69+223529.8	2644	54210	431
J120841.91+355024.8	SDSS J120841.96+355025.2	2103	53467	28
		4613	55591	512
J121015.61+351334.4		10245	58161	799
J121209.31+013627.7	V0379 Vir	518	52282	285
J121607.03+052013.9	SDSS J121607.03+052013.9	844	52378	423
J121913.04+204938.3	SDSS J121913.04+204938.3	2611	54477	376
		5978	56073	185
J122021.17+565456.7	MGAB-V359	8233	57887	28
J122405.58+184102.7	SDSS J122405.58+184102.7	2611	54477	42
J122740.83+513924.9	GP CVn	884	52374	139
		8227	57427	629
J122808.73+454516.3		7425	56777	26
J123255.10+222209.4	SDSS J123255.11+222209.4	2647	54495	200
		5982	56074	964
J123717.98+365535.2		3968	55590	782
J123813.73-033932.9	V0406 Vir	335	52000	85
J123931.98+210806.2	IR Com	2613	54481	523
		5985	56089	232
J124058.02-015919.2	SDSS J124058.03-015919.2	336	51999	358
		2922	54612	406
J124325.92+025547.4	NSV 19466	522	52024	325
		4755	55660	292
J124413.48+593610.2	Gaia16adi	8235	58191	880
J124417.87+300400.8	CSS 080427:124418+300401	2237	53828	560

SDSS name	Other name	Plate	MJD	Fibre
		6478	56341	80
		6481	56363	534
		11397	58522	260
J124426.25+613514.6	V0351 UMa	781	52373	93
		6840	56685	755
J125023.79+665525.5	OV Dra	495	51988	238
		7120	56720	997
		6964	56748	422
J125044.42+154957.3		1770	53171	530
J125510.54+264226.4	MT Com	5972	56334	566
J125609.82+623704.5	ASASSN-16da	6970	56444	107
J125637.10+263643.2	GO Com	2240	53823	92
		5972	56334	606
J125641.29-015851.9	SDSS J125641.29-015852.0	338	51694	382
J125716.08+582501.5		8213	58193	273
		8213	58487	273
J125834.73+640823.0	SDSS J125834.74+640823.1	602	52072	264
J125834.76+663551.5	SDSS J125834.77+663551.6	495	51988	148
J130147.97+434549.4		6621	56366	467
J130514.72+582856.2	SDSS J130514.73+582856.3	958	52410	297
		8200	58174	572
J130527.72+390927.5	ASASSN-17eg	2925	54584	302
		3976	55302	18
		3978	55330	662
		4706	55705	442
J130542.26+180104.0	GP Com	2603	54479	474
J130753.86+535130.5	EV UMa	1039	52707	69
J131223.48+173659.1	2XMMp J131223.4+173659	5424	56033	750
J131908.88+315832.0	ASASSN-14mr	11401	58491	606
J131954.47+591514.8	SDSS J131954.50+591514.5	7117	56685	854
J132104.01+560958.2	V0496 UMa	8204	58146	914
J132411.57+032050.5	PZ Vir	527	52342	323
J132715.28+425932.8	GUVV J132715.2+425932.1	8389	57488	826
J132723.38+652854.2	OZ Dra	496	51973	83
		496	51988	83
J133309.19+143706.9	SDSS J133309.19+143706.9	1775	53847	428
J133540.75+050722.5	SDSS J133540.76+050722.7	853	52374	498
		4759	55649	954

SDSS name	Other name	Plate	MJD	Fibre
J133615.76+380933.4	MGAB-V701	8876	57783	907
J133816.44+371639.8		8877	57782	538
J133940.98+484727.9	V0355 UMa	6744	56399	345
J134323.16+150916.8	HW Boo	1776	53858	576
J134441.83+204408.4	SDSS J134441.83+204408.3	2654	54231	23
J140203.08+461333.8	ASASSN-16fy	8499	57431	407
J140429.36+172359.5	RX J1404.4+1723	2757	54509	112
		5449	56030	938
J140430.98+525811.1		7027	56448	618
J140430.98+552558.5		8428	57837	669
J141118.31+481257.6	SDSS J141118.31+481257.6	1671	53446	10
J142256.31-022108.0	SDSS J142256.31-022108.1	918	52404	301
J142955.86+414516.8	SDSS J142955.86+414516.8	1395	52825	45
J143209.77+191403.4	SDSS J143209.78+191403.5	2774	54534	107
		5899	56038	474
J143317.77+101122.8	SDSS J143317.78+101123.3	1709	53533	153
		5465	55988	138
J143500.22-004606.3	OU Vir	306	51637	4
		306	51690	20
J143544.02+233638.7	SDSS J143544.02+233638.7	2136	53494	541
J144659.95+025330.3	SDSS J144659.95+025330.3	537	52027	454
J145003.12+584501.8	SDSS J145003.12+584501.9	610	52056	349
J145744.75+404340.6	TT Boo	8494	57104	680
J145758.18+514808.1	SDSS J145758.21+514807.9	1328	52786	618
		8396	57837	408
J150137.18+550122.4	SDSS J150137.22+550123.4	792	52353	44
		8408	57874	38
J150240.97+333423.8	NZ Boo	1648	53171	408
J150441.76+084752.6	SDSS J150441.76+084752.6	1717	53883	260
J150551.60+065948.5	SDSS J150551.58+065948.7	4856	55712	812
J150722.15+523040.2	OV Boo	6720	56390	764
J150903.71+465056.6	CSS 130324:150904+465057	8518	58193	870
J151302.29+231508.4	NY Ser	2155	53820	163
J151413.71+454911.8	PP Boo	1050	52721	171
J151415.60+074445.9		1817	53851	534
		4878	55710	747
		5487	55982	180
J151915.85+064529.0	SDSS J151915.86+064529.1	1834	54562	417

SDSS name	Other name	Plate	MJD	Fibre
		4889	55709	572
J152020.40-000948.3		4012	55327	578
		4014	55630	18
J152212.20+080340.9	SDSS J152212.20+080340.9	1721	53857	209
J152238.83+391352.3	CSS_J152238.7+391351	2936	54626	193
J152419.31+220920.2	SDSS J152419.33+220920.0	2161	53878	189
		3955	55678	80
J152603.67+382216.4		10741	58230	645
J152613.96+081802.3	QW Ser	1721	53857	21
J152717.96+543724.9	SDSS J152717.96+543724.9	614	53437	251
J152857.86+034911.7	SDSS J152857.86+034911.7	592	52025	601
J153015.04+094946.3	SDSS J153015.04+094946.3	1722	53852	141
J153023.63+220646.3	CSS 110920:153024+220646	2161	53878	34
		3949	55650	814
J153213.67+370104.8	SDSS J153213.68+370104.9	1401	53144	443
		4977	56047	401
J153412.17+594832.0	DM Dra	8426	58224	773
J153634.42+332851.9	SDSS J153634.42+332851.9	1355	52823	54
J153817.34+512338.0	SDSS J153817.35+512338.0	796	52401	388
		6722	56431	820
		8407	57839	736
J154104.67+360252.8	BM CrB	1402	52872	445
		10740	58223	592
J154453.60+255348.8	SDSS J154453.60+255348.8	1849	53846	74
J154459.80+464835.3	SDSS J154459.80+464835.4	6032	56067	800
J154539.08+142231.4	CT Ser	2517	54567	581
		4890	55741	952
J154544.88+442830.0	CSS 110428:154545+442830	8511	57901	20
J154953.41+173938.9	SDSS J154953.41+173939.0	2170	53875	276
		3926	55327	616
J155037.27+405439.9	SDSS J155037.27+405440.0	1053	52468	14
J155247.18+185629.1	MR Ser	2170	53875	441
J155252.48+320150.9	SDSS J155252.48+320150.9	1580	53145	583
J155331.11+551614.4	MQ Dra	619	52056	437
J155412.33+272152.4	AP CrB	1654	53498	542
		2459	54339	533
		2459	54544	521
J155531.98-001054.9	V0489 Ser	343	51692	198

SDSS name	Other name	Plate	MJD	Fibre
J155538.12+380250.5		10736	58274	986
J155644.23-000950.2	V0493 Ser	344	51693	315
J155654.47+210718.9	QZ Ser	2171	53557	7
J155656.91+352336.6	BT CrB	1417	53141	508
		10739	58255	796
J155720.75+180720.2	SDSS J155720.75+180720.2	2170	53875	588
J160003.70+331113.8	VW CrB	10921	58251	317
J160111.53+091712.6	SDSS J160111.53+091712.6	1728	53228	551
J160232.13+161731.7	CSS 080424:160232+161732	3922	55333	898
J160419.02+161548.5	SDSS J160419.02+161548.5	2200	53875	292
J160450.18+414328.5	SDSS J160450.16+414328.6	1335	52824	531
		6052	56092	790
		6043	56096	132
J160501.35+203056.9	SDSS J160501.35+203056.9	2205	53793	247
J160712.11+392450.6		10732	58253	356
J160745.02+362320.5	CH CrB	1682	53173	582
		10733	58244	448
J160813.59+301952.2		10917	58252	169
J160932.67+055044.6	SDSS J160932.67+055044.6	1823	53886	411
J161007.50+035232.7	V0519 Ser	1823	53886	92
J161012.52+222110.8	SDSS J161012.52+222110.8	1852	53534	153
J161027.61+090738.4	SDSS J161027.61+090738.4	2526	54582	98
J161030.34+445901.7	SDSS J161030.35+445901.7	814	52355	274
		814	52370	274
		814	52443	280
J161033.63-010223.2	V0386 Ser	345	51690	138
J161332.55-000331.0	SDSS J161332.56-000331.0	346	51693	263
J161853.16+303845.5		10918	58254	222
J161909.10+135145.5	SDSS J161909.10+135145.5	2530	53881	327
J161935.76+524631.8	DDE 32	3442	54983	276
		8062	58251	766
J162207.15+192236.6	V0589 Her	2970	54589	466
J162209.63+360418.1	CSS 111019:162210+360419	10731	58247	364
J162212.44+341147.3	CY CrB	1057	52522	203
J162450.82+451806.8	MGAB-V3563	8542	57933	342
J162501.74+390926.3	V0844 Her	1172	52759	212
J162520.29+120308.7	SDSS J162520.29+120308.7	2531	54572	446
J162558.18+364200.6	SDSS J162558.18+364200.6	10731	58247	182

SDSS name	Other name	Plate	MJD	Fibre
J162608.15+332827.7	SDSS J162608.16+332827.8	1058	52520	433
J162718.38+120434.9	SDSS J162718.39+120435.0	2530	53881	68
		4066	55444	592
J162830.89+240259.1	SDSS J162830.89+240259.1	1572	53177	400
J162936.53+263519.5	V1189 Her	1409	52824	339
J163545.72+112458.0	V0849 Her	2533	54585	156
J163605.01+465204.5	SDSS J163605.01+465204.5	627	52144	479
J163620.62+472442.4		8541	58257	726
J163722.21-001957.1	V2690 Oph	348	51671	103
		348	51696	103
J164248.52+134751.4	SDSS J164248.52+134751.4	2210	53535	592
J164624.78+180808.9	CSS 100616:164625+180808	4062	55383	20
J165244.83+333925.3	SDSS J165244.84+333925.4	1175	52791	617
J165359.05+201010.4	V1227 Her	1568	53169	508
J165658.12+212139.3	V1229 Her	1415	52885	95
J165837.70+184727.4	SDSS J165837.70+184727.4	1567	53172	495
J165951.68+192745.6	SDSS J165951.69+192745.6	1567	53172	578
J170053.29+400357.6	V1237 Her	633	52079	574
		8544	58281	405
J170213.25+322954.1	V1239 Her	973	52426	144
		4992	55723	890
		4993	55738	452
		10901	58397	188
J170244.09+223547.9	V1240 Her	1689	53177	342
		1688	53462	232
J170324.08+320953.1	SDSS J170324.09+320953.2	973	52426	97
J170542.53+313240.7	SDSS J170542.54+313240.8	975	52411	400
J171016.94+403127.5		8544	58281	52
J171145.08+301319.9	V1247 Her	977	52410	402
J171222.06+321856.2	CSS_J171222.0+321856	10904	58402	256
J171247.70+604603.2	SDSS J171247.71+604603.3	351	51695	17
		351	51780	3
J172325.99+330414.1	ASASSN-14gz	4999	55721	420
J172601.95+543230.7	SDSS J172601.96+543230.8	357	51813	51
		367	51997	53
J173008.39+624754.6	SDSS J173008.38+624754.7	352	51694	26
		352	51789	33
J173102.22+342633.2	ASASSN-15cm	2262	54623	418

SDSS name	Other name	Plate	MJD	Fibre
J183131.63+420220.2		2798	54397	340
J204448.91-045928.8	V0485 Aqr	635	52145	387
		1916	53269	424
J204720.76+000007.6	SDSS J204720.76+000007.7	982	52466	477
J204817.84-061044.8	SDSS J204817.85-061044.8	635	52145	127
J204827.90+005008.9	SDSS J204827.91+005008.9	1909	53261	601
J205017.83-053626.8	PW Aqr	636	52176	331
J205914.87-061220.4	QT Aqr	636	52176	599
J210014.11+004445.9	QU Aqr	984	52442	533
J210131.26+105251.5	SDSS J210131.26+105251.5	727	52207	324
J210449.94+010545.8	QV Aqr	1918	53240	347
J210842.62+084429.9	MGAB-V3716	11317	58398	719
J211605.42+113407.4	VV Equ	729	52468	363
J211652.28+014144.3		9161	57691	615
J211936.95+033211.8	CSS 150520:211937+033212	4077	55361	197
J212406.75+010029.8		5143	55828	471
J213040.11-001319.1		9141	57663	946
J213122.40-003937.0	QZ Aqr	9141	57663	28
J213503.93-004129.6	ASASSN-16ep	9142	57664	591
J214140.43+050729.9	SDSS J214140.43+050730.0	4087	55449	144
J214354.60+124457.9	SDSS J214354.60+124458.0	732	52221	589
J215411.12-090121.6	DM Cap	716	52203	299
J220553.97+115553.6	SDSS J220553.98+115553.7	734	52224	30
J220818.52+135330.0		5062	55803	32
J220935.78-001332.5		4200	55499	436
J221009.93+185418.1	CSS 111227:221010+185418	7574	56945	316
J221159.03+302835.1	ASASSN-13am	7708	57664	940
J221333.38+245059.3		7643	57302	812
J221519.79-003257.1	V0344 Aqr	4200	55499	122
J221814.05-005848.8	SDSS J221814.06-005849.2	4201	55443	362
J221832.76+192520.2	Swift J2218.5+1925	7578	56956	264
J221900.24+201831.1		7578	56956	773
J222144.78+184008.2	V0521 Peg	7578	56956	83
J222334.17+074518.8	1RXS J222335.6+074515	5057	56209	470
J222724.50+284403.5	CSS 090531:222724+284404	7650	57575	866
J223212.79+260725.1		7654	57330	730
J223233.67+185037.0	CSS 100520:223234+185036	7577	56944	991
J223252.34+140352.9	SDSS J223252.35+140353.0	738	52521	509

SDSS name	Other name	Plate	MJD	Fibre
J223352.56+225913.4		7586	57186	73
J223439.92+004127.2	SDSS J223439.93+004127.2	376	52143	631
		674	52201	427
J223606.51+291559.9		6586	56485	20
		11633	58463	372
J223623.52+323913.1		11634	58484	597
J223843.83+010820.6	V0349 Aqr	377	52145	540
		674	52201	524
J223909.83+250331.1	CSS 100521:223910+250331	7653	57306	834
J224303.82+221456.0	SDSS J224303.82+221456.0	2252	53565	239
		2252	53613	214
		6307	56205	298
J224736.37+250436.3	CSS 120616:224736+250436	6290	56238	770
J225417.52+074227.1	PQ J225417.5+074227	5060	56181	182
J225613.53+191132.9		5027	56218	886
J225831.18-094931.6	SDSS J225831.18-094931.7	725	52258	306
J225926.51+223902.4		7613	56988	68
J230319.85+274736.0		7706	57575	890
J230351.64+010651.0	HY Psc	380	51792	575
J230425.88+062545.6	KX Psc	11302	58436	544
J230641.47+244055.8	ZTF J230641.45+244055.7	7705	57332	321
J230813.57+254341.0	CSS 130916:230814+254341	7705	57332	816
J230949.12+213516.7	V0405 Peg	2623	54096	199
		2623	54328	193
J231110.88+013002.7	USNO-B1.0 0915-0569037	4288	55501	138
J231552.35+271037.3	CSS 100610:231552+271037	7704	57572	58
J231643.23+011640.2	Karachurin 15	9174	58070	114
J231909.18+331539.6	CSS 111021:231909+331540	7765	58047	703
J231930.43+261518.6	Swift J2319.4+2619	7703	57333	818
J232113.45+251822.3		7669	57329	584
J232553.47+011527.3		9175	58049	76
J232619.40+282649.7	CSS 080930:232619+282650	7702	58017	961
J232727.14+085538.6	V0681 Peg	11293	58462	310
J233003.03+303300.4	CSS 111101:233003+303301	7767	58049	935
J233325.92+152222.1	V0598 Peg	746	52238	614
J233705.01+314149.4		7761	58071	752
J234226.21+324819.8	ASASSN-15nv	7760	58080	770
J234401.83+002116.6	MLS 120926:234402+002117	9158	57664	589

SDSS name	Other name	Plate	MJD	Fibre
J234440.53-001205.8	MLS 100904:234441-001206	4213	55449	38
J234502.47+342923.9	1RXS J234500.2+342913	7759	58401	371
J234814.69+181219.6	CSS 110115:234815+181220	7599	56955	296
J234843.14+250249.9	MASTER OT J234843.23+250250.4	7667	57580	158
J235131.68+270907.7		7697	57574	820
J235603.71+001833.3		7848	56959	739
		9159	57666	787
		9179	57682	284

Appendix C

Supplementary Material - Chapter 6

C.1 Spectra and light curves of previously known CVs

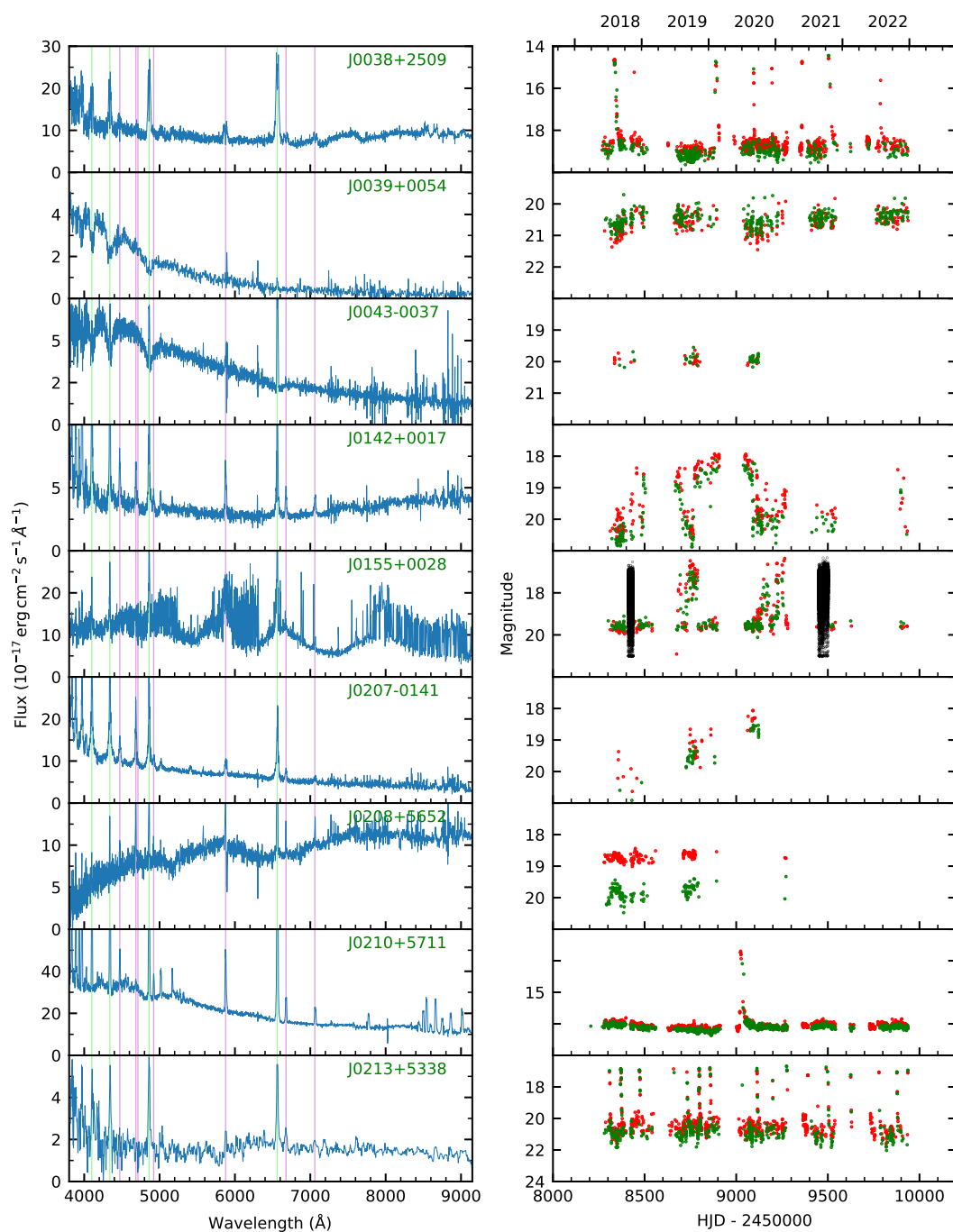


Figure C.1: Left panels: Spectra of the CVs previously known by SDSS-V. Right panels: ZTF light curves of the previously known CVs (r - and g -band). TESS light curves are shown in black.

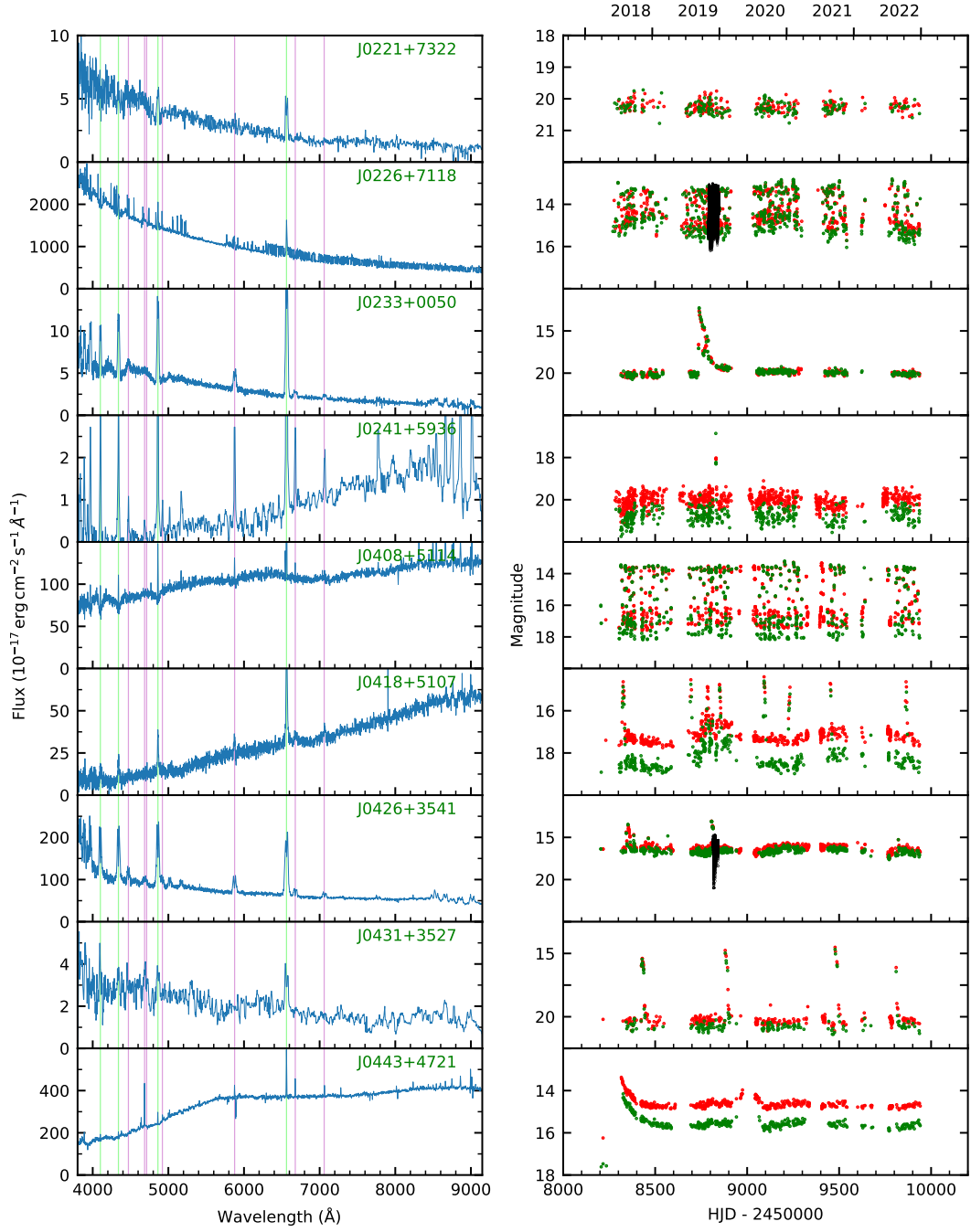


Figure C.2: Left panels: Spectra of the CVs previously known by SDSS-V. Right panels: ZTF light curves of the previously known CVs (r - and g -band). TESS light curves are shown in black.

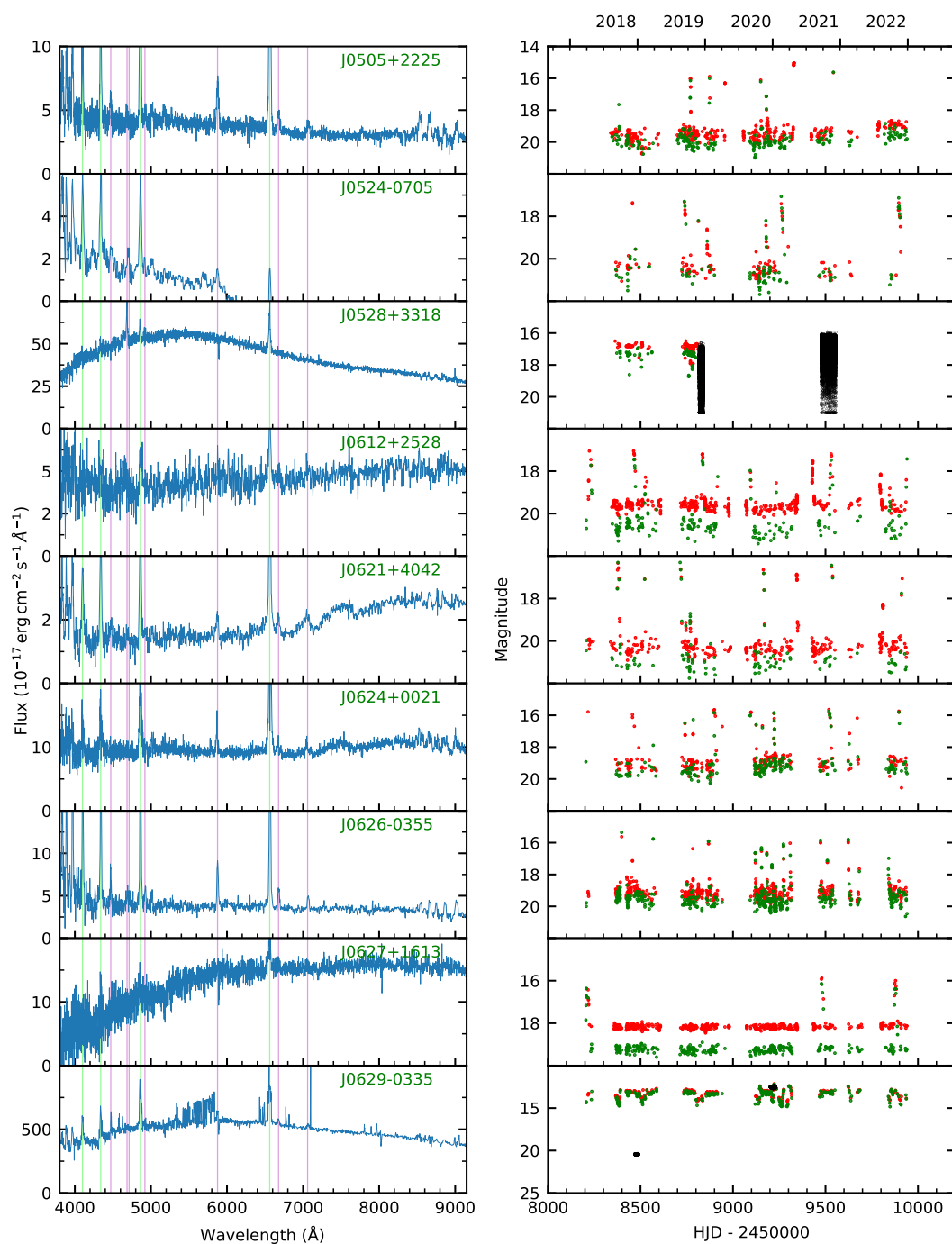


Figure C.3: Left panels: Spectra of the CVs previously known by SDSS-V. Right panels: ZTF light curves of the previously known CVs (r - and g -band). TESS light curves are shown in black.

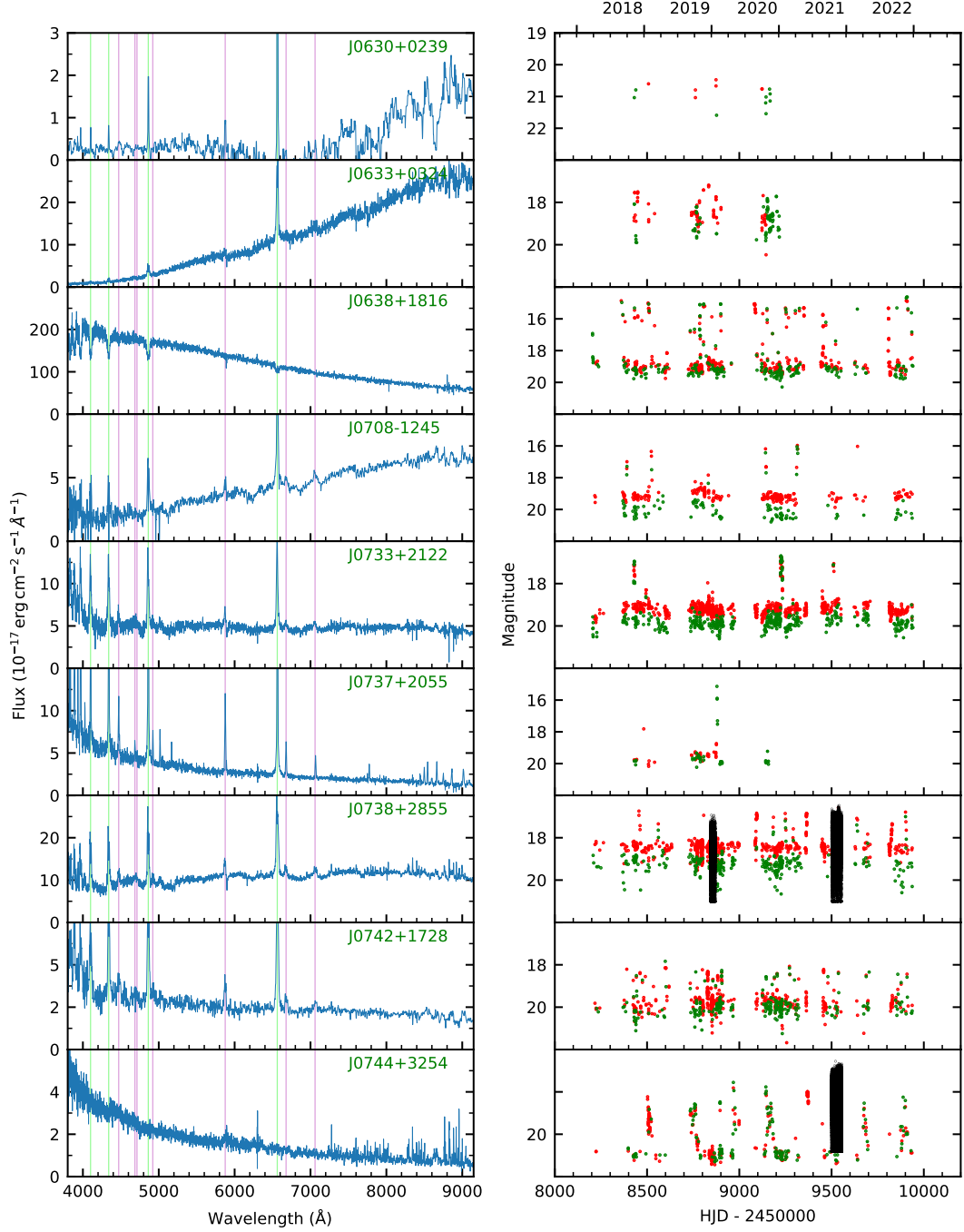


Figure C.4: Left panels: Spectra of the CVs previously known by SDSS-V. Right panels: ZTF light curves of the previously known CVs (r - and g -band). TESS light curves are shown in black.

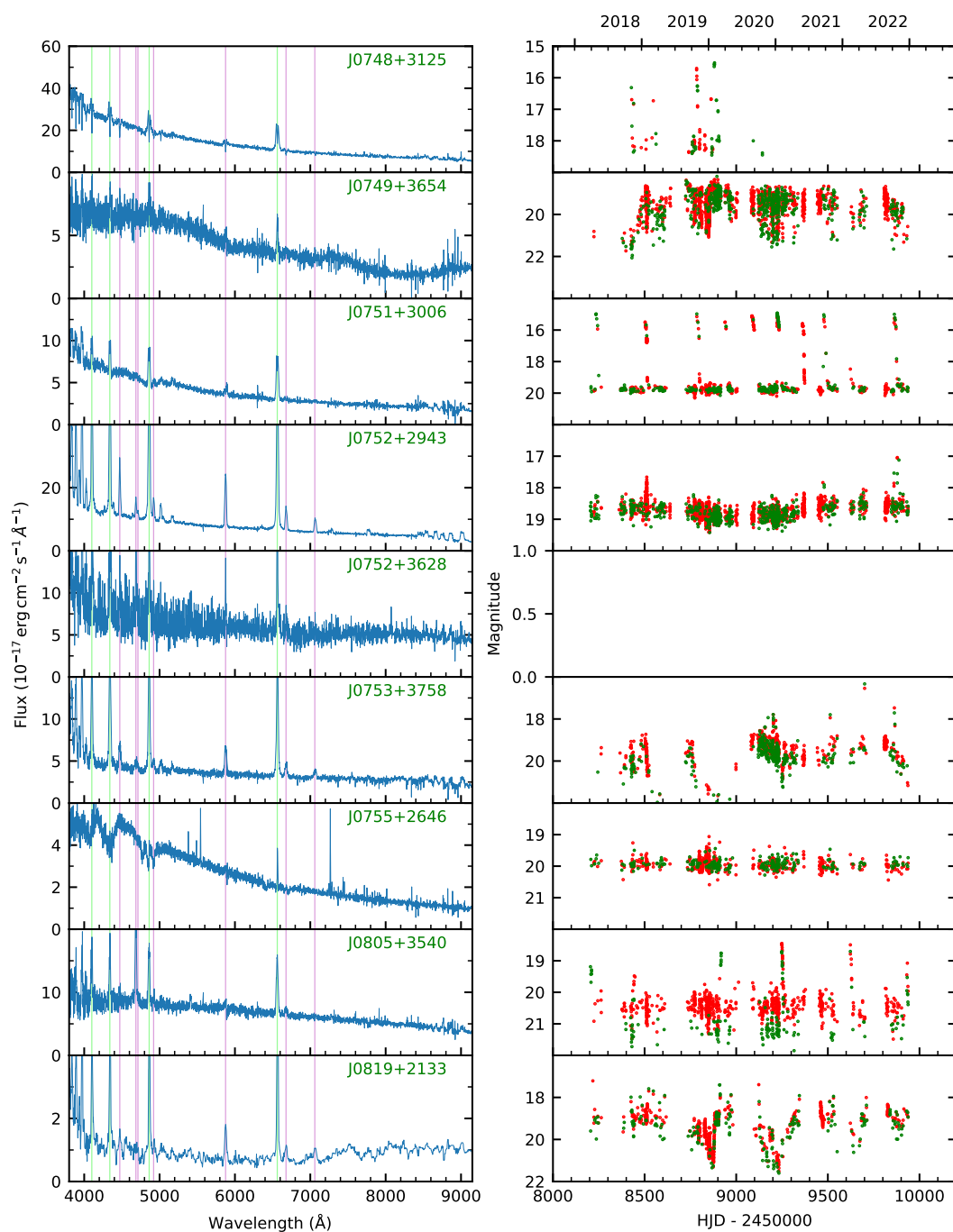


Figure C.5: Left panels: Spectra of the CVs previously known by SDSS-V. Right panels: ZTF light curves of the previously known CVs (r - and g -band). TESS light curves are shown in black.

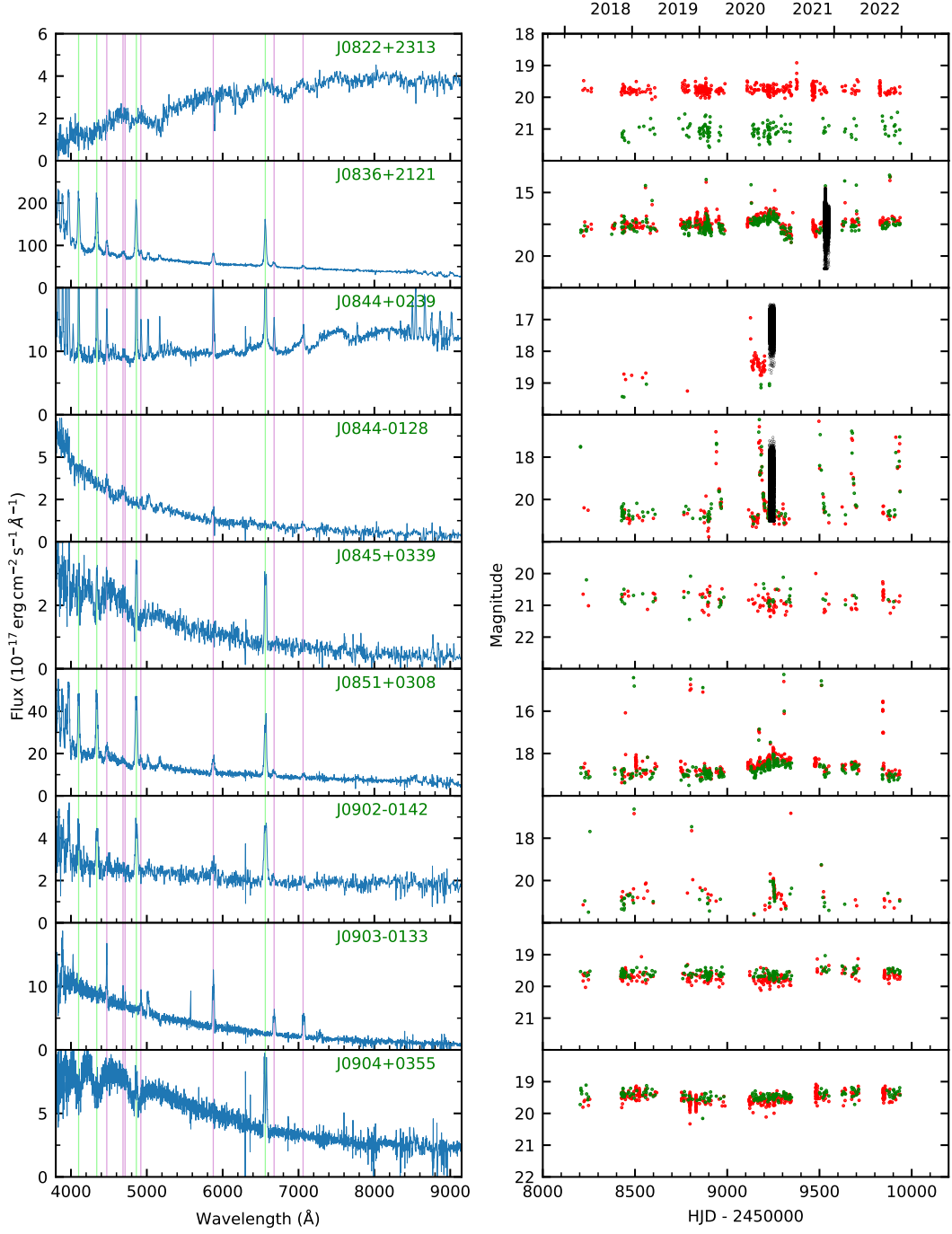


Figure C.6: Left panels: Spectra of the CVs previously known by SDSS-V. Right panels: ZTF light curves of the previously known CVs (r - and g -band). TESS light curves are shown in black.

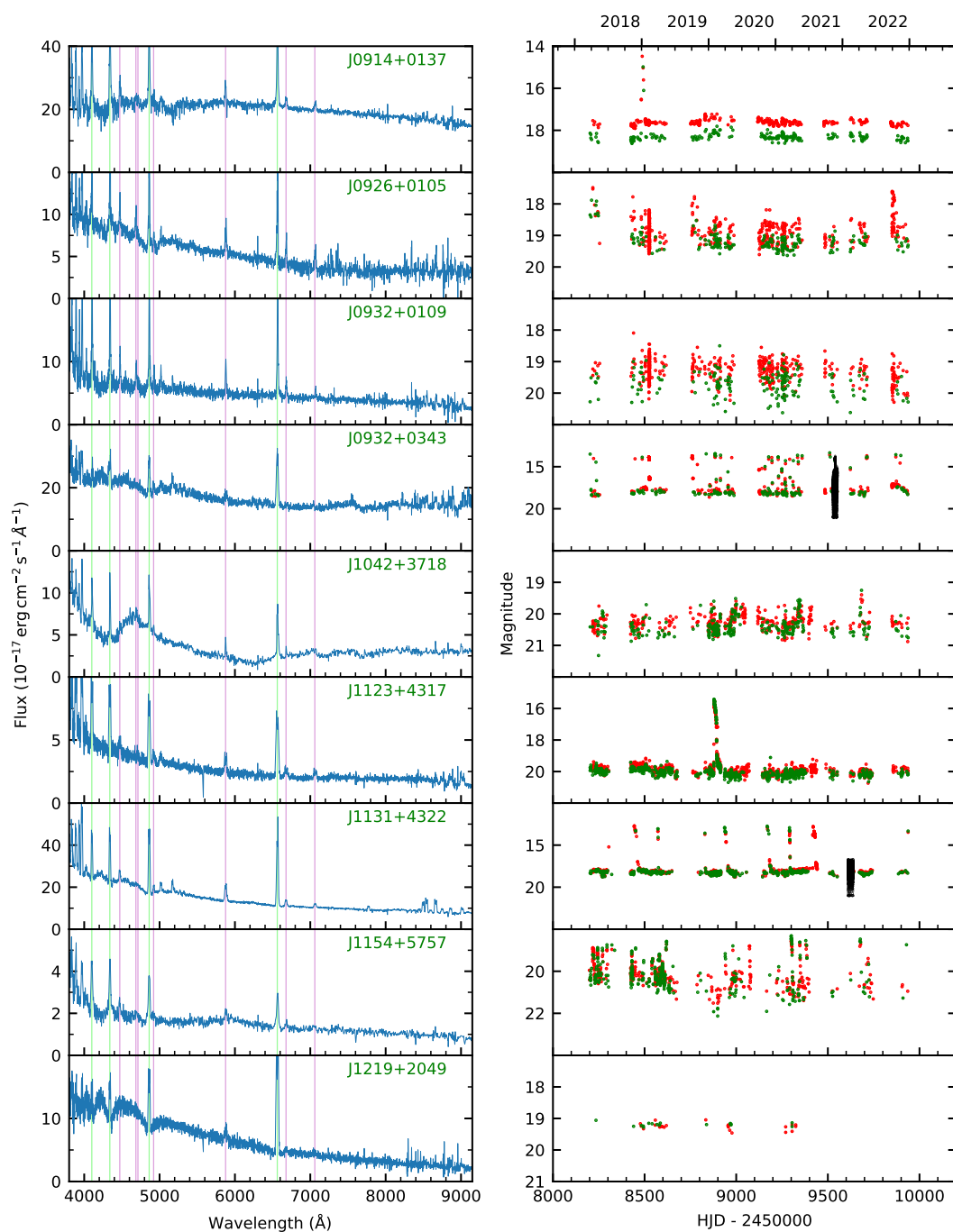


Figure C.7: Left panels: Spectra of the CVs previously known by SDSS-V. Right panels: ZTF light curves of the previously known CVs (r - and g -band). TESS light curves are shown in black.

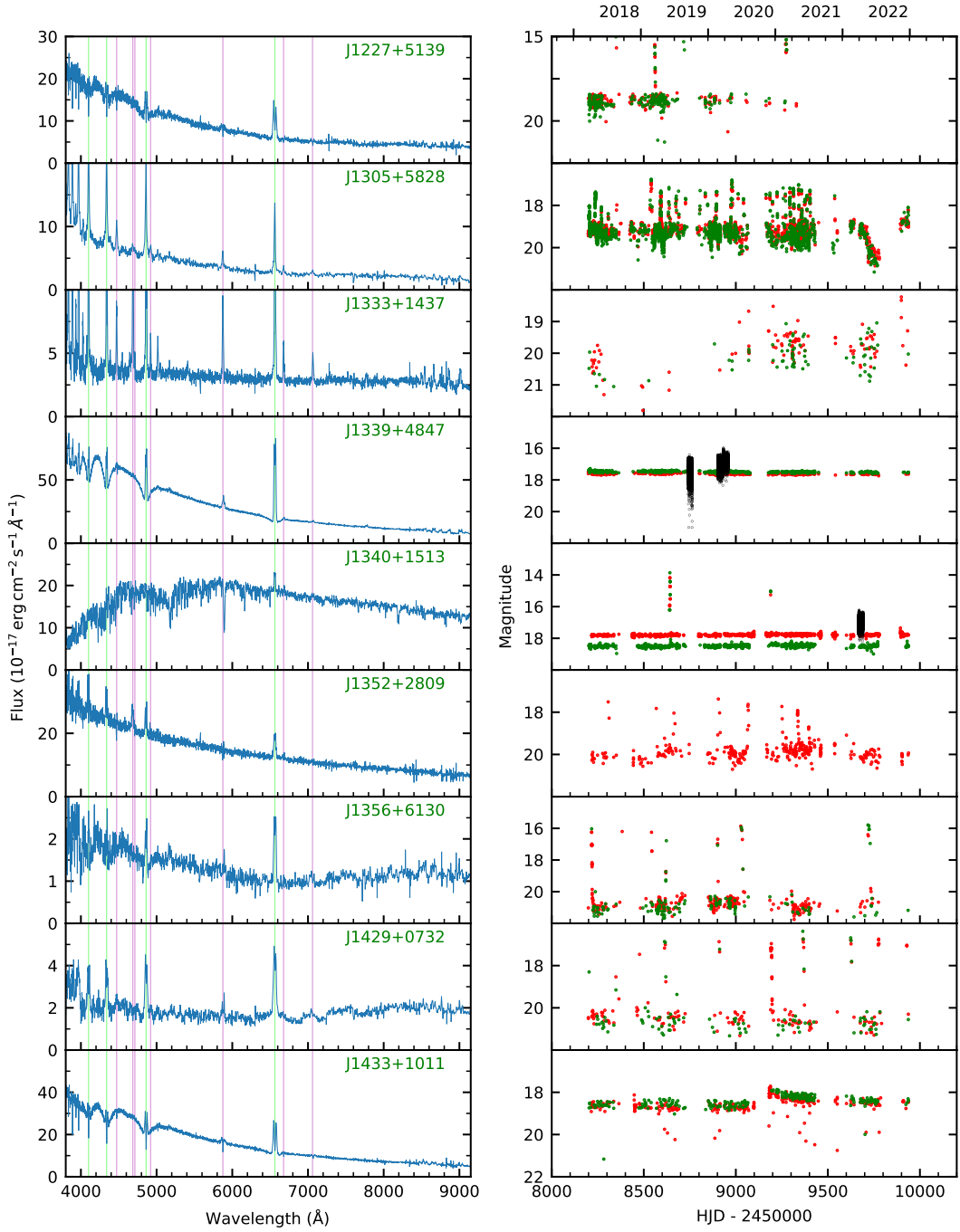


Figure C.8: Left panels: Spectra of the CVs previously known by SDSS-V. Right panels: ZTF light curves of the previously known CVs (r - and g -band). TESS light curves are shown in black.

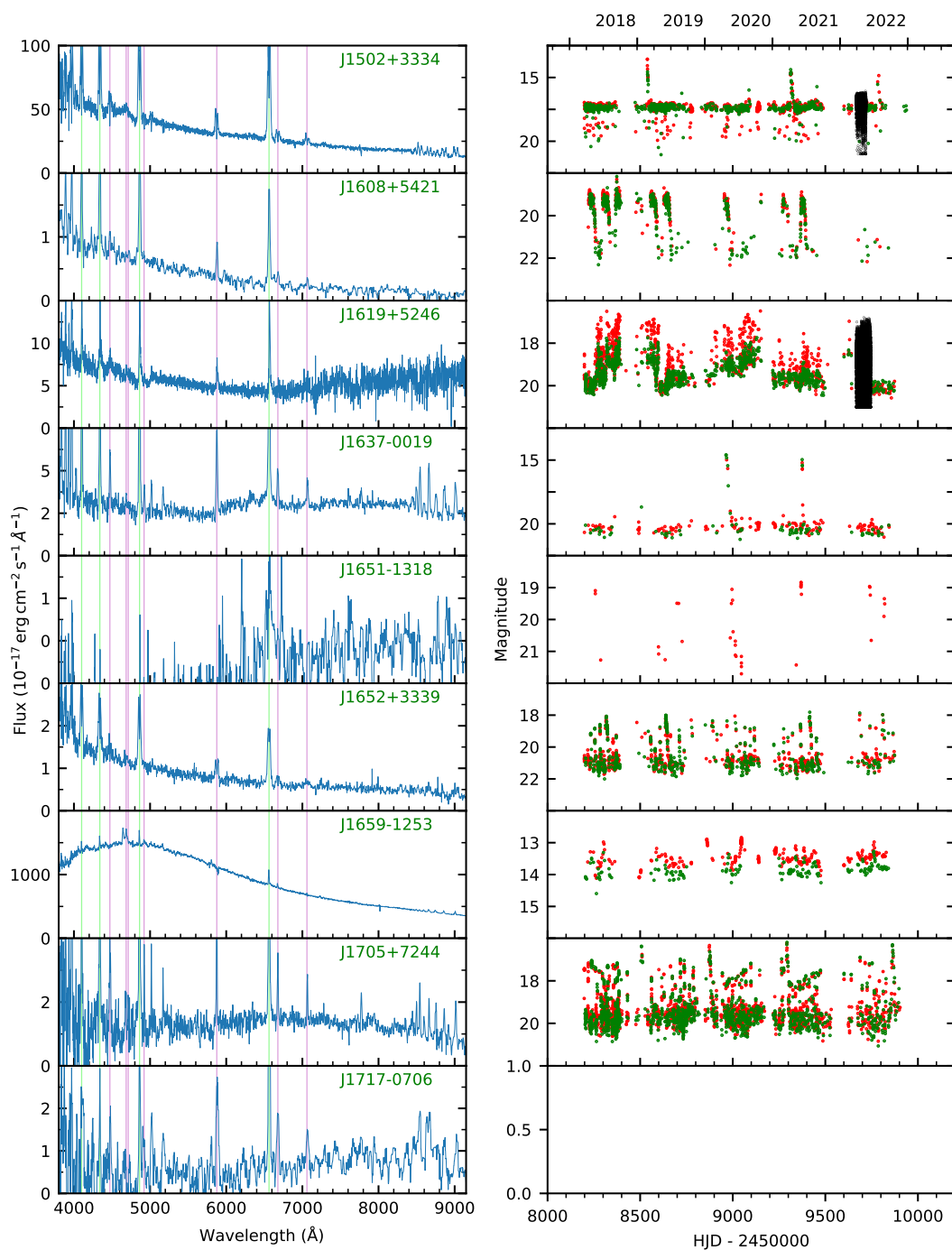


Figure C.9: Left panels: Spectra of the CVs previously known by SDSS-V. Right panels: ZTF light curves of the previously known CVs (r - and g -band). TESS light curves are shown in black.

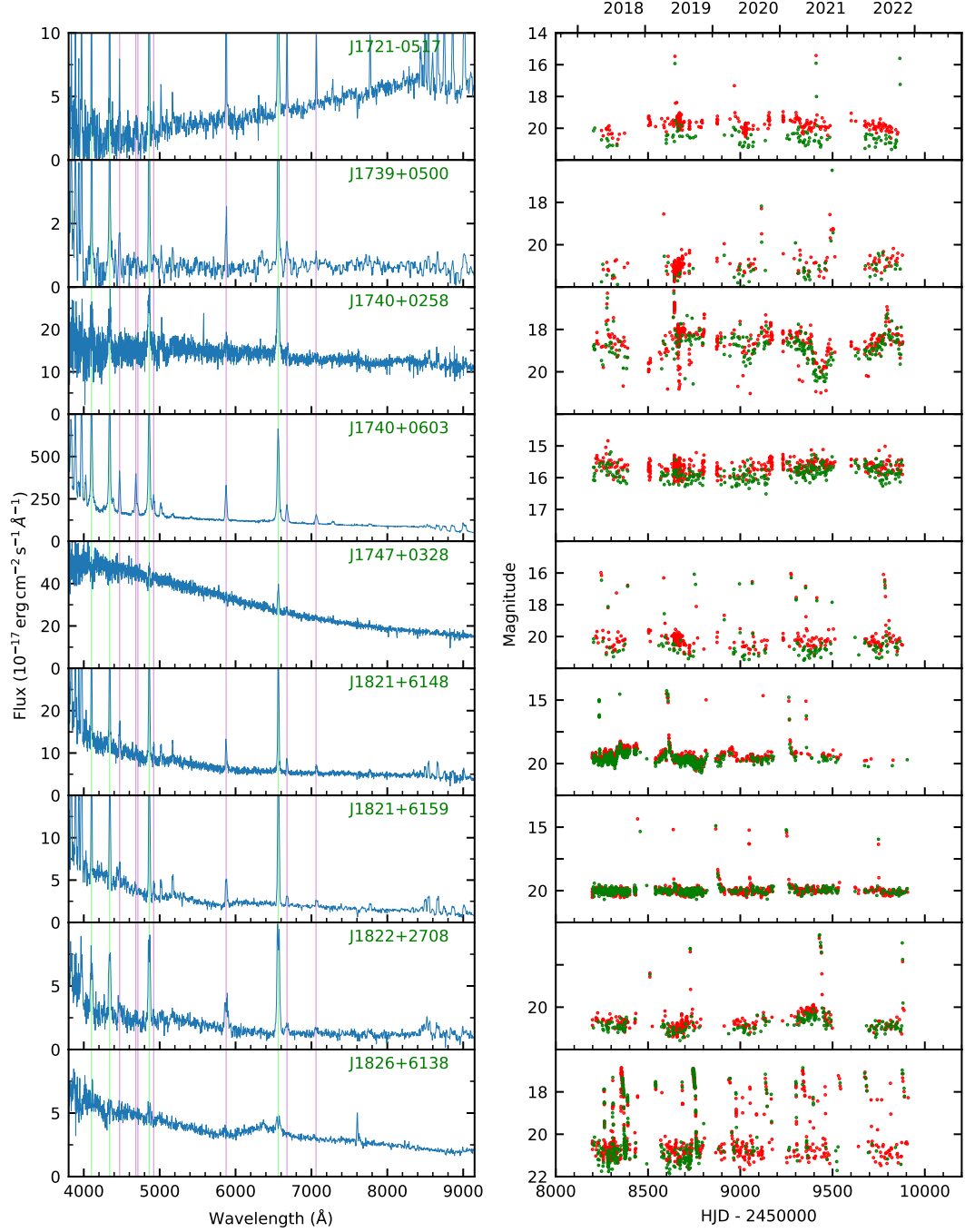


Figure C.10: Left panels: Spectra of the CVs previously known by SDSS-V. Right panels: ZTF light curves of the previously known CVs (r - and g -band). TESS light curves are shown in black.

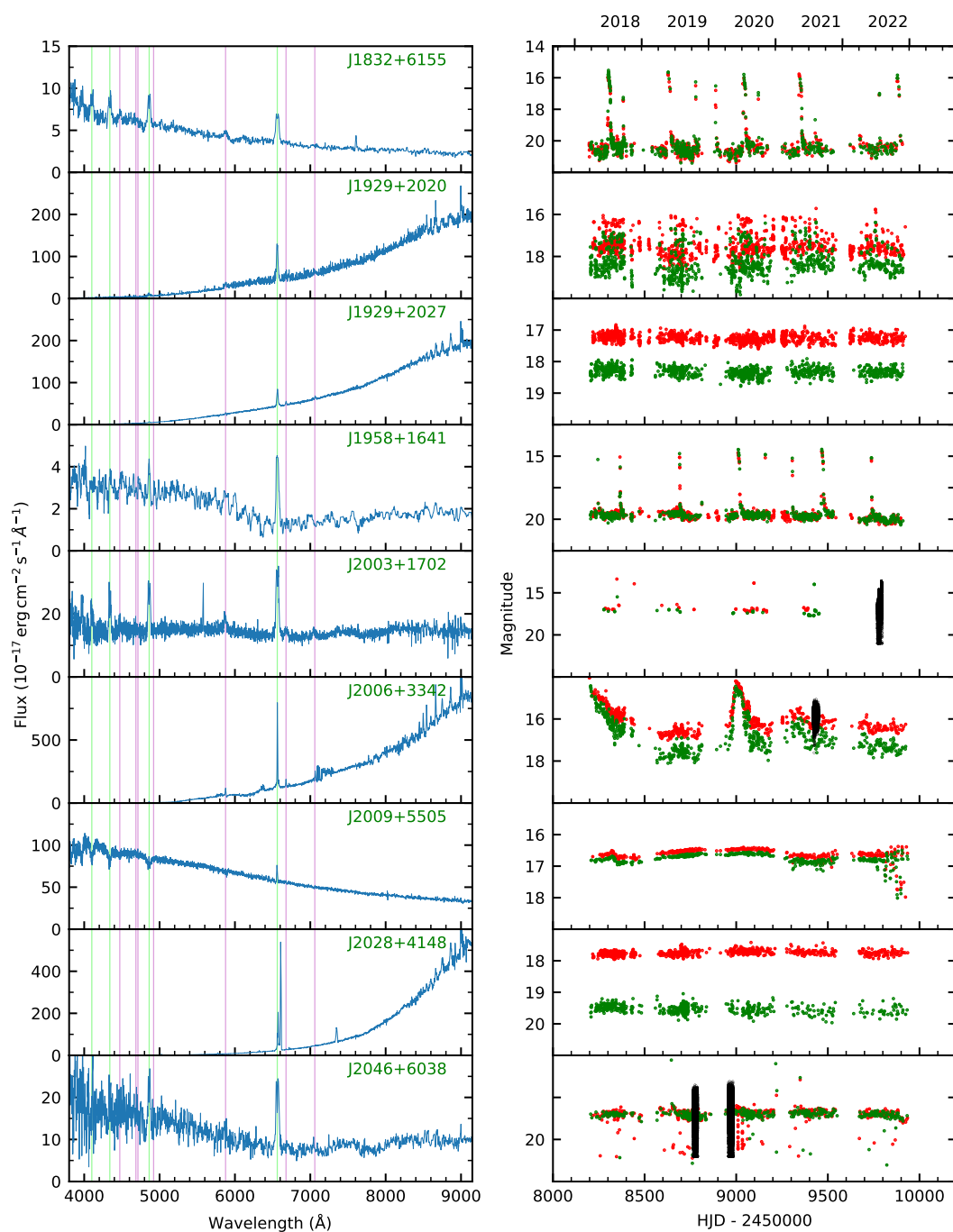


Figure C.11: Left panels: Spectra of the CVs previously known by SDSS-V. Right panels: ZTF light curves of the previously known CVs (r - and g -band). TESS light curves are shown in black.

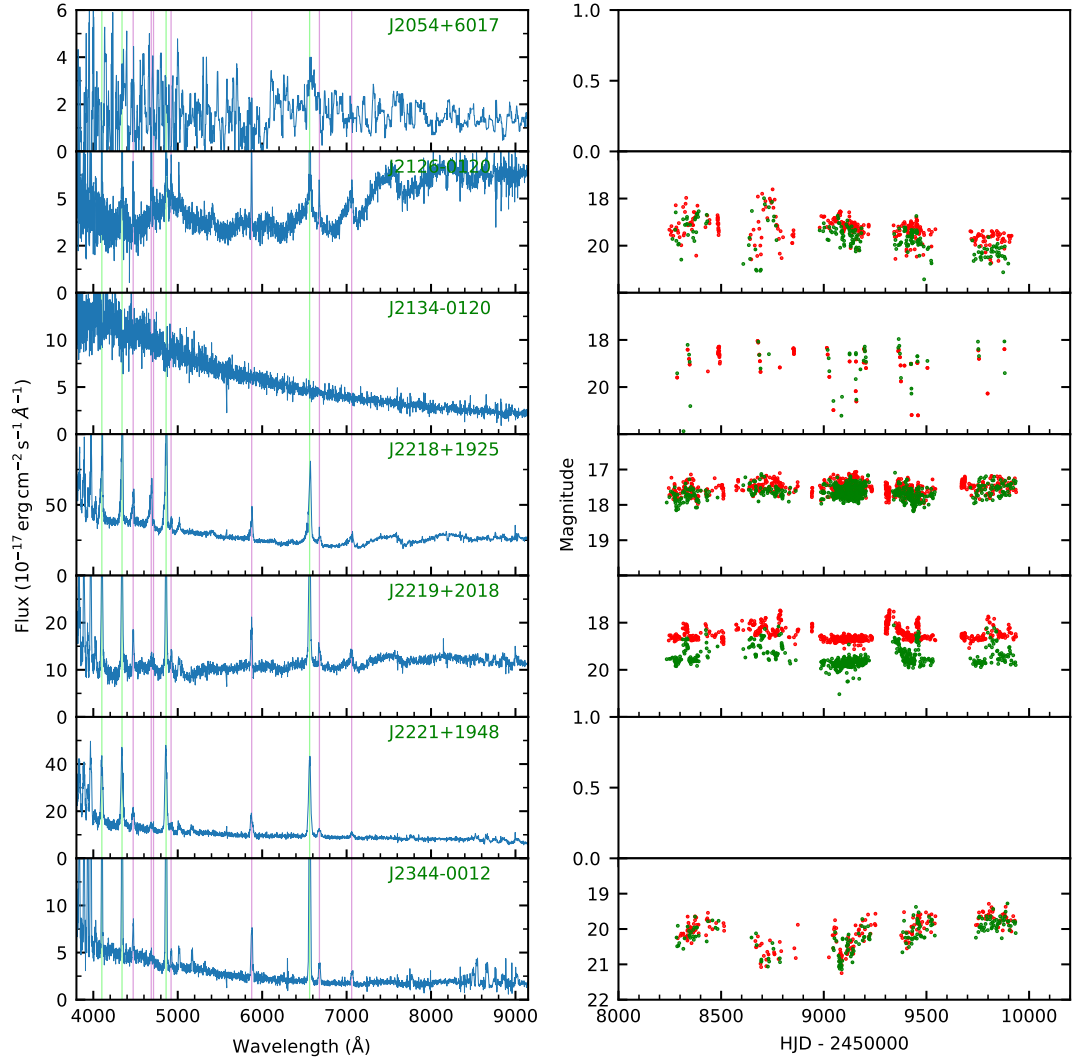


Figure C.12: Left panels: Spectra of the CVs previously known by SDSS-V. Right panels: ZTF light curves of the previously known CVs (r - and g -band). TESS light curves are shown in black.

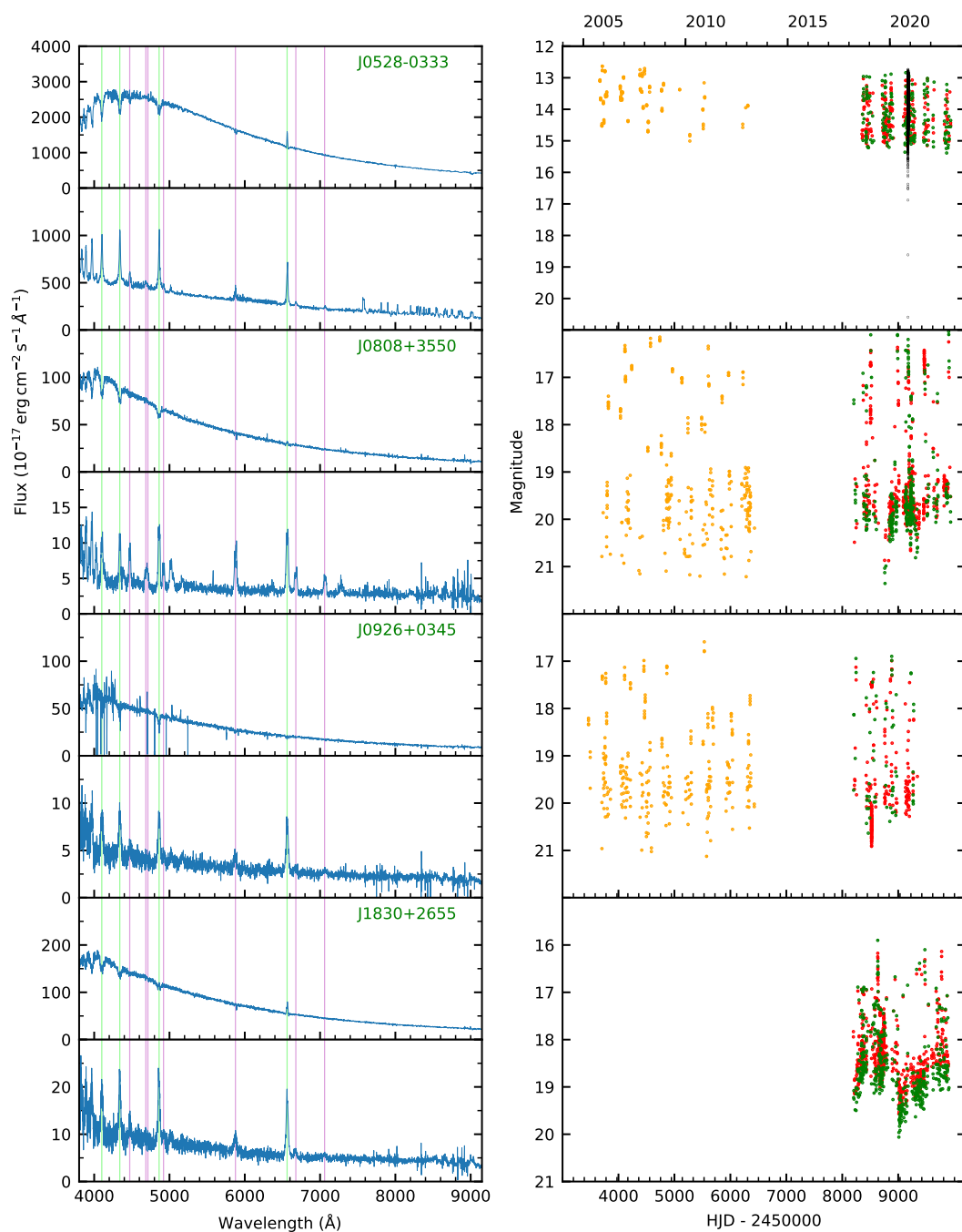


Figure C.13: CV spectra in outburst (upper) and quiescence (lower). Left panels: Spectra of the CVs previously known by SDSS-V. Right panels: ZTF light curves of the previously known CVs (*r*- and *g*-band). TESS light curves are shown in black, CRTS in yellow.